BULGARIAN CHEMICAL COMMUNICATIONS

Preface

Dear reader,

This special issue of the "Bulgarian Chemical Communication" journal is dedicated to the 70th anniversary of Prof. Tsonko Kolev, a prominent Bulgarian scientist working for decades in the field of physical organic chemistry. His scientific achievements and contributions in the fields of spectroscopy, single crystal X-ray diffraction and quantum chemical calculations of new organic materials are profound and were published in 225 research papers. In addition 2 books, 4 chapter of books and an invited review were also produced. All of the published works are cited more than 2800 times.

After approval, the submitted original research papers in this issue are published on-line and as hard copies in the year 2018. The acceptance of the papers was based on the Journal's normal reviewing procedure and the order sequence followed the time of submitted corrected proofs. The final contents of this issue comprise 34 research papers submitted by more than 150 scientists from Bulgarian universities and institutes and from abroad (Germany, USA, France, Turkey).

The published papers cover a very wide range of scientific fields – organic and inorganic materials, new crystalline phases, products for medicine and pharmacy, structure and properties of minerals, ceramic and composite preparations. The investigations are based on a huge complex of modern scientific instrumentation and approaches. The papers in the present issue outline the latest developments in the research of the Bulgarian scientists.

We hope that the interdisciplinary character of this special issue will inspire the scientific audience and attract young researchers.

Special acknowledgements are due to all the authors contributing good scientific essence as well as to all the reviewers making serious efforts to make this issue a success.

Guest editors
Prof. Dr. Ognyan Petrov
and Assoc. Prof. Dr. Yana Tzvetanova
Institute of Mineralogy and Crystallography
Bulgarian Academy of Sciences

Scientific biography of Professor DSc Tsonko Mitev Kolev

Tsonko Mitev Kolev was born on 10 January 1948 in Gradnitsa, district Gabrovo. In 1973 he completed his Master's degree in Organic synthesis and Chemistry of natural pharmaceutical drugs at the Faculty of Chemistry, Sofia University.

In 1975 Tsonko Kolev began to work as Junior scientist in the Laboratory for Structural Organic Chemistry at the Institute of Organic Chemistry, Bulgarian Academy of Sciences under scientific supervision of Prof. Ivan Juchnovski in the field of electronic structure of conjugated organic compounds and the genetically related negative ions, which are intermediates in important organic reactions, by means of the combined application of infrared spectroscopy, quantum chemical methods, the correlation analysis and isotope labelled compounds. They work on the transmission of polar effects of substituents through the systems of conjugated bonds on the characteristic frequencies and intensities, and particularly the exponential decrease of the polar effect of the substituents with the increase of the number of the double bonds in the polyene system. Tsonko Kolev defended his PhD thesis devoted to IR spectral investigation of anion radicals of aromatic ketones in 1982. The infrared spectra of anion-radicals of aromatic ketones (ketyls) were interpreted correctly for the first time by means of isotopic labelled compounds, which led to the correction of a number of errors in band assignment and some corresponding findings concerning the influence of the structure over infrared spectra of these anion-radicals. It was shown that infrared spectroscopy could give information about the form of the orbital of the unpaired electron, as well as about the presence of separate weak interactions between molecular fragments due to the peculiar symmetry of this orbital.

In 1987 Tsonko Kolev has been awarded the Alexander von Humboldt Research Fellowship for Postdoctoral Researchers. He joined the research group of Prof. Dr. Paul Bleckmann at the Faculty of Chemistry, Structural Chemistry Department, University of Dortmund (1987–1988 and 1991–1992).

Tsonko Kolev acquired the academic rank Associate Professor at the Institute of Organic Chemistry, Bulgarian Academy of Sciences in 1992. He organized a working group handling with organic materials for nonlinear optics. In 2001 he defended his Doctor of Sciences degree – dissertation titled "Vibrational and structural analyses of some aromatic, aryl aliphatic ketones, diketones and their derivatives – potential materials for nonlinear optics".

He became Full Professor in Organic Chemistry in 2005.

In the period 2005–2013 Prof. Kolev was Head of the Department of Organic Chemistry at Plovdiv University and Member of the Faculty Council.

Scientific research field

Tsonko Kolev's scientific research fields cover: design, synthesis, spectral and structural elucidation of novel organic materials with large nonlinearoptical (NLO) and electrooptical (EO) coefficients and good photochemical resistance against laser beam.

The following methods were used: spectral ones (IR, Raman, UV-vis and Fluorescent spectroscopy), single crystal X-ray analysis and quantum chemical calculations of hydrogensquarates, squarates and esteramides of squaric acid with amino acids and aminoacid amides.

Another important field of investigation is the synthesis, spectral and structural elucidation of pyridinio betaines of squaric acid. Quantum chemical calculations were performed to obtain electronic structure and vibrational data, using DFT and *ab initio* methods.

In the last years the efforts of Prof. Kolev are directed to the synthesis, spectral and structural elucidation of new stilbazolium salt with enlarged π-conjugated system and their functional thin films deposited by pulsed laser deposition (PLD) using UV TEA N_2 laser onto glass substrates and KCl, NaCl single crystals.

Last but not least, Prof. Kolev works on the complete elucidation of new dicyanoisophorone deriva-

tives – nonlinear optical and electrooptical materials with possibility to tune their mechanical and electrical properties.

Lecturer activities

In the period 2004–2013 Prof. Kolev worked at the Faculty of Chemistry at the University of Plovdiv giving lectures on Organic Chemistry for the Bachelor students. He also gave lectures on Medicinal chemistry, Organic Chemistry, Organic Synthesis and X-ray analysis for the Master degree.

Between 2006 and 2010 he gave lectures at Sofia University on Modern methods of Organic Structural Analysis, Infrared and Raman Spectroscopy and New NLO materials (Master degree).

Since 2014 Prof. Kolev is lecturer at the South West University in Blagoevgrad, course Instrumental methods in Organic Chemistry for the Master students.

Scientific Supervisor

Since 2000 Prof. Kolev is Scientific Supervisor of 9 PhD students: Zornitza Glavcheva, Denitsa Yancheva, Mariana Topuzova, Rumyana Bakalska, Plamen Angelov, Emilia Cherneva, Tsanko Tsanev, Mina Todorova and Daniela Petrova.

Scientific projects

Manager and lecturer at the International Summer School on Applied Spectroscopy and X-Ray Analysis for young scientists and PhD students from Bulgaria, Poland, Czech Republic, Serbia, Macedonia, Slovenia, Croatia, Albania, Turkey, Hungary and Romania held every summer between 2004 and 2009 in the Institute of Organic Chemistry, Bulgarian Academy of Sciences supported by Deutscher Akademischer Austauschdienst (DAAD).

Scientific projects BUL 001 96 (1996–1998) and BUL 006 99 (1999–2001) between the Institute of Organic Chemistry, Bulgarian Academy of Sciences, and Bundesministerium für Bildung und Forschung.

Scientific projects between the Institute of Organic Chemistry, Bulgarian Academy of Sciences,

and Deutscher Akademischer Austauschdienst (DAAD) 2002–2004 and 2005–2007.

"Sandwich program" with PhD student Zornitza Glavcheva at the University of Dortmund, supported by Alexander von Humboldt Stiftung (2001).

Award "Institutspartnerschaft" (2003–2004) with Prof. Rüdiger Wortmann (Technical University Kaiserslautern) and Prof. Kolev (Institute of Organic Chemistry, Bulgarian Academy of Sciences) supported by Alexander von Humboldt Stiftung. As a result of this project series of nonlinear optical chromophores containing a cyclobutenedione fragment as electron-acceptor group have been synthesized and investigated and their linear and nonlinear optical properties were proven by electro-optical absorption measurements in solution. The negative values of the static hyperpolarizabilities of the NLO-phores studied, associated with dipolar ground-state structures, increase significantly on going from donor to acceptor substituent.

Prof. Kolev was Invited Professor at the University of Dortmund (1994).

For the "Sandwich" program at the University of Dortmund supported by Deutscher Akademischer Austauschdienst (DAAD) Prof. Kolev chose PhD student Tsanko Tsanev (2008).

In the period 2009–2010 Prof. Kolev was co-principal investigator of a German-Bulgarian Research Project supported by the German Research Society (DFG) grant SP 255/21-1 dedicated to NLO and EO properties of organic materials at Technical University of Dortmund, Germany.

Scientific contributions

The basic and most essential scientific contributions of Prof. Kolev, consist in both experimental and theoretical studies on the field of design, synthesis, spectral and structural elucidation of novel organic materials with large nonlinearoptical (NLO) and electrooptical (EO) coefficients and good photochemical resistance against laser beam. The spectral (IR, Raman, UV-vis and Fluorescent spectroscopy) and single crystal X-ray analysis and quantum chemical calculations of hydrogensquarates, squarates and esteramides of squaric acid with amino acids and amino acid amides. As a results 8 new structural motifs of hydrogensquarates are established: Ib, IIb, IIIb, 4b, 4c, VIII, IXa, IXb.

The synthesis, spectral and structural elucidation of series pyridinio betaines of squaric acid are performed. Quantum chemical calculations are made to obtain electronic structure and vibrational data, using DFT and *ab initio* methods. In the last years the efforts of prof. Kolev are directed to the synthesis, spectral and structural elucidation of new stibazolium salts with enlarged π-conjugated system and their functional thin films deposited by pulsed
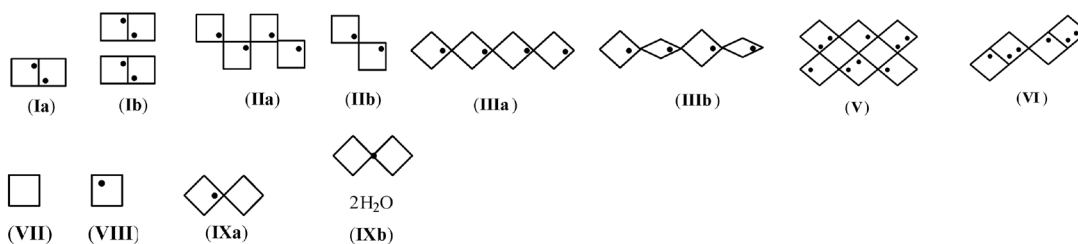
(Ia) **(Ib)** **(IIa)** **(IIb)** **(IIIa)** **(IIIb)** **(V)** **(VI)**

(VII) **(VIII)** **(IXa)** 2H₂O **(IXb)**

laser deposition (PLD) using UV TEA N₂ laser onto glass substrates and KCl, NaCl single crystals. The effective $\chi^{(2)}$ values are determined to be 1.40 and 0.95 pm/V for p and s polarization, respectively, so the $\chi^{(2)}$ in the p polarization case is enhanced by about 45%, with respect to the s case. The chemical diagram of (E)-1-Ethyl-4-(2-(4-hydroxynaphthalen-1-yl)vinyl)quinolinium Bromide is shown below:
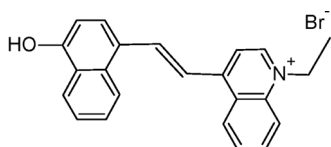

The determined effective $\chi^{(3)}$ value was found to be 6.5×10^{-20} m² V⁻² one of the best values measured for organic compounds. These results were published in the Journal of Physical Chemistry C (2012), 116, 7144−7152.

The complete elucidation of series of new dicyanoisophorone derivatives – nonlinear optical and electro optical materials with possibility to tune of their optical and mechanical properties. As a result of this investigation it was found second-order optical properties of anionic 3-dicyanomethylen-5,5-dimethyle-1-[2-(4-hydroxyphenyl)ethenyl)]-cyclohexene (1) with crystalline sizes from 10 nm to 300 nm were studied. An electric field enhancement of effective second-order susceptibility at 1064 nm for the crystallites incorporated into the oligoetheracrylate photopolymer matrices from 3.1 pm/V to 7.8 pm/V was discovered corresponding to hyperpolarizability increase from $0.12.10^{-30}$ esu to $0.21.10^{-30}$ esu. The evaluated intrinsic hyperpolarizability achieves value about 0.037, which is comparable with the best organic molecule. Further investigations of Prof. Kolev and researchers from France, Germany and Poland were on physics of the NLO materials on the basis of compounds with the quinoide like structure.

(I)
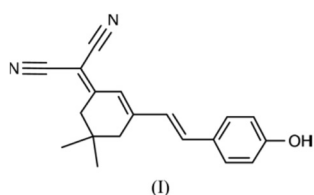
The novel composites based on the 1-methyl-4-[2-(3-methoxy-4-oxocyclohexadienyliden) ethyliden]-1,4-dihydropyridine (I) chromophore incorporated into the polymer PMMA matrices in 7.5% weight content deposited on mica substrate They have found that the SHG at 1,064 nm was increased saturating after 4–5 min. of the dc-treatment. The main alignment process was observed during first 2 min of the dc-field poling. Afterwards, the process was saturated achieving the maximal values after about 8 min. It was crucial that more flexible for alignment was temperature of about 350 K. They have measured values of second order optical effect of about122 pm/V at 1,064 nm fundamental laser wavelength. This effect show very weak reversibility after the dc-field switching off.

The linear and nonlinear optical properties of different substituted piridinio betaines of squaric acid were established by electro-optical absorption measurements (EOAM) in dioxane solution. It was found all chromophores studied exhibit intense absorption bands in the visible region within 372–441 nm, accompanied with decrease in dipole moment upon excitation.
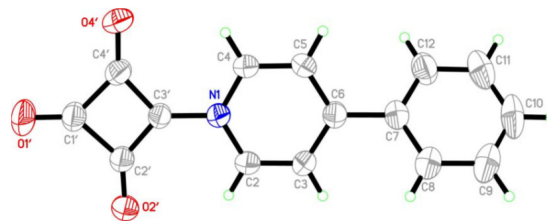
The static hyperpolarizabilities of the NLO-phores studied depend strongly on the substituent in the pyridinium ring and increase significantly going from donor to acceptor substituent. Specifically, the noncentrosymmetrically crystallizing 4-benzoyl compound showed the highest static hyperpolarizability β_0 −26.19.

Prof. Kolev published 225 research papers, 2 books, 4 chapters of books and an invited review.

The books and chapter of books are listed below:

1. Kolev, T. (2007) *Quantum chemical, spectroscopic and structural study of hydrochlorides, hydrogensquarates and ester amides of squaric acid of amino acid amides, Chapter of book "Progress in Quantum Chemistry Research" E. Hoffman (Ed),*

Nova Science Publishers, Inc., Hauppauge, NY 11788, USA, ISBN: 1-60021-621-8.

2. Kolev, T. (2008) *Quantum Chemical, Spectroscopic and Structural Study of Hydrochlorides, Hydrogens Squarates and Ester Amides of Squaric Acid, Book – 95 pages Nova Science Publishers, Inc., Hauppauge, NY 11788, USA, ISBN: 978-1-60456-431-0.*

3. Koleva, B., Kolev, T. M., Spiteller, M. (2011) Book chapter: *"Spectroscopic Analysis and Structural Elucidation of Small Peptides", in "Advances in Chemistry Research vol. 3, pages 675–755 J. C. Taylor (Ed.), Nova Science Publishers, Inc., Hauppauge, NY, 11788, USA.*

4. Ivanova, B., Kolev, T. (2011) *Linearly Polarized IR Spectroscopy Theory and Applications for Structural Analysis--Book. Taylor and Francis Group, CRC Press, Boca Raton, USA ISBN: 978-1-4398-2559-4.*

5. Kolev, T., Spiteller, M., Koleva, B. (2010) *Spectroscopic and structural elucidation of amino acid derivatives and small peptides – experimental and theoretical tools, Amino Acids, Review, 38, 45-50.*

6. Tsonko Kolev, Rumyana Bakalska, Mina Todorova (2016) *Efficient π electrons delocalization in two styrylquinolinium dyes – organic materials for second order nonlinear application Chapter of book "BULGARIAN-GERMAN SCIENTIFIC COOPERATION: PAST, PRESENT, AND FUTURE" PROCEEDINGS OF THE HUMBOLDT-KOLLEG Sofia, November 26–28, 2015, Faber Publishing House, 2016 pp. 209–221, ISBN 978-619-00-0517-9.*

The citations for the period 1990–2018 are 2426 in total (Scopus) and 2845 (Google). The most cited article is: Kolev, T., Velcheva, E., Stamboliyska, B., Spiteller, M. (2005) DFT and Experimental Studies of the Structure and Vibrational Spectra of Curcumin, International Journal of Quantum Chemistry, 102, 1069–1079 – 255 citations until July 2018.
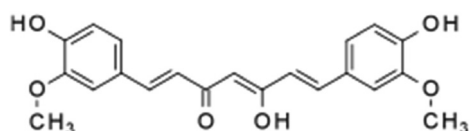
In this work Prof. Kolev has unambiguously shown by vibrational spectroscopy and DFT calculations that the compound possesses outstanding antioxidant activity due to enol form which keeps the molecule conjugated.

Article in journal with highest impact factor: Kolev, T., Yancheva, D., Stoyanov, St. (2004) Synthesis, Spectral and Structural Elucidation of Some Pyridinium Betaines of Squaric Acid – Potential Materials for Nonlinear Optical Applications, Advanced Functional Materials, 14, 799 –804 – IF 10.48. An example of 4-dimethylamino pyridinio-betaine of squaric acid is presented on the following figure:
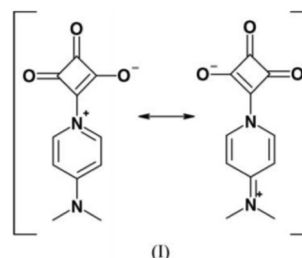
Scientific Awards

In 2010 Prof. Kolev received the Award of Plovdiv University for the best scientist on the field of Natural Sciences.

In 2011 he received the National Pitagor Award (Pythagoras) of the Ministry of Education and Sciences for the best scientist on the field of Natural Sciences.

In 2012 Prof. Kolev is nominated for corresponding member of Bulgarian Academy of Sciences by Plovdiv University for his achievements in the field of physical organic chemistry and organic material science.

He was awarded Alumni Program of Alexander von Humboldt Foundation (2013–2015) with host Prof. Dr. Dr. h. c. Michael Spiteller, Institute of Environmental Research at the Technical University (TU) Dortmund.

Family life

Prof. Kolev has two daughters – Martina and Tsonka. Together with granddaughter Sophia they love spending time together in Gradnitsa village – the birth place of Prof. Kolev, at the foot of the Central Balkan Mountains.

Acknowledgements

Neutral versus protonated uracil: CASPT2 theoretical study of the mechanisms of NH-photodissociation

V. B. Delchev

Department of Physical Chemistry, University of Plovdiv, Tzar Assen 24 Str.,
4000-Plovdiv, Bulgaria

We performed a CASCF(10,8)//CASPT2(10,8) level relaxed scans of the excited-state reaction paths of the N_1-H and N_3-H bonds of uracil and its doubly protonated form. The optimized state was the repulsive $^1\pi\sigma^*$ excited state which was recognized as a driven state. The results showed that the protonation of uracil disfavors the H-photodetachment processes in the compound because it leads to an increase of the reaction energy barrier along the $^1\pi\pi^*$ and $^1\pi\sigma^*$ excited-state reaction paths. Moreover the protonation of the oxygen atoms leads to the stabilization of the $^1n\pi^*$ excited state.

Keywords: CASPT2 calculations; Excited-state reaction paths; MP2 optimizations; Uracil.

INTRODUCTION

Pyrimidine nucleobases are major building blocks of the macromolecules of nucleic acids [1]. They are major chromophores in living organisms [2–11]. They absorb UV light and relax non-radiatively through internal conversion to the ground state. In this manner the pyrimidine nucleobases serve as a barrier against the damaging impact of UV rays [2–5].

Lots of papers regard the pyrimidine nucleobases from the stand point of their photostability [12–15]. Merchan *et al*. [16] have proposed a unified model for the ultrafast relaxation of excited pyrimidine nucleobases. It has been assumed that the deactivation occurs through internal conversion and conical intersections S_0/S_1 [16–20]. The conical intersections S_0/S_1 have twisted geometries around the double CC bonds in the aromatic rings. These are so-called "ethylene-like" conical intersections since they are found to explain the internal conversion of the $^1\pi\pi^*$ excited states in ethylene [21].

It has been found that the photodetachment and photoattachement of protons from the O-H and N-H bonds in pyrimidine derivatives occur along the reaction path of the repulsive $^1\pi\sigma^*$ excited state [13, 17]. The mechanism is known as PIDA (photoin-duced dissociation-association) [13–15]. Despite the large number of papers treating the photophysical phenomena in pyrimidine nucleobases there is still a gap regarding the influence of protonation of pyrimidine bases on the PIDA reactions. In other words, it is not known how the protonation of uracil, in particular, changes the photophysics of the compound.

The aim of the paper is to throw light upon the mechanism of proton photodetachment (the first step of the PIDA mechanism) of neutral and doubly protonated uracil. The comparison would reveal the influence of the acidification of the uracil water solution to the tautomerization of the compound when irradiated with UV light.

THEORETICAL AND EXPERIMENTAL METHODS

The ground-state equilibrium geometries of two forms of uracil (neutral and protonated) were optimized at the CASSCF(10,8) and MP2 levels of theory. The harmonic vibrations were calculated to prove that the studied systems are located in minima on the PES. The energies of the systems were computed using the CASSCF(10,8)//CASPT2(10,8) protocol, the last accounting for the second order correlation energy correction.

The adiabatic $^1\pi\sigma^*$ excited-state reaction paths were optimized with the CASSCF(10,8)//CASPT2

(10,8) protocol either using symmetry restrictions, symmetry C_S. Applying symmetry aids to construct a proper active space and to keep it constant during the CASSCF optimizations. Within the C_S symmetry space it is possible to divide the orbitals into two groups: $a' - n, \sigma^*$; and $a'' - \pi, \pi^*$. Furthermore the excited states are grouped into two groups: $A' - {}^1\pi\pi^*$, and $- A'' - {}^1n\pi^*, {}^1\pi\sigma^*$. The adiabatic electronic-state reaction paths were referred to the MP2 energies of the two systems under study.

All calculations were performed using the aug-cc-pVDZ basis set. They all refer to the gas phase systems.

For recording of the UV spectra we preapared two water solutions of uracil with concentration of 2.10^{-4} mol/L. We set the pH of the first solution 6.28 which is prepared directly from bidestiled water and uracil (without additional acidification). For the preparation of the acidic solution we added drop by drop concentrated HCl acid to the initial solution up to pH=3.80. At this pH the molar ratio between uracil molecules and the added protons is 1:2. In other words the molar ratio is completely enough to protonate the two oxygen atoms of uracil with two protons, i.e. to produce the doubly protonated uracil UH_2^{2+}. The UV spectra of the two solutions were recorded on a LAMBDA 9 UV-Vis/NIR spectrometer operating between 200 and 900 nm.

RESULTS AND DISCUSSIONS

Ground-state equilibrium geometries

The MP2-optimized ground state equilibrium geometries of the studied systems are presented in Fig. 1.

The two structures are planar. The associated protons to the oxygen atoms in the system UH_2^{2+} lye in the molecular plane as well. Further, they form extremely short $H^+....O_{7/8/}$ bonds which are in the length interval of the covalent bonds. The formation of this bonds provokes a shortening of the C=O bonds of about 0.07 Å. In other words the protonation of the oxygens could be a way to stabilize the ${}^1n\pi^*$ excited state as it has been reported previously for similar compounds [12, 22].

Excited-state reaction paths of the NH-dissociation mechanisms

The N_3-H photodissociation mechanisms of the two systems U and UH_2^{2+} are presented in Fig. 2.

Fig. 2a represents the N_3-H photodissociation mechanism of pure uracil. As seen the spectroscopically active ${}^1\pi\pi^*$ excited state can be populated, in the Franck-Condon area, by a direct excitation of ground-state uracil with UV light. The adiabatic
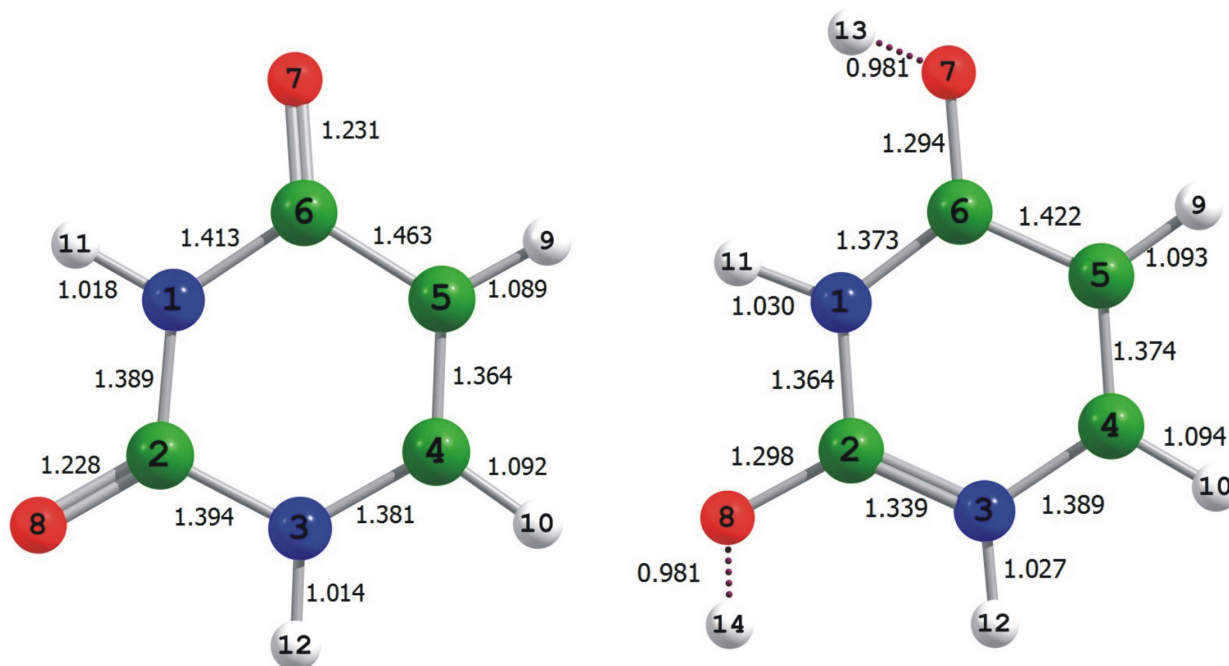

Fig. 1. MP2-ground-state equilibrium geometries of the studied systems. The structures were optimized with the aug-cc-pVDZ basis functions
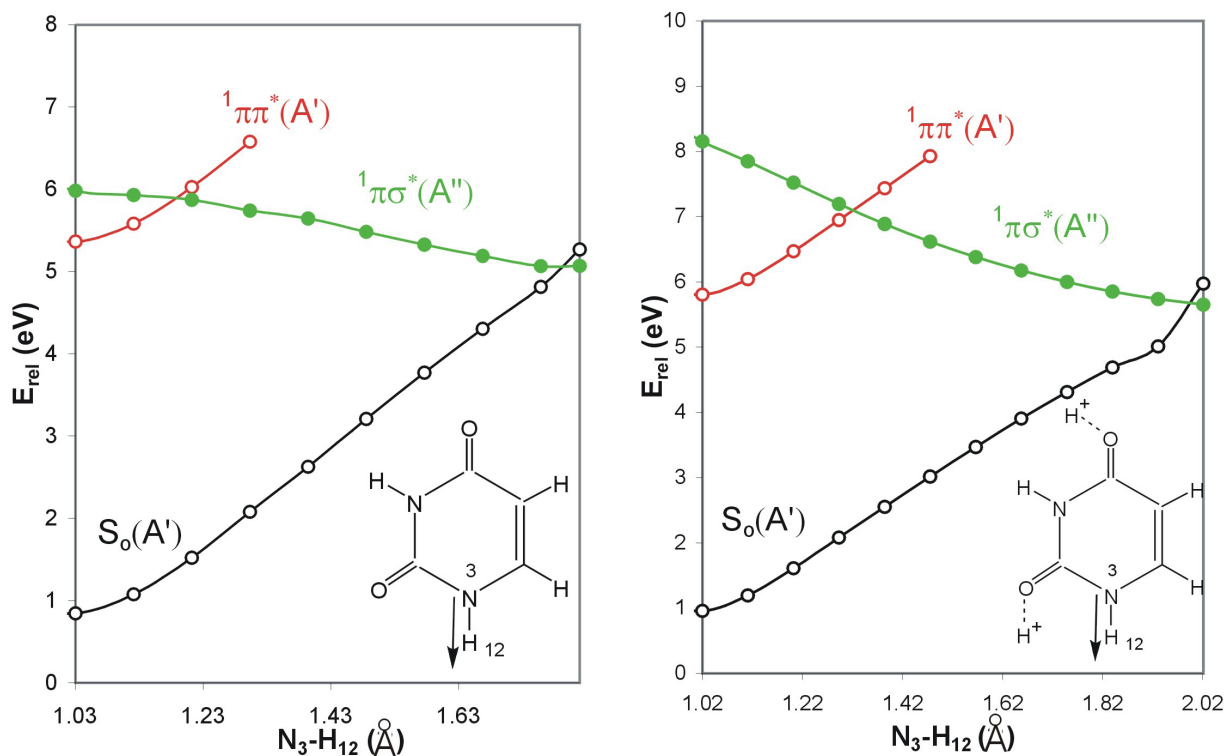
Fig. 2. Excited-state reaction paths of the N_3-H photodissociation processes of a) uracil U and its doubly protonated form b) UH_2^{2+}. The adiabatic energies of the electronic states are calculated using the MP2/aug-cc-pVDZ energies of the ground state equilibrium geometries as reference values: U (-413.779025 a.u.) and UH_2^{2+} (-414.259424 a.u.). The optimized excited state is designated with full circles along the reaction path

vertical excitation energy of the $^1\pi\pi^*$ excited state is 5.36 eV (232 nm). In the Franck-Condon region the driven and repulsive $^1\pi\sigma^*$ excited state has rather high adiabatic excitation energy (5.98 eV or) to be populated directly when the solution of U is irradiated with UV light. However the $^1\pi\sigma^*$ excited-state reaction path goes down along the reaction coordinate and leads to a crossing with the ground-state reaction path of the compound. The population of the $^1\pi\sigma^*$ excited state can be achieved from the bright $^1\pi\pi^*$ excited state along its excited-state reaction path and a conical intersection $^1\pi\pi^*/$ $^1\pi\sigma^*$. The energy barrier of this excited-state internal conversion process is relatively low, ~ 0.5 eV. The conical intersection S_0/S_1 is about 5.06 eV. Therefore the energy gradient along the $^1\pi\sigma^*$ excited-state reaction path from the Franck-Condon point to the crossing point is only 0.87 eV.

In Fig. 2b are given the excited-state reaction paths of the same mechanism in the doubly protonated system UH_2^{2+}. As seen the initial population of the $^1\pi\pi^*$ excited state requires higher energy, 5.81 eV (214 nm) as compared to pure U. The popu-

lation of the driven $^1\pi\sigma^*$ excited state in the Franck-Condon region is practically impossible because of the very high adiabatic excitation energy, 8.16 eV (152 nm). Theoretically the last state could be populated by internal conversion through a conical intersection $^1\pi\pi^*/$ $^1\pi\sigma^*$, however the energy barrier of the process is quite high, 1.33 eV.

The photodissociation processes of the bond N_1-H of the systems U and UH_2^{2+} are illustrated in Fig. 3. The results in Fig. 3a show that the population of the $^1\pi\pi^*$ excited state of U starts over 6.15 eV (under 202 nm). The $^1\pi\sigma^*$ excited state have very high vertical excitation energy (7.64 eV), which makes the direct population of this state impossible. The excited state can be populated along the reaction coordinate through the $^1\pi\pi^*$ excited-state reaction path and a conical intersection $^1\pi\pi^*/^1\pi\sigma^*$. This internal conversion process passes through an energy barrier of 0.63 eV.

In the same way the driven $^1\pi\sigma^*$ excited state of UH_2^{2+} can be populated through a much larger energy barrier of 1.23 eV (Fig. 3b). However the adiabatic excitation energy of the $^1\pi\pi^*$ excited state
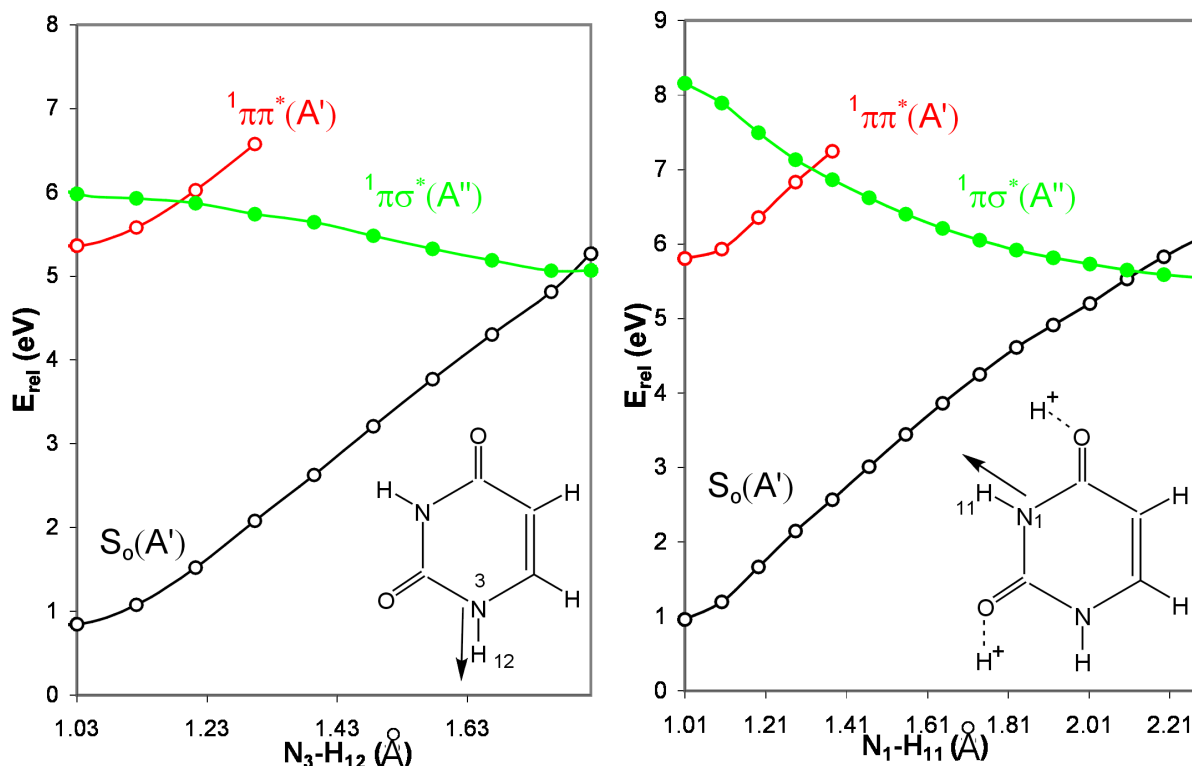
Fig. 3. Excited-state reaction paths of the N_1-H photodissociation processes of a) uracil U and its doubly protonated form b) UH_2^{2+}. The adiabatic energies of the electronic states are calculated using the MP2/aug-cc-pVDZ energies of the ground state equilibrium geometries as reference values: U (-413.192969 a.u. – found with the aug-cc-pVDZ / 6-31G basis sets) and UH_2^{2+} (-414.259424 a.u.). The optimized excited state is designated with full circles along the reaction path.

in the Franck-Condon area of UH_2^{2+} is a bit lower as compared to uracil. Conversely, the $^1\pi\sigma^*$ excited state is higher.

The difference in the adiabatic excitation energies of U in the Franck-Condon are in Fig. 2a and Fig. 3a comes from the fact that we used different basis sets for atoms. For example for the atoms N_1 and H_{11} we used the aug-cc-pVDZ basis set and the 6-31G for all the remaining atoms. That was only way to locate the σ^*-MO on the N_1-H_{11} bond. Usually this antibonding orbital has very high energy and it is outside the active space. This computational trick agrees well with the experimental absorption spectra of water solutions of pure and protonated uracil, which are presented in Fig. 4.

The spectra in Fig. 4 shows that the neutral uracil U (pH=6.28) has a bit lower intensities of the bands than the doubly protonated form (pH=3.80). The reason might be the better conjugation of the oxygen atoms in the protonated form than in neutral uracil. The main absorption maxima in both spectra correspond to $\pi\rightarrow\pi^*$ electron transitions in the two systems under study.

CONCLUSION

We performed a CASCF(10,8)//CASPT2(10,8) level study in order to find out the influence of the acidification of the water solution of uracil on the mechansim of NH-photodissociation. The NH-dissociation mechanisms have been found to play a key role in the photochemistry of nucleobases and their analogues [13–15, 17]. The research led to the next major conclusions:

1. The protonation of the oxygen atoms leads to the stabilization of the $^1n\pi^*$ excited state which is in accord with previous investigations [12, 22].

2. The population of the $^1\pi\pi^*$ excited state of U requires lower excitation energy than the population of the same state of UH_2^{2+}. Moreover the population of the $^1\pi\sigma^*$ excited state along the reaction path of N_3-H elongation passes through a larger energy barrier for UH_2^{2+} than for neutral uracil. In this case the protonation of uracil disfavors the H-photodetachment process.

3. The protonation of uracil disfavors the photodissociation of the N_1-H bond either. However the

REFERENCES

1. D. L. Nelson, M. M. Cox, Lehninger Principles of Biochemistry (5th edition), W.H.Freeman & Co Ltd., New York, 2008.
2. P. R. Callis, *Annu. Rev. Phys. Chem.*, **34**, 329 (1983).
3. M. H. Daniels, W. W. Hauswirth, *Science*, **171**, 675 (1971).
4. A. R. Reuther, H. Iglev, R. Laenen, A. Laubereau, *Chem. Phys. Lett.*, **325**, 260 (2000).
5. C. E. Crespo-Hernandez, B. Cohen, P. M. Hare, B. Kohler, *Chem. Rev.*, **104**, 1977 (2004).
6. B. Cohen, C. E. Crespo-Hernandez, B. Kohler, *Faraday Discuss.*, **127**, 000 (2004).
7. J. -M. L. Pecourt, J. Peon, B. Kohler, *J. Am. Chem. Soc.*, **122**, 9348 (2000).
8. J. -M. L. Pecourt, J. Peon, B. Kohler, *J. Am. Chem. Soc.*, **123**, 10370 (2001).
9. B. Cohen, P. Hare, B. Kohler, *J. Am. Chem. Soc.*, **125**, 13594 (2003).
10. K. H. Kraemer, *Proc. Natl. Acad. Sci.*, **94**, 11 (1997).
11. [11] H. Muktar, C. A. Elmets, *Photochem. Photobiol.*, **63**, 355 (1996).
12. A. L. Sobolewski, W. Domcke, C. Hattig, *J. Phys. Chem. A*, **110**, 6301 (2006).
13. A. L. Sobolewski, L. Adamowicz, *J. Phys. Chem.*, **100**, 3933 (1996).
14. A. L. Sobolewski, *Chem. Phys. Lett.*, **211**, 293 (1993).
15. B. Chmura, M. Rode, A. Sobolewski, L. Lapinski, M. Nowak, *J. Phys. Chem. A*, **112,** 13655 (2008).
16. M. Merchan, R. Gonzalez-Luque, T. Climent, L. Serrano-Andres, E. Rodriguez, M. Reguero, D. Pelaez, *J. Phys. Chem. B*, **110**, 26471 (2006).
17. V. B. Delchev, A. L. Sobolewski, W. Domcke, *Phys. Chem. Chem. Phys*., **12**, 5007 (2010).
18. D. Keefer, S. Thallmair, S. Matsika, R. de Vivie-Riedle, *J. Am. Chem. Soc.*, **139**, 5061 (2017).
19. S. Matsika, *J. Phys. Chem. A*, **108**, 7584 (2004).
20. S. Matsika, M. Spanner, M. Kotur, T. C. Weinacht, *J. Phys. Chem. A*, **117**, 12796 (2013).
21. M. Barbatti, J. Paier, H. Lischka, *J. Chem. Phys.*, **121**, 11614 (2004).
22. M. Etinski, C. M. Marian, *Phys. Chem. Chem. Phys.*, **12**, 15665 (2010).
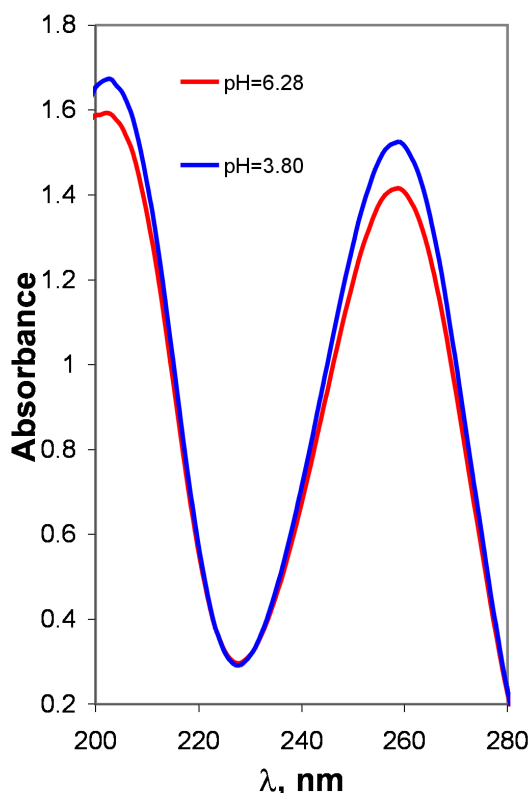
Fig. 4. UV-absorption spectra of water solutions of uracil at different pH

reduction of the energy barrier as compared to the N$_3$-H bond is lower.

НЕУТРАЛЕН ИЛИ ПРОТОНИРАН УРАЦИЛ: CASPT2 ТЕОРЕТИЧНО ИЗСЛЕДВАНЕ НА МЕХАНИЗМИТЕ НА NH-ФОТОДИСОЦИАЦИЯ

В. Б. Делчев

Катедра Физикохимия, Пловдивски университет „Паисий Хилендарски", ул. Цар Асен 24, 4000 – гр. Пловдив, България, E-mail: vdelchev@uni-plovdiv.net

(Резюме)

Проведено е релаксационно сканиране на реакционните пътища на възбудените състояния на връзките N_1-H и N_3-H в урацила и неговата протонирана форма. Теоретичните изчисления са извършени на CASCF(10,8)//CASPT2(10,8) теоретично ниво. Резултатите показват, че протонирането на урацила възпрепятства фотодисоциацията на тези връзки, тъй като води до по-високи енергетични бариери по реакционните пътища на $^1\pi\pi^*$ и $^1\pi\sigma^*$ възбудените състояния, отколкото в неутралния урацил. Освен това протонирането на кислородните атоми на урацила предизвиква стабилизация на $^1n\pi^*$ възбуденото състояние.

Predicting molecular properties using theoretical parameters: substituted pyridines

Gergana Koleva, Boris Galabov*

Department of Chemistry and Pharmacy, University of Sofia,
1 James Bourchier Blvd, Sofia 1164, Bulgaria

The potential of three alternative theoretical quantities – NBO atomic charges, Hirshfeld charges, and electrostatic potential at nuclei (EPN) values – in predicting molecular properties is examined for a series of 37 substituted pyridines. These molecular parameters were evaluated using density functional theory computations at ωB97X-D/aug-cc-pVTZ. Correlations with experimental basicities (pK_b) and proton affinities (PA) as well as with theoretically estimated hydrogen bonding energies (for complexes with HF and H_2O) show that the EPN values at the pyridine nitrogen (V_N) provide the best predictive power among the considered theoretical parameters.

Keywords: pyridines, atomic charges, electrostatic potential at nuclei, Density functional theory, hydrogen bonding.

INTRODUCTION

In this research, we examine the potential application of theoretical molecular parameters in predicting the reactivity of 3- and 4-substituted pyridines with respect of hydrogen bonding and in characterizing their proton affinities and basicities. Quantifying chemical reactivity has been in the focus of theoretical studies for decades. Important developments on this respect represent the methods employing the properties of the frontier orbitals, first considered quantitatively by Fukui [1, 2]. The modern versions of these methods usually employ density functional theory (DFT) computations [3–5]. These methods yield quantities that characterize the global reactivity of molecules (chemical potential, global hardness, softness, electrophilicity index, nucleophilicity index) [3–7]. For many systems, however, such information is not sufficient, since it does not describe local (atomic sites) reactivities and positional selectivities. To avoid these problems, a number of localization methods have been proposed [5, 8, 9]. Implicit in these methods are variously defined theoretical atomic charges.

The accuracy of reactivity predictions in applying such procedures depends, therefore, on the particular definition of atomic charges. Computed atomic charges are frequently employed in rationalizing chemical reactivity [10–19]. A considerable advantage of these quantities is their straightforward physical interpretation. An alternative to these methods is the application of the molecular electrostatic potential (MESP) [20, 21]. MESP maps as well as minimum and maximum MESP values (V_{min}, V_{max}) have been successfully applied in quantifying chemical reactivity, especially for processes, where the electrostatic interaction between the reactants is important [22–25]. It should be underlined that MESP computations do not involve additional approximations aside from those inherent in evaluating the molecular wave function. We have proposed the electrostatic potential at nuclei (EPN, V_Y) as a local reactivity descriptor and have shown that EPN quantifies the reactivity of molecules toward hydrogen bonding as well as for a number of chemical reactions [26]. EPN was first introduced by Wilson in 1962 [27]. Politzer and Truhlar [20] defined the potential at nuclei Y by the expression:

$$V_Y \equiv V(\mathbf{R}_Y) = \sum_{A(\neq Y)} \frac{Z_A}{|\mathbf{R}_A - \mathbf{R}_Y|} - \int \frac{\rho(\mathbf{r})}{|\mathbf{r} - \mathbf{R}_Y|} d\mathbf{r} \qquad (1)$$

In Eqn. 1, R_A and Z_A are the position vector and the charge of nucleus A. $\rho(\mathbf{r})$ is the electron density

* To whom all correspondence should be sent:
E-mail: galabov@chem.uni-sofia.bg

function. The singular term $R_A = R_Y$ is excluded. In essence, the V_Y value reflects the potential at the position of nucleus Y (R_Y), determined by the positive charges of all nuclei except nucleus Y and the entire electron density. This definition of V_Y limits the applicability of this quantity in rationalizing reactivities only to series of structurally related molecules. Providing that the structural changes in such series be at some distance to the reaction center, the shifts of V_Y follow quite well the variations in the electron density near atom Y [28].

In the present research, we focus on examining by theoretical methods a series of 37 substituted pyridines. Extensive experimental data on the proton affinities (PA) and basicities (pK_b) of these systems are available [29, 30]. Both of these properties are inherently associated with the chemical reactivity of the molecules. These data offer an excellent opportunity for testing the performance of alternative theoretical quantities in characterizing and predicting these properties.

Herein, we report results from the application of Hirshfeld [31] and NBO [32] atomic charges and of the electrostatic potential at nuclei in analyzing and predicting both experimental (basicities, pK_b, and proton affinities, PA) and theoretical (hydrogen bonding energies) quantities for a series of 37 3- and 4-monosubstituted pyridines. Popelier *et al.* [33] correlated the basicities of substituted pyridines with electron density parameters derived from the Atoms in Molecule (AIM) approach. A multi-parameter analysis yielded in good correlations for 3- and 4-substituted derivatives. Hopkins *et al.* [34] have established a good correlation between experimental relative hydrogen bonding basicities and the gas-phase proton affinities for a series of nineteen 3- and 4-substituted pyridines. Blanco *et al.* [35] conducted a theoretical study (at B3LYP/6-31+G**) of the effects of monosubstitution in pyridines involving the atoms from the second and third rows in the periodic table. These authors established an excellent correlation between theoretically estimated proton affinities and MESP minimum values. Theoretical computations using semi-empirical molecular orbital computations have also been applied in examining the substituent effects on the pK_a values in nitrogen containing organic compounds including pyridines [36]. Habbibi-Yangjeh *et al.* [37] applied a combined principal component analysis-genetic algorithm-neural network approach in predicting the basicities of substituted pyridines.

COMPUTATIONAL METHODS

The geometries of reactants, complexes between substituted pyridines and HF, and H_2O, respec-

tively, were fully optimized using the ωB97X-D hybrid functional [38], combined with correlation-consistent aug-cc-pvtz basis set [39]. The ultrafine grid was used for the numerical integrations. The interaction energies were corrected for the basis set superposition error by the Boys-Bernardi counterpoise method [40] in all the complexes. Harmonic vibrational frequency computations were evaluated to ensure that the optimized structures are true minima. All computed parameter values refer to isolated molecules and complexes in the gas phase. The computations employed the Gaussian 09 program package [41]. Cartesian coordinates and energies of all optimized structures are given in the Supplementary Material.

RESULTS AND DISCUSSION

The conducted computations include complete optimizations of isolated pyridine derivatives and their hydrogen bonded complexes with two model proton donating molecules: hydrogen fluoride and water. The employed ωB97X-D density functional has been shown to perform well for both thermochemistry and noncovalent interactions [42]. Besides, Medvedev *et al.* [43] reported recently that the inherent in these computations B97 hybrid functional [44] is among the best performing functionals in deriving the electron density distributions in molecules. As emphasized, the present research centres on examining how well charge related parameters (atomic charges, electrostatic potentials) correlate with the experimental basicities and proton affinities as well as with theoretically derived hydrogen bonding energies. Table 1 presents the results for NBO and Hirshfeld charges at the pyridine nitrogen for the series of monomeric 3- and 4-substituted derivatives. The shifts of the electrostatic potential at the nitrogen atom with respect the unsubstituted pyridine (ΔV_N) are shown in column five. Table 1 contains also the computed hydrogen bonding energies (ΔE) for the complexes with HF and H_2O and the experimental pK_b and gas-phase proton affinities. The last four rows of Table 1 contain the correlation coefficients for the relationships between the theoretical parameters (q^{NBO}, $q^{Hirshfeld}$, ΔV_N) and the considered experimental (pK_b, PA) and theoretical (ΔE) values. Figure 1 illustrates some of these relationships. As expected, the correlations between ΔV_N and the hydrogen bonding energies (ΔE) are excellent. The correlation coefficient for the complexes with hydrogen fluoride is $r = 0.993$. Energy decomposition analysis has shown a very strong participation of the electrostatic energy term in hydrogen bonding [45].

Table 1. ωB97X-D/aug-cc-pvtz calculated values of atomic charges, experimental basicities (pK_b)[a] and proton affinities (PA)[b] of 3-, and 4-substituted pyridines, and complexation energies ($\Delta E = E_{el} + ZPC + BSSE$) of hydrogen bonding complexes between the pyridines and HF (ΔE^{HF}) and H_2O (ΔE^{water})

	subs.	q_N^{NBO} [a.u.]	$q_N^{Hirshfeld}$ [a.u.]	ΔV_N[c] [volt]	pK_b	PA [kcal mol⁻¹]	ΔE^{HF} [kcal mol⁻¹]	ΔE^{water} [kcal mol⁻¹]
1	H	−0.428	−0.167	0.000	8.83	222.28	−11.30	−5.15
2	3-Br	−0.410	−0.156	0.396	11.15	217.50	−10.16	−4.62
3	3-C(CH₃)₃	−0.423	−0.169	−0.149	8.18	−	−11.82	−5.48
4	3-CH(CH₃)₂	−0.423	−0.169	−0.130	8.28	−	−11.74	−5.43
5	3-CH₂CH₃	−0.423	−0.168	−0.115	8.20	226.44	−11.69	−5.39
6	3-CH₃	−0.423	−0.168	−0.107	8.32	225.48	−11.66	−5.35
7	3-Cl	−0.410	−0.156	0.392	11.16	215.92	−10.16	−4.58
8	3-CN	−0.416	−0.153	0.748	12.55	209.61	−9.14	−4.19
9	3-COCH₃	−0.431	−0.165	0.321	10.74	218.98	−10.63	−4.97
10	3-CONH₂	−0.422	−0.159	0.244	10.67	219.48	−10.42	−4.92
11	3-COOCH₃	−0.430	−0.163	0.244	10.87	221.23	−10.72	−4.86
12	3-COOCH₂CH₃	−0.430	−0.164	0.211	10.65	−	−10.82	−4.95
13	3-COOH	−0.428	−0.162	0.347	11.93	−	−10.37	−4.71
14	3-F	−0.407	−0.156	0.358	11.03	215.59	−10.32	−4.66
15	3-NH₂	−0.408	−0.165	−0.141	7.97	228.11	−11.88	−5.49
16	3-NHCOCH₃	−0.408	−0.159	−0.037	9.63	−	−11.17	−5.31
17	3-NO₂	−0.415	−0.151	0.818	13.21	−	−9.05	−4.24
18	3-OCH₃	−0.408	−0.162	−0.032	9.09	225.31	−11.38	−5.20
19	3-OH	−0.407	−0.162	0.110	9.20	222.16	−11.17	−5.26
20	3-SCH₃	−0.412	−0.160	0.063	9.58	223.83	−10.97	−5.08
21	4-Br	−0.426	−0.164	0.294	10.29	219.36	−10.54	−4.73
22	4-C(CH₃)₃	−0.435	−0.174	−0.208	8.01	228.90	−12.00	−5.48
23	4-CH(CH₃)₂	−0.436	−0.174	−0.185	7.98	228.42	−11.86	−5.44
24	4-CH₂CH₃	−0.436	−0.174	−0.172	8.13	227.32	−11.81	−5.42
25	4-CH₃	−0.437	−0.174	−0.164	8.00	226.39	−11.77	−5.40
26	4-CH=CH₂	−0.430	−0.169	−0.047	8.38	225.65	−11.46	−5.20
27	4-Cl	−0.429	−0.165	0.275	10.17	218.96	−10.57	−4.76
28	4-CN	−0.405	−0.150	0.734	12.10	210.47	−9.44	−4.20
29	4-COCH₃	−0.410	−0.157	0.321	10.50	218.62	−10.57	−4.89
30	4-COOCH₃	−0.410	−0.157	0.270	10.74	221.47	−10.66	−4.84
31	4-COOCH₂CH₃	−0.411	−0.158	0.237	10.55	−	−10.69	−4.86
32	4-COOH	−0.407	−0.154	0.380	12.16	−	−10.35	−4.65
33	4-NH₂	−0.469	−0.192	−0.486	4.89	234.16	−12.79	−5.92
34	4-NO₂	−0.400	−0.147	0.811	12.77	208.97	−9.26	−4.10
35	4-OCH₃	−0.457	−0.184	−0.279	7.53	229.86	−12.06	−5.55
36	4-OCH₂CH₃	−0.458	−0.185	−0.319	7.33	−	−12.20	−5.66
37	4-SCH₃	−0.443	−0.176	−0.113	8.06	228.30	−11.58	−5.32
r with pK_b		0.681	0.906	**0.965**; y = 5.457x + 8.976				
r with PA		0.695	0.894	**0.988**; y = −19.29x + 224.5				
r with ΔE^{HF}		0.651	0.890	**0.993**; y = 2.753x − 11.34				
r with ΔE^{water}		0.633	0.874	**0.987**; y = 1.352x − 5.212				

[a] From ref. [29]. [b] From ref. [30]. [c] $\Delta V_N = V_N(Y–C_5H_4N) − V_N(C_5H_5N)$.
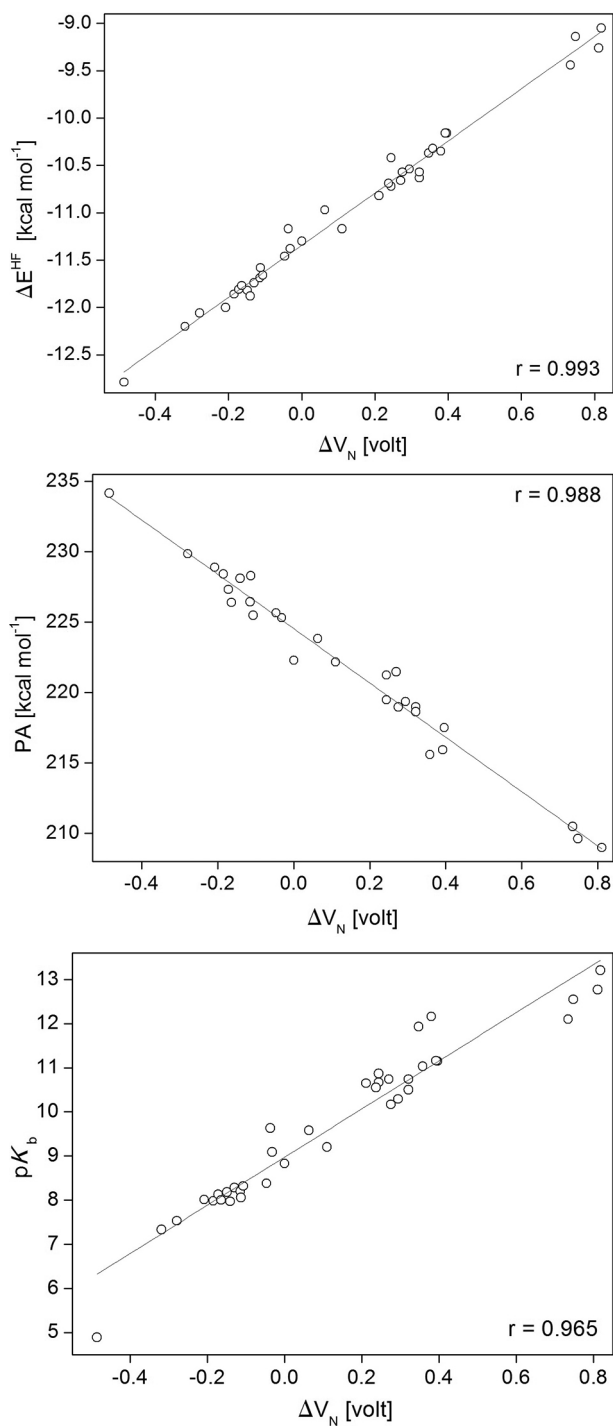
Fig. 1. Dependences between the theoretical electrostatic potential at the N atom in 3- and 4-monosubstituted pyridines and theoretically evaluated hydrogen bonding energies for complexes with HF (ΔE) as well as with the experimental basicities (pK_b) and proton affinities (PA).

An excellent correlation of ΔV_N with the experimental proton affinities for the substituted pyridine is also established ($r = 0.988$). As expected, electrostatic effects dominate the interaction of the

pyridine nitrogen lone pair with the incoming proton. The dependency between shifts of electrostatic potential with basicities (pK_b) is still satisfactory ($r = 0.965$) though with lower correlation coefficient. The pK_b values refer to equilibrium in water solution. Thus, very high linearity with the computed for the gas-phase shifts of electrostatic potentials at the pyridine nitrogen may not be expected. Still, the found relationship for 37 substituted pyridine may be used in predicting, at least qualitatively, basicity values.

The two tested atomic charges (NBO and Hirshfeld) do not provide satisfactory correlations with the studied theoretical and experimental quantities (Table 1). Nonetheless, the Hirshfeld charges perform better than the NBO atomic charges for all studied relationships. Popelier and Green [46] have discussed that hydrogen fluoride may not be the best choice for a model proton-donating species in describing basicities of molecules. These authors quantified the basicities of a series of 41 organic bases belonging to different classes in terms of the change of the energy of the proton-donating molecule in going from monomer to complex. Employing water as a model hydrogen donor resulted in much improved correlations. In view of these results, we conducted additional computations for the series of 37 pyridine derivatives using water as a model proton-donating species. The computed hydrogen bonding energies are given in the last column of Table 1. The correlation coefficients for the relationships with q^{NBO}, $q^{Hirshfeld}$, and ΔV_N are shown in the last row of the table. For the present series of pyridine derivatives, the obtained correlations with atomic charges and ΔV_N confirm the reported results for the complexes with hydrogen fluoride.

CONCLUSIONS

The results from this research outline a simple approach in analyzing and predicting properties for series structurally related molecules using theoretical computations. The conducted investigation considered experimental proton affinities (PA), experimental basicities (pK_b), and theoretically evaluated hydrogen bonding energies (ΔE) for 37 pyridine derivatives with substituents at positions 3 and 4. ωB97X-D/aug-cc-pVTZ computations provided the theoretical NBO charges, Hirshfeld charges, and electrostatic potential at nuclei (EPN) values, all associated with the nitrogen atom in the isolated pyridines. Among the three tested theoretical parameters, the electrostatic potential at the nitrogen (V_N) provides the best predictive potential for the properties considered.

REFERENCES

1. K. Fukui, T. Yonezawa, H. Shingu, *J. Chem. Phys.*, **20**, 722 (1952).
2. K. Fukui, H. Fujimoto, Frontier Orbitals and Reactions Paths, World Scientific, Singapore, 1997.
3. R, G. Parr, W. Yang, Density Functional Theory of Atoms and Molecules, Oxford University Press, New York, 1989.
4. Electronegativity: Structure and Bonding, K. D. Sen, C. K. Jorgersen (eds), Springer, Berlin, 1993.
5. P. Geerlings, F. De Proft, W. Langenaeker, *Chem. Rev.*, **103**, 1793 (2003**)**.
6. R. G. Parr, L. V. Szentpaly, S. Liu, *J. Am. Chem. Soc.*, **121**, 1922 (1999**)**.
7. Z. Zhou, R. G. Parr, *J. Am. Chem. Soc.*, **112**, 5720 (1990**)**.
8. W. Langenaeker, F. De Proft, P. Geerlings, *J. Phys. Chem.*, **99**, 6424 (1995).
9. a) P. K. Chattaraj, U. Sarkar, D. R. Roy, *Chem.* Rev., **106**, 2065 (2006); b) P. K. Chattaraj, U. Sarkar, D. R. Roy, *Chem.* Rev., **107**, PR46 (2007).
10. W. J. Herren, L. Radom, P. v. R. Schleyer, J. A. Pople, Ab initio Molecular Orbital Theory, Wiley, New York, 1986.
11. R. F. W. Bader, Quantum Theory of Atoms in Molecules, Oxford University Press, Oxford, 1990.
12. F. A. Carey, R. J. Sundberg, Advanced Organic Chemistry Part A: Structure and Mechanisms, Springer, New York, 2004, p 62.
13. S. M. Bachrach, Computational Organic Chemistry, Wiley-Interscience, 2007.
14. K. B. Wiberg, P. R. Rablen, *J. Comp. Chem.*, **14**, 1504 (1993).
15. H. Szatylowicz, T. Siodła, T. M. Krygowski, *ACS Omega*, **2**, 1746 (2017).
16. N. Sadlej-Sosnowska, *J. Phys. Chem.* A, **111**, 11134 (2007).
17. H. Szatylowicz, T. Siodla, O. A. Stasyuk, T. M. Krygowski, *Phys. Chem. Chem. Phys.*, **18**, 11711 (2016).
18. N. Sadlej-Sosnowska, *Chem. Phys. Lett.*, **447**, 192 (2007).
19. T. M. Krygowski, N. Sadlej-Sosnowska, *Struct. Chem.*, **22**, 17 (2011).
20. P. Politzer in: Chemical Applications of Atomic and Molecular Electrostatic Potentials, P. Politzer, D. G. Truhlar (eds), Plenum Press, New York, 1981, p 7.
21. S. R. Gadre, P. K. Bhadane, S. S. Pundlik, S. S Pingale in: Molecular Electrostatic Potential: Concepts and Applications, J. S. Murrey, K. Sen (eds), Elsevier, Amsterdam, 1996.
22. P. Politzer, L. Abrahmsen, P. Sjoberg, *J. Am. Chem. Soc.*, **106**, 855 (1984).
23. P. Politzer, K. Jayasuriya, P. Sjoberg, P. R. Laurence, *J. Am. Chem. Soc.*, **107**, 1174 (1985).
24. C. H. Suresh, S. R. Gadre, *J. Org. Chem.*, **62**, 2625 (1997).
25. C. H. Suresh, S. R. Gadre, *J. Am. Chem. Soc.*, **120**, 7049 (1998).
26. a) P. Bobadova-Parvanova, B. Galabov, *J. Phys. Chem.* A, **102**, 1815 (1998); b) P. Bobadova-Parvanova, B. Galabov *J. Phys. Chem.* A, **103**, 6793 (1999); c) B. Galabov, D. Cheshmedzhieva, S. Ilieva, B. Hadjieva, *J. Phys. Chem*. A, **108**, 11457 (2004); d) B. Galabov, S. Ilieva, G. Koleva, W. D. Allen, H. F. Schaefer III, P. von R. Schleyer, *WIREs Comput. Mol. Sci.*, **3**, 37 (2013).
27. E. B. Wilson, *J. Chem. Phys.*, **36**, 2232 (1962).
28. B. Galabov, V. Nikolova, S. Ilieva, *Chem. Eur. J.*, **19**, 5149 (2013).
29. J. A. Dean, Lange's Handbook of Chemistry, McGraw-Hill, New York, 1999.
30. NIST Chemistry WebBook, NIST Standard Reference Database Number 69, National Institute of Standards and Technology (NIST): Gaithersburg, MD, 2005, available at http://webbook.nist.gov/chemistry/ (accessed June 23, 2017)
31. a) F. L. Hirshfeld, *Theor. Chem. Acc.*, **44**, 129 (1977); b) J. P. Ritchie, *J. Am. Chem. Soc.*, **107**, 1829 (1985); c) J. P. Ritchie, S. M. Bachrach, *J. Comp. Chem.*, **8**, 499 (1987).
32. a) A. E. Reed, R. B. Weinstock, F. Weinhold, *J. Chem. Phys.*, **83**, 735 (1985); b) A. E. Reed, L. A. Curtiss, F. Weinhold, *Chem. Rev.*, **88**, 899 (1988).
33. G. I. Hawe, I. Alkorta, P. L. A. Popelier, *J. Chem. Inf. Mod.*, **50**, 87 (2010).
34. H. P. Hopkins Jr., C. J. Alexander, S. Z. Ali*, J. Phys. Chem.*, **82**, 1268 (1978).
35. F. Blanco, D. H. O'Donovan, I. Alkorta, J. Elguero, *Struct. Chem.*, 19, 339, (2008).
36. B. G. Tehan, E. J. Lloyd, M. G. Wong, W. R. Pitt, E. Gancia, D. T. Manallack, *Quant. Struct.-Act. Relat.*, **21**, 473 (2002).
37. A. Habibi-Yangjeh, E. Pourbasheer, M. Danandeh-Jenagharad, *Monatsh. Chem.*, **139**, 1423 (2008).
38. J.-D. Chai, M. Head-Gordon, *Phys. Chem. Chem. Phys.*, **10**, 6615 (2008).
39. a) T. H. Dunning Jr., *J. Chem. Phys.*, **90**, 1007 (1989); b) R. A. Kendall, T. H. Dunning Jr., R. J. Harrison, *J. Chem. Phys.*, **96**, 6796 (1992); c) D. E. Woon, T. H. Dunning Jr., *J. Chem. Phys.*, **98**, 1358 (1993).
40. a) S. F. Boys, F. Bernardi, *Mol. Phys.*, **19**, 553 (1970); b) S. Simon, M. Duran, J. J. Dannenberg, *J. Chem. Phys.*, **105**, 11024 (1996).
41. M. J. Frisch, G. W. Trucks, H. B. Schlegel, G. E. Scuseria, M. A. Robb, J. R. Cheeseman, G. Scalmani, V. Barone, G. A. Petersson, H. Nakatsuji, X. Li, M. Caricato, A. Marenich, J. Bloino, B. G. Janesko, R. Gomperts, B. Mennucci, H. P. Hratchian, J. V. Ortiz, A. F. Izmaylov, J. L. Sonnenberg, D. Williams-Young, F. Ding, F. Lipparini, F. Egidi, J. Goings, B. Peng, A. Petrone, T. Henderson, D. Ranasinghe, V. G. Zakrzewski, J. Gao, N. Rega, G. Zheng, W. Liang, M. Hada, M. Ehara, K. Toyota, R. Fukuda, J. Hasegawa, M. Ishida, T. Nakajima, Y. Honda, O. Kitao, H. Nakai, T. Vreven, K. Throssell, J. A. Montgomery, Jr., J. E. Peralta, F. Ogliaro, M. Bearpark, J. J. Heyd, E. Brothers, K. N. Kudin, V. N. Staroverov, T. Keith, R. Kobayashi, J. Normand,

K. Raghavachari, A. Rendell, J. C. Burant, S. S. Iyengar, J. Tomasi, M. Cossi, J. M. Millam, M. Klene, C. Adamo, R. Cammi, J. W. Ochterski, R. L. Martin, K. Morokuma, O. Farkas, J. B. Foresman, D. J. Fox, Gaussian09, Revision A.02, Gaussian, Inc., Wallingford CT, 2009.

42. L. A. Burns, Á. Vázquez-Mayagoitia, B. G. Sumpter, C. D. Sherrill, *J. Chem. Phys*., **134**, Article Number 084107 (2011).

43. M. G Medvedev, I. S. Bushmarino, J. Sun, J. P. Perdew, K. A. Lyssenko, *Science*, **355**, 49 (2017).

44. a) A. D. Becke, *J. Chem. Phys*., **107**, 8554 (1997); b) H. L. Schmider, A. D. Becke, *J. Chem. Phys*., **108**, 9624 (1998).

45. B. Galabov, P. Bobadova-Parvanova, S. Ilieva, V. Dimitrova, *J. Mol. Struct*., **630**, 101 (2003).

46. A. J. Green, P. L. Popelier, *J. Chem. Inf. Model.*, **54**, 553 (2014).

ПРЕДСКАЗВАНЕ НА МОЛЕКУЛНИ СВОЙСТВА С ПОМОЩТА НА ТЕОРЕТИЧНИ ПАРАМЕТРИ: ЗАМЕСТЕНИ ПИРИДИНИ

Г. Колева, Б. Гълъбов

Факултет по химия и фармация, Софийски университет „Св. Климент Охридски"
бул. Джеймс Баучер 1, София 1164

(Резюме)

Потенциалът на три алтернативни теоретични величини – NBO атомни заряди, Hirshfeld заряди и електростатични потенциали върху ядрата (EPN) – да предсказват молекулни свойства е оценен при проучване върху серия от 37 заместени пиридинови производни. Тези молекулни параметри са определени с помощта на изчисления, ползващи теорията на плътностния функционал с метода ωB97X-D/aug-cc-pVTZ. Корелации с експериментално определени константи на базичност (pK_b), както и с теоретично определени енергии на водородно свързване (за комплекси с HF и H_2O), показват, че измежду изследваните параметри, стойностите на EPN за позицията на пиридиновия азотен атом, предоставят най-добри възможности за предсказване на молекулни свойства при пиридинови производни.

New fluorescent PAMAM dendron with sensor and microbiological activity

D. Staneva[1], E. Vasileva-Tonkova[2], I. Grabchev[3]*

[1] University of Chemical Technology and Metallurgy, 1756 Sofia, Bulgaria
[2] Stephan Angeloff Institute of Microbiology, Bulgarian Academy of Sciences, 1113 Sofia, Bulgaria
[3] Sofia University "St. Kliment Ohridski", Faculty of Medicine, 1407 Sofia, Bulgaria

A new dendron containing Eosin Y as fluorescence unit has been synthesized and characterized. The basic photophysical characteristics of dendron have been investigated in organic solvents with different polarity and the results have been compared to the modified Eosin Y. In *N,N*-dimethylformamide solution, the newly synthesized dendron quench its fluorescence intensity in the presence of metal cations (Li^+, Na^+, K^+, Ag^+, Co^{2+}, Zn^{2+}, Mn^{2+}, Ni^{2+}, Cu^{2+}, Fe^{3+} and Cr^{3+}) depending from the nature of metal cations. It has also been observed than the fluorescence intensity is not affected from pH of the medium. Antimicrobial activity of the new dendron was tested in meat-peptone broth towards some model bacteria and yeasts.

Keywords: Eosin Y, dendron, PAMAM, sensor, environment pollutants, antimicrobial activity.

INTRODUCTION

The monitoring and rapid control of the environment pollutants is at the core of the development of new analytical systems for their detection. Especially suitable for these purposes are fluorescence optical sensors responsive to light irradiation in the presence of certain analytes with a change of their fluorescence emission. Therefore, in recent years, research has been focused on finding the possibility to increase the sensitivity, selectivity and appropriate working range of new sensor systems, depending on their application areas. An innovative area is the use of dendrimer or dendritic macromolecules, which are a new form of organization of polymeric materials [1]. For sensing applications dendrimers must be functionalized with fluorescent dyes because dendrimer molecules do not exhibit intrinsic photophysical properties. As fluorescent fluorophores for dendrimer and dendron modification are used 1,8-naphthlimide, xanthene dyes, dansyl, acridine, naphthalene, etc. [2–7].

In our laboratory we perform systematic investigations on the synthesis and photophysical properties of new luminescent polyamidoamine (PAMAM) and polypropyleneamine (PPA) dendrimers modified with 1,8-naphthalmide units in their periphery [7]. Several fluorescent tripods based of 1,8-naphthalimide with sensor properties have also been described [8–10]. Xanthene dyes, such as eosin Y, are a very interesting and special class of environmentally sensitive fluorophores which participate as a signal fragment in the design of different sensor systems [11]. They have low toxicity *in vivo*, and moderately high water solubility. They exhibit different tautomeric structures with different photolytic forms, either proton "on" or "off" depending on pH [12].

In this paper we describe the synthesis and characterization of a new PAMAM dendron from second generation. Its basic photophysical characteristics have been investigated in organic solvents of different polarity. The behaviour of fluorescent intensity in media with different pH and the ability to detect metal ions have been investigated. *In vitro* antimicrobial activity against Gram-positive and Gram-negative bacteria and yeasts has also been tested.

EXPERIMENTAL

Materials and methods

The synthesis of acylated eosin Y (E) with chloroacetyl chloride has been described recently (Scheme 1) [13]. Dendron D has been synthesized

---

* To whom all correspondence should be sent:
E-mail: i.grabchev@chem.uni-sofia.bg

by the procedure described by Ghosh et. al. [14]. Absorption spectra were performed using "Thermo Spectronic Unicam UV 500" spectrophotometer. The fluorescence spectra were taken on a "Cary Eclipse" spectrophotometer. Organic solvents were of spectroscopic grade and used without special treatment. The effect of the metal ions on fluorescence intensity was measured by adding a few μl of stock solution (c = 10^{-3} mol l^{-1}) of the metal cations to a known volume of the ligand solution (3 ml). The addition was limited to 0.08 ml, so that dilution remained insignificant [15]. $NaNO_3$, KNO_3, $LiNO_3$, $AgNO_3$, $Cu(NO_3)_2.3H_2O$, $Ni(NO_3)_2.6H_2O$, $Mn(NO_3)_2.6H_2O$, $Co(NO_3)_2.6H_2O$, $Zn(NO_3)_2.4H_2O$, and $Cr(NO_3)_3$, $Fe(NO_3)_3$ salts were the metal cation sources, and were used as obtained from Sigma-Aldrich. IR spectra were recorded on an Infrared Fourier transform spectrometer (IRAffinity-1 Shimadzu) with the diffuse-reflectance attachment (MIRacle Attenuated Total Reflectance Attachment) at a 2 cm^{-1} resolution. ^1H (600.13 MHz) and ^{13}C (150.92 MHz) spectra were acquired on an AVANCE AV600 II+NMR spectrometer. The measurements were carried out in a DMSO-d_6 solution at ambient temperature. The chemical shifts were referenced to a tetramethylsilane (TMS) standard. Electrospray mass spectroscopic measurements were carried out using a Hewlett–Packard Series 1100 MSD.

Synthesis of dendron ED

A solution 0.709 g (1mmol) of compound **E** and 1.24g, (1mmol) of **D** in 50 ml acetone was refluxed in the presence of 0.1500, (1.1 mmol) K_2CO_3 for 8 hours. The process was controlled by thin-layer chromatography and the final product was filtered off with very high yield and purity after pouring the liquor into 500 ml of water. The resulting precipitate was washed with water, and then dried in vacuum at 40°C. Yield: 1.36g, 85.0%.

FT-IR (KBr) cm^{-1}: 1736, 1652, 1619, 1557, 1507, 1455, 1346, 1230, 1085, 1057, 973, 879, 762, 707, 645; ^1H-NMR (DMSO-d6, 600 MHz, ppm): 9.06 (s, 1H, COOH), 8.42 (d, 1 H, j = 7.8 Hz, H-Ar), 8.08 (t. 2H, j = 5.6 Hz, NHCO), 7.90 (d, 1 H, j = 7.4 Hz H-Ar), 7.64 (d, 1 H, j = 7.2 Hz, H-Ar), 7.38 (d, 1 H, j = 7.8 Hz, H-Ar), 6.90 (t, 1 H, j = 7.8 Hz, H-Ar), 4.42 (t. 2H, j = 6.4 Hz, -OCH_2-CO), 3.80 (m, 18H, N-CH_2), 3.61 3.62 (s. 12H, OCH_3), 3.44 (br. 2H, OCH_2), 3.22 (q, 4H, NCH_2C$\underline{H}_2$CONH), 2.91 (br, 4H, NCH_2C$\underline{H}_2$NH), 2.64 (t, 8H, j = 6.5 Hz, NCH_2C$\underline{H}_2$COOCH_3) 2.33 (t, 8H, j = 6.5 Hz, NCH_2C$\underline{H}_2$COOCH_3). API-ES-MS calc. for (1320.8) found 1321.7 (M+H)$^+$; Elemental analysis: $C_{50}H_{59}N_5O_{17}Br_4$ (1320.8): C 45.42% (calc. 45.58%); H 4.46% (calc. 4.39%); N 5.30% (calc. 5.41%)

Antimicrobial assay

The antimicrobial activity of the newly synthesized dendron ED was evaluated in meat-peptone broth towards Gram-positive bacterium *Bacillus subtilis*, Gram-negative bacterium *Pseudomonas aeruginosa* and the yeasts *Candida lipolytica*. Aliquots of sample solution in DMSO (0.1%) were added in test tubes with sterile meat-peptone broth achieving final concentration 50 μg/ml and then inoculated with 1% of each overnight indicator culture. Test tubes without added compound were also prepared for each strain. After incubation of the strains at 26°C for 24h under shaking, the microbial growth was determined by measuring the optical density at 600 nm (OD_{600}). Three independent experiments were carried out and averages are reported.

RESULTS AND DISCUSSION

Scheme 1 presents the synthetic rout of fluorescent dendron **ED**. Initial compound (**E**) was synthesised by the reaction of eosin Y with chloroacetyl chloride following the method described recently [13]. This compound has been used as fluorescent units for the synthesis of fluorescent PAMAM dendron by the reaction with dendron **D**. The final solid product (**ED**) was obtained in high yield, filtrated, washed with water and dried under vacuum.

The basic spectral characteristics of compound **E** and Dendron **D** have been investigated in organic solvents with different polarity and the results have been summarised in Table 1 and Table 2: the absorption (λ_A) and fluorescence (λ_F) maxima, the extinction coefficient (ε), Stokes shift ($\nu_A - \nu_F$), and quantum yield of fluorescence (Φ_F).

Compound **E** has absorption maxima in the region λ_A = 528–540 nm and the respective fluorescence maxima are at λ_F = 547–560 nm. These results suggest that the polarity of the organic solvents influence the position of the absorption and fluorescence maxima. At the organic solvents containing hydroxyl groups, both types of maxima are hypochromically displaced, with this effect being most pronounced for methanol. This is due to the possibility of the formation of hydrogen bonds. The similar results have been obtained for the dendron **ED**. That means the bonding to the dendron chain do not affect the chromophoric system of the monomeric compound **E**. The normalized absorption and fluorescence spectra of dendron **ED** in n-butanol solution are plotted in Fig. 1. As seen the absorption and fluorescence spectra have bands with a single maximum, without vibrational structure. The fluorescence curve is an approximately equal mirror
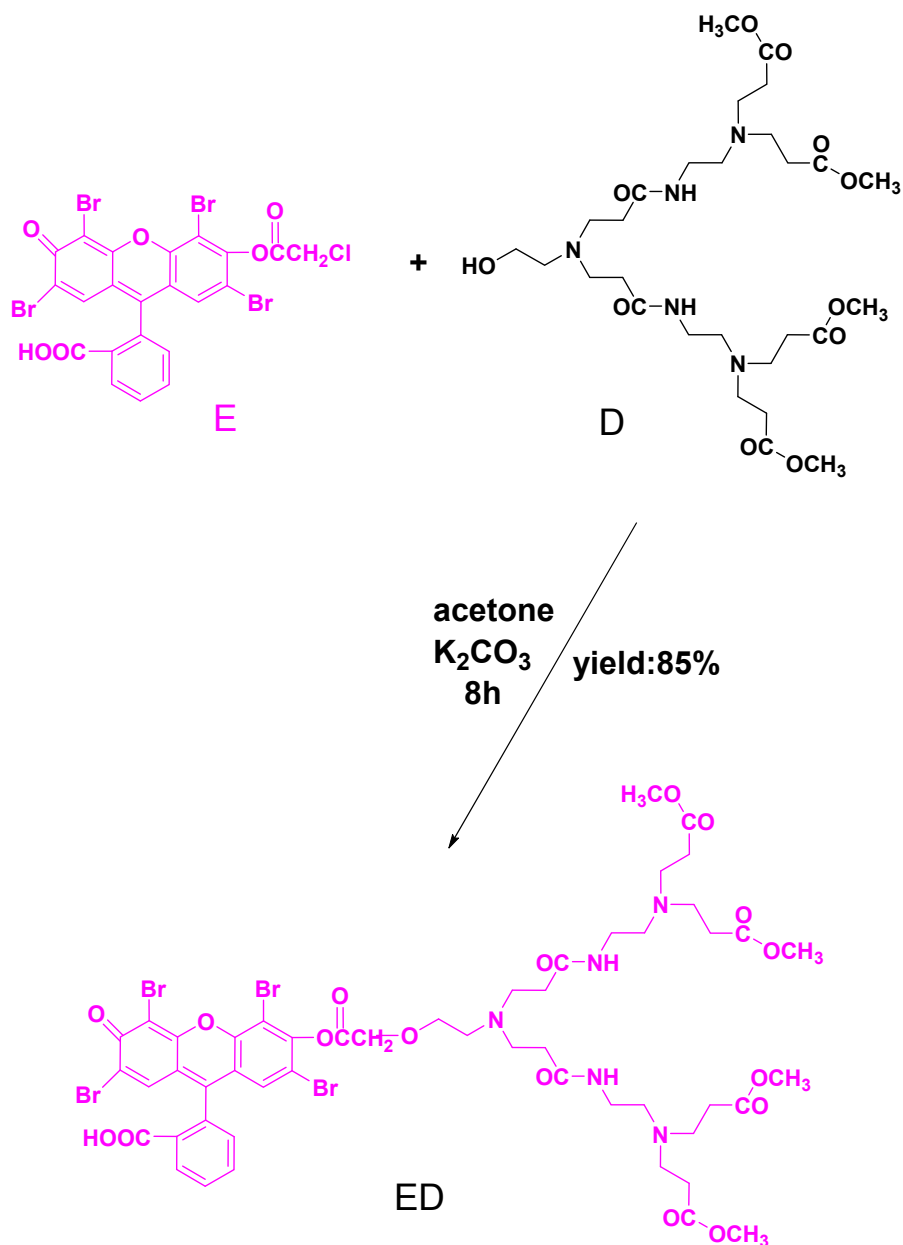
Scheme 1. Synthesis of Dendron **ED**.

Table 1. Photophysical characteristics of compound **E** in organic solvents

	λ_A nm	ε l mol^{-1} cm^{-1}	λ_F nm	$\nu_A - \nu_F$ cm^{-1}	$\lambda\Phi_F$	f
Acetonitrile	539	61300	557	600	0.64	0.345
N,N-dimethylformamide	538	64200	556	602	0.60	0.349
n-Buthanol	530	68000	550	686	0.62	0.366
2-propanol	531	54720	549	617	0.58	0.249
Methanol	528	58970	547	657	0.54	0.289
Chloroform	537	55320	556	636	0.29	0.256
Dichlorometane	537	54300	560	764	0.26	0.241
Tetrahydrofuran	540	66700	559	629	0.28	0.371

Table 2. Photophysical characteristics of dendron **ED** in organic solvents

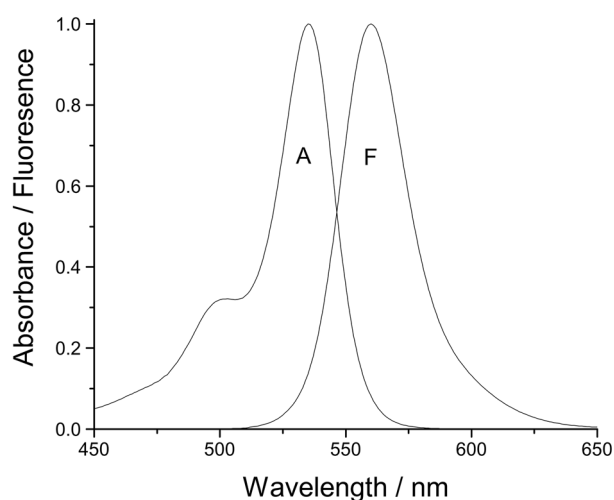|	λ_A nm	ε l mol^{-1} cm^{-1}	λ_F nm	$\nu_A - \nu_F$ cm^{-1}	Φ_F	f
Acetonitrile	538	114000	560	730	0.76	0.542
N,N-dimethylformamide	536	119000	556	671	0.66	0.539
n-Butanol	533	129000	559	872	0.64	0.599
2-propanol	534	130000	560	869	0.56	0.590
Methanol	526	114250	557	1058	0.49	0.534
Chloroform	537	113300	557	668	0.21	0.496
Dichlorometane	536	130600	557	703	0.20	0.558
Tetrahydrofuran	539	149385	560	695	0.24	0.603

Fig. 1. Normalized absorption (A) and fluorescence (F) spectra of dendron ED in butanol solution (c = 1×10^{-6} mol l^{-1}).

The Stokes shift is a parameter, which indicates the difference in the properties and structure of the dyes between the ground state S_0, and the first excited state S_1 and it has been estimated according to Equation (2):

$$(\nu_A - \nu_F) = (1/\lambda_A - 1/\lambda_F) \times 10^{-7} \qquad (2).$$

The Stokes shift values for both compounds are very similar and do not imply any change in the chromophores systems in the excited state. The values are typical for this class of compounds.

The ability of compounds **E** and **ED** to emit absorbed light energy has been characterized by the fluorescence quantum yield Φ_F using Rhodamine 6G as a standard. It has been calculated on the basis of the absorption and fluorescence spectra in organic solvents using Equation (3).

$$\Phi_F = \Phi_{st} \frac{S_u}{S_{st}} \frac{A_{st}}{A_u} \frac{n_{Du}^2}{n_{Dst}^2} \qquad (3)$$

where the Φ_F is the emission quantum yield of the sample, Φ_0 is the emission quantum yield of standard, Ast and Au represent the absorbance of the standard and sample, respectively, while Ist and Iu are the integrals of the emission of the standard and sample respectively, and n_{Dst} and n_{Du} is the refractive index of the standard and sample.

As seen from the data in Table 1 and Table 2, the quantum yield depend strongly from the polarity of the solvents. Higher values have been obtained in polar solvents which are more than three times compared to the non polar solvents.

image of the absorption curve what is indicative of the molecular structure of the dendrimer in excited state and prevailing fluorescence emission.

An important characteristic of the fluorescence compounds is the oscillator strength (*f*) which reveals the effective number of electrons whose transition from ground S_0 to excited S_1 state gives the absorption area in the spectrum. Values of the oscillator strength can be calculated using Equation (1):

$$f = 4.32 \times 10^{-9} \, \Delta\nu_{1/2} \, \varepsilon max \qquad (1),$$

where $\Delta\nu_{1/2}$ is the width of the absorption band (in cm^{-1}) at 1/2 εmax.

The values obtained for **E** are: *f* = 0.249–0.366 and for the dendron **ED** the values are higher *f* = 0.496–0.603. The higher values correlate well with the hypochromic effect of the **ED** in the respective organic solvents.

Influence of pH on the fluorescence intensity of E and ED

The influence of pH on the absorbance and fluorescence intensity of compounds **E** and **ED** have
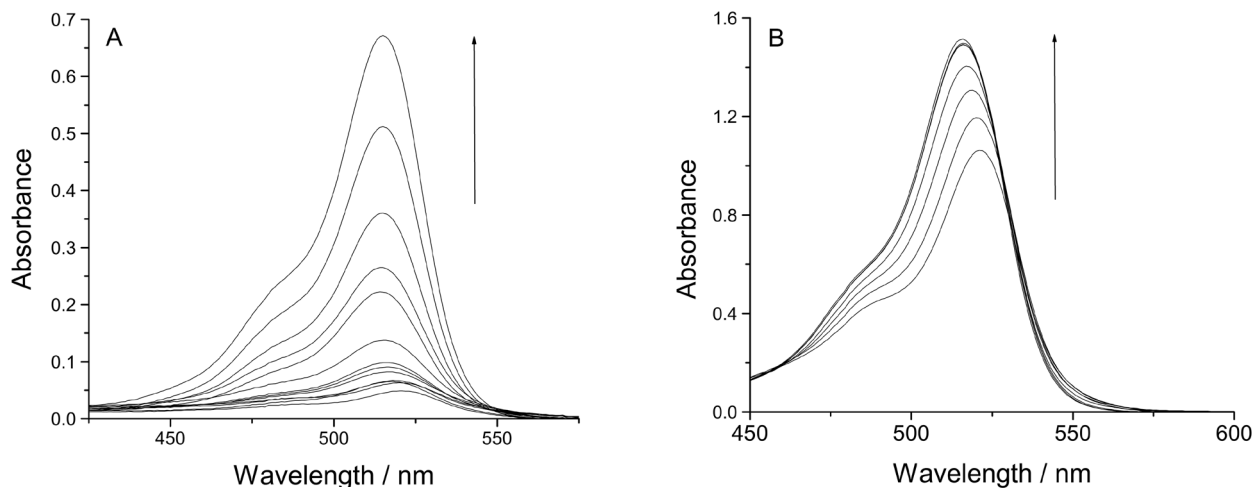
Fig. 2. Effect of pH in range from 3.5 to 12.0 on absorbance of compound **E** (A) and Dendron **ED** (B) in ethanol/water solution (1:4 v/v).

been investigated in ethanol/water (1:4 v/v) solution. In Fig. 2 are plotted the absorption spectra of both compounds in the pH range from 3.5 to 12.0. In the case of monomer compound **E** ($c = 1 \times 10^{-6}$ mol l^{-1}) the absorption maxima change it position from λ_A = 522 nm in acidic medium to λ_A = 515 (Fig. 2A). Also, a drastic increase in the molar absorbance of the compound was observed, with the molar extinction coefficient of ε = 49900 l mol^{-1} cm^{-1} in acidic medium was increase to ε = 67100 l mol^{-1} cm^{-1} in the alkaline medium. The same investigations were conducted for dendron **ED** and the results obtained are shown in Fig. 2B. It can be seen the effect of pH on absorption of dendron **ED** is less pronounced. In this case, a hypochromic displacement of the absorption maximum was observed by 10 nm, but the molar extinction coefficient increased significantly less.

Figure 3 presents the normalized fluorescence intensity of compounds **E** and **ED** depending on the pH of the medium. Figure 3 shows that both compounds have different behaviour. For compound **E**, the fluorescence intensity slightly increased in the interval pH = 3.5–10.0 after which in strong alkaline medium (pH = 10–12) the emitted fluorescence has increased significantly. In the case of dendron **ED**, the influence of pH of the medium is negligible and the fluorescence has almost the same intensity in the interval of pH 3.5–12.0.

*Influence of metal cations on the photophysical properties of **ED***

Different metal ions (Li$^+$, Na$^+$, K$^+$, Ag$^+$, Co^{2+}, Zn^{2+}, Mn^{2+}, Ni^{2+}, Cu^{2+}, Fe^{3+} and Cr^{3+}) upon the fluorescent intensity of DMF solutions of **ED** has been
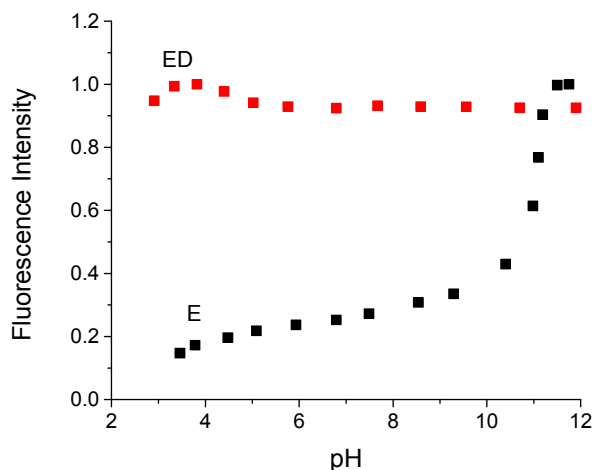

Fig. 3. Dependence of fluorescence intensity from pH of compounds **E** and **ED**.

studied with regards with its potential applications as a detector for metal ions. DMF has been chosen for the fluorescence experiments because it is good solvent for dendron **ED**, metal salts used as well as for the formed metal complex.

In DMF solution the free of metal cations, dendron **ED** has a good fluorescence emission with quantum yields Φ_F = 0.66. Fluorescence emission decreases after the addition of metal ions into the solution and the effect of the guest metal cations in the solution is signalled by fluorescence quenching factor (FQ) (Fig. 4). The fluorescence enhancement factor FQ = F_0/F is determined from the ratio of initial fluorescence intensity (F_0 before metal ions addition) and minimum fluorescence intensity (F after addition of metal ions). As seen in Fig. 3, the
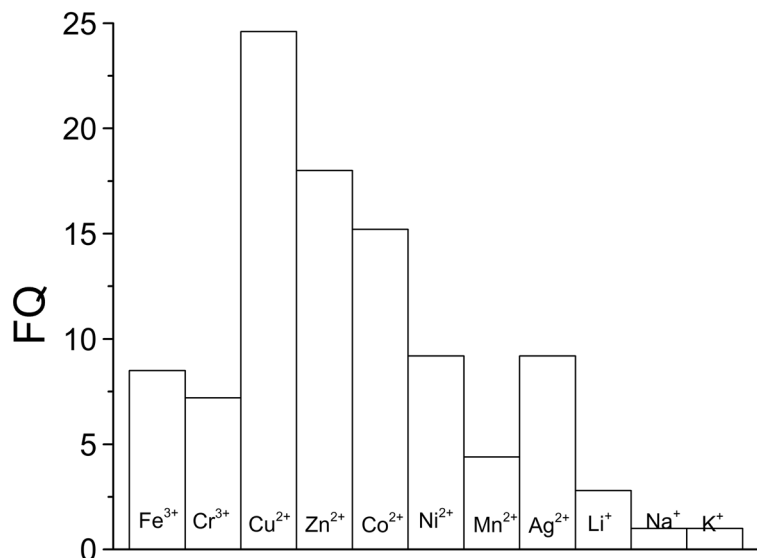
Fig. 4. Fluorescence quenching factor (*FQ*) of **ED** (c = 1×10^{-6} mol l^{-1}) in the presence of different metal cations (c = 1×10^{-6} mol l^{-1}) in DMF solution.

metal cations lead to a decrease in the fluorescence intensity which is different for each metal ion. The highest value is observed in the presences of Cu^{2+} (FQ=24.6). A good reduction of the fluorescent emission has been observed for Zn^{2+} and Co^{2+}. An average fluorescence quenching has been observed in the presence of Ag^+, Ni^{2+}, Cr^{3+} and Fe^{3+}. Metal ions such as Li^+ and Mn^{2+} cause a slight reduction, while alkali metal ions as Na^+ and K^+, have not effect on the fluorescence intensity of dendron **ED**. The rank of the response can be presented as follows: Cu^{2+} > Zn^{2+} > Co^{2+} > Ni^{2+} ≈ Ag^+ ≈ Fe^{3+} ≈ Cr^{3+} > Mn^{2+} > Li^+ > Na^+ ≈ K^+.

Most probably during the complex formation Cu^{2+} are the most competitive in the reaction with tertiary nitrogen atoms comprised dendron structure. That ensures a stability of the complex thus formed which is greater than that of complexes formed with the other metal ions studied.

In order to quantify the effect of Cu^{2+} on the fluorescence intensity we have performed detailed titration experiments. The typical change in the fluorescence intensity of **ED** induced by Cu^{2+} is plotted in Fig. 5 as an example. As seen, the addition of Cu^{2+} leads to a reduction in the fluorescence intensity. A pronounced increase in the fluorescence intensity
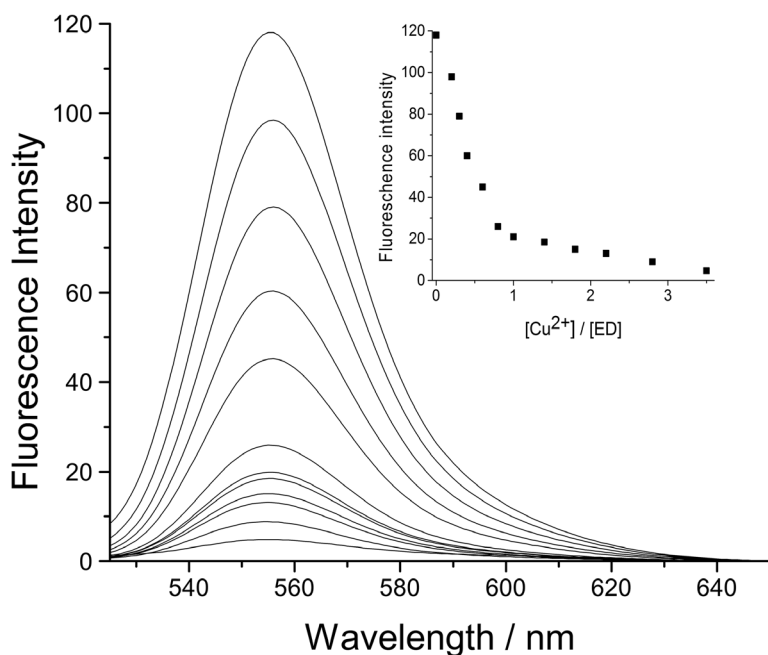

Fig. 5. Fluorescence spectra of **ED** (c = 1×10^{-6} mol l^{-1}) in DMF at various concentrations of Cu^{2+} cations. The concentrations of Cu^{2+} cations are in the order of increasing intensity from 0 to 4×10^{-6} mol l^{-1}.

has been observed by increasing the concentration of Cu^{2+} cations up to 1.0×10^{-6} mol l^{-1} and above this concentration the change in the fluorescence intensity is negligible. The inset in Fig. 5 shows the plots of fluorescence intensity versus Cu^{2+} concentration which demonstrate than one metal ion coordinate with **ED**. From Fig. 5 also it is seen that during the titration with Cu^{2+} ions the position of the fluorescence maximum do not change its position in the presence of Cu^{2+} ions. This indicates that Cu^{2+} ions do not coordinates directly with the chromophor system of Eusin Y unites. The possible coordination of metal ions with dendron **ED** is with him aliphatic part as it is presented in Scheme 2.

The fluorescence titration profile shows that a linear curve appears (R = 0.982) in $0 \div 8 \times 10^{-7}$ mol l^{-1} concentration range of Cu^{2+} cations (Fig. 6). A detection limit of 9.2×10^{-8} mol l^{-1} for Cu^{2+} has been determined [16]. Such a linear curve and a detection limit are sufficient enough to sense and determine Cu^{2+} ions.

In this case the formed metal complex probably destabilizes the planarity of the Eosin Y chromophore system. The non-radiative deactivation during the transition from S_1 to the S_0 prevails leads to decrease in the fluorescence quantum yield (Fig. 7). The lowest Φ_F has been observed in the presence of Cu^{2+} cations ($\Phi_F = 0.02$).

Antimicrobial activity of ED

The results for antimicrobial activity showed that the new dendron **ED** in concentration 50 µg/ml inhibited the growth of the used test cultures (Fig. 8).
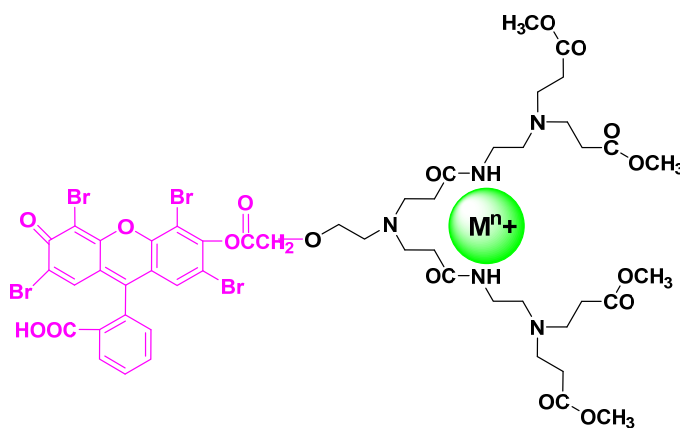
Scheme 2. Proposed mechanism of complexation.
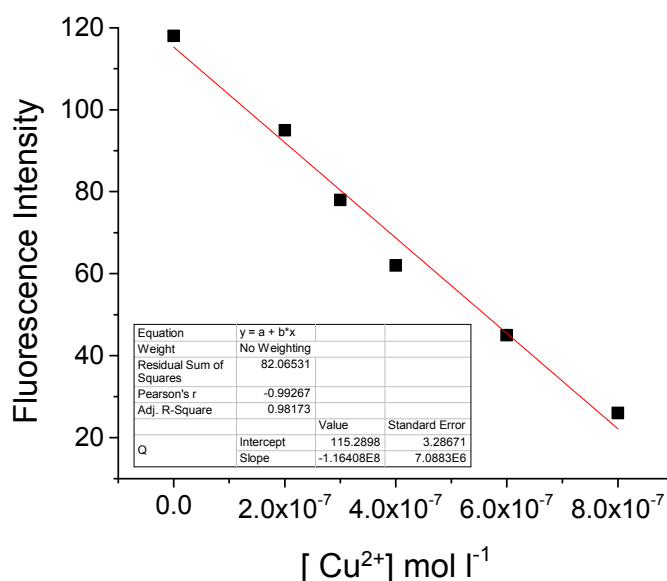
Fig. 6. Dependence of fluorescence intensity of dendron **ED** (c = 1×10^{-6} mol l^{-1}) in the presence of different amount of Cu^{2+}.
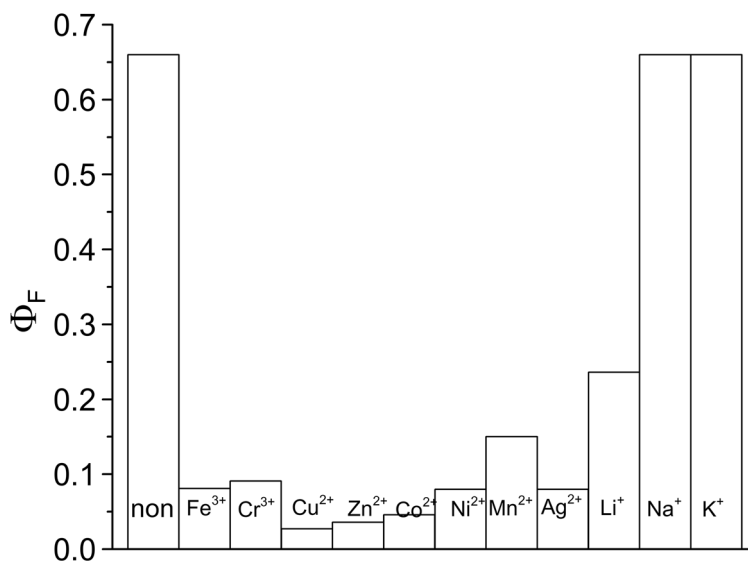
Fig. 7. Quantum yield of dendron **ED** (c = 1×10⁻⁶ mol l⁻¹) in DMF solution in presence of metal ions.
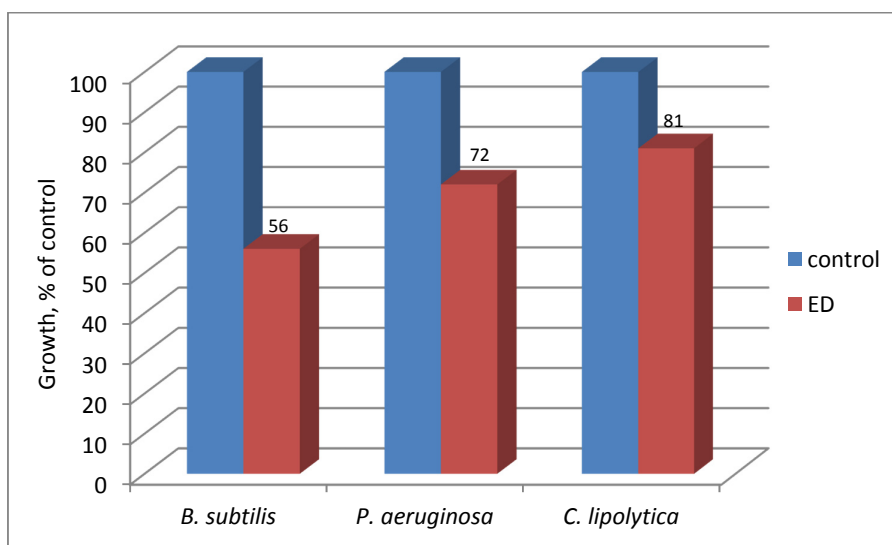
Fig. 8. The effect of **ED** on the growth of *B. subtilis, P. aeruginosa* and *C. lipolytica* tested in meat-peptone broth (MPB).

Gram-positive *B. subtilis* was sllightly more sensitive than Gram-negative *P. aeruginosa*: ED decreased the growth of *B. subtilis* and *P. aeruginosa* by 44% and 28%, respectively. This could be attributed to the different outer structural arrangement of the bacterial cell walls: Gram-negative bacteria have an additional outer membrane when compared to Gram-positive bacteria. The yeasts *C. lipolytica* showed higher resistance to ED than the bacterial strains with growth reduction of 19%.

CONCLUSION

A new fluorescent PAMAM dendron has been synthesized and characterized. Its basic photophysical characteristics have been investigated in organic solvents of different polarity and it has been found solvent dependence. The influence of various metal cations Li^+, Na^+, K^+, Ag^+, Co^{2+}, Zn^{2+}, Mn^{2+}, Ni^{2+}, Cu^{2+}, Fe^{3+} and Cr^{3+}) on the fluorescence intensity of the new Dendron has been investigated in DMF

solution with regard to its potential application as a fluorescent sensor for metal ions. It has been shown that the fluorescence intensity depends strongly on the nature of metal cations. Fluorescence quenching has been observed. The new compound exhibited good antimicrobial activity against Gram-positive and Gram-negative bacteria and yeasts, which makes this new PAMAM dendron interesting for biological applications.

REFERENCES

1. E. Sorsak, J. Volmajer Valh, S. Kornet Urek, A. Lobnik, *Analyst*, **140**, 976 (2015).
2. P. Passaniti, M. Maestri, P. Ceroni, G. Bergamini, F. Vogtle, H. Fakhrnabavi, O. Lukin, *Photochem. Photobiol. Sci.*, **6**, 471 (2007).
3. K. Kaastrupa, H. D. Sikes, *RSC Adv.*, 5, 15652 (2015).
4. T. H. Ghaddar, J. K. Whitesel, M. A. Fox, J. Phys. Chem. B, **105**, 8729 (2001).
5. V. Balzani, P. Ceroni, S. Gestermann, C. Kauffmann, M. Gorka, F. Vögtle, *Chem. Commun*., **2000**, 853 (2000).
6. P. Froehling, *Dyes Pigments*, **48**, 187 (2001).
7. I. Grabchev, D. Staneva, R. Betcheva, *Curr. Med. Chem*., **19**, 4976 (2012).
8. I. Grabchev, P. Bosch, D. Staneva, *J. Photochem. Photobiol. A*, **222**, 288 (2011).
9. D. Staneva, M. S. I. Makki, T. R. Sobahi, P. Bosch, R. M. Abdel-Rahman, A. Asiri, I. Grabchev, *J. Lumin*., **162**, 149 (2015).
10. V. Bojinov, N. Georgiev, *J. Chem. Technol. Metallurgy*, **46**, 3 (2011).
11. J. Gao, P. Wang, R. W. Giese, *Anal. Chem.*, **74**, 6397 (2002).
12. M. O. Okuom, M. V. Wilson, A. Jackson, A. E. Holmes, *Int. J. Spectrosc*., **2013**, Art. 245376 (2013).
13. D. Staneva, I. Grabchev, P. Bosch, *Int. J. Polym. Mater*., **64**, 838 (2015).
14. S. Ghosh, A. Banthia, *Tetrahedron Lett*., **42**, 501 (2001).
15. S. Banthia, A. Samanta, *J. Phys. Chem. B*, **110**, 6437 (2006).
16. T. Little, *BioPharm. Int.*, 28, 48 (2015).

НОВ ФЛУОРЕСЦЕНТЕН ПАМАМ ДЕНДРОН СЪС СЕНЗОРНА И МИКРОБИОЛОГИЧНА АКТИВНОСТ

Д. Станева[1], Е. Василева-Тонкова[2], И. Грабчев[3]*

[1] *Химикотехнологичен и Металургичен Университет, 1756 София, България*

[2] *Стефан Ангелов Институт по Микробиология, БАН, 1113 София, България*

[3] *Софийски Университет „Св. Климент Охридски", Факултет по медицина, 1407 София, България*

(Резюме)

Синтезиран и охарактеризиран е нов дендрон, съдържащ еозин Y като флуоресцентен фрагмент. Изследвани са основните фотофизични характеристики на дендрона в органични разтворители с различна полярност и получените резултати са сравнени с модифициран еозин Y, използван при синтеза на флуоресцентния дендрон. В присъствието на различни по природа метали катиони (Li$^+$, Na$^+$, K$^+$, Ag$^+$, Co^{2+}, Zn^{2+}, Mn^{2+}, Ni^{2+}, Cu^{2+}, Fe^{3+} и Cr^{3+}) новосинтезираният дендрон гаси флуоресцентната си интензивност, като гасенето зависи от природата на металните катиони. Установено е, че интензитетът на флуоресценцията на дендрона не се влияе от pH на средата, за разлика от модифицирания момомерен еозин Y. Тествана е антимикробната активност на дендрона в месо-пептонен бульон спрямо някои бактерии и дрожди.

Novel asymmetric azaquinolizinium monomethine cyanine dyes versus a Thiazole Orange analog: a comparison of photophysical and dsDNA binding properties

A. A. Vasilev[1], M. I. Kandinska[1]*, Y. Zagranyarski[1], D. Sucunza[2], J. J. Vaquero[2], O. D. Castaño[2], S. E. Angelova[2,3]

[1] Faculty of Chemistry and Pharmacy, Sofia University "St. Kliment Ohridski", 1164 Sofia, Bulgaria
[2] Departamento de Química Orgánica y Departamento de Química Física, Universidad de Alcalá, E-28871 Alcalá de Henares, Madrid, Spain
[3] Institute of Organic Chemistry with Centre of Phytochemistry, Bulgarian Academy of Sciences, 1113 Sofia, Bulgaria

New asymmetric monomethine cyanine dyes containing an azaquinolizinium core have been synthesized using novel 4-chloropyridopyrimidinium chlorides as building blocks. The photophysical properties of the dyes have been compared to those of a novel monomeric tricationic Thiazole Orange (TO) analog. Compounds **8** and **13** have very low fluorescence in TE buffer in the absence of dsDNA, but after binding to dsDNA a dramatic increase in the fluorescence intensity was observed. Computational tools (DFT and TDDFT calculations) have been employed in studying the relationship between the chemical structure and the optical properties of the chromophores.

Keywords: cyanine dyes, DNA, fluorescence, azaquinolizinium salts, Thiazole Orange.

INTRODUCTION

Asymmetric cyanine dyes have attracted considerable interest due to their excellent nucleic acid staining properties. In the absence of DNA, such dyes have negligible fluorescence but upon binding to biomolecule they usually exhibit a large enhancement of the fluorescence intensity [1]. As a result, cyanine dyes are widely used as fluorophores for DNA detection and visualization in various applications [2–4]. A wide range of novel examples with similar properties based mainly on TO and Oxazole Yellow (YO) have been designed, synthesized and commercialized [5, 6]. In this scientific area two general strategies for discovering more efficient fluorescent nucleic acid stains have been used. The first approach is to improve the already well known bio-labels. The second approach is to design and create new types of fluorophores based on novel heterocyclic compounds. As an extension of our previous studies on the synthesis and exploration of the properties of new nucleic acid fluorescent stains [7], we report here a synthetic route for the preparation of new asymmetric azaquinolizinium monomethine cyanine dyes and compare their photophysical properties with those of a new tricationic analog of TO. Computational tools are employed in an effort to understand the relationships between the chemical structure and the optical properties of the fluorochromes.

EXPERIMENTAL

All solvents used in the present work were HPLC grade and commercially available. Column chromatography was performed on Silica gel 60, pore size 60 Å, 230–240 mesh, 40–63 μm particle size (Fluka). The starting materials **1a**, **1b**, **2** and **3** are commercially available and they were used as supplied. Melting points were determined on a Büchi MP B-545 apparatus and are uncorrected. NMR spectra were obtained on a Bruker Avance II+ 600 spectrometer in CDCl$_3$ and on a Bruker III HD Avance-500 spectrometer in DMSO-d$_6$. UV-vis spectra were measured on a Unicam 530 UV-VIS spectrophotometer and the fluorescence spectra were obtained on a Cary Eclipse fluorescence spectrophotometer (Varian, Australia). Intermediates **7** and **9** were synthesized by methods described in the

---

literature [8]. Details about the synthesis and the purification of dye **13** will be published elsewhere.

Synthesis of 2,2-dimethyl-5-((pyridin-2-ylamino) methylene)-1,3-dioxane-4,6-dione (4a) and 5-(((4-bromopyridin-2-yl)amino)methylene)-2,2-dimethyl-1,3-dioxane-4,6-dione (4b)

A mixture of 2-aminopyridine (**1a**) or 4-bromo-2-aminopyridine (**1b**) (10 mmol), Meldrum's acid (1.1 equiv. toward **1a** or 1.25 equiv. toward **1b**) and triethyl orthoformate (12 ml) was stirred at 100°C for 30 min. The excess of triethyl orthoformate was evaporated under reduced pressure. The crude product was purified by recrystallization from methanol (**4a**) or recrystallization from chloroform (**4b**). **4a:** Yield 93%, ^{1}H-NMR (δ (ppm), CDCl$_3$, 600 MHz): 1.76 (s, CH$_3$, 6H); 7.04 (dt, CH, $^3J_{HH}$ = 8.1 Hz, $^4J_{HH}$ = 0.7 Hz, 1H); 7.18 (ddd, CH, $^3J_{HH}$ = 7.4 Hz, $^3J_{HH}$ = 4.9 Hz, $^4J_{HH}$ = 0.8 Hz, 1H); 7.76 (ddd, CH, $^3J_{HH}$ = 8.1 Hz, $^3J_{HH}$ = 7.5 Hz $^4J_{HH}$ = 1.9 Hz, 1H); 8.42 (dd, CH, $^3J_{HH}$ = 4.8 Hz, $^4J_{HH}$ = 1.0 Hz, 1H); 9.42 (d, CH, $^3J_{HH}$ = 13.5 Hz, 1H); 11.30 (d, NH, $^3J_{HH}$ = 12.8 Hz, 1H). **4b:** Yield 93%, ^{1}H-NMR (δ (ppm), CDCl$_3$, 600 MHz): 1.76 (s, 6H, CH$_3$); 7.27 (d, 1H, $^4J_{HH}$ = 0.6 Hz); 7.33 (dd, 1H, CH, $^3J_{HH}$ = 5.3 Hz, $^4J_{HH}$ = 0.8 Hz); 8.24 (d, 1H, CH, $^3J_{HH}$ = 5.3 Hz); 9.38 (d, 1H, CH, $^3J_{HH}$ = 13.3 Hz); 11.27 (d, 1H, NH, $^3J_{HH}$ = 13.0 Hz).

Synthesis of 4H-pyrido[1,2-a]pyrimidin-4-one (5a) and 8-bromo-4H-pyrido[1,2-a]pyrimidin-4-one (5b)

A mixture of **4a** (3 mmol) or **4b** (3 mmol) and *Dowtherm A* (20 ml) was refluxed for 30 min. The reaction mixture was filtered through silica and washed with hexane to remove *Dowtherm A* and the compound was eluted with ethyl acetate (**5a**) or dichloromethane/ethyl acetate (**5b**). **5a**: Yield 90%, Mp: 129–130°C (from methanol); ^{1}H-NMR (δ (ppm), CDCl$_3$, 600 MHz): 6.47 (d, CH, $^3J_{HH}$ = 6.3 Hz, 1H); 7.19 (td, CH, $^3J_{HH}$ = 7.0 Hz, $^3J_{HH}$ = 1.3 Hz, 1H); 7.69 (d, CH, $^3J_{HH}$ = 8.9 Hz, 1H); 7.77 (ddd, CH, $^3J_{HH}$ = 8.4 Hz, $^3J_{HH}$ = 6.6 Hz, $^4J_{HH}$ = 1.5 Hz, 1H); 8.31 (d, CH, $^3J_{HH}$ = 6.3 Hz, 1H); 9.10 (d, CH, $^3J_{HH}$ = 7.1 Hz, 1H). **5b**: Yield 87%. ^{1}H-NMR (δ (ppm), CDCl$_3$, 600 MHz): 6.44 (d, CH, $^3J_{HH}$ = 6.4 Hz, 1H); 7.23 (dd, CH, $^3J_{HH}$ = 7.6 Hz, $^3J_{HH}$ = 2.1 Hz, 1H); 7.85 (dd, CH, $^4J_{HH}$ = 2.1 Hz, $^5J_{HH}$ = 0.7 Hz, 1H); 8.25 (d, CH, $^3J_{HH}$ = 6.4 Hz, 1H); 8.90 (dd, CH, $^3J_{HH}$ = 7.6 Hz, $^5J_{HH}$ = 0.7 Hz, 1H).

Synthesis of 4-chloropyrido[1,2-a]pyrimidin-5-ium chloride (6a) and 8-bromo-4-chloropyrido[1,2-a] pyrimidin-5-ium chloride (6b)

To a solution of **5a** (1 mmol) or **5b** (1 mmol) in dichloromethane were added phosphoryl chloride

(5 mmol) and DMF (1 drop). The reaction mixture was refluxed and stirred vigorously under argon for 4 h. Then was allowed to cool down to room temperature and diethyl ether (40 mL) was added. The resulting precipitate was filtered and dried in a desiccator. The target compounds **6a** and **6b** are highly hygroscopic and unstable. They were used in the next step without further purification. **6a:** Yield 95%; **6b:** Yield 98%.

Synthesis of 4-((4H-pyrido[1,2-a]pyrimidin-4-ylidene)methyl)-1-benzylquinolin-1-ium iodide (8) and 2-((8-bromo-4H-pyrido[1,2-a]pyrimidin-4-ylidene)methyl)-3-(3-(pyridin-1-ium-1-yl)propyl) benzo[d]thiazol-3-ium iodide (10)

Compound **6a** (1 mmol) or **6b** (1 mmol) and an appropriate quaternary ammonium salt **7** or **9** (1.2 mmol) were finely ground in a mortar and the mixture was transferred to a 50 ml reaction flask, equipped with a condenser and an electromagnetic stirrer. The flask was flushed with argon and methanol (10 mL) was added. The reaction mixture was heated at 50°C for 5 min and DIPEA (2.1 mmol) was added dropwise. Then the mixture was stirred at room temperature for 2 h and the resulting precipitate was filtered off and air dried. The target dyes were purified by flash column chromatography (dichloromethane/methanol mixture of increasing polarity up to 10/1) and subsequently crystallized from methanol/diethyl ether = 1/3. **8:** Yield 82%, Mp: 174–175°C; ^{1}H-NMR (δ(ppm), DMSO-d$_6$, 500 MHz): 5.74 (d, $^3J_{HH}$ = 22.0 Hz, CH, 1H), 5.81 (s, CH$_2$, 2H), 6.31 (brs, CH, 1H), 7.25–7.43 (m, CH, 9H), 7.59–7.63 (m, CH, 2H), 7.75–7.71 (m, CH, 2H), 7.84 (m, CH, 1H), 8.09 (brs, CH, 2H). ^{13}C-NMR (δ (ppm), DMSO-d$_6$, DEPT 135 MHz): 56.7 (CH$_2$), 109.13 (CH), 109.69 (CH), 118.55 (CH), 126.59 (CH), 126.69 (CH), 126.99 (CH), 127.05 (2CH), 126.52 (CH), 128.41 (CH), 128.55 (CH), 129.51 (2CH), 129.53 (CH), 129.66 (CH), 129.76 (CH), 133.20 (CH), 144.09 (CH). Elemental analysis for C$_{25}$H$_{20}$IN$_3$ (Mw = 489.07) C(%): Calculated 61.36; Found 60.92; H(%) Calculated 4.12; Found 4.00; N (%): Calculated 8.59; Found 8.73. **10:** Yield 41%, Mp: 251–251°C; ^{1}H-NMR (δ(ppm), DMSO-d$_6$, 500 MHz): 1.22–1.26 (m, CH$_2$, 2H), 2.61–2.68 (m, NCH$_2$, 2H), 4.51 (brs, N$^+$CH$_2$, 2H), 6.42 (s, CH, 1H), 7.19–7.22 (m, CH, 3H), 7.43–7.48 (m, CH, 2H), 7.59–7.64 (m, CH, 4H), 7.86 (brs, CH, 1H), 8.09 (brs, CH, 2H), 8.25–8.83 (m, CH, 2H). ^{13}C-NMR (δ (ppm), DMSO-d$_6$, DEPT 135 MHz): 29.59 (CH$_2$), 57.97 (NCH$_2$), 57.98 (N$^+$CH$_2$), 113.22 (CH), 125.22 (CH), 125.83 (CH), 128.52 (CH), 128.54 (CH), 128.57 (CH), 128.63 (CH), 128.69 (CH), 145.21 (CH), 150.23 (CH), 153.20 (CH), 153.79 (CH), 153.88 (CH), 171.12 (CH), 175.41 (CH). Elemental

analysis for $C_{24}H_{21}BrI_2N_4S$ (Mw = 729.88) C(%): Calculated 39.42; Found 39.48; H(%): Calculated 2.89; Found 2.67; N (%): Calculated 7.66, Found 7.82.

COMPUTATIONAL

The molecular ground state geometries of the cationic fragments of **8**, **10** and **13** with/without Cl⁻ counterions were fully optimized using B3LYP [9, 10] functional. The diffuse function-augmented 6–31G(d,p) [11–13] basis set was adopted for all atoms. C_1 symmetry was assumed for all systems and default convergence criteria were used; local minima were verified by establishing that the Hessians had zero negative eigenvalues. The structures with counterions were optimized in methanol by using IEFPCM (Integral Equation Formalism Polarizable Continuum Model) [14] method. TDPBE0/6–311+G(2d,p) calculations were performed to compute the 20 lowest excited states of each structure. Solvent effects were included in TDDFT calculations (via IEFPCM). All calculations were performed using Gaussian 09 [15]. The PyMOL molecular graphics system was used to generate the molecular graphics images [16].

RESULTS AND DISCUSSION

The 4*H*-pyrido[1,2-*a*]pyrimidin-4-one scaffold is a privileged structure [17–19] in medicinal chemistry. In general this compound is synthesized from 2-aminopyridine using β-diesters as ring-closure reagents (such as *Meldrum's* acid, for example) [20–25].

Applying reaction conditions modified by us [26–29], the 4*H*-pyrido[1,2-*a*]pyrimidin-4-one derivatives **5a** and **5b** were prepared in high yields and their structures were confirmed by NMR spectroscopy (Scheme 1).

The chlorination of intermediates **5a** and **5b** in DCM in the presence of DMF as a catalyst (Scheme 1) furnished the target 4-chloropyridopyrimidinium salts **6a** and **6b** in excellent yields (Scheme 2).

Monomethine cyanine dyes such as TO or its analogs can be synthesized according to Brooker's method [2, 30–33], running along with side reactions and including the evolution of methyl mercaptan (methanethiol) – the toxic by-product with a very unpleasant odor [34]. In an effort to avoid these problems, the azaquinolizinium dyes **8** and **10** and the novel tricationic TO analog **13** (Scheme 2) were synthesized by an environmentally more benign method that was successfully applied previously by our group [35–37].

The newly synthesized cyanine dyes **8**, **10** and **13** were characterized by NMR and UV-VIS spectroscopy and by elemental analysis.

The photophysical properties of dyes **8** and **10** were evaluated and the data were compared to those of the new tricationic TO analog **13**. Three absorption bands were observed for a methanol solution of dye **8** at wavelengths of 562 nm, 590 nm and 710 nm and these can be associated with different types of aggregates [38]. Similar behavior was observed for a methanol solution of dye **10** (Fig. 1A) with a hypsochromically shifted shoulder (H-aggregates) toward the main absorption signal.
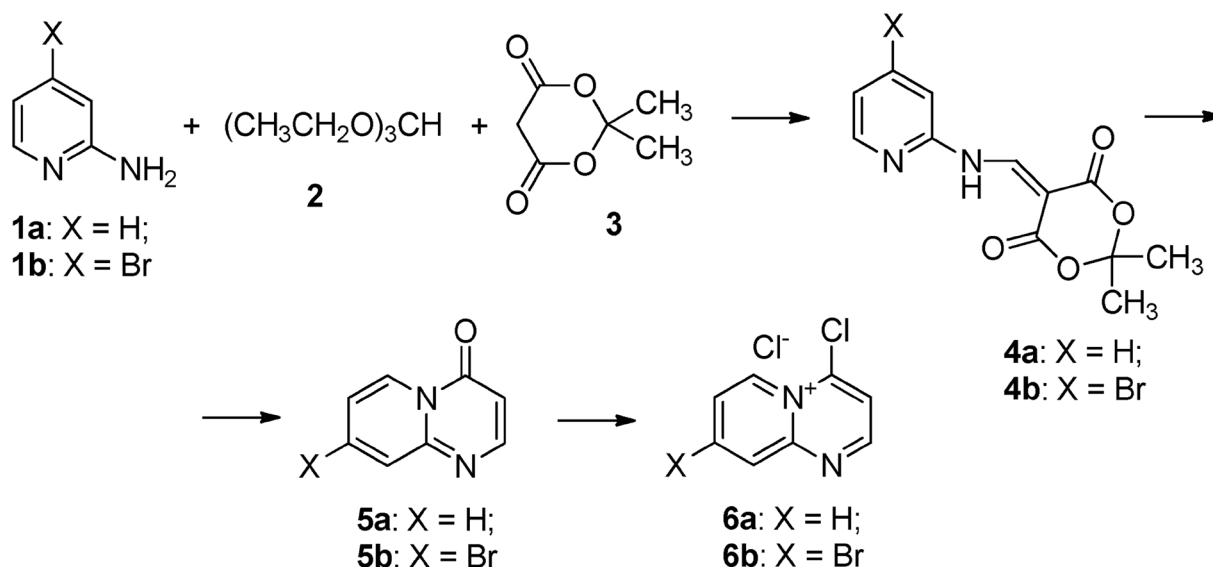
Scheme 1
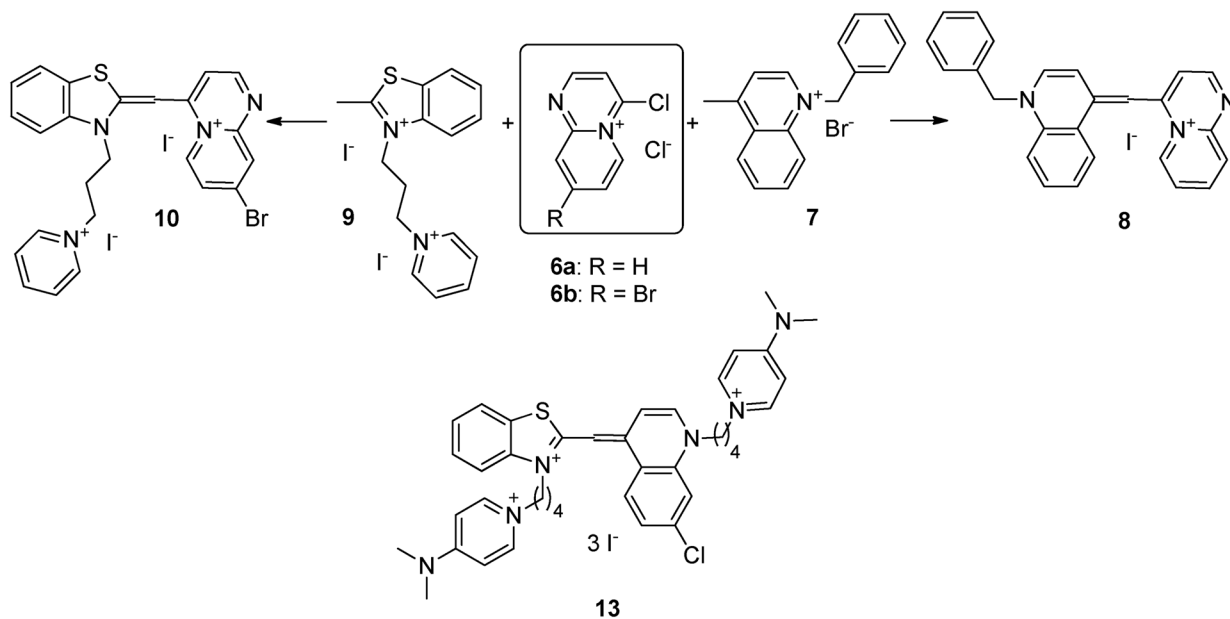
Scheme 2

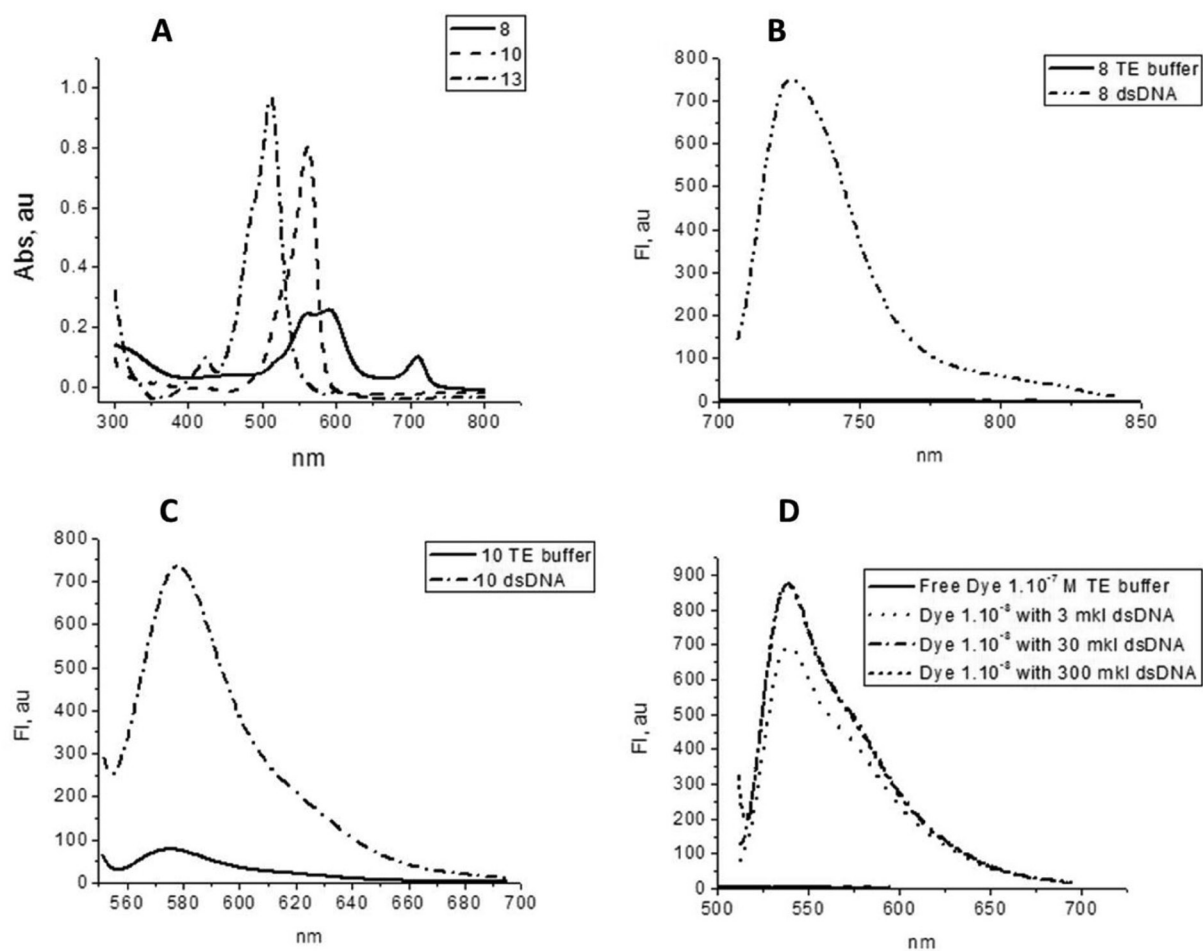**Fig. 1.** (A) Absorption spectra of dyes **8**, **10** and **13** in methanol (1.10^{-5} M); (B) Increase in the fluorescence of dye **8** in the presence of dsDNA in TE buffer solution; (C) Change in the fluorescence of dye **10** in TE buffer in the presence of dsDNA; (D) Fluorescence of free dye **13** in TE buffer and varied concentration of dsDNA.

Table 1. Photophysical properties of dyes 8, 10 and 13 in methanol and in TE buffer in the absence and in the presence of dsDNA

Dye	Absorption			Fluorescence				
	Abs^a	Abs^b	Abs^c	$\lambda_{max}^{\,d}$	$I_{fl0}^{\,d}$	$\lambda_{max}^{\,e}$	$I_{fl}^{\,e}$	Ratio I_{fl}/I_{fl0}
8	562 (24 500)	556	561	598	22	-----	-----	----
	590 (25 600)			629	1.6	-----	-----	-----
	710 (9 960)	706	710	718	0.6	726	750	1250
10	562 (80 600)	559	567	578	51	578	734	14
13	513 (97 000)	513	521	538	4.3	538	875	203

[a] λ_{max} (nm) and molar absorptivity ε (l.mol^{-1}.cm^{-1}) of free dyes in methanol; [b] λ_{max} (nm) of free dye in TE buffer; [c] λ_{max} (nm) of dye-dsDNA complex in TE buffer; [d] λ_{max} (nm) and I_{fl0} of free dye in TE buffer; [e] λ_{max} (nm) and I_{fl} of complex dye-dsDNA in TE buffer.

The absorption spectrum of dye **8** in TE buffer in the absence of DNA contains two peaks at 556 nm and 706 nm and these are shifted bathochromically to 561 nm and 710 nm, respectively, in the same buffer in the presence of dsDNA (Table 1). A bathochromic shift of the absorption signal for dye **10** was observed in TE buffer from 559 nm for the free dye to 567 nm in the presence of dsDNA (Table 1). These effects provide evidence for intercalation, as reported in other investigations into cyanine dyes [39].

Dye **8** shows three fluorescence bands in TE buffer. Fluorescence was not observed in the presence of dsDNA in the buffer solution upon excitation at the shorter wavelength bands (598 nm and 629 nm). The longest wavelength fluorescence band of **8** at 718 nm is characterized by very low intrinsic fluorescence intensity, but excitation at 718 nm in the presence of dsDNA led to a dramatic increase in the fluorescence intensity by up to 1250-fold (Table 1). Dye **10** showed a similar to **8** change in the fluorescence intensity in the presence of dsDNA, but its very high fluorescence in the free state does not make it suitable as a fluorescent label for

dsDNA detection. Dye **13** showed an even higher fluorescence intensity in the presence of dsDNA, but its intrinsic fluorescence (4.3 au, Table 1) led to a decrease in the ratio I_{fl}/I_{fl0} (Table 1). One probable explanation for the observed photophysical properties of compound **13** is that the presence of the halogen substituent connected to the chromophore leads to an increase in the hydrophobicity and thus to the formation of fluorescent aggregates in the TE-buffer solution.

The TDDFT method was used to generate the absorption spectra of the cationic fragments of dyes **8**, **10** and **13** (presented in Fig. 2 with the respective atom color scheme) with Cl$^-$ counterions optimized in methanol.

TDPBE0/6-311+G(2d,p) calculations in methanol predicted absorption maxima at 482 nm, 450 nm and 466 nm for **8**, **10** and **13**, respectively; a typical systematic overestimation of the excitation energies by the TDDFT schemes was observed [40]. It can be proposed that different dimers may originate from **8**; data for the most stable dimer are presented in Table 2 and the optimized structure of this dimeric form is represented in Fig. 3.
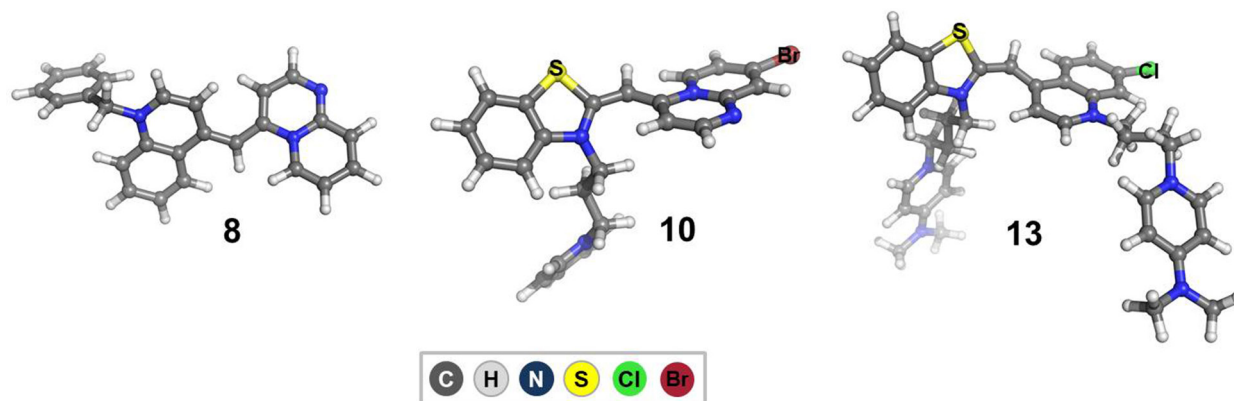

Fig. 2. B3LYP optimized structures of the cations of dyes **8**, **10** and **13**.

Table 2. TDPBE0/6-311+G(2d,p) calculated excitation wavelengths, λ (nm), and oscillator strengths, f, of the cationic fragments of dyes **8**, **10** and **13** with Cl$^-$ counterions in methanol

Compound	λ	f
8	482	0.8798
	431	0.0590
8_dimer	502	0.0202
	496	0.1692
	486	0.1137
	475	1.1770
	426	0.0565
10	450	0.7059
	423	0.1029
13	466	0.9049

Simulated with a Gaussian broadening with a full width at half-maximum (fwhm) 0.06–0.07 eV and a height proportional to the oscillator strength for each transition spectra are presented in Figure 3. At this broadening the **8_dimer** spectrum qualitatively reproduced the splitting in the experimental absorption spectrum of dye **8** in methanol solution, i.e., the monomer-dimer equilibrium of dye **8** can be hypothesized.

CONCLUSION

Three novel dyes were synthesized and their photophysical properties were investigated. Two of the dyes (**8** and **13**) possess typical features of fluorescent DNA labels. In the absence of DNA, these dyes have negligible fluorescence, but after binding to DNA a dramatic increase in the fluorescence intensity was observed. Dye **8** is worth highlighting because excitation at 706 nm led to a significant (1250-fold) increase in the fluorescence in the presence of dsDNA. Computational tools were employed in an effort to understand the relationship between the chemical structure and the optical properties of the chromophores. The results are
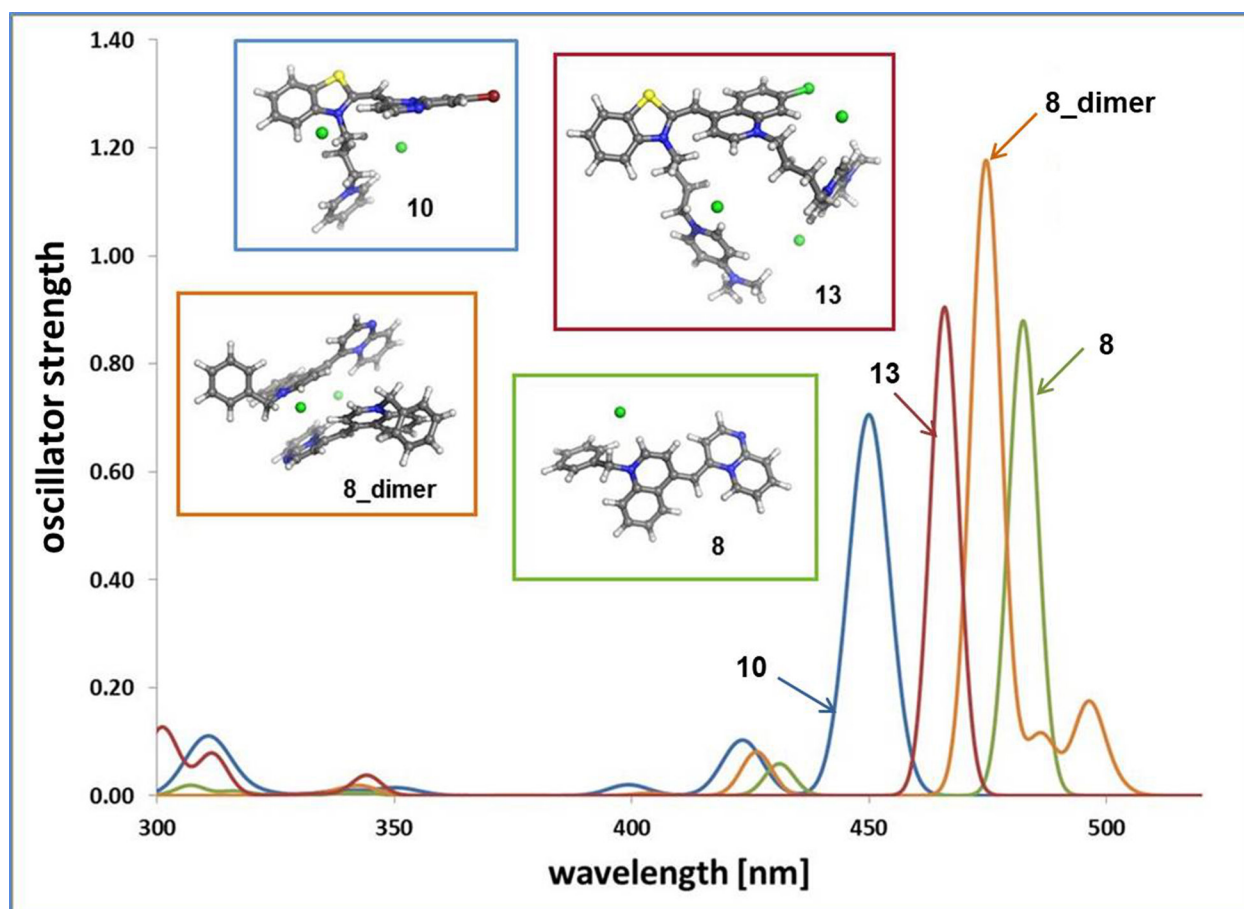
Fig. 3. TDPBE0/6-311+G(2d,p) simulated spectra of the cationic fragments of dyes **8** (monomer and dimer), **10** and **13** with Cl$^-$ counterions in methanol.

promising and warrant further investigations into the newly synthesized dyes as fluorogenic labels for DNA analysis in research and medical science. Additional quantum-chemical calculations, including the simulation of fluorescence spectra of new azaquinolizinium heterocycle-containing dyes, subsequent design of new analogs and further experiments in order to examine their DNA binding mechanism are planned.

REFERENCES

1. H. S. Rye, S. Yue, D. E. Wemmer, M. A. Quesada, R. P. Haugland, R. A. Mathies, A. N. Glazer, *Nucleic Acids Res.*, **20**, 2803 (1992).
2. L. G. Lee, C. H. Chen, L. A. Chiu, *Cytometry*, **7**, 508 (1986).
3. S. Berndl, S. D. Dimitrov, F. Menacher, T. Fiebig, H. A. Wagenknecht, *Chem. Eur. J.*, **22**, 2386 (2016).
4. P. R. Bohländer, M. L. Abba, F. Bestvater, H. Allgayer, H. A.Wagenknecht, *Org. Biomol. Chem.*, **14**, 4961 (2016).
5. T. Deligeorgiev, A. Vasilev, in: Functional Dyes, Kim S-H (ed.), Elsevier, Amsterdam, New York, Tokyo, (137) 2006.
6. R. P. Haugland, Molecular Probes: Handbook of fluorescent probes and research chemicals, Molecular Probes Inc., 9th ed., 2014.
7. T. G. Deligeorgiev, N. I. Gadjev, A. A. Vasilev, V. A. Maximova, I. I. Timcheva, H. E. Katerinopoulos, G. K..Tsikalas, *Dyes and Pigments*, **75**, 466 (2007).
8. K. Bernhard, S. Jäggli, P. Kreienbuhl, U. Schieter, US4883887 (1989).
9. A. D. Becke, *J. Chem. Phys.*, **98**, 5648 (1993).
10. C. Lee, W. Yang, R. G. Parr, *Phys. Rev. B*, **37**, 785 (1988).
11. W. J. Hehre, R. Ditchfield, J. A. Pople, *J. Chem. Phys.*, **56**, 2257 (1972).
12. T. Clark, J. Chandrasekhar, G. W. Spitznagel, P. v R.Schleyer, *J. Comp. Chem.*, **4**, 294 (1983).
13. M. J. Frisch, J. A. Pople, J. S. Binkley, *J. Chem. Phys.*, **80**, 3265 (1984).
14. J. Tomasi, B. Mennucci, R. Cammi, *Chem. Rev.*, **105**, 2999 (2005).
15. M. J. Frisch et al., Gaussian 09, Revision D.01, Gaussian, Inc., Wallingford CT, 2013.
16. The PyMOL Molecular Graphics System, Version 1.7.6.6, Schrödinger, LLC.
17. R. W. DeSimone, K. S. Currie, J. W. Mitchell, J.W. Darrow, D. A. Pippin, *Comb. Chem. High Throughput Screen*, **7**, 473 (2004).
18. B. E. Evans, K. E. Rittle, M. G. Bock, R. M. DiPardo, R. M. Freidinger, W. L. Whitter, G. F. Lundell, D. F. Veber, P. S. Anderson, R. S. L. Chang, V. J. Lotti, D. J. Cerino, T. B. Chen, P. J. Kling, K. A. Kunkel, J. P. Springer, J. Hirshfield, *J. Med. Chem.* 31, 2235 (1988).
19. C. A. Lipinski, F. Lombardo, B. W. Dominy, P. J. Feeney, *Adv. Drug Delivery Rev.*, **46**, 3 (2001).
20. V. V. Lipson, N. Y. Gorobets, *Mol. Diversity*, **13**, 399 (2009).
21. A. E. Gaber, H. McNab, *Synthesis*, **14**, 2059 (2001).
22. G. Y. Lesher, E. J. Froechlich, M. D. Gruett, J. H. Bailey, R. P. Brundage, *J. Med. Chem.*, **5**, 1063(1962).
23. G. S. Bisacchi, *J. Med. Chem.*, **58**, 4874 (2015).
24. R. Wise, J. M. Andrews, L. J. Edwards, *Chemother.*, **23**, 559 (1983).
25. L. A. Mitscher, P. N. Sharma, D. T. Chu, L. L. Shen, A. G. Pernet, *J. Med. Chem.*, **30**, 2283 (1987).
26. T. T. Curran, in: Named Reactions in Heterocyclic Chemistry; J.-J. Li, E. J. Corey, (eds.), Wiley Interscience, New York, 423 (2005).
27. T. D. White, A. C. Alt, P. Kevin, K. P. Cole, J. M. Groh, M. D. Johnson, R. D. Miller, *Org. Process Res. Dev.*, **18**, 1482 (2014).
28. A. M. Molnar, Z. Mucsi, G. Vlad, K. Simon, T. Holczbauer, B. Podanyi, F. Faigl, I. Hermecz, *J. Org. Chem.*, **76**, 696 (2011).
29. L. Lengyel, T. Zs. Nagy, G .Sipos, R. Jones, G. Dormán, L. Ürge, F.Darvas, *Tetrahedron Lett.*, **53**, 738 (2012).
30. I. Crnolatac, L. Tumir, N. Lesev, A. Vasilev, T. Deligeorgiev, K. Miskovic, L. Glavas-Obrovac, O. Vugrek, I. Piantanida, *Chem. Med. Chem.*, **8**, 1093 (2013).
31. T. Deligeorgiev, N. Gadjev, A. Vasilev, K-H. Drexhage, S. M. Yarmoluk, *Dyes and Pigments*, 70, 185 (2006).
32. L. G. Brooker, G. Keyes, W. Williams, *J. Am. Chem. Soc.*, **64**, 199(1942).
33. B. Beilenson, F. M. Hamer, *J. Chem. Soc.*, **13**, 143 (1939).
34. W. A. Sexton, *J. Chem. Soc.*, **13**, 470 (1939).
35. T. Deligeorgiev, A. Vasilev, T. Tsvetkova, K-H. Drexhage, *Dyes and Pigments*, **75**, 658 (2007).
36. T. Deligeorgiev, A. Vasilev, K-H. Drexhage, *Dyes and Pigments*, **74**, 320 (2007).
37. A. A. Vasilev, M. I. Kandinska, S. S. Stoyanov, S. B. Yordanova, D. Sucunza, J. J. Vaquero, O. D. Castaño, S. Baluschev, S. E. Angelova, *Beilstein J. Org. Chem.*, **13**, 2902 (2017).
38. T. Yu. Ogulchansky, V. M. Yashchuk, M. Yu. Losytskyy, I. O. Kocheshev, S. M. Yarmoluk, *Spectrochimica Acta Part A*, **56**, 805 (2000).
39. R. S. Kumar, E. H. Turner, *J. Photochem. Photobiol. A: Chemistry*, **74**, 231 (1993).
40. Fundamentals of Time-Dependent Density Functional Theory, M. A. L. Marques, N. T. Maitra, F. M. S. Nogueira, E. K. U. Gross, A. Rubio (eds), Springer-Verlag, Berlin Heidelberg, 2012.

СРАВНЯВАНЕ НА ФОТОФИЗИЧНИТЕ И ДНК-СВЪРЗВАЩИ СВОЙСТВА НА НОВИ АСИМЕТРИЧНИ АЗАХИНОЛИЗИНИЕВИ МОНОМЕТИНОВИ ЦИАНИНОВИ БАГРИЛА С НОВ АНАЛОГ НА ТИАЗОЛ ОРАНЖ

А. А. Василев[1], М. И. Къндинска[1]*, Ю. Загранярски[1], Д. Сукунза[2], Х. Х. Вакеро[2], О. Д. Кастаньо[2], С. Е. Ангелова[2,3]

[1] *Факултет по химия и фармация, Софийски университет „Св. Климент Охридски“, 1164 София, България*
[2] *Катедра по органична химия и катедра по физикохимия, Университет на Алкала,*
Е-28871 Алкала де Енарес, Мадрид, Испания
[3] *Институт по органична химия с Център по фитохимия, Българска академия на науките,*
1113 София, България

(Резюме)

Синтезирани са нови асиметрични монометинови цианинови багрила, съдържащи азахинолизиниев фрагмент, с използването на 4-хлоропиридопиримидиниеви хлориди като изходни съединения. Фотофизичните свойства на багрилата са сравнени с тези на нов мономерен трикатионен аналог на Тиазол Оранж (ТО). Съединения 8 и 13 се характеризират с много ниска собствена флуоресценция в ТЕ буфер в отсъствие на двДНК, но след свързване с двДНК се наблюдава значително увеличение на интензитета на флуоресценцията им. Изчислителни методи (DFT и TDDFT изчисления) са използвани за изследване на връзката между химичната структура и оптичните свойства на хромофорите.

Acetylcholinesterase inhibitors selected by docking-based screening – proof-of-concept study

G. Stavrakov[1,2], I. Philipova[2], A. Lukarski[1], I. Valkova[1,3], M. Atanasova[1], I. Dimitrov[1], S. Konstantinov[1], I. Doytchinova[1,3]*

[1] Faculty of Pharmacy, Medical University of Sofia, 2 Dunav str., Sofia 1000, Bulgaria
[2] Institute of Organic Chemistry with Centre of Phytochemistry, Bulgarian Academy of Sciences, Acad. Bonchev 9, Sofia 1113, Bulgaria
[3] Drug Design and Development Lab, Sofia Tech Park JSC, 111 Tsarigradsko Shose Blvd., Sofia 1784, Bulgaria

The enzyme acetylcholinesterase (AChE) plays an important role in the pathogenesis of neurodegenerative diseases. Its inhibition improves the cholinergic function and moderately delays the disease progress. In the present study, we performed a docking-based virtual screening for novel hits binding to AChE on the standard lead-like set of ZINC database containing more than 6 million small molecules. Two of the top best best-scored hits were tested *in vitro* for AChE affinity and neurotoxicity. Both compounds bind to the enzyme with affinities in the micromolar range but are moderately toxic. They are promising for further lead optimization to increase affinity and reduce toxicity. The present study proves the concept that the virtual screening is a reliable technique for discovery of novel AChE inhibitors.

Keywords: acetylcholinesterase, molecular docking, virtual screening, isothermal titration calorimetry, neurotoxicity.

INTRODUCTION

The enzyme acetylcholinesterase (AChE) is available in the cholinergic chemical synapses in the central nervous system and in neuromuscular junctions. It is located on the post-synaptic membrane and its function is to terminate the neurotransmission by hydrolysing the acetylcholine (ACh). In neurodegenerative diseases, like Alzheimer's disease, the cholinergic neurons are extensively lost leading to decline in memory and cognition [1, 2]. The inhibition of AChE enhances the levels of ACh and improves the cholinergic transmission.

The binding site of AChE is a deep and narrow gorge (Fig. 1) [3]. At the bottom of this gorge is located the catalytic anionic site (CAS) where the quaternary trimethylammonium choline moiety of ACh binds and is hydrolysed. Along the gorge are situated additional binding domains like the acyl pocket determining the selective binding of ACh and the oxyanion hole hosting a molecule of structural water. At the entrance of the binding gorge is situated the peripheral anionic site (PAS) which
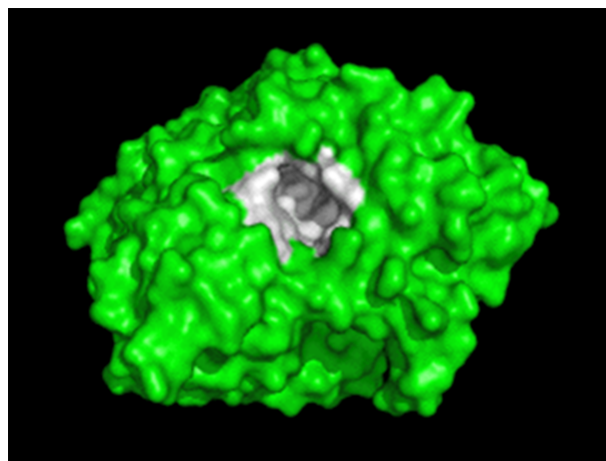
Fig. 1. Binding gorge (light grey) of *rh*AChE (pdb code: 4EY6).

modulates the catalysis allosterically and takes non-cholinergic functions like amyloid deposition [4], cell adhesion and neurite outgrowth [5].

Several AChE inhibitors (AChEIs) are approved as anti-Alzheimer's drugs and many others are under development [6–10]. In the present study, we describe a docking-based virtual screening on ZINC database leading to the identification of several new

---
* To whom all correspondence should be sent:
E-mail: idoytchinova@pharmfac.mu-sofia.bg

hits. Two of them (Fig. 2) were synthesized and tested for AChE binding affinity and neurotoxicity.

Fig. 2. Structures of the new hits derived by docking-based virtual screening.

EXPERIMENTAL

Database and docking protocol

ZINC (zinc.docking.org) contains several databases of biologically active structures. We selected the Standard Lead-like database which consists of 6,053,287 small molecules with molecular weights between 250 and 350 g/mol, *logP* up to 3,5 and up to 7 rotatable bonds. The set was dow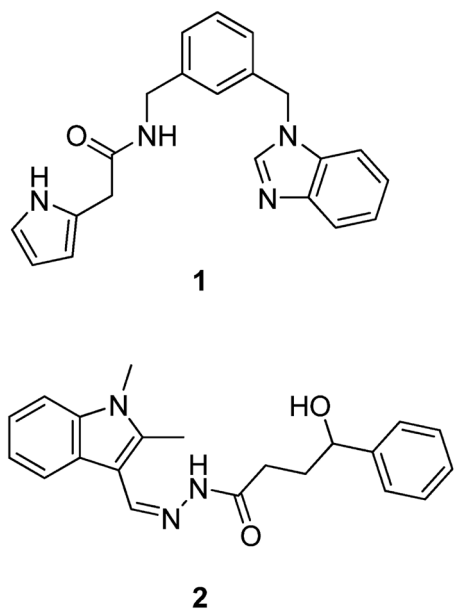nloaded in March 2015. The molecules were docked into the X-ray structure of human recombinant acetylcholinesterase (*rh*AChE, pdb id: 4EY6, R = 2.15 Å) [3]. The docking simulations were performed by GOLD v. 5.1.(CCDC Ltd., Cambridge, UK) using the following settings: scoring function ChemPLP, flexible ligand, rigid protein, radius of the binding site 6Å, no structural water molecules in the binding site, 10 runs for each compound. The AChEI galantamine (GAL) was used as a positive control.

Calculation of drug-like properties

Six drug-like properties were calculated by ACD/LogD v.9.0 (Advanced Chemistry Development, Inc.): molecular weight *Mw*, distribution coefficient at pH 7.4 *logD*$_{7.4}$, polar surface area *PSA*, free rotat-

able bonds *FRB*, number of hydrogen-bond donors *HBD* and hydrogen-bond acceptors *HBA*. The ability of compounds to cross the blood-brain barrier (BBB) by passive diffusion was predicted by the BBB Predictor (http://www.cbligand.org/BBB/). The BBB predictor includes eight models for BBB permeability prediction.

Chemistry

Reagents were commercial grade and used without further purification. Thin layer chromatography (TLC) was performed on aluminium sheets pre-coated with Merck Kieselgel 60 F$_{254}$ 0.25 mm (Merck). Flash column chromatography was carried out using Silica gel, for chromatography, 0.035–0.070 mm, 60 A (Acros) and Aluminum oxide for chromatography; basic; 0.05–0.15 mm; pH 9.5±0.5 (Fluka). Commercially available solvents for reactions, TLC and column chromatography were used after distillation (and were dried when needed). Melting points of the compounds were determined using "Electrothermal" MEL-TEMP apparatus (uncorrected). The NMR spectra were recorded on a Bruker Avance II+ 600 spectrometer (600.13 MHz for ^{1}H and 150.92 MHz for ^{13}C NMR) with TMS as internal standard for chemical shifts (δ, ppm). ^{1}H and ^{13}C NMR data are reported as follows: chemical shift, multiplicity (s = singlet, d = doublet, t = triplet, q = quartet, br = broad, m = multiplet), coupling constants (Hz), integration, identification. The assignment of the ^{1}H and ^{13}C NMR spectra was made on the basis of DEPT, COSY and HSQC, experiments. Elemental analyses were performed by Microanalytical Service Laboratory of Faculty of Pharmacy, Medical University of Sofia, using Vario EL*3* CHNS(O).

Synthesis of 3-((1H-benzo[d]imidazol-1-yl)methyl)benzonitrile 3.

Benzimidazole (0.236 g, 2 mmol) was mixed with 0.5 ml 50% aq.NaOH and after 10 min at r.t. a clear solution was obtained. DMSO (0.2 ml) was added, followed by 3-(bromomethyl)benzonitrile (0.432 g. 2.2 mmol). The reaction mixture was stirred at 30 °C for 1 hour, diluted with water and extracted with CH$_2$Cl$_2$. The combined organic phases were washed with water, dried and concentrated. The product was purified by flash column chromatography on silica gel (CH$_2$Cl$_2$/EtOAc = 1:1) to give 0.461 g, 99% of the desired product as white crystals; m.p. 99–101 °C. ^{1}H NMR (CDCl$_3$, 600 MHz) δ = 8.04 (s, 1H, benzimid.), 7.87 (d, *J* = 7.9 Hz, 1H, benzimid.), 7.62 (d, *J* = 7.6 Hz, 1H, arom.), 7.49 (s, 1H, arom.), 7.46 (t, *J* = 7.8 Hz, 1H, benzimid.), 7.37 (dd, *J* = 7.9, 0.7 Hz, 1H, benzimid.), 7.33 (t, *J* = 7.8 Hz, 1H, benzimid.), 7.29 (t, *J* = 7.6 Hz, 1H, arom.), 7.22 (d, *J* = 7.6 Hz, 1H, arom.), 5.45 (s, 2H, CH$_2$) ppm.

^{13}C NMR (CDCl$_3$, 150.9 MHz) δ = 142.92 (CH), 137.16 (C), 133.46 (C), 132.00 (CH), 131.09 (CH), 130.29 (CH), 130.00 (CH), 123.60 (CH), 122.77 (CH), 120.65 (CH), 118.09 (C), 113.30 (C), 109.67 (CH), 47.95 (CH$_2$) ppm.

Synthesis of (3-((1H-benzo[d]imidazol-1-yl)methyl)phenyl)methanamine 4.

To a solution of nitrile **3** (0.111 g, 0.476 mmol) in dry THF (6 ml) was added portionwise at 0 °C LiAlH$_4$ (0.090g, 2.380 mmol). The mixture was refluxed for 3 hours and cooled on ice bath, diluted with ether and carefully quenched by adding dropwise 0.09 ml water, followed by 0.09 ml 10% aq.NaOH and 0.27 ml water (Fieser workup). After additional 30 min stirring at r.t. the mixture was filtered through a pad of Celite and the filtrate was concentrated. The product was purified by flash column chromatography on silica gel (CH$_2$Cl$_2$/CH$_3$OH/NH$_4$OH = 20:1:0.05) to give 0.063 g, 56% of the desired amine **4** as waxy solid. ^{1}H NMR (CDCl$_3$/CD$_3$OD = 6:1, 600 MHz) δ = 8.01 (s, 1H, benzimid.), 7.78 (d, *J* = 7.7 Hz, 1H, benzimid.), 7.34–7.26 (m, 3H, benzimid., 2H, arom.), 7.17 (s, 1H, arom.), 7.10 (d, *J* = 7.6 Hz, 1H, arom.), 5.38 (s, 2H, CH$_2$N), 3.81 (s, 2H, C*H*$_2$NH$_2$) ppm. ^{13}C NMR (CDCl$_3$/CD$_3$OD = 6:1, 150.9 MHz) δ = 142.92 (CH), 142.66 (C), 135.58 (2C), 133.47 (C), 129.25 (CH), 127.12 (CH), 125.90 (CH), 125.83 (CH), 123.22 (CH), 122.49 (CH), 119.66 (CH), 110.07 (CH), 48.66 (CH$_2$), 45.35 (CH$_2$) ppm.

Synthesis of methyl 2-(1H-pyrrol-2-yl)acetate 5.

A 50 ml Schlenk flask was loaded under argon atmosphere with pyrrole (0.201 g, 3 mmol) and dry THF (10 ml). The mixture was cooled to –10 °C and EtMgBr (3M in Et$_2$O, 1.2 ml, 3.6 mmol) was added dropwise. The reaction was allowed to reach r.t. and was stirred for 30 min. It was again cooled to –10 °C and methyl bromoacetate (0.550 g, 3.6 mmol) was added. After stirring for 30 min at r.t. the reaction was quenched with aq.NH$_4$Cl, extracted with EtOAc, dried and concentrated. The product was purified by flash column chromatography on silica gel (petroleum ether/EtOAc = 10:1) to give 0.120 g, 29% of the desired ester **5** as yellowish oil. ^{1}H NMR (CDCl$_3$, 600 MHz) δ = 8.71 (br, 1H, NH), 6.76–6.75 (m, 1H, pyrrole), 6.15–6.14 (m, 1H, pyrrole), 6.03–6.02 (m, 1H, pyrrole), 3.72 (s, 3H, CH$_3$), 3.69 (s, 2H, CH$_2$) ppm. ^{13}C NMR (CDCl$_3$, 150.9 MHz) δ = 171.63 (CO), 123.09 (C), 117.76 (CH), 108.27 (CH), 107.34 (CH), 52.16 (CH$_3$), 32.99 (CH$_2$) ppm.

Synthesis of N-(3-((1H-benzo[d]imidazol-1-yl)methyl)benzyl)-2-(1H-pyrrol-2-yl)acetamide 1.

A mixture of amine **4** (0.058 g, 0.244 mmol) and ester **5** (0.034 g, 0.244 mmol) was heated for 3 hours at 80 °C. The reaction was cooled to r.t. and directly subjected to flash column chromatography on basic aluminum oxide (EtOAc = 10:1) to give 0.019 g, 23% of the desired product **1** as white crystals; m.p. 146–148 °C. ^{1}H NMR (CDCl$_3$, 600 MHz) δ = 9.14 (br, 1H, NH-pyrrole), 7.91 (s, 1H, benzimid.), 7.81 (d, *J* = 7.7 Hz, 1H, benzimid.), 7.30–7.26 (m, 3H, benzimid.), 7.23 (t, *J* = 7.6 Hz, 1H, arom.), 7.10 (d, *J* = 7.6 Hz, 1H, arom.), 7.06 (d, *J* = 7.6 Hz, 1H, arom.), 6.88 (s, 1H, arom.), 6.72–6.70 (m, 1H, pyrrole), 6.28 (t, *J* = 5.5 Hz, 1H, CONH), 6.11 (m, 1H, pyrrole), 5.98–5.97 (m, 1H, pyrrole), 5.26 (s, 2H, CH$_2$N), 4.29 (d, *J* = 6.1 Hz, 2H, C*H*$_2$NHCO), 3.51 (s, 2H, C*H*$_2$CONH) ppm. ^{13}C NMR (CDCl$_3$, 150.9 MHz) δ = 170.74 (CO), 143.45 (C), 143.23 (CH-benzimid.), 139.17 (C), 135.89 (C), 133.77 (C), 129.25 (CH-arom.), 127.22 (CH-arom.), 126.00 (CH-arom.), 125.44 (CH-arom.), 124.23 (C), 123.30 (CH-benzimid.), 122.52 (CH-benzimid.), 120.16 (CH-benzimid.), 118.26 (CH-pyrrole), 110.10 (CH-benzimid.), 108.50 (CH-pyrrole), 107.75 (CH-pyrrole), 48.54 (CH$_2$N), 42.88 (C*H*$_2$NHCO), 35.49 (C*H*$_2$CONH) ppm. C$_{21}$H$_{20}$N$_4$O (344.41): calcd. C 73.23; H 5.85; N 16.27, found C 73.16, H 6.11, N 16.08.

Synthesis of racemic 4-hydroxy-4-phenylbutane-hydrazide 6 [6].

To a solution of 5-phenyldihydrofuran-2(3*H*)-one (1.135 g, 7 mmol) in EtOH (14 ml) was added hydrazine hydrate (0.491 g, 9.8 mmol) and the mixture was refluxed for 2 hours. After cooling to rt, the product crystallized and was filtered. The crystals were washed with EtOH (4 ml) and dried under vacuum to give 0.987 g, 73% of the desired product as white crystals.

Synthesis of racemic N'-((1,2-dimethyl-1H-indol-3-yl)methylene)-4-hydroxy-4-phenylbutane-hydrazide 2.

A mixture of hydrazide **6** (0.056 g, 0.288 mmol), 1,2-dimethyl-1*H*-indole-3-carbaldehyde (0.050 g, 0.288 mmol) and a pinch of p-toluenesulfonic acid (PTSA) in abs.EtOH (4 ml) was refluxed for 30 min. The mixture was concentrated under vacuum till dry. Crystallization from Et$_2$O/MeOH = 10:1 followed by filtration gave 0.088 g, 88% of the desired product **2** as yellow crystals; m.p. 170–172 °C. ^{1}H NMR (CDCl$_3$, 600 MHz) δ = 9.62 (s, 1H, NH), 8.11 (d, *J* = 7.7 Hz, 1H, indole), 8.08 (s, 1H, HC=N), 7.43 (d, *J* = 7.4 Hz, 2H, arom.), 7.34 (t, *J* = 7.5 Hz, 2H, arom.), 7.28–7.20 (m, 1H, arom., 3H, indole), 4.90 (t, *J* = 6.0 Hz, 1H, C*H*OH), 4.02 (br, 1H, OH), 3.64 (s, 3H, NCH$_3$), 3.09-3.04 (m, 1H, C*H*$_2$CHOH), 3.01-2.96 (m, 1H, C*H*$_2$CHOH), 2.48 (s, 3H, CH$_3$), 2.25–2.22 (m, 2H, CH$_2$CO) ppm. ^{13}C NMR (CDCl$_3$, 150.9 MHz) δ = 175.80 (CO), 144.80 (C), 140.57

(CH=N), 140.41 (C), 137.20 (C), 128.31 (2CH-arom.), 127.17 (CH-indole), 125.76 (2CH-arom.), 124.94 (C), 122.32 (CH-indole), 121.27 (CH-indole), 121.18 (CH-indole), 108.88 (CH-arom.), 107.35 (C), 73.86 (CHOH), 33.78 (CH_2CO), 29.64 (CH_2OH), 29.55 (CH_3N), 10.58 (CH_3) ppm. $C_{21}H_{23}N_3O_2$ (349.18): calcd. C 72.18; H 6.63; N 12.03, found C 72.40, H 6.89, N 12.07.

Isothermal titration calorimetry (ITC) protocol

The ITC measurements were performed on NanoITC tool (TA Instuments, Lindon, UT, USA) with 190 μL sample cell and 50 μL syringe. The lyophilized AChE from *Electrophorus electricus* (electric eel) (Sigma Aldrich, St. Luis, MO, USA) was reconstructed in 50 mM TRIS-HCl pH 7.4 buffer with the 0.1% addition of BSA as an enzyme stabilizing factor, according to the manifacturer's instuctions. The tested compounds were prepared in 5 mM stock solutions in DMSO or ethanol and diluted to 0.5 mM in 50 mM TRIS-HCl pH 7.4 buffer. All samples were degassed prior the experiments. The AChE solution was placed into the sample cell and titrated by the tested compounds in 25 steps of 2 μL at 5 min intervals at 25°C. The blank samples (buffer lacking AChE) were titrated at the same conditions. The corresponding K_d values were calculated using NanoAnalyze software (TA Instuments, Lindon, UT, USA).

Neurotoxicity test

Murine neuroblastoma NEURO-2A cells (German collection DSMZ, Braunschweig, Germany) were cultivated under standard conditions: complete medium (90% DMEM, 10% heat inactivated FBS and 1 × non-essential amino acids); 37°C and 5% CO_2 in fully humidified atmosphere. The cell line was kept in the logarithmic growth phase by splitting 1:4 once a week using trypsin/EDTA. About 30% of the cells grow like neuronal cells.

For the experimental evaluation of the cytotoxicity NEURO-2A, cells were plated in 96-well flat bottomed cell culture plates at the recommended density of 1×10^6 cells/25 cm^2. After 24 hours the cells were treated with various concentrations of the investigational compounds and after 72-hr incubation, a MTT-dye reduction assay was performed [7]. Briefly, at the end of incubation, a MTT stock solution (10 mg/ml in PBS) was added (10 μl/well). Plates were further incubated at 37°C for 4 hr. Next, the formazan crystals were dissolved by the addition of 110 μl/well 5% formic acid in 2-propanol (v/v). Absorption was measured at 580 nm wavelength on an automated ELISA reader Labexim LMR1. At least six wells per concentration were used, and data were processed using the GraphPad Prism 5.0 software 2.

RESULTS

Docking-based screening of ZINC database on rhAChE

The dockings were performed with flexible ligands and rigid binding site lacking structural water molecules. The RMSD value for the docked pose of GAL was 0.204 Å. Among the top ten best-scored hits by ChemPLP were compounds **1** and **2**. (Table 1). Both compounds consisted of two aromatic moieties connected by a linker of 3-7 carbon chain containing NHCO group. Compound **1** has one additional phenyl ring. The docking poses showed that the first aromatic moiety binds in CAS, the aliphatic chain stretches along the binding gorge and the second aromatic ring binds in PAS (Figure 3).

The molecular weights of both compounds are below 350 (Table 1). Compound **1** ($logD_{7.4} = 4.09$) is more hydrophilic than compound **2** ($logD_{7.4} = 4.09$) although the *PSA* of **1** is slightly less than that of **2**. Compound **1** has one rotatable bond less than compound **2** and both compounds have equal number of

Table 1. Docking score, *ee*AChE affinity and neurotoxicity of the tested compounds

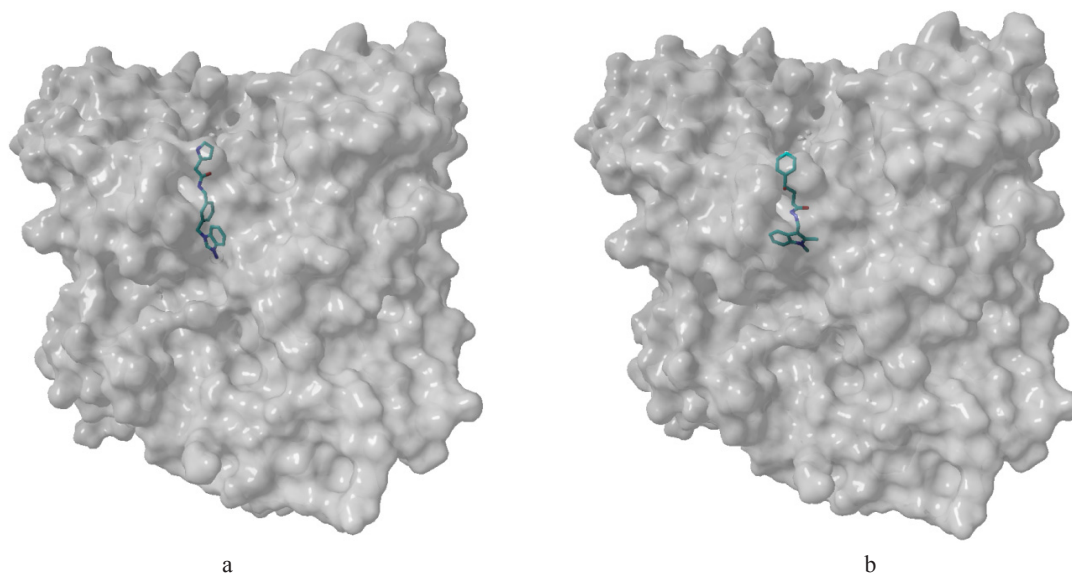| ID	ZINC ID	ChemPLP score	K_d μM ITC	IC_{50} μM Neuro2A	Mw	$logD_{7.4}$	PSA	FRB	HBD	HBA	BBB
1	89571446	99.28	10.191	45.092 ± 3.526	344.41	1.91	62.71	6	2	5	Yes
2	83312851	99.29	2.872	69.722 ± 16.930	349.43	4.09	66.62	7	2	5	Yes
GAL	–	74.560*	388.2	> 50*	287.35	1.12	41.93	1	1	2	Yes

*Ref. [8].

a   b

Fig. 3. Docking poses of **1** (a) and **2** (b) in the complexes with *rh*AChE.

HB donors and acceptors. The drug-like properties show that both compounds will have good permeability though the gastro-intestinal tract. They are BBB permeable by passive diffusion according to all 8 models included in the BBB Predictor.

Chemistry

The choice of synthetic strategy was based on theoretical fragmentation of the target structures to key building blocks. Thus, amide bonding between benzimidazole containing benzylamine **4** and 2-pyrroleacetate **5** was foreseen for the synthesis of compound **1** (Scheme 1). The first building block was synthesised *via* deprotonation of benzimidazole with aq.NaOH [9] and subsequent nucleophilic substitution of the commercially available 3-(bromomethyl)benzonitrile to give intermediate **3**, which was reduced with $LiAlH_4$ to the corresponding amine **4**. The ester **5** was synthesised by reacting the *in situ* prepared Grignard derivative of pyrrole [10] with methyl bromoacetate. Pyrolysis of the two building blocks resulted in the formation of the target compound **1**.

The synthesis of hydrazone **2** was based on the condensation of 1,2-dimethyl-1*H*-indole-3-carbaldehyde with initially prepared hydrazide **6** (Scheme 2). The latter was prepared *via* ring opening of racemic gamma-phenyl-gamma-butyrolactone with hydrazine hydrate according to literature procedure [6]. The target compound **2** was synthesised by heating of hydrazine **6** with the chosen aldehyde in absolute ethanol. The addition of cata-

lytic amount of p-toluenesulfonic acid was crucial for the success of the condensation.
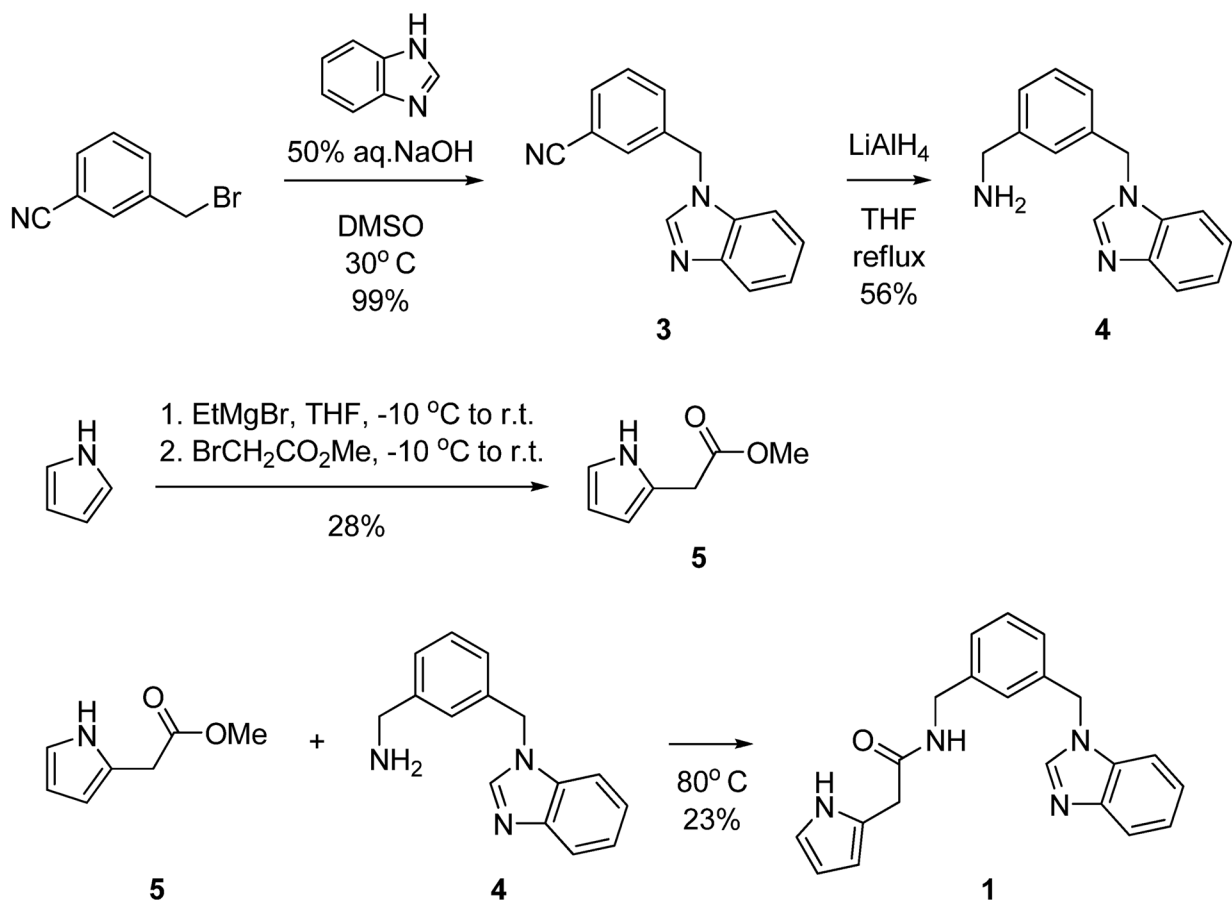
Binding affinity to AChE

The binding affinity of the best-scored compounds was tested *in vitro* by ITC as described in Experimental. AChE from electric eel (*ee*AChE) was used in the measurements. The UniProt alignment of *rh*AChE (UniProt: P22303) and *ee*AChE (UniProt: O42275) have showed that all 17 residues forming the binding gorges are identical [11]. Thus, the target *ee*AChE is a good and cheaper alternative of *rh*AChE. The K_d values of the tested compounds are given in Table 1. The K_d values for compounds **1** and **2** are 10.191 μM and 2.872, respectively. Both of them have higher affinity than GAL (K_d = 388.2 μM).

Neurotoxicity on Neuro-2A cells

The neurotoxicity of the compounds was tested on NEURO-2A cells as described in Experimental. Both of them are moderately toxic with IC_{50} values of 45 μM for compound **1** and 70 μM for compound **2**.

DISCUSSION

The standard lead-like set of ZINC database was virtually screened by molecular docking on *rh*AChE and two of the best-scored structures were tested *in*

Scheme 1. Synthesis of compound **1**.
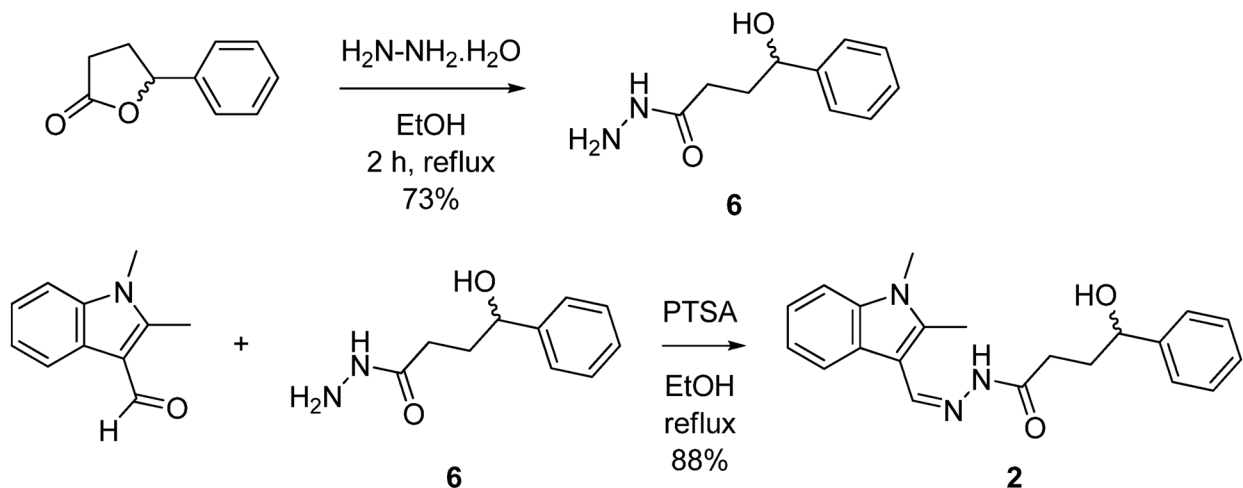
Scheme 2. Synthesis of compound **2**.

vitro for binding affinity to the enzyme and neuro-toxicity. The drug-like properties were calculated and showed that both structures are able to permeate through the intestinal mucosa. The compounds bind well to the enzyme with K_d in the micromolar range and have higher affinity than that of GAL.

Compound **1** is a neutral molecule with $logD_{7.4}$ of 4.09 and micromolar affinity to AChE (K_d =
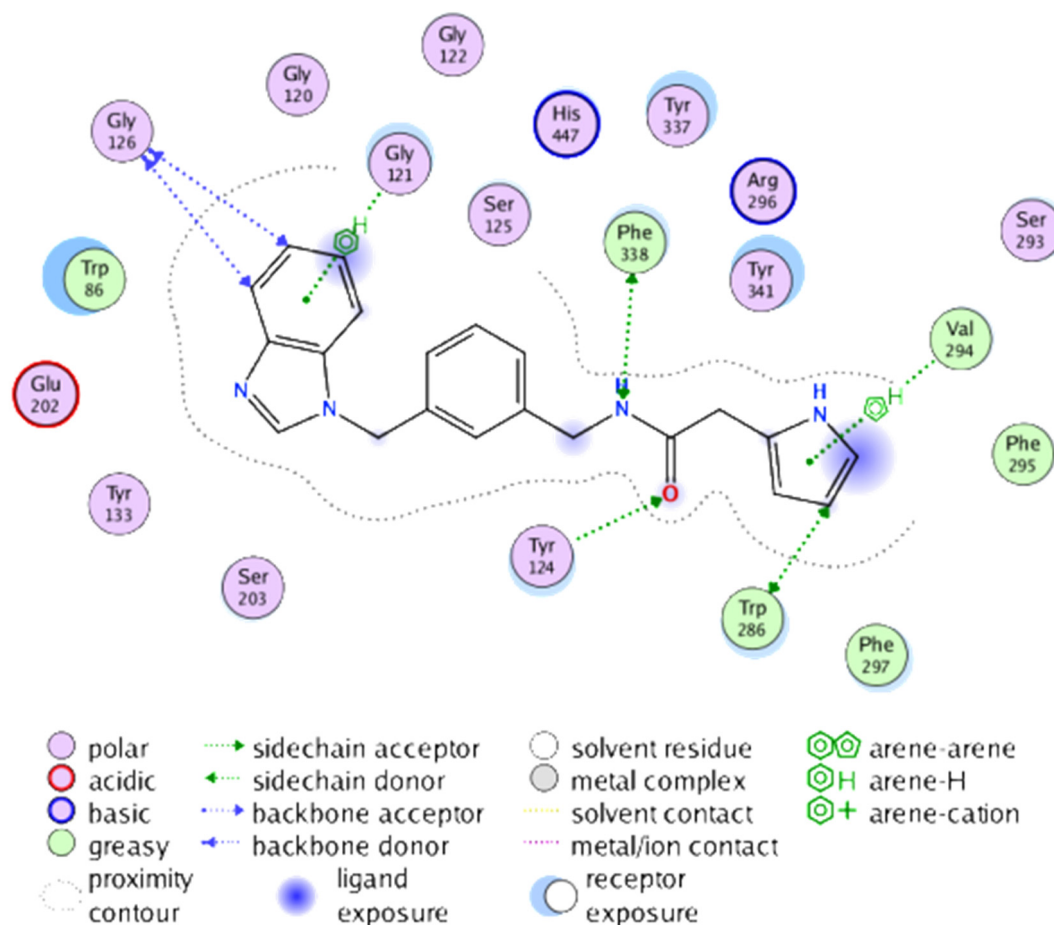
Fig. 4. 2D interaction plot of the complex **1** – *rh*AChE derived by MOE 2016.0801 (Chemical Computing Group, Montreal, Canada).

10.191 µM). It is able to cross the GIT and BBB but is more toxic on Neuro-2A cells (IC_{50} = 45 µM) than GAL. The docked pose of **1** into *rh*AChE shows that the benzimidazole fragment binds in CAS, while the pyrrole ring is placed in PAS (Figure 4). Hydrogen bonds are formed between Phe338 and NH and between Tyr124 and carbonyl oxygen atom from the linker. Gly121 and Gly126 from CAS interact with the benzimidazole fragment while Trp286 and Val294 from PAS – with the pyrrole ring.

Compound **2** is a weak base with $logD_{7.4}$ of 1.91, micromolar affinity to AChE (K_d = 2.872 µM), good intestinal and BBB permeability and moderate toxicity (IC_{50} = 70 µM). The indole moiety stacks with Trp86 in CAS, while the phenyl ring is positioned in PAS making interactions with Trp286, Val294, Phe295 and Tyr341 (Figure 5). A hydrogen bond is formed between Tyr124 and the carbonyl oxygen

atom from the linker. Phe297 and Phe338 are involved in hydrophobic interactions with the linker.

In conclusion, both structures identified as hits by docking-based virtual screening showed high affinity to AChE and moderate neurotoxicity. They could be considered for further lead optimization to increase affinity and reduce toxicity. The present study was a preliminary proof-of-concept.

REFERENCES

1. R. T. Bartus, R. L. Dean III, B. Beer, A. S. Lippa, *Science*, **217**, 408 (1982).
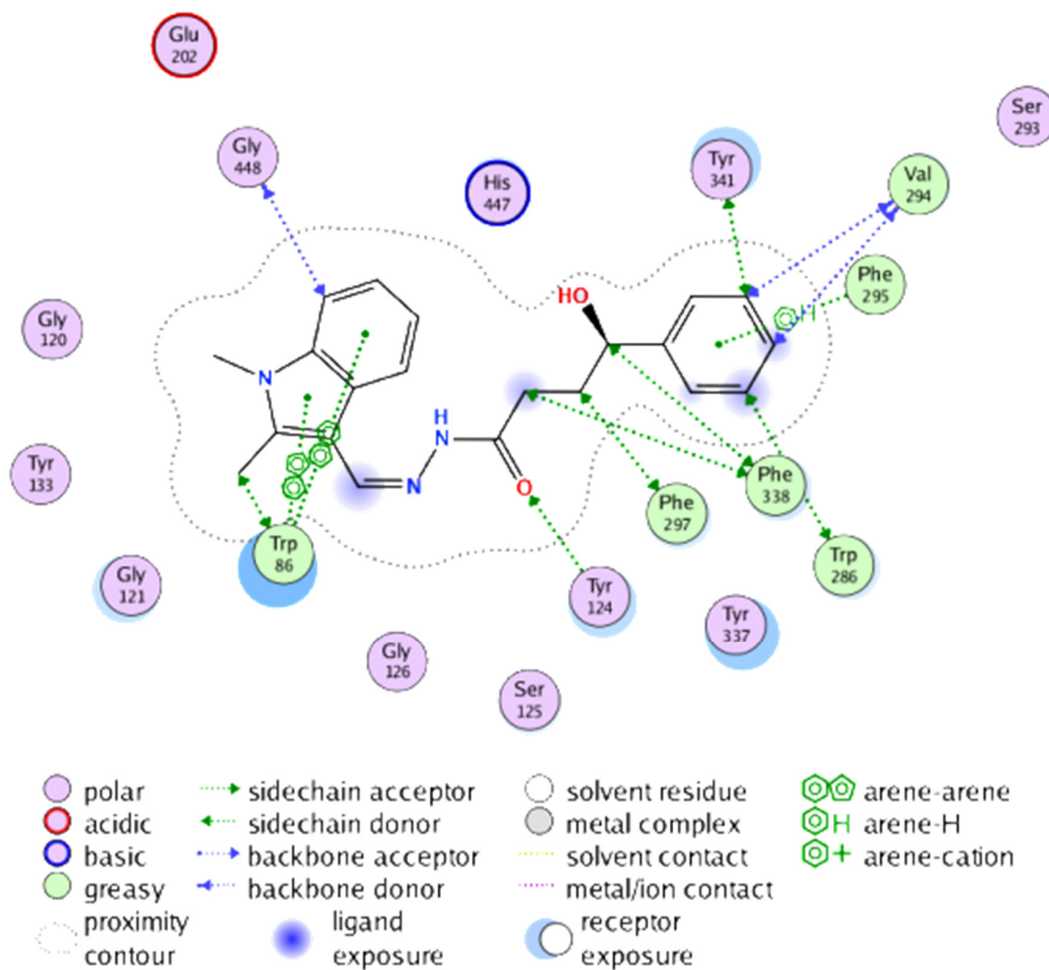2. R. T. Bartus, *Exp. Neurol.*, **163**, 495 (2000).

Fig. 5. 2D interaction plot of the complex **2** – *rh*AChE derived by MOE 2016.0801 (Chemical Computing Group, Montreal, Canada).

3. J. Cheung, M. J. Rudolph, F. Burshteun, M. S. Cassidy, E. N. Gary, J. Love, M. C. Franklin, J. J. Height, *J. Med. Chem.*, **55**, 10282 (2012).
4. F. J. Carvajal, N. C. Inestrosa, *Front. Mol. Neurosci.*, **4**, 19 (2011).
5. G. Johnson, S. W. Moore, *Curr. Pharm. Des.*, **12**, 217 (2006).
6. M. Schulze, *Synth. Commun.*, **40**, 3415 (2010).
7. G. Momekov, D. Ferdinandov, A. Bakalova, M. Zaharieva, S. Konstantinov, M. Karaivanova, *Arch.*
Toxicol., **80**, 555 (2006).
8. G. Stavrakov, I. Philipova, D. Zheleva-Dimitrova, I. Valkova, E. Salamanova, S. Konstantinov, I. Doytchinova, *Chem. Biol. Drug Des.*, **90**, 709 (2017).
9. B. Pilarski, *Liebigs Ann. Chem.*, **6**, 1078 (1983).
10. A. D. Abell, B. K. Nabbs, *Bioorg. Med. Chem.*, **9**, 621 (2001).
11. G. Stavrakov, I. Philipova, D. Zheleva, M. Atanasova, S. Konstantinov, I. Doytchinova, *Mol. Inf.*, **35**, 278 (2016).

ИНХИБИТОРИ НА АЦЕТИЛХОЛИНЕСТЕРАЗАТА, ИЗБРАНИ ЧРЕЗ ДОКИНГ-БАЗИРАН СКРИНИНГ – ДОКАЗВАНЕ НА КОНЦЕПЦИЯТА

Г. Ставраков[1,2], И. Филипова[2], А. Лукарски[1], И. Вълкова[1,2], М. Атанасова[1],
И. Димитров[1], С. Константинов[1], И. Дойчинова[1,2]*

[1] *Фармацевтичен Факултет, Медицински Университет – София, ул. Дунав 2, София 1000, България*
[2] *Институт по Органична химия с Център по Фитохимия, ул. Акад. Г. Бончев, бл.9, София 1113, България*
[3] *Лаборатория за разработване и охарактеризиране на фармацевтични форми, София Тех парк,*
бул. Цариградско шосе 111, София 1784, България

(Резюме)

Ензимът ацетилхолинестераза (AChE) играе важна роля в патогенезата на невродегенеративните заболявания. Неговото инхибиране подобрява холинергичната функция и умерено забавя напредъка на болестта. В настоящото изследване проведохме виртуален скрининг, базиран на молекулен докинг на 6 053 287 съединения от базата данни ZINC върху AChE. Две от съединенията с най-добър резултат бяха синтезирани и тествани *in vitro* за афинитет към AChE и невротоксичност. И двете съединения се свързват с ензима с афинитет в микромоларния диапазон, но са умерено токсични. Те са подходящи за по-нататъшна оптимизация с цел увеличаване на афинитета и намаляване на токсичността. Настоящото изследване доказва, че виртуалният скрининг е надежден метод за откриване на нови AChE инхибитори.

Rhodium-modified carbonaceous electrodes: application to electrochemical sensing of hydrogen peroxide

Y. L. Lazarova, T. M. Dodevska*

University of Food Technologies, Department of Organic chemistry and Inorganic chemistry,
26 Maritza Blvd., Plovdiv 4002, Bulgaria

In this research, a fast, simple and reproducible procedure for electrochemical modification of carbonaceous carriers with rhodium has been reported. Rhodium was electrodeposited by means of cyclic voltammetry at various scan rates. The electrochemical behaviour in the electroreduction of H_2O_2 of the graphite and glassy carbon electrodes, modified applying the here presented procedure, was studied using cyclic voltammetry and chronoamperometry at pH 7.0. The applicability of the modified electrodes for sensitive quantitative amperometric detection of hydrogen peroxide at low applied potentials (0 V and –0.1 V vs. Ag/AgCl, 3M KCl) has been demonstrated. As an optimized electrode, modified glassy carbon type Rh_v100/GC exhibited excellent electrocatalytic performance – fast, stable and sensitive (493 μA mM^{-1} cm^{-2}) response, low detection limit (1.5 μM H_2O_2) and wide linear range (up to 5.5 mM), making it one of the promising candidates for efficient non-enzymatic amperometric detection of H_2O_2.

Keywords: carbonaceous materials, rhodium, electrodeposition, hydrogen peroxide reduction, electrocatalyst.

INTRODUCTION

In the development of efficient electrode-catalysts, it is particularly important to obtain on chemically inert electrically conductive carrier metal deposits with high specific catalytic activity in the target reaction. In this connection, dispersing the catalytically active phase onto the surface of solid carbonaceous carriers not only significantly reduces the cost of the produced catalysts but also repeatedly increases their activity.

The studies of the deposition of micro- and nanosized structures of rhodium (Rh) are motivated by the well-known catalytic activity of this metal and its extreme resistivity towards acids and bases, rendering Rh-structures broadly applicable and potentially aging resistant. Rhodium shows outstanding catalytic properties in various reactions such as the reduction of nitrate and nitrite ions [1], hydrogenation of CO, CO_2, alkenes and arenes [2, 3], C-C cross-coupling [4], decomposition of methane and some oxidation reactions [5–8]. Rhodium is an excellent catalyst in $(NO)_x$ removal [9], so it is a common component of the three-way catalyst used for the simultaneous conversion of nitrogen oxides, CO and hydrocarbons in automobile exhausts.

It is well known that the catalytic properties of the metal deposits depend on the particles size and shape, and morphology of the metal phase onto the carrier surface. These parameters are determined both by the nature, physical characteristics and pretreatment of the carrier, as well as by the procedure for deposition. Numerous studies proved the electrodeposition as an attractive method for modifying various electrode materials. The great advantage of electrochemical techniques is the possibility of strict and accurate control allowing high reproducibility of the modification procedure. The required equipment is standard for any electrochemical laboratory and offers a wide range of possibilities electrodeposition to be performed in potentiostatic or potentiodynamic conditions as well as by applying pulse techniques.

Based on the above, the present study deals with the optimization of electrochemical procedure for obtaining stable rhodium deposits onto carbonaceous electrodes (glassy carbon and spectroscopic graphite). With aim to develop a non-enzymatic sensor for rapid and sensitive quantitative detection of H_2O_2, an industrially and biologically relevant analyte, the catalytic activity of the so-obtained modified electrodes in the reduction of H_2O_2

* To whom all correspondence should be sent:
E-mail: dodevska@mail.bg

at potentials around and below 0 V (vs. Ag/AgCl, 3M KCl) was investigated. Hydrogen peroxide is used as an oxidizing and bleaching agent in the pharmaceutical, cosmetic, textile and paper industries; in the food industry H_2O_2 is used in the artificial aging of wines and as a sterilizing agent in the dairy industry; in medicine the excess of H_2O_2 in human body is associated with oxidative stress, aging, cancer and progressive neurodegenerative diseases. Moreover, the development of effective materials with pre-defined operational parameters for quantitative determination of H_2O_2 at low potentials is relevant not only for the establishment of amperometric analysis of H_2O_2, but also for developing selective first generation biosensors.

MATERIALS AND METHODS

Materials

Two types carbonaceous carriers were used as working electrodes: 1/ disc from glassy carbon (GC) with diameter of the working surface 3 mm and visible surface area of *ca.* 7.07 mm^2 (Metrohm) and 2/ disc from spectroscopic graphite (Gr) with diameter of the working surface 5.6 mm and visible surface area *ca.* 25 mm^2 (RWO, Ringsdorf, Germany).

$RhCl_3.nH_2O$, HCl, H_2O_2 (30% (v/v) aqueous solution), $Na_2HPO_4.12H_2O$, $NaH_2PO_4.2H_2O$ were purchased from Fluka. All chemicals used were of analytical grade. Phosphate buffer solution, 0.1 M, (PBS) was made of sodium phosphates (monobasic and dibasic) dissolved in double distilled water with pH adjusted with H_3PO_4 and NaOH using a pH meter MS2006 (Microsyst, Bulgaria). Double distilled water was used to prepare aqueous solutions.

Apparatus and measurements

The electrochemical measurements were performed using computer controlled electrochemical workstation EmStat2 (PalmSens BV, The Nederland), equipped with PSTrace 2.5.2 licensed software, in a conventional thermostated three-electrode cell, including a working electrode (modified with rhodium electrode), an Ag/AgCl (3 M KCl) reference electrode, and a platinum auxiliary electrode.

All the electrochemical measurements were carried out at a temperature of 25°C. To remove oxygen, the background solution was purged with pure argon. Cyclic voltammograms (CVs) were recorded at scan rates from 10 to 100 mV s^{-1}. Peak intensities of CVs were reported with baseline correction. The amperometric experiments (calibrations) were performed by successive addition of aliquots of 3.10^{-2} M H_2O_2 freshly prepared solution to background elec-

trolyte (0.1 M PBS) in the cell (30 mL initial volume) with simultaneous registration of the current at a constant potential.

The experimental data were processed by software package 'OriginPro 8'.

Electrochemical deposition of Rh

Before modification, the GC electrode surface was carefully polished with 0.3 and 0.5 µm alumina slurry on a polishing cloth (LECO, USA), the graphite electrode was carefully polished to mirror-like finish with emery paper with decreasing particle size (P800, P1200 and P2000). After polishing, the electrodes were sonicated in double distilled water for 3 min and allowed to dry at room temperature for few minutes. The rhodium was electrodeposited from electrolyte 0.1 M HCl, containing 2.0% $RhCl_3$, by means of cyclic voltammetry. The electrode surface was seeded with rhodium particles when starting the cycle at –0.3 V, then the scan goes up to 0.9 and back to –0.3 V.

RESULTS AND DISCUSSION

In order to establish the effect of electrodeposition scan rate on the activity of the catalysts in electroreduction of H_2O_2, GC electrodes were modified at scan rates of 50, 100 and 200 mV s^{-1}, respectively. To indicate the type of the modified electrode we take the following notation: Rh_scan rate/GC (for example: GC modified by applying a rate of 50 mV s^{-1} will be denoted in the text as Rh_v50/GC).

The presence of Rh-deposits on the glassy carbon carrier was confirmed by CV, recorded in an electrolyte 0.1 M PBS (pH 7.0). Fig. 1 shows CVs
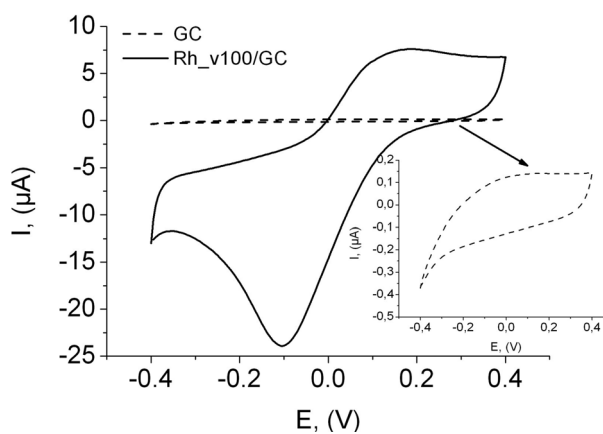

Fig. 1. CVs of the bare GC electrode (dash line) and of the modified Rh_v100/GC electrode (solid line) recorded in 0.1 M PBS (pH 7.0); scan rate of 50 mV s^{-1}.

of the unmodified GC electrode and modified electrode type Rh_v100/GC, registered in the potential range from –0.4 to 0.4 V at scan rate of 50 mV s^{-1}. No redox peak is observed on the CV of the bare GC electrode (enlarged in inset plot). Compared with bare GC electrode, the background current of the modified electrode is apparently larger, which indicates that the effective electrode surface area is significantly enhanced.

Further experiments were carried out to evaluate the electrocatalytic activity of the modified electrode Rh_v100/GC in the electroreduction of H_2O_2. Fig. 2 presents CVs recorded in 0.1 M PBS
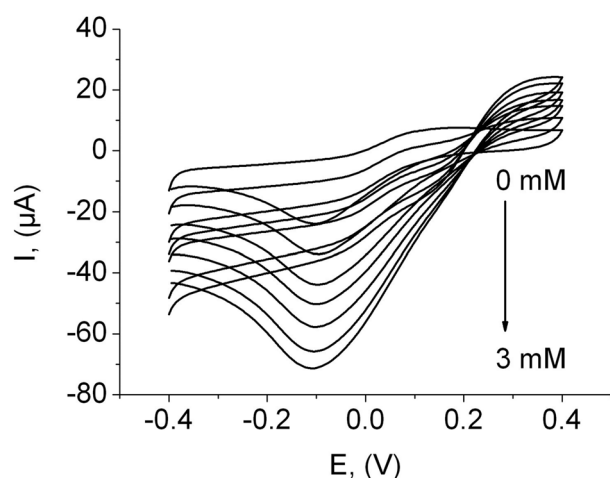
pH 7.0 at various concentrations of H_2O_2. When the concentration of H_2O_2 in the electrolyte is increased from 0.5 to 3.0 mM, cathodic peak current at –0.1 V progressively increases. A plot of concentration vs. cathodic peak current exhibits a linear dependency over entire experimental range. This phenomenon indicates that the modified electrode not only reduces H_2O_2, but can also be used for amperometric determination of H_2O_2.

Chronoamperometry (CA) under stirred conditions as an electrochemical technique has a much higher current sensitivity than cyclic voltammetry. The performance of the modified electrodes regarding the sensing of H_2O_2 was evaluated using CA according to detection limit, linear range, response time and stability. The amperometric response of the prepared electrodes was registered after successive additions of H_2O_2 stock solution under potentials of –0.1 and 0 V.

Fig. 3A displays the authentic record of the signal of GC electrodes, modified at different scan rates, to successive concentration increments over 0.5 to 7.0 mM H_2O_2 range. Cathode currents in presence of H_2O_2, resulting from its electrochemical reduction, were observed for the proposed electrochemical systems. Upon addition of H_2O_2 the modified electrodes show increasing reduction currents (staircase current response), corresponding to the electrochemical conversion of the analyte. As can be seen electrodes type Rh_v50/GC and Rh_v200/GC do not yield the desired response. Significant disadvantage of type Rh_v200/GC being a high noise level, recorded even at relatively low H_2O_2 concentrations. At the same time type Rh_v50/GC exhibits much lower current response than the other two modified electrodes. Analogous results in the

Fig. 2. CVs of modified electrode Rh_v100/GC in 0.1 M PBS (pH 7.0) at scan rate of 50 mV s^{-1} with increasing H_2O_2 concentration (from inner to outer) 0.0, 0.5, 1.0, 1.5, 2.0, 2.5 and 3.0 mM.
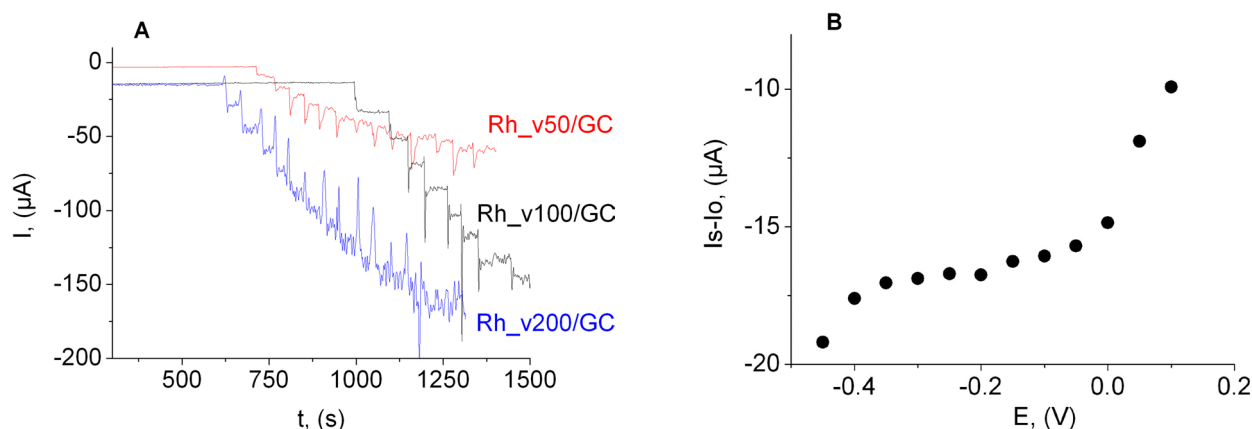

Fig. 3. A) Authentic record of the amperometric response at the modified electrodes type Rh_v50/GC, Rh_v100/GC and Rh_v200/GC for successive additions of H_2O_2 into stirred 0.1 M PBS (pH 7.0) at an applied potential of –0.1 V. B) The steady-state current as a function of potential applied at electrode type Rh_v100/GC when 0.5 mM H_2O_2 is present.

analytical behavior of the three modified electrodes were obtained in the CA study at an applied potential of 0 V. Based on the observed, electrode type Rh_v100/GC was used in further investigations. The polarization curve (Fig. 3B) over the potential range from -0.45 to 0.1 V, registered in 0.1 M PBS (pH 7.0) with 0.5 mM H_2O_2 present, clearly shows interval of potentials where the cathodic current hardly varies (a "plateau region"). The plateau region for the modified electrode occurred between –0.4 and 0 V.

The background subtracted steady-state response (I_S-I_0) of the electrode in PBS (pH 7.0) is presented in Fig. 4. At an applied potential of –0.1 V the linear response was proportional to the H_2O_2 concentration up to 5.5 mM (correlation coefficient of 0.99_4) with a sensitivity of 34.88 $\mu A\ mM^{-1}$ (or 493 $\mu A\ mM^{-1}\ cm^{-2}$). At a potential of 0 V the linearity was up to 3.5 mM H_2O_2 (0.97_8) with a sensitivity of 23.36 $\mu A\ mM^{-1}$ (330 $\mu A\ mM^{-1}\ cm^{-2}$).

The modified electrode responded rapidly producing steady-state signal within 8 s. A well-defined current response was observed during the successive additions of 10 μM H_2O_2 (detection limit of 1.5 μM at a signal-to-noise ratio of 3), which evidences a stable and efficient catalytic property of rhodium deposits (Fig. 5).

In order to assess the impact of type of carbonaceous carrier on the activity of the electrocatalysts, graphite electrode (Gr) has been modified using the same procedure for electrodeposition of Rh (denoted in text as type Rh_v100/Gr). The chronoamperometric data at potential of 0 V suggest that the analytical detection of H_2O_2 with a modified graphite Rh_v100/Gr is distinguished by twice lower sensitivity (230 $\mu A\ mM^{-1}\ cm^{-2}$), short linear dynamic range (up to 2.8 mM), slower response (15 s), higher background current and noise (detection limit of 10 μM). The probable reason for the observed differences in the electrochemical behavior of the two modified electrodes is highly porous surface of the graphite carrier, used for the development of catalyst type Rh_v100/Gr.

The long-term operational stability and reproducibility of the signal of the modified electrode are essential for its applicability as a sensing element. In this connection, the reproducibility of the current signal for the electrode type Rh_v100/GC to 0.5 mM H_2O_2 at an applied potential of 0 V was examined. The relative standard deviation (RSD) was calculated to be 3.2% for 5 successive measurements (current responses were 16.8, 17.3, 15.9, 16.5 and 17.0 μA, respectively).

Further, the reproducibility of the proposed procedure of electrodeposition of Rh was studied by analysis of the same concentration of H_2O_2 (0.5 mM) using four equally prepared electrodes type Rh_v100/GC. The electrodeposition procedure had good reproducibility with a RSD of 6.7%. Here, it should be noted the key role of the pre-treatment process of the electrode surface preceding the procedure of electrodeposition.

The modified electrode was stored in air over a 3 months period. During the first two weeks there was a gradual decrease to 87% of its initial current response, probably due to processes of recrystallization of the metal phase; after this period the electrode activity remained practically unchanged. The long-term stability of the electrode is in general comparable to the stability of other modified electrodes, applied for H_2O_2 sensing: 85.3% after 1 week of storage [15], 87% (1 month) [16], 92% (3 weeks) [17].

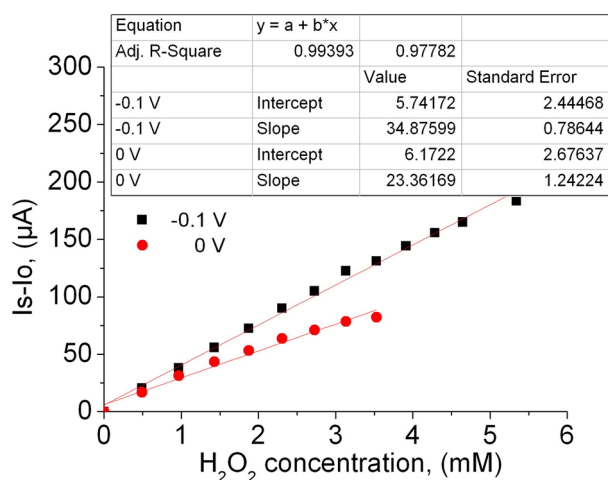| Equation	y = a + b*x		
Adj. R-Square	0.99393	0.97782	
		Value	Standard Error
-0.1 V	Intercept	5.74172	2.44468
-0.1 V	Slope	34.87599	0.78644
0 V	Intercept	6.1722	2.67637
0 V	Slope	23.36169	1.24224

Fig. 4. Calibration plot for electrode type Rh_v100/GC; 0.1 M PBS (pH 7.0); applied potentials: –0.1 V and 0 V.
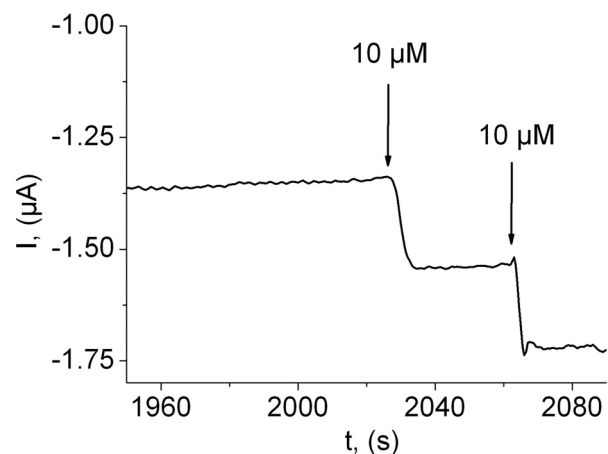

Fig. 5. Authentic record of the amperometric response of modified electrode Rh_v100/GC upon additions of 10 μM H_2O_2 in 0.1 M PBS (pH 7.0); potential of 0 V.

Table 1. Comparison of the operational characteristics of amperometric sensors for H_2O_2 detection, based on modified glassy carbon electrodes, with the achieved in the present work

Electrode modifier	E, V	Sensitivity, $\mu A\ mM^{-1}\ cm^{-2}$	Linear range, M	Detection limit, M	Ref.
Ag/NFM	-0.58[a]	157.0	$1.0\times10^{-5}\sim1.6\times10^{-2}$	4.0×10^{-6}	10
$Ir^{IV}Ox.H_2O$	-0.3[a]	6.15[c]	$5.0\times10^{-6}\sim1.5\times10^{-4}$	5.0×10^{-6}	11
GR-AuNPs	-0.4[a]	3.0[d]	$2.0\times10^{-5}\sim2.8\times10^{-4}$	6.0×10^{-6}	12
PtNWs-CNTs-CHIT	-0.1[b]	260.0	$1.0\times10^{-6}\sim3.0\times10^{-2}$	–	13
Co_3O_4 NWs	-0.2[a]	80.74	up to 5.35×10^{-3}	1.0×10^{-5}	14
Ag	-0.2[a]	104.53[*]	$5.0\times10^{-6}\sim1.2\times10^{-2}$	5.0×10^{-7}	15
PVA/MWCNTs/PtNPs	0[a]	122.63	$2.0\times10^{-6}\sim3.8\times10^{-3}$	7.0×10^{-7}	16
Pd/PEDOT NSs	-0.2[b]	215.3	up to 1.0×10^{-3}	2.84×10^{-6}	17
ERGO-AgNPLs	-0.5[a]	183.5	$2.0\times10^{-5}\sim1.0\times10^{-2}$	3.0×10^{-6}	18
Rh_v100/GC	-0.1[a]	493.0	$2.0\times10^{-6}\sim5.5\times10^{-3}$	1.5×10^{-6}	This work
Rh_v100/Gr	0[a]	230.0	$2.0\times10^{-5}\sim2.8\times10^{-3}$	1.0×10^{-5}	

[*]Calculated from the data in paper;

[a] Reference electrode: Ag/AgCl, 3 M KCl (0.200 V vs. SHE);

[b] Reference electrode: saturated calomel electrode (SCE) (0.242 V vs. SHE);

[c] the unit is: $nA\ \mu M^{-1}\ cm^{-2}$;

[d] the unit is: $\mu A\ \mu M^{-1}\ cm^{-2}$.

NFM – nanofibrous membrane, GR – graphene, ERGO – electrochemically reduced graphene oxide, CNTs – carbon nanotubes, MWCNTs – multiwall carbon nanotubes, NPLs – nanoparticles, NWs – nanowalls, NSs – nanospheres, CHIT – chitosan, PVA – poly(vinyl alcohol), PEDOT – poly(3,4-ethylenedioxythiophene).

The performance of the Rh_v100/GC catalyst, developed in this study, was compared with other modified electrodes. In Table 1 we have summarized various H_2O_2 sensors, based on modified glassy carbon electrodes, with respect to the applied potential, sensitivity, linear dynamic range and limit of detection. All data presented are recorded in supporting electrolyte buffer solution with pH in the range 6.0–7.5 in the H_2O_2 electroreduction mode. It can be seen that the proposed Rh_v100/GC electrode shows an excellent sensitivity, several times higher than that obtained by using other glassy carbon electrodes modified with metal or metal oxide particles.

CONCLUSION

In conclusion, a fast, simple and reproducible procedure for electrochemical modification of carbonaceous carriers with rhodium has been demonstrated in this study. The graphite and glassy carbon electrodes, modified applying the presented procedure, were used for the electrocatalytic reduction of H_2O_2 and their applicability for amperometric detection of H_2O_2 in micromolar concentrations has been proven. The modified glassy carbon type Rh_v100/GC exhibited excellent electrocatalytic performance – fast and stable response, low

detection limit (1.5 μM) and wide linear range (up to 5.5 mM) for H_2O_2 detection at low applied potential (–0.1 V vs. Ag/AgCl, 3M KCl). The developed electrocatalyst provides a new approach to construct a highly sensitive and selective amperometric biosensors of first generation (based on hydrogen peroxide-producing enzymes) for quantitative detection of biologically important compounds. Further experiments, such as the practical application of this modified electrode as a transducer in the construction of glucose and L-lactate biosensors, are underway.

REFERENCES

1. I. Casella, M. Contursi, *Electrochim. Acta*, **138**, 447 (2014).
2. S. Garcìa, L. Zhang, G. Piburn, G. Henkelman, S. Humphrey, *ACS Nano*, **8**, 11512 (2014).
3. K. Park, K. Jang, H. Kim, S. Son, *Ang. Chem. Int. Edit.*, **46**, 1152 (2007).
4. V. Kanaru, S. Humphrey, J. Kyffin, D. Jefferson, J. Burton, M. Ambruster, R. Lambert, *Dalton Trans.*, 7602 (2009).
5. R. Ortiz, O. Marquez, J. Marquez, C. Gutierrez, *Portug. Electrochim. Acta*, **24**, 105 (2006).
6. E. Horozova, N. Dimcheva, M. Miteva, Z. Jordanova, *Bulg. Chem.Commun.*, 40, 129 (2008).

7. Q. Yuan, Z. Zhou, Z. Zhuang, X. Wang, *Inorg. Chem.*, **49**, 5515 (2010).
8. B. Sathe, B. Balan, V. Pillai, *Energy & Environm. Sci.*, **4**, 1029 (2011).
9. H. Beyer, K. Kohler, *Appl. Catal. B: Environm.*, **96**, 110 (2010).
10. D. Li, L. Luo, Z. Pang, X. Chen, Y. Cai, Q. Wei, *RSC Adv.*, **4**, 3857 (2014).
11. P. Liu, S. Sun, Y. Chen, M. Chuang, *Electrochim. Acta*, **187**, 256 (2016).
12. J. Hu, F. Li, K. Wang, D. Han, Q. Zhang, J. Yuan, L. Niu, *Talanta*, **93**, 345 (2012).
13. F. Qu, M. Yang, G. Shen, R. Yu, *Biosens. Bioelectron.*, **22**, 1749 (2007).
14. W. Jia, M. Guo, Z. Zheng, T. Yu, E. Rodriguez, Y. Wang, Y. Lei, *J. Electroanal. Chem.*, **625**, 27 (2009).
15. X. Qin, H. Wang, X. Wang, Z. Miao, Y. Fang, Q. Chen, X. Shao, *Electrochim. Acta*, **56**, 3170 (2011).
16. Y. Fang, D. Zhang, X. Qin, Z. Miao, S. Takahashi, J. Anzai, Q. Chen, *Electrochim. Acta*, **70**, 266 (2012).
17. F. Jiang, R. Yue, Y. Du, J. Xu, P. Yang, *Biosens. Bioelectron.*, **44**, 127 (2013).
18. L. Zhong, S. Gan, X. Fu, F. Li, D. Han, L. Guo, L. Niu, *Electrochim. Acta*, **89**, 222 (2013).

МОДИФИЦИРАНИ С РОДИЙ ВЪГЛЕРОДНИ ЕЛЕКТРОДИ: ПРИЛОЖЕНИЕ ЗА ЕЛЕКТРОХИМИЧНА ДЕТЕКЦИЯ НА ВОДОРОДЕН ПЕРОКСИД

Я. Л. Лазарова, Т. М. Додевска*

Университет по хранителни технологии, кат. „Органична химия и неорганична химия“, бул. „Марица“ 26, Пловдив 4002, България

(Резюме)

Настоящото изследване представя бърза, семпла и възпроизводима процедура за електрохимично модифициране на въглеродни носители с родий. Електрохимичното поведение при електроредукция на H_2O_2 на графитов и стъклографитов електрод, модифицирани чрез представената тук методика, е изучено чрез циклична волтамперометрия и хроноамперометрия при pH 7.0. Показана е приложимостта на модифицираните електроди за количествена амперометрична детекция на H_2O_2 при ниски работни потенциали (0 V и –0.1 V vs. Ag/AgCl, 3M KCl). Модифицираният електрод тип Rh_v100/GC, получен чрез електроотлагане на родий при определената като оптимална скорост на разгъване на потенциала (100 mV s⁻¹), показва отлично поведение – бърз, стабилен и чувствителен отклик, нисък откриваем минимум (1.5 μM H_2O_2) на аналита и широка област на линейна зависимост на сигнала (до 5.5 mM), което го характеризира като подходящ трансдюсер за неензимна амперометрична детекция на H_2O_2.

Mechanism of therapeutic action of abiogenic Li^+ and Ga^{3+} ions: insights from theoretical studies

N. Kircheva, T. Dudev*

Faculty of Chemistry and Pharmacy, Sofia University "St. Kliment Ohridski", 1 James Bourchier Avenue, Sofia1164, Bulgaria

Lithium and gallium (Li^+ and Ga^{3+}) exhibit no known biological functions and are categorized as abiogenic ions. However, they are used in medicine (in the form of soluble salts) as a first-line drugs for treatment of bipolar disorder (Li^+) or cancer-related hypercalcemia (Ga^{3+}) as well as a drug with antiproliferative action in clinical trials (Ga^{3+}). Even though their therapeutic effects are well known, there are many unanswered questions concerning their mechanism of action. The main hypotheses posit competition between Li^+ and the native Mg^{2+}, and between Ga^{3+} and the cognate Fe^{3+} ions for binding to some metalloenzymes involved in cell signaling and cell proliferation, respectively. The conducted theoretical research explains some of the most accepted hypotheses about the therapeutic action of the two alien cations. The factors governing the competition between biogenic and abiogenic cations in protein binding sites are also revealed. The theoretical results are in line with experimental data.

Keywords: lithium, gallium, mechanism of action, theoretical study.

INTRODUCTION

Since the beginning of time mankind has struggled not only to understand the laws of nature but also to apply them for the general benefit. Over the centuries, medicine and pharmacy have been prioritized areas of research/application achieving tremendous success in their development [1, 2]. Nowadays the term "drug" is usually associated with a variety of organic/peptide/polypeptide compounds from different classes of medications. Inorganic substances, however, such as metal salts or complexes, can also exert curative effect and be employed in treating health disorders.

About 40% of all known proteins contain metal cations, which appear as indispensable players in a plethora of essential tasks such as protein structure stabilization, enzyme catalysis, hormone secretion, signal transduction, blood coagulation, respiration and photosynthesis [1, 3, 4, 5]. In the course of evolution biological function has been bestowed on about two dozen metal species based on their bioavailability and chemical properties. They are known as "biogenic" or "native" ions, among which the most common are Na^+, K^+, Mg^{2+}, Ca^{2+} and Zn^{2+} and the redox-active transition metal cations $Mn^{2+/3+/4+}$, $Fe^{2+/3+}$ and $Cu^{+/2+}$ [3, 4, 5]. Other (abiogenic) metal ions, excluded from the evolutionary process, such as Hg^{2+}, Pb^{2+}, Al^{3+}, upon entering the host organism, could disrupt cellular functions by competing with some of the above-mentioned native ions thus intoxicating the recipient. On the other hand, there are a few alien metal cations (Li^+, Sr^{2+} and Ga^{3+}) with no known vital functions in humans, that exert therapeutic effects based on their similarity with some cognate metals. In this review we focus on lithium and gallium that have been an object of investigation of our group for some time. We summarize the most accepted hypotheses concerning the mechanism of action as well as the applications of Li^+ and Ga^{3+} in medicine. Using the methods of the theoretical chemistry we have tried to shed light on the suggested competition between the biogenic and alien metal ions.

MECHANISM OF ACTION

Lithium

Lithium has been applied in the form of soluble salts in concentration range of 0.6–1.2 mM to treat patients suffering from bipolar disorder [6]. This illness affects 1–3% of the world's population and

* To whom all correspondence should be sent:
E-mail: t.dudev@chem.uni-sofia.bg

is characterized by episodes of mania and depression separated by periods of normal behavior [6, 7]. Although the beneficiary effect of lithium therapy has been known for decades, its mechanism of action is still enigmatic. Several hypotheses have been put forward. Among them, the most accepted one posits competition between the alien Li$^+$ and the native Mg^{2+} and subsequent inhibition of several overexpressed enzymes involved in cell signaling, such as inositol monophosphatase (IMPase) and glycogensynthase kinase 3β (GSK-3β) [4, 6–8]. Lihium's direct inhibition of IMPase has led to the formation of the "inositol depletion hypothesis" – by decreasing the free inositol levels, lithium dampens the activation of downstream signaling pathways in neurons [6–9]. The other enzyme of interest – GSK-3β, is a component of many signaling pathways responsible for specific neurotransmission in the brain [4, 6, 7, 9, 10]. Note, however, that other essential magnesium enzymes in the cell remain unaffected by lithium action. Furthermore, another channel of lithium's therapeutic action has been recently suggested: lithium not only competes with magnesium to bind enzymes but it can also associate with magnesium-loaded ATP to modulate the native receptor's response involved in cell signaling [10, 11].

Lithium is expected to compete mainly with magnesium due to the similarity in their physicochemical properties. The "diagonal rule" brings Li$^+$ closer to Mg^{2+} than to its fellow alkali metals from group IA. This is proven by the fact that both Li$^+$ and Mg^{2+} are "hard" nonpolarizable cations with affinity towards hard "O" – containing ligands. They also have similar ionic radii (R_{ion}) for a given coordination number (CN): R_{ion}(Li$^+$) = 0.59 Å and R_{ion}(Mg^{2+}) = 0.57Å for CN = 4, and R_{ion}(Li$^+$) = 0.76 Å and R_{ion}(Mg^{2+}) = 0.72 Å for a CN = 6 [12]. Still they differ in their ionic charge (+1 for Li and +2 for Mg) and hydration free energies: –123.5 kcal/mol (Li$^+$) and –455.5 kcal/mol (Mg^{2+}) [13]. Although there are a few experiments proving lithium's ability to compete with magnesium for binding the above-mentioned enzymes and ATP-complexes [6, 7, 9, 11], there still remain questions about the ability of Li$^+$ to substitute for Mg^{2+} in IMPase and GSK-3β but not in other essential Mg^{2+}-containing enzymes in the cell. Also, the exact geometry/conformation and protonation state of the active ATP-Mg-Li complex has not been known.

Gallium

The first use of gallium in medicine was as a tumor-imaging ^{67}Ga-scan which was in time replaced by the more effective PET-scan [14]. But due to its ability to concentrate especially in liver cancer cells it was investigated for antiproliferative action.

As a side effect it was found that infusion of gallium nitrate reduces blood-level calcium and so it is nowadays used as Ganite^{TM} to treat patients with cancer-related hypercalcemia [15]. However, newer gallium compounds such as gallium maltolate and *tris*(8-quinolonato)gallium(III) (KP46) have already passed the preclinical examination with promising results of their anticancer action [16–20]. Ga^{3+} could also be used in a combination with other antitumor drugs like cis-platinum or tiosemicarbazones [21, 22]. The rationale behind gallium's anticancer effect lies upon its action as an iron mimetic species [14, 19, 23, 24] and iron-competitor in tumor cells, that need iron for their fast proliferation. Sharing the same oxidation state and similar ionic radius with Fe^{3+} (R_{ion}(Ga^{3+}) = 0.620 Å in octahedral complexes compared with R_{ion}(Fe^{3+}) = 0.645 Å for high spin complexes as well as tetrahedral ionic radius 0.47 Å (Ga^{3+}) and 0.49 Å (Fe^{3+})) gallium could deceive the cell machinery and be taken up as iron. The two metal ions have also similar ionization potential and electron affinity values [5, 14]. However, while Fe^{3+} may undergo redox-reactions under physiological conditions, Ga^{3+} is redox-inactive and cannot participate in redox reactions in metalloenzymes.

Gallium's most probable target in tumor cells is the enzyme ribonucleotide reductase (RR) [5, 14, 18, 19, 24]. RR is a heterodimer which consists of two homodimeric M1 and M2 subunits. RRM1 contains a substrate (nucleotide diphosphate) and two effector-binding sites while RRM2 consists of a binuclear iron center and a tyrosil free radical. Its main purpose is the *de novo* synthesis of deoxyribonucleotides from ribonucleotides [25]. The iron center is of extreme importance because it is responsible for the generation of the radical which is later used in the redox reaction with the nucleotide-substrates. In the iron center, Fe^{2+} is oxidized to Fe^{3+}. Substituting the Fe^{3+} cation with the redox-inactive Ga^{3+} renders the enzyme inactive. Although it is a widely accepted hypothesis and there is some experimental evidence [14], the intimate mechanism of the competition between the two metal ions is poorly understood.

Another hypothesis of gallium's therapeutic action states that it may compete with iron for human transferrin (Tf), a glycoprotein, transporting Fe^{3+} in the bloodstream [26], as well as that the newly formed Tf-Ga^{3+} complex may compete with the Tf-Fe^{3+} complex for the Tf-receptor which would lead to decrease in the native ion's intracellular concentration level [5, 14, 24].

The last and newest hypothesis concerning gallium's mechanism of action coincides with the information that it is able to form complexes with different nucleotide-diphosphates [14, 26]. Since the substrates for RR are namely NDP (for example

ADP) the probable NDP-Ga^{3+} complex may directly inhibit the enzyme by blocking its substrate-binding site. This hypothesis is an object of ongoing investigation from our group.
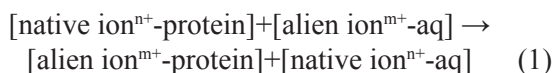
METHODS

Models used

Interactions between the metal and ligands from its first coordination shell are electrostatic in origin and dominate the energetics of the metal loaded binding site. Thus, we modeled the first coordination sphere of the enzymes of interest as a complex with either the native or the alien cation and evaluated the thermodynamic parameters of the respective substitution reaction (see below) [4, 5, 10]. The side chains of Asp^-/Glu^-, Asn/Gln and the backbone of the peptide are modeled as acetate (CH_3COO^-), acetamide (CH_3CONH_2) and *N*-methylacetamide ($CH_3CONHCH_3$), respectively, whereas the neutral His and ionized Tyr are presented as imidazole and phenolate, respectively. The preferable coordination number of the metal ions has been taken into account. The metal-binding centers of the enzymes were modeled in accordance with the respective Protein Data Bank (PDB) X-ray structures.

Reaction modeled

The competition between the native (Mg^{2+}/Fe^{3+}) and alien (Li^+/Ga^{3+}) cations can be described by the following model reaction:

$$[\text{native ion}^{n+}\text{-protein}]+[\text{alien ion}^{m+}\text{-aq}] \rightarrow$$
$$[\text{alien ion}^{m+}\text{-protein}]+[\text{native ion}^{n+}\text{-aq}] \quad (1)$$

In eq.1 [native/alien ion^{n+}-protein] and [native/alien ion^{n+}-aq] represent the metal cation bound inside the enzyme active site and outside binding cavity, respectively. The outcome of the competition between the two metal cations is assessed by the free energy evaluated in an environment characterized by a dielectric constant $\varepsilon = x$:

$$\Delta G^x = \Delta G^1 + \Delta G_{solv}^{\ x}([\text{alien ion}^{m+}\text{-protein}]) +$$
$$\Delta G_{solv}^{\ x}([\text{native ion}^{n+}\text{-aq}]) - \Delta G_{solv}^{\ x}([\text{native ion}^{n+}\text{-protein}]) - \Delta G_{solv}^{\ x}([\text{alien ion}^{m+}\text{-aq}]) \quad (2)$$

A negative value implies an alien-ion selective site, while a positive one means that the abiogenic ion cannot substitute for the native metal. ΔG^1 is the gas-phase free energy for the modeled reaction, and $\Delta G_{solv}^{\ x}$ is the free energy for transferring a molecule from the gas phase to a medium characterized by a dielectric constant $\varepsilon = x$.

DFT/CDM calculations

All calculations in the gas phase were done using either the Gaussian 03 [27] or the Gaussian 09 [28] programs. For each study the most adequate combination of DFT functional/basis set was chosen in order to reproduce the experimental data for the known metal ion-complexes [29–31]. After the full optimization of each structure and evaluating its electronic energy (E_{elect}), vibrational frequency calculations were performed. No imaginary frequencies were found indicating that the optimized structure corresponds to a minimum in its potential energy surface. For each method/basis set the vibrational frequencies were scaled by the corresponding empirical factor [32, 33] and were used to compute the thermal energies, including the zero-point energy (E_T) and entropy (S) corrections, in line with the statistical mechanical formulas [34]. The reaction free energy in the gas phase, ΔG^1, at room temperature, $T = 298.15$ K, was calculated according to the formula:

$$\Delta G^1 = \Delta E_{elec} + \Delta E_T + \Delta PV - T\Delta S, \quad (3)$$

where ΔE_{elec}, ΔE_T, ΔPV (work term*)* and ΔS are the differences between the products and the reactants.

Continuum dielectric method (CDM) calculations of the optimized metal constructs were performed [4, 5, 10] mimicking buried protein cavities characterized with dielectric constant $\varepsilon = 4$, partially solvent accessible active centers with $\varepsilon = 10$, or solvent exposed binding sites with $\varepsilon \approx 30$.

RESULTS

Li⁺ vs Mg²⁺ in GSK-3β and IMPase polynuclear sites

Crystallographic data indicates that GSK-3β possesses a solvent-accessible binuclear magnesium binding site (PDB entry 1PYX), where the two metals are bridged by an aspartate amino acid residue. Accordingly, the active site structure was modeled, optimized and its Li^+/Mg^{2+} selectivity assessed (Fig. 1). The calculations reveal that the binuclear binding site is vulnerable to Li^+ attack: the substitution of either of the Mg^{2+} cations by Li^+ is favorable in both buried and solvent-exposed sites (Fig. 1, negative ΔG^ε, $\varepsilon = 4$–30).

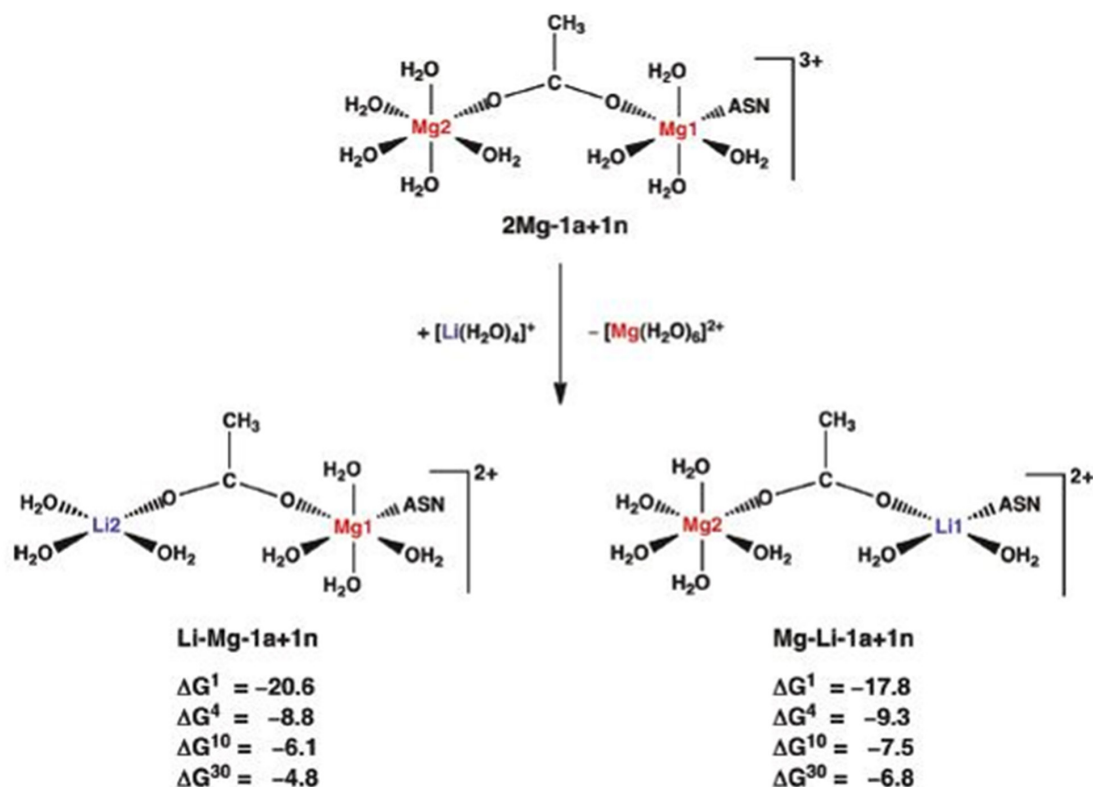IMPase, a key trinuclear Mg^{2+} enzyme of the phosphatidylinositol signaling pathway, is another

Fig. 1. Free energies, ΔG^ε (in kcal/mol) for $Mg^{2+} \rightarrow Li^+$ substitution in a model GSK-3β binuclear active center. Calculations are performed at B3LYP/6-31+G(3d,p) level [4].

putative target for Li⁺ therapy. The calculations predict that solvent exposed binding sites 2 and 3 (Fig. 2) are prone to $Mg^{2+} \rightarrow Li^+$ substitution, evidenced by negative ΔG^{30}. Results obtained imply that displacing Mg^{2+} from binding site 2 is more thermodynamically favorable than that from binding site 3 (lower ΔG^{30} for the former than latter). These findings are in line with the experimental ⁷Li NMR data which shows that, first of all, Li⁺ can displace Mg^{2+} from IMPase active centers, and, second, that the site of the Li⁺ attack is, indeed, center 2 [35]

The calculations answer the question why Li⁺ competes successfully with Mg^{2+} in signal transducing proteins, such as GSK-3β and IMPase, but not in other essential Mg^{2+} proteins. This is because the binding sites of the former enzymes possess high *positive* charge density (complex net charge 3+ for GSK-3β and 2+ for IMPase) and are solvent-exposed, whereas the binding sites of majority of the Mg^{2+} essential enzymes have higher *negative* charge density (overall charge between −1 and +1) and are buried into the protein structure (results not shown) [4].

Li⁺ in Mg²⁺-ATP complexes

Lithium has been hypothesized to bind to Mg^{2+}-loaded adenosine triphosphate (ATP) forming a Mg^{2+}-ATP-Li⁺ complex which, when protein-bound, may elicit different responses from key ATP-dependent enzymes/receptors involved in cell signaling [36]. The last hypothesis is supported by recent experiments showing that the Mg^{2+}-ATP-Li⁺ complex can indeed modulate the neuronal purine receptor response [11]. The P2X receptor, a ligand-gated ion channel that mediates the influx of extracellular Ca^{2+} into the cytoplasm, exhibited prolonged activation when stimulated by Mg^{2+}-ATP-Li⁺ as compared to the „native" Mg^{2+}-ATP. Therefore, when Mg^{2+} is already bound to ATP, which phosphate(s) best accommodate Li⁺ binding? Is the native Mg^{2+}-ATP conformation altered by Li⁺ coordination, thus affecting enzyme/receptor recognition?

The calculations reveal how the metal cation type and its binding mode affect the ATP conformation. Li⁺ bidentate binding via β and γ phosphates and OH⁻ metal bridge to Mg^{2+}-loaded ATP (Fig. 3) did not significantly alter the ATP conformation or
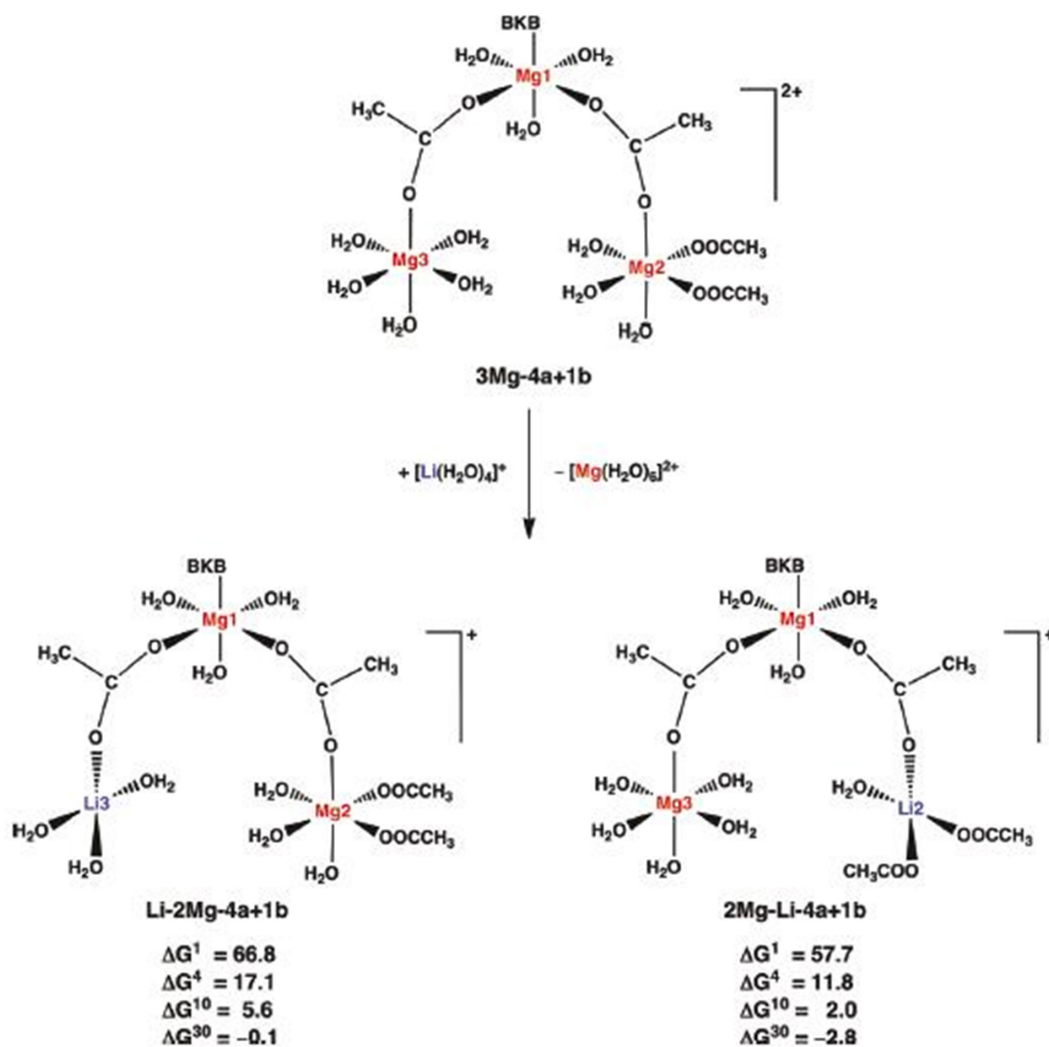
Fig. 2. Free energies, ΔG^ε (in kcal/mol) for $Mg^{2+} \rightarrow Li^+$ substitution in a model IMPase trinuclear binding site. Calculations are performed at B3LYP/6-31+G(3d,p) level [4].
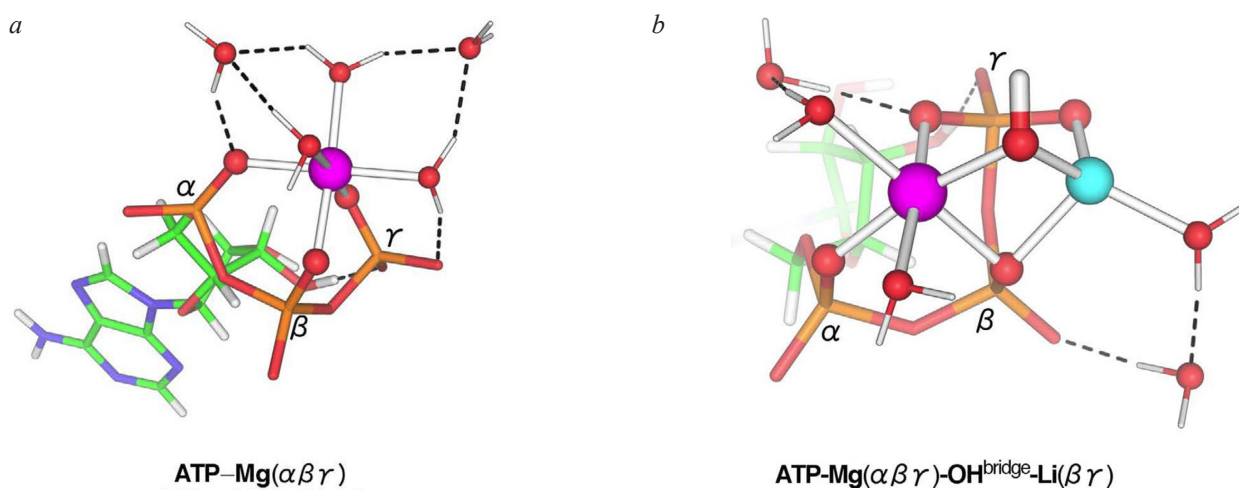

Fig. 3. M062X/6-311++G(d,p) optimized structures of the most stable (a) Mg^{2+}-ATP complex, where the metal binds in a tridentate fashion to the α, β and γ phosphates, and (b) Mg^{2+}-ATP-Li⁺ complex where Li⁺ binds to the Mg^{2+}-ATP tridentate complex in a βγ-bidentate mode via OH⁻ metal bridge [9].

the properties of the P–O bonds: The P–O bond lengths in the Mg^{2+}-ATP (Fig. 3a) and Mg^{2+}-ATP-Li$^+$ (Fig. 3b) complexes are identical (1.693 Å), while the bond polarities, estimated by the difference between the P and O Hirschfeld charges, are 0.81e and 0.83e, respectively.

These findings have important consequences for Mg^{2+}-ATP and Mg^{2+}-ATP-Li$^+$ recognition by cellular receptors. Since these two types of metal complexes have the same charge, similar overall ATP conformation and P–O bond properties, the Mg^{2+}-ATP-Li$^+$ complex might fit in the host receptor and trigger cellular response. Indeed, experiments show that Mg^{2+}-ATP-Li$^+$, like the native Mg^{2+}-ATP construct, is recognized by purinergic receptors and can activate subsequent signaling pathways [11]. Hence, Li$^+$ binding to Mg^{2+}-loaded ATP may permit recognition of the Mg^{2+}-ATP-Li$^+$ complex by certain host enzymes/receptors and activate specific signaling pathways.

Ga^{3+} vs Fe^{3+} in transferrin and ribonucleotide reductase

How selective are the metal binding sites of transferrin and ribonucleotide reductase, a key Fe^{3+} transport protein and an essential non-heme iron enzyme, respectively, for the two competing species, Ga^{3+} and Fe^{3+}? In answering this question, we have modeled the respective metal-loaded binding sites and evaluated the free energy of metal substitution [5].

The calculations demonstrate that Ga^{3+} cannot displace Fe^{3+} from a buried metal binding site evidenced by a positive ΔG^4 of metal exchange (= 0.9 kcal/mol) in Figure 4. This is in line with experimental estimates showing that the metal center, which is buried, exhibits greater affinity for Fe^{3+} than Ga^{3+} (ΔG^{exp} for Fe^{3+}→Ga^{3+} substitution = 2.4 kcal/mol [37]. However, transferrin remains the main carrier of gallium in the bloodstream as only one-third of its binding sites are loaded with Fe^{3+} [14, 24] thus the unoccupied binding centers can accomodate the incoming Ga^{3+} and, subsequently, deliver the alien metal to its target.

Ribonucleotide reductase contains two ferric-active centers which both, as the calculations imply, are prone to Fe^{3+}→Ga^{3+} substitution in solvent accessible binding pockets (negative ΔG^{32} in Figure 5). The Fe2^{3+} binding site, characterized with lower free energies of metal exchange than its Fe1^{3+} counterpart, seems to be the more likely target for Ga^{3+} attack. Therefore, the active sites loaded with the redox-inactive Ga^{3+} apper, in line with the postulated hypothesis (see above), defunct thus lowering the elevated levels of the enzyme in malignant cells.

CONCLUSIONS

This review summarizes the most accepted hypotheses about the mechanism of therapeutic action of the two abiogenic cations Li$^+$ and Ga^{3+}. Using the tools of the computational chemistry it sheds light on the intimate mechanism of the competition between Li$^+$ and Mg^{2+}, and Ga^{3+} and Fe^{3+} in protein binding sites. This, however, does not preclude efforts for deeper understanding the biochemistry and curative effect of abiogenic metal cations: The lithium's use as a preventive treatment for Alzheimer's disease or other neurodegenerative disorders calls for further investigations. Gallium, on the other hand, is also known for its antimicrobial and anti-inflammatory
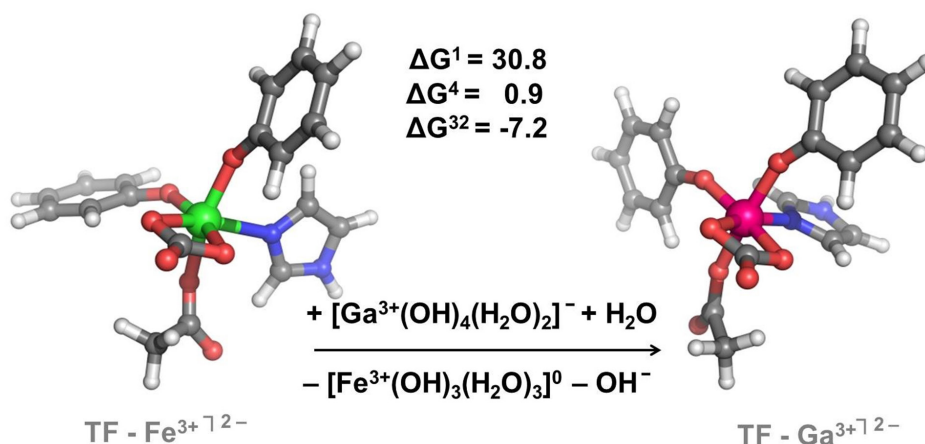

$\Delta G^1 = 30.8$
$\Delta G^4 = 0.9$
$\Delta G^{32} = -7.2$

$+ [Ga^{3+}(OH)_4(H_2O)_2]^- + H_2O$

$- [Fe^{3+}(OH)_3(H_2O)_3]^0 - OH^-$

TF - Fe^{3+}⌐$^{2-}$

TF - Ga^{3+}⌐$^{2-}$

Fig. 4. ΔG^x (in kcal/mol) for Fe^{3+}→Ga^{3+} substitution in a model transferrin binding site. Calculations are performed at B3LYP/6-31+G(3d,p) level of theory [5].

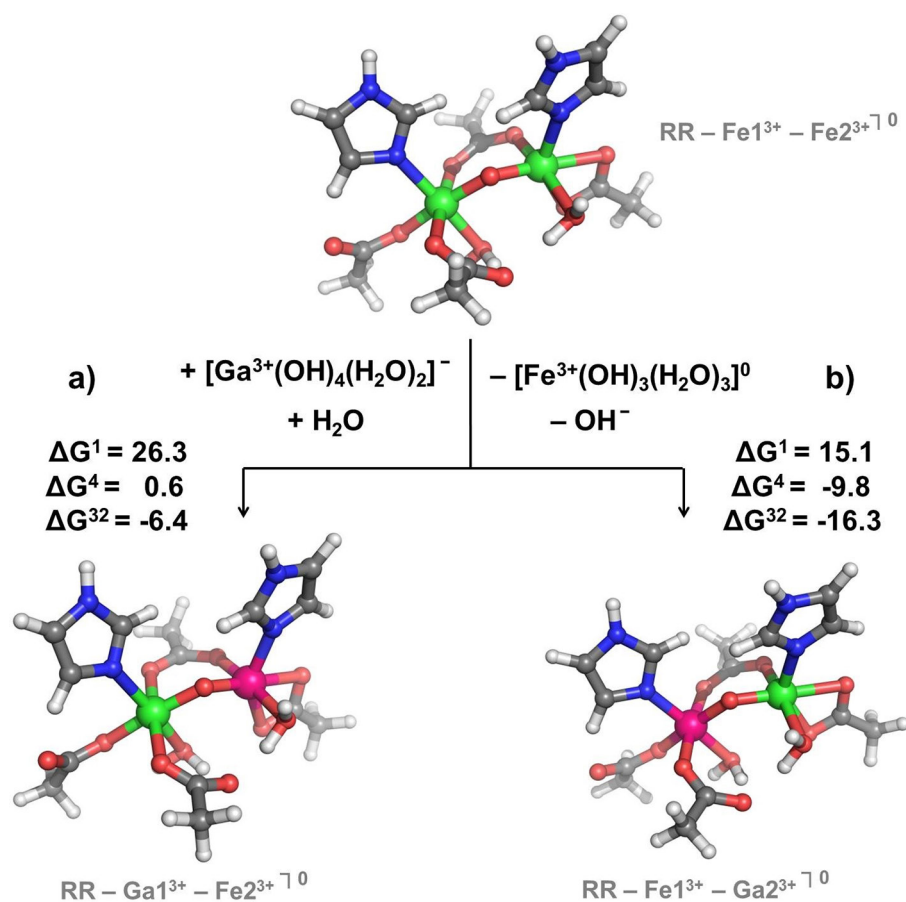**Fig. 5.** ΔG^x (in kcal/mol) for Fe^{3+}→Ga^{3+} substitution in a model ribonucleotide reductase active center. Calculations are performed at B3LYP/6-31+G(3d,p) level of theory [5].

actions, but the underlying mechanism/s of its curative effect is/are still enigmatic. The beneficiary effect of Sr^{2+}, another abiogenic metal, for human health and its mode of action have still to be elucidated.

REFERENCES

1. C. Orvig, M. J. Abrams, *Chem. Rev.*, **99**, 9, 2201 (1999).
2. Y. Ellahioui, S. Prashar, S. Gómez-Ruiz, *Inorganics*, **5**, 1, 4 (2017).
3. T. Dudev, C. Lim, *Chem. Rev.*, **114**, 1, 538 (2014).
4. T. Dudev, C. Lim, *J. Am. Chem. Soc.*, **133**, 24, 9506 (2011).
5. V. Nikolova, S. Angelova, N. Markova, T. Dudev, *J. Phys. Chem. B*, **120**, 9, 2241 (2016).
6. T. D. Gould, J. A. Quiroz, J. Singh, C. A. Zarate, H. K. Manji, *Mol. Psychiatry*, **9**, 8, 734 (2004).
7. F. Marmol, *Prog. Neuro-Psychopharmacology Biol. Psychiatry*, **32**, 8, 1761 (2008).
8. M. J. Berridge, R. F. Irvine, *Nature*, **341**, 6239, 197 (1989).
9. K. M. Brown, D. K. Tracy, *Ther. Adv. Psychopharmacol.*, **3**, 3, 163 (2013).
10. T. Dudev, C. Grauffel, C. Lim, *Sci. Rep.*, **7**, January, 1 (2017).
11. K. T. Briggs, G. G. Giulian, G. Li, J. P. Y. Kao, J. P. Marino, *Biophys. J.*, **111**, 2, 294 (2016).
12. R. D. Shannon, *Acta Crystallogr. Sect. A*, **32**, 5, 751 (1976).
13. C. V. Friedman, H. L.; Krishnan, *Plenum Press New York*, **3**, 1 (1973).
14. C. R. Chitambar, *Biochim. Biophys. Acta - Mol. Cell Res.*, **1863**, 8, 2044 (2016).
15. P. Melnikov, A. Malzac, M. de B. Coelho, *Acta Ortopédica Bras.*, **16**, 1, 54 (2008).
16. C. R. Chitambar, D. P. Purpi, J. Woodliff, M. Yang, J. P. Wereley, *J. Pharmacol. Exp. Ther.*, **322**, 3, 1228 (2007).
17. S. K. Bharti, S. K. Singh, *Int. J. PharmTech Res.*, **1**, 4, 1406 (2009).
18. C. R. Chitambar, *Future Med. Chem.*, **4**, 10, 1257 (2012).

19. C. R. Chitambar, *Int. J. Environ. Res. Public Health*, **7**, 5, 2337 (2010).
20. A. D. Melting, *L.R.Bernstein*, 1 (2013).
21. P. Collery *et al.*, *Anticancer Res.*, **32**, 7, 2769 (2012).
22. C. R. Chitambar, W. E. Antholine, *Antioxid. Redox Signal.*, **18**, 8, 956 (2013).
23. B. Desoize, *Anticancer Res.*, **24**, 3 A, 1529 (2004).
24. P. Collery, B. Keppler, C. Madoulet, B. Desoize, *Crit. Rev. Oncol. Hematol.*, **42**, 3, 283 (2002).
25. Y. Aye, M. Li, M. J. C. Long, R. S. Weiss, *Oncogene*, **34**, 16, 2011 (2014).
26. L. G. Marzilli, B. De Castro, J. P. Caradonna, R. C. Stewart, C. P. Van Vuuren, *J. Am. Chem. Soc.*, (1980).
27. J. A. Frisch, M. J.; Trucks, G. W.; Schlegel, H. B.; Scuseria, G. E.; Robb, M. A.; Cheeseman, J. R.; Montgomery, Jr., J. A.; Vreven, T.; Kudin, K. N.; Burant, J. C.; Millam, J. M.; Iyengar, S. S.; Tomasi, J.; Barone, V.; Mennucci, B.; Cossi, M.; Scalmani, G.; R, "Gaussian 03." Gaussian, Inc, Pittsburgh, PA, 2003.
28. J. A. Frisch, M. J.; Trucks, G. W.; Schlegel, H. B.; Scuseria, G. E.; Robb, M. A.; Cheeseman, J. R.; Montgomery, Jr., J. A.; Vreven, T.; Kudin, K. N.; Burant, J. C.; Millam, J. M.; Iyengar, S. S.; Tomasi, J.; Barone, V.; Mennucci, B.; Cossi, M.; Scalmani, G.; R, "Gaussian 09," *Gaussian Inc.* Wallingford CT, 2009.
29. T. Dudev, L. Chang, and C. Lim, *Biochemistry*, **15**, 12, 4091 (2005).
30. T. Dudev, C. Lim, *J. Am. Chem. Soc.*, 24, 1553 (2006).
31. T. Dudev, C. Lim, *J. Am. Chem. Soc.*, **131**, 23, 8092 (2009).
32. I. M. Alecu, J. Zheng, Y. Zhao, D. G. Truhlar, *J. Chem. Theory Comput.*, **6**, 9, 2872 (2010).
33. M. W. Wong, *Chem. Phys. Lett.*, **256**, 4–5, 391 (1996).
34. D. A. McQuarrie, Statistical Mechanics. Harper and Row: New York, 1976.
35. A. Haimovich, U. Eliav, A. Goldbourt, *J. Am. Chem. Soc.*, **134**, 12, 5647 (2012).
36. Birch_Response_to_DaSilvia_1976.pdf., Nature, p. 681 (1976).
37. W. R. Harris, L. Messori, *Coord. Chem. Rev.*, **228** (2002).

МЕХАНИЗЪМ НА ТЕРАПЕВТИЧНО ДЕЙСТВИЕ НА АБИОГЕННИТЕ ЙОНИ Li$^+$ И Ga^{3+}: ИЗВОДИ ОТ ТЕОРЕТИЧНИ ИЗСЛЕДВАНИЯ

Н. Кирчева, Т. Дудев*

Факултет по химия и фармация, Софийски университет „Св. Климент Охридски", бул. „Джеймс Баучер" № 1, София 1164, България

(Резюме)

Литият и галият (Li$^+$ и Ga^{3+}) не проявяват биологични функции в живите организми и се определят като абиогенни йони. Въпреки това те се използват в медицината (под формата на разтворими соли) като лекарства от първа линия за лечението на биполярно разстройство (Li$^+$) и на хиперкалциемия при раково болни пациенти (Ga^{3+}), както и като лекарство с антипролиферативно действие в клинични изпитания (Ga^{3+}). Макар че терапевтичните им ефекти са добре известни, съществуват много въпроси без отговор, засягащи механизма им на действие. Основните хипотези предполагат конкуренция между Li$^+$ и нативния Mg^{2+}, както и между Ga^{3+} и биогенния Fe^{3+} за свързване с някои металоензими, участващи съответно в клетъчната сигнализация или делене. Проведените теоретични изследвания обясняват някои от най-широко разпространените хипотези за терапевтичното действие на двата абиогенни йона. Факторите, управляващи конкуренцията между биогенните и абиогенните катиони в активните центрове на протеините, също биват разкрити. Теоретичните резултати са в съответствие с експериментални данни от литературата.

New phase obtained at mutual transformations of zinc hydroxy-salts

Ts. Stanimirova[1]*, Z. Delcheva[2], N. Petrova[2]

[1] *University of Sofia "St. Kliment Ohridski", Faculty of Geology and Geography, Department of Mineralogy, Petrology and Economic Geology, 15 Tzar Osvoboditel Blvd., 1000 Sofia, Bulgaria*
[2] *Institute of Mineralogy and Crystallography – Bulgarian Academy of Sciences, 107 Acad. G. Bonchev Str., 1113 Sofia, Bulgaria*

The hydroxy-salt minerals are normally stable over a small range of external conditions (such as Eh, pH, T, P, concentration of solutions, etc.). Therefore, they are converted easily into each other through changes in the crystal structure. The investigated initial zinc hydroxy salts are characterized by specific layered structures in which the zinc cations are both octahedrally and tetrahedrally coordinated as the ratio of octahedrally to tetrahedrally-coordinated zinc atoms is 3:2 or 3:1. In the process of detailed examination of the transformations during reaction of Zn-hydroxy nitrates (3:2 ratio) with sulfate solutions, Zn-hydroxy sulfates (3:1 ratio) with nitrate solutions and exchange reactions of Zn-hydroxy sulfate samples with alkali iodides, a stable phase with powder diffraction pattern not described in the ICDD database was obtained. Data of XRD, SEM-EDS, DTA-TG-MS and FTIR were used to characterize the new phase. The obtained new phase is characterized by a greater value of d_{001} = 17.84 Å comparing to that of the initial samples (d_{001} between 9.70–11.10 Å). The chemical data shows the only presence of cations of zinc and sulfur. The new phase chemical formula calculated from the chemical and thermal analyses could be defined as $Zn_4(OH)_6SO_4 \cdot 2 – 2.25H_2O$. The formation conditions as well as the mechanism of transformation were described and discussed: the new phase is formed at pH = 4.5–8 and the main mechanism of transformation is dissolution and subsequent crystallization.

Keywords: new Zn-hydroxy sulfate phase, characteristic data, transformation mechanism.

INTRODUCTION

Zinc hydroxy-salts are widespread in nature and are of interest in different areas. Primary sulfides of zinc are an important component of sulfide ores. In the oxidation zones, zinc is predominantly represented by hydroxy salts ($Zn_{1+x}(OH)_2A_{x/m}{}^{m-} \cdot nH_2O$, where A = Cl^-, CO_3^{2-}, SO_4^{2-}), carbonates (smithsonite) and silicates (hemimorphite) [1–2]. Zinc hydroxy-salt minerals have been also described as zinc and brass shifting products as well as zinc-containing slags [3–4]. Podda et al. [5] have established that the precipitation of hydrozincite from mine waters occurs due to photosynthetic microorganisms.

The excellent resistance of zinc and zinc-plated steel under natural conditions is due to the formation of a protective corrosion layer of zinc hydroxy-salts (zinc rust). The mineral composition of this layer highly depends on the exposure environment and its protective action is determined by both the morphology and the arrangement of the layer crystals [6]. Zinc hydroxide salts have been also investigated for other useful properties: ion-exchange and sorption properties [7–11], photo-catalytic properties [12], hydrogen-gas sensing properties [13], and as precursors of nanosized ZnO for various applications [14–15].

The hydroxy salt minerals normally are stable over a small range of external conditions (e.g. Eh, pH, T, P, concentration of solutions, component ratio, impurities, etc.) and are commonly associated with many other minerals of similar compositions in same parageneses. Unlike stable rock-forming minerals, these minerals react to minor environmental changes through changes in the crystal structure [16–17]. The strict limits of the conditions of formation and stability imply complete or partial dissolution and subsequent crystallization as a transformation mechanism of their mutual transformations.

* To whom all correspondence should be sent:
E-mail: stanimirova@gea.uni-sofia.bg

The investigated zinc hydroxy salts are characterized by specific layered structures in which the zinc cations are both octahedrally and tetrahedrally coordinated. The fundamental building unit of the structures is a sheet of octahedra with vacancies that share upper and lower faces with tetrahedra (Fig. 1). The octahedron is built mainly of OH groups as only in the structures of zinc hydroxy-sulfates some of the OH groups of the zinc octahedron are substituted by oxygen atoms of the sulfate groups. Zn-tetrahedra consist of three OH-groups of the octahedral layer (of the free octahedron), and the fourth (apical) position is directed to the interlayer and is occupied by a H_2O molecule, chlorine anions or oxygen atoms of the CO_3 group. The ratio of filled to vacant octahedral sites is 3:1 or 6:1 and respectively, the ratio of octahedrally to tetrahedrally-coordinated zinc atoms is 3:2 or 3:1. Thus, the octahedral-tetrahedral layer can be characterized as "interrupted decorated sheet" [18]. The zinc-hydroxide layer has a positive charge, which is compensated by the non-hydroxide anions in the structures. The hydroxide layer in the structure of Zn hydroxy sulfates (gordaite and Ca-gordaite) has a negative charge because of the simultaneous occupation of the two types of non-hydroxide anion sites in the tetrahedra and octahedra. This "excess" charge is compensated by $[Na(H_2O)_6]^+$ or $[Ca(H_2O)_9]^{2+}$ groups introduced into the interlayer. Sodium or calcium cations act as "anionic bond-valence absorbers" while the water molecules as bond-valence transformers in the sense of Schindler & Hawthorne [19]. This variety of different functionalities in the mineral structures of the group is a prerequisite for mutual transformations by different mechanisms: ionic (cationic and anionic) exchange, water-anion exchange; dehydration – rehydration, etc. On the other hand, the field and experimental studies show that the mutual transformations of hydroxy-salt minerals are typical of the weathering zones and are one of the reasons for the varied paragenesis.

Consecutive conversion was also observed in experiments to form zinc rust on galvanized steel under different conditions: in the Cl environment the sequence is ZnO-hydrozincite- simonkolleite-gordaite, while in the urban or industrial environment it is ZnO-hydrozincite- namuwite and with the time the ZnO and the hydrozincite gradually disappear [21–22].

The reactions of zinc hydroxy-nitrate with Zn-, Ni- and Co-chloride solutions are the first experimental study of transformations of zinc hydroxy salts [23]. The system has been studied later and pseudomorphic and topotaxic character of the transformations with oriented nucleation and crystal growth has been proposed [24]. Reactions of the
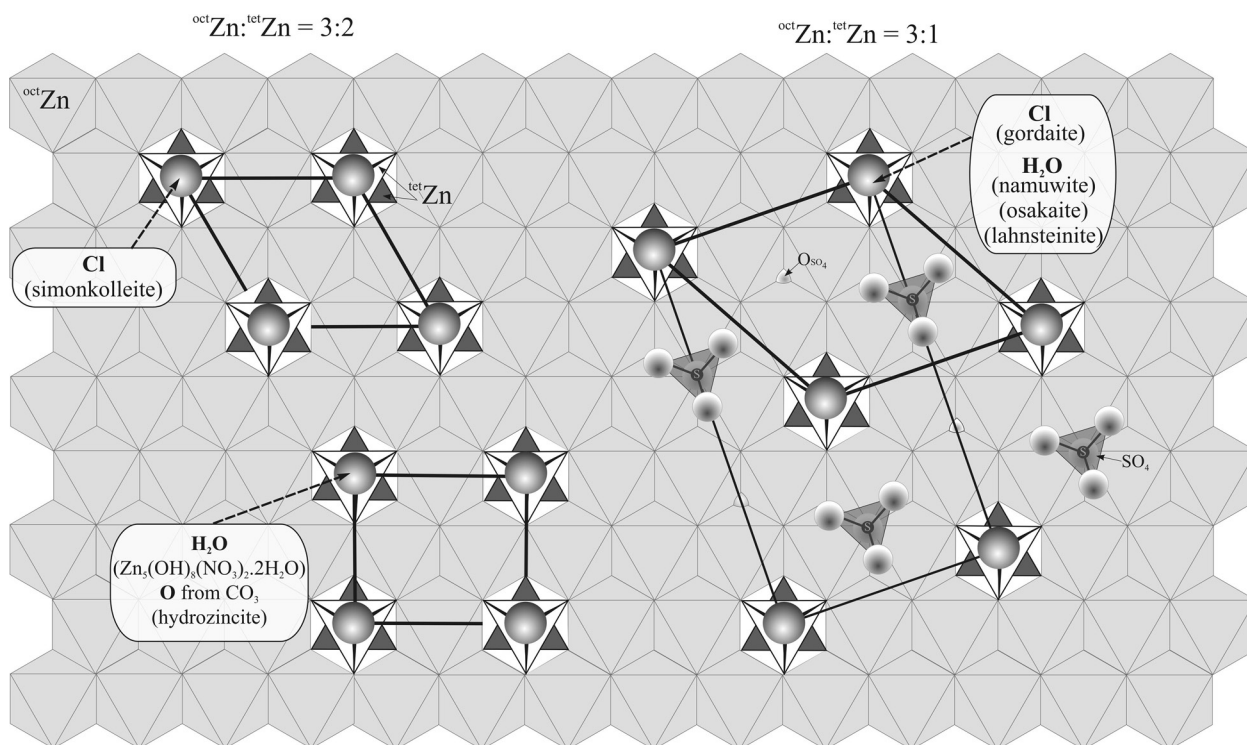

Fig. 1. Unit cells and atom distributions of Zn-hydroxy-salts on projection 001 of Zn hydroxide sheet.

same precursor with terephthalate and benzoate aqueous solutions have been studied allowing an ion exchange mechanism with a change in the arrangement of the vacant octahedra [7].

In the process of a detailed examination of the transformation mechanisms (in both the 3:1 and 3:2 systems) during reaction of Zn-hydroxy nitrates with sulfate solutions and Zn-hydroxy sulfates (namuwite, gordaite) with nitrate solutions and the exchange relationships in the sulfate agents, a stable phase with powder diffraction pattern not described in the ICDD database was obtained.

The aim of this work is to present the characterization data of this new phase (chemical composition, XRD, FTIR, thermal behavior: DTA-TG-MS, SEM: morphology) and to give an idea of the formation conditions and the transformation mechanism.

EXPERIMENT

Initial materials: In the present study synthetic analogues of Zn-hydroxy-salts minerals were used. This is due to the inaccessibility of a sufficient amount of mono-mineral in natural conditions and the fact that the natural samples are always with isomorphic impurities (mainly copper) which would hamper the interpretation of the results. In all experiments analytical grade chemicals were used.

Namuwite ($Zn_4(OH)_6(SO_4) \cdot 4H_2O$) was obtained by mixing of 1g ZnO powder with 30 ml 0.5M solution of $ZnSO_4$ with periodic stirring for 72 hours.

Gordaite ($NaZn_4(OH)_6(SO_4)Cl \cdot 6H_2O$) was obtained by mixing of 1g ZnO powder with 30 ml mixed solution of 0.5M $ZnSO_4$ and 1.5M NaCl in a ratio 1:1 at periodic stirring for 120 hours.

Ca-gordaite ($CaZn_8(OH)_{12}(SO_4)_2Cl_2 \cdot 9H_2O$) obtained through reaction between 1g mixed ZnO-CaO powder in a ratio 5:1 and 30 ml mixed solution of 1M $ZnSO_4$ and 1M $ZnCl_2$ in a ratio 1:1 at periodic stirring for 72 hours.

Nitrate compound ($Zn_5(OH)_8(NO_3)_2 \cdot 2H_2O$) was obtained by alkalization of 1M $Zn(NO_3)_2$ solution by titration with 1M NaOH or by urea [$(NH_2)_2CO$)] hydrolysis at 95 °C to pH=7.

After syntheses, the obtained samples were washed in distilled water and dried in air at room temperature.

Obtaining of new phase: *1) During reaction of both Zn-hydroxy nitrates with sulfate solutions and Zn-hydroxy sulfates with nitrate solutions:* The samples of initial $Zn_5(OH)_8(NO_3)_2 \cdot 2H_2O$ were treated with sodium or ammonium sulfate at pH 5, 6, 7 and 8 for 24–48 h; The samples of initial namuwite and gordaites were treated with $NaNO_3$ at 25 and 55 °C, $Mg(NO_3)_2$, $Sr(NO_3)_2$.

All experiments were performed at room temperature with periodic stirring. The resulting products were washed with distilled water, filtered and dried in air.

2) During attempts of exchange reaction in sulfate samples with alkali iodides: The initial samples of namuwite, gordaite and Ca-gordaite were dispersed in solutions of NaI or KI. The solid to solution ratio was adjusted to provide at least a tenfold excess of exchangeable ion. The reaction duration was one – three days. The resulting products were washed with distilled water, filtered and dried in air.

All experiments of synthesis, exchange and transformation are repeated at least twice.

Analyses: The initial and treated samples (new phase) were characterized by X-ray powder diffraction (XRD), scanning electron microscopy (SEM), Fourier transformed infrared spectroscopy (FTIR) and differential thermal analyses and the thermogravimetry with mass-spectroscopy (DTA-TG-MS).

The powder XRD patterns were recorded on a TuR M62 diffractometer using filtered Co Kα radiation in the 2Θ range 4–80°, step size 0.02°.

The SEM investigations and chemical analysis of some samples were performed by SEM fitted with energy dispersive spectrometer (EDS). Apparatus JEOL – model JSM-6010PLUS/LA, 20kV accelerating voltage and spot size 65 nm.

The infrared spectra were recorded by a Tensor 37 FTIR Bruker spectrometer in the spectral region 400–4000 cm^{-1}. The spectra were collected at room temperature on samples prepared by the standard KBr pallet technique after N_2-purging and with a spectral resolution of 4 cm^{-1} after averaging over 72 scans.

The DTA-TG-MS were carried out on the DTA-TG analyzer SETSYS2400, SETARAM at the following conditions: temperature range from 20 to 1000 °C, in a static air atmosphere, with a heating rate of 10 °C min^{-1}, and 10–15 mg samples weight. Simultaneous analysis of the evolved gases was performed via mass spectrometry using an OmniStar mass spectrometer connected to the TG apparatus. The intensities related to the main m/z value of the following volatiles H_2O (18), O_2 (32) and SO_2 (64) were examined.

RESULTS AND DISCUSSION

Initial samples: The powder X-ray diffraction shows that all obtained products are pure and well crystallized materials (Fig. 2a, c, e). The XRD-patterns correspond to the phases in the ICDD database as follows: $Zn_5(OH)_8(NO_3)_2 \cdot 2H_2O$ – PDF card No 24-1460; namuwite – PDF card No 35-0528;
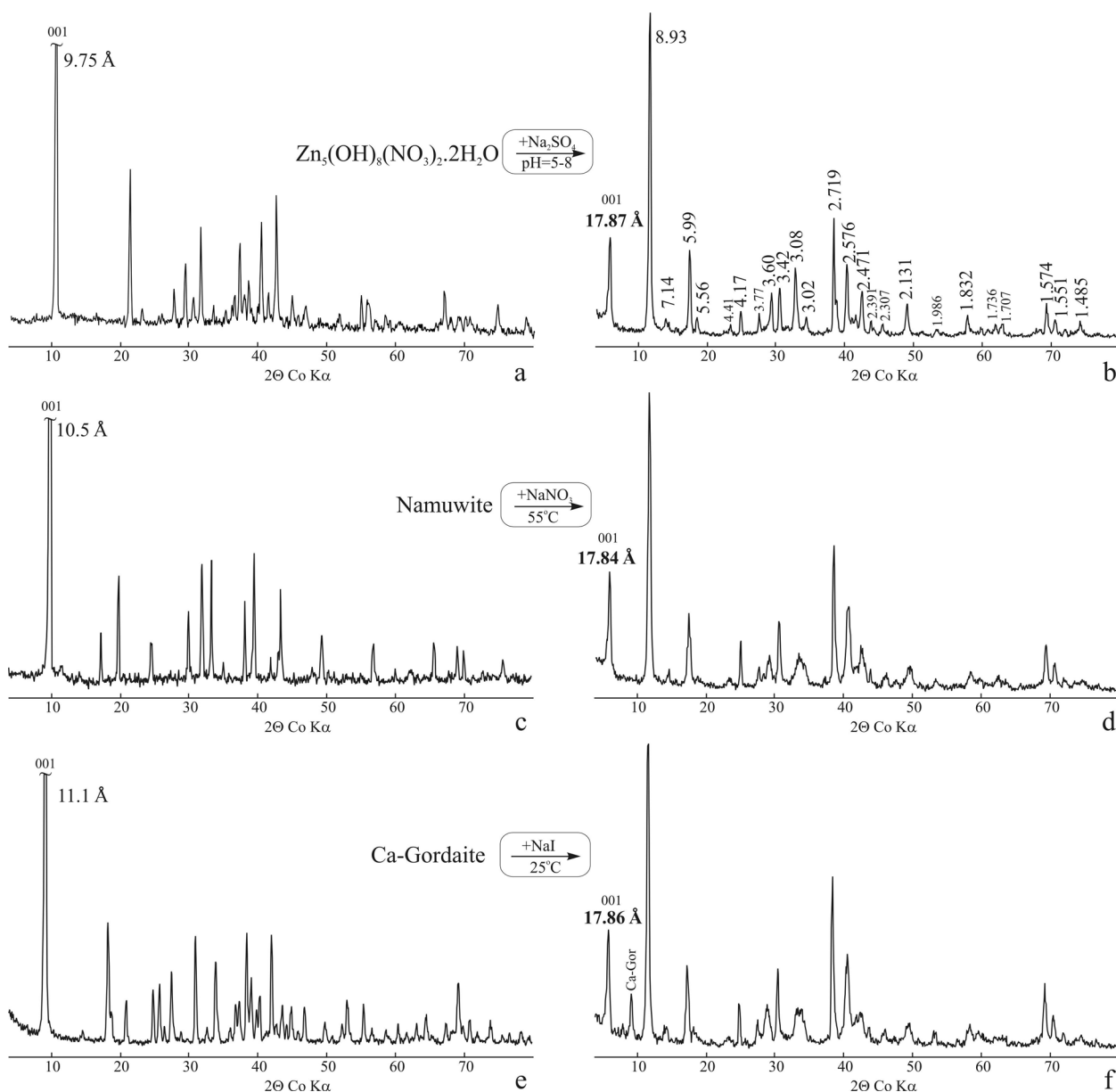
Fig. 2. Powder XRD patterns of: *a–b*) initial and treated with Na$_2$SO$_4$ Zn$_5$(OH)$_8$(NO$_3$)$_2$·2H$_2$O; *c–d*) initial and treated with NaNO$_3$ namuwite; *e–f*) initial and treated with NaI Ca-gordaite.

gordaite – PDF card No 88-1359 and Ca-gordaite – PDF card No 89-0851.

Plated to finely lined crystals with hexagonal or trigonal outlines are observed in SEM in accordance with the hexagonal symmetry of the octahedral layers of the initial samples. The size of the crystals depends on the method of synthesis. The NaOH precipitated crystals have a cross-sectional area of up to 2 μm and a thickness of 0.03–0.1 μm. Crystals obtained by hydrolysis of urea as well as from ZnO are in the order of magnitude larger than previous ones and reach cross-sections of 10–30 μm and

thickness of 0.5 to 2 μm (Fig. 3a, c, e). Among the crystals of Zn$_5$(OH)$_8$(NO$_3$)$_2$.2H$_2$O phase (Fig. 3a) according to its monoclinic symmetry (SG C2/m, a = 19.48 Å, b = 6.238 Å, c = 5.517 Å [25]), various pinacoid and prism crystal forms are observed as their relative development varies depending on the synthesis method. The gordaite crystals (SG P-3; a = 8.3556 Å, c = 13.0252 Å according to [26]) are scaly specimens with characteristic spiral subdivisions on the basal wall (Fig. 3c). The namuwite mineral (SG P-3; a = 8.33Å, c = 10.54Å according to [27]) is represented by finely flaky to finely

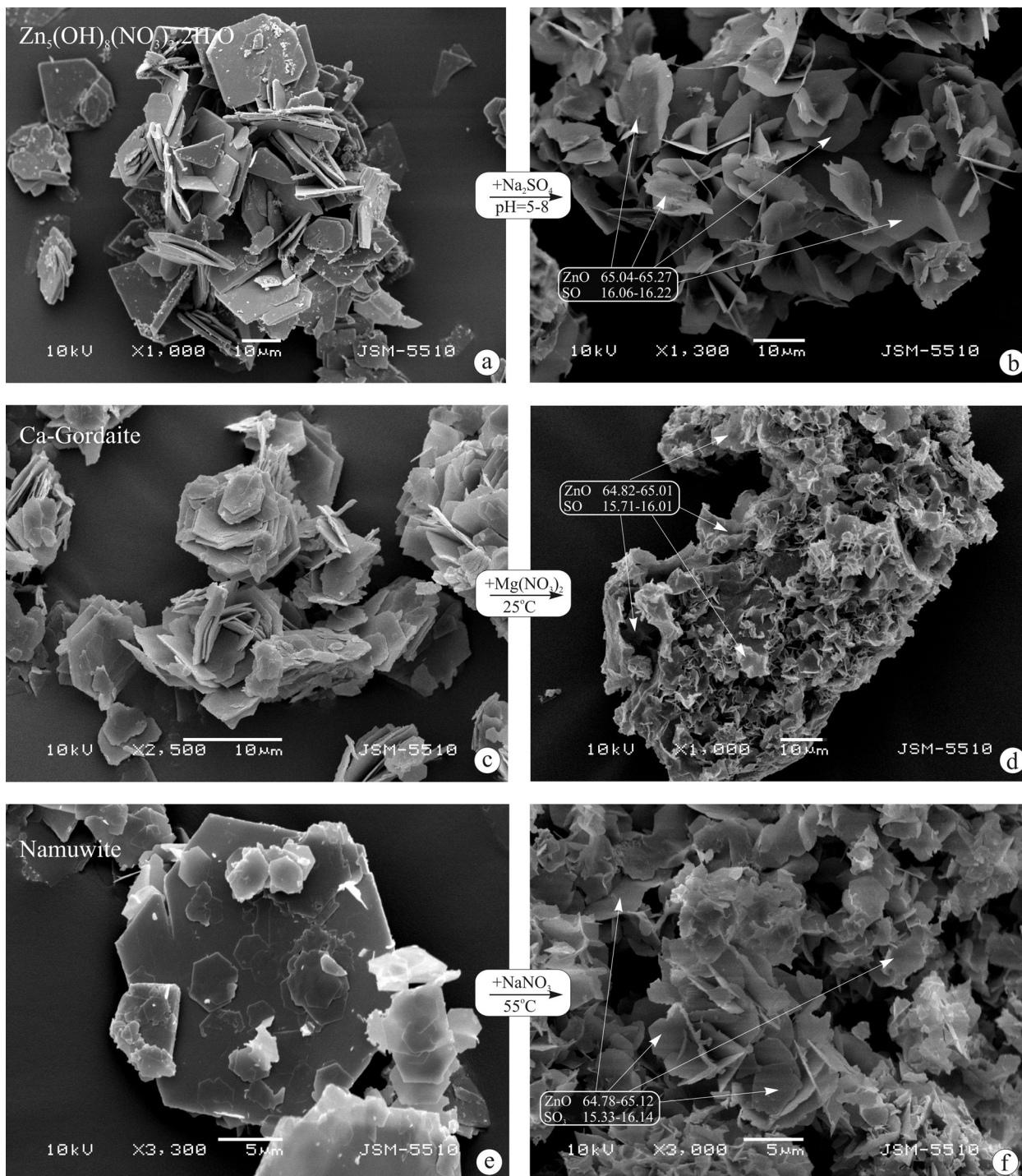**Fig. 3.** SEM microphotographs of: *a–b*) initial and treated with Na_2SO_4 $Zn_5(OH)_8(NO_3)_2 \cdot 2H_2O$; *c–d*) initial and treated with $Mg(OH)_2$ Ca-gordaite; *e–f*) initial and treated with $NaNO_3$ namuwite. Chemical data of new phase obtained by EDS are also presented.

cryptic crystals (sometimes bent), with hexagonal outlines (Fig. 3e).

The new phase: During investigation of the transformation relationships between nitrate hydroxy salts (^{oct}Zn : ^{tet}Zn ratio = 3:2) and sulfate hydroxy salts (3:1 ratio) an unidentified phase in the ICDD database was obtained (Fig. 2b). This phase is a product of two type of reactions: interaction between both the nitrate hydroxy salts with sulfate solutions (Na_2SO_4 and $(NH_4)_2SO_4$; pH = 4.5–8)

and the sulfate hydroxy salts with nitrate solutions ($NaNO_3$, $Mg(NO_3)_2$ and $Sr(NO_3)_2$).

As can be seen, the phase is characterized by a greater value of the d-spacing of the first reflection (d_{001} = 17.84 Å), which is in multiple dependence with other reflexes of 8.93 Å and 5.99 Å. The hk0 characteristic lines of the sulfate zinc hydroxy salts (d_{110} = 4.17 Å, d_{210} = 2.719 Å, d_{140} = 1.574 Å) are also registered in the XRD pattern of the new phase (Fig. 2b), which suggests the similarity or proximity of the hydroxide layers. The EDS chemical data of the products obtained from both types of hydroxy sulfate in the presence of various nitrates shows that only cations of zinc and sulfur were found in the phase composition without presence of an alkaline or alkaline earth cations and other non-sulfate anions (Fig. 3 b, d, f). At that way, this phase can be defined as zinc-hydroxy sulfate hydrate. Such kinds of the known minerals are osakaite ($Zn_4(OH)_6SO_4·5H_2O$), namuwite ($Zn_4(OH)_6SO_4·4H_2O$) and lahnsteinite ($Zn_4(OH)_6SO_4·3H_2O$). The thermal study data, however, shows that the water content is less than that of the hydroxy-sulfate salt minerals – namuwite and gordaite (Fig. 4). The new phase chemical formula calculated from the chemical and thermal analyses could be defined as $Zn_4(OH)_6SO_4·$ 2–2.25H_2O. Less hydrated zinc hydroxy sulfate compounds are known and investigated in the lit-
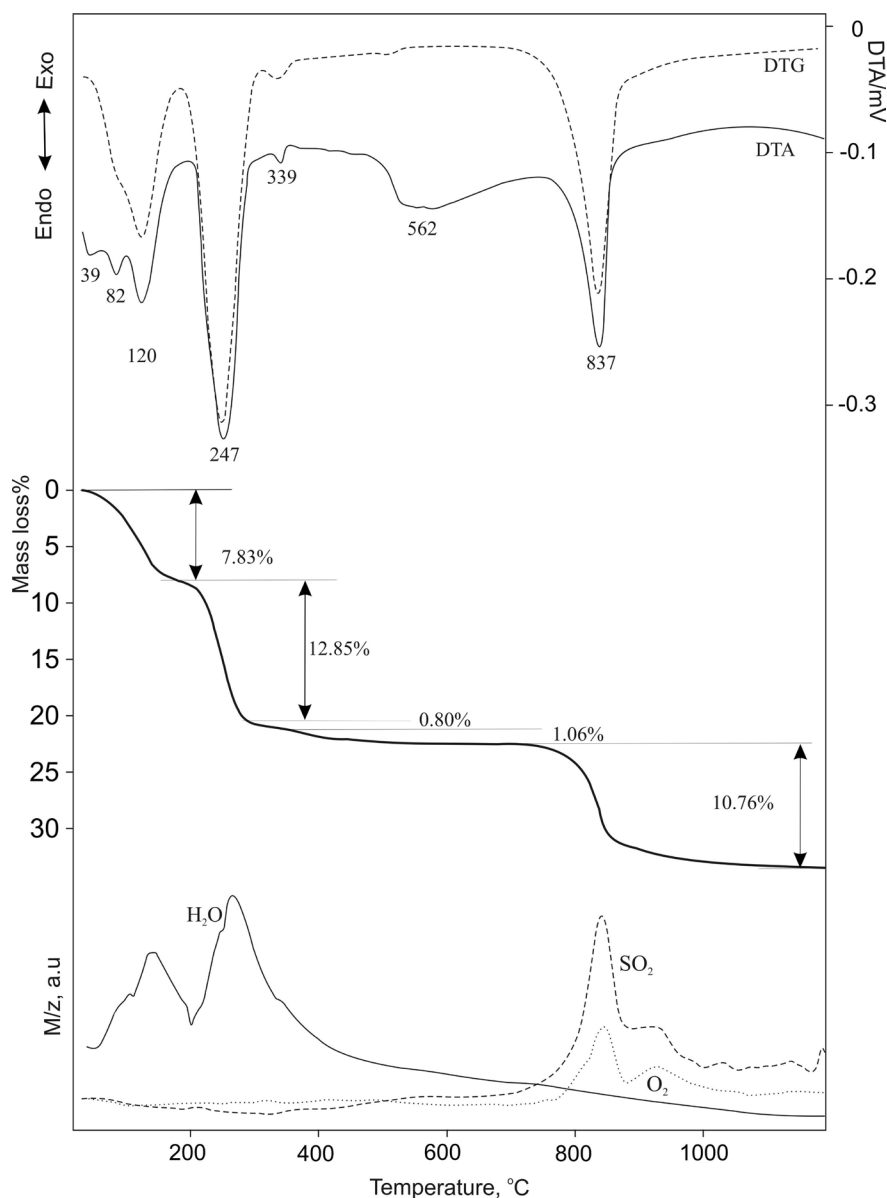
Fig. 4. DTA-TG(DTG)-MS data of the new phase obtained by treatment of $Zn_5(OH)_8(NO_3)_2·2H_2O$ with Na_2SO_4.

erature $(Zn_4(OH)_6SO_4 \cdot 2H_2O$; $Zn_4(OH)_6SO_4 \cdot 1H_2O$ and $Zn_4(OH)_6SO_4 \cdot 0.5H_2O)$, which however have been characterized by a completely different diffraction pattern [25, 28–30]. The comparison of the FTIR spectra of the new phase with the other sulfate hydroxy salts also shows some differences. Except the SO_4 (600, 1111 и 1060 cm^{-1}) and OH (3344 cm^{-1}) absorption bands, a weak water band (1624 cm^{-1}) and two weak bands at 1391 and 1506 cm^{-1} which very precisely correspond to a bi-

dentate bonded carbonate group [31] are also observed in the infrared spectrum of the phase obtained from $Zn_5(OH)_8(NO_3)_2 \cdot 2H_2O$ and Na_2SO_4 (Fig. 5b).

The presence of carbonate may be due to the NaOH used for synthesis of the starting zinc hydroxy nitrate. Since EDS shows no presence of carbonate, it could be assumed that the carbonate is most probably surface adsorbed.

It is interesting to note that a phase with the same powder XRD diffraction pattern has been obtained
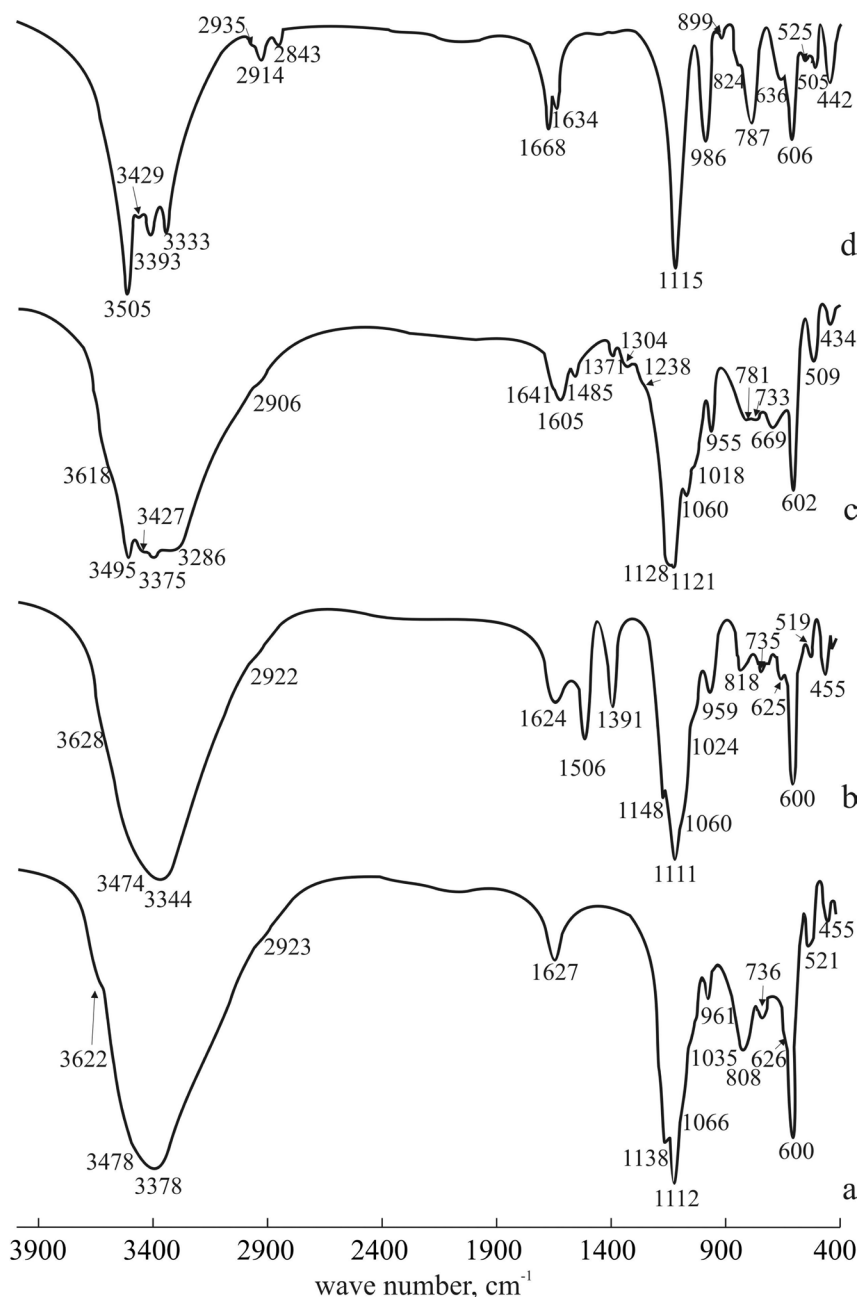

Fig. 5. FTIR spectra of: *a*) the new phase obtained by treatment of namuwite with NaI; *b*) the new phase obtained by treatment of $Zn_5(OH)_8(NO_3)_2 \cdot 2H_2O$ with Na_2SO_4; *c*) namuwite; *d*) gordaite.
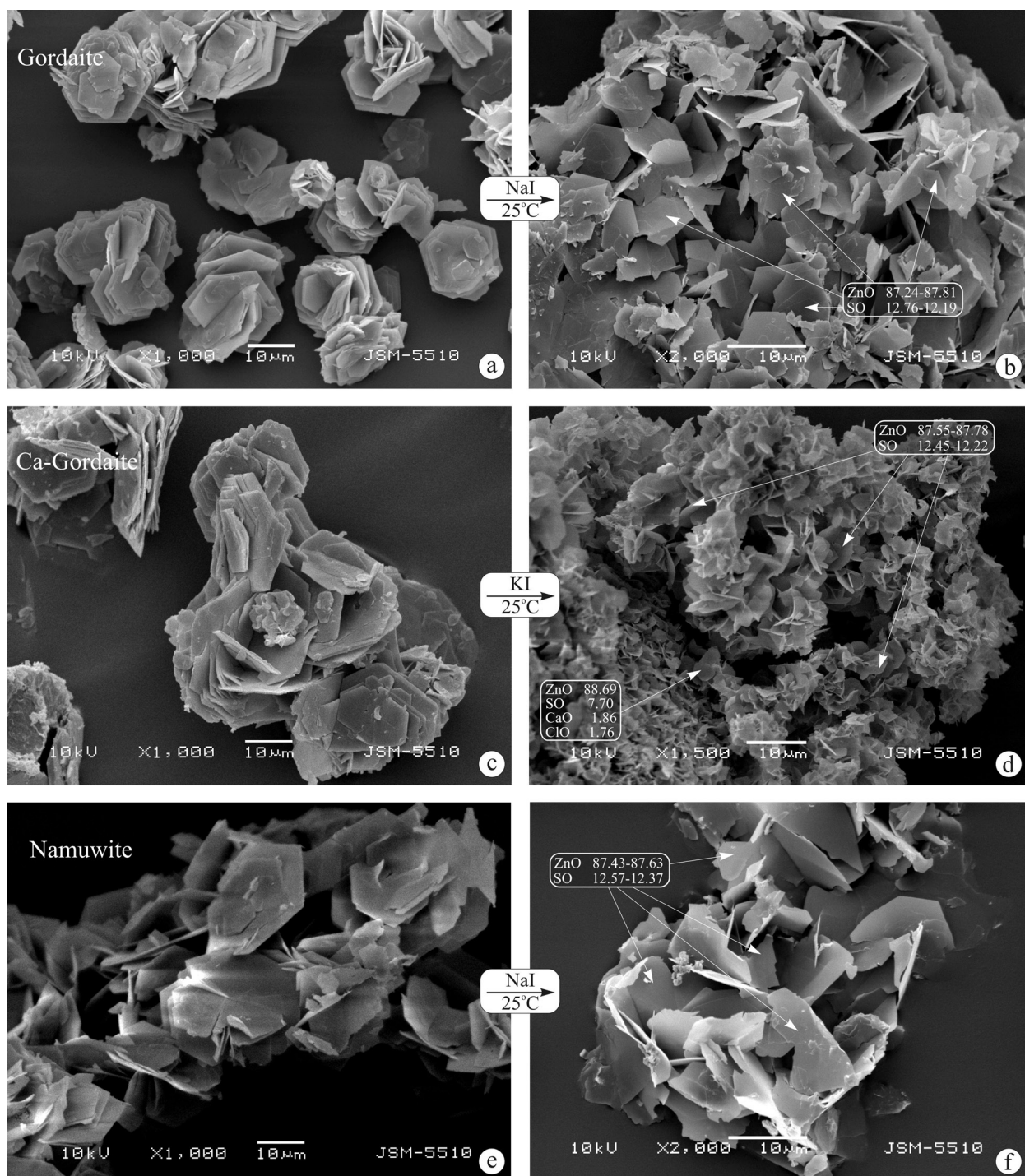
Fig. 6. SEM microphotographs of: *a–b*) initial and treated with NaI gordaite; *c–d*) initial and treated with KI Ca-gordaite; *e–f*) initial and treated with NaI namuwite. Chemical data of new phase obtained by EDS are also presented.

in the cation exchange reactions of the sulfate hydroxy-salt mineral gordaite with solution of LiNO$_3$ and Ca(NO$_3$)$_2$ [32–33]. The authors of this study claim that their obtained products are gordaites with compensating interlayer cations of Li$^+$ or Ca^{2+}. The greater value of the d-spacing of the first reflection

they attributed to the bigger water content in the interlayer space, caused by the high hydration ability of Li$^+$ and Ca^{2+}. Unfortunately, chemical data for the presence of the two cations as well as any data for the increased content of interlayer water has not been provided in their study. Most likely, in their

case, in an attempt to cation exchange in gordaites with nitrate salts, the same new phase was obtained.

Mechanism of the new phase formation: SEM data shows that the studied phase forms extremely thin, often curved hexagonal crystals with no relation to the orientation of the precursor crystals (Fig. 3b, d, f). This result suggests that the main mechanism of transformation is dissolution and subsequent crystallization.

From a crystal chemical point of view, the formation of pure hydroxy sulfates of the type $Zn_4(OH)_6SO_4 \cdot nH_2O$ in the presence of nitrates could be explained by the peculiarities of the apical position of the Zn tetrahedron from the hydroxide layer. This position is loaded with a half positive charge and can be occupied by water molecules in the minerals osakaite-namuwite-lahnsteinite or by chlorine anions in the structures of the gordaites. Apparently, the position could not be occupied by a large monovalent anion. In support of this, is also the structure peculiarities of the starting zinc hydroxy nitrate $Zn_5(OH)_8(NO_3)_2 \cdot 2H_2O$ in which the apical position of the zinc tetrahedra is occupied by water molecules (Fig. 1), and the NO_3 groups are located freely between the zinc tetrahedra [25].

The results of the experiments show that the pH of the solutions has a controlling role for the formation of one or another representative of zinc hydroxy sulfates by reaction between $Zn_5(OH)_8(NO_3)_2 \cdot 2H_2O$ and sulfate solutions. It was found that at pH = 4.5–8, the new phase was formed, while under more acidic conditions (pH from 4.5 to 2.5), namuwite was obtained.

To investigate the effect of the size of the monovalent anion on its ability to occupy the apical position of the zinc tetrahedra, a series of experiments was performed by treating the two major types of zinc hydroxy sulfates (namuwite and gordaite) with solutions of NaI and KI. Sodium and potassium iodide solutions were selected for two reasons: (i) the large iodine size and (ii) the neutral character (pH ≈ 7) of the NaI and KI solutions. As in the case of nitrate anions the I⁻ anion is very large in order to be able to occupy the apical position, and as a result, the studied new phase was again obtained (Fig. 1c).

The chemical and morphological data (Fig. 6) of the products obtained by treatment with iodide solutions showed that the resulting products are completely identical to the investigated new phase obtained in the presence of nitrate anions. The DTA-TG(DTG)-MS curves showed also identical thermal behavior. Only difference was observed in the FTIR spectrum, where the presence of carbonate was not registered (Fig. 5a), which supports the assumption that in the product obtained by reaction between $Zn_5(OH)_8(NO_3)_2 \cdot 2H_2O$ and sodium or ammonium sulfate solutions, the carbonate could be surface adsorbed. However, the ability of the structure to absorb and include a carbonate group should not be completely excluded.

CONCLUSIONS

(i) A new zinc hydroxy sulfate phase with a composition $Zn_4(OH)_6SO_4 \cdot 2–2.25H_2O$ was obtained. The conditions of three different ways of synthesis were established and described: during transformation reaction of Zn-hydroxy nitrates with sulfate solutions; Zn-hydroxy sulfates with nitrate solutions and exchange reaction of Zn-hydroxy sulfate samples with alkali iodides;

(ii) Data of XRD, SEM-EDS, DTA-TG-MS and FTIR were presented for characterizing the new phase;

(iii) The formation conditions as well as the mechanism of transformation were described and discussed: the new phase is formed at pH = 4.5–8 and the main mechanism of transformation is dissolution and subsequent crystallization. The possible reasons for its formation were discussed as well.

REFERENCES

1. R. E Bevins, S. Turgoose, P. A. Williams, *Mineralogical Magazine*, **46**, 51 (1982).
2. 2. M. Ohnishi, I. Kusachi, S. Kobayashi, *Can. Mineral.*, **45**, 1511 (2007).
3. K. Schmetzer, G. Schnorrer-Kohler, O. Medenbach, *Neues Jahrb. Mineral., Monatsh.*, **145**, (1985).
4. P. C. Burns, A. C. Roberts, A. J. Nikischer, *Eur. J. Mineral.*, **10**, 923 (1998).
5. F. Podda, P. Zuddas, A. Minaci, M. Pepi, F. Baldi, *Appl. Environ. microbiol.*, **66**, 5092 (2000).
6. P. Volovitch, C. Allely, K. Ogle, *Corrosion science*, **51**, 1251 (2009).
7. S. P. Newman, W. Jones, *J. Solid State Chem.*, **148**, 26 (1999).
8. T. Hongo, T. S. Lemur, S. Satokawa, A. Yamazaki, *Appl. Clay Sci.*, **48**, 455 (2010).
9. R. Marangoni, L. P. Ramos, F. Wypych, *Journal of colloid and interface science*, **330**, 2, 303 (2009).
10. M. Z. Hussein, N. Hashim, A. H. Yahaya, Z. Zainal, *Solid State Sciences*, **12**, 5, 770 (2010).
11. M. Z. Hussein, N. S. S. Abdul Rahman, S. H. Sarijo, Z. Zainal, *International journal of molecular sciences*, **13**, 6, 7328 (2012).
12. W. Liang, W. Li, H. Chen, H. Liu, L. Zhu, *Electrochimica Acta*, **156**, 171 (2015).
13. J. Sithole, B. D. Ngom, S. Khamlich, E. Manikanadan, N. I. Manyala, M. L. Saboungi, D. Knoessen, R. Nemutudi, M. Maaza, *Appl. Surface Sci.*, **258**, 20, 7839 (2012).
14. T. Biswick, A. Jones, W. A, Pacula, E. Serwicka, *J. Solid State Chem.*, **179**, 49 (2006).

15. A. Moezzi, M. B. Cortie, A. M. McDonagh, *Dalton Trans.*, **42**, 14432 (2013).
16. F. C. Hawthorne, *Mineral. Magazine*, **62**, 2, 141 (1998).
17. 17. F. C. Hawthorne, M. Schindler, *Zeitsch. Kristall.- Crystalline Materials*, **223**, 01-02, 41 (2008).
18. F. C. Hawthorne, *Zeitschrift fur Kristallographie,* **201**, 183 (1992).
19. F. C. Hawthorne, M. Schindler, *Can. Mineral.*, **38**, 751 (2000).
20. M. Schindler, F. Hawthorne, *Canad. Mineral.*, **39**, 5, 1225 (2001).
21. I. Odnevall, C. Leygraf, *Corrosion science*, **34**, 1213 (1993).
22. I. Odnevall, C. Leygraf, *Corrosion science*, **36**, 1551 (1994).
23. W. Feitknecht, W. Lotmar, *Helv. Chim. Acta*, **18**, 1369 (1935).
24. W. Stählin, H. R. Oswald, *J. Solid State Chem*., **3**, 252 (1971).
25. W. Stählin, H. R. Oswald, *Acta Cryst.*, **B26**, 860 (1970).
26. G. Adiwidjaja, K. Frise, K-H. Klaska, J. Schlüter, *Z. Kristallogr*., **212**, 704 (1997).
27. L. A. Groat, *Am. Mineral.*, **81**, 238 (1996).
28. I. J. Bear, I. E. Gray, I. C. Madsen, I. E. Newnham, L. J. Rogers, *Acta Crystallogr.*, **B 42**, 32 (1986).
29. I. J. Bear, I. E. Gray, I. C. Madsen, I. E. Newnham, L. J. Rogers, *Aust. J. Chem.*, **40**, 539 (1987).
30. Ts. Stanimirova, T. Kerestedjian, G. Kirov, *Appl. Clay Sci.*, **135**, 16 (2017).
31. K. Nakamoto, Infrared and Raman spectra of inorganic and coordination compounds, 5th ed., Wiley, New York, 1997.
32. S. A. Maruyama, K. C. Molgero Westrup, S. Nakagaki, F. Wypych, *Appl. Clay Sci.*, **139**, 108 (2017).
33. S. A. Maruyama, F. Krause, S. R. Tavares Filho, A. A. Leitro, F. Wypych, *Appl Clay Sci.*, **146**, 100 (2017).

НОВА ФАЗА, ПОЛУЧЕНА ПРИ ВЗАИМНИ ТРАНСФОРМАЦИИ НА ЦИНКОВИ ХИДРОКСИ-СОЛИ

Ц. Станимирова[1], З. Делчева[2], Н. Петрова[2]

[1] Софийски Университет „Св. Климент Охридски“, Геолого-географски факултет, Катедра „Минералогия, петрология и полезни изкопаеми“, бул. „Цар Освободител“ 15, София 1000, България
[2] Институт по минералогия и кристалография – Българска Академия на Науките, ул. „Акад. Г. Бончев“, бл. 107, София 1000, България

(Резюме)

Минералите хидроксисоли обикновено са стабилни в тесен диапазон на външни условия (като Eh, pH, T, P, концентрация на разтвори и др.). Поради тази причина, те се превръщат лесно един в друг чрез промени в кристалната им структура. Изследваните изходни цинкови хидроксисоли се характеризират със специфични слоести структури, в които цинковите катиони са координирани октаедрично и тетраедрично, като отношението на октаедрично- към тетраедрично координираните цинкови атоми е 3:2 или 3:1. В процеса на подробно изследване на трансформациите по време на взаимодействие на Zn-хидрокси нитрати (отношение 3:2) със сулфатни разтвори, Zn-хидрокси сулфати (отношение 3:1) с нитратни разтвори и обменни реакции на Zn-хидроксисулфатни образци с алкални йодиди, е получена стабилна фаза с прахова дифракция, която не бе намерена в базата данни на ICDD. За охарактеризиране на новата фаза са използвани данни от XRD, SEM-EDS, DTA-TG-MS и FTIR. Получената нова фаза се характеризира с по-голяма стойност $d_{001} = 17,84$ Å в сравнение с тази на изходните образци (d_{001} между 9,70–11,10 Å). Химичните данни показват само наличието на катиони на цинк и сяра. Новата фаза има химична формула $Zn_4(OH)_6SO_4 \cdot 2{-}2,25H_2O$, която е изчислена от химичните и термичните анализи. Описани и дискутирани са условията на образуване, както и механизма на трансформация: новата фаза се образува при pH = 4,5–8 и основният трансформационен механизъм е разтваряне с последваща кристализация.

A new polymorph of Bisacodyl

V. Dyulgerov, Hr. Sbirkova-Dimitrova, L. Tsvetanova,
R. Rusew*, Boris Shivachev

*Institute of Mineralogy and Crystallography "Acad. Ivan Kostov",
Bulgarian Academy of Sciences, Acad. G. Bonchev Str.,
bl. 107, 1113 Sofia, Bulgaria*

A new polymorph structure of bisacodyl, (pyridin-2-ylmethylene)bis(4,1-phenylene) diacetate, was determined. The starting bisacodyl was extracted from suppositories with petroleum ether and the precipitate was recrystallized from acetone. The purity of the recrystallized product was verified with powder X-ray diffraction. The single crystal structure of bisacodyl shows that the compound crystallizes in a noncentrosymmetric manner in orthorhombic $P2_12_12_1$ space group, with unit cell parameters $a = 8.06862(18)$ Å, $b = 8.27567(18)$ Å, $c = 28.3631(7)$ Å.

Keywords: bisacodyl, polymorph, single crystal, powder diffraction.

INTRODUCTION

Bisacodyl, (pyridin-2-ylmethylene)bis(4,1-phenylene) diacetate, [4-[(4-acetyloxyphenyl)-pyridin-2-ylmethyl]phenyl] acetate); is a stimulant laxative, widely used for the relief of occasional constipation [1, 2]. It is an over-the-counter drug sold under different brand names: Dulcolax, Correctol, Bisacolax, Bisac-Evac, Alophen, Feen-A-Mint. Bisacodyl is a white or almost white crystalline powder poorly adsorbed *in vivo* as it is practically insoluble in water. It is soluble in acetone, sparingly soluble in ethanol (96% *v/v*) and it dissolves in dilute mineral acids [3]. Bisacodyl mode of action requires its hydrolyzation by intestinal deacetylase enzymes to bis-(p-hydroxyphenyl)-pyridyl-2-methane (BHPM) [4, 5]. BHPM is also the active metabolite of sodium picosulfate [6]. Bisacodyl can be administered orally or as suppositories. Though oral administration of Bisacodyl is easier the observed side effects (stomach or abdominal irritation, pains, vomiting) have forced the implementation of pharmaceutical approaches such as "controlled" pH-, time-, and enzyme-dependent release [4, 7]. Normally, new drug formulations are permitted only if they contain a particular polymorph (solid form), or a defined mixture of polymorphs (solid forms) [8], of the Active Pharmaceutical Ingredients. Consequently, it is important to control the crystallization conditions in order to allow the crystallization of only one particular solid form. In order to avoid problems linked with the crystallization of undesired solid forms (e.g. amorphous *vs* crystalline) or the crystallization of a new and unexpected crystal polymorph usually polymorphic screening is performed [9]. Up to now, data for only one crystal structure of Bisacodyl could be located in the databases (CCDC-CSD). The Bisacodyl structure was originally solved by powder diffraction ([10], **polymorph 1**) in $P\bar{1}$ space group (SG). In the present work we have identified and report the crystal structure a new polymorph (**polymorph 2**) of Bisacodyl (space group $P2_12_12_1$). Interestingly the crystals were grown from acetone, like those (space group $P\bar{1}$) structure reported in [10].

EXPERIMENTAL

Bisacodyl purification and preparation of solid form: 20 suppositories of bisacodyl (10 mg) were dissolved in 20 ml petroleum ether (b.p. 40–60 °C). After precipitation, the petroleum ether was decanted and the crude bisacodyl was washed with petroleum ether (2×10 ml). The bisacodyl precipitate was dried in air for 24 h and then recrystallized from acetone at room temperature which resulted in formation of colorless crystals.

---

* To whom all correspondence should be sent:
E-mail: r.rusev93@gmail.com

POWDER X-RAY DIFFRACTION (PXRD)

The PXRD investigations were performed on an X-ray powder diffractometer D2 Phaser (Bruker AXS) using Cu$K\alpha$ radiation, with a step size 0.02° 2θ and a collection time of 8 s per step. The simulated XRPD patterns were calculated with Mercury software (version 3.9) [11].

SINGLE CRYSTAL X-RAY ANALYSIS

A suitable single crystal of bisacodyl was selected and mounted on a glass capillary. All intensity and diffraction data were collected on an Agilent SupernovaDual diffractometer equipped with an Atlas CCD detector using micro-focus Cu Kα radiation (λ = 1.54184 Å) at 290 K. Collection and data reduction program was CrysAlisPro, Rigaku Oxford Diffraction, 2017, version 1.1.171.37.35 [12]. The crystal structure was solved by direct methods and refined by the full-matrix least-squares method on F^2 with ShelxS and ShelxL programs [13]. All non-hydrogen atoms were located successfully from Fourier maps and were refined anisotropically. Hydrogen atoms were placed at calculated positions using a riding scheme (Ueq = 1.2, aromatic C-H = 0.93 Å and Ueq =1.5, methyl C-H = 0.96 Å). The ORTEP [14] drawing of the molecule present in the asymmetric unit (ASU) and the most important crystallographic parameters from the data collection and refinement are shown in Figure 1 and Table 1 respectively. The figures concerning crystal structure description and comparison were prepared using Mercury software (version 3.9) [11].
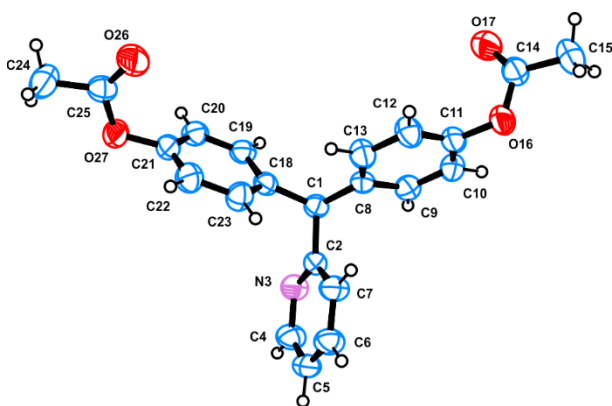
Table 1. Most important crystallographic parameters for data collection and refinement of bisacodyl

Empirical formula	$C_{22}H_{19}NO_4$
Formula weight	361.38
Temperature/K	290
Crystal system	Orthorhombic
Space group	$P2_12_12_1$
a/Å	8.06862(18)
b/Å	8.27567(18)
c/Å	28.3631(7)
α/°	90
β/°	90
γ/°	90
Volume/Å³	1893.90(8)
Z	4
ρ_{calc} g/cm³	1.267
μ/mm^{-1}	0.714
F(000)	760.0
Crystal size/mm³	0.25 × 0.2 × 0.2
Radiation	Cu Kα (λ = 1.54184)
2Θ range for data collection/°	11.138 to 149.058
Index ranges	$-9 \le h \le 9, -9 \le k \le 4, -34 \le l \le 31$
Reflections collected/ Independent	6518/3717
R_{int} / R_{sigma}	0.0236/0.0289
Data/restraints/ parameters	3717/0/246
Goodness-of-fit on F^2	1.046
Final R indexes [$I >= 2\sigma (I)$]	R_1 = 0.0386 wR_2= 0.0993
Final R indexes [all data]	R_1 = 0.0435 wR_2= 0.1047
Largest diff. peak/hole / e Å^{-3}	0.12/–0.16
Flack parameter	–0.25(17)
CCDC number	1831419

Fig. 1. ORTEP drawing of the molecule present in the asymmetric unit (atomic displacement parameters are at 50% probability); hydrogen atoms are shown as spheres with arbitrary radii.

RESULTS AND DISCUSSION

The comparison of the powder and the single crystal generated diffraction patterns clearly shows the existence of two polymorphic forms (Fig. 2). The assessment of the purity of the polymorph 1 from powder patterns of ref. [10] and this shown on Fig. 2 suggests that the employed purification procedure yields cleaner bisacodyl substance than that one purchased from Heowns Biochem Technologies LLC (considering the observed halo in the 5–15 2θ° region of [10]).

The new polymorph of Bisacodyl crystalizes in the orthorhombic $P2_12_12_1$ space group with one molecule in the ASU and four molecules in the unit cell (Z = 4) (Fig. 1). The values for the most bond lengths, angles and torsion angles (Table 2) are comparable with the other similar structures from the
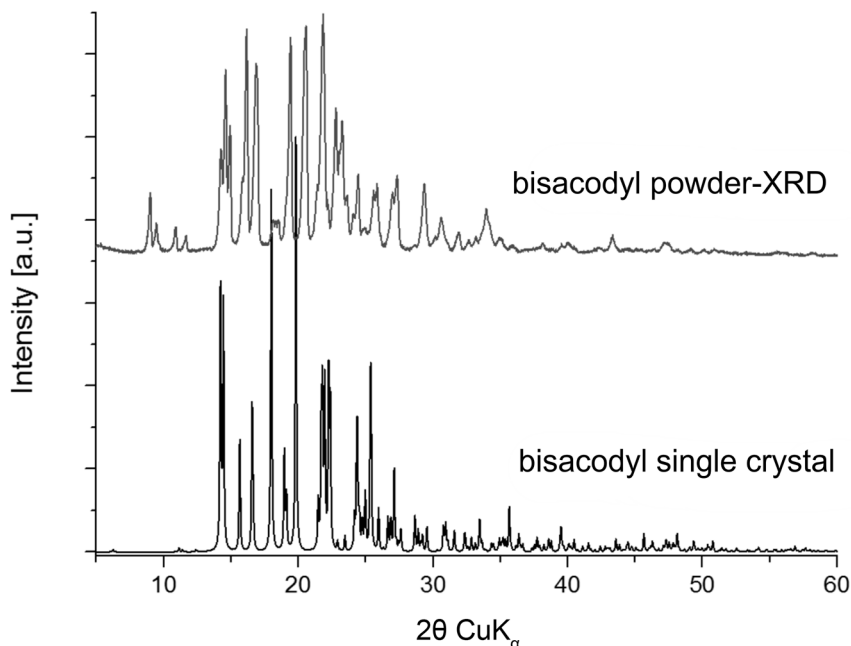
Fig. 2. Comparison between the powder and single crystal generated diffraction patterns of **polymorph 2**.

Table 2. Selected bond lengths, angles and torsion angles of the crystal structure of **polymorph 2**

Bond lengths	Å	Angles	°
N3—C2	1.335 (3)	C22—C21—O27	119.2 (3)
N3—C4	1.340 (4)	C25—O27—C21	118.4 (2)
C1—C8	1.523 (3)	C18—C1—C2	109.97 (18)
C1—C2	1.526 (3)	O17—C14—C15	126.4 (3)
C1—C18	1.525 (3)	O17—C14—O16	122.7 (2)
C11—O16	1.406 (3)	N3—C4—C5	124.3 (2)
O27—C21	1.411 (3)	O27—C25—C24	110.9 (2)
O16—C14	1.350 (3)	O26—C25—C24	126.3 (3)
O27—C25	1.337 (3)	Torsion angles	°
O17—C14	1.187 (3)	C21—O27—C25—O26	0.6 (5)
C25—O26	1.173 (3)	C2—C1—C8—C9	75.2 (3)

CSD-database 5.38 [10, 15–17]. A detailed comparison molecular packing similarity [18] of bisacodyl from **polymorph 1** [10] and **polymorph 2** shows an overall root mean square deviation (*rms*) of 1.017 and reveals that main difference is in the orientation of the acetate moieties (Fig. 3). Indeed the minimal variations of molecular geometry are the reason for the existence of the two polymorphic forms. The existence of a third polymorph form, which differs by the orientation of only one of the acetate moieties can be envisaged. The geometry around the – CH center is also interesting. Because of the two identical substituents (phenyl acetate) the C is not
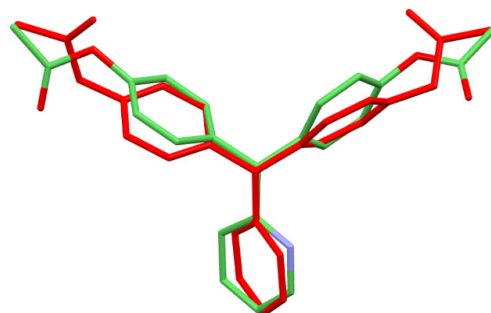

Fig. 3. Overlaid molecules [100] of **polymorph 1** (in green) [10] and **polymorph 2** (in red). The main difference between the forms is the torsion of the acetate moieties.

truly "chiral" and the polymorph in ref. [10] crystallizes in centrosymmetric SG $P\bar{1}$. Nevertheless the second polymorph crystallizes in a noncentrosymmetric manner (SG 19) with only one molecules in the ASU. Having in mind that the active metabolite of bisacodyl BHMP is hydrolyzed by intestinal enzymes one could expect that after the production of one –OH moiety the enzymes will continue to act only on the correct *R* or *S* 4-((4-hydroxyphenyl)(pyridin-2-yl)methyl)phenyl acetate. Thus for the reduction of the administered bisacodyl dose (e.g. by a factor of two) one should obtain the "correct" molecular orientation in the solid form.

Weak hydrogen bonding interactions (C—H···O) could be located in the structure (Table 3, Fig. 4). In both polymorphs the number of the weak interactions is two. However in the present structure the two C—H···O involve aromatic C-H (Fig. 4b) while in **polymorph 1** one of the detected interactions is obtained from a methyl group (Fig. 4a, e.g. C-H$_{methyl}$…O with H…*A* distance of 2.718 Å).

As the bisacodyl molecule features only classical hydrogen bond acceptors (2 × C=O), no hydrogen bond donors, and it is practically insoluble in water, the three dimensional crystal packing is governed by the network of weak interactions and the minimization of free spaces. Indeed the three dimensional packing of the bisacodyl molecules in **polymorph 2** shows a zig-zag orientation alongside *b*–axis and S-shaped orientation alongside *a*-axis (Fig. 5).

CONCLUSIONS

In this work, we describe the crystal structure and solid state behavior of a new bisacodyl polymorph. The single-crystals of the new polymorph form were obtained by a standard procedure followed by recrystallization from acetone. The single crystal structure data of **polymorph 2** showed a high molecular similarity with polymorph 1 with an overall *rm*s of 1.017 and only the orientation of the two acetate moieties is different. However, we found significant differences for **polymorph 2**: it crystallizes in a noncentrosymmetric manner ($P2_12_12_1$) and C-H$_{aromatic}$…O weak interactions stabilizing the three-dimensional packing are prefered over C-H$_{methyl}$…O ones. The existence of a third polymorph modification, differing by the orientation of only one acetate moiety should be envisaged.

Table 3. Weak intermolecular hydrogen bonding interactions of **polymorph 2**

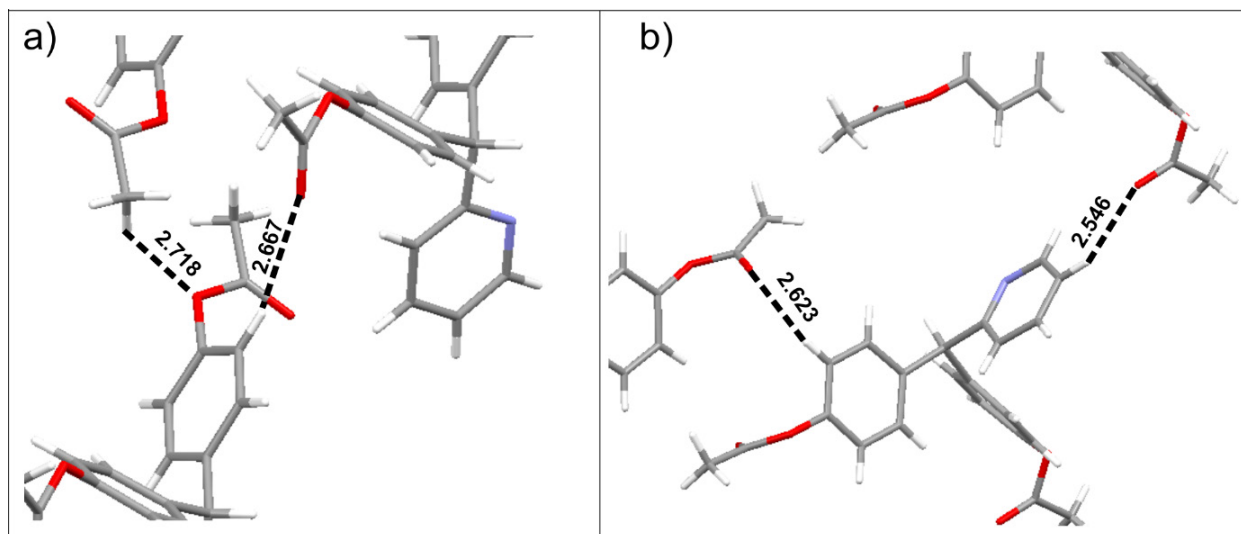| D—H···A	D—H (Å)	H···A (Å)	D···A (Å)	D—H···A (°)
C10—H10···O17i	0.93	2.623	3.333 (4)	134
C5—H5···O26ii	0.93	2.546	3.243 (3)	132
Symmetry codes: (i) −x+1, y−1/2, −z+1/2; (ii) x−1, y−1, z.				

Fig. 4. Observed weak interactions in a) **polymorph 1** and b) **polymorph 2**
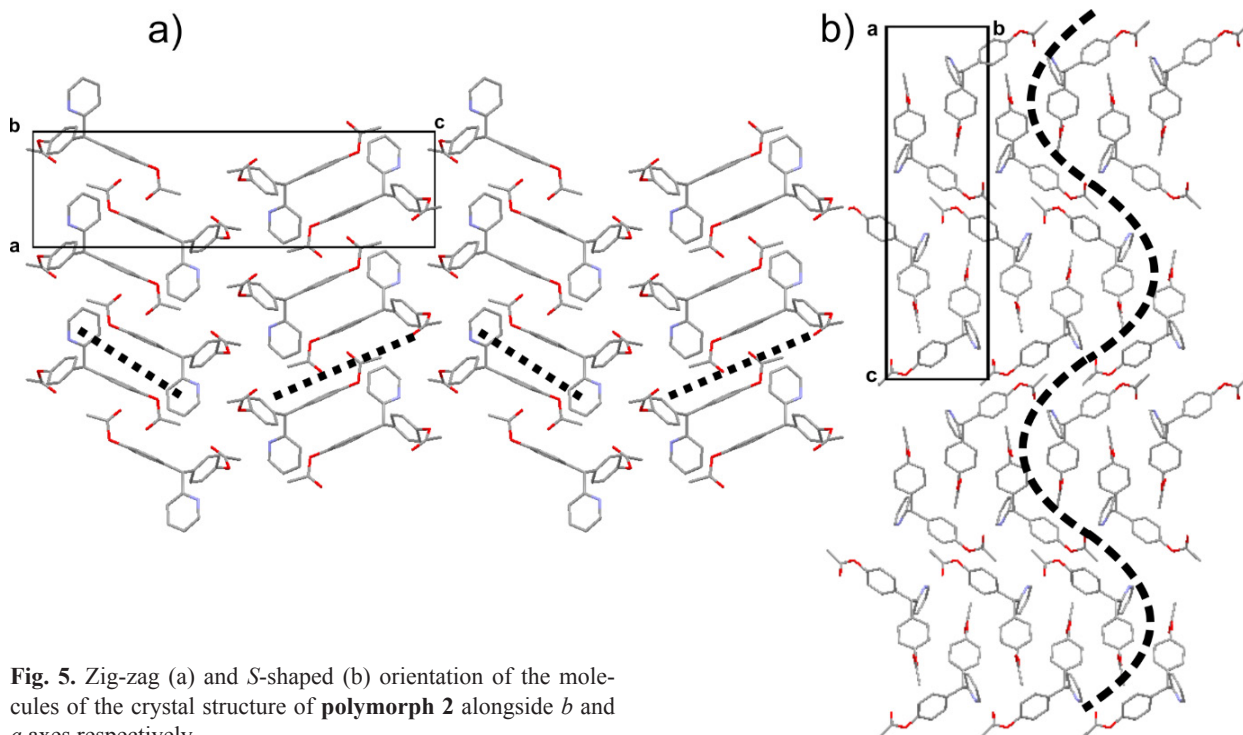
Fig. 5. Zig-zag (a) and *S*-shaped (b) orientation of the molecules of the crystal structure of **polymorph 2** alongside *b* and *a* axes respectively.

REFERENCES

1. E. M. H. Mathus-Vliegen, K. van der Vliet, I .J. W. der Storm, J. S. Stadwijk, *Diseases of the Colon & Rectum*, **61**, 2, 239 (2018).
2. G. Pala, G. Coppi, E. Crescenzi, *Arch Int Pharmacod T*, **164**, 2, 356 (1966).
3. European Pharmacopoeia Commission, Council of Europe, European pharmacopoeia 9-th edition, Maisonneuve, Sainte Ruffine, 2016.
4. H. J. Park, H. J. Jung, M. J. Ho, D. R. Lee, H. R. Cho, Y. S. Choi, J. Jun, M. Son, M. J. Kang, *European Journal of Pharmaceutical Sciences*, **102**, 172 (2017).
5. W. J. Adams, A. P. Meagher, D. Z. Lubowski, D. W. King, *Diseases of the Colon & Rectum*, **37**, 229 (1994).
6. [6] R. Jauch, R. Hankwitz, K. Beschke, H. Pelzer, *Arzneimittel-Forschung*, **25**, 1796 (1975).
7. D. R. Friend, *Advanced Drug Delivery Reviews*, **57**, 247 (2005).
8. W. Beckmann, *Engineering in Life Sciences*, **3**, 113 (2003).
9. [9] E. H. Lee, *Asian Journal of Pharmaceutical Sciences*, **9**, 163 (2014).
10. S. S. Li, X. Q. Wu, Q. Wang, P. X. Tang, H. Li, *Powder Diffraction*, **29**, 295, (2014).
11. C. F. Macrae, I. J. Bruno, J. A. Chisholm, P. R. Edgington, P. McCabe, E. Pidcock, L. Rodriguez-Monge, R. Taylor, J. van de Streek, P. A. Wood, *Journal of Applied Crystallography*, **41**, 466 (2008).
12. CrysAlis PRO, in: Agilent Technologies, UK Ltd, Yarnton, England, 2011.
13. G. M. Sheldrick, *Acta Crystallographica A*, **64**, 112 (2008).
14. L. Farrugia, *Journal of Applied Crystallography*, **45**, 849 (2012).
15. N. C. Habermehl, F. Mohr, D. J. Eisler, M. C. Jennings, R. J. Puddephatt, *Canadian Journal of Chemistry*, **84**, 111 (2006).
16. B. Nath, D. Kalita, J. B. Baruah, *Solid State Sciences*, **14**, 880 (2012).
17. R. J. Sarma, J. B. Baruah, *Chemistry – A European Journal*, **12**, 4994 (2006).
18. J. Rohlicek, E. Skorepova, M. Babor, J. Cejka, *Journal of Applied Crystallography*, **49**, 2172 (2016).

НОВ ПОЛИМОРФ НА БИЗАКОДИЛ

В. Дюлгеров, Хр. Сбиркова-Димитрова, Л. Цветанова,
Р. Русев*, Б. Шивачев

*Институт по минералогия и кристалография „Акад. Иван Костов", Българска академия
на науките, ул. „Акад. Г. Бончев", бл. 107, 1113 София, България*

(Резюме)

Определена е кристалната структура на нов полиморф на бизакодил. Изходният продукт е екстрахиран от супозитори с петролев етер, а преципитатът е прекристализиран с ацетон. Чистотата на прекристализирания продукт е проверена с помощта на прахов рентгенофазов анализ. Монокристалният рентгеноструктурен анализ показа, че молекулите на бизакодил кристализират по нецентросиметричен начин в орторомбичната $P2_12_12_1$ пространствена група, с параметри на елементарната клетка $a = 8.06862(18)$ Å, $b = 8.27567(18)$ Å, $c = 28.3631(7)$ Å. Сравнението между праховата рентгенограма на пречистения бизакодил и на полиморфа, докладван от Li et al., навежда на мисълта, че приложената екстракция дава продукт с висока чистота.

Ureates and hydrates of magnesium chloride, nitrate and tetrafluoroborate

R. Rusev, L. Tsvetanova, B. Shivachev,
K. Kossev*, R. Nikolova

*Institute of Mineralogy and Crystallography "Acad. Iv. Kostov", Bulgarian Academy of Sciences,
Acad. G. Bonchev str., building 107, 1113 Sofia, Bulgaria*

Five magnesium complexes two of which with tetrafluoroborate anion $[U_6Mg]^{2+}.2BF_4^- - \mathbf{1}$, $[(H_2O)_6Mg]^{2+}.2BF_4^- - \mathbf{2}$, two with chloride anion – $[U_6Mg]^{2+}.2Cl^-.4U - \mathbf{3}$, $[U_4Mg(H_2O)_2]^{2+}.2Cl^- - \mathbf{4}$ and one with nitrate anion – $[U_6Mg]^{2+}.2NO_3^- - \mathbf{5}$, have been synthesized. Crystals suitable for X-ray diffraction have been obtained by slow evaporation from aqueous solutions. The single crystal X-ray studies showed that compounds **1** and **2** crystallize in orthorhombic $P2_12_12$ ($a = 9.964(5)$, $b = 11.979(6)$, $c = 9.638(5)$) and in orthorhombic $Pnnm$ ($a = 5.4322(6)$, $b = 13.2050(12)$, $c = 7.6786(6)$) space groups respectively. Compounds **3** and **4** crystallize in the monoclinic $P2_1/c$ space group with unit cell parameters $a = 9.6317(8)$, $b = 7.2241(7)$, $c = 23.506(3)$, $\beta = 94.045(9)$ and $a = 8.0168(16)$, $b = 14.844(2)$, $c = 28.662(4)$, $\beta = 94.194(16)$ respectively. Compound **5** crystallizes in the triclinic $P–1$ space group with $a = 7.1917(6)$, $b = 8.279(3)$ $c = 9.555(9)$, $\alpha = 71.01(6)$, $\beta = 89.17(3)$, $\gamma = 84.158(19)$.

Keywords: magnesium tetrafluoroborate, magnesium chroride, magnesium nitrate, ureate, hydrate, single crystal.

INTRODUCTION

It is well known that Mg^{2+} coordinates with ligands containing urea moiety. Up to now single crystal studies of magnesium complexes with formamide [1], DMF [2], methylurea [3] and dimethylurea [4] have been conducted. Such studies exploit the Mg^{2+} bioavailability and its role as co-factor in many enzymes [5], for energy production in the transformation of adenosine triphosphate (ATP) and adenosine diphosphate (ADP) [6], in the DNA extension by Polymerase and for the building of the chlorophyll center [7]. From the above mentioned magnesium complexes, those involving urea are extensively characterized including bromide [8, 9], sulfate [10, 11], formate [12, 13], dihydrogen phosphate [14], chlorate [15] and nitrate [16] salts. The diversity of the Mg^{2+}-urea complexes (excluding the formate and dihydrogen phosphate salts) can be generalized in two main structural types: $[U_6Mg]^{2+}$ and $[U_4Mg(H_2O)_2]^{2+}$. In all cases the magnesium is octahedrally coordinated [17, 18]. Here we report

the synthesis and crystal structure analysis of five magnesium complexes: two with tetrafluoroborate anion $[U_6Mg]^{2+}.2BF_4^- - \mathbf{1}$, $[(H_2O)_6Mg]^{2+}.2BF_4^- - \mathbf{2}$, two with chloride anion – $[U_6Mg]^{2+}.2Cl^-.4U - \mathbf{3}$, $[U_4Mg(H_2O)_2]^{2+}.2Cl^- - \mathbf{4}$ and one with nitrate anion – $[U_6Mg]^{2+}.2NO_3^- - \mathbf{5}$.

MATERIALS AND METHODS

Single crystal samples of the synthesized complexes were obtained by slowly evaporation from aqueous solution of the corresponding magnesium salt and urea in equimolar proportions at room temperature. All compounds (except MgO – Merck) were purchased from Sigma-Aldrich and were used with no further purification.

Synthesis of hexakis(urea-O) magnesium bis(tetrafluoroborate), $[U_6Mg]^{2+}.2BF_4^-$, **1**

Magnesium tetrafluoroborate was prepared according to a modified methodology [19] by reacting magnesium oxide and tetrafluoroboric acid in an equilibrium manner.

MgO (4.03 g, 0.1 mol) was mixed in 10 ml distilled water and 13 ml (8.78 g, 0.1 mol) of 48%

HBF_4 were added dropwise with stirring. After one hour a clear solution of magnesium tetrafluoroborate was formed. The water was removed in vacuo to give a quantitative yield of $[(H_2O)_6Mg]^{2+}2BF_4^-$ as a microcrystalline phase.

Hexaaqua magnesium tetrafluoroborate (305.9 mg, 0.001 mol) and urea (360.4 mg, 0.006 mol) were dissolved in 10 ml distilled water and after slow evaporation of the aqueous solution single crystal samples of **1** were obtained.

Synthesis of hexakis(aqua) magnesium bis(tetrafluoroborate), $[(H_2O)_6Mg]^{2+}.2BF_4^-$, **2**

Hexaaqua magnesium tetrafluoroborate (305.9 mg, 0.001 mol) was dissolved in 10 ml distilled water and after slow evaporation single crystal samples of **2** were obtained.

Synthesis of hexakis(urea-O) magnesium dichloride tetraurea, $[U_6Mg]^{2+}.2Cl^-.4U$, **3**

Anhydrous magnesium chloride (95.21 mg, 0.001 mol) and urea (600.6 mg, 0.02 mol) were dissolved in 10 ml distilled water and after slow evaporation of the aqueous solution single crystal samples of **3** were obtained.

Synthesis of bis(aqua) tetrakis(urea-O) magnesium dichloride, $[U_4Mg(H_2O)_2]^{2+}.2Cl^-$, **4**

Anhydrous magnesium chloride (95.21 mg, 0.001 mol) and urea (240.2 mg, 0.004 mol) were dissolved in 5 ml distilled water and after slow evaporation of the aqueous solution single crystal samples of **4** were obtained.

Synthesis of hexakis (urea-O) magnesium dinitrate, $[U_6Mg]^{2+}.2NO_3^-$, **5**

MgO (4.03 g, 0.1 mol) was dissolved in 5 ml distilled water and 6.5 ml (6.04 g, 0.1 mol) of 65% HNO_3 were added dropwise. The mixture was then stirred for one hour. The excess water was removed by heating. After the reaction mixture cool down colorless crystals of Hexaaqua magnesium nitrate $[(H_2O)_6Mg]^{2+}.2NO_3^-$ were obtained.

Hexaaqua magnesium nitrate (256.4 mg, 0.001 mol) and urea (360.4 mg, 0.006 mol) were dissolved in 10 ml distilled water and after slow evaporation of the aqueous solution single crystal samples of **5** were obtained.

Single crystal X-ray diffraction

Suitable single crystals of compounds **1-5** were mounted on a glass capillaries. The intensity and diffraction data for compound **1** were collected on an Enraf-Nonius CAD-4 diffractometer equipped with a scintillation detector and using graphite monochromated Mo Kα radiation (λ = 0.71073). Diffraction data for compounds **2–5** were collected on an Agilent SupernovaDual diffractometer equipped with an Atlas CCD detector using micro-focus Mo Kα radiation (λ = 0.71073). Collection and data reduction program was CrysAlisPro, Rigaku Oxford Diffraction, 2017, version 1.1.171.37.35 [20]. Due to the thermal instability (i.e. high hygroscopicity, lack of diffraction after 10–15 min) of compounds **2–4** at ambient conditions data collection were performed by flash freezing the crystals at 150 K in N_2 stream using Cobra, Oxford cryosystem. The crystal structures were solved by direct methods with ShelxS and refined by the full-matrix least-squares method of F^2 with ShelxL programs [21, 22]. All non-hydrogen atoms were located successfully from Fourier maps and were refined anisotropically. Hydrogen atoms were placed at calculated positions using a riding scheme (Ueq = 1.2 for N-H = 0.86 Å). The ORTEP [23] drawings of the molecules present in the asymmetric unit and the most important crystallographic parameters from the data collection and refinement are shown in Figure 1–5 and Table 1 respectively. The figures concerning crystal structure description and comparison were prepared using Mercury software (version 3.9) [24]. Selected bonds lengths, angles and torsion angles are given in Tables 2 and 3.

RESULTS AND DISCUSSION

Crystal structures of magnesium tetrafluoroborate ureates or hydrates have not been previously reported. The conducted search in the ICDD and ICSD databases returned only a powder diffractogram of anhydrous magnesium tetrabluorobate. Subsequent search for crystal structure data of magnesium chlorides urea salts also did not return results. The case of magnesium nitrate ureas is a little bit different as such compounds have been investigated since the 1930s [25]. The authors managed to define the space group and unit cell parameters of $[U_4Mg (H_2O)_2]^{2+}.2NO_3^-$. Later, other authors report the isolation of ureas of magnesium nitrate with variable urea and water content in the crystal structure [26–28]. Interestingly, there are data for only one crystal structure: $[U_4Mg(H_2O)_2]^{2+}.2NO_3^-$ [16]. Among the magnesium halides only two crystal structures of two urea complexes of magnesium

Table 1. Most important data collection and refinement parameters for compounds **1–5**

Compound	1	2	3	4	5
Empirical formula	$C_6H_{24}B_2F_8MgN_{12}O_6$	$B_2F_8H_{12}MgO_6$	$C_{10}H_{40}Cl_2MgN_{20}O_{10}$	$C_4H_{20}Cl_2MgN_8O_6$	$C_6H_{24}MgN_{14}O_{12}$
Formula weight	558.30	306.03	695.83	371.49	508.70
Temperature/K	290	150	150	150.0	290
Crystal system	Orthorhombic	Orthorhombic	Monoclinic	Monoclinic	Triclinic
Space group	$P2_12_12$	$Pnnm$	$P2_1/c$	$P2_1/c$	$P–1$
a/Å	9.964(5)	5.4322(6)	9.6317(8)	8.0168(16)	7.1917(6)
b/Å	11.979(6)	13.2050(12)	7.2241(7)	14.844(2)	8.279(3)
c/Å	9.638(5)	7.6786(6)	23.506(3)	28.662(4)	9.555(9)
α/°	90	90	90	90	71.01(6)
β/°	90	90	94.045(9)	94.194(16)	89.17(3)
γ/°	90	90	90	90	84.158(19)
Volume/Å³	1150.3(10)	550.80(9)	1631.5(3)	3401.7(10)	535.0(6)
Z	2	2	2	8	1
ρ_{calc} (g/cm³)	1.612	1.845	1.416	1.451	1.579
μ/mm⁻¹	0.192	0.288	0.292	0.454	0.171
F(000)	572.0	308.0	732.0	1552.0	266.0
Crystal size/mm³	0.2×0.15×0.1	0.3×0.25×0.25	0.25×0.2×0.2	0.35×0.3×0.3	0.25×0.2×0.2
Radiation, λ [Å]	Mo$K\alpha$ λ = 0.71073	Mo$K\alpha$ λ = 0.71073	Mo$K\alpha$ λ = 0.71073	Mo$K\alpha$ λ = 0.71073	Mo$K\alpha$ λ = 0.71073
2Θ range for data collection/°	4.226 to 55.922	6.17 to 55.912	5.902 to 56.832	5.67 to 57.068	7.33 to 56.866
Reflections collected	5745	1442	6794	14528	3595
Reflections independent	2777	606	3332	7093	2173
R_{int}/ R_{sigma}	0.0466/0.0575	0.0244/0.0232	0.0673/0.1073	0.1143/ 0.1854	0.0205/0.0333
Data/restraints/parameters	2777/0/159	606/0/72	3332/0/196	7093/0/383	2173/0/151
Goodness-of-fit on F^2	1.041	1.077	1.051	1.133	1.058
Final R indexes [$I>=2\sigma(I)$]	$R_1 = 0.0416$ $wR_2 = 0.0975$	$R_1 = 0.0530$ $wR_2 = 0.1420$	$R_1 = 0.0647$ $wR_2 = 0.1096$	$R_1 = 0.1398$ $wR_2 = 0.3503$	$R_1 = 0.0438$ $wR_2 = 0.1028$
Final R indexes [all data]	$R_1 = 0.0681$ $wR_2 = 0.1087$	$R_1 = 0.0717$ $wR_2 = 0.1613$	$R_1 = 0.1494$ $wR_2 = 0.1491$	$R_1 = 0.2545$ $wR_2 = 0.4473$	$R_1 = 0.0555$ $wR_2 = 0.1127$
Largest diff. peak/hole /e Å⁻³	0.29/–0.23	0.35/–0.25	0.27/–0.25	1.39/–1.09	0.50/–0.34

Table 2. Selected bonds for structures **1–5**

Compounds	1	2	3	5	4		4	
Bonds	Å	Å	Å	Å	Bonds	Å	Bonds	Å
Mg1—O1	2.059(2)	2.065(2)	2.057(3)	2.067(2)	Mg11—O11	2.092(7)	Mg12—O12	2.064(8)
Mg1—O2	2.052(2)	2.061(3)	2.074(3)	2.0414(16)	Mg11—O21	2.015(7)	Mg12—O22	2.063(7)
Mg1—O3	2.105(2)	–	2.078(2)	2.0907(14)	Mg11—O31	2.096(7)	Mg12—O32	2.083(8)
O1—C1	1.250(4)	–	1.242(4)	1.246(3)	Mg11—O41	2.066(7)	Mg12—O42	2.056(7)
O2—C2	1.250(3)	–	1.240(5)	1.236(3)	Mg11—O51	2.100(8)	Mg12—O52	2.040(9)
O3—C3	1.254(4)	–	1.256(5)	1.253(2)	Mg11—O61	2.038(8)	Mg12—O62	2.096(8)
C1—N11	1.316(5)	–	1.338(5)	1.339(3)	O11—C11	1.240 (12)	O12—C12	1.247(12)
C1—N12	1.328(5)	–	1.344(5)	1.331(3)	O21—C21	1.247(13)	O22—C22	1.249(13)
C2—N21	1.332(4)	–	1.319(5)	1.332(3)	O31—C31	1.261(12)	O32—C32	1.241(12)
C2—N22	1.317(4)	–	1.339(6)	1.334(3)	O41—C41	1.238(13)	O42—C42	1.210(12)
C3—N31	1.336(4)	–	1.327(5)	1.327(3)	N21—C11	1.319(13)	C42—N82	1.289(17)
C3—N32	1.328(5)	–	1.325(4)	1.329(3)	C31—N51	1.345(17)	C21—N41	1.314(18)

Table 3. Selected Angles and Torsion angles for structures **1**–**5**

Compounds	1	2	3	5	Compound	4
Angles	°	°	°	°	Angles	°
O2—Mg1—O1	84.11(9)	89.22(9)	86.92(10)	88.45(8)	O22—Mg12—O32	93.5(3)
O2—Mg1—O3	95.54(9)	–	88.03(10)	90.65(6)	O12—Mg12—O22	88.5(3)
C1—O1—Mg1	139.8(2)	–	135.1(3)	143.52(14)	C11—O11—Mg11	162.3(7)
C2—O2—Mg1	141.89(19)	–	133.8(2)	140.78(14)	C12—O12—Mg12	155.6(7)
C3—O3—Mg1	132.9(2)	–	133.8(3)	133.56(14)	C31—O31—Mg11	138.0(7)
N11—C1—N12	117.6(3)	–	116.9(4)	117.4(2)	N32—C22—N42	117.9(12)
N22—C2—N21	117.5(3)	–	116.9(4)	118.3(2)	N52—C32—N62	115.3(10)
N32—C3—N31	117.1(3)	–	117.4(4)	117.76(19)	N81—C41—N71	118.2(11)
Torsion angles	°	°	°	°	Torsion angles	°
Mg1—O1—C1—N12	12.9(6)	–	175.6(2)	–175.21(17)	Mg12—O42—C42—N72	–149.60(15)
Mg1—O2—C2—N22	16.5(6)	–	–157.3(3)	–179.17(17)	Mg12—O32—C32—N62	178.51(15)
Mg1—O3—C3—N32	4.1(5)	–	–176.0(2)	158.97(16)	Mg11—O11—C11—N11	103.68(12)

bromide: hexaurea magnesium bromide tetra urea $[U_6Mg]^{2+}$ 2Br⁻.4U [8] and diaqua tetraurea magnesium dibromide $[U_4Mg(H_2O)_2]^{2+}$2Br⁻ [9] have been reported. Following the synthesis by using the technique of slow evaporation from an aqueous solution, we were able to grow single crystals of five magnesium salts: two with tetrafluoroborate anion $[U_6Mg]^{2+}.2BF_4^-$ – **1**, $[(H_2O)_6Mg]^{2+}.2BF_4^-$ – **2**, two with chlorine anion – $[U_6Mg]^{2+}.2Cl^-.4U$ – **3**, $[U_4Mg(H_2O)_2]^{2+}.2Cl^-$ – **4** and one with nitrate anion – $[U_6Mg]^{2+}.2NO_3^-$ – **5**. The problem with the crystal structure determination of urea complexes of magnesium chlorides is associated with their relative in-

stability at ambient temperature. Actually, the performed room temperature data collection resulted in good diffraction of the crystals for 10–15 minutes after what diffraction disappeared almost instantly. The attempted X-ray powder data collection was also unsuccessful. Thus we performed single crystal data collection by flash freezing the crystals in N_2 at 150 K.

Compound 1, $[U_6Mg]^{2+}.2BF_4^-$ crystallizes in orthorhombic $P2_12_12$ space group with one BF_4^- molecule and ½ of the $[U_6Mg]^{2+}$ moiety in the asymmetric unit. The Mg–O and urea bond lengths and angles are comparable to those analogous com-
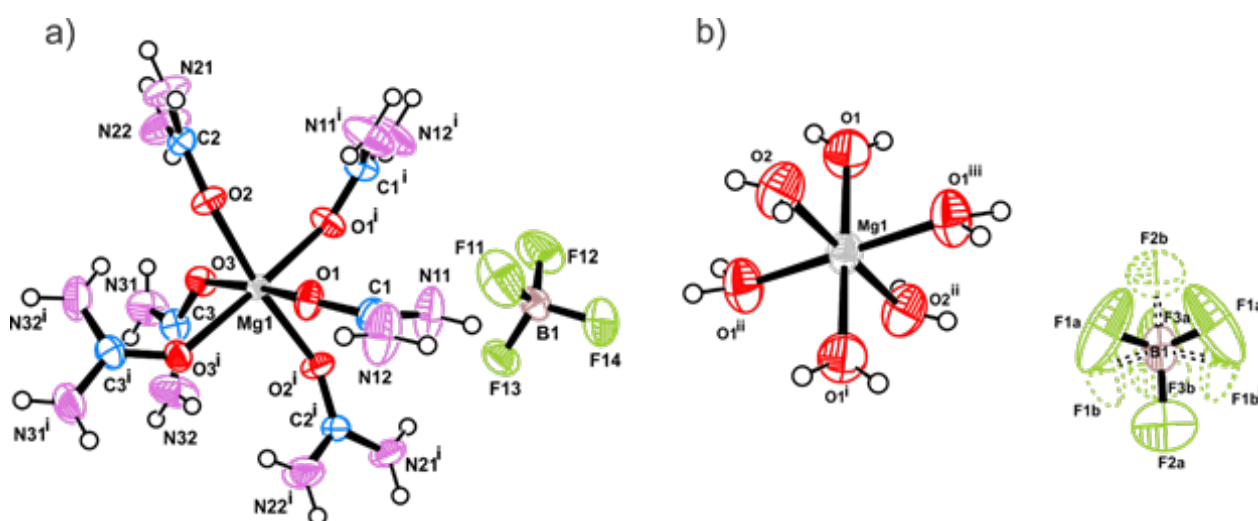

Fig. 1. View of the molecular structures of compounds **1** – a) (symmetry operation: i: *1-x,1-y,z*) and **2** – b) (symmetry operations: (i): *x,y,1-z*; (ii): *2-x,1-y,z* (iii): *2-x,1-y,1-z* with atomic numbering scheme. Atomic displacement parameters for the non-H atoms are drawn at the 50% probability level; the H atoms are presented with spheres with arbitrary radii. The minor disordered component (44%) of the BF_4^- is shown as dashed lines.

pounds [10, 11, 14, 16] Table 2 and 3. Magnesium coordination is octahedral, very slightly distorted, with four Mg–O distances of ~2.0 Å and two longer distances 2.1 Å. The four oxygen atoms exhibiting shorter bond distances with Mg are nearly planar (the mean plane defined by the four oxygen has an *rms* of 0.103 Å). The Mg–O geometry is stabilized trough six N-H…O intramolecular hydrogen bonds (Table 4). The BF_4^- moiety tetrahedral geometry is close to the expected ideal geometry: three of the bond lengths are nearly identical (~1.37 Å) and one is shorter 1.349 Å, while the angles F-B-F vary from 107.7 to 110.5°. All of the F atoms are involved in halogen bonding F…N with NH from urea (Table 3).

Compound 2, $[(H_2O)_6Mg]^{2+}.2BF_4^-$, crystallizes in orthorhombic *Pnnm* space group. The magnesium octahedral coordination is completed by six water molecules. The octahedra is "perfect" as Mg, O1 and O2 atoms are situated on special positions. The two Mg–O distances have comparable values (~2.06 Å) and are intermediate to those of compound **1** where Mg is coordinated by six urea oxygens. The BF_4^- molecule is disordered over two position with a major component of 56%. For compound **2** no intramolecular hydrogen bond interactions could be located. Similarly to compound **1** the all F atoms (from BF_4^-) are involved in halogen bonding interactions of O–H…F type (Table 5).

Table 4. Hydrogen bonded geometry (Å, °) for compound **1**

D—H$\cdots A$	D—H	H$\cdots A$	$D\cdots A$	D—H$\cdots A$
N21—H21$A\cdots$F1³i	0.86	2.34	3.092 (4)	147
N21—H21$B\cdots$O³ⁱi	0.86	2.40	3.108 (4)	141
N21—H21$B\cdots$O¹ⁱⁱi	0.86	2.42	3.157 (4)	144
N32—H32$A\cdots$O³i	0.86	2.46	3.065 (4)	128
N32—H32$A\cdots$O²i	0.86	2.63	3.156 (5)	121
N32—H32$A\cdots$F1²ⁱv	0.86	2.64	3.055 (4)	111
N32—H32$B\cdots$F1¹v	0.86	2.24	3.056 (5)	158
N32—H32$B\cdots$F1⁴v	0.86	2.53	3.278 (5)	146
N22—H22$A\cdots$O3	0.86	2.53	3.263 (4)	143
N22—H22$A\cdots$F1³ⁱi	0.86	2.38	2.936 (4)	123
N22—H22$B\cdots$O²ⁱⁱi	0.86	2.52	3.297 (4)	150
N22—H22$B\cdots$O¹ⁱⁱi	0.86	2.51	3.224 (4)	142
N31—H31$A\cdots$F1³ⁱi	0.86	2.42	3.152 (4)	143
N31—H31$B\cdots$F1²v	0.86	2.64	3.444 (5)	157
N12—H12$B\cdots$F1⁴ᵛi	0.86	2.25	3.073 (5)	159
N11—H11$A\cdots$F11	0.86	2.19	2.825 (4)	130
N11—H11$B\cdots$F1²ᵛi	0.86	2.18	3.027 (4)	170

Symmetry operations: (i) −x+1, −y+1, z; (ii) −x+3/2, y−1/2, −z+1; (iii) x+1/2, −y+1/2, −z+1; (iv) x−1/2, −y+3/2, −z+1; (v) x, y, z+1; (vi) x−1/2, −y+3/2, −z.

Table 5. Hydrogen bonded geometry (Å, °) for compound **2**

D—H$\cdots A$	D—H	H$\cdots A$	$D\cdots A$	D—H$\cdots A$
O1—H1$A\cdots$F1Aⁱ	0.94	2.02	2.888(13)	153
O1—H1$A\cdots$F1Bⁱ	0.94	2.26	3.106(11)	149
O1—H1$A\cdots$F1Bⁱi	0.94	2.63	3.219(10)	121
O1—H1$B\cdots$F2Aⁱi	0.87	2.42	3.011(7)	126
O1—H1$B\cdots$F3Aⁱⁱi	0.87	2.26	2.967(9)	139
O1—H1$B\cdots$F3Bⁱⁱi	0.87	2.27	2.984(7)	140
O1—H1$B\cdots$F2Bⁱv	0.87	2.54	3.055(8)	119
O2—H2$\cdots$F1Av	0.80	2.28	3.075(14)	169
O2—H2$\cdots$F1Bv	0.80	2.24	2.974(10)	153

Symmetry operations: (i) −x+1, −y+1, z; (ii) −x+1/2, y+1/2, −z+1/2; (iii) x+1/2, −y+1/2, z−1/2; (iv) −x+3/2, y+1/2, −z+1/2; (v) x+1/2, −y+1/2, z+1/2.

Compound 3 $[U_6Mg]^{2+} \cdot 2Cl^- \cdot 4U$, crystallizes in monoclinic $P2_1/c$ space group (Fig. 2) and features the same $[U_6Mg]^{2+}$ cations as compound **1**. Here the counterion is Cl^- instead of the BF_4^- present in compound **1**. In **3** along with the cationic $[U_6Mg]^{2+}$ and anionic (Cl^-) parts two additional urea molecules can be located. The Mg–O values are similar to those of **1**, around 2.07 Å and similarly to **1** the

$[U_6Mg]^{2+}$ octahedra is stabilized by intramolecular hydrogen bonds (Table 6). Halogen bonding N-H···Cl is also observed. Due to the presence of the additional urea molecules the three-dimensional packing is stabilized by a multitude of hydrogen bonding interactions (Table 6). The three-dimensional arrangement of the $[U_6Mg]^{2+}$ cations in the crystal structure leads to the formation of "cavities" (voids,
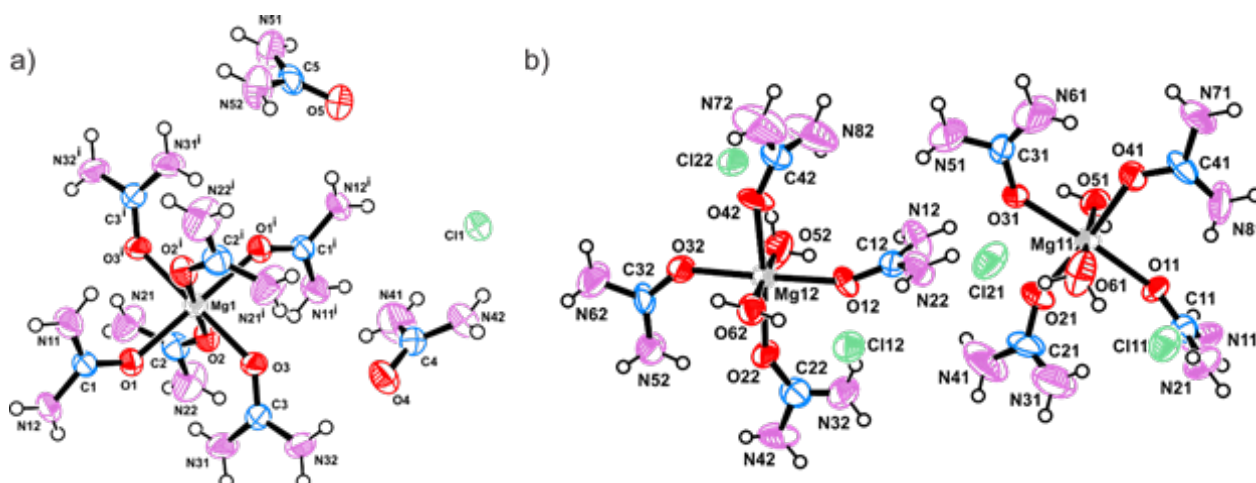
Fig. 2. ORTEP view of the molecular structures of compounds **3** – a) and **4** – b) with atomic numbering scheme. Atomic displacement parameters for the non-H atoms are drawn at the 50% probability level; the H atoms are presented with spheres with arbitrary radii.

Table 6. Hydrogen bonded geometry (Å, º) for compound **3**

D—H···A	D—H	H···A	D···A	D—H···A
N31—H31A···O2	0.86	2.59	3.150 (4)	124
N31—H31A···O1	0.86	2.36	2.983 (4)	129
N31—H31B···Cl1^i	0.86	2.49	3.317 (4)	162
N21—H21A···O3^{ii}	0.86	2.19	2.949 (5)	146
N21—H21B···N12^{iii}	0.86	2.60	3.282 (5)	137
N32—H32A···O4	0.86	2.10	2.955 (5)	175
N32—H32B···O4^{iv}	0.86	2.35	2.999 (4)	133
N51—H51A···O5^v	0.86	2.08	2.932 (4)	172
N51—H51B···Cl1^{vi}	0.86	2.63	3.430 (3)	156
N42—H42A···Cl1^{vii}	0.86	2.60	3.419 (4)	159
N42—H42B···Cl1^{viii}	0.86	2.82	3.333 (4)	120
N52—H52A···O5^{ix}	0.86	2.24	3.076 (5)	163
N52—H52B···Cl1^{vi}	0.86	2.92	3.661 (3)	145
N22—H22A···N42^i	0.86	2.52	3.329 (5)	157
N22—H22B···O5^x	0.86	2.63	3.261 (5)	131
N41—H41B···Cl1	0.86	2.57	3.433 (4)	177
N12—H12A···O5^{ii}	0.86	2.18	3.019 (5)	165
N12—H12B···Cl1^{ii}i	0.86	2.77	3.404 (3)	132
N11—H11A···O2^{i}i	0.86	2.22	2.934 (4)	141
N11—H11B···O4^{x}i	0.86	2.15	2.930 (4)	151

Symmetry operations: (i) $-x, -y+1, -z+1$; (ii) $-x+1, -y+1, -z+1$; (iii) $x, y-1, z$; (iv) $-x, -y+2, -z+1$; (v) $-x+1, y-1/2, -z+3/2$; (vi) $x+1, y, z$; (vii) $x, y+1, z$; (viii) $-x, y+1/2, -z+3/2$; (ix) $-x+1, y+1/2, -z+3/2$; (x) $x, -y+1/2, z-1/2$; (xi) $-x+1, -y+2, -z+1$.
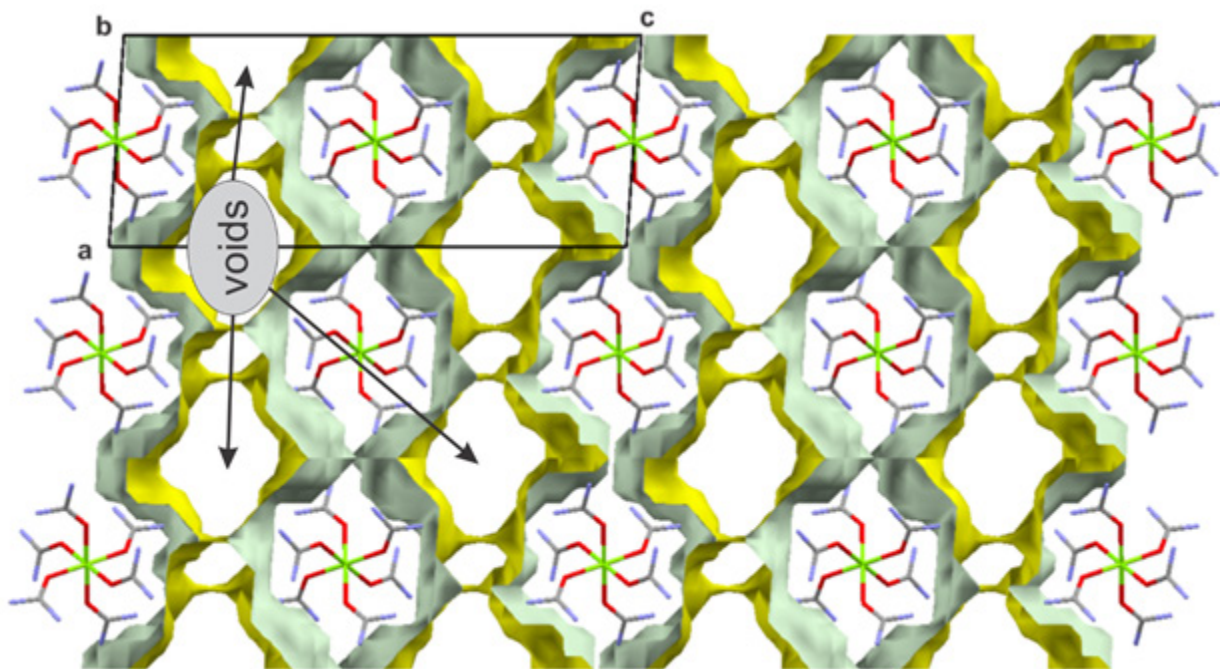
Fig. 3. Observed formation of "cavities" (voids) in the crystal structure of **3** (note that the urea molecules and Cl⁻ have been omitted from the illustration).

Fig. 3) that occupy 42.6% of the unit cell volume (e.g. 695.47 from 1631.5(3) Å^3, the urea molecule have been omitted from this calculation). Due to the smaller size of the monoatomic Cl⁻ (compared to the BF$_4$⁻), the stabilization of the crystal structure of **3** requires the inclusion of urea to fill the empty spaces.

Compound 4, crystallizes in monoclinic $P2_1/c$ space group (Fig. 2b) with two molecules $[U_4Mg(H_2O)_2]^{2+}.2Cl^-$ in the asymmetric unit and is nearly isostructural to $[U_6Mg]^{2+}.2Br^-.4U$ reported in ref. [8]. The bond lengths and angles for the two molecules are nearly identical and are comparable with those of compounds **1–3**, **5** (Tables 2 and 3). The geometry of the two molecules differs

slightly, mainly due to the different orientation of the urea to the mean plane formed by the O-$_{UREA}$ participating in Mg coordination (Fig. 4).

Again, as for compounds **1–3**, the $[U_4Mg(H_2O)_2]^{2+}$ octahedra is stabilized by intramolecular hydrogen bonds (Table 7). The three-dimensional packing of the molecules stabilizing the crystal structure generates a significant number of intermolecular halogen and hydrogen bonds (Table 7). The "inclusion" of additional urea/water molecules (to fill the gaps in the structure) is not necessary as the presence of the two water molecules in the Mg coordination sphere permits denser packing of $[U_4Mg(H_2O)_2]^{2+}$ moieties (closer contact, nearly interpenetration, Fig. 5).
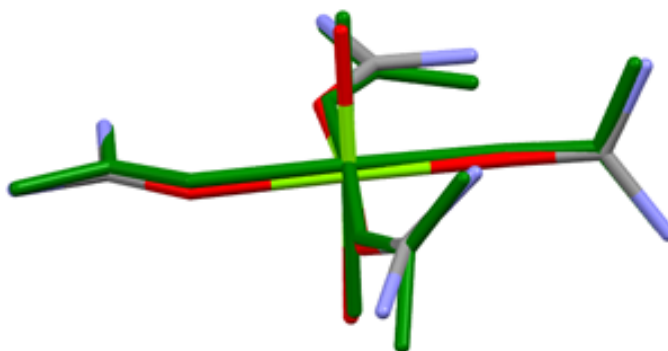

Fig. 4. Overlay of the molecules present in the asymmetric unit of **4** (*rms* 0.604 Å).

Table 7. Hydrogen bonded geometry (Å, °) for compound **4**

D—H$\cdots A$	D—H	H$\cdots A$	$D\cdots A$	D—H$\cdots A$
O51—H51$A\cdots$Cl21^i	0.91	2.25	3.096 (8)	156
O51—H51$B\cdots$Cl11^i	0.90	2.29	3.122 (8)	154
O61—H61$A\cdots$Cl11	0.88	2.41	3.067 (8)	132
O61—H61$B\cdots$Cl21	0.88	2.46	3.044 (9)	124
O52—H52$A\cdots$Cl12^i	0.88	2.38	3.193 (9)	153
O52—H52$B\cdots$Cl22	0.88	2.40	3.076 (9)	134
N22—H22$A\cdots$Cl12	0.88	2.52	3.396 (10)	171
N22—H22$B\cdots$O31	0.88	2.23	3.019·(11)	150
N12—H12$A\cdots$Cl12^i	0.88	2.58	3.416 (10)	158
N12—H12$B\cdots$O31	0.88	2.37	3.128 (11)	144
N21—H21$A\cdots$Cl11	0.88	2.49	3.365 (10)	179
N21—H21$B\cdots$O32^{ii}	0.88	2.53	3.294 (11)	145
N11—H11$A\cdots$Cl11^i	0.88	2.46	3.328 (10)	172
N11—H11$B\cdots$O32^{ii}	0.88	2.37	3.163 (12)	150
N52—H52$C\cdots$O22	0.88	2.11	2.896 (12)	148
N52—H52$D\cdots$Cl22^{iii}	0.88	2.57	3.413 (10)	161
N42—H42$A\cdots$Cl11^{iv}	0.88	2.75	3.576 (13)	156
N42—H42$B\cdots$Cl21^{iv}	0.88	2.49	3.254 (10)	146
N71—H71$A\cdots$Cl22^v	0.88	2.77	3.647 (12)	173
N71—H71$B\cdots$Cl12^{vi}	0.88	2.73	3.376 (9)	132
N71—H71$B\cdots$Cl2^{1v}i	0.88	2.99	3.684 (12)	137
N31—H31$B\cdots$O6^{2i}v	0.88	2.56	3.434 (14)	171
N72—H72$A\cdots$Cl2^{2vi}i	0.88	2.99	3.771 (15)	149
N62—H62$D\cdots$Cl2^{2ii}i	0.88	2.67	3.489 (12)	155
N41—H41$B\cdots$Cl1^{2i}v	0.88	2.41	3.260 (12)	163
N32—H32$A\cdots$O12	0.88	2.11	2.872 (14)	145
N32—H32$B\cdots$Cl1^{2i}v	0.88	2.46	3.319 (11)	166
N82—H82$B\cdots$O5^{1vii}i	0.88	2.33	3.198 (13)	171
N61—H61$C\cdots$O41	0.88	2.06	2.842 (17)	148
N61—H61$D\cdots$Cl2^{2}v	0.88	2.76	3.273 (13)	118
N61—H61$D\cdots$Cl1^{1i}x	0.88	2.74	3.558 (14)	154
N51—H51$C\cdots$Cl1^{1i}x	0.88	2.53	3.375 (13)	160
N51—H51$D\cdots$N22	0.88	2.74	3.319 (16)	124
N81—H81$A\cdots$O11	0.88	2.05	2.862 (14)	152
N81—H81$B\cdots$Cl2^{1v}i	0.88	2.25	3.119 (12)	169

Symmetry operations: (i) x−1, y, z; (ii) x, y−1, z; (iii) −x+1, −y+2, −z+1; (iv) −x+2, −y+1, −z+1; (v) −x+1, y−1/2, −z+1/2; (vi) −x+2, y−1/2, −z+1/2; (vii) x+1, y, z; (viii) −x+1, y+1/2, −z+1/2; (ix) −x+2, y+1/2, −z+1/2.
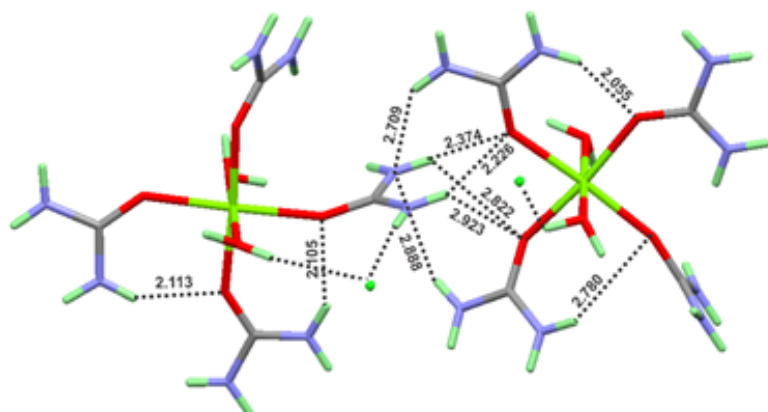

Fig. 5. Representation of the dense packing of the $[U_4Mg(H_2O)_2]^{2+}$ moieties observed in **4** (hydrogen bonds are shown as dotted lines, distances are in Å).

Compound 5, $[U_6Mg]^{2+}.2NO_3^-$, crystallizes in the triclinic P–1 space group with 1/2 molecule in the asymmetric unit (Fig. 6).The bond lengths and angles of the nitro group and $[U_6Mg]^{2+}$ fragment are comparable to those of compounds **1–4** (Tables 2 and 3). Here the difference is in the anion – the nitro group – which is more bulky than the Cl⁻ and more compact than BF_4^-. As for compounds **1–4** the intramolecular and intermolecular hydrogen bonds stabilizing the molecular geometry of the $[U_6Mg]^{2+}$ and the three-dimensional packing are also observed (Table 8).

According to the structural data obtained from compounds **1–5** the Mg octahedral coordination is very conservative. The Mg–O distances are not affected by the change coordinating moiety urea *vs* water (Table 9) or by the change of anion moiety (Cl⁻, NO3⁻, BF_4^-). The rotation of the urea around the Mg–O_{UREA} bond is not hampered and allows the
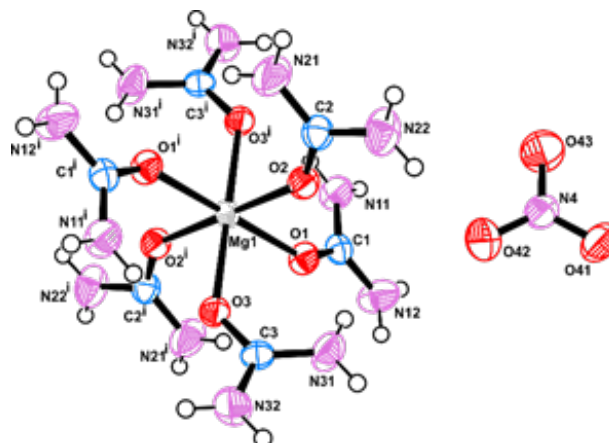
Fig. 6. ORTEP view of compound **5** with atomic numbering scheme (symmetry operation (i); *x,y,z*). Displacement ellipsoids for the non-H atoms are drawn at the 50% probability level. The H atoms are presented with spheres with arbitrary radii.

Table 8. Hydrogen bonded geometry (Å, °) for compound **5**

D—H⋯A	D—H	H⋯A	D⋯A	D—H⋯A
N22—H22A⋯O42	0.86	2.31	3.107 (4)	153
N22—H22B⋯N32ⁱ	0.86	2.65	3.502 (4)	174
N31—H31A⋯O1	0.86	2.35	3.035 (3)	137
N31—H31B⋯O43ⁱⁱ	0.86	2.34	3.091 (3)	146
N21—H21A⋯O1ⁱⁱⁱ	0.86	2.43	3.082 (3)	133
N21—H21A⋯O41ⁱᵛ	0.86	2.33	2.953 (4)	130
N21—H21B⋯O43ᵛ	0.86	2.36	3.157 (4)	155
N32—H32A⋯O2ⁱⁱ	0.86	2.53	3.114 (3)	126
N32—H32A⋯O3ᵛⁱ	0.86	2.51	3.267 (3)	148
N32—H32B⋯O43ⁱⁱ	0.86	2.19	2.975 (4)	152
N11—H11A⋯O3ⁱⁱⁱ	0.86	2.29	3.031 (4)	145
N11—H11B⋯O41ᵛⁱⁱ	0.86	2.30	3.064 (3)	148
N12—H12A⋯O41ᵛⁱⁱⁱ	0.86	2.64	3.307 (3)	136
N12—H12A⋯O42ᵛⁱⁱⁱ	0.86	2.17	3.018 (3)	169
N12—H12B⋯O41ⁱˣ	0.86	2.63	3.345 (3)	142
N12—H12B⋯O43ᵛⁱⁱ	0.86	2.39	3.029 (3)	131

Symmetry operations: (i) −*x*+1, −*y*, −*z*+1; (ii) *x*−1, *y, z*; (iii) −*x*+1, −*y*+1, −*z*+1; (iv) *x, y, z*+1; (v) −*x*+2, −*y*, −*z*+1; (vi) −*x*, −*y*+1, −*z*+1; (vii) −*x*+2, −*y*+1, −*z*; (viii) −*x*+1, −*y*+1, −*z*; (ix) *x, y*+1, *z*.

Table 9. Average Mg–O distances and negative and positive deviations from average for compounds **1–5**

Compound	Bond Mg—O (Å)	Angle O—Mg1—O (°)
1	2.072 (−0.013; +0.028)	90 (−5.9; +5.54)
2	2.063 (−0,002; +0.002)	90 (−0.06; +0.68)
3	2.070 (−0.003; +0.012)	90 (−3.08; +1.42)
4	2.071 (−0.028; +00.33)	90 (−2.5; +3.5)
5	2.067 (−0.024; +0.025)	90 (−1.55; +0.65)

87

formation of intermolecular halogen and hydrogen bonds that stabilize the three-dimensional packing of the crystal structures. Both the cation and anion "sizes" are affecting the crystal packing.

CONCLUSIONS

The crystal structure of five magnesium complexes have been determined. The structures reveal the traditional octahedral coordination of Mg. The change of anion (Cl^-, NO_3^-, BF_4^-) does not induce changes in the octahedral Mg coordination. When magnesium chloride forms a complex with six molecules of urea, additional urea molecules are included in the crystal structure. No such "inclusion" is observed for the other magnesium salts BF_4^- and NO_3^-. This is explained by the large size of the coordinated cation $[U_6Mg]^{2+}$ and the small size of the anion (Cl^-). The three-dimensional packing of the cation produces voids in the structure that cannot be completely filled by the small anion. In order to minimize the "free spaces" additional urea molecules are required. Therefore, the crystal structure is stabilized by incorporating two additional urea molecules with each chlorine anion and the compound crystallizes as $[U_6Mg]^{2+}.2Cl^-.4U$.

SUPPLEMENTARY MATERIALS

ICSD No XX1, XX1, xx4 xx3 and XX1 contains the supplementary crystallographic data for compounds **1–5** respectively. Further details of the crystal structure investigation(s) may be obtained from Fachinformationszentrum Karlsruhe, 76344 Eggenstein-Leopoldshafen, Germany (fax: (+49)7247-808-666; e-mail: crysdata(at)fiz-karlsruhe.de, http://www.fiz-karlsruhe.de/request_for_deposited_data.html) on quoting the appropriate CSD number.

REFERENCES

1. L. Pavanello, P. Visonà, A. Marigo, S. Bresadola, G. Valle, *Inorganica chimica acta*, **216**, 261 (1994).
2. B. L. Barker, D. Aubry, F. R. Fronczek, S. F. Watkins, G. G. Stanley, *Acta Crystallographica Section E: Structure Reports Online*, **62**, m942 (2006).
3. M. Nardelli, L. Coghi, *Ric. Sci.*, **29**, 134 (1959).
4. A. S. Antsyshkina, K. K. Palkina, N. E. Kuz'mina, V. T. Orlova, G. G. Sadikov, *Russ. J. Inorg. Chem*, **42**, 1468 (1997).
5. D. Rogolino, M. Carcelli, M. Sechi, N. Neamati, *Coordination Chemistry Reviews*, **256**, 3063 (2012).
6. C. Hsiao, M. Tannenbaum, H. VanDeusen, E. Hershkovitz, G. Perng, A. Tannenbaum, L. D. Williams, *Nucleic acid metal ion interactions. London: The Royal Society of Chemistry*, 1 (2008).
7. E. Susan, in: Biology of Plants, 7-th ed, P. Raven, R. Evert, S. Eichhorn (eds), WH Freeman, New York, 2005, p. 119.
8. Ł. Lebioda, K. Stadnicka, J. Sliwinski, *Acta Crystallographica Section B: Structural Crystallography and Crystal Chemistry*, **35**, 157 (1979).
9. Ł. Lebioda K. Lewiński, *Acta Crystallographica Section B: Structural Crystallography and Crystal Chemistry*, **36**, 693 (1980).
10. T. Todorov, R. Petrova, K. Kossev, J. Macicek, O. Angelova, *Acta Crystallographica Section C: Crystal Structure Communications*, **54**, 456 (1998).
11. T. Todorov, R. Petrova, K. Kossev, J. Macicek, O. Angelova, *Acta Crystallographica Section C: Crystal Structure Communications*, **54**, 1758 (1998).
12. K. Yamagata, N. Achiwa, M. Hashimoto, N. Koyano, Y. Iwata, I. Shibuya, *Acta Crystallographica Section C: Crystal Structure Communications*, **48**, 793 (1992).
13. K. Yamagata, N. Koyano, N. Achiwa, M. Fujino, Y. Iwata, I. Shibuya, *Journal of Magnetism and Magnetic Materials*, **104**, 849 (1992).
14. T. D. Hayden, E. E. Kim, K. Eriks, *Inorganic Chemistry*, **21**, 4054 (1982).
15. T. Todorov, R. Petrova, K. Kossev, J. Macícek, O. Angelova, *Acta Crystallographica Section C: Crystal Structure Communications*, **54**, 927 (1998).
16. E. Frolova, K. Palkina, A. Kochetov, V. Danilov, *Russian Journal of Inorganic Chemistry*, **57**, 416 (2012).
17. J. P. Glusker, A. K. Katz, C. W. Bock, *The Rigaku Journal*, **16**, 8 (1999).
18. C. W. Bock, A. Kaufman, J. P. Glusker, *Inorganic Chemistry*, **33**, 419 (1994).
19. Harold S. Booth (ed.), Inorganic Syntheses, Vol. 1, McGraw-Hill Book Company, Inc., New York and London, 1939.
20. CrysAlis PRO, Agilent Technologies, UK Ltd, Yarnton, England, 2011.
21. G. Sheldrick, *Acta Crystallographica Section C*, **71**, 3 (2015).
22. G. M. Sheldrick, *Acta Cryst. A*, **64**, 112 (2008).
23. L. Farrugia, *Journal of Applied Crystallography*, **45**, 849 (2012).
24. C. F. Macrae, I. J. Bruno, J. A. Chisholm, P. R. Edgington, P. McCabe, E. Pidcock, L. Rodriguez-Monge, R. Taylor, J. van de Streek, P. A. Wood, *Journal of Applied Crystallography*, **41**, 466 (2008).
25. J. Yee, R. Davis, S. Hendricks, *Journal of the American Chemical Society*, **59**, 570 (1937).
26. M. Sosnowski, *J. Scienska. Roczn. Chemii*, **31**, 1223 (1957).
27. В. М. Какабадзе, З. Г. Николайшвили, И. Б. Мшвенперадзе, *Докл. АН СССР*, **5**, 1156 (1965).
28. V. Orlova, E. Konstantinova, V. Kosterina, M. Sherbanski, I. Lepeshkov, *Journal of thermal analysis*, **33**, 929 (1988).

УРЕАТИ И ХИДРАТИ НА МАГНЕЗИЕВ ХЛОРИД, НИТРАТ И ТЕТРАФЛУОРОБОРАТ

Р. Русев, Л. Цветанова, Б. Шивачев, К. Косев*, Р. Николова

Институт по минералогия и кристалография „Акад. Иван Костов",
Българска академия на науките, „Акад. Георги Бончев",
бл. 107, 1113 София

(Резюме)

Получени са пет комплекса на магнезий и е определен кристалният им строеж. Два с тетрафлуороборатен анион – $[U_6Mg]^{2+} \cdot 2BF_4$ – **1** и $[(H_2O)_6Mg]^{2+} \cdot 2BF_4$ – **2**, два с хлориден – $[U_6Mg]^{2+} \cdot 2Cl^- \cdot 4U$ – **3** и $[U_4Mg(H_2O)_2]^{2+} \cdot 2Cl$ – **4**, както и един с нитратен – $[U_6Mg]^{2+} \cdot 2NO_3^-$ – **5**. Образци за монокристален рентгеноструктурен анализ са израстнати чрез бавно изпарение от воден раздвор на съответната магнезиева сол и карбамид. Два от тях кристализират в моноклинна сингония $[U_6Mg]^{2+}$ $2Cl^- \cdot 4U$ и $[U_4Mg(H_2O)_2]^{2+}$ $2Cl^-$, пространствена група – Р 2_1/с с параметри на елементарната клетка a = 9.6317(8), b = 7.2241(7), c = 23.506(3), β =94.045(9) и a = 8.0168(16), b = 14.844(2), c = 28.662(4), β= 94.194(16) съответно, един в триклинна – $[U_6Mg]^{2+}$ $2NO_3^-$ пространствена група – Р–1 с параметри на елементарната клетка a = 7.1917(6), b = 8.279(3) c =9.555 (9), α = 71.01(6), β = 89.17(3), γ = 84.158(19) и два в орторомбична $[U_6Mg]^{2+} 2BF_4^-$ кристализира в пространствена група – $P2_12_12$, с параметри на елементарната клетка a = 9.964(5), b = 11.979(6), c = 9.638(5)), а $[(H_2O)_6Mg]^{2+} 2BF_4^-$ в пространствена група – Pnnm с параметри на елементарната клетка a = 5.4322(6), b = 13.2050(12), c = 7.6786(6).

Auto-freeze drying by zeolites

G. Kirov[1], N. Petrova[2]*, Ts. Stanimirova[1]

[1] University of Sofia "St. Kliment Ohridski", Faculty of Geology and Geography, Department of Mineralogy, Petrology and Economic Geology, 15 Tzar Osvoboditel Blvd., 1000 Sofia, Bulgaria
[2] Institute of Mineralogy and Crystallography – Bulgarian Academy of Sciences, 107 Acad. G. Bonchev Str., 1113 Sofia, Bulgaria

Combining the processes of freezing and drying by means of adsorption with dehydrated zeolite was proposed as a new auto-freeze drying process. This work describes the changes of temperature and mass of the dried product (carrot) and of the adsorbent (zeolite Na-A) during the auto-freeze drying process and the influence of different factors on them. Based on the analysis of the changes of the water states in both the product and the adsorbent, a strategy for harnessing the full adsorption capacity of the zeolite and significantly reducing of the reaction time was suggested. The zeolite freeze drying system works effectively using mainly low-temperature heat and could be functioned by solar or waste heat. The system gives opportunity to recuperate and reuse the heat flows to further enhance of energy effectiveness.

Keywords: auto-freeze drying, zeolite Na-A, water state, energy effectiveness.

INTRODUCTION

The freeze drying produces the highest quality end output for heat-sensitive products compared to other drying methods. Due to the low temperatures (below 0 °C) required for the process, the tastes, as well as any nutritive qualities of the products, are retained. The separation of water is achieved by the sublimation of ice, through which the structure, the form, and the size of the tissue are conserved. The porous structure of the dried product permits its quick rehydration [1–3]. However, the freeze drying is also the most expensive process compared to other drying methods due to high capital and processing costs, as well as its significant duration.

The freeze drying can be carried out in vacuum [1] or in a suitable atmosphere [4]. With contemporary technology, sub-zero temperatures and removal of the vapor are ensured by refrigerating machines [1]. In literature, vacuum systems with removal of the vapor from pre-frozen products through adsorption have been described [5, 6], but have never been developed. An atmospheric freeze drying system with silica-gel as adsorbent has been described by Rahman and Mujumdar [7].

Zeolites are the most effective sorbents for deep drying of gazes and liquids [8, 9]. They are capable of drying solid products through contact reactions [10, 11] or air dehumidification by adsorption [12].

Tchernev [13, 14] has first shown that the sorption properties of zeolites are very effective in adsorption cooling and this led to the creation of various freezing, heating, cooling and conditioning systems, driven by low temperature heat such as solar heat or waste energy. Unlike the other solid adsorbents, zeolites adsorb actively even at very low partial pressure of the adsorbate and at relatively high temperatures [8]. In the zeolite-water adsorption systems, cooling is obtained through evaporation of water in the evaporator. When the water molecules of a water-containing product enter the vapor phase, they preserve a significant amount of the latent heat of evaporation (2447 kJ/kg water) and thus, the temperature of water is reduced to the freezing point. Then, the cooling continues at the expense of the sublimation of the ice.

Kirov and Kirov [15] use this effect in an auto-freezing adsorption dryer with an extremely simple construction and maintenance. A prototype device with natural zeolite (clinoptilolite) activated at 400 °C achieves cooling to –25 °C with high drying rates. In later publication [16] the behavior of the freeze dried product and the sorbent (zeolite A) has been studied.

* To whom all correspondence should be sent:
E-mail: nadia5@mail.bg

In this work, we present an auto-freezing zeolite system and describe the results of its trials in the one-stage freeze drying of carrot tissue. The influence of different factors on the temperature of the product and on the kinetics of the drying are taken into consideration as well. Based on the analysis of the change of the water state in both the product and the adsorbent, a two-step process is proposed with the aim of strategically utilizing the full adsorption capacity of the zeolite and the maximal reduction of the reaction time.

MATERIALS AND EXPERIMENTAL EQUIPMENT

As a model product, an orange carrot from a local market was used. It was cut into ribbons thick 0.3–0.5 mm, wide 3 mm and long 25–120 mm, without further treatment. By drying at 105 °C to a constant mass, a dry residue of 12–13% of the initial wet product is obtained. As adsorbent, Na-A zeolite (manufactured by Zeochem), in the form of pills, with a diameter of 2–3 mm was used. The zeolite was activated in an electric furnace for 1.5 h at 350 °C and cooled to room temperature in a closed vessel, the zeolite lost 22.0 mass% upon thermal activation.

A scheme of the equipment for auto-freeze drying experiment is shown on Fig. 1. The adsorber is a cylindrical glass bottle with an inner diameter of 70 mm and a height of 120 mm. Three glass tubes used to measure the temperature of the sorbent are welded at a distance of 20, 60 and 95 mm from the bottom of the glass equipment. This gives the possibility of monitoring the average temperatures of
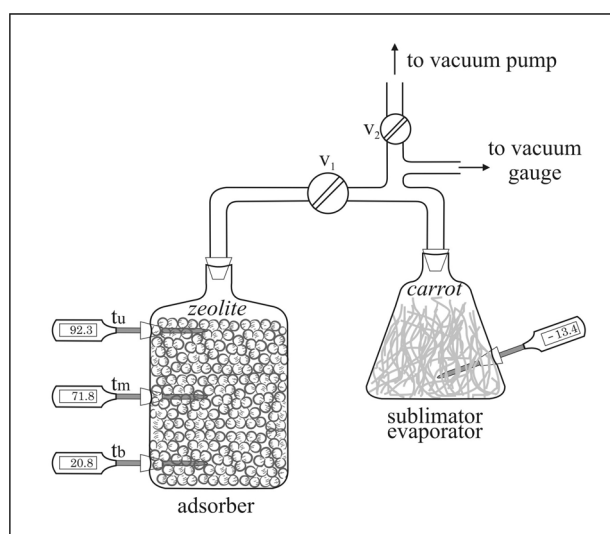

Fig. 1. Experimental equipment used for vacuum freeze drying.

three layers 40 mm apart from each other: upper (t_u), middle (t_m) and bottom (t_b). The sublimator is an Erlenmeyer flask with a welded tube for a thermometer 15 mm from the bottom. The two vessels are connected by a glass tube through a vacuum valve (v_1) with aperture of 8 mm. Through a second valve (v_2), the system is connected to the vacuum pump (Labortechnik, Ilmenau), with end pressure 67 Pa and a capacity of 2.5 cubic meters per hour.

Digital thermometers with a precision of 0.1 °C and electronic balance with a precision of 0.1 g were used.

RESULTS AND DISCUSSION

The driving force behind the drying process is the difference in partial pressure of water in the environment and the moisture pressure in the product. This difference reaches magnitudes triggering the auto-freezing of the product in the vacuum system. The vigorous adsorption of the water vapors from the zeolite maintains the difference long enough and the drying continues at the expense of the sublimation. The degree of freezing is regulated by a multitude of factors, namely the pressure in the system and the state of the water in both the product and the zeolite.

One-stage experiments

Procedure. 45 g of product are loaded in the sublimator immediately after their grating at room temperature. The adsorber is loaded with 330 g dehydrated zeolite, activated in an electric oven in a layer thick of 1.5–2 cm at a heating rate of 10 °C/min and kept 30 minutes at 250 °C. The sorbent is cooled to 150–160 °C, after which is reintroduced in the adsorber and put into vacuum in order to prevent the sorption of nitrogen from the air at lower temperatures. The cooling zeolite adsorbs the remaining nitrogen and oxygen molecules in the chamber and the pressure drops by one order of magnitude. The sublimator is joined with the system and the product is joined with the adsorber after 1–2 minutes of vacuum pumping. The cooling of the product begins during the vacuum pumping and is accelerated after the junction to the adsorber, which acts as an adsorption pump.

The temperature of the product and the sorbent are constantly monitored during 12 hours. The mass of the product and of the zeolite is recorded both at the beginning and at the end of the experiments (continuously during two of the experiments).

The conditions of four experiments are: In experiment 1 (exp. 1), the adsorber is cooled down and the sublimator is heated by the surrounding

air. In other runs, the sublimator is heated with a 100 W infrared lamp (exp. 2) or insulated with a layer of expanded vermiculite thick 3 cm (exp. 3). In particular cases the adsorber is cooled with filter paper jacket immersed with cooled water (exp. 4). The data about the four experiments are provided in Table 1.

The changes in temperature in the sublimator and the adsorber in experiment 1 are given on Fig. 2a. In this experiment there is only spontaneous heat exchange with the surrounding air. In the first minutes, because of the vigorous evaporation of the water from the carrot, the temperature drops fast. The product freezes for two minutes and reaches −14 °C at the 14th minute. Meanwhile, the adsorption of the water vapor causes the heating of the surface layer of the sorbent to over 100 °C. In the following hours, the temperature in the sublimator slowly rises and reaches 0 °C after 8 hours and 10 °C after 12 hours. During this period, the temperature of the surface layer of the zeolite decreases at the room temperature. The adsorption continues in the deeper layers and they remain above the room

temperature until the end of the experiment. The weighing of the product and the sorbent at the end shows that the carrot has lost 66.2% of the initial mass, and the mass of the zeolite has augmented by just as much adsorbed water.

The kinetics of the drying can be seen on the gravimetric curve in Fig. 2b. On the curve of exp. 1 there are three segments: steep, declining and a final, almost horizontal. In the steep area, 1/4 of the water from the carrot evaporates. In the first 10 minutes the rate of the dehydration is more than 2%/min and in the following 10 minutes – around 1%/min. In the declining area the dehydration rate constantly decreases to average 0.08%/min for the following 6–8 hours. Finally, the drying ceases, its rate drops under 0.03%/min. In exp. 2, from the 75th minute the sublimator is heated with an infrared lamp which moves from 60 cm from the bottom to 30 cm from it at the end of experiment. One can see, that the introduction of heat activates the drying process – the curve become steeper and the product is fully dried after 570 minutes. The product, however, stays frozen only 145 minutes and reaches 36.6 °C

Table 1. Comparison of the results obtained in one-stage (experiments 1, 2, 3 and 4) and two-stage freeze drying (experiments 5-1 and 5-2)

| Experiment No	1	2	3	4	5-1	5-2
Extreme temperature and time to reach it, °C/min						
Product	−14.1° /14'	−14.6° /16'	−14.6° /30'	−15.4° /10'	−11° /11'	−16° /17'
Sorbent (upper)	107° /10'	115° /3'	110° /10'	97° /7'	78° /13'	68° /17'
Sorbent (middle)	68° /15'	77° /16'	73° /20'	92° /10'	84° /77'	32° /90'
Sorbent (bottom)	26° /36'	37° /260'	29° /720'	25° /30'	32° /95'	24° /170'
Time to reach 0 °C in the product, min						
	460	145	does not reach	540	390	95
Temperature in the end of experiment, °C						
Product	9.6	36.6	−2.2	6	2	19
Sorbent (upper)	22	27	29	18	37	31
Sorbent (middle)	42	38	36	22	44	26
Sorbent (bottom)	26	31	30	20	32	21
Duration of the experiments, min						
	720	570	720	720	420	300
Mass loss in the product, %						
	66.2	87.1	64.0	74.7	56.2	87.3
Degree of filling, % from maximum sorption capacity						
	41.3	54.0	39.7	46.4	94.9	34.3
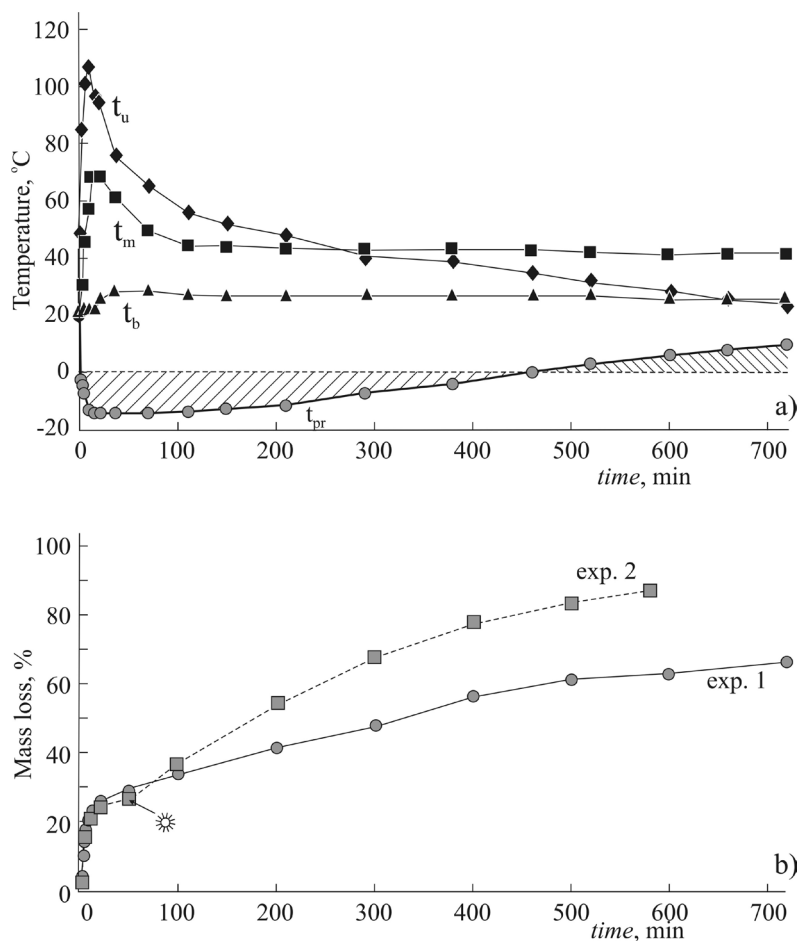
Fig. 2. a) Temperature of the product (t_{pr}) and of three levels of the sorbent (t_u, t_m and t_b) during experiment 1; b) mass loss of the product during experiments 1and 2. The turning on an infra-red lamp is marked with a star.

by the end of the experiment (Table 1). As could be expected, the insulation of the sublimator (exp. 3) has an influence mainly on the frozen state's duration, with the minimal temperature and the drying rate close to those in exp. 1. Cooling the adsorber (exp. 4) causes a decrease in product temperature, thus increase of the time spent of a frozen state (Table 1). As one can see, the application of various effects enables control over the drying conditions. Furthermore, each of those can be applied at given moments of the process regarding the features of the drying product.

As can be seen (Fig. 2b), the rate of drying almost diminishes to zero, even though the sorption capacity of the zeolite is half used. The cause of this is that during the drying process, the states of the product and the sorbent continuously change – the channels of zeolite structure are filled with water molecules and the product is dried more and more, a dry crust is formed, which hinders the diffusion of the water vapors. Analysis of the evolution of

the state of the water in the product and zeolite during the experiment showed a significant discrepancy [17], which influences the effectiveness of the drying process. The weakest bonded moisture of the product is adsorbed at the most active sorption sites in the zeolites, while the strongest bonded water should be evaporated under influence of weakly active centers. A significant improvement to the efficiency of the process could be made by performing the process in the backward flow – to adsorb low-bond product moisture on less active adsorption places in the zeolite and the strongly associated – on the most active places. Unfortunately, this process is technically difficult to perform in the adsorption drying of solid products. A harmonization of the water state of both product and zeolite has been proposed by the application of a two-stage drying process, which provides full consumption of the adsorption capacity of the zeolite, maximal drying of the product and a reduction of duration of the drying cycle by 2 times [17].

Two-stage experiment

Procedure. The used equipment is the same as described above, but with a larger sublimator (400 ml flask) loaded with 80 grams of grated carrot. At the start, 330 g of zeolite are activated up to 250 °C. After the activation, the zeolite is used in a preliminary stage to dry the product during 40 minutes. After that, the partially dried carrot is replaced with a freshly grated carrot and the adsorber is cooled to room temperature. This is the starting point of the two-stage cycle. In the first stage, the zeolite has already used 1/3 adsorption capacity, but due to the large content of free water in the fresh carrot, the product freezes spontaneously and stays frozen for the next few hours, while the sorbent reaches upwards of 90% of its capacity. In the second stage the zeolite is changed with a freshly-activated batch, which adsorbs the remaining strongly-bounded moisture in the product. The dried product is then changed with a fresh one and a new cycle can begin with the partially used zeolite.

The results from a two-stage experiment are given on Fig. 3 and Table 1 as well. In the first stage (exp. 5–1), the middle zeolite layer plays the main role, as the upper layer has already used a part of its capacity in previous stage (Fig. 3a). The temperature of the bottom layer increases, because it also adsorbs. The gravimetric curve (Fig. 3b) has a steep beginning section and then gradually a smooth bend. In these stages the carrot losses 45.0 g water, which is 56.2% of the initial mass of the product, and the zeolite (sown as Z_1) uses up more than 90% of its sorption capacity.

The process is reactivated (exp. 5–2) after the change of the adsorber with fully dehydrated zeolite (sown as Z_2): the product freezes again for about one hour, and another steep area can be seen on the gravimetric curve. Thus, after 10 hours of drying the product loses 80% of its mass. The full drying is achieved by heating the sublimator with an infrared lamp (to 27 °C) for two more hours (Fig. 3b). In the second stage, Z_2 adsorbs 24.6 g water or 34.3% of the capacity and can still dry out partially a second portion of fresh carrot.
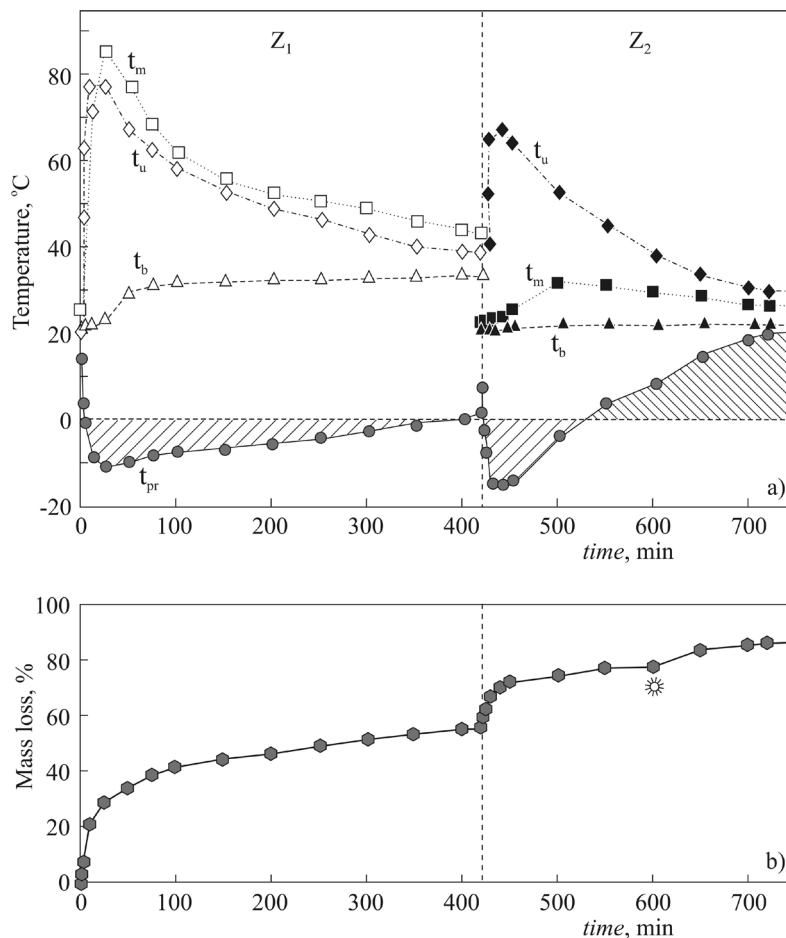

Fig. 3. a) Temperature of the product (t_{pr}) and of the sorbent (t_u, t_m, t_b) during a two-stage experiment; b) mass loss of the product during drying with two adsorbents. The turning on an infra-red lamp is marked with a star.

The results from the two-stage experiment confirm the conclusions from the two-stage contact drying [17]: full consumption of the sorption capacity of the zeolite, drying to a maximal degree (when needed) and reduction of the drying process duration.

Dried product. A SEM photograph of the dried carrot is shown on Fig. 4. According to literature data for freeze dried carrot [3], the preservation of the cellular structure is very well achieved, with big and regular pores. After rehydration the carrot has an odor and taste almost identical to the original. The fully dried product keeps the orange color, the form and the dimensions of the bands of carrot. The dried product is very hydroscopic.
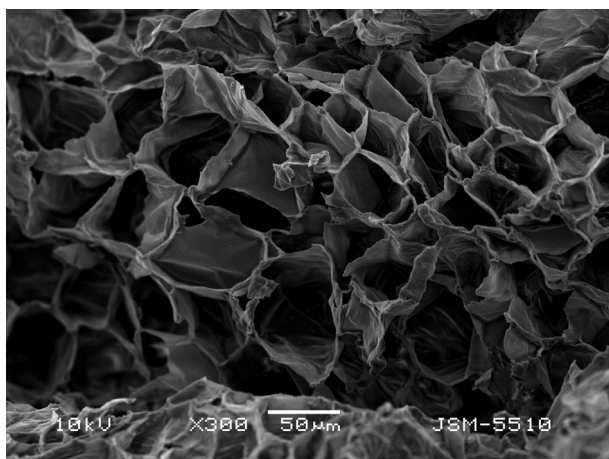
Fig. 4. SEM photography of a freeze dried carrot (exp. 2).

Heat flows in the zeolite freeze drier. There are two heat inflows in the system: (i) to dehydrate (activate) the zeolite at a temperature of 200–250 °C and (ii) to provide the latent heat of sublimation and evaporation with a temperature of 30–60 °C. Unlike the conventional freeze driers, which use only electric energy, the zeolite installations can use a number of other heat sources, including solar and waste energy. In these cases, only the vacuum pump is powered with electricity, for no more of 10–12 minutes in drying cycle.

Heat is produced in three heat outflows: (i) the condensation and cooling of water vapor, produced by the activation of the zeolite; (ii) the cooling of activated zeolite from 250 °C to room temperature and (iii) the heat of adsorption of water vapor in zeolite.

Each of the three heat outflows can be used to deliver latent heat for sublimation/evaporation in the product, but the first and third sources are more fitting to this end. Moreover, as was proved, the removal of the adsorption heat from adsorber enhances its effectiveness. The temperature of activated zeolite is high enough so that the heat outflow can be used for preheating the next portion of adsorbent.

CONCLUSIONS

The zeolite freeze drying system ensures fast auto-freezing and full drying of water containing products matching the high standards set by the industry demands, even in a device with extremely simple construction and very limited maintenance. The temperature of the product and the kinetics of the drying process can be influenced by the introduction of heat, by insulating the evaporator, cooling the adsorber or pre-freezing of the product, along with other methods, which enable the process to switch between specific customer expectations with ease.

On the basis of the analysis of water states in the product and zeolite, a two-stage experimental scheme providing the full use of the sorption capacity of the sorbent and a steep reduction in cycle duration is suggested. The dried product has a well-preserved cellular structure, high pore content and can be reverted back to the original state with quick rehydration.

The zeolite freeze drying systems can be driven by low-temperature heat, such as waste or solar energy, since the vacuum pump only works for less than 2% of the drying process duration. The system offers ways to recuperate the heat outflows and reach high energy efficiency.

REFERENCES

1. A. I. Liapis, R. Bruttini, in: Handbook of Industrial Drying, A. S. Mujumdar (ed.), Marsel Dekker, NY, 1999.
2. Sh. Sokhansanj, D. S. Jayas, in: Handbook of Industrial Drying, A. S. Mujumdar (ed.), Marsel Dekker, NY, 1999.
3. A. Rayes, R. Vega, R. Bustos, C. Areneda, *Drying Technology*, **26**(10), 1272 (2008).
4. I. C. Claussen, T. S. Ustad, I. Stommen, P. M. Walde, *Drying Technology*, **25**(6), 947 (2007).
5. A. Takasaka, Y. Matsuda, in: New developments in zeolite science and technology, Y. Marakami, A. Iijimma, J. M. Ward (eds), Kodansha and Elsevier, Tokyo, Amsterdam, 1986.
6. G. A. Bell, J. D. Mellor, *CSIRO Food Research Quarterly*, **50**(2), 48 (1990).
7. S. M. A. Rahman, A. S. Mujumdar, *Drying Technology*, **26**(4), 393 (2008).

8. D. W. Breck, Zeolite molecular sieves, John Willey & Sons, N.Y., London, Sidney, Toronto, 1974.
9. G. V. Tsitsishvili, T. G. Andronikashvili, G. N. Kirov, L. D. Filizova, Natural zeolites, Ellis Horwood, N.Y., London, Sidney, Toronto, Tokyo, Singapore, 1992.
10. Z. Alikhani, G. S. V. Raghavan, A. S. Mujumbar, *Drying Technology*, **10**(3), 783 (1992).
11. T. Kudra, A. S. Mujumbar, in: Handbook of Industrial Drying, A. S. Mujumbar (ed.), Marsel Dekker, NY, 1999.
12. M. Djaeni, P. Bartels, J. Sanders, G. van Straten, A. J. B. van Boxtel, *Drying Technology*, **25**(1), 225 (2007).
13. D. I. Tchernev, in: Natural Zeolites: Occurrence, Properties, Use, L. B. Sand, F.A Mumpton (eds.), Pergamon Press, NY, 1978.
14. D. I. Tchernev, in: Natural Zeolites'93*, D. V. Ming, F. A. Mumpton (eds.), Int. Comm. Natural Zeolites, Brockport, NY, 1995.
15. G. N. Kirov, D. G. Kirov, *Bulgarian Patent* 48534 (1989).
16. D. G. Kirov, L. Filizova, G. N. Kirov, in: Book of extended abstracts of Zeolite 2010 – 8th International Conference on the Occurrence, Properties, and Utilization of Natural Zeolites, Bulgaria, Sofia, July 10–18, 2010.
17. G. N. Kirov, N. Petrova, Ts. Stanimirova, *Drying Technology*, **35**(16), 2015 (2017).

САМО-ЗАМРАЗИТЕЛНО СУШЕНЕ СЪС ЗЕОЛИТИ

Г. Киров[1], Н. Петрова[2], Ц. Станимирова[1]

[1] Софийски Университет „Св. Климент Охридски", Геолого-географски факултет, Катедра „Минералогия, петрология и полезни изкопаеми", бул. „Цар Освободител" 15, София 1000, България
[2] Институт по минералогия и кристалография – Българска академия на науките, ул. „Акад. Г. Бончев", бл. 107, София 1113, България

(Резюме)

Предложен е нов подход за само-замразително сушене посредством комбиниране на процесите на замразяване и сушене чрез адсорбция с дехидратиран зеолит. Тази работа описва промените в температурата и теглото на изсушения продукт (морков) и на адсорбента (зеолит Na-A) по време на процеса на сушене чрез само-замразяване и влиянието на различни фактори върху него. Въз основа на анализа на промените в състоянието на водата както в продукта, така и в адсорбента беше предложен подход за оползотворяване на пълния адсорбционен капацитет на зеолита и значително намаляване на реакционното време. Системата за само-замразително сушене със зеолит работи ефективно предимно с нискотемпературна топлина като може да функционира със слънчева или отпадъчна топлина. Системата дава възможност за възстановяване и повторно използване на топлинните потоци за по-нататъшно повишаване на енергийната ефективност.

Preparation of hydroxyapatite/hyaluronan biomimetic nano-hybrid material for reconstruction of critical size bone defects

R. Ilieva[1], E. Dyulgerova[2], O. Petrov[3]*, M. Tarassov[3], A. Gusiyska[2], R. Vasileva[2]

[1] *Institute of General and Inorganic Chemistry, Bulgarian Academy of Sciences,*
Acad. G. Bontchev Str., Bl. 11, 1113 Sofia, Bulgaria
[2] *Faculty of Dental Medicine, Medical University, 1 G. Sofiiski Str., 1431 Sofia, Bulgaria*
[3] *Institute of Mineralogy and Crystallography, Bulgarian Academy of Sciences,*
Acad. G. Bontchev Str., Bl. 107, 1113 Sofia, Bulgaria

Sintered bi-phase calcium phosphate material was subjected to dry high-energy milling for 40 hours to obtain crystalline nano-metric hydroxyapatite. During milling the tertiary calcium phosphate got fully amorphous. Powder XRD analysis was used for phase control and crystallite size measurements. The morphological studies were performed by SEM and TEM and showed formation of granulated agglomerates. The obtained material was additionally milled with 1% hyaluronan for times of 2, 5, and 10 hours and the initially formed agglomerates were subsequently disintegrated to form well homogenized nano-hydroxyapatite particles of a hybrid hydroxyapatite/hyaluronan material, which was used for filling of bone defects with critical sizes in cases of apical periodontites. Test clinical studies showed good healing process.

Keywords: hydroxyapatite, high-energy milling, hybrid hydroxyapatite/hyaluronan, apical periodontites.

INTRODUCTION

The development of bone–like materials with optimized function are general problems and have been developed to meet and provide promising ways to repair and replace damaged bone areas [1, 2]. As it is well known human bone is a nanocomposite with organic/inorganic structural components. In regenerative processes the extracellular matrix plays a critical role in supporting and directing bone cells adhesion, proliferation and differentiation. Therefore, in development of bone-like materials it is desirable to create biomimetic nanostructured engineering scaffolds providing structural support for initial cell adhesion [3, 4]. Therefore, recently, research has been focused towards bone-like biomaterials, which might substitute bone as a natural functional nanostructure.

In this regard, calcium orthophosphates have substantial potential due to their chemical similarity with natural bone mineral – they are biocompatible, bioactive, and biodegradable and have the ability to form a direct chemical bond with the surrounding tissues and are non-toxic, non-inflammatory and non-immunogenic agents [5–8]. Hydroxyapatite (HA) has been preferably proposed as substitute for defective bones or teeth.

Nowadays, significant research effort has been dedicated to develop inorganic nano-sized crystalline hydroxyapatite (nHA) because of crystallite size, active surface and potential biological activity [9–11]. Moreover, nHA particles will provide an increased ratio of high surface area to volume and their ultrafine structure similar to biological apatite can suitably affect their biological activity in biomedical application. Recently, HA at nano-level has playing increasing role in various biomedical applications [12, 13]. Thus, with the development of nanotechnologies, considerable efforts are focused on controlling the morphology and size of materials [14–17]. Moreover, nHA with ultrafine structure imitates the natural bone mineral as an extracellular matrix component and can cause an increased binding capacity of macromolecules, optimized bone cell–surface protein interaction, promoting the attachment and growth of osteoblast-like cells [18, 19, 20–23]

Even after extensive investigations related to bio-mineralization many intermediate stages in synthesis and preparation of nHA are still unclear.

---

* To whom all correspondence should be sent:
E-mail: opetrov@dir.bg

Therefore, various parameters that affect size, shape, and crystallinity of nHA still need to be further studied.

Biomimetic composite materials have recently drawn considerable attention [24, 25]. In investigation of critical size bone defects (intraosseous wounds of size that do not heal by natural regenerative processes) they are subjects of repair and regeneration and require substitute materials as scaffolds, to provide osteogenic processes and formation of new bone [26].

Strategies in bone tissue regeneration nowadays are related with scaffolds mimicking the natural extracellular matrix as templates for cells. Hence, of particular interest are nanocomposite and organic/inorganic hybrid biomaterials based on selective combination of biodegradable polymers and bioactive inorganic nanomaterials [27]. Generally, the focus is based on nHA as filler in combination with biodegradable natural or synthetic polymers. It was demonstrated that a HyA matrix is a promising biomimetic material [28, 29]. These studies suggest that HyA-containing scaffold materials are efficacious in bone repairing. HyA is well known as hyaluronan or hyaluronate (Na salts of hyaluronic acid) [30], being linear glycosaminoglycan polysaccharide consisting of repeated disaccharide units of negatively charged high–molecular–weight linear polymer, with repeated unites of N-acetyl glucosamine and glucuronic acid and in water they form three dimensional (3D) network [31]. The long chains of HyA macromolecules with a large number of carboxyl, hydroxyl and amino groups have a strong capacity to bind various ions [32]. As a consequence of this specificity they are ideal network of mineralizing template [33]. Furthermore, through HyA complex interactions with extracellular matrix components and cell surfaces regulation of cellular behavior controlling the tissue macro and micro environments occurs [34] and could induce osteoblast differentiation and bone formation [35]. In presence of endotoxins hyaluronic acid is produced by fibroblasts and is a potential anti-inflammatory agent [36]. The anti-inflammatory effect may be due to the action of HyA as a scavenger draining prostaglandins, metalloproteinases and other bioactive molecules [37, 38, 39]. Additionally, HyA is essential component of the periodontal ligament and plays role in cell adhesion, migration and differentiation modulated binding proteins and cell–surface receptors such as CD44 [40] and is a significant factor in growth, development and repair of tissue [41, 42]. Relating to the unique properties of HyA it is possible that nano-hybrid with hydroxyapatite can produce more effective bone filler-like materials that provide the necessary features for more efficient healing of bone defects.

The choice of hyaluronic acid (HyA) is chiefly based upon its natural abundance in soft tissues and high chemical affinity with hydroxyapatite (HA) and the ability to enhance anisotropic growth in bio-mineralization [43]. Moreover, hyaluronic acid based materials have been intensively investigated for tissue engineering repair of bone, cartilage and in reconstructive dentistry [44–46]

In oral and maxillofacial surgery, bone defects are always challenging problems for reconstructive orthopedic craniofacial procedures, and various treatments have been proposed in this consideration [47, 48]. Synthetic bone grafts are among the promising approaches in this field. It is of interest to refer clinical results for Endodontic Orthograde treatment of apical bone defect in chronical apical periodontal lesions (49–52).

As a result of all above mentioned about the biological activity of nHA, HyA and composites of HyA/nHA, we hypothesized that it will be of theoretical, practical and biomedical clinical interest to prepare nHA, and nano hybrid of HyA/nHA and to be tested as new filling materials in endodontics treatment of critical size apical bone defects.

The purpose of the present study is to prepare nano–hybrid of nano-hydroxyapatite (nHAp) and hyaluronan (Na salt of Hyaluronic acid – NyA-Na) in varying ratio of nHAp/HyA in attempt to optimize their physical-chemical and mechanical properties, and to be used as a test filling material for orthograde endodontic treatments.

MATERIALS AND METHODS

Nano hydroxyapatite was prepared by top down method using high energy milling process of the sintered bi-phasic calcium phosphate. The obtained material was used to prepare nano-hybrid of nHA/HyA.

1. Synthesis and methodology

Biphasic calcium phosphate was prepared by sintering of precursor precipitate sample obtained by chemical wet precipitation method in a typical process by double decomposition of 1M calcium nitrate solution (prepared from $Ca(NO_3)_2 x4H_2O$) in de-ionized water and di-ammonium hydrogen phosphate (prepared with $(NH_4)_2HP0_4$, 0.6 M), in stoichiometric ratios for hydroxyapatite Ca/P ~1.67 under controlled temperature and pH = 10.5–11 conditions [56] (the used salts of calcium nitrate and ammonium hydrogen phosphate are of analytical grade Merck). However, this method has some inherent disadvantage such as difficulty to control the pH value over pH = 9, to avoid the formation of

Ca-deficient HA, which during the sintering forms tertiary calcium phosphate (TCP).

At the end of the maturation for period of 24 h the precipitate was centrifuged, filtered and washed 3 times with de-ionized water. The resulting crystalline apatite was dried at 100 °C for 10 h to use as a starting material. Afterwards, this material was sintered stepwise at 1100 °C for 1 h. at a heating rate 50 °C min^{-1}. It is well known that depending on the degree of Ca deficiency of the precipitate the molar composition of the resulting bi-phase composition of TCP/HA can vary [53, 54] and for these reasons, we have characterized the processes in a step-like manner to follow calcination in the interval 800–1100 °C (more details are presented in our work [56]).

The obtained sintered material subsequently was dry milled in agate planetary ball mill ('pulverisette'6 Fritsch) at 600 rev/min, working in a programmed manner with agate bolls (10 mm diameter) in standard mass of 30 g of sample. Nanocrystalline HA (nHA) was obtained after 40 h milling and was used to prepare nano-hybrid from HyA-Na solution in different ratios of HA/HyA-Na, as it is described below.

2. Characterization of the nano-sized apatite material

The concentration of calcium in the sintered material was determined potentiometrically and by EDTA complex-metrically titration in the presence of Cu EDTA at pH = 10, using a Cu ion-selective electrode and Ag/AgCl reference electrode. The concentration of P-PO$_4^{3-}$ was measured spectrophotometrically by NOVA 60 equipment, using Merck and Spectroquant® test kits.

For SEM study, nano-metric materials were suspended in water, transferred on specimen stubs, dried and then coated with conductive material (Au) for observation in SEM JEOL JSM-5510 at accelerating voltage of 10 kV and electron beam current of 2–20 nA to reveal the textural details of nano-metric agglomerations after dry milling for 40 hours.

For TEM study, nano-metric materials were suspended in de-ionized water, sonicated for 15 min and then transferred on formvar coated TEM grids and observed in TEM JEOL JEM-2100 at 200 kV.

Powder nano-metric samples were ground in an agate mortar for 10 min, suspended in de-ionized water and sonicated for 15 min. After allowing setting for 20 min the supernatant was collected and was collected and redropped on formvar coated grids and observed in TEM JEOL JEM-2100 at 200 kV.

The crystalline phases in all samples were determined by powder X-ray diffraction (XRD) with a Bruker D8 diffractometer, operating at 40 kV and 40 mA with Cu Ka radiation. Scans were performed over the range of 2Θ 10–80° (step size 0.01°, counting time 1 s). The crystallite sizes were determined using the Scherrer equation, $D = K \lambda/(\beta_{1/2} \cos \Theta)$, where D is the crystal size in nanometers, K is the Scherrer constant, λ is the x-ray wavelength, and β is the experimental full-width at half-maximum intensity of the diffraction measured peak.

3. Preparation of nano-hybrid HA/HyA-Na

Nano hybrid samples prepared from 40h milled HA and HyA in ratio 3:1 were subjected to second wet milling for 2 and 5 h and then characterized by powder XRD for phase content and crystallite sizes.

Then, hyaluronan with 1% concentration (denoted as L) was mixed with nHA milled material (denoted as S) in different experimentally chosen ratios S/L from 0.2 to 3.3. From the obtained mixed materials, as dense pastes there were molded samples in rubber-molds with diameter of 10 mm and height of 5 mm, dried in air for 24 h at room temperature. The initial and final setting times of the nano hybrid material prepared in the rubber-molds were determined by the Vicar Needle method (ASTM C191-9 1993). The formation features are shown in Table 1.

Table 1. Formation mechanisms of the prepared nano hybrid materials

Solid to liquid ratio	Liquid phase	Formation features	
		Initial setting time, min	Final setting time, min
3.3	HyA/HA	6	60
2.8	Hya/HA	15	60
2.0	HyA/HA	20	60
1.4	HyA.HA	27	60

4. Micro environmental tested behavior of hybrid HA/HyA

The prepared samples of hybrid **HA/HyA** were used for testing their environmental behavior. The air-dried solid samples of HA/HyA were placed in distilled water and in simulated body fluid (SBF) (prepared according to Kukubo, 1990). The solid samples taken out from the rubber-molds were air-dried for 24 h, and then were immersed in a solution at ratio of 1:20 S/L. All experiments were conducted at room temperature under static conditions. The changing values of pH in the solution were kinetically followed for a period of 30 h at room temperature. The same procedure was used in the case of distilled water.

5. Test-clinical studies

For testing biogenic repair capability of the obtained nano-hybrid of nHA/HyA through healing processes on the critical size bone defects there were carried out chronical periodontal bone lesions on clinical compromised teeth with periapical lesions and ill prognosis. Orthograde root canal filling process was used. Clinical treatment was carried out after obtaining the patient's consent to the guidelines of ethical committee of Faculty of Dental Medicine of the Medical University of Sofia.

Preparation of nano-hybrid of HA/HyA for clinical use was obtained by mechanical mixing in ratio 4:1 of nHA/HyA. (The nano-HA was autoclave sterilized and the used HyA is a pharmaceutical product for injection application).

Fig. 1. SEM image of nHA milled for 40 hours. Bar – 0.2 μm.

RESULTS AND DISCUSSION

Synthesis and modification

The synthesis procedure and reaction conditions strongly influence the type of the precipitated calcium phosphate phases and the morphology, size and specific surface area of the particles [57–60].

The elemental chemical analysis of the obtained material gave for calcium and phosphate the ratio of Ca/P 1.63.

The morphological characterization of the obtained nHA material after 40 h milling showed continuous decrease of particle sizes until some lower size limit when many defects in the crystal lattice are accumulated and the phase of TCP is almost fully transformed in amorphous phase, as it was shown earlier in our work [56].
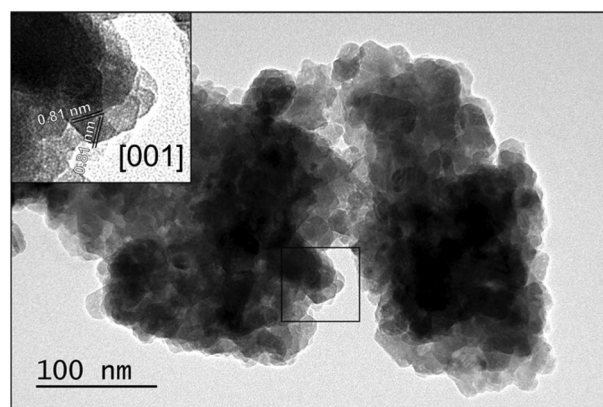

Fig. 2. TEM bright-filed image of nHA aggregates (after milling for 40 hours). The insert shows enlarged area marked in the image center with indicated d-spacing typical for the zone [001] of apatite.

Scanning and transmission electron microscopy (SEM, TEM)

The SEM study of the sample after 40 hour milling showed the presence of 20–100 nm nanoparticles self-organized into aggregates with size 200–800 nm (Fig. 1). The aggregates are randomly shaped being occasionally connected with each other to form much larger and porous agglomerates. These agglomerates most probably are secondary assemblies being formed due to the preparation procedure for SEM study.

The sonication procedure used for the TEM sample preparation allows to substantially exclude the secondary aggregation and to observe the actual microstructure of the milled material. This case is well illustrated in Fig. 2 where two steady aggregates with size 300×500 and 200×300 nm are shown. The aggregates consist mainly of platy (thin) hex-

agonally shaped nanocrystals with size 10–30 nm. The most developed face of the crystals is {001}. The insert on the left-top part of the figure shows an enlarged fragment from the central part of the image (delineated as square) where the hexagonal nHA crystal demonstrates two-dimensional lattice fringes (high-resolution image) corresponding to d-spacings equal to 0.81 nm and angle of 60°, which is typical for the zone [001] of apatite. A part of nHA is presented by slightly elongated platy nanocrystals with the aspect ratio close to 2 and the length varying between 30 and 60 nm. The crystal structure of the studied in TEM nanocrystals is not perfect. This fact is well demonstrated in Fig. 3, where high-resolution image of defect and comparatively large HA nanocrystal in zone [010] is shown. It is well visible that the two-dimensional lattice fringes are characterized by different contrast and clarity.
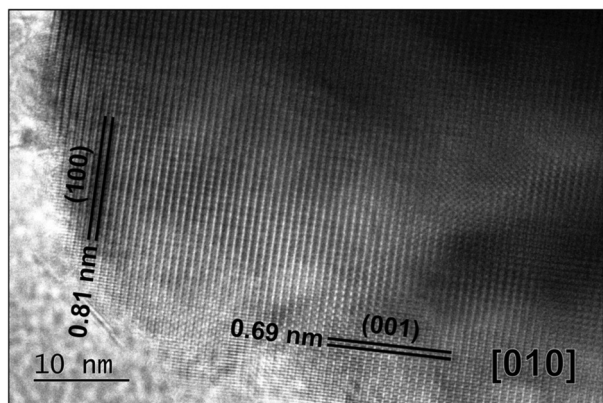
Fig. 3. HRTEM image of defect HA nanocrystal whose [010] zone axis is parallel to the electron beam. d-spacing 0.81 nm for (100) and 0.69 nm for (001) typical for the [010] zone of apatite are drawn in the image. Defect structure of the nanocrystal is characterized by the presence slightly oriented domains with size of about 10 nm.

In some places of the image, the two-dimensional lattice is transformed into one-dimensional lattice. There are light and dark areas. All these data indicate the presence of differently oriented domains constructing the nanocrystal.

Powder X-ray diffraction

The prepared nano-apatite by stepwise dry milling process for 40 h and the hybrid material of nano-HA/HyA was subject to powder X-ray diffraction analysis. In the model studies hyaluronan was used as crystal modifier controlling shape and size. The results from powder XRD analysis are shown on the Figure 4.

The crystallite size determination gave about 70 nm for the as-syntesized sample and about 30 nm for the milled sample for 40 h, which value is preserved for the mixed HA-HyA sample milled for 5 hours.

The lowest pattern (Fig. 4a) shows presence of major hydroxyapatite and whitlockite (TCP phase) in the as-synthesized ceramic. After milling for 40 h the phase TCP gets amorphous (Fig. 4b). It can be stated that the mixed HA-HyA sample after additional milling for 5 hours contains three components – nano-crystalline (HA), amorphous (TCP) and HyA (hyaluronan) (Fig. 4c). Possible disaggregation due to hyaluronan addition is expected and can e registered by granulometric methods in future.

Micro environmental behavior of samples

The obtained series of nano-materials from the tested ratios (Table 1) were molded in rubber-molds

were used for testing their microenvironment behavior and mechanochemical properties.

The micro environmental behavior of the test air dried samples were studied in distilled water
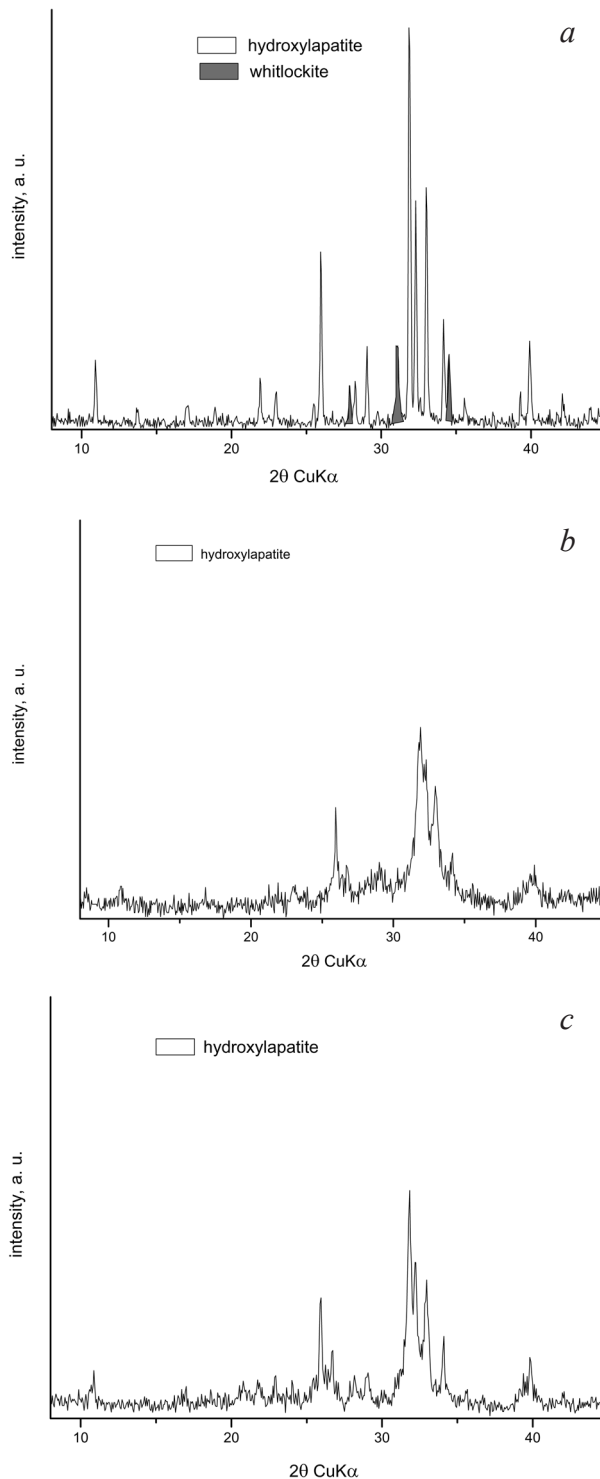
Fig. 4. Powder XRD patterns of the used materials: *a*, XRD pattern of as-synthesized Ca-P ceramics; *b*, XRD pattern of Ca-P ceramic milled for 40 h; *c*, XRD pattern of Ca-P ceramic milled for 5 h with hyaluronan.

with pH = 6.9 and in simulated body fluid (SBF) prepared according to Kokubo (1990) at pH = 7.2–7.4. The test samples were immersed in liquid and the pH value of the liquid phase was measured for a period of 30h. The results revealed that the finer the powder the higher is the amount of the liquid needed for preparation of plastic material that remains compact after drying (solid to liquid ratio of 3.3). The results from the *in vitro* micro environmental behavior testing of compact dried sample moulds in SBF and in distilled water are presented on Fig. 5.

The results of the microenvironmental behavior show the tendency for keeping pH values in the interval 8.4–9.2 for the entire studied time. These values of pH are relevant to biological reactions and bio-compatibility.

Test clinical studies – a case report

A 37 years old female was referred for endodontic retreatment on tooth #36. The radiographic examination revealed a tooth with unsatisfied endodontic treatment and large periapical lesion – PAI5 (critical size bone defect). The patient felt pain on percussion. The endodontic treatment plan included the removal of old root canal filling, precise inspection and preparation of apical zone into the canals.

The canals were prepared using ProTaper Universal instruments (Dentsply Maillefer) and classic endodontic irrigating protocol – 2.5% NaOCl, 17% EDTA and distilled water. Final preparation of the endodontic space with apical bone lesion was filled with hybrid HA/HyA and after that was obturated with bioceramic sealer TotalFill (FKG, Switzerland) and gutta-percha.

It is know [62] that hyaluronic acid and synthetic calcium phosphate have osteoconductive and biodegradable properties and that was confirmed bu our presented clinical case (Fig. 6).

SUMMARY OF THE OBTAINED RESULTS

The most commonly used technique for the formation of HA is the precipitation of precursors, involving wet chemical reaction between calcium and phosphate salts under controlled pH and temperature. Having in mind the complexity of the processes involved in the precipitation synthesis it is obvious that understanding the mechanism in the individual history of the samples used is an intriguing task.

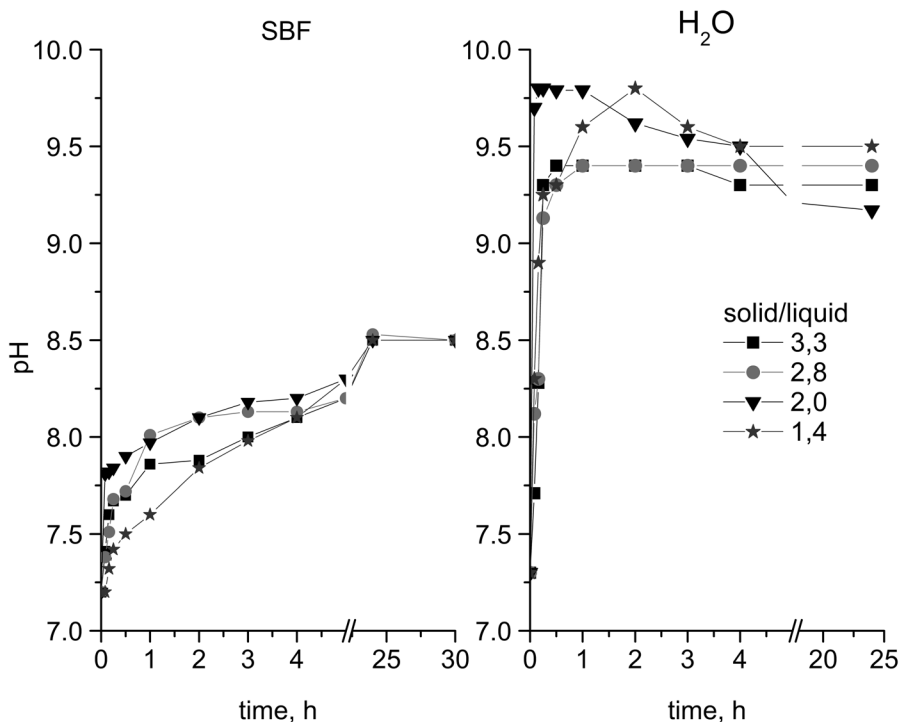This work confirmed that synthesis procedures and reaction conditions strongly influence the char-

Fig. 5. pH changes in SBF and in distilled water at *in vitro* testing of molds of CaP nano-crystalline particles with sodium hyaluronate (solid/liquid 3.3; SBF pH = 7.2–7.4; water pH = 7).
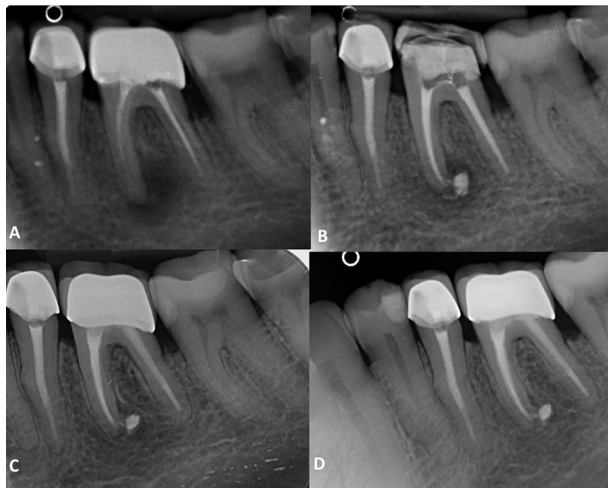
Fig. 6. *A*, Diagnostic radiograph of tooth #36; *B*, Control radiograph after definitive root canals obturation; *C*, Control radiograph after 6 months follow up period; *D*, Control radiograph after 12 months follow up period.

acteristics of nanoparticles obtained by top-down milling processes – their particles morphology, size and specific surface area, etc. [55–61].

In these contexts interesting features of the mechanical high energy milling processes is to be used for top-down preparation of nanoscale hydroxyapatites with particle and crystallite sizes relevant to the bio mineralized structures. As a result, the milling process is one of the pathways of choice to prepare nano-sized bone substituted material. There is a great clinical need for advanced biomaterials with enhanced functionality in order to improve quality of life of patients and to reduce the healthcare burden of a global aging population.

Furthermore, the various parameters that affect size and shape of crystallinity of nano scale HA (1–100 nm) still need further study. We hypothesize that this material has higher potential to be used as bone building blocks in repair processes and probably to be self-organized matrix with biological activity.

Another problem posed the results from wet milling of nano-HA with HYA-Na solution receiving materials with nano-particles of 20–25 nm or smaller. These results also would be subjects of more detailed future experimental studies and crystallographical analysis.

The vantage point to prepare nanocrystals is a great challenge maximizing in vivo targeting efficiency. Applications of macromolecules for functionalization of mineral nano-particles have been widely investigated and it was proven to be effective for bone repair strategy.

The obtained results are related to the new challenges in 21 century of endodontics studies on the clinical application of new materials that can adopt to ever-changing microenvironment of the root canal system (composite-like HA/HYA materia). Our test-clinical study in the cases of apical bone lesions as critical bone size defects show healing with nano-hydroxyapatite as an orthogonal filling material.

CONCLUSION

In this study a series of nano-hybrid materials of NyA/nHA with nano-hydroxyapatite and hyaluronan (sodium HyA) in different chosen experimental ratios of the components were investigated. The obtained material was chemically, morphologically and structurally studied. The composition of the liquid phase and the solid/liquid ratio on the formation features and mechanical strength of the materials were investigated. It was found that high energy milling stimulates the binding capacity of the received nano-material. The performed studies revealed that the obtained nano-hydroxyapatite by high-energy milling is with crystallite size about 30 nm. SEM and TEM investigations show aggregates of nHA crystallites. Hybrid material of nHA and 1% hyalorunan additionally milled was applied in test treatment of bone defects with critical dimensions, which lead to good clinical results.

REFERENCES

1. L. Zhang, T. Webster, *Nanotechnology*, **4**(1), 66 (2009).
2. R. Langer, J. Vacanti, *Tissue Engineering, Science*, **260**(5110), 920 (1993).
3. M. Tibbitt, K. Anseth, *Biotechnol. Bioeng.*, **103**(4), 655 (2009).
4. A. Mistry, A. Mikos, *Adv. Biochem. Eng. Biotechnol.*, **94**, 1 (2005).
5. J. Elliot, Structure and Chemistry of the Apatites and other Calcium Orthophosphates (Studies in Inorganic Chemistry, vol. 18), Elsevier, Amsterdam, 1994.
6. L. Hench, *J. Am. Ceram. Soc.*, **74** (7), 1487 (1991).
7. M. Jarcho, *Clinical Orthopaedics and Related Research*, **157**, 259 (1981).
8. M. Ogiso, *J. Biomed. Mater. Res.: Appl. Biomater.*, **43** (3), 318 (1998).
9. C. Combes, C. Rey, *Biomaterials*, **23**, 2817 (2002).
10. M. Gorbunoff, *Analytical Biochemistry*, **136** (2), 440 (1984).
11. L. Hench, *J. Am. Ceram. Soc.*, **74** (7), 1487 (1991).

12. T. Webster, R. Siegel, R. Bizios, *Biomaterials*, **21**, 1803 (2000).
13. X. Zhu, O. Eibl, C. Berthold, L. Scheideler, J. Geis-Gerstorfer, *Nanotechnology*, **17**, 2711 (2006).
14. P. Kumta, C. Sfeir, D-H. Lee, *Acta Biomaterialia*, **1**, 65 (2005).
15. T. Hirai, M. Hodono, I. Komasawa, *Langmuir*, **16**, 955 (2000).
16. D. Walsh, S. Mann, *Chemistry of Materials*, **8**, 1944 (1996).
17. K. Hing, S. Best, W. Bonfield, *J. Mater. Sci.: Materials in Medicine*, **3**, 135 (1999).
18. Huang J., SM. Best, W.Bonfieu, RA. Brooks, et al., In vitro assessment of the biological response to na-no-size Hydroxyapatite. J Mater Sci.Mater Med 15, 441–445 (2004)
19. A. Zhao, W. Graysona, T. Maa, B. Bunnell, W. Luc, *Biomaterials*, **27**, 1859 (2006).
20. J. Liuyun, L/ Yubao, Z. Li, L. Jianguo, *J Mater Sci: MaterMed*, **19**, 981 (2008).
21. T. Webster, R. Cergun, W. Doremus, W. Siegel, R Bizios. *J. Biomend Mater. Res.,* **51**(3), 475 (2000).
22. G. Wei, P. Ma, *Biomaterials*, **25**(19), 4739 (2004).
23. M. Sato, M. Sambito, A. Aslani, N. Kalkhoran, E. Slamovich, T. Webster,. *Biomaterials*, **27**(11), 2358 (2006).
24. E. Place, E. Evans, M. Stovens, *Nat. Mater*, **8**, 457 (2009).
25. J. Zhao, X. Lu, K. Duan, L. Guo, S. Zhou, J. Weng, *Colloids Surf. B., Bio Interfaces*, **74**, 159 (2009).
26. T. Einhorn, *Clin. Orthop. Res*.**367**, 59 (1999).
27. B. Allo, D. Costa, S. Dixon, K. Mequanint, A. Rizkalla, *J. Func. Mater,* **3**(2) 432 (2012).
28. K. Tanaka, T. Goto, T. Myazakki, Y. Morita, S. Kobayashi, S. Tagahashi, *J. Dent. Res*., **90**, 906 (2011).
29. M. Bohner, *Eur. Cell Mater*., **20**,1 (2010).
30. T. Laurent,.J. Frazer, *FASEB Journal,* **6**(7), 2397 (1992).
31. J. Fraser, T. Laurent U. Laurent, J *Intern Med.,* **242** (1), 27 (1997).
32. E. Balazs*, Federation Proceeding* **17** (4), 1086 (1958).
33. Chen Z H , X L Ren, HH Zhou X D Li: The role of hyaluronic acid in bio mineralization Front Mater Sci. 6(4)283-296(2012)
34. P. Rajan, D. Nair, C. Kumar, L. Dusanapudi, *Univ. Res. Jour. of Dentistry,* **3**(3), 123 (2013).
35. L. Hung, Y. Cheng, P. Koo, K. Lee, L. Qin, J. Cheng, S. Kumta, *J. Biomed. Mater. Res*., **66A**, 880 (2003).
36. R. Moseley, R. Waddington, G. Emery, *Dent. Updata,* **29**, 144 (2002).
37. T. Laurent, U. Laurent, J. Frazer; *Ann. Rheum. Dis*, **54**, 429 (1995).
38. H. Larjava, J. Heino, V. Kahari, T. Krusius, E. Viorio, *J. Dent. Res*., **68**, 20 (1989).
39. M. Pogrel, M. Lowe, R. Stern, *Arch. Oral Biol.,* **41**, 667 (1996).
40. O. Oksala, T. Salo, R.Tammi, L. Hakiknen, M. Jalkanen et al., J Histochem. Cytochem., **43**, 125 (1995).
41. I. Hakansson, L. Hallgren, P. Venge, J. Clin. Invest., **66**, 298 (1980).
42. R. Mendes,.G. Silva, M. Lima, M. Callari, S. Almeida, et al., *Arch. Oral Biol*., **53**, 1156 (2008).
43. Y. Ishikawa, J. Komotori, M. Srnna, *Current Nanoscience*, **2**(3) 1 (2006).
44. M. Yoshikawa, N. Tsuji,T. Toda, H. Ohgushi, *Materials Science and Engineering C*., **27**(2) 220 (2007).
45. Y. Ishikawa, J. Komotori, M. Scenna, *Current Nanoscience*, **2**(3), 191 (2006).
46. S. Ahmadzadeh-Asl, S. Hesaraki, A. Zamaniam, *Adv. Appl. Ceramics*, **110**(6), 340 (2011).
47. J. Currey, Bones structure and mechanics, Princeton University press, Princeton, NJ, 2002.
48. T. Einhorn, *Clin. Orthop. Res*., **367**, 59 (1999).
49. A. Gusiyska, R Ilieva, *IJCR*, 7(1), 11564 (2015).
50. A. Gusiyska, PhD Thesis, Medical University, Sofia, 2012.
51. A. Gusiyska, *J. IMAB*, **20**(5), 601 (2014).
52. A. Gusiyska, *IJSR*, **3**(12), 2390 (2014).
53. J. Marchi, P. Greil, J. Bressiani, A. Bressiani, F. Muller, *Int. J. Appl. Ceram. Technol*., **6**(1), 60 (2009).
54. M. Tami, M. Nakamura, T. Isshiki, K. Nishio, H. Endoh, A.Nakahira, *J.Mater. Sci. Mater. Med*., **12**, 617–(2001).
55. D. Erchart, C. Drouet, H. Sfihi, C. Ray, C. Combes, in: Research advances, Kendall B. Jason (ed.), Nova Science Publishers, NY, 2007, p. 93.
56. R. Ilieva, E. Dyulgerova, O. Petrov, R. Aleksandrova, R. Titorenkova, Adv. Appl. Ceram., **112**(4), 219 (2012).
57. C. Qiu, X. Xiao, R. Liu, H. She, *Mater. Sci. Technol*, **24**, 612 (2008).
58. P. Shanthi, M. Ashok, T. Balasubramanian, A. Riyasdeen, M. Akbarsha, *Mater. Lett*., **63**, 2123 (2009).
59. J. Yao, W. Tjandra, Y. Chen, K. Tam, J. Ma J., B. Soh, *J. Mater. Chem*, **13**, 3053 (2003).
60. Y. Liu, W. Wang, Y. Zhan, C. Zheng, G. Wang, *Mater. Lett*., **56**, 496 (2002).
61. P. Shanthi, R. Mangalaraja, A. Uthirakumar, S. Velmathi, T. Balasubramanian, M. Ashok, *J. Colloid Interface Sci*., **350**, 39 (2010).
62. K. Suzuki, T. Anada, T. Miyazaki, N. Miyatake, Y. Honda, K. Kishimoto, M. Hosaka, H. Imaizumi, E. Itoi, O. Suzuki, *Acta. Biomater*., **10**, 531 (2014).
63. G. Glickman, A. Koch, *JADA*, **131**, 39 (2000).

ПОЛУЧАВАНЕ НА ХИДРОХИЛАПАТИТ/ХИАЛУРОНОВ БИОМИМЕТИЧЕН НАНОХИБРИДЕН МАТЕРИАЛ ЗА РЕКОНСТРУКЦИЯ НА КОСТНИ ДЕФЕКТИ С КРИТИЧЕН РАЗМЕР

Р. Илиева[1], Е. Дюлгерова[2], О. Петров[3]*, М. Тарасов[3],
А. Гусийска[2], Р. Василева[2]

[1] *Институт по обща и неорганична химия, Българска академия на науките,*
ул. Акад. Г. Бончев, блок 11, 1113 София, България
[2] *Факултет по дентална медицина, Медицински Университет, ул. Г. Софийски №1, 1431 София, България*
[3] *Институт по минералогия и кристалография, Българска академия на науките,*
ул. Акад. Г. Бончев, блок 107, 1113 София, България

(Резюме)

Синтерован бифазна калциевофосфатен материал е подложен на високоенергийно смилане в продължение на 40 часа за получаване на нанокристален хидроксилапатит. По време на смилането трикалциевият фосфат напълно се аморфизира. Прахов рентгенов анализ е използван за фазов контрол и определяне на размера на кристалитите. Морфоложките изследвания са направени със СЕМ и ТЕМ анализи, които показаха формирането на агломерати от гранули. Полученият материал беше допълнително млян с 1% хиалурон за времена 2, 5, и 10 часа, при което първоначалните агломерати бяха дезинтегрирани до формиране на добре хомогенизирани нанохидроксилапатитови частици в хибриден хидроксилапатит/хиалуронов материал, който беше използван за запълване на костни дефекти с критичен размер в случаите на апикални пародонтити. Тестовите клинични изследвания показаха добър лечебен процес.

The crystal structures of L-leucinium hydrogensquarate monohydrate and DL-leucinium hydrogensquarate

R. W. Seidel[1,#]*, S. Zareva[2]

[1] *Lehrstuhl für Analytische Chemie, Ruhr-Universität Bochum, Universitätsstr. 150, 44780 Bochum, Germany*
[2] *Sofia University "St. Kliment Ohridski", Faculty of Chemistry and Pharmacy,*
1 James Bourchier Blivd., 1164 Sofia, Bulgaria
[#] *Current address: Institut für Pharmazie, Martin-Luther-Universität Halle-Wittenberg,*
Wolfgang-Langenbeck-Str. 4, 06120 Halle (Saale), Germany

The crystal structures of L-leucinium hydrogensquarate monohydrate (**1**) and DL-leucinium hydrogensquarate (**2**) are reported. Compound **1** crystallizes in the monoclinic space group $P2_1$ with two formula units in the asymmetric unit ($Z = 4$, $Z' = 2$) and exhibits *pseudo* inversion symmetry. The crystal structure of **1** features two crystallographically distinct stacked hydrogen-bonded β-chains of hydrogensquarate ions interconnected by hydrogen-bonded water molecules, surrounded by hydrogen-bonded L-leucininium ions, resulting in an intricate O-H···O and N-H···O hydrogen-bonded layer structure. Compound **2** crystallizes in the monoclinic space group $P2/n$ with $Z = 4$. Similar to **1**, the hydrogensquarate anions form β-chains in the crystal structure. Two symmetry-related β-chains are stacked and interconnected by hydrogen-bonded DL-leucinium ions, likewise affording an intricate O-H···O and N-H···O hydrogen-bonded sheet structure.

Keywords: leucine, amino acid, squaric acid, hydrogen bonding, crystal structure, *pseudo* symmetry.

INTRODUCTION

Squaric acid, $H_2C_4O_4$ (Scheme 1), is a remarkably strong diprotic organic acid. A pK_{a1} value of 0.51 ± 0.02 was obtained by conductometric determination [1] and $pK_{a1} = 0.55 \pm 0.15$ and $pK_{a2} = 3.480 \pm 0.023$ (at 25 °C) were determined by potentiometric titration [2]. Based on earlier studies, $pK_{a1} = 1.2–1.7$ was reported in a review article by Gilli *et al.* [3]. In any case, the strong acidity has been attributed to resonance stabilization of the corresponding anions, *i. e.* hydrogensquarate, $HC_4O_4^-$ (Scheme 1), and squarate, $C_4O_4^{2-}$ [4].

Since the 1990s, squaric acid anions have frequently been used as counterions for protonated organic bases in molecular salt crystals. A wide variety of such proton-transfer compounds can be found in the Cambridge Structural Database [5]. An early account of the crystal chemistry of squaric acid anions was given by Gilli *et al.* [3]. These authors ascribed the interest in these anions for crystal engineering to the following factors: first, the fact that donating and accepting hydrogen bonds are confined to the molecular plane; second, the strength of the O-H···O hydrogen bonds that hydrogensquarate ions can form to one another; third, the ability of squaric acid to readily transfer a proton to an aromatic base, which in turn forms a charge-assisted N-H···O hydrogen bond to the anion. Three modes of association of hydrogensquarate ions *via* O-H···O hydrogen bonds frequently encountered in the solid-state, *viz.* 1,2-dimers (α-dimers), 1,2-chains (α-chains) and 1,3-chains (β-chains) [3], are illustrated in Scheme 1.

Research into solid-state supramolecular chemistry of proton-transfer compounds of squaric acid and α-amino acids is driven by the general chemical and biological interest in α-amino acids and by the possibility to synthesize non-centrosymmetric crystals from enantiopure chiral α-amino acids. Noncentrosymmetry in the crystals is a requirement for desired non-linear optical properties of these materials. Kolev *et al.* [6–16] and others [17–19] have reported on the structures and properties of a variety of salts of squaric acid and α-amino acids and derivatives. Very recently, Yadav *et al.* reported a study on optical, piezoelectric, dielectric and mechanical properties of L-asparaginium hydrogen squarate hemihydrate crystals [20], which were first synthesized and structurally characterized by Kolev *et al.*

---

squaric acid hydrogensquarate

1,2-dimer (α–dimer) 1,2-chain (α–chain)

1,3-chain (β–chain)
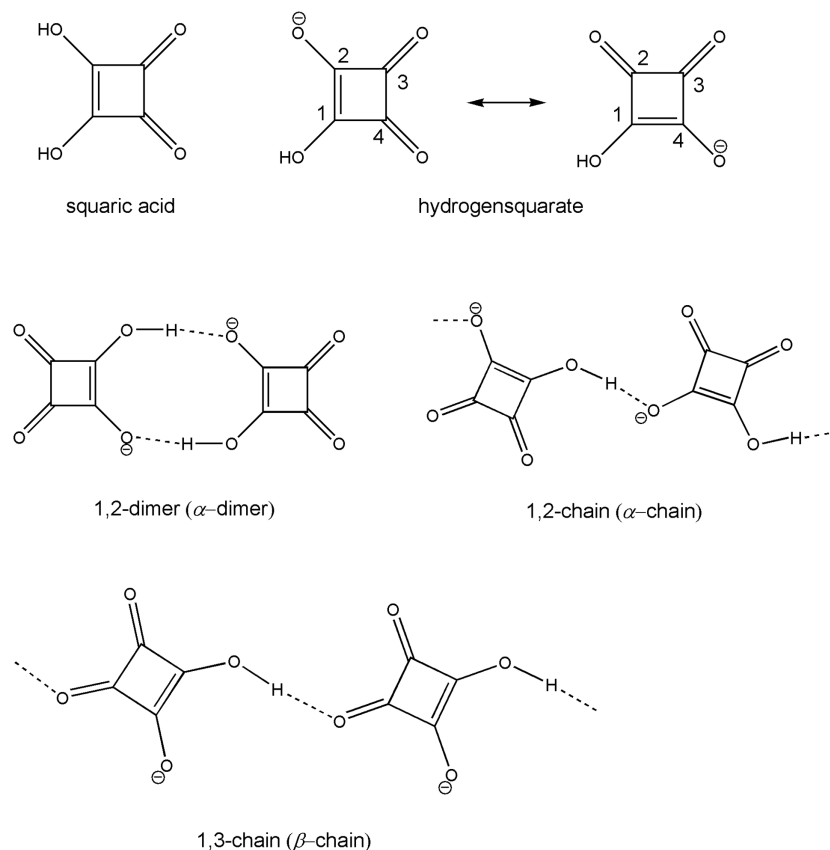
Scheme 1. Chemical diagrams of squaric acid, hydrogensquarate resonance structures and some common hydrogen-bonded associations of hydrogensquarate [3].

[8]. Motivated by these results, we herein report the syntheses and crystal structures of L-leucinium hydrogensquarate monohydrate (**1**) and DL-leucinium hydrogensquarate (**2**). Chemical diagrams of the D- and L-form of the amino acid leucine are depicted in Scheme 2.
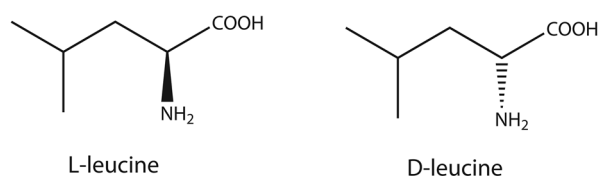
L-leucine D-leucine

Scheme 2. Chemical diagrams of L-leucine and D-leucine.

EXPERIMENTAL SECTION

Preparation of 1 and 2

224 mg (2 mmol) of squaric acid were dissolved in 30 mL of deionised water at 70 °C by continuous stirring for six hours. When the solution became clear, 262 mg (2 mmol) of L-leucine or DL-leucine were added for the preparation of **1** and **2**, respectively. Stirring was continued for three hours without heating. Subsequently, the product was filtered off and purified by multifold recrystallization from deionised water.

Single-crystal X-ray analysis

The X-ray intensity data for **1** were collected on a Siemens P4 four-circle diffractometer with a scintillation detector, using graphite-monochromated Mo-K$_a$ radiation from a fine focus sealed X-ray tube. Unit cell parameters were determined by least-squares fit to the θ values of 15 automatically centred reflections ($7.5° < \theta < 15.0°$). The intensity data were collected in the ω scan mode. The data were corrected for Lorentz and polarisation effects. An absorption correction based on ψ scans was carried out [21]. The diffraction data for **2** were collected on a Bruker SMART X2S diffractometer, using Mo-K$_\alpha$ radiation from a XOS X-beam microfocus X-ray source with a doubly curved silicon crystal monochromator. The data were processed with CrysAlisPro [22]. An absorption correction based

on multiple-scanned reflections [23] was carried out with ABSPACK in CrysAlisPro.

The crystal structures were solved by direct methods using SHELXS-97 [24] and refined by full-matrix least-squares refinement on F^2 using SHELXL-2018/3 [25]. The absolute structure of **1** was deduced from the known absolute configuration of the L-leucine starting material used for the synthesis. Anisotropic displacement parameters were introduced for all non-hydrogen atoms. Hydrogen atoms except for water molecules were placed at geometrically calculated positions and refined with the appropriate riding model. The positions of water hydrogen atoms were located *via* difference Fourier syntheses and subsequently refined with O-H distances restrained to target values of 0.82(2) Å. Crystal data and refinement details for **1** and **2** are given in Table 1. Representations of the crystal and molecular structures were drawn with DIAMOND [26]. Crystal data and refinement details are listed in Table 1.

CCDC 1433510 (**1**) and 1831823 (**2**) contain the supplementary crystallographic data for this paper. The data can be obtained free of charge from the Cambridge Crystallographic Data Centre *via* www.ccdc.cam.ac.uk/getstructures.

RESULTS AND DISCUSSION

Reaction of enantiopure L-leucine with an equimolar amount of squaric acid in aqueous solution afforded the crystalline monohydrate **1**, whereas treatment of racemic DL-leucine with squaric acid under the same reaction conditions yielded crystalline anhydrous **2**. Compound **1** crystallizes in the Sohncke space group $P2_1$. Figure 1 depicts the asymmetric unit of **1**, which comprises two L-leucinium ions, two hydrogensquarate ions and two water molecules, *i. e.* two formula units ($Z' = 2$). The two crystallographically unique hydrogensquarate ions are related by *pseudo* inversion symmetry. The ADDSYM routine in PLATON [27] calculates that the *pseudo* inversion symmetry expands to 94 % of the entire structure (*pseudo* space group $P2_1/n$). The *pseudo* symmetry encountered here is not a simple disorder, because the $h0l$: $h + l = 2n + 1$ reflections are not absent and the crystal structure

Table 1. Crystal data and refinement details for **1** and **2**

|	1	2
Empirical formula	$C_{10}H_{17}NO_7$	$C_{10}H_{15}NO_6$
M_r	263.24	245.23
λ (Å)	0.71073	0.71073
Crystal size (mm³)	$0.23 \times 0.13 \times 0.11$	$0.54 \times 0.30 \times 0.25$
Crystal system	Monoclinic	Monoclinic
Space group	$P2_1$	$P2/n$
T (K)	294(2)	300(2)
a (Å)	14.2880(17)	13.4301(19)
b (Å)	6.119(2)	6.0440(6)
c (Å)	15.0909(18)	14.9714(19)
β (°)	95.433(10)	92.189(12)
V (Å³)	1313.5(6)	1214.3(3)
Z	4	4
ρ_{calc} (g cm⁻³)	1.331	1.341
μ (mm⁻¹)	0.114	0.112
$F(000)$	560	520
θ range (°)	2.063–24.991	2.000–25.053
Reflections collected / unique	3351 / 2977	6853 / 2141
R_{int}	0.0201	0.0394
Observed reflections [$I > 2\sigma(I)$]	2583	1714
Goodness-of-fit on F^2	1.024	1.112
Parameters / restraints	338 / 4	159 / 0
$R1$ [$I > 2\sigma(I)$]	0.0417	0.0712
$wR2$ (all data)	0.1160	0.1527
Residuals (eÅ⁻³)	0.295 / –0.271	0.412 / –0.223
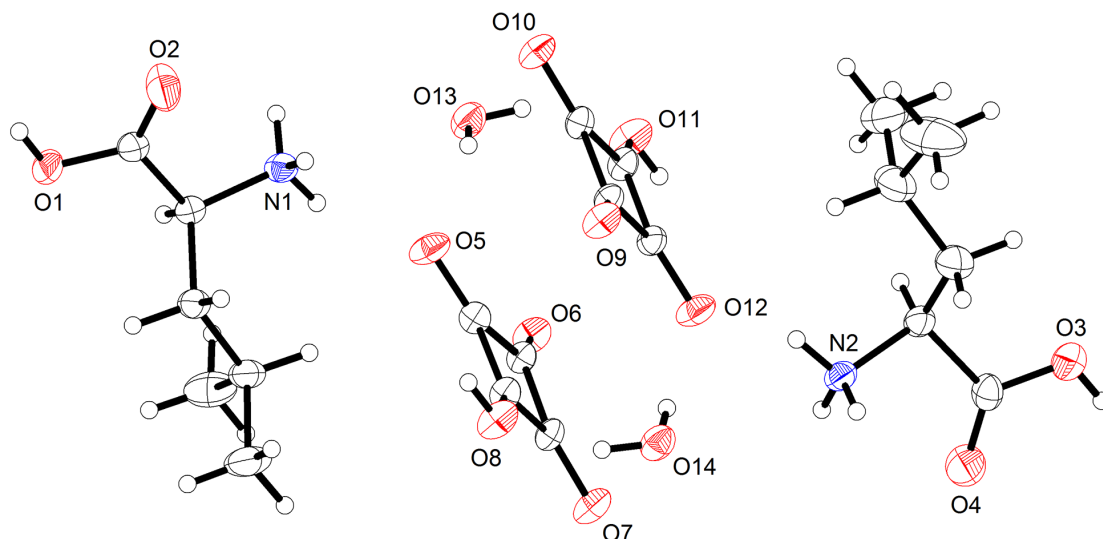
Fig. 1. Asymmetric unit of **1**. Displacement ellipsoids are drawn at the 30% probability level. Hydrogen atoms are represented by small spheres of arbitrary radii.

could be refined satisfactorily in the space group $P2_1$ with a non-disordered model. For some recent examples of *pseudo* symmetric crystal structures in the literature, see, for instance, references [28, 29]. In contrast to **1**, the asymmetric unit of **2** comprises only one formula unit (Fig. 2). Compound **2** crystallizes in the centrosymmetric space group $P2/n$.

In the crystal structure of **1**, the hydrogensquarate ions are joined by O-H···O hydrogen bonds, resulting in two crystallographically distinct β-chains extending by translational symmetry in the *b* axis direction (Fig. 3). The O-H···O distances within the β-chains are 2.571(4) and 2.57(4) Å, indicating strong hydrogen bonds. As aforementioned, the
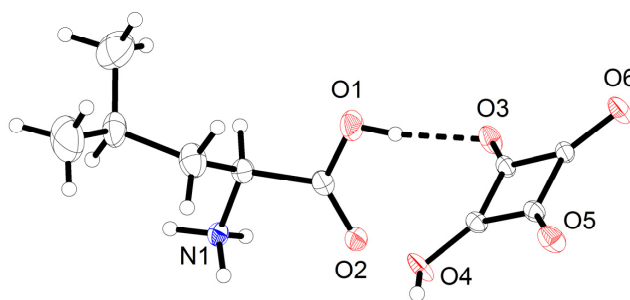
Fig. 2. Asymmetric unit of **2**. Displacement ellipsoids are drawn at the 30% probability level. Hydrogen atoms are represented by small spheres of arbitrary radii. The dashed line represents a hydrogen bond.
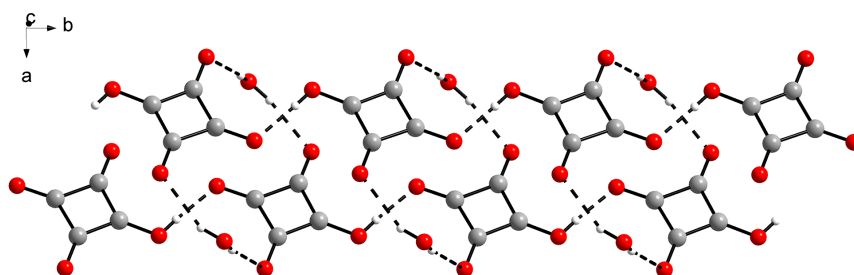
Fig. 3. View of the two crystallographically distinct oppositely extending stacked β-chains of hydrogensquarate ions in **1**, interconnected by water molecules, approximately along the *c* axis direction. Hydrogen bonds are represented by dashed lines.

hydrogensquarate ions in the distinct oppositely extending chains are related by *pseudo* inversion symmetry. The stacking distance between the chains is approximately 3.3 Å with respect to the mean planes. The water molecules interconnect the two *β*-chains *via* O-H⋯O hydrogen bonds with an average hydrogen bond distance of 2.85 Å. The hydrogen-bonded strands of hydrogensquarate *β*-chains and water molecules are laterally linked by the L-leucinium ions *via* the carboxy and the protonated amino group. The carboxy groups form hydrogen bonds to hydrogensquarate oxygen atoms with distances of 2.610(4) and 2.618(4) Å. The average N-H⋯O hydrogen bond distance is 2.89 Å. In the crystal, an intricate two-dimensional hydrogen bond network parallel to (10$\bar{1}$) results (Fig. 4). A comprehensive listing of the hydrogen bond parameters in **1** can be found in the supporting crystallographic data.

As shown in Figure 5, the crystal structure of **2** likewise features hydrogen-bonded *β*-chains of hydrogensquarate ions extending by translational symmetry in the *b* axis direction. The O-H⋯O

hydrogen bond distance is 2.592(3) Å. In contrast to **1**, however, the stacked *β*-chains in **2** do not extend oppositely but in the same direction. The two *β*-chains forming a stack are symmetry-related by a crystallographic twofold rotation axis, as also observed in the crystal structure of L-asparaginium hydrogen squarate hemihydrate [8, 20]. The stacking distance, *i. e.* the distance between the mean planes through the hydrogensquarate four-membered rings, is 3.21 Å and similar to that observed in **1**. It has been pointed out that *β*-chains of hydrogensquarate ions are strongly hydrophilic and therefore usually surrounded by water molecules in the crystal [3], as observed in **1**. Therefore, it is interesting to note that the structure of **2** is solvent-free, *i. e.* anhydrous, and the *β*-chains are exclusively surrounded by carboxy and protonated amino groups of the DL-leucinium ions, although **2** crystallized from water under the same conditions as **1**. The DL-leucinium ions link the stacks of *β*-chains into a two-dimensional hydrogen bond network parallel to (101) in the crystal (Fig. 6). The O-H⋯O
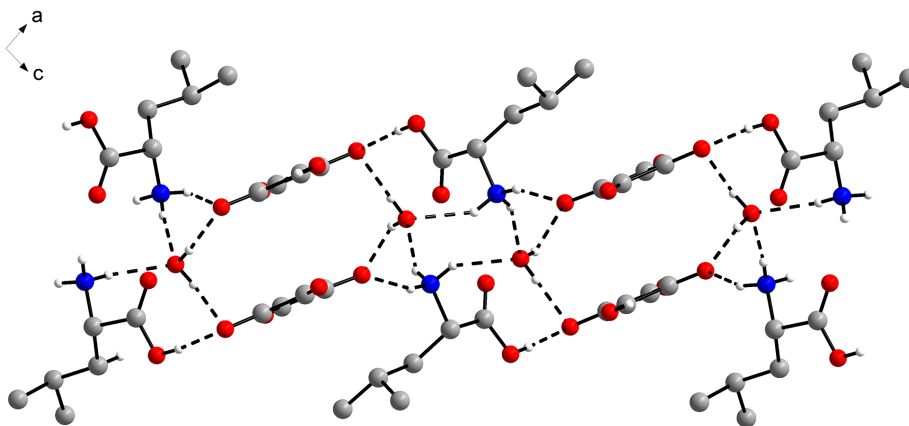

Fig. 4. O-H⋯O and N-H⋯O hydrogen-bonded sheet structure of L-leucinium ions, hydrogensquarate ions and water molecules in **1**, viewed along the *b* axis direction (along the *β*-chains). Hydrogen bonds are represented by dashed lines. Carbon-bound hydrogen atoms are omitted for clarity.
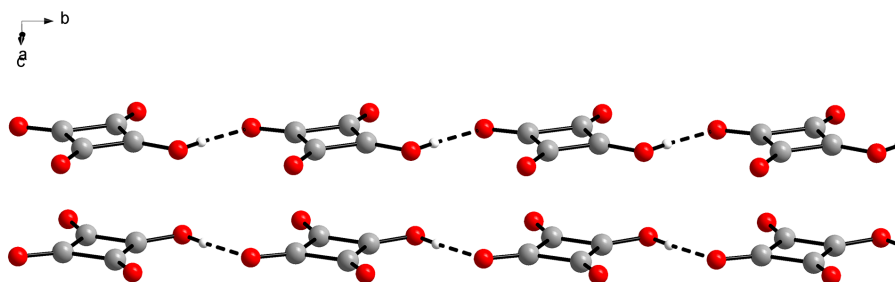

Fig. 5. View of two symmetry-related stacked *β*-chains of hydrogensquarate ions in **2**, extending in the same direction. Hydrogen bonds are represented by dashed lines.
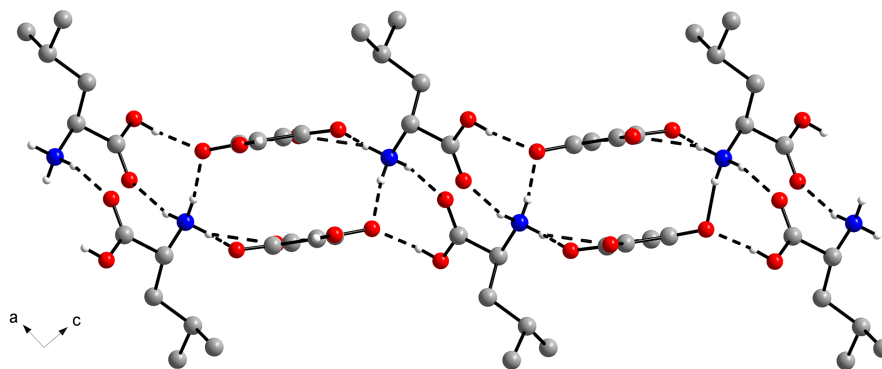
Fig. 6. O-H⋯O and N-H⋯O hydrogen-bonded sheet structure of DL-leucinium ions, hydrogensquarate ions in **2**, viewed along the *b* axis direction (along the *β*-chains). Hydrogen bonds are represented by dashed lines. Carbon-bound hydrogen atoms are omitted for clarity.

hydrogen bond distance involving the carboxy group is 2.592(3) Å. The protonated amino group forms a hydrogen bond to a carboxy oxygen atom of a neighbouring molecule [N-H⋯O: 2.840(3) Å] and another to a hydrogensquarate oxygen atom [N-H⋯O: 2.882(3) Å] and a donating bifurcated hydrogen bond to two hydrogensquarate oxygen atoms with an average N-H⋯O hydrogen bond distance of 2.96 Å. In contrast to **1**, there is structural evidence for a weak hydrogen bond between the α-CH group of the leucinium ion and a hydrogensquarate oxygen atom [C-H⋯O: 3.546(4), <CHO: 157.5°]. A comprehensive listing of the hydrogen bond parameters in **2** can be found in the supporting crystallographic data.

A survey of the Cambridge Structural Database [5] (CSD; version 5.39 with February 2018 updates) yielded a number of structurally characterized salts consisting of protonated α-amino acids and hydrogensquarate counterions. Similar to **2**, DL-serinium hydrogensquarate (CSD refcode: BUTBOJ) crystallizes solvent-free from a methanol/water mixture [16], but, in contrast to **2**, the hydrogensquarate ions form α-chains in the crystal. Topologically, the hydrogensquarate ions also form α-chains in the solvent-free structure of L-serinium hydrogensquarate (CSD refcode: PAZCUO) [8], but the flat hydrogensquarate ions are twisted to one another. α-Chains are also found in the monohydrate structure of the hydrogensquarate of (*R*)-1-phenylglycine (CSD refcode: TEHYUA) [7], a non-natural α-amino acid. The aforementioned L-asparaginium hydrogen squarate hemihydrate crystallizes from aqueous solution (CSD refcodes: NUIFUY and NUYFUI01) [8, 20] and features *β*-chains of hydrogensquarate ions in the crystal, similar to those in **2** but also surrounded by water molecules. *β*-Chains are also encountered in L-alaninium amide hydrogensquar-

ate monohydrate (CSD refcode: PAZFUS) [11] and L-prolinamidium hydrogensquarate (CSD refcode: TECMUK) [12]. The crystal structures of solvent-free L-argininium hydrogensquarate (CSD refcode: TIDCAK) [6] and L-argininamidium bis(hydrogen square) (CSD refcode: WEJCEU) [13] and show α-dimers of the hydrogensquarate ions. In the crystal structure of histidinium hydrogensquarate (CSD refcode: TIWXAY) [17], L-lysinium hydrogensquarate monohydrate (CSD refcode: CONVAD) [15] and the hydrogensquarate of the α-amino acid derivative L-leucineamide (CSD refcode: YUKFUG) [14], isolated hydrogensquarate ions surrounded by the respective cations are observed. Interestingly, in the hemihydrate structure of the hydrogensquarate of the non-proteinogenic α-amino acid L-canavanine (CSD refcode: HIVSUA) [10], the hydrogensquarate are 1,2- and 1,3-connected through O-H⋯O hydrogen bonds in an alternating fashion, resulting in a zigzag chain.

CONCLUSIONS

We have synthesized and structurally characterized hydrogensquarates of enantiopure L-leucine and racemic DL-leucine. The former, compound **1**, is a monohydrate and the latter, compound **2**, is solvent-free. The present study expands the series of structurally characterized squaric acid salts of the proteinogenic amino acids. As required by the enantiopure chiral L-leucinium ion, **1** crystallizes in a Sohncke space group. The entire crystal structure, however, fits 94% with *pseudo* centrosymmetry. In both **1** and **2**, the hydrogensquarate ions exhibit a 1,3-chain (*β*-chain) hydrogen bonding pattern. It is expected that the present study sparks future research into the properties of the compounds studied

and further investigations on the solid-state supramolecular chemistry of squaric acid salts of amino acids in general.

REFERENCES

1. R. I. Gelb, *Anal. Chem.*, **43**, 1110 (1971).
2. L. M. Schwartz, L. O Howard, *J. Phys. Chem.*, **74**, 4374 (1970).
3. G. Gilli, V. Bertolasi, P. Gilli, V. Ferretti, *Acta Cryst.*, **B57**, 859 (2001).
4. R. West, D. L. Powell, *J. Am. Chem. Soc.*, **85**, 2577 (1963).
5. C. R. Groom, I. J. Bruno, M. P. Lightfoot, S. C. Ward, *Acta Cryst.*, **B72**, 171 (2016).
6. O. Angelova, V. Velikova, T. Kolev, V. Radomirska, *Acta Cryst.*, **C52**, 3252 (1996).
7. O. Angelova, R. Petrova, V. Radomirska, T. Kolev, *Acta Cryst.*, **C52**, 2218 (1996).
8. T. Kolev, R. Stahl, H. Preut, L. Koniczek, P. Bleckmann, V. Radomirska, *Z. Kristallogr. – New Cryst. Struct.*, **213**, 167 (1998).
9. T. Kolev, R. Stahl, H. Preut, P. Bleckmann, V. Radomirska, *Z. Kristallogr. – New Cryst. Struct.*, **213**, 169 (1998).
10. T. Kolev, Z. Glavcheva, R. Stahl, H. Preut, P. Bleckmann, V. Radomirska, *Z. Kristallogr. – New Cryst. Struct.*, **214 (**1999).
11. T. Kolev, M. Spiteller, W. S. Sheldrick, H. Mayer-Figge, *Acta Cryst.*, **E61**, o4292 (2005).
12. T. Kolev, D. Yancheva, M. Spiteller, W. S. Sheldrick, H. Mayer-Figge, *Acta Cryst.*, **E62**, o463 (2006).
13. T. Kolev, M. Spiteller, W. S. Sheldrick, H. Mayer-Figge, *Acta Cryst.*, **C62**, o299 (2006).
14. T. Kolev, S. Zareva, H. Mayer-Figge, M. Spiteller, W. S. Sheldrick, B. B. Koleva, *Amino Acids*, **37**, 693 (2009).
15. T. Kolev, H. Mayer-Figge, R. W. Seidel, W. S. Sheldrick, M. Spiteller, B. B. Koleva, *J. Mol. Struct.*, **919**, 246 (2009).
16. T. Kolev, T. Pajpanova, T. Dzimbova, S. Zareva, M. Spiteller, *J. Mol. Struct.*, **1102**, 235 (2015).
17. I. L. Karle, D. Ranganathan, V. Haridas, *J. Am. Chem. Soc.*, **118**, 7128 (1996).
18. M. Aniola, Z. Dega-Szafran, A. Katrusiak, M. Szafran, *New J. Chem.*, **38**, 3556 (2014).
19. N. Tyagi, N. Sinha, H. Yadav, B. Kumar, *RSC Adv.*, **6**, 24565 (2016).
20. H. Yadav, N. Sinha, S. Goel, B. Singh, I. Bdikin, A. Saini, K. Gopalaiah, B. Kumar, *Acta Cryst.*, **B73**, 347 (2017).
21. A. C. T. North, D. C. Phillips, F. S. Mathews, *Acta Cryst.*, **A24**, 351 (1968).
22. CrysAlisPRO, Rigaku Oxford Diffraction, Yarnton, Oxfordshire, England (2016).
23. R. H. Blessing, *Acta Cryst.*, **A51**, 33 (1995).
24. G. M. Sheldrick, *Acta Cryst.*, **A64**, 112 (2008).
25. G. M. Sheldrick, *Acta Cryst.*, **C71**, 3 (2015).
26. K. Brandenburg, DIAMOND, Crystal Impact GbR, Bonn, Germany (2012).
27. A. L. Spek, *Acta Cryst.*, **D65**, 148 (2009).
28. G. J. Reiss, *Z.Kristallogr. – New Cryst. Struct.*, **228**, 431 (2013).
29. Z. Hong, Y.-L. Zhan, D.-R. Yu, Y. Li, W.-J. Yuan, H.-Y. Zhang, *Z. Kristallogr. – New Cryst. Struct.*, **232**, 893 (2017).

КРИСТАЛНИ СТРУКТУРИ НА L-ЛЕВЦИНИЕВ ХИДРОГЕНСКВАРАТ МОНОХИДРАТ И DL-ЛЕВЦИНИЕВ ХИДРОГЕНСКВАРАТ

Р. В. Зайдел[1,#]*, С. Й. Зарева[2]

[1] *Катедра „Аналитична химия“, Рурски университет, Бохум, ул. „Университетска“ 150, 44780 Бохум, Германия*
[#] *Настоящ адрес: Институт по Фармация, Университет „Мартин Лутер“–Хале-Витенберг, ул. „Волфганг Лангенбек“ 4, 06120 Хале, Германия*
[2] *Софийски университет „Св. Климент Охридски“, Факултет по химия и фармация, бул. „Дж. Баучер“ 1, 1164 София, България*

(Резюме)

Представени са кристалните структури на L-левциниев хидрогенскварат монохидрат (**1**) и DL-левциниев хидрогенскварат (**2**). Съединение **1** кристализира в моноклинна пространствена група $P2_1$ като асиметричната единица се състои от два левциниеви катиона и два хидрогенскваратни аниона ($Z = 4$, Z' = 2) и показва псевдоинверсионна симетрия. Кристалната структура на **1** се характеризира с две кристалографски различно подредени β-вериги от хидрогенскваратни йони, свързани с водни молекули чрез водородни връзки, обградени от свързани с водородни връзки L-левциниеви йони, което води до образуването на слоеста структура със сложни O–H⋯O и N–H⋯O водородни връзки. Съединение **2** кристализира в моноклинна пространствена група $P2/n$ със $Z = 4$. Подобно на **1**, хидрогенскваратните аниони образуват β-вериги в кристалната структура. β-веригите са свързани с водородни връзки с DL-левциниевия йон, като по този начин се получава сложна структура от слоеве, свързани с O–H⋯O и N–H⋯O водородни връзки.

Structural peculiarities of natural chabazite modified by ZnCl$_2$ and NiCl$_2$

L. T. Dimowa[1], I. Piroeva[2], S. Atanasova-Vladimirova[2], R. Rusew[1], B. L. Shivachev[1]*

[1] *Institute of Mineralogy and Crystallography, Bulgarian Academy of Sciences,*
"Acad. Georgi Bonchev" str., building 107, 1113 Sofia, Bulgaria
[2] *Academician Rostislav Kaishev Institute of Physical Chemistry, "Acad. Georgi Bonchev" str.,*
building 11, 1113 Sofia, Bulgaria

Chabazite single crystals were modified to NH_4^+, Zn^{2+} and Ni^{2+} chabazite forms and characterized by EDS/SEM, DTA/TG, FTIR and single crystal X-ray diffraction. The modification procedure includes successive conversion of the starting natural chabazite $(Na_{0.37}Ca_{1.56})Al_{3.63}Si_{8.36}O_{24}.xH_2O)$ into its ammonium form (NH4-CHA) where after the NH4-CHA form is converted to either zinc or nickel forms by ion-exchange with 1M $ZnCl_2$ and $NiCl_2$ water solutions at 100 °C. The EDS, FTIR and structural studies revealed remains of ammonium cations in Zn and Ni exchanged forms. The structural analyses disclosed that the water molecules present within the CHA framework tend to occupy sites that are usually related with nearby cation(s) sites. As the cation amounts required for the framework charge compensation is limited the water molecules amounts are also adjusting to this detail. The distribution of the water molecules in the 8-membered ring is of radial type.

Keywords: chabazite, microporous, single crystal, ion exchange.

INTRODUCTION

Crystalline open-framework materials such as aluminosilicate zeolites belong to a family of microporous materials that are attractive due to their rich structural chemistry and their various usage: as catalysts, in gas separation, ion exchange, low-*k* dielectric (thin film) materials, for H$_2$ and CO$_2$ gas storage [1–9]. Nowadays, in order to accommodate the industrial demand and increased technological requirements, the performed investigations target to improve the properties of existing crystalline open-framework materials and to discover new ones exhibiting better structure-property characteristics. This is achieved through modifications of currently available microporous materials and by the targeted design and synthesis of new ones [10–13]. The properties of "porous" materials are usually associated with their pore size, channel systems, thermal, mechanical and chemical stability. In the case of alumo-, titano-, zircono- and "other-" silicate zeolites used as catalysts, their catalytic activity is also related to the number and type of acid centers present in the structure [8, 14–16]. The efficiency of zeolites in catalytic reactions, gas separation, sorption, etc. applications can be better understood if in-depth knowledge of the structural features of existing materials is available. Therefore the investigations mainly target the pore size dimensions, the channel shape and size, the connectivity of the building blocks and the modification of the framework chemical composition [17, 18]. The detailed knowledge of structural features of existing materials is also critical for the design and synthesis of new ones. [19, 20]. However, in-depth structural characterization is a challenging task, because sufficiently bigger single crystals are difficult to grow. The synthesis of microporous materials usually produces microcrystalline powders, the characterization techniques are limited to powder diffraction, chemical analyses and spectroscopic methods. Moreover, typical optimization for industrial applications includes the maximization of the specific surface and/or volume of the samples through lowering the crystallite size e.g. going in the "nano" scale [13, 21, 22]. Thus most single crystal studies are performed on naturally grown samples. Chabazite is a natural microporous aluminosilicate with common formula $(M^{(I),(II)})_2Al_4Si_8O_{24}.nH_2O$ [23] where M = Na, K, Ag, Cs, Ca, Sr, Ba, Cd, Mn, Co, and Cu are the

* To whom all correspondence should be sent:
blshivachev@gmail.com

framework charge compensating cations. Natural chabazite(s) shows considerable variation in Si/Al ratio [24, 25]. Based on the dominant non-framework cation (natural) chabazite is usually referred as Ca-CHA, K-CHA, Na-CHA, Sr-CHA. The CHA structure consists of six-membered double rings (D6R) which are connected with tilted four-membered rings (4MR). As a result 8-membered twisted rings (8MR) with diameters of ~3.9 Å can be detected. The three-dimensional arrangement of the D6R (e.g. hexagonal prisms), 4MR and 8MR produces a $[4^{12}6^88^6]$ cavity 11.0 x 6.6 x 6.6 Å^3 in size, opened in all directions through the 8MR. Thus a three-dimensional system of channels is observed Fig. 1.
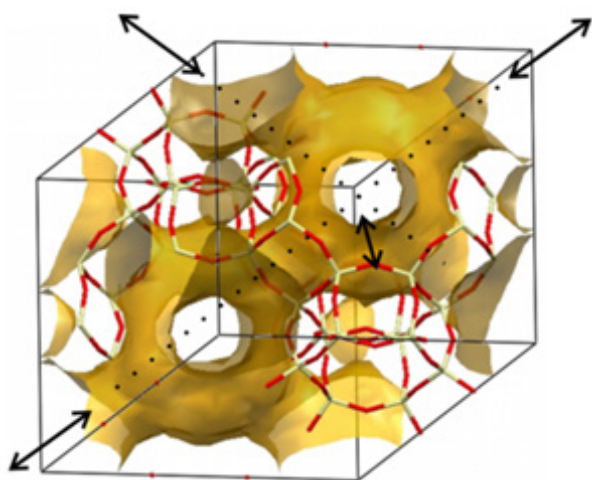
Fig. 1. Observation of the CHA framework surface (contoured with probe diameter of 2.4 Å) leading to the appearance of 3D channel system.

The large size of the CHA $[4^{12}6^88^6]$ cavity promotes the high sorption specificity for large cations such as alkali and alkaline Cs$^+$, K$^+$, Sr^{2+} [26]. CHA specific chemical and structural features (high specific surface and volume, thermal stability above 450 °C, simultaneous existence of small and large pores, voids and cavities, presence of acidic centers) makes it a material with likely application for bulk gas adsorption, gas separation, heavy oil cracking etc. Unfortunately, industrial scale deposits of chabazite are relatively rare and mostly unexploited (e.g. Bowie, Arizona, US; Gads Hill, Tasmania, AU). The natural chabazite deposits feature impurities e.g. parasite crystal phases, amorphous content etc. On the other hand, CHA with industrial quality (higher than 90%) can be easily produced from chabazite ore by combining gravity concentration, magnetic separation, semi-synthetic caustic digestion [27] or alternatively from commercial HY or

K/NaY by "zeolite to zeolite conversion" [16, 20, 28] e.g. adjusting the Si/Al ratio using highly basic solutions (1–3M KOH) and additional amounts of SiO₂. The synthesis of CHA usually yields micro size crystals and thus hampers the detailed structural investigations. In this work we present structural studies of natural chabazite single crystals exchanged with ammonium, zinc and nickel cations.

EXPERIMENTAL

Materials

The starting material is a natural light gray chabazite (CHA) consisting of tightly packed single crystals with indeterminate habitus. The ion exchange was conducted in Teflon autoclaves using double distilled water (ddH₂O). For the preparation of exchange solutions the following Sigma-Aldrich reagents were used: NH₄Cl (A9434), ZnCl₂ (208086) and NiCl₂ x H₂O (364304).

Cation exchange

Initially natural chabazite was converted into ammonium form (NH4-CHA) by ion exchange with 1M NH₄Cl solution. Typically ~15 mg of CHA single crystals were added to 5 ml of 1M NH₄Cl and the mixture was heated to 90 °C with orbital shaking (40 rpm). After 40 hours the NH₄Cl solution was removed and replaced with fresh 1M NH₄Cl. This procedure (supplying fresh 1M NH₄Cl) was performed two times producing a total exchange time of 120 h (5 days). Finally, the NH₄Cl solution was discarded and the NH4-CHA was washed several times with ddH₂O. The resulting NH4-CHA was allowed to dry at room temperature for at least 24 hours. The zinc and nickel forms of chabazite were prepared starting from NH4-CHA by ion exchange with 1M ZnCl₂ and 1M NiCl₂ solutions at 100 °C for a total exchange time of 168 hours and using a similar procedure as for NH4-CHA (every 56 hours the 1M ZnCl₂ or 1M NiCl₂ solution were substituted with fresh ones).

Scanning electron microscopy

Scanning electron microscopy (SEM) microanalyses of the samples were performed on a JEOL JSM 6390 electron microscope (Japan) in conjunction with energy dispersive X-ray spectroscopy (EDS) Oxford INCA Energy 350, equipped with ultrahigh resolution scanning system (ASID-3D) in regimes of secondary electron image (SEI). The accelerating voltage was 15 kV, I ~65 nA, the pressure was of the order of 10^{-4} Pa. The single crys-

tals were directly placed on an adhesive carbon tape (Agarscientific) and coated with Au for 30 sec.

The DTA/TG data were obtained on a Setaram Setsys equipment. The experiment was carried out by placing approximately 2–3 mg of the CHA samples into a corundum crucible with heating of 10 °C min⁻¹ from ambient temperature to 800 °C and under flowing argon gas (20 ml min⁻¹). Baseline curves, measured under the same experimental conditions were acquired to account for buoyancy effects. The peak fitting of the DTA data was performed with a Gaussian type of function using Fityk [29].

The FTIR spectra of the chabazite samples (KBr pellets) were recorded in the transmission mode at room temperature using a TENSOR 37 Bruker spectrometer in the 400–4000 cm⁻¹ range. Before spectra collection the CHA samples were dried and crushed (grounded). The pellets were prepared using 50 mg KBr and 0.5 to 1 mg of (NH4, Zn, Ni)-CHA.

Single Crystal X-ray

Crystals of ammonium, zinc and nickel exchanged chabazite suitable for X-ray analyses were mounted on a glass capillary and all diffraction data were recorded from those crystals. Diffraction data were collected at room temperature by ω-scan technique, on an Agilent Diffraction SuperNovaDual four-circle diffractometer equipped with Atlas CCD detector using mirror-monochromatized Mo$K\alpha$ ($\lambda = 0.7107$ Å) radiation from micro-focus source. The determination of cell parameters, data integration scaling and absorption correction were carried out using the CrysAlisPro program package [30]. The structures were solved by direct methods [31] and refined by full-matrix least-square procedures on F^2 [31]. The natural and exchanged chabazite crystals were isotypical, space group R$\bar{3}$m (No 166) with one molecule per asymmetric unit. A summary of the main fundamental crystal and refinement data is provided in Table 1.

Table 1. Important crystallographic and refinement details for ammonium, zinc and nickel exchanged chabazite

	NH4-CHA	Ni-CHA	Zn-CHA
Molecular weight	2784.84	2743.21	3056.50
Crystal system	Trigonal	Trigonal	Trigonal
Space group	R$\bar{3}$m	R$\bar{3}$m	R$\bar{3}$m
T(K)	290	290	290
Radiation, wavelength (Å)	Mo Kα, 0.71073	Mo Kα, 0.71073	Mo Kα, 0.71073
a (Å)	13.8520(3)	13.7972(5)	13.8485(7)
b (Å)	13.8520(3)	13.7972(5)	13.8485(7)
c (Å)	14.9061(3)	14.8847(7)	14.8504(8)
V(Å³)	2476.96(9)	2453.88(17)	2466.5(2)
α (°)	90	90	90
β (°)	90	90	90
γ (°)	120	120	120
Z	1	1	1
F_{000}	1409.4	1498	1510
d (mg. m⁻³)	1.867	1.856	2.058
μ (mm⁻¹)	0.554	1.340	1.590
Cell parameters	from 4113 reflections	from 4030 reflections	from 2508 reflections
Crystal habit, color	prism, colorless	prism, colorless	prism, colorless
Crystal size (mm³)	0.30×0.28×0.27	0.30×0.28×0.27	0.29×0.26×0.23
Radiation source	SuperNova (Mo) X-ray	SuperNova (Mo) X-ray	SuperNova (Mo) X-ray
Monochromator	mirror	mirror	mirror
Data collection	ω scans	ω scans	ω scans
Reflections collected/I>2σ (I)	7385/1373	8111/1300	5710/1217
Parameters	55	61	68
$R1$ ($F^2 > 2\sigma$ (F^2))	0.037	0.052	0.049
$wR2$ (all data)	0.110	0.172	0.150
Extinction correction	none	none	none
$\Delta\rho_{max}/ \Delta\rho_{min}$ (e Å⁻³)	0.71/–0.70	1.38/–0.82	0.79/–0.61

DISCUSSION

The most employed and important technique used to modify zeolites is ion exchange. Ion-exchange properties of natural chabazite(s) have been well studied [9, 32, 33]. Normally the ion exchange process is not as lengthy but the use of single crystals, with limited exchange surface and almost certainly having crystal defects, hampering the ion exchange, implies longer exchange times and higher cation concentrations. As the 1M ZnCl₂ and NiCl₂ solutions have acidic character (pH around 4.7 at room temperature) the extension of the ion exchange period cannot be prolonged indeterminably due to the expected structural damage and eventual destruction of the CHA framework. The SEM images of the samples (Fig. 2) do not show noticeable degradation on the surface. This observation is further supported by conducted standardless EDS chemical composition analyses showing a persistent Si/Al molar ratio on a randomly nominated points on the surface of the samples (Table 2). This result is important from practical point of view, because it

shows that no significant variation of the chabazite Si/Al framework is produced during the 7 days modification with acidic solutions of ZnCl₂ and NiCl₂. The positive/negative charge balance ($M^{+/2+}/Al^-$) is also very well-adjusted in natural, Zn- and Ni-CHA, being very close to the theoretical estimation. In the case of NH4-CHA the charge-balance should take into account that the exchange procedure may introduce both NH_4^+ and NH_3 species, indiscernible by EDS and most chemical analyses [14]. As SEM observation are carried out in vacuum (10^{-4} torr) the water molecules tend to leave the porous structure of chabazite and thus their content cannot be accurately deduced using standard EDS analyses (although the Oxford INCA Energy 350 detector outputs the oxygen amounts). For that reason TG analyses were preferred for the estimation of water content in zeolites. The DTA/TG results for the four samples, CHA, NH4-CHA, Zn-CHA and Ni-CHA are shown on Fig. 3. The TG curves of CHA and Ni-CHA show one stage weight losses while the NH4-CHA and Zn-CHA weight losses occur clearly in two stages. The principal weight losses
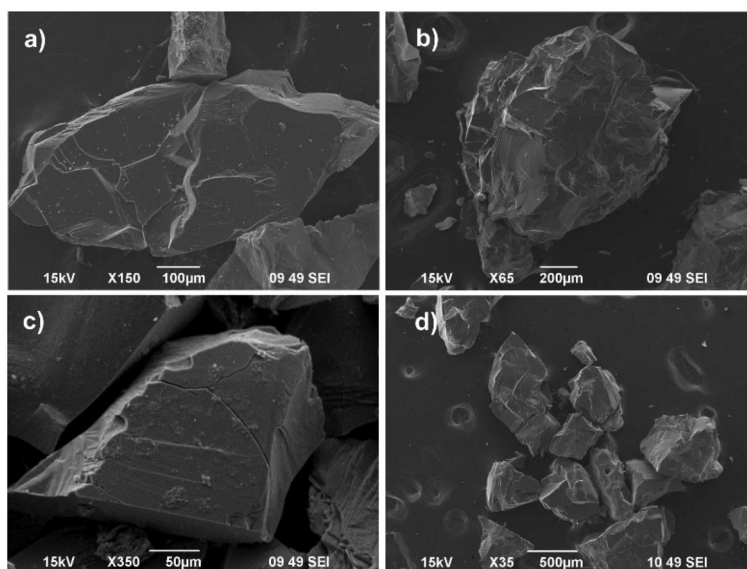

Fig. 2. SEM morphology of *a*) natural CHA, *b*) NH4-CHA, *c*) Zn-CHA, and *d*) Ni-CHA.

Table 2. Chemical compositions of natural and ammonium, zinc and nickel exchanged chabazite

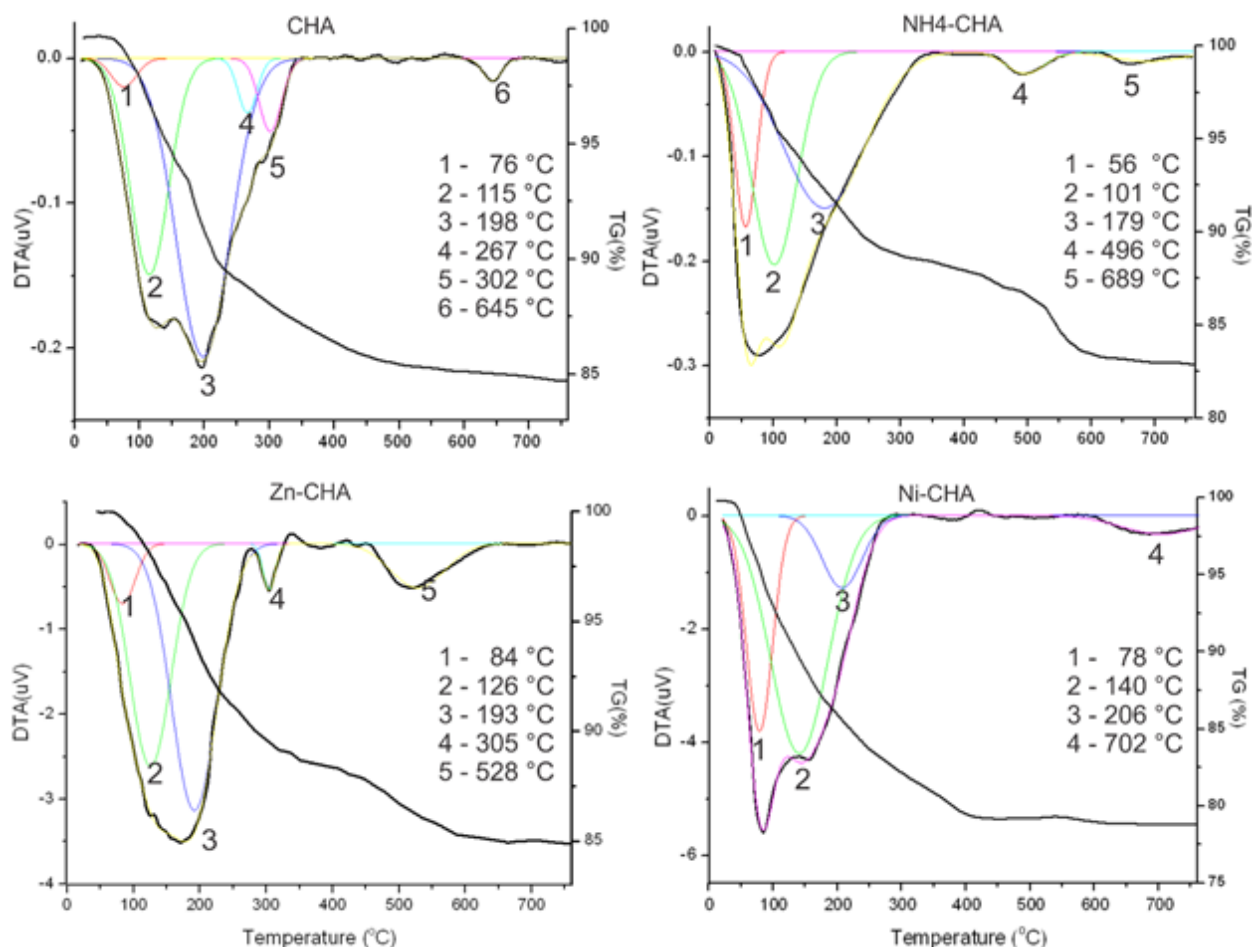| Chabazite form	Extra-framework cations	Framework and waters	Si/Al ratio	Charge compensation
CHA natural	$(Ca_{1.59}Na_{0.37})$	$Al_{3.63}Si_{8.37}O_{24}$ nH_2O	2.30	$M^{+/2+}/Al^- = 3.48/3.63$
NH4-CHA	$(N_{5.58})$	$Al_{3.52}Si_{8.48}O_{24}$ x nH_2O	2.41	$NH_4^+/Al^- = 5.58/3.52$
Ni-CHA	$(Ni_{1.43}N_{1.18})$	$Al_{3.96}Si_{7.82}O_{24}$ x nH_2O	1.87	$M^{+/2+}/Al^- = 4.04/3.96$
Zn-CHA	$(Zn_{1.44}N_{0.96})$	$Al_{3.67}Si_{8.33}O_{24}$ x nH_2O	2.26	$M^{+/2+}/Al^- = 3.84/3.67$

Fig. 3. DTA/TG data for a) natural CHA b) NH4-CHA c) Zn-CHA and d) Ni-CHA.

occur during the first stage (up to ~340 °C) and are mainly related to the release of water molecules and ammonium, in the case of NH4-CHA.

The tentative "peak fitting" of the DTA curves showed that the broad region (20 to ~340 °C) can be further subdivided (Fig. 3). In all four samples the fitting shows a peak in the 60–85 °C region that can be explained by "low temperature" desorption (release) of physisorbed water. The next two peaks (90–220 °C) are also common for the four CHA samples. The first one (~90 to 150 °C) can be explained by the breakup and release of hydrogen bonded water molecules, present in the channels. The second one (~150 to 220 °C) can be attributed to the more strongly coordinated H_2O molecules e.g. those that complement the cation coordination. Interestingly, in the cases of natural CHA and Zn-CHA the DTA data discloses *endothermic* effects in the region around 300 °C. As such effects are not present in the NH4- and Ni-CHA (Fig. 4) their assignment is a little bit delicate. An assumption is that due to the release of part of the H_2O molecules

complementing the cation coordination sphere, the cations start to migrate and occupy positions closer to the negatively charged CHA framework sites (compensating their positive/negative charge). Thus the cations would "attract" even more strongly the remaining H_2O molecules and the release will occur even "slowly" and at higher temperatures. The process is beneficial for both the framework and the cations. Such explanation is also in agreement with TG data, showing a change of TG slope and thus the speed of weight losses. In the case of NH4-CHA the peak at ~490 °C is associated with the release of the ammonium (such effect is not observed in the other three samples). At higher temperatures (above 560 °C) the completion of the dehydration process and the release of remaining NH_4^+ are finalized.

The four FTIR spectra (natural, NH_4^+, Zn and Ni chabazite, Fig. 5) show analogous spectral bands related to the chabazite framework, NH_4^+, OH and H_2O molecules. The main feature is the presence of the bands associated with NH_4^+ vibration (~1420 cm⁻¹ and a shoulder around 2800 cm⁻¹)
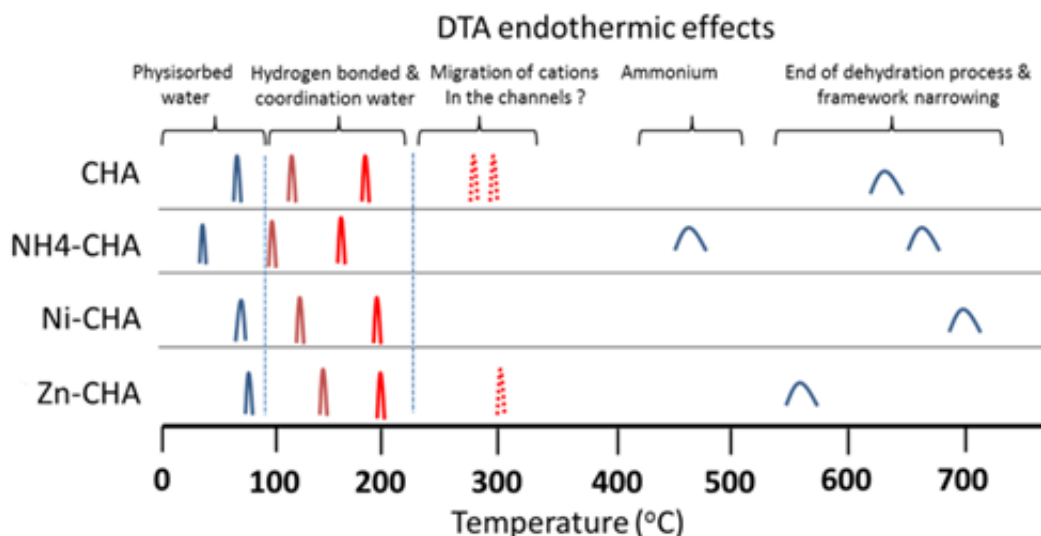
Fig. 4. DTA *endo* effects and associates processes in natural chabazite and exchanged NH4-CHA, Zn-CHA and Ni-CHA.
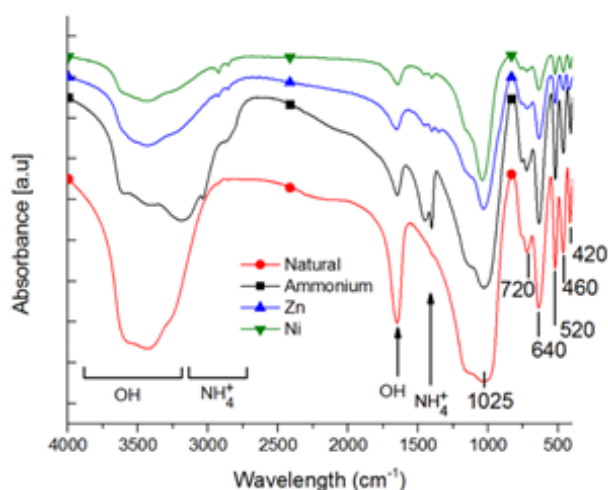

Fig. 5. FTIR spectra of natural CHA, NH4-CHA, Zn-CHA and Ni-CHA.

in the exchanged chabazite. These bands are very well pronounced and intensive for NH4-CHA, not present for natural CHA while for Ni- and Zn-CHA the low intensity of these bands (~1455, ~1400, ~1340, ~2930 and ~2850) suggests only minimal remains of NH_4^+.

The IR absorption bands associated with the chabazite framework vibrations are visible in the 400–1200 cm⁻¹ range. As one can see the relative intensity and position of the six bands (420, 460, 520, 640, 720 and 1025) is not affected by the performed cation exchange. According to [34] CHA type phases are characterized by the presence of a triplet of

peaks near 420, 455 and 510 cm⁻¹. These bands are clearly visible in our spectra at 420, 460, 520 cm⁻¹ and thus FTIR data also supports that the conducted ion exchange is not affecting the structure of CHA. The meticulous assignment of the absorption bands related to the chabazite framework vibrations is usually associated to two types of vibrations representative for CHA building units (TO_4 tetrahedra, T = Si or Al). Those related to internal O–T–O symmetric, asymmetric stretching and bending and those that are characteristic for T–O–T linkages (involving a bridging oxygen atom). Thus the bands at 460, 640, 720 and 1025 cm⁻¹ are associated to the O–T–O vibrations. The O–T–O asymmetric stretching vibrations occur at 1025 cm⁻¹ while the symmetric stretching vibrations located at 640 and 720 cm⁻¹ can be subdivided to internal (640 cm⁻¹) and external (720 cm⁻¹). The 460 cm⁻¹ band is characteristic for tetrahedra O–T–O bending. The bands around 420 and 520 cm⁻¹ are due to external linkage vibrations between tetrahedrons (T–O–T). The shoulder at ~1140 cm⁻¹ results specifically from Si–O–Si asymmetric stretching mode.

The band at 1650 cm⁻¹ reflects the bending vibration of H_2O molecules present in the CHA channels [35]. In addition the symmetric and asymmetric H_2O vibrations produce a broad peak in the 3000–3600 cm⁻¹ region (also disclosing hydrogen bonding interactions).

Single crystal analyses were conducted for NH4-, Zn- and Ni-CHA. The structure solution and refinement allowed the location of the cations, ammonium (nitrogen atoms) and some of the H_2O molecules present in the CHA framework. The positions of ex-
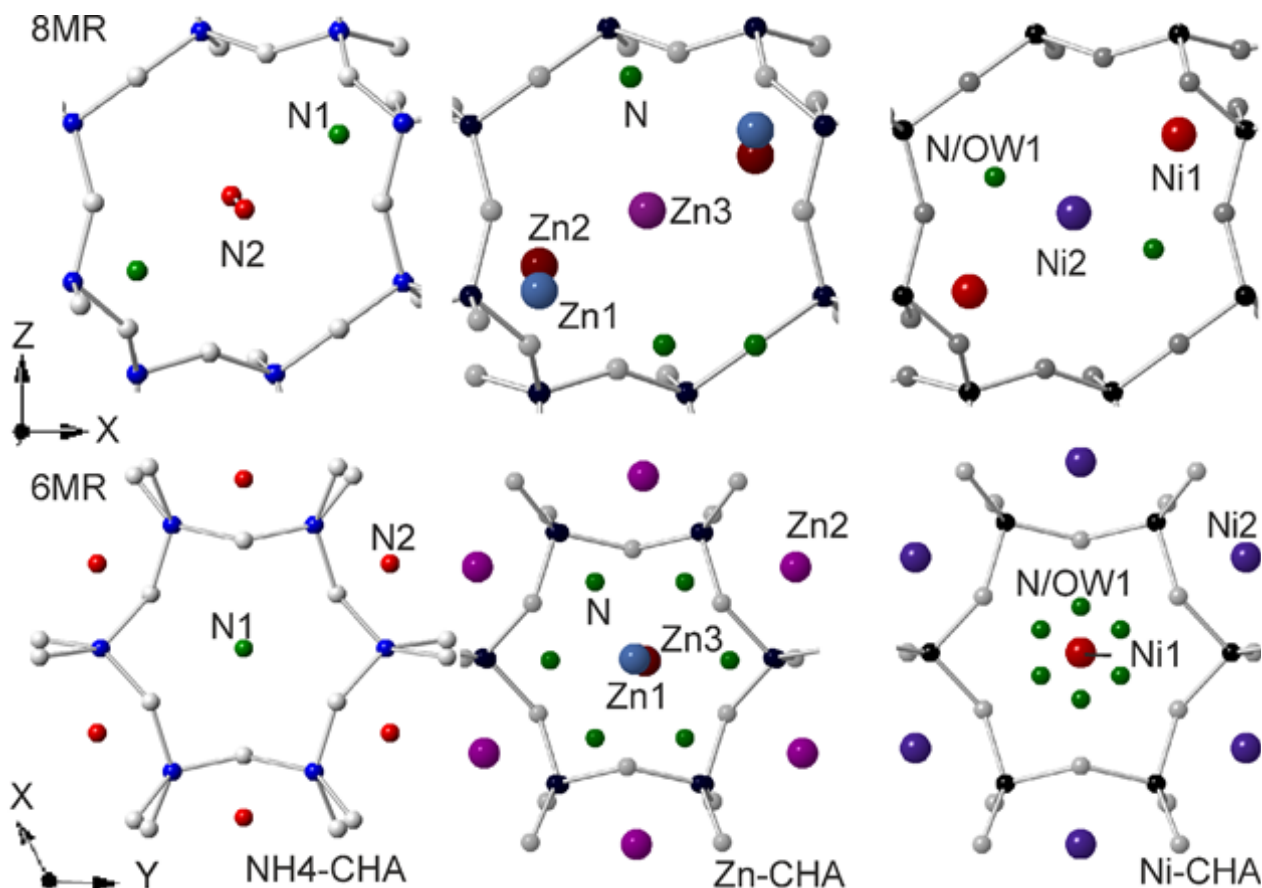
Fig. 6. Representation of NH_4^+, Zn and Ni cations location when viewed along 8MR and 6MR axes.

changeable cations, ammonium and H_2O molecules were obtained from difference Fourier. The location of hydrogen atoms from difference Fourier map was not always possible[1]. In the case of Zn-CHA and Ni-CHA the positions of hydrogen atoms associated with H_2O molecules were not determined. In the structure refinements, the occupancies of Si^{4+} and Al^{3+}, belonging to the aluminosilicate framework, were adjusted to the values obtained from the EDS chemical analysis while.

Previous structural studies of exchanged and dehydrated CHA have shown that there are several (three, four or five) "general" positions for the cations [36–39]. The present NH4-CHA refinement unveils the existence of two H_2O sites (OW1 and OW2) [38] and two ammonium (Nitrogen) sites (N1 and N2). Unfortunately NH_4^+ and H_2O are with similar MW, N and O scatter almost identically and

there is no real possibility to differentiate between them from X-ray data − leaving the assignment to the observed electron density "open". Thus when viewed along the axis of the D6R prism (e.g. along *c*) N1 position seems to be in the center of the D6R (Fig. 6 second row) while in reality they are displaced out of the prism and are near the border of the $[4^{12}6^88^6]$ cavity (e.g. along *b*). The N2 nitrogen site is located at the center of the $[4^{12}6^88^6]$ cavity (Fig. 6 top row). Both nitrogen sites are close to a framework oxygen: N1 is near O2 (N1…O2 distance of 2.940 Å), N2 is near three oxygen atoms O1, O3 and O4 (N2…O1, N2…O3, N2…O4 distances are 3.20, 3.32 and 3.396 Å respectively). Interestingly N1, OW1 and OW2 participate also in a series of hydrogen bonding interactions producing a complex motif.

The refinement of "disordered" OW1 required some attention and ended with 34% occupancy, in accordance to its 12 fold symmetry operation replication near the borders of the D6R. The chemical compositions of NH4-CHA obtained from X-ray refinement and by EDS are quite similar, with values of 5.21 and 5.58 for N (based on 24 framework oxygen).

---

[1] The location of hydrogen atoms from X-ray is contestable as H features only one electron and the resulting scattering intensity is very weak and in addition is usually displaced toward the N or O atoms.

The results of the NH4-CHA refinement are comparable with those of Gualtieri and Passaglia [38].

According to the EDS data the subsequently conducted ion exchange (with 1M $ZnCl_2$ or $NiCl_2$ solutions) of the NH4-CHA form resulted in a partial displacement of ammonium molecules by Zn and Ni cations (as FTIR data suggest residual remains of ammonium). The refinement of the Zn- and Ni-CHA structures shows that the Zn^{2+} and Ni^{2+} cations occupy/displace the ammonium N1 and N2 sites. The ammonium, remaining Zn- and Ni-CHA structures, is displaced from the center of the rings, closer to the Si/Al framework (sharing its site with a H_2O molecule).

In Zn-CHA, the cations Zn^{2+} occupy three positions: Zn1 and Zn2 and Zn3. The resulting Zn1 site is in a threefold position when it is observed along *c*. Like N1 this position is situated out of the 6DR prism, and is near the border of the $[4^{12}6^88^6]$ cavity. Position Zn2 corresponds to N2 (e.g. in the center of the $[4^{12}6^88^6]$ cavity). Interestingly no suitable coordination H_2O molecules could be detected for Zn2. In Zn-CHA H_2O molecules are distributed into four positions OW1, OW2/N, OW3, and OW4 Position OW1 coordinates Z1 and Zn3 positions The H_2O molecules seem to be positioned concentrically/radially when viewed along the threefold axis of the D6R prism [40]. Position OW3 appears on the D6R axis (coordinates Z1 and Zn3 positions) while OW4 and OW2/N are displaced from the axis and closer to the border of the prism. These H_2O molecules, situated in the $[4^{12}6^88^6]$ cavity are complementing the cation coordination. Position OW4 is the highly occupied in Zn-CHA (occupancy of 1), while OW1 OW2 and OW3 are less 0.32, 0.12 and 0.04 respectively. In Ni-CHA the cations (Ni^{2+}) occupy two positions Ni1 and Ni2. The sites correspond to N1 and N2 and thus to Zn1 and Zn2.

In Ni-CHA three water sites were located: OW1, OW2 and OW3 with occupancy of 0.21, 0.29, and 0.18 respectively. Positions OW1 and OW2 are analogous to those of the Zn-CHA. The distance OW1...Ni2 is 2.38 Å. Position OW3 is situated in the $[4^{12}6^88^6]$ cavity with distance OW3...N1 2.68 Å.

CONCLUSIONS

Single crystals of natural chabazite were completely exchanged by NH4 cations. The subsequent ion exchange of the chabazite ammonium form (NH4-CHA) with 1M $ZnCl_2$ and $NiCl_2$ solution produced Zn-CHA and Ni-CHA forms. The exchange of NH_4^+ by Zn^{2+} and Ni^{2+} was not complete according to FTIR and EDS microanalyses. The Ni and Zn cations substitute easily two of the two ammonia positions observed in NH4-CHA: the position "N1"

near the border of the $[4^{12}6^88^6]$ cavity the other position "N2" at the center of the $[4^{12}6^88^6]$ cavity. The remaining NH_4^+ in Zn-CHA and Ni-CHA shares a water position.

SUPPLEMENTARY MATERIALS

ICSD No 426116, 426117 and 426118 contains the supplementary crystallographic data for NH4-, Zn- and Ni-CHA respectively. Further details of the crystal structure investigation(s) may be obtained from Fachinformationszentrum Karlsruhe, 76344 Eggenstein-Leopoldshafen, Germany (fax: (+49)7247-808-666; e-mail: crysdata(at)fiz-karlsruhe.de, http://www.fiz-karlsruhe.de/request_for_deposited_data.html) on quoting the appropriate CSD number.

REFERENCES

1. J. Shang, G. Li, R. Singh, P. Xiao, J. Z. Liu,P. A. Webley, *J. Phys. Chem. C*, **114**, 22025 (2010).
2. I. Georgieva, L. Benco, D. Tunega, N. Trendafilova, J. Hafner, H. Lischka, *J. Chem. Phys.*, **131** (2009).
3. R. K. Singh, P. Webley, *Adsorption-Journal of the International Adsorption Society*, **11**, 173 (2005).
4. V. Van Speybroeck, K. Hemelsoet, K. De Wispelaere, Q. Y. Qian, J. Van der Mynsbrugge, B. De Sterck, B. M. Weckhuysen, M. Waroquier, *Chemcatchem*, **5**, 173 (2013).
5. F. Goltl J. Hafner, *Microporous and Mesoporous Materials*, **166**, 176 (2013).
6. J. Shang, G. Li, R. Singh, Q. F. Gu, K. M. Nairn, T. J. Bastow, N. Medhekar, C. M. Doherty, A. J. Hill, J. Z. Liu,P. A. Webley, *J. Am. Chem. Soc.*, **134**, 19246 (2012).
7. D. P. Smith, *Water Environ. Res.*, **83**, 373 (2011).
8. J. Weitkamp, *Solid State Ionics*, **131**, 175 (2000).
9. A. A. Zagorodni, Ion exchange materials: properties and applications, Elsevier, Amsterdam; Boston, 2007, 1st edn.
10. V. A. Nikashina, A. N. Streletsky, I. V. Kolbanev, I. N. Meshkova, V. G. Grinev, I. B. Serova, T. S. Yusupov, L. G. Shumskaya, *Clay Miner.*, **46**, 329 (2011).
11. E. A. Eilertsen, S. Bordiga, C. Lamberti, A. Damin, F. Bonino, B. Arstad, S. Svelle, U. Olsbye, K. P. Lillerud, *Chemcatchem*, **3**, 1869 (2011).
12. M. Majdan, S. Pikus, Z. Rzaczynska, M. Iwan, O. Maryuk, R. Kwiatkowski, H. Skrzypek, *J. Mol. Struct.*, **791**, 53 (2006).
13. G. J. D. Soler-illia, C. Sanchez, B. Lebeau, J. Patarin, *Chem. Rev.*, **102**, 4093 (2002).

14. M. V. Vener, X. Rozanska, J. Sauer, *Phys. Chem. Chem. Phys.*, **11**, 1702 (2009).
15. K. Suzuki, G. Sastre, N. Katada,M. Niwa, *Phys. Chem. Chem. Phys.*, **9**, 5980 (2007).
16. H. S. Shin, I. J. Jang, N. R. Shin, S. H. Kim, S. J. Cho, *Res. Chem. Intermediat.*, **37**, 1239 (2011).
17. M. Hammes, M. Valtchev, M. B. Roth, K. Stowe,W. F. Maier, *Appl. Catal. B-Environ.*, **132**, 389 (2013).
18. V. Valtchev, G. Majano, S. Mintova, J. Perez-Ramirez, *Chem. Soc. Rev.*, **42**, 263 (2013).
19. F. Chen, Y. Liu, R. E. Wasylishen, Z. H. Xu, S. M. Kuznicki, *J. Nanosci. Nanotechno.*, **12**, 1988 (2012).
20. F. N. Ridha, Y. X. Yang, P. A. Webley, *Microporous and Mesoporous Materials*, **117**, 497 (2009).
21. E. P. Ng, D. Chateigner, T. Bein, V. Valtchev, S. Mintova, *Science*, **335**, 70 (2012).
22. T. Babeva, R. Todorov, B. Gospodinov, N. Malinowski, J. El Fallah, S. Mintova, *J. Mater. Chem.*, **22**, 18136 (2012).
23. C. Baerlocher, L. B. McCusker, D. H. Olson, Atlas of zeolite framework types, Elsevier B.V., 2007, 7-th edn.
24. B. de Gennaro, A. Colella, P. Aprea,C. Colella, *Microporous and Mesoporous Materials*, **61**, 159 (2003).
25. H. Lee, P. K. Dutta, *Microporous and Mesoporous Materials*, **38**, 151 (2000).
26. J. Cejka, H. V. Bekkum, A. Corma, F. Schuth, Introduction to Zeolite Science and Practice (vol. 168), Elsevier Science Bv, Amsterdam, 2007.
27. S. M. Kuznicki, C. C. H. Lin, J. Bian, A. Anson, *Clays Clay Miner.*, **55**, 235 (2007).
28. M. Bourgogne, J. L. Guth, R. Wey, *US Patent* 4 503 024 (1985).
29. M. Wojdyr, *J. Appl. Crystallogr.*, **43**, 1126 (2010).
30. Agilent, CrysAlis PRO, Agilent Technologies, UK Ltd, Yarnton, England, 2011.
31. G. M. Sheldrick, *Acta Crystallogr.*, *A* **64**, 112 (2008).
32. J. Zhang, R. Singh,P. A. Webley, *Microporous and Mesoporous Materials*, **111**, 478 (2008).
33. M. Trzpit, S. Rigolet, J. L. Paillaud, C. Marichal, M. Soulard,J. Patarin, *J. Phys. Chem. B*, **112**, 7257 (2008).
34. E. M. Flanigen, L. B. Sand, Molecular Sieve Zeolites (Advances in Chemistry Series, vol. 101–102), American Chemical Society, Washington, D.C., 1971.
35. M. Falk, *Spectrochim. Acta A*, **40**, 43 (1984).
36. A. Alberti, E. Galli, G. Vezzalini, E. Passaglia, P. F. Zanazzi, *Zeolites*, **2**, 303 (1982).
37. L. J. Smith, H. Eckert,A. K. Cheetham, *J. Am. Chem. Soc.*, **122**, 1700 (2000).
38. A. F. Gualtieri, E. Passaglia, *Eur. J. Mineral.*, **18**, 351 (2006).
39. F. N. Ridha P. A. Webley, *Sep. Purif. Technol.*, **67**, 336 (2009).
40. A. Nakatsuka, H. Okada, K. Fujiwara, N. Nakayama, T. Mizota, *Microporous and Mesoporous Materials*, **102**, 188 (2007).

СТРУКТУРНИ ОСОБЕНОСТИ НА ПРИРОДЕН ХАБАЗИТ, МОДИФИЦИРАН ЧРЕЗ ZnCl$_2$ И NiCl$_2$

Л. Т. Димова[1], И. Пироева[2], С. Атанасова-Владимирова[2], Р. Русев[1], Б. Л. Шивачев[1]*

[1] Институт по минералогия и кристалография „Акад. Иван Костов", Българска академия на науките, ул. „Акад. Георги Бончев", бл. 107, 1113 София, България
[2] Институт по физикохимия, Българска академия на науките, ул. „Акад. Георги Бончев", бл. 11, 1113 София, България

(Резюме)

Монокристали от природен хабазит са модифицирани до получаването на NH$_4^+$, Zn^{2+} и Ni^{2+} форми, които са характеризирани чрез ЕДС/СЕМ, ДТА/ТГ, ИЧ, както и монокристален рентгеноструктурен анализ. Процедурата на модифициране включва последователното преминаване на изходния природен хабазит (Na$_{0.37}$Ca$_{1.56}$)Al$_{3.63}$Si$_{8.36}$O$_{24}$xH$_2$O) в неговата амониева форма (NH4-CHA). Тази NH4-CHA форма се използва като изходна при последвалия йонен обмен с цинкови и никелови катиони. Йонният обмен се осъществява в 1М ZnCl$_2$ и NiCl$_2$ водни разтвори при 100 °C. ЕДС и ИЧ анализи, както и рентгеноструктурните проучвания, разкриха остатъци от амониеви катиони в Zn и Ni обменени форми. Структурните уточнения разкриват, че водните молекули, налични в структурата на хабазита, са склонни да заемат места, които обикновено са свързани с близки места на катионите. Тъй като катионните количества, необходими за компенсиране заряда на скелета, са ограничени, то и молекулите на водата също се приспособяват към тази особеност. Разпределението на водните молекули в 8-членния пръстен е от радиален тип.

Crystal structure and spectral study of 3-methylpyridazinium hydrogensquarate

S. Y. Zareva*, G. G. Gencheva

Sofia University "St. Kliment Ohridski", Faculty of Chemistry and Pharmacy,
*1 James Bourchier Blivd., 1164 Sofia, Bulgaria*

The crystal structure of 3-Methylpyridazinium hydrogensquarate was determined by single-crystal X-ray diffraction technique. The compound crystallizes in the monoclinic space group $P2_1/c$. The crystal packing shows the formation of layers of hydrogen squarate anions and 3-methylpyridazinium cations, connected by strong hydrogen O-H$\cdots$O and N-H$\cdots$O bonds. The novel derivative of squaric acid was spectroscopically characterized in solution by UV/Vis- and in solid state by means of FTIR-spectroscopy.

Key words: Single crystal X-ray diffraction, FTIR, UV/Vis.

INTRODUCTION

The diazines and the substituted azines are studied because of their important properties in biology, medicinal chemistry and fundamental chemistry of the heterocycles [1–4]. Recently the synthesis, the crystal structure and the spectroscopic properties of cyano-bridged two-dimensional coordination polymers with axially bonded 3-methylpyridazine (3-MetPy) were published by Gör *et al.* [5] with vibrational assignment of the bands from the IR and Raman spectra to the corresponding normal vibrations.

The hydrogen-bonded supramolecular patterns found in crystals of squaric acid (H_2Sq) and its anions hydrohensquarate (HSq) and squarate (Sq) were extensively studied [6–21]. The self-assembly of hydrogensquarate was studied of many researchers: Angelova [6–7], Kolev et al. [8–14] but the detailed study of crystal structure and spectral characteristics have been given by Koleva et al. [15–20]. Concerning the crystal chemistry of HSq anion [21], it was proved that it exists in different supramolecular organizations, such as chains, dimmers, tetramers, etc.. In water solution, H_2Sq has a protic behavior with formation of both anions HSq and Sq. The presented paper is dedicated to study of the ability of the squaric acid to protonate an organic base, namely 3-MetPy, and thus to form an
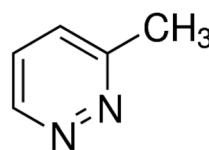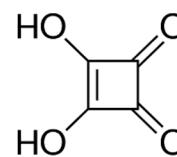
3-Methylpyridazine   Squaric acid

Scheme 1. Starting compounds.

organic salt (Scheme 1). Here, the synthesis, crystal structure and spectroscopic characteristics of a novel compound 3-methylpyridazinium hydrogensquarate have been presented and discussed in order to give an additional information about the arrangement of the HSq-anions in its solid state

EXPERIMENTAL

Synthesis

The starting compounds for the synthesis of 3-methylpyridazinium hydrogensquarate (3MPHSq), 3-methylpyridazine, $C_5H_6N_2$ and squaric acid, $C_4H_2O_4$ were purchased from Sigma Aldrich (USA). The base, 3-MetPy (2 mmol, 0.188 g) dissolved in ethanol (10 mL) was added with continuous stirring to the 45 mL aqueous solution of H_2Sq (2 mmol, 0.228 g) and then the solution obtained was stirred

---

* To whom all correspondence should be sent:
E-mail: ahsz@chem.uni-sofia.bg

for 24 h at 40 °C. The resulting colorless crystals were filtered off, washed with ethanol, and dried on P_2O_5 at 298 K, yield 88%. The product was purified by multiple recrystallizations from distilled water. Crystals suitable for X-ray diffraction of 3MPHSq were grown by slow evaporation from double-distilled water.

Experimental methods

The IR-spectra (KBr-disks and Nujol mulls) were measured on a Thermo Nicolet 6700 FTIR-spectrometer (4000–400 cm^{-1}, 2 cm^{-1} resolution, 32 scans).

UV-spectra of solutions of the compound in ethanol (Uvasol, Merck) at concentration of 2.5×10^{-5} M were recorded at room temperature on a Thermo Scientific Evolution 300 UV-VIS-spectrophotometer (10 mm quartz cells have been used).

A colorless plate crystal of 3MPHSq with the size $0.50 \times 0.30 \times 0.12$ mm^3 was selected for data collection with a Bruker SMART X2S diffractometer using a monochromatic Mo-Kα ($\lambda = 0.71073$ Å) mi-crofocus source with a Bruker APEX-II CCD detector at 300.15 K. APEX II software was used for data collection, cell refinement and data reduction [23]. Absorption corrections based on equivalent reflections were applied using SADABS-2008. The crystal structure was solved by direct method using SHELXS-97 [24]. All non-hydrogen atoms of the molecule were located from the electron-density map. All hydrogen atoms were placed in calculated positions. To refine the structure, the program SHELXL97 [25], version 2014/7 implemented in program OLEX2 was used [26]. Full-matrix least-squares refinement was carried out till the final refinement cycles converged to an $R = 0.0476$ and $wR(F^2) = 0.1187$ for the observed data. The OLEX software was applied to prepare the materials for publication. The crystallographic, X-ray data collection and refinement statistics for the compound are given in Table 1. Selected bond lengths and bond angles are summarized in Table 2 and hydrogen bonding interactions are given in Table 3. ORTEP diagram for the studied compound is shown on Fig. 1. CCDC 1831416 contains the supplementary crystallographic data

Table 1. Crystal data and structure refinement for 3MPHSq

|	
Empirical formula	$C_{18}H_{16}N_4O_8$
Formula weight	416.35
Temperature/K	300.15
Crystal system	monoclinic
Space group	$P2_1/c$
a/Å	9.7853(14)
b/Å	21.557(3)
c/Å	8.8921(13)
α/°	90
β/°	90.270(5)
γ/°	90
Volume/Å^3	1875.7(4)
Z	4
ρ_{calc} g/cm^3	1.474
μ/mm^{-1}	0.118
F(000)	864.0
Crystal size/mm^3	$0.5 \times 0.3 \times 0.12$
Radiation	MoKα ($\lambda = 0.71073$)
2Θ range for data collection/°	3.778 to 50.086
Index ranges	$-11 \leq h \leq 11, -24 \leq k \leq 25, -10 \leq l \leq 10$
Reflections collected	16920
Independent reflections	3297 [$R_{int} = 0.0997, R_{sigma} = 0.0817$]
Data/restraints/parameters	3297/0/280
Goodness-of-fit on F^2	0.984
Final R indexes [I>=2σ (I)]	$R_1 = 0.0476, wR_2 = 0.1187$
Final R indexes [all data]	$R_1 = 0.0733, wR_2 = 0.1296$
Largest diff. peak/hole / e Å^{-3}	0.23/-0.27
CCDC number	1831416
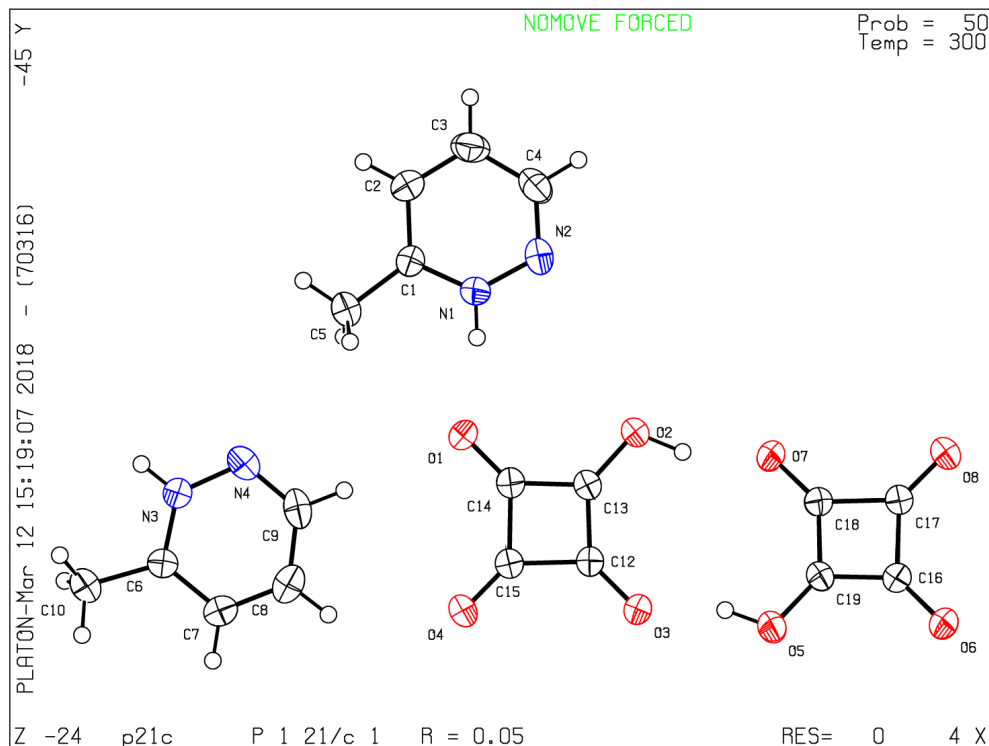
Fig. 1. Asymmetric unit of 3MPHSq. Displacement ellipsoids are drawn at the 50% probability level; hydrogen atoms are drawn at arbitrary size.

for the compound [27]. The drawings were prepared using Mercury version 3.3 [28].

RESULTS AND DISCUSSION

The compound 3MPHSq crystallizes in monoclinic $P2_1/c$ space group. The asymmetric unit contains two hydrogen-squarate anions and two 3-methylpyridazinium cations (Fig. 1). All molecular geometry parameters exhibit typical values [15–21]. The hydrogen-squarate ions form classical α-dimers [21], (Fig. 2) via hydrogen-bonding interactions. The observed O5-H5···O3 and O2-H2···O7 distances, respectively, 2.536 and 2.561 Å indicate strong hydrogen bond formation in the dimeric structure.

The two 3-methylpyridazine base are protonated at the N1- and N3-atoms, respectively and thus the formed pyridazinium cations (3-MetPyH) are joined to each HSq ions from the dimmer by N3-H3···O6 and N1-H1···O1 hydrogen bonds (2.676 and 2.684 Å, Tabl. 2). Thus the hydrogen bonding network leads to formation of tetramers along *a*-axis from two hydrogen-squarate ions and two side pyridazinium cations with length approximately of 1.5 nm (16.581 Å). In the crystal structure, the te-
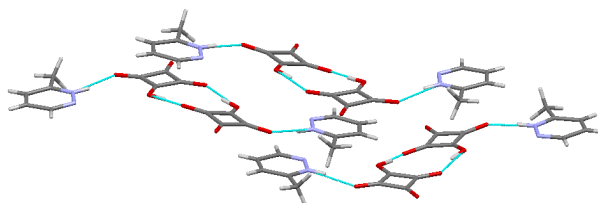
Fig. 2. Hydrogen-bonding pattern in the structure of 3MPHSq. Hydrogen bonds are represented by dashed lines.

tramers build finite wavy layers as the shortest distance between them is 4.488 Å. The reported structure is the first crystallographically characterized salt of 3-methylpyridazine.

The presence of aromatic heterocyclic six-membered rings containing two N-atoms is probably the reason for the layered structure formation. The interaction between the layers is most probably at the expense of van der Waals forces.

Infrared and UV-spectra

The experimental IR-spectrum of 3MPHSq is characterized by a broad absorption band within the 3400–2100 cm^{-1} range corresponding to overlapped

125

Table 2. Selected geometrical parameters for 3MPHSq (Å, °)

Bond Lengths			
O4 —C15	1.228(2)	C1—C2	1.397(3)
O2—C13	1.317(2)	C4—C3	1.398(3)
O1—C14	1.248(2)	C3—C2	1.363(3)
O3—C12	1.255(2)	C9—C8	1.402(3)
N1—N2	1.343(2)	C15—C14	1.497(3)
N1—C1	1.327(2)	C12—C13	1.421(3)
N2—C4	1.311(3)	C13—C14	1.424(3)
C5—C1	1.489(3)	C15—C12	1.496(3)
Bond Angles			
C1—N1—N2	126.76(18)	O3—C12—C1	137.1(2)
C4—N2—N1	115.46(19)	C13—C12—C15	89.50(16)
N1—C1—C5	118.42(18)	O2—C13—C12	135.99(19)
O4—C15—C12	135.7(2)	O2—C13—C14	130.50(19)
N1—C1—C2	117.0(2)	O1—C14—C15	134.2(2)
C2—C1—C5	124.60(19)	O1—C14—C13	136.5(2)
N2—C4—C3	123.5(2)	C13—C14—C15	89.35(16)
C2—C3—C4	118.2(2)	O3—C12—C15	133.35(19)
C3—C2—C1	119.1(2)	C12—C15—C14	87.63(16)
C12—C13—C14	93.51(17)	O4—C15—C14	136.6(2)

Table 3. Hydrogen Bonds and weak C–H…O interactions (Å, °) in the crystal structure of 3MPHSq

D—H··A	d(D-H)	d(H-A)	d(D-A)	D-H-A
O2—H2A··O7[1]	0.95(3)	1.65(3)	2.561(2)	159(2)
O5—H5···O3[2]	0.94(3)	1.63(3)	2.536(2)	160(2)
N1—H1···O1[3]	0.86	1.84	2.684(2)	168.5
N3—H3A··O6	0.86	1.83	2.676(2)	169.0
C4—H4···O6	0.93	2.47	3.396(3)	172.4
C2—H2···O3[5]	0.93	2.53	3.367(3)	150.4
C9—H9···O1[6]	0.93	2.43	3.361(3)	176.3
C7—H7···O7[7]	0.93	2.53	3.387(3)	152.9
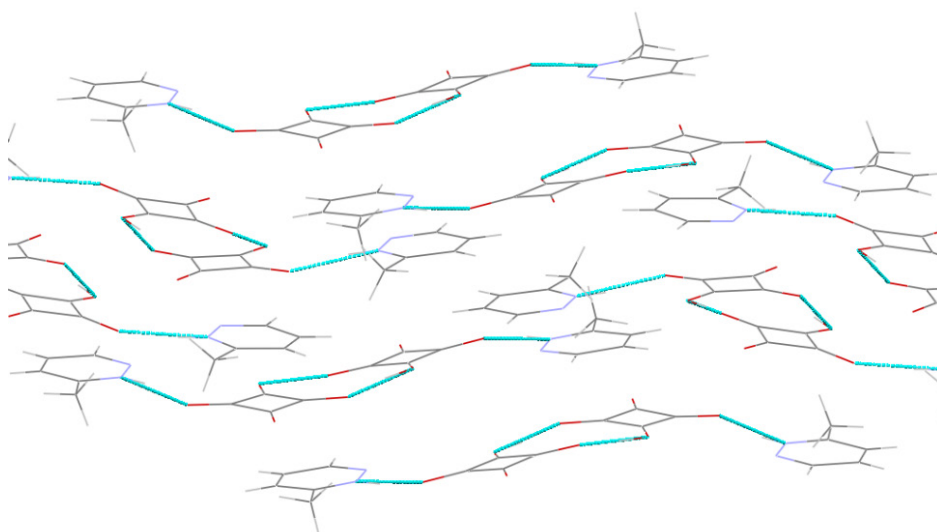
Fig. 3. O–H···O and N–H···O bonded layers in the structure of 3MPHSq.

$\nu_{OH(Sq)}$ and $\nu_{N^+H(3-MetPyH)}$ stretching vibrations. The series of bands within the 3100–3000 cm^{-1} and 2965 and 2800 cm^{-1} regions correspond to the stretching vibration $\nu_{3MetPyCH}$ and $\nu_{(CH_3)}$ modes. The bands in the interval 1810–1590 cm^{-1} belong to $\nu^s_{C=O(Sq)}$, $\nu^{as}_{C=O(Sq)}$ and $\nu_{C=C(Sq)}$ stretching vibrations of the hydrogensquarate anion. The bands at 1644 cm^{-1} and 1605 cm^{-1} can be attributed to ν_{N^+H} bending vibrations as the bands at 1545 and 1385 cm^{-1} could be assigned to $\nu^{as,s}(COO^-)$ of the one-deprotonated carboxylic group.

The observed shift of the bands belonging to NH$^+$(base), -C=O (HSq) and COO$^-$ (HSq) in respect to the free acid and base (Fig. 4, Table 4) prove the participation of the groups in hydrogen-bond formation. The assignments of the bands are in accordance with theoretical data published in [15, 22].

The molecular structure in solution was studied by ultraviolet absorption spectroscopy, which in general is regarded as very useful to study the chemical behavior and the electronic orientation of the substituents in heteroaromatic molecules [29]. The base 3-MetPy shows the characteristic $\pi \rightarrow \pi^*$ at 263 (lgε=4.5) and $n \rightarrow \pi^*$ at 315 nm (lgε = 4.0) (Fig. 5).

In the spectrum of the studied compound 3-MetPySq, only the band for $\pi \rightarrow \pi^*$ band (lgε =

Table 4. Assignment of the experimental IR- bands 3MPHSq

Assignment	IR bands of 3MPHSQ [cm^{-1}]
νCH	3057
νOH$_{Sq}$	2730
νOH$_{Sq}$	2651
νOH$_{Sq}$	2572
νOH$_{Sq}$	2504
νOH$_{Sq}$	2159
νOH$_{Sq}$	2082
ν^s(C=O)$_{Sq}$	1805
ν^{as}(C=O)$_{Sq}$	1663
8a + νSq	1644
19a; 19b	1538
ν(C=C)$_{Sq}$)	1596
ν(C—O$^-$)$_{Sq}$	1542
ν(C—C)$_{Sq}$	1470
νC—CH$_3$	1250
ν(C—C)$_{Sq}$	1169
ν(C—C)$_{Sq}$	1142
ν(C—C)$_{Sq}$	1095
r(CH$_3$)	1049
δCH(ring)	1020

Fig. 4. FTIR-spectrum of 3-Methylpyridazinium hydrogensquarate – KBr pellet.
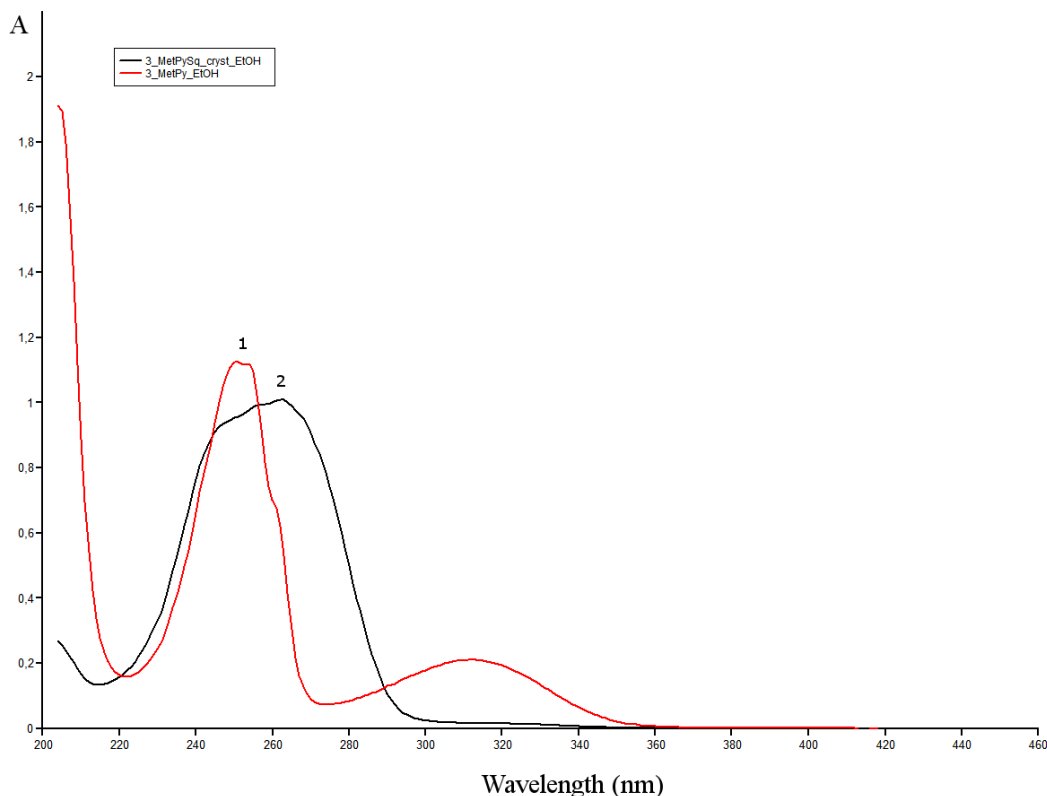
Fig. 5. UV-spectra of 3-Methylpyridazine (1) and 3-Methylpyridazinium hydrogensquarate (2) dissolved in ethanol at concentration 2.5.10-5 molL-1.

4.8) was observed. As a consequence of the protonation of one of the nitrogen atoms (Fig. 5), a hypsochromic shift of the $n\rightarrow\pi^*$ band leads to overlay with the more intensive $\pi\rightarrow\pi^*$ band.

CONCLUSION

The new compound 3-methylpyrdazinium hydrogensquarate has been synthesized, isolated, spectroscopically and structurally characterized, using single crystal X-ray diffraction, IR spectroscopy and UV-spectroscopy. The effects of N-protonation on the optical properties are elucidated by the comparison of the data of the protonated and neutral compound. The compound crystallizes in the monoclinic $P2_1/c$ space system and the structure consists of infinite layers. The hydrogensquarate ions form stable α-dimers via inter anion hydrogen-bonding interactions. The observed O5-H5···O3 and O2-H2···O7 distances, respectively, 2.536 and 2.561 Å indicate strong hydrogen bond formation in the dimeric structure. We reported for the first time the structural motif of α-dimer with formation of hydrogen bonds with different distances (2.536 and 2.561 Å).

REFERENCES

1. D. Mantu, M. C. Luca, C. Moldoveanu, G. Zbancioc, I. I. Mangalagiu, *Eur. J. Med. Chem.*, **45**, 5164 (2010).
2. R. M. Butnariu, I. I. Mangalagiu, *Med. Chem.*, **17**, 2823 (2009).
3. C. Moldoveanu, G. Mangalagiu, G. Drochioiu, M. Caprosu, M. Petrovanu, I. Mangalagiu, New Potential Anti-tuberculosis Compounds Derived from Diazine, in: Al. I. Cuza (Ed.), An. St. Univ., 2003.
4. A. M. Zbancioc, G. Zbancioc, C. Tanase, A. Miron, C. Ursu, I. I. Mangalagiu, *Lett. Drug Des. Discov.*, **7**, 644 (2010).
5. K. Gör, G. Kürkçüoğlu, O. Yeşilel, O. Büyükgüngörd, *Inorg. Chim. Acta*, **414,** 15 (2014).
6. O. Angelova, R. Petrova, V. Radomirska, T. Kolev, *Acta Cryst. C*, **52**, 2218 (1996).
7. O. Angelova, V. Velikova, T. Kolev, V. Radomirska, *Acta Cryst. C*, **52**, 3252 (1996).
8. T. Kolev, Z. Glavcheva, R. Stahl, H. Preut, P. Bleckmann, V. Radomirska, *Acta Cryst. C*, **53**, IUC9700010 (1997).
9. T. Kolev, H. Preut, P. Bleckmann, V. Radomirska, *Acta Cryst. C*, **53**, 805 (1997).
10. T. Kolev, H. Preut, P. Bleckmann, V. Radomirska, *Z. Kristallogr. – New Cryst. Struct.*, **212**, 414 (1997).

11. T. Kolev, R. Stahl, H. Preut, P. Bleckmann, V. Radomirska, *Z. Kristallogr. – New Cryst. Struct.*, **212**, 415 (1997).
12. T. Kolev, R. Stahl, H. Preut, V. Koniczek, P. Bleckmann, V. Radomirska, *Z. Kristallogr. – New Cryst. Struct.*, **212**, 417 (1997).
13. T. Kolev, R. Stahl, H. Preut, V. Koniczek, P. Bleckmann, V. Radomirska, *Z. Kristallogr. – New Cryst. Struct.*, **213** (1), 167 (1998).
14. T. Kolev, R. Stahl, H. Preut, P. Bleckmann, V. Radomirska, *Z. Kristallogr. – New Cryst. Struct.*, **213** (1), 169 (1998).
15. B. B. Koleva, T. Kolev, R. W. Seidel, M. Spiteller, H. Mayer-Figge, W. S. Sheldrick, *J. Phys. Chem. A*, **113**, 3088 (2009)
16. B. B. Koleva, T. Kolev, R. W. Seidel, Ts. Tsanev, H. Mayer-Figge, M. Spiteller, W. S. Sheldrick, *Spectrochim. Acta, Part A*, **71**, 695 (2008).
17. B. B. Koleva, T. Tsanev, T. Kolev, H. Mayer-Figge, W. S. Sheldrick, *Acta Cryst. E*, **63**, o3356 (2007).
18. T. Kolev, B. Koleva, R. Sedel, M. Spitreller, W. Sheldrick, *Acta Cryst. E*, **63**, o4852 (2007).
19. T. Kolev, B. Koleva, M. Spitreller, *Amino Acids*, **33**, 719 (2007).
20. T. Kolev, B. Koleva, M. Spiteller, *J. Mol. Struct.*, **877**, 79 (2008).
21. G. Gilli, V. Bertolasi, P. Gilli, V. Ferretti, *Acta Cryst. B*, **57**, 859 (2001).
22. T. Kolev, T. Pajpanova, T. Dzimbova, S. Zareva, M. Spiteller, *J. Mol. Struct.*, **1102**, 235 (2015).
23. Bruker (2012). SADABS. Bruker AXS Inc., Madison, Wisconsin, USA; Bruker (2013). APEX2 and SAINT. Bruker AXS Inc., Madison, Wisconsin, USA.
24. G. M. Sheldrick, *Acta Cryst. A*, **64**, 112 (2008).
25. G. M. Sheldrick, *Acta Cryst.*, *C* **71**, 3 (2015).
26. O. V. Dolomanov, L. J. Bourhis, R. J. Gildea, J. A. Howard, H. Puschmann, *J. Appl. Cryst.*, **42**, 339 (2009).
27. The crystallographic data for 3MPHSq were deposited at the Cambridge Crystallographic Data Centre and allocated the deposition number CCDC 1831416. Copies of the data can be obtained, free of charge, on application to CCDC, 12 Union Road, Cambridge CB2 1EZ, UK; tel: +441223762910; fax: +441223336033; e-mail: deposit@ccdc.cam.ac.uk; http://www.ccdc.cam.ac.uk/deposit.
28. C. F. Macrae, I. J. Bruno, J. A. Chisholm, P. R. Edgington, P. McCabe, E. Pidock, L. Rodriguez-Monge, R. Taylor, J. Van de Streek, P. A. Wood, *J. Appl. Crystallogr.*, **41**, 466 (2008).
29. F. Peral, E. Gallego, *Spectrochim. Acta Part A*, **59**, 1223 (2003).

КРИСТАЛНА СТРУКТУРА И СПЕКТРАЛНИ ХАРАКТЕРИСТИКИ НА 3-МЕТИЛПИРИДАЗИНИЕВ ХИДРОГЕНСКВАРАТ

С. Й. Зарева, Г. Г. Генчева

Софийски университет „Св. Климент Охридски", Факултет по химия и фармация, бул. „Дж. Баучер" 1, 1164 София, България

(Резюме)

Кристалната структура на 3-метилпиридазиниевия хидрогенскварат беше определена посредством монокристална рентгенова дифракция. Изследваното съединение кристализира в моноклинна пространствена група $P2_1/c$, като формира слоеве от хидрогенскваратни аниони и 3-метилпиридазиниеви катиони, свързани със здрави водородни О−Н⋯О и N−Н⋯О връзки. Новополученото съединение е охарактеризирано в разтвор и в твърдо състояние съответно чрез УВ- и ИЧ-спектроскопия.

Divalent metal ions binding to lactose: a DFT computational study

S. Angelova[1]*, V. Nikolova[2], T. Dudev[2]

[1] Institute of Organic Chemistry with Centre of Phytochemistry, Bulgarian Academy of Sciences, 1113 Sofia, Bulgaria
[2] Faculty of Chemistry and Pharmacy, Sofia University "St. Kl. Ohridski", 1164 Sofia, Bulgaria

In recent years, there has been a growing interest in searching ways to enrich various food products with minerals essential for good health. One of the food products which is important and it is a main part of the people's diet is milk. The main minerals with which the milk is enriched are Ca, Mg, Zn, etc. However, very little information is available about the competition between metals for binding to natural or artificial nutrients in milk. The purpose of this study is to elucidate the factors determining the interactions of lactose, one of the natural ingredients of milk with Ca^{2+}, Mg^{2+} and Zn^{2+} cations. DFT calculations of complexes of lactose and Ca^{2+}, Mg^{2+} and Zn^{2+} cations at M062X/6-31G(d,p) level of theory are performed. The influence of physicochemical properties, such as ionic radius, preferred coordination and hydration numbers of the metal cation, and influence of the medium on the process of metal binding are estimated.

Keywords: lactose, metal binding, calcium, magnesium, zinc.

INTRODUCTION

Dairy products are a popular part of the diet and are perceived to be healthy. They are a reliable source of calcium, a mineral that the body needs for numerous functions, including building and maintaining bones and teeth, nerve impulses transmission, blood clotting, regulation of the heart's rhythm, etc. The calcium bioavailability of milk is good (about 30 to 35%) and much higher than that of plant foods [1, 2]. The difference in the calcium bioavailability is due to the food composition: milk contains components that act synergistically to promote calcium absorption (lactose, vitamin D, casein phosphopeptides) while plant food contain some inhibitory substances, such as oxalates and phytates.

Food fortification (enrichment) is a strategy for decreasing micronutrient malnutrition at the global level ("A world free from hidden hunger" initiative) by increasing the content of essential micronutrients, i. e. vitamins and minerals (including trace elements) in the food [3, 4]. Milk and dairy products are typically fortified with minerals such as Ca, Mg, Fe and Zn [5, 6]. All minerals used as milk fortificants are considered to be a category "A" risk

as they can interact with each other in terms of absorption and high intakes of one may lead to insufficiency of another [7]. The negative effect of high dietary intakes of calcium and phosphorus on zinc absorption as a result of interactive effects has been demonstrated [6]. Zinc is essential for many basic physiological functions; the human body has a limited zinc storage capacity and zinc deficiency can develop very rapidly when intakes are low. A potential mechanism by which calcium interferes with zinc absorption is competition for a divalent cation channel across the brush border membrane [8, 9]. On the other hand calcium levels in the human body have to be balanced with magnesium: adequate levels of magnesium are needed in order to properly use calcium; magnesium deficiency affects calcium metabolism and alters levels of certain hormones that regulate calcium in the body. Several studies have reported that calcium and magnesium intakes influence each other's absorption [10, 11]. Very little information is available about the competition between metals for binding to natural or artificial nutrients in milk [12]. The goal of this paper is to shed light on this issue and examine the interactions between lactose, naturally occurring sugar in milk, which is used as fortificant in some fortified milks for children [13], and calcium, magnesium and zinc ions (also naturally occurring and/or added as mineral fortificants to milk). The sub-aims of the pre-

_____

* To whom all correspondence should be sent:
E-mail: sea@orgchm.bas.bg

sent study are: (a) to clarify whether and to what extent the properties of the metal ion govern the metal binding affinity and selectivity for lactose; (b) to assess the role of external factors such as the dielectric properties of the medium in the process of metal binding and competition in these complexes. In achieving these aims, we conducted DFT calculations combined with the PCM (Polarizable Continuum Model, one of the most widely used implicit continuum solvation model) computations for the complexes resembling Ca^{2+}, Mg^{2+} and Zn^{2+} ions binding to lactose.

COMPUTATIONAL DETAILS

The molecules of galactose, glucose, bare and hydrated metal cations Ca^{2+}, Mg^{2+} and Zn^{2+} and their complexes were optimized using the Gaussian 09 program package [14]. The calculations were performed at M062X/6-31G(d,p) level of theory. This combination method/basis set was chosen because it reliably reproduces the metal – oxygen bond distances in the 1:2 Ca-lactose complex: the M062X/6-31G(d,p) calculated $Ca-O_{lactose}$ average distance, 2.506 Å, is very close to the experimental one – 2.500 Å [15]. All optimized structures were verified to be minima of the potential energy surface by means of frequency calculations. No imaginary frequencies were found for any of the structures. The differences between the products and reactants of electronic energies, ΔE_{el}, thermal energies, including zero-point energy, ΔE_{th}, and entropies, ΔS were used to evaluate the gas-phase free energy of the complex formation, ΔG, at T = 298.15 K according to the equation (PΔV below is a work term):

$$\Delta G = \Delta E_{el} + \Delta E_{th} + P\Delta V - T\Delta S \qquad (1)$$

The influence of the solvent was estimated by PCM (Polarizable Continuum Model) calculations [16, 17] as implemented in the Gaussian 09 [14]. All the structures were fully optimized in water environment ($\varepsilon \approx 78$) and the respective ΔE_{el}^{78}, ΔE_{th}^{78} and ΔS^{78} were used to evaluate the free energy in solution, ΔG^{78} (following eq. 1).

The complex formation is thermodynamically favorable if the calculated value of ΔG is negative, and the process is unfavorable if the value of ΔG is positive.

All the calculations reported herein are corrected for basis set superposition errors (BSSE) using the counterpoise procedure of Boys and Bernardi [18] as coded in Gaussian 09 package [14]. The PyMOL molecular graphics system was used in generating the molecular graphics images [19].

RESULTS AND DISCUSSION

Ca-lactose complex: The crystal structure of the hydrated calcium bromide complex of lactose (4-O-β-D-galactopyranosyl-D-glucopyranose) (Fig. 1; [15]) was taken as a basis for our modeling study (see below). In the experimental structure the calcium ion binds two lactose molecules and four water molecules [15]. First lactose molecule is coordinated to the calcium ion through two oxygen atoms of its galactose moiety and the second one is coordinated through two oxygen atoms of its glucose unit. There are no close contacts between calcium cations and bromide anions (the closest bromide-calcium distance is about 5 Å) [15].

Note that the galactose moiety of the first lactose molecule and the glucose moiety of the second one are not connected directly to the metal and, apparently, do not contribute significantly to the energetics of the complex formation, if at all. Thus, the surrounding of Ca^{2+} can be represented in a simplified manner by using a model in which calcium ion
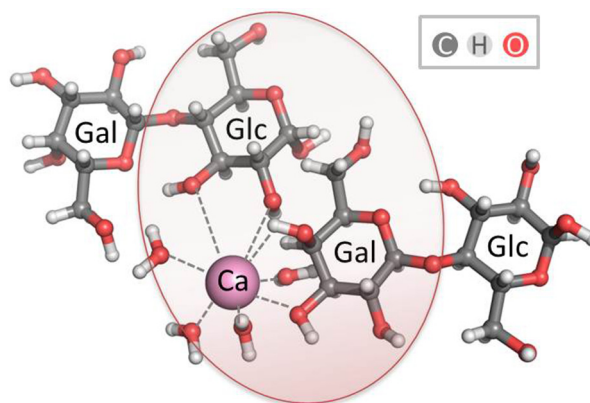

Fig. 1. Environment of the calcium ion in the Ca-lactose complex [15]. Gal = galactose, Glc = glucose.

binds to one galactose molecule, one glucose molecule and four water molecules (Fig. 2). Thus, after omitting the non-metal-coordinating sugar moieties, the immediate surrounding of the calcium cation is preserved the same as in the crystal structure above (Fig. 1): the metal coordination shell is composed of four water molecules and two sugar rings. The resultant construct was fully optimized where the Ca^{2+} cation is octacoordinated to the surrounding ligands (Fig. 2) with metal-oxygen bond distances $Ca^{2+}-O_{glucose/galactose}$ in the range 2.43÷2.69 Å.

Mg- and Zn-lactose model system complexes: Mg^{2+} and Zn^{2+} cations in the respective complexes
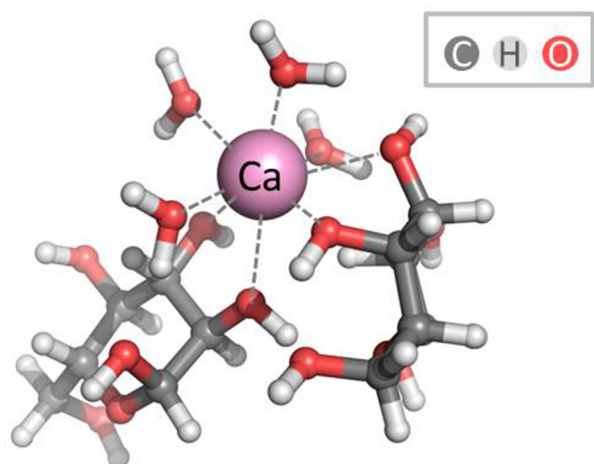
Fig. 2. Fully M062X/6-31G(d,p) optimized structure of the Ca-complex.

were located at the same position as the Ca^{2+} cation in the model system (Fig. 2). The ligand surrounding of the metal entities was also kept the same. The systems were allowed to fully relax upon geometry optimization. The resultant optimized structures of the respective metal complexes are shown in Figure 3. Note that the coordination number of Mg^{2+} and Zn^{2+} cations in the complex was reduced to 6 as the two sugar moieties bind the metal in a monodentate fashion (Fig. 3).

Thermodynamic parameters for the reaction Gal + Glc + M^{2+} + nH_2O →[M-complex]$^{2+}$ with bare metal cations are given in Figure 3. Data presented indicate that there is a rough correlation between the metal cation radius and ΔG values: the smaller the cationic radius is (and higher is the respective charge density of the cation), the more thermodynamically favorable is the complex formation. Ionic
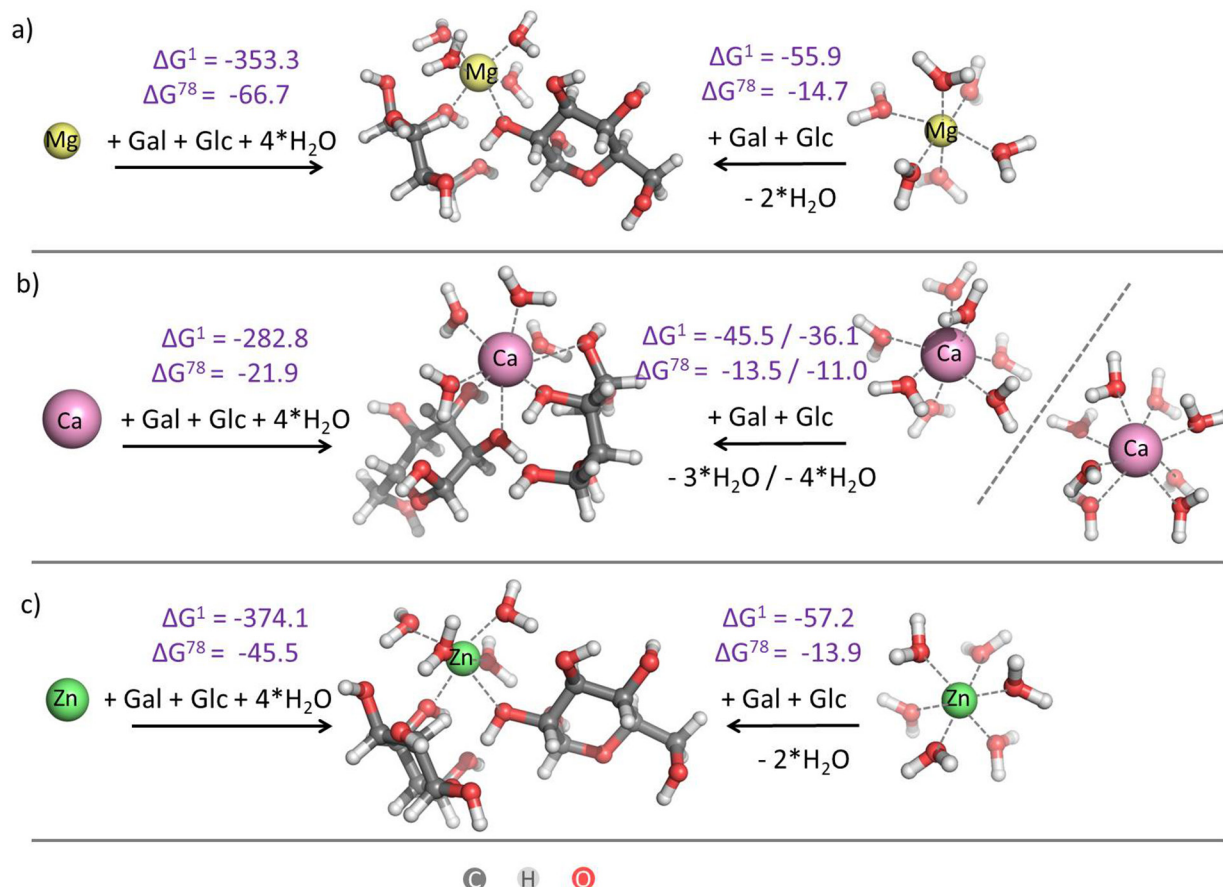
Fig. 3. M062X/6-31G(d,p) optimized structures of Mg^{2+} (a), Ca^{2+} (b) and Zn^{2+} (c) cations bound to a model lactose (middle). The free energies ΔG^1 and ΔG^{78} (in kcal/mol) for the complex formation reactions for non-hydrated (left-hand side) and hydrated metal (right-hand side) cations are shown. ΔG^1 refers to reaction free energy in the gas phase, whereas ΔG^{78} refers to reaction free energies in an environment characterized by an effective dielectric constant of 78 (water).

radii of metal cations and their coordination numbers are presented in Table 1. Mg^{2+} and Zn^{2+} cations in octahedral configuration have smaller ionic radii than Ca^{2+} and the reactions of the complex formation with these cations are characterized by lower ΔG values than their Ca^{2+} counterparts. The higher Louis acidity of Zn^{2+}, as compared to Mg^{2+} and Ca^{2+}, also enhances its competitiveness with respect to its rivals. Calcium cation has a larger ionic radius and the respective ΔG values for the [Ca-complex]$^{2+}$ formation are higher.

Table 1. Effective ionic radii of metal cations (Å) [20]

Cation	Coordination	Ionic radius[a]
Mg^{2+}	VI	0.72
Ca^{2+}	VII	1.06
Ca^{2+}	VIII	1.12
Zn^{2+}	VI	0.74

All of the reactions of the complex formation with bare metal cations are characterized with quite large negative formation free energies in the gas phase. Solvation effects, however, greatly attenuate the free energy gains in the gas phase although the reactions are predicted to be still exergonic (occur spontaneously) in aqueous medium. Since the solvation effects seem to play a significant role in the process, we increased the level of modeling and incorporated water molecules around the cations to take explicitly into account the first hydration shell: metal ions in aqueous solution are hydrated. The structures of the hydrated metal ions in aqueous solution can display a variety of configurations depending on the size and electronic properties of the metal ion. The metal ions with an ionic radius in the range 0.55–0.98 Å are expected to be octahedral, while those with an ionic radius larger than 0.98 Å are expected to have higher coordination numbers [21]. Indeed, the experimentally found hydration numbers and configurations for the studied metals are as follows: for Mg^{2+} and Zn^{2+} – coordination number 6 and regular octahedral configuration; for Ca^{2+} – coordination numbers 7 or 8 and capped octahedron or square antiprismatic configurations, respectively [22, 23]. These basic configurations of the hydrated metal ions ([$Mg(H_2O)_6$]$^{2+}$, [$Ca(H_2O)_7$]$^{2+}$, [$Ca(H_2O)_8$]$^{2+}$, [$Zn(H_2O)_6$]$^{2+}$) in aqueous solution are used to re-model the reaction of complex formation with lactose.

Calculations demonstrate that hydration of the metal cations significantly increase the reaction free energies making the process of the ligands-(hydrated metal cation) complex formation less favorable than that of the respective ligands-(bare metal cations) counterparts. The metal binding to the ligands, however, is still favorable as evidenced by the negative ΔG^1 and ΔG^{78} values in Figure 3. Among the three metal cations, the complex formation with Mg^{2+} and Zn^{2+} cations is appears to be more advantageous than that of the Ca^{2+} complexes (more negative ΔG^1 and ΔG^{78} values for the former than the latter). The reactions with hepta- and octahydrated Ca^{2+} cations are characterized with different free energies as the difference in ΔG^1 values is more pronounced. The model with implicit and explicit water consideration gives ΔG^{78} values for the three metal cations studied in the range of $-14.7 \div -11.0$ kcal/mol.

CONCLUSIONS

By employing density functional theory (DFT) calculations at M062X/6-31G(d,p) level combined with continuum dielectric method (PCM) computations, the thermodynamic descriptors (ΔG^1 and ΔG^{78}) of the metal (Ca^{2+}, Mg^{2+} and Zn^{2+}) binding to a model representing lactose have been evaluated and the interaction between the binding partners assessed. The DFT calculations confirm the experimental findings [8] that Ca^{2+} ion binds favorably to lactose as the free energy of the complex formation is negative. Mg^{2+} and Zn^{2+} can successfully compete with Ca^{2+} ion for the lactose binding as evidenced by the negative (and lower than those for Ca^{2+}) ΔG^1 and ΔG^{78} values.

The calculations reveal few key factors governing the process of Ca^{2+}, Mg^{2+} and Zn^{2+} cations binding to a lactose model system with omitted non-metal-coordinating sugar moieties:
- The physicochemical properties of the metal cation – its ionic radius, coordination and hydration number, and Louis acidity;
- The dielectric properties of the medium.

It can be assumed that naturally occurring and/or added as fortificants to milk Ca^{2+}, Mg^{2+} and Zn^{2+} cations and lactose can interact in a competitive manner.

REFERENCES

1. L. Gueguen, A. Pointillart, *J. Am. Coll. Nutr.*, **19**, 119s (2000).
2. G. Unal, S. N. El, S. Kilic, *Int. J. Food Sci. Nutr.*, **56**, 13 (2005).

3. S. Muthayya, J. H. Rah, J. D. Sugimoto, F. F. Roos, K. Kraemer, R. E. Black, *PLoS ONE*, **8(6)**, e67860 (2013).
4. H. K. Biesalski, Hidden Hunger, Springer-Verlag Berlin Heidelberg, 2013.
5. E. Ocak, R. Rajendram, in: Fortification of Milk with Mineral Elements., V. Preedy, R. Srirajaskanthan, V. Patel (eds.), Humana Press, New York, 2013.
6. S. A. Abrams, S. A. Atkinson, *The Journal of Nutrition*, **133**, 2994S (2003).
7. H. M. Meltzer, A. Aro, N. L. Andersen, B. Koch, J. Alexander, *Public Health Nutr.* **6**, 281 (2003).
8. R. F. Bertolo, W. J. Bettger, S. A. Atkinson, *J. Nutr. Biochem.,* **12**, 73 (2001).
9. R. F. Bertolo, W. J. Bettger, S. A. Atkinson, *J. Nutr. Biochem.,* **12**, 66 (2001).
10. J. Z. Hendrix, N. W. Alcock, R. M. Archibald, *Clinical Chemistry.,* **9**, 734 (1963).
11. Y. Toba, Y. Kajita, R. Masuyama, Y. Takada, K. Suzuki, S. Aoe, *The Journal of Nutrition*, 130, 216 (2000).
12. S. Perales, R. Barbera, M. J. Lagarda, R. Farre, *J. Agric. Food Chem.*, **54**, 4901 (2006).
13. H. Crawley, S. Westland, in: Fortified milks for children: a worldwide review of fortified milks marketed for children over 1 year of age, 2013.
14. M. J. Frisch et al., Gaussian 09, Revision D.01, , Gaussian, Inc., Wallingford CT, 2013.
15. C. E. Bugg, *J. Am. Chem. Soc.*, **95**, 908 (1973).
16. S. Miertuš, E. Scrocco, J. Tomasi, *Chemical Physics*, **55,** 117 (1981).
17. S. Miertuš, V. Frecer, M. Májeková, *J. Mol. Struct: THEOCHEM*, **179**, 353 (1988).
18. S. F. Boys, F. Bernardi, *Mol. Phys.*, **19**, 553 (1970).
19. The PyMOL Molecular Graphics System, 1.7.6.6, Schrödinger, LLC (2015).
20. R. Shannon, *Acta Cryst. A*, **32**, 751 (1976).
21. I. Persson, *Pure Appl. Chem.*, **82**, 1901 (2010).
22. H. Ohtaki, T. Radnai, *Chem. Rev.*, **93**, 1157 (1993).
23. G. Johansson, in: Advances in Inorganic Chemistry, A. G. Sykes (ed), vol. 39, Academic Press, 1992, pp.159–232.

ИЗСЛЕДВАНЕ С ТЕОРИЯ НА ФУНКЦИОНАЛА НА ПЛЪТНОСТТА НА СВЪРЗВАНЕТО НА ДВУВАЛЕНТНИ МЕТАЛНИ ЙОНИ С ЛАКТОЗА

С. Ангелова[1]*, В. Николова[2], Т. Дудев[2]

[1] Институт по органична химия с Център по фитохимия, БАН, 1113 София, България
[2] Факултет по химия и фармация, СУ „Св. Климент Охридски" 1164 София, България

(Резюме)

През последните години нараства интересът към търсене на начини за обогатяване на различни хранителни продукти с минерали, които са полезни за здравето. Един от хранителните продукти, който е важен и е основна част от диетата на хората е млякото. Основните минерали, с които се обогатява млякото са Ca, Mg, Zn и др. Въпреки това все още има малко информация за конкуренцията на свързването на металите с изкуствените и естествени съставки на млякото. Целта на това изследване е да се изяснят факторите, определящи взаимодействието на лактозата, една от естествените съставки на млякото, с Ca^{2+}, Mg^{2+} и Zn^{2+} катиони. Направени са изчисления с теория на функционала на плътността на комплекси на лактоза и Ca^{2+}, Mg^{2+} и Zn^{2+} катиони на ниво M062X/6-31G(d,p). Оценено е влиянието на физикохимичните свойства на металните катиони, като йонен радиус, предпочитано координационно и хидратационно число, оценено е и влиянието на средата върху процеса на метално свързване.

Surface chemical states of cellulose, chitin and chitosan studied by density functional theory and high-resolution photoelectron spectroscopy

K. L. Kostov[1],*, E. Belamie[2, 3], B. Alonso[2], T. Mineva[2]

[1] Institute of General and Inorganic Chemistry, Bulgarian Academy of Sciences, 1113 Sofia, Bulgaria
[2] ICGM-MACS, UMR 5253 CNRS-ENSCM-UM, Institut Charles Gerhardt de Montpellier, 240,
Avenue du Professeur Emile Jeanbrau, 34090 Montpellier cedex 5, France
[3] Ecole Pratique des Hautes Etudes, PSL Research University, 75014 Paris, France

A combined theoretical and experimental approach has been applied to study the 1s electron-energy surface properties of cellulose, chitin, synthesized chitin nanorods and chitosan using density functional theory and high-resolution photoelectron spectroscopy. This allows to reliably distinguish the contributions of surface hydrocarbon impurities in the photoelectron spectra and to examine in detail the chemical states of the polysaccharide surfaces. Although a stoichiometric structure is suggested for the cellulose surface as more likely, a mechanism for possible degradation of the surface including removal of the OH group bonded to glucose ring is also contemplated. The good agreement between theoretical and experimental results allows suggesting a chitosan-like structure for the surfaces of as-prepared chitin and of chitin nanorods. In addition to the dominant concentration of amino NH_2 groups on these surfaces, a small amount of acetyl amine NH_2COCH_3 groups is also observed on the as-prepared chitin. It is possible that protonated amino NH_3^+ functional groups instead of acetyl amine are present on the crystalline surface of chitin nanorods. The possible destructive role of X-ray radiation on the studied surfaces is also discussed.

Keywords: DFT, XPS, cellulose, chitin, chitosan.

1. INTRODUCTION

In the surface area of the solids, the bulk field equilibrium is disturbed, causing a modification of its structure, often accompanied by a change in the chemical state of the surface atoms. On the other hand, the solids interact with the environment through their surfaces, and this process also causes changes in their chemical state. Therefore, in order to understand the mechanism of this interaction, which is of utmost importance for the modern life, the knowledge of the surface chemical state stands out with great significance. Experimentally, the X-ray photoelectron spectroscopy (XPS) is an appropriate method for analyzing the changes in the electron-energy structure of surface atoms and hence their chemical state. Due to the small inelastic free paths of the photoemitted electrons in the order of several nanometers, this method provides chemical information mainly for the top surface atoms. However, due to the variety of chemical bonds involving surface atoms, as in the case of polysaccharide surfaces, the photoelectron spectral regions often show complex structures. Their interpretation requires the use of theoretical methods, among which the methods of density functional theory (DFT) are highlighted. This combined theoretical and experimental approach provides a thorough and reliable analysis of the chemical state of the surface atoms.

Objects of the present study are the surfaces of some polysaccharides (cellulose, chitin, chitosan) and the interest in them is dictated by their extremely wide practical applications (see for example refs. 1–3 and references therein). For example, mats of fibers can be used as technical papers or as textiles for medical applications. In the form of nanorods, crystalline cellulose and chitin possess self-assembly properties leading to interesting applications, notably in optics due to the birefringence of the cholesteric mesophases. These nano-objects can also be used as templates for porous materials with designed textures, very useful in heterogeneous catalysis. Because of these applications, the

* To whom all correspondence should be sent:
E-mail: klkostov@gmail.com

polysaccharides have been studied extensively, but we focus only on those studies concerning the electron-energy structure of surface atoms.

The previous XPS studies have resolved mainly three C 1s peak contributions [4–10] as the first peak at lowest binding energy is attributed to carbon atoms in C-C and C-N bonds, the second peak at higher energies has been assigned as carbons in C-O-C, C-OH and the highest binding-energy third peak is interpreted as due to O-C-O bonding [4, 11]. In our study we are able not only to give more detailed information but also, in some aspects, to give a new interpretation of the experimental results. It seems that in the analysis of the N 1s photoelectron region there is a better consensus in the literature. A lower binding energy has been measured for the amino NH_2 group of chitosan with respect to acetyl amine $NHCOCH_3$ of chitin [4, 5, 7, 11]. The energy difference between them varies within 1.0–1.5 eV. However, it is possible that this varying energy difference is due to the presence of a third chemical state of nitrogen, for example positively charged nitrogen [12–15].

The experimental O 1s photoelectron region of cellulose, chitin and chitosan is less informative showing a broad asymmetric peak which is often fitted with 2 or 3 peak contributions with ambiguous interpretationin the previous studies [4, 7, 9]. All contradictions and incompleteness in characterization of the surface electron structure of cellulose, chitin and chitosan motivate our present study. It uses a combined theoretical (DFT) and experimental (XPS) approach allowing reliable results to be obtained for the stoichiometry and the chemical state of the uppermost layers.

2. EXPERIMENTAL AND THEORETICAL DETAILS

2.1. Apparatus

The X-ray photoelectron experiments have been carried out on AXIS Supra electron spectrometer (Kratos Analytical Ltd., a Shimadzu Group Company) with base vacuum in the analysis chamber of ~10^{-9} mbar. The spectra have been recorded using a monochromatic Al K_α excitation radiation with photon energy of 1486.6 eV. The photoemitted electrons are separated, according to their kinetic energy, by a 180°-hemispherical analyser. The detection system is characterized by hybrid type (electrostatic and magnetic) lenses of the analyser, charge neutralizer operating with low-energy electrons. The used spot size aperture in front of the electrostatic lenses and the analyser pass energy of 20 eV determine an instrumental resolution of

0.54 eV (full width at half maximum (FWHM) of Ag $3d_{5/2}$ peak). However, for isolator samples, the actual resolution is ~0.9 eV (measured by the half-width of the narrowest C 1s peak of cellulose) due to the charging effect caused by the electron photoemission.

The peak positions and areas have been evaluated by a symmetrical Gaussian-Lorentzian curve fitting. The concentrations (in at.%) of the observed chemical elements were calculated by normalizing the areas of the corresponding photoelectron peaks to their relative sensitivity factors using the commercial software of the spectrometer. The accuracy of the binding energy determination is within ± 0.1 eV. The corresponding error in concentration determination is around 1 at.%.

2.2. Theoretical details

All the calculations were carried out with Density Functional Theory based computer program deMon2k [16] with the generalized gradient-corrected PW91 [17] approximation for the exchange-correlation functionals. Empirical dispersion term as implemented in deMon2k was introduced in the geometry optimization [18]. The atoms were described with the double-zeta quality basis sets [19]. The 3-units models of cellulose, chitin and chitosan (see below) were optimized at the same level of theory. The 1s binding energies of carbon and nitrogen were computed using the Slater Transition state approach [20], as generalized later on within DFT by Janak [21]. Following this approach, the binding energy, E_b, is computed from the negative of the orbital energy ε_{1s} occupied by n = 0.5 electron: $E_b(1s) = -\varepsilon_{1s}(n)$.

2.3. Energy calibration

In our previous studies [22–24] the reported XPS results have been obtained using a spectrometer wherein the ultra-high vacuum is achieved by diffusion pumps. The energy scale calibration has been performed by normalizing the C 1s line of adsorbed adventitious hydrocarbons to 284.6 eV (equal to C 1s energy after their adsorption on conductive silver surface). In the present study, oil-free vacuum pumps were used which minimizes the adsorption of such hydrocarbons and their eventual C 1s peak is screened from the intense peaks of C 1s complex structure of studied materials. In this case we used the results from theoretical considerations normalizing the calculated C 1s binding energies of carbons having similar chemical environments as those in a benzene ring to 285 eV. The calibration procedure is similar to that used in our previous study on some coumarin-containing compounds [25].

2.4. Materials

The cellulose sample was purchased from GE Healthcare (Whatman – Chromatography paper 4 Chr, Cat. No. 3004-614). Flakes of chitin provided by France Chitine (http://www.france-chitine.com) and chitosan (high molecular weight, Aldrich) have been also studied. These samples are called "as-prepared chitin" and "as-prepared chitosan", respectively.

The sample of compressed chitin nanorods has been prepared in the Charles Gerhardt Institute (CNRS, Montpellier, France). The average length and diameter of these chitin monocrystalline nanorods are around 260 nm and 3 nm, respectively. The synthesis procedure and the properties of chitin nanorods are described in refs. 26 and 27.

3. RESULTS AND DISCUSSION

3.1. Cellulose

The studied 3-units model (Fig. 1) is constructed based on the bulk structure of cellulose.

The calculated 1s binding energies of the central-unit atoms are shown in Table 1. As mentioned in sect. 2.3 the energy scale is calibrated by normalizing the C 1s core-level energy of C2 carbon atom to 285.0 eV. The C4 and C5 carbon atoms have very close binding energies of 286.47 and 286.50 eV, respectively. Therefore, they would give a common peak contribution to the C 1s photoelectron spectrum with an area twice as large as the individual contributions of the remaining carbon atoms. The energies for the C6 and C3 carbon atoms are around these values, respectively, of 286.64 and 286.28 eV. The
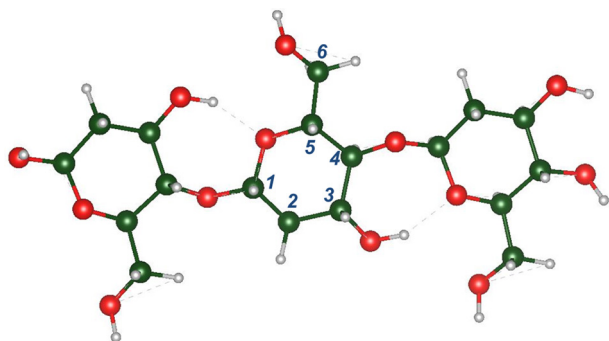
Fig. 1. (Color online) Structural model of cellulose including three units. The carbon and oxygen atoms are colored in green and red, respectively. The small circles with gray contour indicate hydrogen atoms. The hydrogen bonds are also marked with dash gray lines.

lowest C 1s energy of 285.0 eV has been calculated for the C2 carbon atom bonded to two carbon atoms of the glucose ring. Its neighbor, the C1 carbon atom, which is chemically bonded to two oxygen atoms, is characterized by the highest binding energy of 287.75 eV. Therefore, in the cellulose unit, six carbon atoms in five different chemical environments can be identified with concentration ratio of 2:1:1:1:1. Also, four non-equivalent oxygen atoms exist in the structural unit: O1 linked two adjacent glucose rings, O2 from the glucose ring, O3 and O4 from both OH groups bonded to CH_2 group and to the carbon C3 from glucose ring, respectively. Their theoretically calculated O 1s binding energies are also shown in Table 1.

Using the areas of C 1s- and O 1s-peaks and their relative sensitivity factors in XPS the carbon-to-oxygen concentration ratio has been calculated to be C:O = 67:33 (at. %), which is different from the bulk stoichiometric ratio of 60:40 (assuming 6 carbon and 4 oxygen atoms in the cellulose unit). Note that the same concentration ratio of C:O = 67:33 (at.%) can be obtained assuming the presence of 6 carbon atoms and 3 oxygen atoms in the surface unit of the cellulose. On the other hand the calculated concentration ratio suggested an excess of carbon amount which can be explained with the presence of adsorbed hydrocarbon contaminations often measured on the polymer surfaces [28]. Therefore, we can consider two cases: (i) modification of the cellulose surface expressed in removing of one oxygen atom from the structural unit and (ii) the cellulose surface conserves its stoichiometry but there are adsorbed hydrocarbon contaminations.

(i) Modification of the cellulose surface

The approach to detecting eventual surface modification of cellulose involves deconvolution of experimental spectra using the theoretically calculated binding energies from Table 1 for a stoichiometric structural unit of cellulose and analysis of the resulting deviations from this stoichiometry.

The deconvolution of the experimental C 1s spectrum with five peaks with an area ratio equal to the stoichiometric carbon concentration ratio of 2:1:1:1:1 is shown in Fig. 2a.

If the individual fit peaks are interpreted in the manner shown in Table 1, the best match with the theoretical data is obtained. The energy differences (ΔE) between peak maxima of different C 1s fit-contributions and corresponding theoretically calculated values for the C1, C2, C4, C5 and C6 atoms are less than 0.1 eV (Table 1, modified surface). Note that this matching is within the experimental error (± 0.1 eV), which highlights the good agreement between the proposed interpretation and the experimental data for these carbon at-

Table 1. Theoretical 1s binding energies (in eV) of different carbon (C) and oxygen (O) atoms from the central unit of cellulose (see Fig. 1) compared to the experimental values derived by the deconvolutions of photoelectron spectra for modified and unmodified cellulose surface. ΔE is the difference between experimental and theoretical 1s energies

atom, electron-level	theory (eV)	Modified surface		Unmodified surface	
		exp (eV)	ΔE (eV)	exp (eV)	ΔE (eV)
C1	287.75	287.8	0.05	287.8	0.05
C2	285.00	285.0	0	285.0	0
C3	286.28	284.5	−1.78	286.3	0.02
C4	286.47	286.4	−0.07	286.5	0.03
C5	286.50	286.4	−0.10	286.5	0.00
C6	286.64	286.6	−0.04	286.7	0.06
other carbon		~289.0		~289.0	
O1 glyc. bond	535.06	532.8	−2.26	532.8	−2.26
O2 ring	534.96	532.8	−2.16	532.8	−2.16
O3 OH-CH2	535.53	533.3	−2.23	533.3	−2.23
O4 ring-OH	534.57			532.3	−2.27
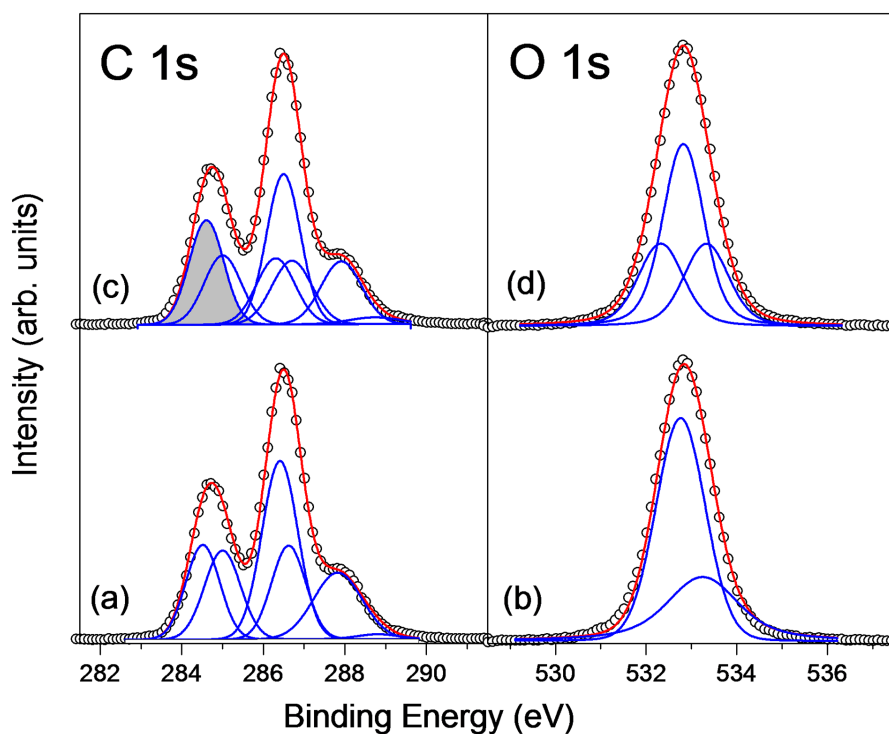
Fig. 2. (Color online) C 1s- and O 1s- photoelectron regions of cellulose (open circles) and their deconvolutions. Spectra (**a** and **b**) corresponds to modified surface by removing of the OH group bonded to glucose ring. Spectra (**c** and **d**) correspond to stoichiometric surface and contain a peak of surface contaminations (colored in gray). The peak contributions and their sum are marked in blue and red, respectively.

oms. However, there is a large exception concerning the carbon atom C3 from the cellulose structural unit (Fig. 1). The deconvolution suggests that its C 1s binding energy should be 284.5 eV instead of 286.3 eV calculated theoretically (Table 1). The difference between the theoretical and experimental C 1s energies of C3 carbon is 1.78 eV, which is too large to be explained by the error of both theoretical and experimental approaches. Most likely, the explanation is in the sensitivity of the experimental method to the upper surface atoms of the cellulose, whereas the theoretical model is based on the cellulose bulk structure. Therefore a large C 1s chemical shift can be proposed for surface C3 carbon atom with respect to its bulk bonding and respectively a chemical modification of this surface atom can be suggested.

As it was mentioned above the experimental concentration ratio has been calculated to be C:O = 67:33 (at.%), which could correspond to the presence of 6 carbon atoms and 3 oxygen atoms in the surface unit of the cellulose. Indeed, the removal of an oxygen atom (respectively the OH group) attached to the C 3 carbon atom would cause a large chemical shift of its C 1s binding energy. In this case the C3 carbon atom could have a similar chemical state like C2 and a close C 1s binding energy, respectively.

The hypothesis for cellulose surface modification connected with the absence of OH group bonded to surface C3 carbon can be proved considering the O 1s core-level results. In contrast to the C 1s region the O 1s spectrum is characterized by a single symmetrical peak at 532.8 eV with half-width (FWHM) of 1.3 eV (Fig. 2b). This makes the interpretation of the chemical states of the individual oxygen atoms in cellulose unit difficult and it can be done only with theoretical help. In Table 1 the calculated O 1s binding energies of the four non-equivalent oxygen atoms from the stoichiometric cellulose unit are shown. It can be seen that the oxygen atoms of the glucose ring and those connecting two adjacent rings have almost the same binding energies of ~ 535.0 eV. Between both hydroxyl groups bonded to the glucose ring and to the C6 carbon atom, respectively, there is an O 1s chemical shift of 1 eV. By using these values, the experimental O 1s spectrum may be fitted with two contributions (2 oxygen atoms related to glucose ring and one oxygen atom from OH group bonded to C6 carbon) with area ratio of 2:1 according the hypothesis of absence of the OH group bound to the glucose ring. The deconvolution may be considered as satisfactory if a relatively broad fit peak of the OH group with a larger Lorenz contribution is allowed (Fig. 2b).

The energy difference of about 2.2 eV between theoretical and experimental fit values exist (Table 1).

This value can be considered as a systematical error related to the energy scale calibration for the different carbon and oxygen atoms. In our study we use for the calibration of O 1s energy the normalization of C 1s binding energy of C5 carbon atom to 285 eV (Table 1). A similar systematical error has been also observed in our previous study of coumarin-containing compounds [25].

(ii) Stoichiometric cellulose surface with adsorbed hydrocarbon contaminations

However, there are indications for another interpretation of the C 1s results that could be more realistic since it is difficult to explain the reasons for removing the OH group from the surface structure of the cellulose. In sect. 2.3 we noted that the hydrocarbon contaminations (CH$_x$) are characterized with C 1s binding energy at 284.6 eV and this value can be used for the energy calibration of photoelectron measurements of nonconductive materials. Also, in the next section 3.2 such a peak of surface contaminations has been detected for chitin and chitosan surfaces. In this connection, the presence of such impurities can also be assumed on the surface of the cellulose. To prove this hypothesis, a new deconvolution of the C1s spectrum has been made using 6 peak contributions: one peak of eventual hydrocarbon impurities at 284.6 eV and 5 other peak contributions of stoichiometric cellulose unit following the theoretically calculated binding energies and the stoichiometric ratio of the areas of these peaks in a 2:1:1:1:1 ratio (Fig. 2c). Within this hypothesis, as shown in Table 1 (unmodified surface), the agreement between the theoretical and experimental data is very good. Also the symmetrical O 1s experimental spectrum can be fitted very well using 3 contributions with area ratio of 1:1:2 (Fig. 2d). These contributions correspond to the four oxygen atoms in the cellulose unit including those from both OH unit groups (O3 and O4) with binding energy difference of 1 eV as mentioned above and also two oxygen atoms (O1 and O2, related to the glucose ring) with equal O 1s-energies at 532.8 eV. Therefore, the area of the last contribution is twice as large as the other peak contributions. The agreement with the theoretically calculated binding energies is again very good if the systematical error of 2.2 eV of the energy scale is neglected (Table. 1).

Also, ignoring the fit peak of proposed contaminations at 284.6 eV, the calculated ratio of carbon and oxygen concentrations of 62:38 is close to the cellulose stoichiometry (60:40). Hence, this second hypothesis (called "unmodified surface") characterizes the cellulose surface as stoichiometric but also containing a certain amount of adsorbed hydrocarbon impurities. The first hypothesis (modified cellulose surface) implies some degree of degradation

of the cellulose chains involving the cleavage of OH groups linked to the glucose ring. Regardless of the realistic nature of this hypothesis, it definitely gives information about a possible mechanism (or at least as a mechanism step) for the degradation of the cellulose surface, which, eventually, could be one of the reasons for the existence of the detected hydrocarbon impurities.

Nevertheless 6 non-equivalent carbon atoms and 4 non-equivalent oxygen atoms exist in the cellulose unit, in the previous studies [29, 30] only two of the measured C 1s-peaks at 286.7 and 288.1 eV are attributed to cellulose carbons in –CH(OH) and –O-CH-O-, respectively. The measured third peak, in ref. 28, at 284.6 eV has been attributed only to contaminations. Two O 1s-peaks have been suggested to exist at 532.9 and 533.5 eV connected to oxygen atoms in -O- and -OH bonding, respectively [29, 30]. In comparison to these studies we are able to give significant more detailed description on the chemical states of different carbon and oxygen atoms and their C 1s- and O 1s-binding energies (Table 1).

For the complete characterization of the C 1s photoelectron spectra, the presence of a low intensity peak at about 289 eV, characteristic of carboxylic carbon, should be noted (Fig. 2a, c). Its negligible amount is an indication for the high quality of the cellulose surface and also for low influence of the X-ray radiation (and also electron exposure from the charge neutralization gun) on cellulose stoichiometry [28].

3.2. Chitin and chitosan

Again, as for cellulose, three-unit structural models of chitin and chitosan have been analyzed theoretically (Fig. 3a and 3b) based on earlier experimental studies (for example refs. 5 and 31). The main difference between both models is the different functional groups connected to the C2 carbon atom: acetyl amine $NHCOCH_3$ for chitin (Fig. 3a) and amino NH_2 group for chitosan (Fig. 3b), respectively.

Now, the C2 atoms have quite different chemical environments than the cellulose C2 carbon atom, which C 1s binding energy has been chosen for the experimental energy-scale calibration (sect. 3.1). Therefore, in the case of chitin and chitosan, another carbon atom should be chosen for energy calibration. Considering the structural models of the polysaccharides (Fig. 1 and Fig. 3), the C5 carbon atom can be proposed as a suitable candidate because it has a similar chemical environment in all three studied compounds. Its calibrated theoretical binding energy for cellulose is at 286.5 eV (Table 1). This value is used to calibrate the calculated C 1s binding-ener-
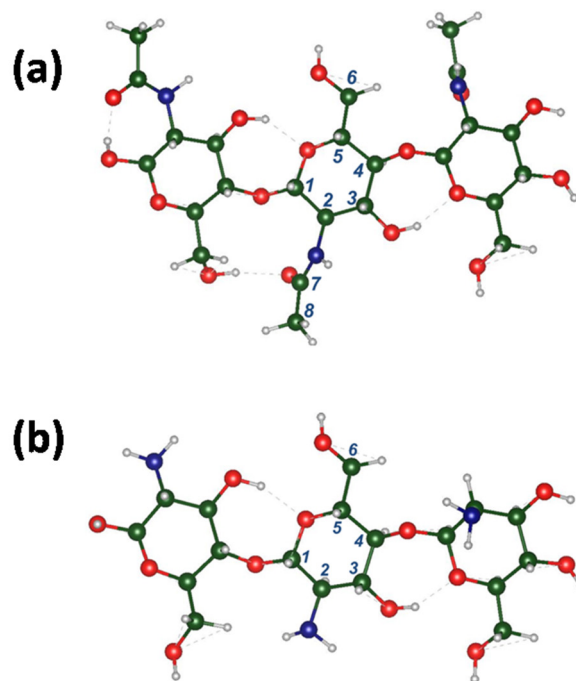
Fig. 3. (Color online) Structural models including 3-units of chitin (**a**) and chitosan (**b**). The carbon and oxygen atoms are colored in green and red, respectively. Blue-colored circles denote nitrogen atoms. The small circles with gray contour indicate hydrogen atoms and the hydrogen bonds are marked with dash gray lines.

gies for chitin and chitosan. The resulting energies are shown in Table 2.

In contrast to cellulose, determination of the corresponding C 1s energies for different carbon atoms of as-prepared chitin, chitin nanorods and as-prepared chitosan is quite difficult because significant deviations from ideal stoichiometry are seen mainly in the contents of carbon atoms. Evidence for this is found in the concentrations of the surface atoms (Table 3).

Also the photoelectron spectra show a complex structure in which individual peak contributions are not as clearly resolved as in the case of cellulose (Fig. 4).

From Table 3 it can be concluded that the contents of nitrogen and oxygen atoms in the case of as-prepared chitosan and chitin nanorods are close to those in the ideal chitosan unit structure. Also, excluding the intense peak at about 284.5 eV, the remainder of the C 1s spectra can be very well matched to the chitosan spectrum and its deconvolutions with chitosan-like contributions give a good agreement with the theoretically calculated binding energies (Table 2). Therefore it seems that the sur-

Table 2. Theoretical 1s binding energies (in eV) of different carbon (C), nitrogen (N) and oxygen (O) atoms from the central units of chitin and chitosan (see Fig. 3) compared to the experimental values for as-prepared chitin, chitin nanorods and as-prepared chitosan derived by the deconvolutions of the photoelectron spectra

Atom	Chitin			Chitosan	
	theory (eV)	as-prepared exp (eV)	nanorods exp (eV)	theory (eV)	exp (eV)
C1	287.31	287.7	287.8	287.36	287. 8
C2	286.67	286.1	286.1	285.43	285.2
C3	286.36	286.1	286.1	286.06	286.1
C4	285.36	285.4	285.4	286.37	286.1
C5	286.50	286.7	286.5	286.50	286.5
C6	286.49	286.7	286.5	286.50	286.5
C7	288.02	288.7	288.5		
C8	285.11	285.3	285.4		
other carbons		284.4	284.5		284.5
N NHCOCH$_3$	401.00	401.0	401.5?		
N NH$_3^+$			401.5?		
N -NH$_2$		399.7	399.6	399.90	399.3
O1 glyc. bond	534.85	532.8	532.7	535.30	532.7
O2 ring	534.17	532.3	532.1	534.80	532.0
O3 OH-CH2	535.73	532.8	532.7	535.38	532.7
O4 ring-OH	535.47	531.6	531.6	534.52	531.7
O5 NHCOCH$_3$	534.02				

Table 3. Concentrations of carbon, nitrogen and oxygen atoms (in at.%) for as-prepared chitin, chitin nanorods and as-prepared chitosan. The experimental values are compared with the ideal concentrations (stoichiometry) and also with the number of the carbon-, nitrogen- and oxygen-atoms in one structural unit of the studied compounds shown below the atomic percentages

		Carbon	Nitrogen	Oxygen
Chitin	exp.	66.5 11.3	5.9 1	27.6 4.7
	ideal	57.1 8	7.1 1	35.7 5
Chitin nanorods	exp.	65.8 9.7	6.8 1	27.4 4.0
	ideal	57.1 8	7.1 1	35.7 5
Chitosan	exp.	73.4 14.1	5.2 1	21.4 4.1
	ideal	54.5 6	9.1 1	36.4 4

face chemical states of chitosan and chitin nanorods are very similar. Note that the individual fit contributions have areas corresponding to the ideal chitosan stoichiometry. For example, each component of the two intensive contributions at about 286.5 and 286.1 eV in Fig. 4c corresponds to two carbon atoms (with close theoretically calculated C 1s binding energies) of the chitosan unit cell. Accordingly, their areas are twice as large as those of the other chitosan components (Fig. 4c). .

As mentioned above, the intense peak contribution at 284. 5 eV is an exception to this ideal chitosan-like structure. Note that the C 1s binding energy of adventitious hydrocarbons adsorbed on silver surface is measured at 284.6 eV (see sect. 2.3). Also, a similar binding energy is received for the surface C2 carbon atom of cellulose (Fig. 4d) existing in CH$_2$ group. Therefore, the lowest energy peak in Fig. 4 can be attributed to CH$_x$ hydrocarbon
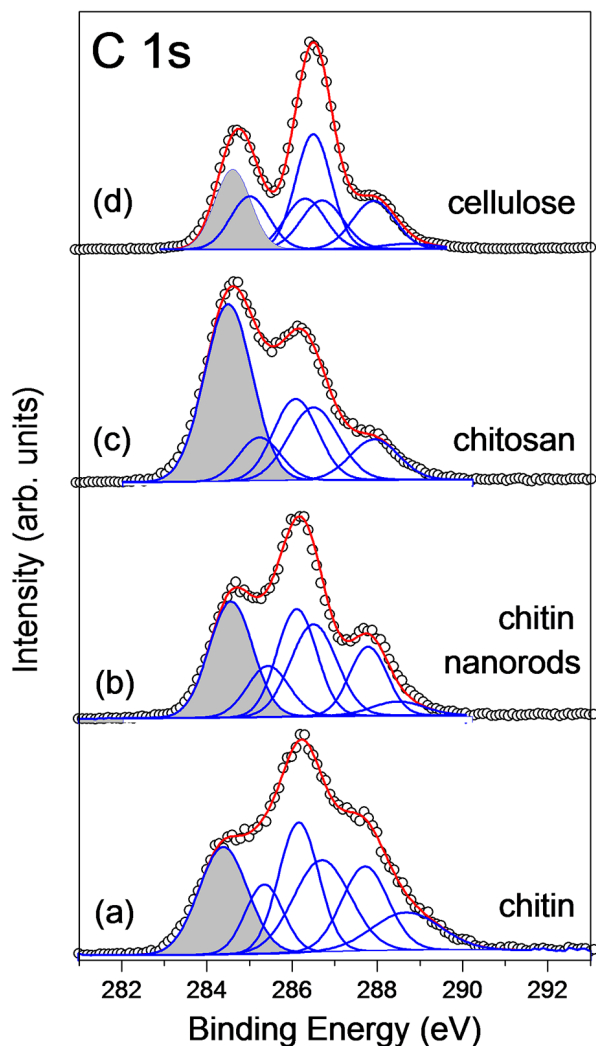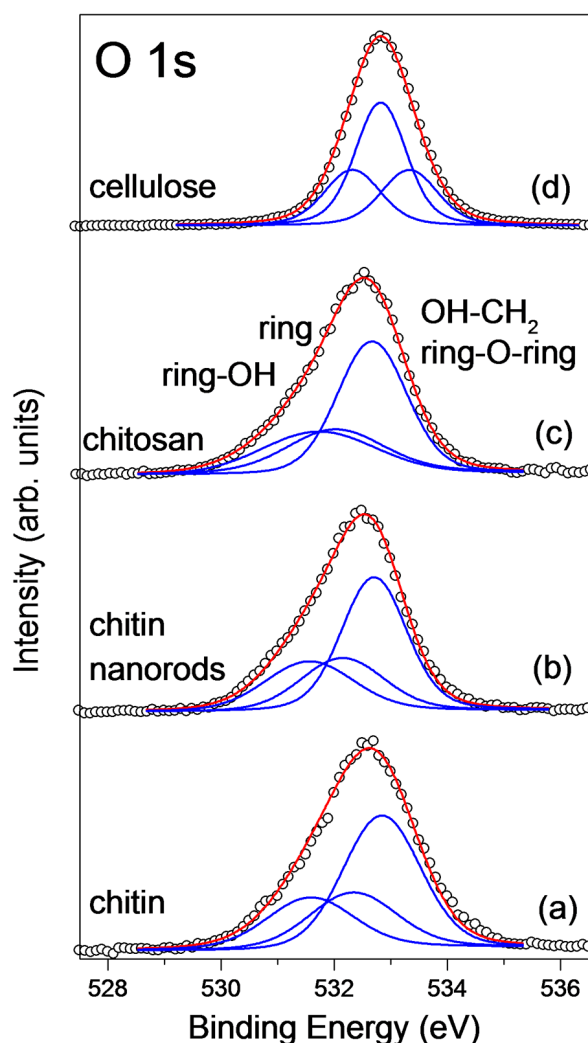
Fig. 4. (Color online) C 1s- photoelectron spectra (open circles) of as-prepared chitin (**a**), chitin nanorods (**b**), as-prepared chitosan (**c**) compared to the spectrum of cellulose (**d**). The peak contributions and their sum are colored in blue and red, respectively. The intense peak contribution corresponding to hydrocarbon contaminations is colored in gray.

Fig. 5. (Color online) N 1s- photoelectron spectra (open circles) of chitin (**a**), chitin nanorods (**b**) and chitosan (**c**). The peak contributions and their sum are colored in blue and red, respectively.

groups adsorbed on the surfaces of the studied materials.

Another exception to the ideal chitosan structure is the additional peak at the highest binding energy of 288.5 eV, which appears in the deconvolution of the as-prepared chitin (Fig. 4a) and to a lesser extent in chitin nanorods spectra (Fig. 4b). According to the theoretical considerations this peak can be attributed to C 1s binding energy of C8 carbon atoms from acetyl amine $NHCOCH_3$ group characteristic for the ideal chitin structure (Table 2). Consequently, surface areas with a chitin-like structure could also provide contributions to the C 1s spectra. This can also reflect the deviations of area ratio of the other

fit peaks from the stoichiometric area ratio of chitosan, which is observed in Fig. 4a and 4b.

The presence of nitrogen in two different chemical states on the surfaces of as-prepared chitin and of compressed chitin nanorods is evident from their N 1s photoelectron spectra (Fig. 5).

A single symmetric N 1s peak at 399.3 eV has been observed for the as-prepared chitosan attributed to nitrogen atom in NH_2 group in agreement with the theoretical calculations (Table 2). For as-prepared chitin and chitin nanorods, an additional less intense peak has been observed at 401.0 and 401.5 eV, respectively (Fig. 5a and 5b). According to the theoretical predictions in Table 2, the higher

binding energy of this peak implies the presence of nitrogen atoms from the acetyl amine $NHCOCH_3$ group. However, the significantly more intense N 1s peaks at about 399.6 eV indicate the dominant presence of amino NH_2 groups in comparison to acetyl amine concentration on both chitin surfaces.

The N 1s results are in agreement with the study of Jiang *et al.* [5] where beside the low- binding energy of nitrogen in NH_2 group another chemical state is found shifted by 2 eV to the higher binding energy. On the other hand, for as-prepared chitin and chitin nanorods an energy difference of 0.5 eV exists between N 1s binding energies for suggested acetyl amine $NHCOCH_3$ groups on both surfaces (Table 2). This energy difference is difficult to be explained because the surfaces show very similar electron-energy structure. It is possible that instead of (or in addition to) acetyl amine group there is more positively charged nitrogen on the surface of chitin nanorods, for example in NH_3^+ configuration. Confirmation for such an interpretation can be found in the N 1s spectrum of adsorbed alanine, where two peaks are observed at 401.8 and 401.3 eV related to NH_3^+ and NH_2 groups, respectively [32]. Note that the energy difference between both nitrogen chemical states is exactly 0.5 eV as in the case of as-prepared chitin and chitin nanorods.

In the structural unit of the chitosan-like surface there are 4 oxygen atoms in different chemical environments: in OH-group bonded to CH_2-functional group, into the glucose ring, between two glucose rings, in OH-group bonded to a carbon of this ring. However the experimental O 1s spectra of the three polysaccharides represent wide peaks with a clear broadening at low binding-energy side (Fig. 6). Together with the above discussed similarities of C 1s regions they indicate similar chemical states of the studied surfaces having most probably a chitosan-like structure.

The detailed contributions of the chemically different oxygen atoms to the photoelectron O 1s spectra can be understood only with the theoretical help. The calculated O 1s binding energies are shown in Table 2 for chitin and chitosan units as a better agreement with the experimental data has been found for the chitosan values. The lowest binding energy at 531.6 eV is obtained for the oxygen atoms of an OH group attached to the glucose ring. This is in agreement with the study of Jiang *et al.* [5] but in contrast to other XPS studies [4, 7, 9] where it has been assumed a lower O 1s binding energy for the oxygen atoms in ring-O-ring than the O 1s energy in OH-C configurations.

The differences between O 1s details of chitosan-like and cellulose surfaces indicate the influence of the amino group. Only the oxygen atom linked two adjacent glucose rings conserves its O 1s binding

energy (Table 1 and 2) whereas a chemical shift of ~0.5 eV is observed for the other oxygens in comparison to the cellulose results. The largest chemical shift of 0.7 eV is found for the OH group bonded to the glucose ring.

Similar to the cellulose surface, a large chemical shift of 1.2 eV is observed between binding energies of both OH-groups bonded to carbon from CH_2 and bonded to the glucose ring, respectively (see Table 1 and Table 2). This is in contrast to the literature where the O 1s contributions of both chemically non-equivalent OH groups from the polysaccharide unit have been assigned to one peak at higher binding energies [4, 7, 9, 15].

Fig. 6. (Color online) O 1s- photoelectron spectra (open circles) of as-prepared chitin (**a**), chitin nanorods (**b**) and as-prepared chitosan (**c**) compared to the spectrum of cellulose (**d**). The peak contributions and their sum are colored in blue and red, respectively. The peak interpretation is indicated on the figure.

From the discussed results it can be seen that their chemical states of chitin surfaces differ from those in their volume. Also, large amounts of surface hydrocarbon contaminations have been measured. The question remains to what extent these surface modifications are caused by the influence of the experimental method, i.e. the X-ray radiation and electron exposure. Such influences may be significant in the case of organic substances. For example, in the XPS study of brewer's yeast strains [33], their degradation during experiments have been observed reflected in an increase in surface hydrocarbon contaminations and decrease in the relative surface concentrations of nitrogen and oxygen atoms. Although in this sensitive case, the degradation cannot mask the real properties of the materials, the influence of the X-ray radiation should be carefully examined [28]. In fact, the eventual modifications can be caused not only by X-ray radiation, but mainly by the inelastic scattering of emitted photoelectrons as shown by Graham *et al.* studying organic layers [34].

We have investigated this eventual effect by varying the flux of X-ray radiation, respectively the X-ray power. Our measurements have been carried out at low powers (75–150 W) where no changes in the spectra with the analysis time have been observed. At high X-ray source power of 300–450 W a slight change of the analyzing-area color is visible accompanied with the small intensity increase of the low binding energy peak at 284.5 eV, which is interpreted as due to surface hydrocarbon contaminations. However, even in this case the other main features of the surface spectra are not affected.

4. CONCLUSIONS

The results show that, despite the high resolution and signal strength of the experimental method XPS, reliable analysis is achieved only in combination with theoretical modeling. This approach allows both the concrete understanding of the experimental C 1s-, O 1s-, N 1s- photoelectron spectra, but also the processes leading to the surface chemical modifications.

In the case of cellulose, its C 1s- and O 1s-photoelectron spectra can be described in details following the theoretical interpretation based on the stoichiometry preservation in the surface layers. The comparison with the theoretical calculations allows identifying a peak of surface hydrocarbon contaminations in the complex C 1s spectrum. Moreover, it allows suggesting a mechanism for degradation of the surface related to removal of surface OH group bonded to the glucose ring. This is accompanied by a decrease in C 1s binding energy of the corresponding carbon atom from the ring to 284.5 eV, exactly at the energy position characteristic for the hydrocarbon contaminations. Therefore, the removal of the OH group could be considered as a step in the process of creating surface hydrocarbon impurities.

An intense C 1s peak at 284.5 eV, attributed to surface hydrocarbon contaminations, is also observed for the studied chitin- and chitosan surfaces. Excluding this peak, the rest of their spectra can be well matched to the chitosan spectrum based on the theoretical predictions. According to these proposed chitosan-like structure of the chitin surfaces, the XPS results show a dominant concentration of surface amino NH_2 group. Additionally a small amount of acetyl amine NH_2COCH_3 is also found. For the monocrystalline surface of chitin nanorods, the presence of protonated nitrogen configuration, for example NH_3^+, is not excluded.

The experimental cellulose-, chitin- and chitosan-O 1s spectra can be very well described using theoretically calculated binding energies for the stoichiometric structural unit of corresponding polysaccharide. In contrast to the previous studies a large chemical shift of 1.0–1.2 eV is observed between O 1s energies for both non-equivalent OH-groups from the functional groups of all three polysaccharides.

Within the X-ray fluxes used (X-ray source power of 75–150 W), no spectra change is observed showing that the observed surface chemical modifications of the studied polysaccharides cannot be caused by the X-ray exposure during the experimental analysis.

REFERENCES

1. M. N. V. Ravi Kumar, *React. Funct. Polymers*, **46**, 1 (2000).
2. A. Bhatnagar, M. Sillanpää, *Adv. Coll. Interface Science.*, **152** , 26 (2009).
3. R. Jayakumar, M. Prabaharan, S. V. Nair, S. Tokura, H. Tamura, N. Selvamurugan, *Progress in Materials Science*, **55**, 675 (2010).
4. L. J. Matienzo, S. K. Winnacker, *Macromol. Mater. Eng.*, **287**, 871 (2002).
5. H. Jiang, J. Liang, J. T. Grant, W. Su, T. J. Bunning, T. M. Cooper, W. W. Adams, *Macromol. Chem. Phys.*, **198**, 1561 (1997).

6. Y. Wang, S. Yin, L. Ren, L. Zhao, *Biomed. Mater.*, **4**, 035003 (2009).

7. J. Chen, K. Nan, S. Yin, Y. Wang, T. Wu, Q. Zhang, *Colloids and Surfaces B: Biointerfaces*, **81**, 640 (2010).

8. A. Di Giuseppe, M. Crucianelli, M. Passacantando, S. Nisi, R. Saladino, *J. Catal.*, **276**, 412 (2010).

9. J. Li, J.-F. Revol, R. H. Marchessault, *J. Coll. Interface Science*, **192**, 447 (1997).

10. J. Wang, Z. Wang, J. Li, B. Wang, J. Liu, P. Chen, M. Miao, Q. Gu, *Carbohydrate Polymers*, **87**, 784 (2012).

11. M. C. Burrell, M. D. Butts, D. Derr, S. Genovese, R. J. Perry, *Appl. Surface Sci.*, **227**, 1 (2004).

12. G. Lawrie, I. Keen, B. Drew, A. Chandler-Temple, L. Rintoul, P. Fredericks, L. Grundahl, *Biomacro-molecules*, **8**, 2533 (2007).

13. F. Chen, Z. Shi, K. G. Neoh, E. T. Kang, *Biotech. Bioeng.*, **104**, 30 (2009).

14. Y. Liua, X.-W. Shi, E. Kim, L. M. Robinson, C. K. Nye, R. Ghodssi, G. W. Rubloff, W. E. Bentleye, G. F. Payne, *Carbohydrate Polymers*, **84**, 704 (2011).

15. H. Maachou, M. J. Genet, D. Aliouche, C. C. Dupont-Gillain, P. G. Rouxhet, *Surf. Interface Anal.*, **45**, 1088 (2013).

16. G. Geudtner, P. Calaminici, J. Carmona-Espíndola, J. M. delCampo, V. D. Domínguez-Soria, R. F. Moreno, G. U. Gamboa, A. Goursot, A. M. Köster, J. U. Reveles, T. Mineva, J. M. Vásquez-Pérez, A. Vela, B. Zúñinga-Gutierrez, D. R. Salahub, *Wiley Interdiscip. Rev.: Comput. Mol. Sci.*, **2**, 548 (2012).

17. J. P. Perdew, Y. Wang, *Phys. Rev. B*, **46**, 12947 (1992).

18. A. Goursot, T. Mineva, R. Kevorkyants, D. Talbi, *J. Chem. Theory Comput.*, **3**, 755 (2007).

19. N. Godbout, D. R. Salahub, J. Andzelm, E. Wimmer, *Can. J. Chem.*, **70**, 560 (1992).

20. J. C. Slater, *Phys. Rev.*, **34**, 1293 (1929).

21. J. F. Janak, *Phys. Rev. B*, **18**, 7165 (1978).

22. A. Sachse, V. Hulea, K. L. Kostov, N. Marcotte, M. Y. Boltoeva, E. Belamie, B. Alonso, *Chem. Commun.*, **48**, 10648 (2012).

23. A. Sachse, V. Hulea, K. L. Kostov, E. Belamie, B. Alonso, *Catal. Sci. Technol.*, **5**, 415 (2015).

24. A. Sachse, L. Cardoso, K. L. Kostov, C. Gerardin, E. Belamie, B. Alonso, *Chem. Eur. J.*, **21**, 3206 (2015).

25. N. I. Petkova, R. D. Nikolova, K. L. Kostov, T. Mineva, G. N. Vayssilov, *J. Phys. Chem. A*, **118**, 11062 (2014).

26. E. Belamie, P. Davidson, M. M. Giraud-Guille, *J. Phys. Chem. B*, **108**, 14991 (2004).

27. B. Alonso, E. Belamie, *Angew. Chem. Int. Ed.*, **49**, 8201 (2010).

28. L.-S. Johansson, J. M. Campbell, *Surf. Interface Anal.*, **36**, 1018 (2004).

29. S. Danielache, M. Mizumo, S. Shimada, K. Endo, T. Ida, K. Takaoka, E. Kurmaev, *Polymer Journal*, **37**, 21 (2005).

30. G. Beamson, D. Briggs, High Resolution XPS of Organic Polymers. The Scienta ESCA 3000 Database, John Wiley &Sons, Inc., Chichester, UK, 1992.

31. D. Carlstrom, *J. Biophysic. Biochem. Cyto.*, **3**, 669 (1957).

32. Y. K. Gao, F. Traeger, O. Shekhah, H. Idriss, C. Woell, *J. Coll. Interface Science*, **338**, 16 (2009).

33. P. B. Dengis, P. A. Gerin, P. G. Rouxhet, *Colloids Surfaces B: Biointerfaces*, **4**, 199 (1995).

34. R. L. Graham, C. D. Bain, H. A. Biebuyck, P. E. Laibinis, G. M. Whitesides, *J. Phys. Chem.*, **97**, 9456 (1993).

ХИМИЧЕСКИ СЪСТОЯНИЯ НА ПОВЪРХНОСТИТЕ НА ЦЕЛУЛОЗА, ХИТИН И ХИТОЗАН, ИЗСЛЕДВАНИ ЧРЕЗ ТЕОРИЯТА НА ФУНКЦИОНАЛА НА ПЛЪТНОСТТА И ФОТОЕЛЕКТРОННА СПЕКТРОСКОПИЯ С ВИСОКА РАЗДЕЛИТЕЛНА СПОСОБНОСТ

К. Л. Костов[1], Е. Белами[2, 3], Б. Алонсо[2], Ц. Минева[2]

[1] Институт по обща и неорганична химия, Българска академия на науките, 1113 София, България
[2] Институт Шарл Герар на Монпелие-Френски национален център за научни изследвания,
Университет на Монпелие – Висше национално училище по химия на Монпелие,
Авеню Проф. Емил Жанбро, 34090 Монпелие, Франция
[3] Практическо училище за висши науки, Изследователски университет, 75014 Париж, Франция

(Резюме)

Комбиниран теоретичен и експериментален подход е приложен в изследването на електронните 1s енергетични свойства на повърхностите на целулоза, хитин, синтезирани хитинови нано-пръчки и хитозан, използвайки теорията на функционала на плътността и фотоелектронна спектроскопия с висока разделителна способност. Това позволява надеждно да се различат приносите на повърхностните въглеводородни замърсявания във фотоелектронните спектри и да се оцени в детайли химическите състояния на полизахаридните повърхности. Въпреки че е предположена стехиометрична структура на целулозната повърхност като най-вероятна, е разгледан и механизъм за възможна деградация на повърхността, включващ отстраняване на OH-групата, свързана към глюкозения ринг. Доброто съответствие между теоретичните и експериментални резултати позволява да се предположи хитозан-подобна структура за повърхностите на хитина и хитиновите нанопръчки. В допълнение към доминиращата концентрация на амино NH_2 групи върху тези повърхности, се наблюдава и малко количество ацетил-аминови NH_2COCH_3 групи върху хитина. Възможно е присъствието на протонирани амино NH_3^+ функционални групи, вместо ацетил-аминови, върху кристалните повърхности на хитиновите нанопръчки. Дискутирана е и възможната деструктивна роля на рентгеновото облъчване върху изследваните повърхности.

IR spectral and structural changes caused by the conversion of salophen into oxyanion and dianion

S. Stoyanov, E. Velcheva, B. Stamboliyska*

Institute of Organic Chemistry, Centre of Phytochemistry, Bulgarian Academy of Sciences, Acad. G. Bonchev Str. Bl. 9, Sofia, 1113, Bulgaria

The structures of salophen molecule its oxyanion and dianion have been studied by means of both IR spectra and DFT calculation, employing the B3LYP functional and 6-311++G** basis set. The solvent effect was simulated by using self-consistent the integral equation formalism variant (IEFPCM) model. A good agreement has been found between the theoretical and experimental vibrational characteristic of the particles studied. The theoretical method used gives a good description on the strong spectral changes caused by the conversion of the salophen into anion and dianion. The structural changes which accompany these conversions are also essential. Analysis of the atomic charge changes shows that the first (oxyanionic) charge remains localized mainly within the oxyphenylene fragment while the second (nitranionic) charge spreads mainly over the acetanilide fragment.

Keywords: IR; DFT; Acetaminosalol; Oxyanion; Dianion.

INTRODUCTION

Organic anions are key to many chemical and biological processes and their important role in the synthesis, design of functional materials and drugs induce numerous studies within the field of organic chemistry and all interfacing disciplines [*e.g.* 1–5]. A better knowledge of the structure of organic anions is an essential point in understanding the mechanism of their actions. However, the highly reactive nature of anionic species has limited their structural characterization. The conversions of neutral molecule into anions (oxyanions, carbanions, azanion, dianions, radical-anions, *etc.*) are accompanied by essential changes in the vibration spectra. So, these changes are very informative for the structural variations caused by the same conversions [6]. The structure of large series of organic molecules and their anions have been successfully studied recently on the basis of experimental IR spectra combined with DFT/ computations [7–13]. The title compound is an interesting and convenient object of the molecule → anion→ dianion conversion investigations, as it contains (–OH) and (-CO-NH-) acidic functional groups and can be converted successively into oxyanion and dianion.

Salophen (Phenetsal, Acetaminosalol, (4-acetamidophenyl) 2-hydroxybenzoate) is an ester of salicylic acid and acetaminophenol, used as an antirheumatic, antipyretic, analgesic and intestinal antiseptic [14]. Due to its antimicrobial function, salophen is used as an ingredient in cosmetic products, pharmaceutical compositions, surgical materials, *etc.* [15]. Crystal structure of salophen was recently determined experimentally [16]. Its IR spectra in KBr are included in many databases [14]. Infrared linear dichroic and Raman spectroscopic approach for determination of salophen in binary solid mixtures with caffeine was reported [17]. Neither the detailed IR spectra nor structure of oxyanion and dianion of salophen have been studied theoretically or experimentally. The purpose of the present investigation is to follow the spectral and structural changes, caused by the conversion of salophen molecule into the corresponding anions on the basis of both DFT computations and spectroscopic experiments. Its relative predictive capabilities are evaluated by comparing the theoretically predicted and experimentally frequencies measured in DMSO

EXPERIMENTAL AND COMPUTATION

Salophen (Sigma–Aldrich) was used without additional purification. The salophen anion was prepared by adding solutions of the parent compound in

---

* To whom all correspondence should be sent:
E-mail: bs@orgchm.bas.bg

dimethyl sulfoxide (DMSO) and DMSO-d$_6$ (Fluka) to equimolar quality of dry alkali-metal methoxides and methoxides-d$_3$. The suspensions obtained were stirred for 1 min and then filtered through a siringe-filter. The conversion was practically complete (Fig. 1(A) and Fig. 1(B)). The dianion salophen was prepared by reacting DMSO and DMSO-d$_6$ solutions of the parent compound with an excess of dry alkali-metal methoxides and methoxides-d$_3$. The conversion was also practically complete: in the spectra we found neither the bands of salophen nor those of its anion (cf. Fig. 1(A-C)). The IR spectra were recorded at a resolution of 1 cm^{-1}, by 64 scans on a Tensor 27 FTIR spectrophotometer in a CaF$_2$ cell of 0.13 mm path length for solutions, spectra of the solid state sample were obtained by ATR technique and in KBr pellet.

The quantum chemical calculations the Natural bond orbital (NBO) population analysis [18] were performed using the Gaussian 09 package [19]. The geometry optimizations of the structures investigated were done without symmetry restrictions, using density functional theory (DFT). We employed B3LYP hybrid functional, which combines Becke's three-parameter nonlocal exchange with the correlation functional of Lee et al. [20, 21], adopting 6-311++G** basis sets. To estimate the effect of the solvent (DMSO) on the infrared spectra of studied species, we applied the integral equation formalism of polarizable continuum model (IEFPCM), proposed by Tomasi and coworkers [22, 23]. The stationary points found on the molecular potential energy hypersurfaces were characterized using standard harmonic vibrational analysis. For a better correspondence between experimental and calculated values, we modified the results using the empirical scaling factors. The relative predictive capability of theoretical method used is evaluated by comparing the theoretically predicted and experimentally frequencies measured in DMSO.

RESULTS AND DISCUSSION

Energy analysis

All conformers of salophen and its deprotonated forms were determined from rotation about Ph-N, and N-C, C-O, C-CO bonds. The structures of the most stable conformers are shown in Scheme 1.

Both structures of molecule and anion correspond to *trans*-type conformers with respect to the NH and amide carbonyl groups and *cis*-type conformers with respect to hydroxyl and the ester carbonyl group. The presence of the same conformer for the molecule was also established by crystallographic analysis [16].
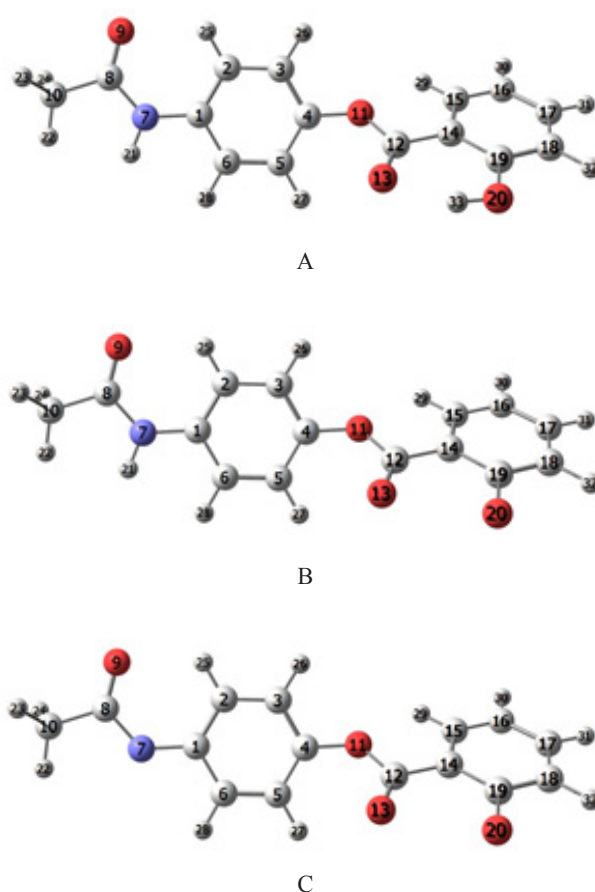
Scheme 1. B3LYP/6311++G** optimized structures of the most stable conformers of molecule A and its oxyanion B and dianion C.

The calculated total energies of the studied species are as follow:

E_{tot} = –935.3485099 H for the salophen molecule A
E_{tot} = –934.8173745 H for the salophen oxyanion B
E_{tot} = –934.1777714 H for the salophen dianion C.

The following deprotonation energies correspond to the above values (see also Scheme 1):

$E^d = E_{tot}(B) – E_{tot}(A) = 1394.230239$ kJ mol^{-1};
$E^d = E_{tot}(C) – E_{tot}(B) = 1668.595$ kJ mol^{-1}.

The energy difference E^d is related to the gas-phase Broensted acidities, and can be used as an approximate measure of these acidities in polar aprotic solvents [24]: low E^d → high acidities → low pKa values. For comparison, the first deprotonation energy is lower than E^d of acedoben (1448.1 kJ mol^{-1}), acetanilide (1489.06 kJ mol^{-1} [12]) and higher than E^d of the stronger acid acesulfame (1324.31 kJ mol^{-1}

[8], in agreement with the experimentally estimated pKa value of 7.87. The second deprotonation energy is essentially higher, and can be compared with the second deprotonation energy of acedoben (1734.1 kJ mol^{-1} [13]). This result is not surprising, having in mind that the products of the second deprotonation are in fact dianions.

Infrared analysis

Let us consider consecutively the IR data of the species studied, which will make it possible to specify the spectral changes, caused by the conversion of the salophen molecule into corresponding anions.

The experimental IR spectra of salophen, measured in DMSO-d$_6$ solution and in solid state (ATR) are shown in Fig. 1.

Based on the differences in the DMSO and solid state spectra in the carbonyl region, it could be assumed that two different forms are present – with and without intramolecular hydrogen bond. The strong intramolecular OH...O=C hydrogen bond existing in solid state produces a C=O ester stretching band with maximum at 1680 cm^{-1}. The DMSO as polar aprotic solvent usually decreases the frequencies of polar groups. But in IR spectra of salophen in solvent this ν(CO) band occurs at a higher frequency (1740 cm^{-1}, Fig. 1), because DMSO breaks the intramolecular hydrogen bond. For this reason

we compared the experimental vibrational characteristics with the calculated ones of conformer, in which the carbonyl group is not intramolecularly hydrogen bonded. It can be seen in Figure 1 that the amide band ν(C=O) is shifted in the solution with 26 cm^{-1}. The numerical values of experimental vibrational characteristics are listed together with the theoretical ones in Table 1. The agreement between the experimental and calculated values is very good – the mean absolute deviation between observed and calculated frequencies is 8.3 cm^{-1}, which value is not away from the lower border of the 8–16 cm^{-1} interval of deviations, typical for the DFT calculations for molecules containing carbonyl groups [8–13].

No experimental data for the ν(OH) and ν(NH) bands were given in the Table 1, as they form a multiplet because of the formation of hydrogen bonds mainly with the solvent. The assignment of the experimental bands to the calculated normal modes in the C–H stretching region (3100–2800 cm^{-1}) is not obvious because there are fewer bands in the experimental spectrum than predicted by the calculations. The highest frequency experimental bands observed in the IR spectrum (3200–3000 cm^{-1}) are assigned to the aromatic C–H stretches, while the lower frequency bands are attributed to the methyl group motions. The calculations resolved and located well the two carbonyl stretching vibrations, those
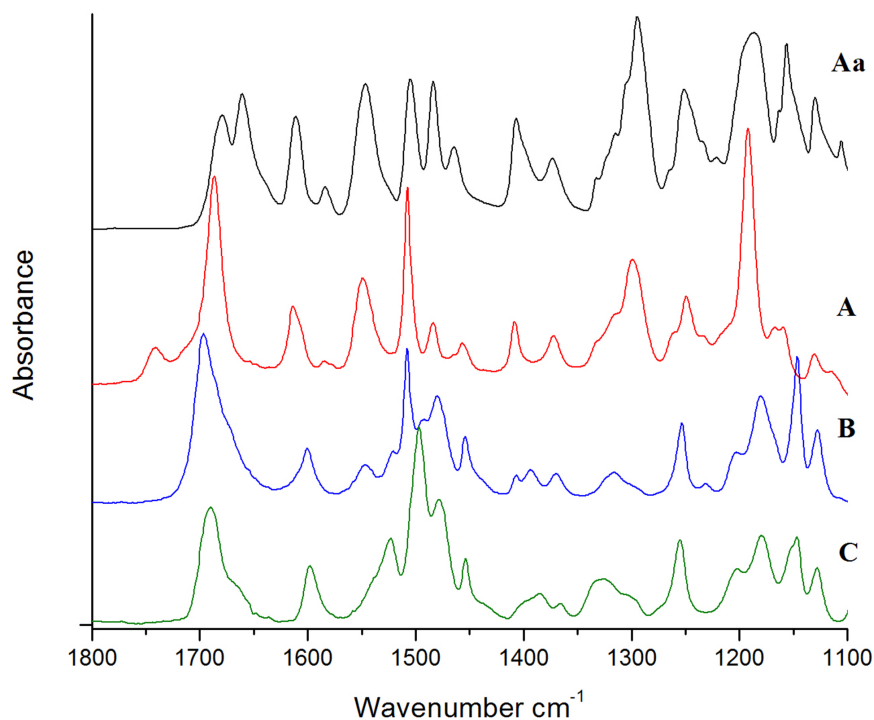
Fig. 1. ATR-FTIR spectrum of salophen (Aa); Infrared spectra of salophen (A), its oxyanion (B) and its dianion (C) in DMSO-d$_6$.

Table 1. Theoretical (B3LYP/6-311++G**) and experimental (solvent DMSO-d_6) vibrational frequencies (in cm^{-1}) and IR integrated intensities (A in km.mol^{-1}) of salophen

No.	$\nu_{calc.}$ [a]	A	Assignments	$\nu_{exp.}$
1.	1739	716.4	ν(C=O) (ester group)	1741
2.	1688	452.8	ν(C=O) (amide group)	1686
3.	1633	32.6	ν^{Ph}(CC), δ^{Ph}(CCH)	
4.	1629	147.3	ν^{Ph}(CC), δ^{Ph}(CCH)	1606
5.	1626	65.7	ν^{Ph}(CC), δ^{Ph}(CCH)	
6.	1609	62.2	ν^{Ph}(CC), δ^{Ph}(CCH)	1584
7.	1543	516.8	δ(HNC), ν(N-C)	1549
8.	1523	322.6	δ^{Ph}(CCH), ν^{Ph}(CC)	
9.	1515	106.5	δ^{Ph}(CCH), δ(HOC)	1507
10.	1473	26.7	δ(CH$_3$)	1483
11.	1466	89.4	δ^{Ph}(CCH), ν^{Ph}(CC)	1467
12.	1455	13.5	δ(CH$_3$)	1456
13.	1419	103.8	δ^{Ph}(CCH), δ(HNC)	1408
14.	1390	58.0	δ(CH$_3$)	
15.	1358	60.7	δ(HOC)	1372
16.	1331	155.7	ν(CN), ν^{Ph}(Ph-N)	1332
17.	1328	133.1	ν(Ph-OC), ν(C-OH)	1319
18.	1316	12.4	δ^{Ph}(CCH), δ(HNC)	
19.	1287	111.4	ν(C-OH)	1299
20.	1263	101.3	ν(C-CH$_3$), ν(Ph-N), ν(CN)	1263
21.	1236	250.7	δ^{Ph}(CCH), ν(Ph-CO)	1249
22.	1230	35.0	ν(Ph-N), δ(CH$_3$)	1233
23.	1194	753.0	ν(Ph-OC)	1192
24.	1192	68.1	δ^{Ph}(CCH), δ(HOC)	
25.	1177	21.0	δ^{Ph}(CCH), ν^{Ph}(CC)	1167
26.	1175	260.1	δ^{Ph}(CCH), ν^{Ph}(CC)	1159
27.	1133	228.4	δ^{Ph}(CCC), ν^{Ph}(CC)	1130
28.	1123	20.9	δ^{Ph}(CCC), ν^{Ph}(CC)	1116
29.	1061	29.9	δ^{Ph}(CCH), ν^{Ph}(CC)	

[a] Scaled by 0.993. [b] Vibrational modes: ν, stretching; δ, bendings. The numbers before the mode symbols indicate % contribution (10 or more) of a given mode to the corresponding normal vibration, according to the potential energy distribution.

of the ester and the amide groups, at 1739 cm^{-1} and 1688 cm^{-1}, respectively. The theory does not reproduce qualitatively well the high integral intensities for the carbonyl bands in the experimental spectrum. DFT calculations predicted well also the IR frequencies of the amide-II and amide-III vibrations measured in DMSO. The amide-II mode δ(HNC) is predicted to appear at 1544 cm^{-1} as a very intense band. Experimentally, a very strong band was detected at 1549 cm^{-1} in DMSO. The stretching ν(N-C) coupled with ν(Ph-N), denoted as amide-III was predicted and measured as an intensive band at 1332 cm^{-1}. The highest intensity band in the theoretical and experimental spectrum at 1192 cm^{-1} is assigned to ν(Ph-CO).

The experimental spectrum of salophen anion in DMSO solvent is shown in Fig. 1(B). It is known that in this solvent the ions exist as free species and there are no anion/counter ion interactions [25]. The

influence of the counterions on the frequencies is neglectful. This makes it possible to compare, in this work, the experimental infrared data for the anions with the theoretical ones. The numerical values of the experimental vibrational data in DMSO-d_6 are listed with the theoretical ones in Table 2.

As above we can find there a good agreement between experimental and scaled theoretical frequencies. The mean deviation between them is 5.6 cm^{-1}. In full agreement between theory and experiment, the conversion of the salophen molecule into the oxyanion is accompanied by an essential decrease in frequency of ester ν(CO) band: predicted 39 cm^{-1}, measured 45 cm^{-1} and has only a weak effect on the amide ν(CO) frequency: predicted decrease 4 cm^{-1}, measured 2 cm^{-1} (Tables 1 and 2; Fig. 1). The shifting between the two carbonyl frequencies expected in this case should amount to a 16 cm^{-1} and it is in agreement with the experimental measured after

Table 2. Theoretical (B3LYP/6-311++G** and experimental (solvent DMSO-d_6) vibrational frequencies (ν in cm^{-1}) and IR integrated intensities (A in km mol^{-1}) of salophen anion

No.	$\nu_{calc.}$ [a]	A	Assignments	$\nu_{exp.}$
1.	1700	1224.8	ν(C=O) (ester group)	1696
2.	1684	469.3	ν(C=O) (amide group)	1684
3.	1633	18.8	ν^{Ph}(CC), δ^{Ph}(CCH)	
4.	1622	83.8	ν^{Ph}(CC), δ^{Ph}(CCH)	
5.	1618	211.4	ν^{Ph}(CC), δ^{Ph}(CCH)	1601
6.	1540	535.9	δ(HNC), ν(N-C)	1546
7.	1529	192.7	δ^{Ph}(CCH)	1521
8.	1522	426.7	δ^{Ph}(CCH), ν^{Ph}(CC)	1508
9.	1483	604.8	ν(C-O$^-$)	1492
10.	1473	194.5	δ(CH$_3$)	1481
11.	1469	27.8	δ^{Ph}(CCH)	1470
12.	1455	13.4	δ(CH$_3$)	1454
13.	1418	91.9	δ^{Ph}(CCH), δ(HNC)	1406
14.	1389	57.8	δ(CH$_3$)	1393
15.	1389	48.3	δ^{Ph}(CCH)	1369
16.	1329	174.4	ν(CN), ν^{Ph}(CC)	1325
17.	1316	14.9	ν(Ph-OC)	1316
18.	1313	6.2	δ^{Ph}(CCH), δ(HNC)	
19.	1270	94.0	δ(HNC), δ(CH$_3$)	
20.	1258	147.0	δ^{Ph}(CCH)	1253
21.	1229	42.1	ν(Ph-N), δ(CH$_3$)	1231
22.	1215	218.7	ν(Ph-OC)	1202
23.	1179	56.3	δ^{Ph}(CCH), ν^{Ph}(CC)	1180
24.	1173	273.6	δ^{Ph}(CCH), ν^{Ph}(CC)	
25.	1153	508.7	δ^{Ph}(CCH), ν^{Ph}(CC)	1146
26.	1121	416.4	δ^{Ph}(CCH), ν^{Ph}(CC)	1127
27.	1120	197.8	δ^{Ph}(CCC), ν^{Ph}(CC)	
28.	1046	12.4	ν(C-CH3), δ(CH$_3$)	

[a] Scaled by 0.993. [b] Vibrational modes: ν, stretching; δ, bendings. The numbers before the mode symbols indicate % contribution (10 or more) of a given mode to the corresponding normal vibration, according to the potential energy distribution.

having decomposed the complex band into components (1696 cm^{-1}, 1684 cm^{-1}, Table 2). The conversion causes also an essential intensity increase of the ester carbonyl ν(CO) bands. In the spectrum of the anion the aromatic skeletal bands of the phenolate ring 8 and 19 (Wilson's notation) are more intense than these in the spectrum of neutral molecule. Conversion of the salophen molecule into the oxyanion virtually did not change the frequencies of δ(HNC) (amide-II) and ν(C-N) (amide-III) bands. Removing the proton from the hydroxyl group of the oxyanion leads to a shift of the ν (Ph–O) coordinate to higher frequency (1492 cm^{-1}), obviously due to the significant shortening of the Ph–O bond.

The experimental spectrum of the dianion studied is shown in Fig. 1(C). Theoretical and experimental IR data for the salophen dianion are compared in Table 3. Again, there is good agreement between experimental and scaled theoretical frequencies. The mean deviation between them is 9.1 cm^{-1}.

Comparison with the other spectra of Fig. 1(B) shows that fundamental spectral changes accompany the second deprotonation of salophen. There is no longer amide band ν(C=O) at the usual place. The theory predicts two new bands characterizing the carboxamide group in the dianion: very strong bands at 1524 cm^{-1} (amide I) and 1393 cm^{-1} (amide III). These bands are actually present in the experimental spectrum (Fig. 1(C)): i.e., at 1522 cm^{-1} and 1386 cm^{-1}. The approximate description of the corresponding normal vibrations (Table 3, No. 6 and 14) are in agreement with the literature data. For the nitranions of acetanilide and of a series of ring-substituted acetanilides, Ognyanova et al. have assigned the strong bands in the 1518–1533 cm^{-1} spectral region as ν(C=O) (amide I) and the medium to strong bands at 1373–1382 cm^{-1} – as ν(C-N) (amide III). In agreement between theory and experiment, the second deprotonation of salophen causes a strong enhancement of the intensity of the aromatic skel-

Table 3. Theoretical (B3LYP/6-311++G**) and experimental (solvent DMSO-d_6) vibrational frequencies (ν in cm^{-1}) and IR integrated intensities (A in km.mol^{-1}) of salophen dianion

No.	$\nu_{calc.}$ [a]	A	Assignments	$\nu_{exp.}$
1.	1706	1150.0	ν(C=O) (ester group)	1689
2.	1629	57.0	ν^{Ph}(CC), δ^{Ph}(CCH)	
3.	1625	182.8	ν^{Ph}(CC), δ^{Ph}(CCH)	
4.	1586	2.3	ν^{Ph}(CC), δ^{Ph}(CCH)	1599
5.	1539	216.3	ν^{Ph}(CC), δ^{Ph}(CCH)	
6.	1524	1018.9	ν(C=O), ν(N-C)	1522
7.	1506	808.6	δ^{Ph}(CCH), ν(Ph-N)	1496
8.	1487	641.7	ν(C-O$^-$)	1478
9.	1477	191.7	δ^{Ph}(CCH)	
10.	1471	10.2	δ(CH$_3$)	
11.	1456	198.5	δ(CH$_3$)	1454
12.	1425	40.7	δ^{Ph}(CCH)	
13.	1394	77.8	δ^{Ph}(CCH)	
14.	1393	643.1	ν(N-C), ν(C-CH3)	1386
15.	1363	88.1	δ(CH$_3$)	1366
16.	1321	29.0	ν(Ph-O-C)	1326
17.	1306	16.4	δ^{Ph}(CCH)	
18.	1292	12.2	δ^{Ph}(CCH)	1255
19.	1265	211.4	δ^{Ph}(CCH)	
20.	1225	6.2	ν(Ph-N), ν(C-CH$_3$)	
21.	1206	64.0	ν(Ph-OC)	1202
22.	1179	377.4	δ^{Ph}(CCH), ν^{Ph}(CC)	1179
23.	1163	10.5	δ^{Ph}(CCH), ν^{Ph}(CC)	
24.	1159	538.2	δ^{Ph}(CCH), ν^{Ph}(CC)	1464
25.	1128	612.9	δ^{Ph}(CCH), ν^{Ph}(CC)	1128
26.	1108	27.3	δ^{Ph}(CCH), ν^{Ph}(CC)	
27.	1046	4.4	δ(CH$_3$)	
28.	1041	51.0	δ^{Ph}(CCH)	
29.	1017	30.9	δ(CH$_3$)	
30.	1017	9.3	δ(CH$_3$)	

[a] Scaled by 0.993. [b] Vibrational modes: ν, stretching; δ, bendings. The numbers before the mode symbols indicate % contribution (10 or more) of a given mode to the corresponding normal vibration, according to the potential energy distribution.

etal bands of the phenylene ring 19 (Wilson's notation). This band is the strongest in the spectrum of the dianion.

Structural analysis of the species studied

According to both the X-ray diffraction experiment [16] and the DFT theory the salophen molecule is composed of atoms lying approximately in two planes: one of the phenylene ring and the carboxamide group, and the other of the salicylate fragment. The twisting angle has been experimentally found to be 93.5° [16]. The same angle for the isolated salophen molecule has been theoretically estimated at 95.5°. The corresponding values for the free salophen anion and dianion are 102.8° and 88.4°, respectively. The theoretical and experimental bond lengths and angles in the salophen and its oxyanion and dianion are listed in Table 4. The conversion of salophen into the oxyanion leads to changes in all the bond lengths, but the strongest ones are the shortening of the C^{19}–O^{20} bond with ca. 0.089 Å and lengthening of the adjacent CC ones with ca. 0.048 Å. The C^{14}–C^{12} bond in the anion is with 0.024 Å shorter while the C^{12}–O^{11} bonds and the C=O^{13} bond are with 0.012 Å and 0.007 Å longer that the same bonds in the molecule. The bond length changes that accompany the conversion of the oxyanion into dianion take place both at the azanionic center and next to it – shortening of the C^{1}–N^{7} and N^{7}–C^{8} and bonds and lengthening of the C^{8}=O^{9} and C^{8}–CH$_3$ bonds (Table 4).

The net electric charges of certain fragments of the species studied and the corresponding charge changes accompanying the conversion molecule → oxyanion → dianion are shown in Table 5.

Table 4. Theoretical (B3LYP/6-311++G**) and experimental bond lengths R (Å) and bond angles A (°) in the salophen, its oxyanion and dianion

	Molecule			Anion		Dianion	
	Experimental[a]	Theoretical	Δ^b	Theoretical	Δ^c	Theoretical	Δ^d
Bond lengths							
$R(C^1,C^2)$	1.397	1.403	−0.006	1.402	−0.001	1.419	−0.017
$R(C^2,C^3)$	1.389	1.388	0.001	1.395	0.007	1.396	−0.001
$R(C^3,C^4)$	1.384	1.390	−0.006	1.389	−0.001	1.389	0.000
$R(C^4,C^5)$	1.376	1.386	−0.010	1.395	0.009	1.393	0.002
$R(C^5,C^6)$	1.393	1.394	−0.001	1.389	−0.005	1.389	0.000
$R(C^6,C^1)$	1.395	1.403	−0.008	1.402	−0.001	1.418	−0.014
$R(C^1,N^7)$	1.414	1.411	0.003	1.413	0.002	1.394	0.019
$R(N^7,C^8)$	1.357	1.370	−0.013	1.368	−0.002	1.334	0.034
$R(C^8,O^9)$	1.228	1.227	0.001	1.228	0.001	1.266	−0.038
$R(C^8,C^{10})$	1.506	1.514	−0.008	1.515	0.001	1.529	−0.014
$R(C^4,O^{11})$	1.415	1.401	0.014	1.389	−0.012	1.399	−0.010
$R(O^{11},C^{12})$	1.350	1.370	−0.020	1.405	0.035	1.394	0.011
$R(C^{12},O^{13})$	1.215	1.208	0.007	1.215	0.007	1.216	−0.001
$R(C^{12},C^{14})$	1.476	1.482	−0.006	1.458	−0.024	1.464	−0.006
$R(C^{14},C^{15})$	1.408	1.407	0.001	1.418	0.011	1.416	0.002
$R(C^{15},C^{16})$	1.380	1.386	−0.006	1.379	−0.007	1.381	−0.002
$R(C^{16},C^{17})$	1.400	1.396	0.004	1.412	0.016	1.411	0.001
$R(C^{17},C^{18})$	1.374	1.387	−0.013	1.374	−0.013	1.375	−0.001
$R(C^{18},C^{19})$	1.404	1.401	0.003	1.449	0.048	1.448	0.001
$R(C^{19},C^{14})$	1.406	1.413	0.007	1.461	0.048	1.460	0.001
$R(C^{19},O^{20})$	1.351	1.357	−0.006	1.268	−0.089	1.270	−0.002
Bond angles							
$A(C^1,C^2,C^3)$	119.6	119.8	−0.2	119.7	0.1	121.3	−1.6
$A(C^2,C^3,C^4)$	119.8	120.1	−0.3	120.5	−0.4	119.6	0.9
$A(C^3,C^4,C^5)$	121.4	120.7	0.7	120.0	0.7	119.7	0.3
$A(C^4,C^5,C^6)$	119.2	119.2	0	119.6	−0.4	120.6	−1
$A(C^5,C^6,C^1)$	120.5	120.8	−0.3	120.7	0.1	121.3	−0.6
$A(C^1,N^7,C^8)$	128.1	129.5	−1.4	129.6	−0.1	122.8	6.8
$A(N^7,C^8,C^{10})$	114.2	114.7	−0.5	114.9	−0.2	114.4	0.5
$A(N^7,C^8,O^9)$	123.9	123.6	0.3	123.6	0	129.0	−5.4
$A(C^4,O^{11},C^{12})$	117.2	118.2	−1	118.6	−0.4	118.5	0.1
$A(O^{11},C^{12},O^{13})$	122.0	122.0	0	119.3	2.7	119.9	−0.6
$A(O^{11},C^{12},C^{14})$	112.7	111.1	1.6	111.5	−0.4	111.7	−0.2
$A(C^{12},C^{14},C^{15})$	122.1	120.2	1.9	119.3	0.9	119.0	0.3
$A(C^{14},C^{15},C^{16})$	121.2	121.7	−0.5	122.7	−1	122.7	0
$A(O^{15},C^{16},O^{17})$	119.0	119.2	−0.2	118.5	0.7	118.4	0.1
$A(C^{16},C^{17},C^{18})$	121.1	120.3	0.8	120.8	−0.5	120.7	0.1
$A(C^{17},C^{18},C^{19})$	120.0	120.7	−0.7	123.3	−2.6	123.3	0
$A(C^{18},C^{19},O^{20})$	117.7	120.4	−2.7	119.9	0.5	120.0	−0.1
$A(C^{18},C^{19},C^{14})$	119.4	119.6	−0.2	114.7	4.9	114.7	0

[a] See Ref. [16]. [b] Algebraic deviations (Å, degrees) between experimental and theoretical values. [c] Algebraic deviations (Å, degrees) between theoretical values of the anion and molecule. [d] Algebraic deviations between theoretical values of the dianion and anion.

Table 5. NBO electronic charges q of the fragments of the species studied

Charge of the fragments	HO/O⁻	Ph	OCO	Ph	NH/N⁻	COCH₃
$q_{molecule}$	−0.17	0.21	−0.37	0.49	−0.22	0.06
q_{anion}	−0.71	−0.12	−0.43	0.45	−0.21	0.01
q_{anion}– $q_{molecule}$	−0.54	−0.33	−0.06	−0.03	0.01	−0.05
$q_{dianion}$	−0.73	−0.17	−0.42	0.28	−0.71	−0.26
$q_{dianion}$– $q_{dianion}$	−0.02	−0.05	0.01	−0.27	−0.50	−0.17

The charge change values $\Delta q = q_{anion} - q_{molecule}$ and $\Delta q = q_{dianion} - q_{anion}$ are usually quite informative in showing the distributions of the new charges in anions [8–13]. According to the present calculations the first (oxyanionic) charge remains localized mainly within the oxyphenylene fragment while the second (nitranionic) charge spreads over the acet-anilide fragment.

CONCLUSION

The spectral and structural changes, caused by the conversion of the salophen molecule into the corresponding oxyanion and dianion have been studied by IR spectra DFT method at B3LYP/6-311++G** level. A comparison of calculated with measured infrared data can be used as a test for the reliability of the structural predictions for various molecules and anions of this and similar types. These predictions can be very useful in cases of molecules and ions for which experimental structural parameters are inaccessible or unknown. IR spectral changes, which take place as a result of the conversion of molecule into anions, were adequately predicted by the same theoretical method.

REFERENCES

1. P. Naumov, G. Jovanovski, S. Tancčeva, S. W. Ng, *Z. Anorg. Allg. Chem.*, 632, 454 (2006).
2. P. Tisovský, R. Šandrik, M. Horváth, J. Donovalová, J, J. Filo, M. Gáplovský, K. Jakusová, M. Cigáň, R. Sokolík, A. Gáplovský, *Molecules*, 22, 1961 (2017).
3. J. L. Castro, M. R. Lopez-Ramirez, J. F. Arenas, J. Soto, J.C. Otero, *Langmuir*, 28, 8926 (2012).
4. S. Y. Lin, H. L. Lin, Y. T. Chi, R. Y. Hung, Y. T. Huang, W. H. Hsieh, C. Y. Kao, *J. Pharm. Innov.*, 11, 109 (2016).
5. E. J. Baran, V. T. Yilmaz, *Coordin. Chem. Rev.*, 250, 1980 (2006)
6. I. N. Juchnovski, I. G. Binev, in: S. Patai, Z. Rappoport (Ed.): The chemistry of functional groups, Suppl. C., Wiley, New York, 1983, p. 107.
7. S. S. Stoyanov, J. A. Tsenov, D. Y. Yancheva, *J. Mol. Struct.*, **1009**, 42 (2012).
8. A. D. Popova, E. A. Velcheva, B. A. Stamboliyska, *J. Mol. Struct.*, **1009**, 23 (2012).
9. E. A. Velcheva, B. A. Stamboliyska, P. J. Boyadjiea, *J. Mol. Struct.*, **963**, 57 (2010).
10. A. D. Popova, M. K. Georgieva, O. I. Petrov, K. V. Petrova, E. A. Velcheva, *Int. J. Quant. Chem.*, **107**, 1752 (2007).
11. Ts. Kolev, E. Velcheva, B. Stamboliyska, *Bulg. Chem. Commun.*, **49**(D), 239 (2017).
12. E. Velcheva, Z. Glavcheva, B. Stamboliyska, *Bulg. Chem. Commun.*, **48**, 514 (2016).
13. E. Velcheva, B. Stamboliyska, S. Stoyanov, *Bulg. Chem. Commun.*, **49**(D), 137 (2017).
14. https://pubchem.ncbi.nlm.nih.gov/compound/1984
15. J. Stopek, *US Patent* 8 758 798 B2 (20014); D. Friedman, *US Patent* 9 186 324 B2(2015).
16. T. Maris, CCDC 779609: Experimental Crystal Structure Determination, Cambridge Crystallographic Data Centre, 2014.
17. B. B. Koleva, T. M. Kolev, M. Spiteller, *J. Pharm. Biomed. Analysis*, **46**, 267 (2008).
18. J. A. Bohmann, F. Weinhold, T. C. Farrar, *J. Chem. Phys.,* **1997**, 107, 1173.
19. M. J. Frisch, G. W. Trucks, H. B. Schlegel, G. E. Scuseria, M. A. Robb, J. R. Cheeseman, G. Scalmani, V. Barone, B. Mennucci, G. A. Petersson, H. Nakatsuji, M. Caricato, X. Li, H. P. Hratchian, A. F. Izmaylov, J. Bloino, G. Zheng, J. L. Sonnenberg, M. Hada, M. Ehara, K. Toyota, R. Fukuda, J. Hasegawa, M. Ishida, T. Nakajima, Y.Honda, O. Kitao, H. Nakai, T. Vreven, J.A. Montgomery, Jr., J. E. Peralta, F. Ogliaro, M. Bearpark, J. J. Heyd, E. Brothers, K. N. Kudin, V. N. Staroverov, R. Kobayashi, J.Normand, K. Raghavachari, A. Rendell, J. C. Burant, S. S. Iyengar, J. Tomasi, M. Cossi, N. Rega, J. M. Millam, M. Klene, J. E. Knox, J. B. Cross, V. Bakken, C. Adamo, J. Jaramillo, R. Gomperts, R. E. Stratmann, O. Yazyev, A. J. Austin, R. Cammi, C. Pomelli, J. W. Ochterski, R. L. Martin, K. Morokuma, V. G. Zakrzewski, G. A. Voth, P. Salvador, J. J. Dannenberg, S. Dapprich, A. D. Daniels, Ö. Farkas, J. B. Foresman, J. V. Ortiz, J. Cioslowski, D. J. Fox, Gaussian 09, Revision A1, Gaussian Inc., Wallingford CT, 2009.
20. A. D. Becke, *J. Chem. Phys.*, **98,** 5648 (1993).
21. C. Lee, W. Yang, G. R. Parr, *Phys. Rev.*, **B37,** 785 (1998).
22. J. Tomasi, M. Perisco, *Chem. Rev.*, **94,** 2027 (1994).
23. J. Tomasi, B. Mennucci, E. J. Cances, *J. Mol. Struct.*, *(THEOCHEM)*, **464** 211 (1999).
24. V. M. Vlasov, L. A. Oshkina, *Org. React.*, **28,** 47 (1993).
25. M. Szwarc, Ions and Ion Pairs in Organic Reactions, Wiley-Interscience, New York, 1972.

ИЧ СПЕКТРАЛНИ И СТРУКТУРНИ ПРОМЕНИ, ПРИЧИНЕНИ ОТ ПРЕВРЪЩАНЕТО НА САЛОФЕН В АНИОН И ДИАНИОН

С. С. Стоянов, Е. А. Велчева, Б. А. Стамболийска*

Лаборатория „Структурен органичен анализ", Институт по органична химия с център по фитохимия, Българска академия на науките, ул. „Акад. Г. Бончев", бл. 9, 1113 София

(Резюме)

Структурите на салофена, неговите анион и дианион са изследвани с помощта на ИЧ спектроскопия и DFT пресмятания. Ефектът на разтворителя е отчетен по метода на самосъгласуваното реактивно поле (IEFPCM). Намерено е добро съответствие между теоретичните и експерименталните вибрационни характеристики на изследваните частици. Използваният теоретичен метод добре предсказва силните спектрални промени, които съпътстват превръщането на салофена в анион и дианион. Установените структурни промени при тези превръщания са също значителни. Анализът на промените в атомните заряди показва, че първият (оксианионен) заряд остава локализиран в оксифениленовия фрагмент, а вторият (азанионен) заряд се делокизира върху ацетанилидния фрагмент.

Syntheses and vibrational spectroscopic characteristics of series ionic merocyanine dyes

M. Todorova[1], R. Bakalska[2]*

[1] *University of Food Technology, Faculty of Technology, Department Organic Chemistry,*
26 Maritsa Blvd., 4000 Plovdiv, Bulgaria
[2] *Plovdiv University, Faculty of Chemistry, Department Organic Chemistry,*
24 Tzar Assen Str., 4000 Plovdiv, Bulgaria

A series ionic merocyanine dyes with enlarged π-conjugated system and varying length of the N-alkyl chain were synthesized and investigated by means of solid-state IR and Raman spectroscopy. Quantum chemical calculations at the DFT level were performed to predict electronic structure and vibrational data. Nearly all IR bands are asymmetric. As a result of electronic interaction due to the intramolecular charge transfer (ICT) which leads to vibrational one, nearly all vibrations are strongly mixed and the intensities are strong influenced. For this reason, the vibrational spectroscopy does not help to estimate the contribution of the two final forms – benzenoid and quinoid in the real electronic structure of the dyes. IR and Raman data for the various dyes are with close numerical values to that of the predicted ones.

Keywords: Merocyanine dye; Styrylquinolinium dye; IR and Raman spectroscopy; DFT calculations.

INTRODUCTION

Merocyanines are systems exhibiting the intramolecular charge transfer (ICT) between the electron-donating and -withdrawing end groups along the conjugated bonds in the polymethine chain, which in terms of the classical resonance theory is described by a linear combination of limiting resonance structures – benzenoid and quinoid, as shown in Scheme 1. Due to their strongly pronounced solvatochromism and the abilities to change their dipole moment essentially at electronic excitation as well as to sensitize various physical and chemical processes, merocyanines find wide application in optoelectronics, nonlinear optics, devices for information recording, in medicine and biology [1–13].

The main method for investigation of the dyes and especially intramolecular charge transfer complex is the electron spectroscopy. NMR spectroscopy has also been used [14], but all these studies were carried out in solutions, and the electronic states of dyes could substantially vary depending on the solvent used. In the crystal, the ICT in merocyanines can be proved by the bond length alternation (BLA) parameter based on the X-ray diffraction study. Vibrational spectroscopy is usually the only method of structural elucidation of dyes in solid state [15]. Kolev and co-workers have successfully applied the X-ray diffraction and vibrational spectroscopy for structural elucidation of dyes in solid state to prove the hyperpolarizabilities of a number of dye chromophores [16–21].

The goal of the present study was to reveal the distinguishing features of the vibrational spectra of merocyanines and to establish general relations between vibrational spectra and their electronic asymmetry determined by donor-acceptor power of the terminal fragments. Therefor we synthesized a series of styrylquinolinium dyes **5–8** with enlarged π-conjugated system, belonging to the merocyanine class. The accent is on the study of the dyes by IR and Raman spectroscopy. Quantum chemical DFT calculations at the B3LYP level of theory using a 6-311++G** basis set were applied for predicting the structure and vibrational data of the chromophore (**5**).

EXPERIMENTAL

The synthesis of dye (**5**) has been reported in the literature [22]. All dyes studied were obtained

---

* To whom all correspondence should be sent:
E-mail: bakalska@uni-plovdiv.net

according to modified by us procedure of higher yields similar to that already outlined for dye (**6**) in our earlier work [12]. The preparation of 1-alkyl-4-methylquinolinium halogenides (**1–4**) was described in Ref. [23].

General method for preparation of hydroxy-substituted dyes (5–8)

A mixture of 1-alkyl-4-methylquinolinium halogenides (1.25 mmol), 4-hydroxynaphtaldehyde (1.25 mmol), piperidine (0.25 mmol) and glacial acetic acid (0.25 mmol) in dry benzene (20 mL) was heated under reflux, equipped with Dean-Stark apparatus and drying tube. After boilling during 6 h, the reaction mixture was cooled; the solid was filtered off, washed with benzene and dried at room temperature. All derived dyes were recrystallized from methanol. Yields 85–95%. All of these salts were characterized by ^{1}H and ^{13}C NMR, UV-Vis and fluorescence, mass spectroscopy and thermal methods [23].

Vibrational and computational methods

The solid state IR and Raman spectra were recorded between 4000 cm^{-1} and 400 cm^{-1} on a VERTEX 70 FT-spectrometer (Bruker Optics). 50 scans were performed for each spectrum with a resolution of 2 cm^{-1}. All density functional theory (DFT) computations were performed with the GAUSSIAN 03 program package [24] employing the B3LYP (Becke's three-parameter non-local exchange) [25, 26] correlation functional and 6-311++G** basis set.

RESULTS AND DISCUSSION

Syntheses

The synthesis of styrylquinolinium dyes (**5–8**) was carried out by Knoevenagel condensation of N-alkyl lepidinium halogenide (**1–4**) and 4-hydroxynaphtaldehyde in the presence of catalyst piperidine/ glacial acetic acid. The synthesis is depicted in Scheme 1. The real dye structure can be represented by a set of the limiting resonance structures – benzenoid and quinoid. Four p-hydroxy substituted dyes with varying the length of the alkyl chain of C1 to C4, namely: 4-[(*E*)-2-(4-hydroxynaphthalen-1-yl) ethenyl]-1-methylquinolinium iodide (**5**); 4-[(*E*)-2-(4-hydroxynaphthalen-1-yl)ethenyl]-1-ethylquinolinium bromide (**6**); 4-[(*E*)-2-(4-hydroxynaphthalen-1-yl)ethenyl]-1-propylquinolinium iodide (**7**); 4-[(*E*)-2-(4-hydroxynaphthalen-1-yl)ethenyl]-1-butylquinolinium bromide (**8**) were investigated.

1: R = Me, X = I	**5:** R = Me, X = I
2: R = Et, X = Br	**6:** R = Et, X = Br
3: R = n Pr, X = I	**7:** R = n Pr, X = I
4: R = n Bu, X = Br	**8:** R = n Bu, X = Br
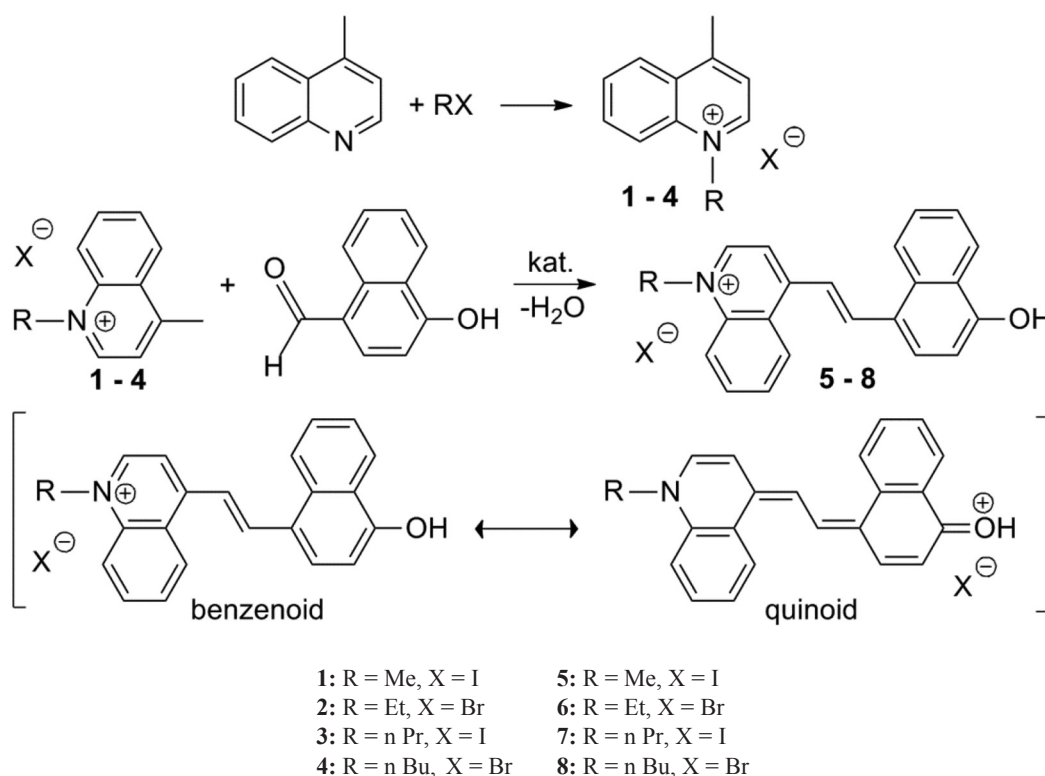
Scheme 1. Reaction scheme for obtaining of merocyanine dyes (**5**)–(**8**) presented with the limiting resonance structures – benzenoid and quinoid.

Vibrational and computational analysis

The accurate assignment of the main experimental frequencies of compounds (**5**)–(**8**) to the corresponding normal modes was supported by B3LYP/6-311++G** calculations. The IR spectra of the series of 4-hydroxy dyes with the same chromophore and different long N-alkyl chain were shown on Figure 1 and in the Table 1 are summarized selected experimental and calculated vibrations. In some cases where more than one band were observed we assigned the band which is closest by frequency to the predicted band by the theoretical method. That phenomenon could be explained with availability of crystal effects [15].

It should be noted that in general the spectral picture in IR spectra is complicated and needs very detailed regard. Nearly all IR bands are asymmetric. Since, the electron interaction between a strong donor – phenolic hydroxyl group and the strongest acceptor – quinolinium fragment leads to vibrational interaction, as a result of this nearly all vibrations are strongly mixed and the intensities are strong influenced. The so-called Davydov splitting and Evans holes effects were observed in all spectra and these phenomenona could be explained with availability of crystal field effects [15]. There is also a characteristic elevation of the spectrum background typical for the salts in the solid state.

In the IR spectra of the merocyanine dyes under study, the stretching vibration of phenolic OH group was found as a broad band in the range 3429–3344 cm^{-1} (Fig. 1). This indicates that a hydrogen bond exists. Only in the IR spectrum of the dye **5** two bands for the stretching vibration of the OH group at 3429 cm^{-1} and 3391 cm^{-1} were detected,

caused by the solid state effects. The stretching vibration bands of the OH group are downshifted of 200 to 400 cm^{-1} in comparison to theoretic ones. The maxima at 2963 cm^{-1} and 2875 cm^{-1} correspond to asymmetric and symmetric C–H stretching vibrations of the methyl group, while these ones in the range 2980–2920 cm^{-1} of the symmetrical and asymmetrical C–H stretching vibrations of methylene group/s.

The bands at about 1618 and 1609 cm^{-1} belong to the skeletal vibration $\nu(\mathrm{C}{=}\mathrm{C})$ of the naphthalene fragment resembling the oscillation 8a. The most intense bands in the infrared spectra of the dyes at about 1588 and 1560 cm^{-1} refer to the highly mixed $\nu_{\mathrm{C=C}}$ and 8a, 8b plane vibrations of the quinoline fragment of the molecules and this one at 1575 cm^{-1} to mixed vibration $\nu(\mathrm{C}{=}\mathrm{C})$ of the naphthalene, $\nu(\mathrm{C}{=}\mathrm{C})$ of the quinoline nucleus and deformation vibration of methyl group. To the in-plane deformation mode $\beta(\mathrm{C–H})$ of the naphthalene fragment correspond two maxima at about 1473 cm^{-1} and 1441 cm^{-1}, respectively. Some bands at about 1351, 1340, 1270 and 1235 cm^{-1} for the $\beta(\mathrm{C–H})$ vibrations of the quinoline part were also observed (Table 1). The maximum corresponding to the C–H deformation vibrations of the methyl group is found at about 1142 cm^{-1}, and those of the out-of-plane $\gamma(\mathrm{C–H})$ of the aromatic rings at about 1004–1014 cm^{-1}. To antiphase vibration $\gamma(\mathrm{C–H})$ of the quinoline fragment corresponds the band at about 970 cm^{-1}.

In the Raman spectra the asymmetric bands are not so much opposed to the IR spectra but both allows better assignment of the bands. For strongly polar chemical bonds such as O–H, C–H, etc., the bands are of low intensity. This explains why in the Raman spectra of the compounds there are miss-
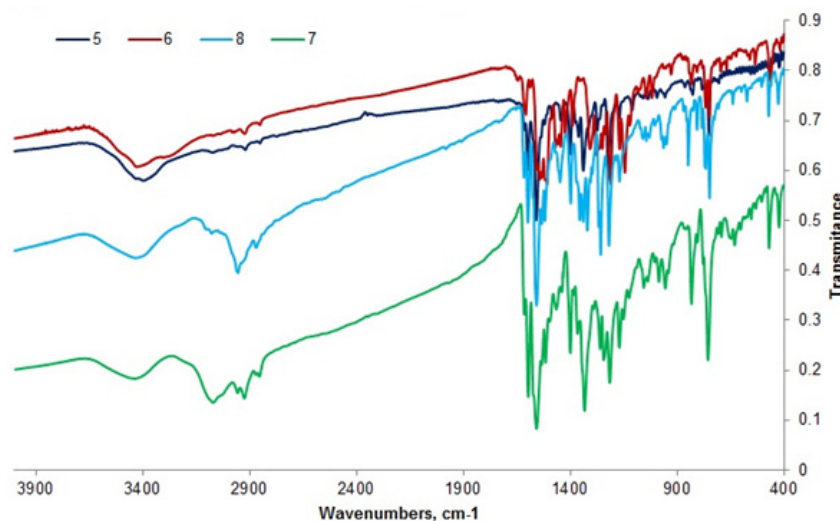
Fig. 1. Solid-state IR-spectra of merocyanine dyes (**5**)–(**8**) in the region of 4000–400 cm^{-1}.

Table 1. Theoretically predicted frequencies, the measured IR and the assignment of the bands to the corresponding normal vibrations of the dyes (**5**)–(**8**)

Vibrational Assignments	Calc. IR Frequency [cm⁻¹]	Observed IR Frequency [cm⁻¹]			
		(5)	**(6)**	**(7)**	**(8)**
ν (OH), pure	3813	3426 3391 br	3426 3290 sh	3429 br	3429 br
νˢ (CH₃), pure	3057	3056	3067	3067	3067
νᵃˢ (CH₂) + νˢ (CH₂)	2978	–	2974	–	–
νᵃˢ (CH₃) +νᵃˢ (CH₂) + νˢ (CH₂)	2958	–	–	2960	2954
νˢ (CH₃) νᵃˢ (CH₂) + νˢ (CH₂)	2929	–	2923	2920	2924 sh
ν (C═C) NF (8a) + ν(C=C)	1627	1622	–	–	–
ν(C═C) NF (8a)	1611	1614	1609	1614	1618
ν(C=C) + ν(C═C) NF + ν(C═C)QF (8b)	1588	1586	1586	1591	1592
ν(C═C) QF + ν(C═C) NF + δ (CH₃)	1575	1575sh	–	1572 sh	1575 sh
ν(C═C)NF(19a) + ν(C═C) QF	1556	1558	1556	1556	1557
δˢ (CH₃) QF + ν(C═C) QF	1519	1520	1518 sh	1514	1518
ν(C═C) NF (19a)	1502	1506	1507	–	–
δᵃˢ (CH₃)	1489	1486	1488	–	–
β(C-H) NF	1473	1473	1471	1465	1470
δˢ(CH₃)+ β(C-H) QF	1459	1467	1458	1458 sh	1454 sh
β(C-H) NF	1441	1439	1445	1439	1447
β(C-H) NF + δˢ (CH₃) + ν(N-C) QF	1425	1421	1423	–	–
β(C-H) C=C + ν(C═C) NF + ν(C-H) QF + δˢ (CH₃)	1406	1400	–	1400	1398
βC-H (C=C) + ν (C-O) NF	1381	1388	1390	1383	-
ν(N-C) QF + δ(C═C) QF + βC-H (C=C) + δ(CH₃)	1377	1375	1377 sh	–	1372 sh
β(C-H) NF + β(C-H) QF + ν(C═C) NF + ν(C═C) QF	1361	1361	–	1365	1356
βC-H (C=C) + β(C-H) NF + β(C-H) QF	1351	1353	1356	–	–
βC-H (C=C) + β(C-H) NF + β(C-H) QF	1334	1338	1343	1343 sh	1339
β(C-H) NF (3)+ βC-H (C=C)	1328	1330	1331	1333	1319
β(C-H) QF + βC-H (C=C) + ν(C-N)	1302	1310	1307	1313	1307
βC-H (C=C) + δ(O-H)	1283	1284	1298	1290	1293
β(C-H) NF + β(C-H) QF	1271	1271	1266	–	1268
ν(C-N) QF+ β(C-H) QF	1254	1249	1249	1259	1258
βC-H (C=C) + δ (O-H) + β(C-H) QF	1235	1236	–	–	–
β(C-H) NF + β(C-H) QF + δ (O-H)	1220	1224	1222	1217	1219
β(C-H) QF + δ(CH₃) + β(C-H) NF	1217	1211	1208	1215	–
β(C-H) NF + δ(CH₃)	1199	1199	–	–	–
β(C-H) NF + β(O-H)	1170	1167	1169	1172	1170
δ (CH₃)	1140	1142	1145	1150	1152
δ(CH₃) + ν(C-N)	1128	1132	1121	1124	1131
β(C-H) NF + β(O-H) + βC-H (C=C)	1082	1083	–	1088 sh	–
β(C-H) QF + βC-H (C=C)	1067	1070	–	–	1073 sh
β(C-H) NF + βC-H (C=C)	1064	–	–	1055	1063
breathing NF + βC-H (C=C)	1036	1037	1039	1036	1045
β(C-H) QF + β(C-H) NF + βC-H (C=C)	1031	1032	–	–	1031
γ(C-H) QF	1019	1018	1019	–	–

Table 1. (continued)

γ(C-H) NF	1012	1014	–	1005	1004
γ(C-H) QF + γC-H (C=C)	997	997	998	987	994
antiphase γ(C-H) QF, pure	970	971	963	–	972
antiphase γ(C-H) NF	953	953	951	955	955
βC-H (C=C) + γC-H (C=C)	898	899	901	–	900
β(C-H) NF + β(C-H) QF	876	875	875	–	870
β(C═══C)NF + β(C=C) + β(C═══C)QF	850	846	852	–	848
γ(C-H) NF + γ(C-H) QF + δ(C═══C)NF	827	830	833	833	825
β(C═══C) QF	814	811	809	–	–
δ(C═══C) NF, δ(C═══C) QF + β(C=C)	801	798	–	806	807
δ(C═══C) NF + γ(C-H) NF + γ(C-H)QF	784	–	–	–	785
"umbrella mode" NF + "umbrella mode" QF	780	782	781	–	–
β(C-H) NF + δ(C-N) QF	776	763	767	758	770
β (C═══C) QF + β (C═══C) NF	712	697	707	709	706
ring puckering QF (4) + NF	666	668	669	–	665
ring puckering NF + QF	654	648	659	654	648
skel. def. QF + NF	627	624	624	633	636
ring puckering γ(C═══C)NF + γ(C═══C)QF, "umbrella mode" NF	611	–	608	605	601
γC-H (C=C) + β(C═══C) QF + γ(C═══C)NF	583	588	586	588	–
γ (C═══C) QF + β (C═══C) NF + γ(O-H)	564	569	569	577	574
β(C═══C) QF + β(C═══C)NF	556	559	559	555	556
β(C═══C) QF + β(C═══C) NF	507	–	512	507	505
β(C═══C) NF + γ(C═══C) QF	500	501	501	–	500
β(C═══C) NF + β(C═══C) QF	485	490	–	490	485
ring puckering NF (4) + QF	478	471	–	471	471
skel. def. NF + β(C═══C) QF	466	461	460	–	464
ring puckering NF + γ(O-H)	431	426	428	–	426

Abbreviations: QF (quinolinium fragment), NF (naphthalene fragment); ν – stretching, δ – deformation, β – in-plane deformation, γ – out-of-plane, τ – torsion vibrations; br. – broad, sh. –shoulder.
Scaling factor –0.9688 [27]

ing bands for O–H and C–H vibrations and why in Fig. 2 the shown region of the Raman spectrum of dye (**8**) is in the range 1800–400 cm⁻¹. The predicted frequencies, selected measured Raman ones and the assignment of the bands to the corresponding normal vibrations were listed in Table 2. The dye (**7**) Raman frequencies were not included in Table 2 because it exhibits a tendency to photodegradation even at the lowest power of the laser source.

As already mentioned, the vibrational spectra are strongly deformed from the charge transfer complex (CT), and it is an evidence of its existence proven by the vibration spectroscopy method. Unfortunately, the vibrational spectroscopy is not enough to quantify the real electronic structure of the molecules according to the contribution of the

two forms – benzenoid and quinoid. The reason is that the vibrations of $\nu_{C=O}$ and $\nu_{C=C}$ are mixed and with close numerical values. It is noteworthy, that the data from the experimental IR and Raman spectra for the various dyes are of close numerical values and within the error. The probable explanation is that for the same chromophore, the influence of the N-alkyl group on the ICT is negligible (weak +I effect). This explanation is also required by the UV-Vis spectra of dyes **5–8**, shown on Fig. 3, all measured in methanol, whose maxima are very close. The shorter-wave absorption bands at 493±2 nm were referred to the CT-band of the benzenoid structures of the dyes, and the longer wavelength bands – to the quinoid forms (Fig. 3, Scheme 1). The longer wavelength band splits into two bands
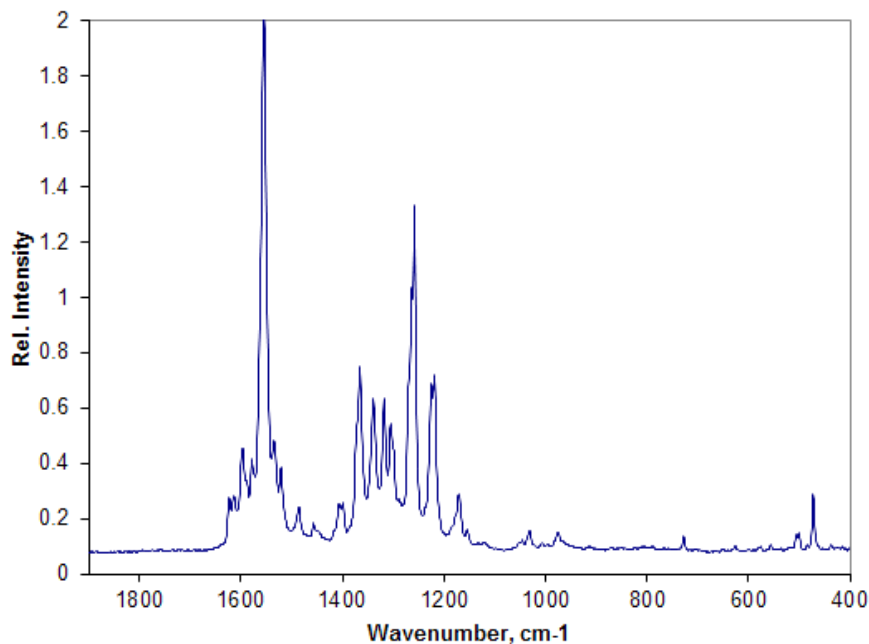
Fig. 2. Raman spectrum of the dye (**8**) in the region of 1800–400 cm⁻¹.

Table 2. Theoretically predicted frequencies, selected experimental Raman frequencies and the assignment of the bands to the corresponding normal vibrations of the dyes (**5**), (**6**) and (**8**)

Vibrational Assignments	Calc. Raman Frequency [cm⁻¹]	Observed Raman Frequency [cm⁻¹]		
		(5)	**(6)**	**(8)**
ν (C≡C) NF (8a) + ν(C=C)	1627	1623	1626	1624
ν(C≡C) NF (8a)	1611	1608	1616	1615
ν(C=C) + ν(C≡C) NF + ν (C≡C) QF (8b)	1588	1590	1595	1595
ν(C≡C) QF+ ν(C≡C) NF + δ(CH₃)	1575	1578	1579	–
ν(C≡C) NF (19a) + ν(C≡C) QF	1556	1552	1552	1555
δˢ (CH₃) QF + ν(C≡C) QF	1519	1520	–	1522
ν(C≡C) QF + δ(CH₃) (19a)	1491	1492	–	1484
δˢ(CH₃)+ β(C-H) QF	1459	1459	–	1458
β(C-H) C=C +ν(C≡C) NF +ν(C-H) QF + δˢ (CH₃)	1406	1402	1397	1408
ν(N-C) QF + δ(C≡C) QF+ βC-H (C=C) + δ(CH₃)	1377	1375	1372	–
β(C-H) NF + β(C-H) QF + ν(C≡C) NF + ν(C≡C) QF	1361	1365	1363	1366
βC-H (C=C) + β(C-H) NF + β(C-H) QF	1334	1343	1336	1340
β(C-H) NF (3)+ βC-H (C=C)	1328	1327	1332	1319
βC-H (C=C) + β(C-H) QF + ν(C-N)	1302	1310	1306	1304
βC-H (C=C) + δ(O-H)	1283	1292	1286	–
β(C-H) NF+ β(C-H) QF	1271	1275	1270	1269
ν(C-N) QF+ β(C-H) QF	1254	1253	–	1258
β(C-H) NF + β(C-H) QF +δ (O-H)	1220	1224	1222	1220
β(C-H) QF + δ(CH₃) + β(C-H) NF	1217	1214	1217	1218
β(C-H) NF + δ(CH₃)	1199	1198	1194	–
β(C-H) NF + β(O-H)	1170	1169	1168	1169

Table 2. (continued)

δ (CH₃)	1140	1147	1146	1149
δ(CH₃) + ν(C-N)	1128	1128	1120	–
β(C-H) NF + β(O-H) + βC-H (C=C)	1082	1088	1090	–
β(C-H) NF + βC-H (C=C)	1064	1059	1069	–
breathing NF + βC-H (C=C)	1036	1036	1044	1045
β(C-H) QF + β(C-H) NF + βC-H (C=C)	1031	1032	–	1029
γ(C-H) QF	1019	1018	1017	–
γ(C-H) NF	1012	1012	1007	–
γ(C-H) QF + γC-H (C=C)	997	995	998	–
antiphaseγ(C-H) QF, pure	970	–	973	978
antiphase γ(C-H) NF	953	945	953	–
β (C≡C) QF + β (C≡C) NF	712	714	705	719
skel. def. QF + NF	627	629	–	629
Ring puckering γ(C≡C) NF + γ(C≡C) QF "umbrella mode" NF	611	608	602	–
γ(C≡C) QF + β(C≡C) NF + γ(O-H)	564	561 sh	573	–
β(C≡C) QF + β(C≡C)NF	556	556	–	557
β(C≡C) QF + β(C≡C) NF	549	542	540	–
β(C≡C) QF + β(C≡C) NF	507	506	–	504
β(C≡C) NF + γ(C≡C) QF	500	501	499	502
ring puckering NF (4) + QF	478	477	479	472
skel. def. NF + β(C≡C) QF	466	465	465	–

Abbreviations: see footnotes under Table 1.
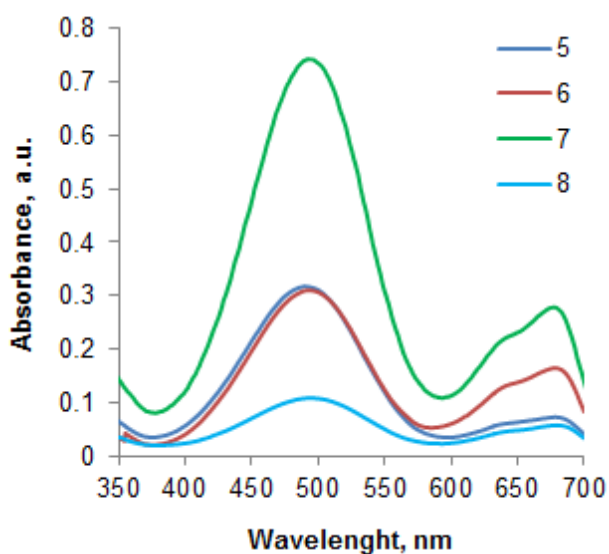
Fig. 3. UV-Vis spectra of merocyanine dyes (**5**)–(**8**) recorded in methanol.

with λ_{max} at 680 nm and 640 nm, demonstrating the aggregation phenomenon.

CONCLUSIONS

The coincidence between the calculated and measured frequencies is good and the complete vibrational analysis can be used for the calculation of the vibrational hyperpolarizability of the dyes.

REFERENCES

1. C. Bosshard, M. Bösch, I. Liakatas, M. Jäger, P. Günter, Nonlinear optical effects and materials, Springer-Verlag, Berlin, 2000.

2. H. S. Nalwa, T. Watanabe, S. Miyata, Nonlinear optics of organic molecules and polymers, CRC Press, Boca Raton, Florida, 1997.
3. L. R. Dalton, P. A. Sullivan, D. H. Bale, *Chem. Rev.*, **110**, 25 (2010).
4. P. Gregory, Industrial Dyes: Chemistry, Properties, Applications, Wiley-VCH, Weinheim, 2003.
5. S.-H. Kim, Functional Dyes, Elsevier, Amsterdam, 2006.
6. T. Kolev, I. V. Kityk, J. Ebothe, B. Sahraoui, *Chem. Phys. Lett.*, **443**, 309 (2007).
7. T. Kolev, B. B. Koleva, M. Spiteller, H. Mayer-Figge, W. S. Sheldrick, *Dyes Pigm.*, **79**, 7 (2008).
8. B. B. Koleva, T. Kolev, R. Nikolova, Y. Zagraniarsky, M. Spiteller, *Cent. Eur. J. Chem.*, **6**, 592 (2008).
9. T. Kolev, B. Koleva, J. Kasperczyk, I. Kityk, S. Tkaczyk, M. Spiteler, A. H. Reshak, W. Kuznik, *J. Mater. Sci.: Mater. Electron.*, **20**, 1073 (2008).
10. B. Koleva, S. Stoyanov, T. Kolev, I. Petkov, M. Spiteller, *Spectrochim. Acta, Part A*, **71**, 1857 (2009).
11. A. V. Kulinich, A. A. Ishchenko, *Russ. Chem. Rev.*, **78**, 141 (2009).
12. H. E. Ouazzani, S. Dabos–Seignon, D. Gindre, K. Iliopoulos, M. Todorova, R. Bakalska, P. Penchev, S. Sotirov, T. Kolev, V. Serbezov, A. Arbaoui, M. Bakasse, B. Sahraoui, *J. Phys. Chem. C*, **116**, 7144 (2012).
13. Y. Hubenova, R. Bakalska, E. Hubenova, M. Mitov, *Bioelectrochemistry*, **112**, 158 (2016).
14. A. V. Kulinich, A. A. Ishchenko, U. M. Groth, *Spectrochim. Acta, Part A*, **68**, 6 (2007).
15. B. Ivanova, T. Kolev, CRC Press, Taylor & Francis Group, Boca Raton, London, New York, 2012.
16. T. Kolev, B. B. Koleva, S. Stoyanov, M. Spiteller, I. Petkov, *Spectrochim. Acta, Part A*, **71**, 1857 (2009).
17. S. Stoyanov, B. B. Koleva, T. Kolev, I. Petkov, M. Spiteller, *Pol. J. Chem.*, **82**, 2167 (2008).
18. T. Kolev, T. Tsanev, S. Kotov, H. Mayer-Figge, M. Spiteller, W. S. Sheldrick, B. Koleva, *Dyes Pigm.*, **82**, 95 (2009).
19. B. B. Koleva, T. Kolev, M. Lamshoeft, M. Spiteller, W. Sheldrick, *Spectrochim. Acta A*, **74**, 1120 (2009).
20. R. Bakalska, M. Todorova, H. Sbirkova, B. Shivachev, T. Kolev, *Dyes Pigm.*, **136**, 919 (2017).
21. M. Todorova, R. Bakalska, T. Kolev, *Spectrochim. Acta A*, **108**, 211 (2013).
22. S. Hunig, O. Rosenthal, *Justus Liebigs Ann. Chem.*, **592**, 161 (1955).
23. M. Todorova, PhD Thesis, Plovdiv University, Plovdiv, 2015.
24. M. J. Frisch, G. W. Trucks, H. B. Schlegel, G. E. Scuseria, M. A. Robb, J. R. Cheeseman, G. Scalmani, V. Barone, B. Mennucci, G. A. Petersson, H. Nakatsuji, M. Caricato, X. Li, H. P. Hratchian, A. F. Izmaylov, J. Bloino, G. Zheng, J. L. Sonnenberg, M. Hada, M. Ehara, K. Toyota, R. Fukuda, J. Hasegawa, M. Ishida, T. Nakajima, Y. Honda, O. Kitao, H. Nakai, T. Vreven, J. A. Montgomery, Jr., J. E. Peralta, F. Ogliaro, M. Bearpark, J. J. Heyd, E. Brothers, K. N. Kudin, V. N. Staroverov, R. Kobayashi, J. Normand, K. Raghavachari, A. Rendell, J. C. Burant, S. S. Iyengar, J. Tomasi, M. Cossi, N. Rega, J. M. Millam, M. Klene, J. E. Knox, J. B. Cross, V. Bakken, C. Adamo, J. Jaramillo, R. Gomperts, R. E. Stratmann, O. Yazyev, A. J. Austin, R. Cammi, C. Pomelli, J. W. Ochterski, R. L. Martin, K. Morokuma, V. G. Zakrzewski, G. A. Voth, P. Salvador, J. J. Dannenberg, S. Dapprich, A. D. Daniels, O. Farkas, J. B. Foresman, J. V. Ortiz, J. Cioslowski, and D. J. Fox, Gaussian 03, Gaussian Inc., Wallingford CT, 2003.
25. P. J. Stephens, F. J. Devlin, C. F. Chabalowski, M. J. Frisch, *J. Phys. Chem.*, **98**, 11623 (1994).
26. C. T. Lee, W. T. Yang, R. G. Parr, *Phys. Rev. B*, **37**, 785 (1988).
27. J. Merrick, D. Moran, L. Radom, *J Phys Chem A*, **111**, 11683 (2007).

СИНТЕЗ И ВИБРАЦИОННИ СПЕКТРОСКОПСКИ ХАРАКТЕРИСТИКИ НА СЕРИЯ ЙОННИ МЕРОЦИАНИНОВИ БАГРИЛА

М. Тодорова[1], Р. Бакалска[2]*

[1] *Университет по хранителни технологии, Технологичен факултет, Катедра Органична химия, бул. „Марица" 26, 4000 Пловдив, България*
[2] *Пловдивски университет „П. Хилендарски", Химически факултет, Катедра Органична химия, ул. „Цар Асен" 24, 4000 Пловдив, България*

(Резюме)

Серия йонни мероцианинови багрила с разширена π-спрегната система и различна дължина на N-алкилната верига бяха синтезирани и изследвани чрез твърдофазна ИЧ и раманова спектроскопия. За да се предскажат електронната структура и вибрационните характеристики, бяха извършени квантово-химични изчисления на ниво DFT. Почти всички инфрачервени ивици са асиметрични. В резултат на електронното взаимодействие, дължащо се на вътремолекулния пренос на заряд (ICT), което води до вибрационно взаимодействие, почти всички трептения са силно смесени, а интензитетите им са силно повлияни. Поради тази причина, вибрационната спектроскопия не дава възможност да се оцени приносът на двете крайни форми бензеноидна и хиноидна в реалната електронна структура на багрилата. Експерименталните и инфрачервени и раманови ивици за различните багрила са с близки числови стойности, както и с изчислените.

3-nitrotyrosine as a serum biomarker of nitroxidative stress and insulin resistance in nascent metabolic syndrome

T. R. Stankova[1]*, G. T. Delcheva[1], K. I. Stefanova[1], A. I. Maneva[1],
S. V. Vladeva[2, 3], G. A. Tsvetkova[4]

[1] Department of Chemistry and Biochemistry, Faculty of Pharmacy, Medical University – Plovdiv, Plovdiv, Bulgaria
[2] Department of Endocrinology and Metabolic Disorders, University Hospital "Kaspela", Plovdiv, Bulgaria
[3] Medical College, Medical University – Plovdiv, Plovdiv, Bulgaria
[4] Department of Clinical Laboratory, University Hospital "Kaspela", Plovdiv, Bulgaria

Metabolic syndrome (MetS) represents a cluster of metabolic abnormalities, including central obesity, hypertension, hypertriglyceridemia, low HDL cholesterol and hyperglycaemia. There is increasing evidence that nitroxidative stress is closely related to MetS and its metabolic and cardiovascular complications. 3-nitrotyrosine (NT), a stable product of a posttranslational protein modification, has appeared as a marker of nitroxidative stress. Studies on circulating NT levels in MetS are limited and discordant. Therefore, the aim of the current study was to determine the serum NT levels in patients with nascent MetS. It also revealed the association between NT, serum fasting glucose and homeostasis model assessment (HOMA-IR)-estimated insulin resistance.

The study involved 63 patients with nascent MetS and 34 healthy controls. Serum NT concentrations were determined using an ELISA method. The levels of NT did not differ significantly between patients with MetS and the control group [12.59 (3.79–22.68) nmol/L vs. 4.23 (1.73–18.32) nmol/L; $p = 0.08$, respectively]. However, subjects with five MetS components had significantly higher NT concentrations [28.13 (19.27–38.58) nmol/L; n = 20], compared to patients with only three MetS components [6.24 (1.8–9.8) nmol/L; n = 17, $p<0.0001$] and to controls ($p<0.0001$). A significant positive correlation between NT concentrations and glycaemia was evident only in the presence of all five MetS components ($r = 0.485$, $p = 0.03$). Nitrotyrosine correlated positively with HOMA-IR in all MetS patients ($r = 0.287$, $p = 0.025$).

Nitroxidative stress might be associated with insulin resistance in subjects with MetS and increases proportionally to the number of components of the syndrome.

Keywords: nitrotyrosine, nitroxidative stress, metabolic syndrome, insulin resistance.

INTRODUCTION

Metabolic syndrome (MetS) represents a constellation of metabolic disturbances, comprising central obesity, hypertension, dyslipidemia – hypertriglyceridemia and low levels of high-density lipoprotein (HDL) cholesterol, and hyperglycaemia [1]. Although there has been a significant debate regarding the criteria and concept of the syndrome, it is unequivocally linked to an increased risk of developing type 2 diabetes (T2DM) and cardiovascular diseases (CVD). It is generally accepted that insulin resistance (IR) is the major underlying mechanism responsible for development of MetS [2, 3]. IR is the pivotal predisposing factor and the best indicator of future onset of T2DM, since it normally precedes impaired glucose tolerance (IGT) and fasting hyperglycaemia [3]. The precise molecular mechanisms that link metabolic abnormalities observed in MetS to IR and CVD have not been clarified yet. Many lines of evidence suggest that oxidative stress (OxS) may represent such a link, since it is implicated in each individual component of the syndrome [3, 4]. Increased OxS appears to be a deleterious factor resulting in decreased peripheral insulin sensitiv-

* To whom all correspondence should be sent:
E-mail: tedy.stankova@gmail.com

ity, β-cell dysfunction and adipokine dysregulation [2–4]. OxS may contribute to the development of T2DM by activating stress-signaling pathways, such as the nuclear factor (NF)-κB pathway [5]. Several recent studies have supported the concept that direct exposure of mammalian skeletal muscle to OxS results in stimulation of the serine kinase p38 mitogen-activated protein kinase (p38 MAPK), which is associated with diminished insulin-dependent stimulation of insulin signaling elements and glucose uptake [6, 7]. Overproduction of reactive oxygen species (ROS) can also activate another MAPK- c-jun N-terminal kinase (JNK1) which has recently been connected to obesity-induced IR [8].

It is also well established that inflammation is closely related to OxS, since the pathways, generating mediators of inflammation such as interleukins (IL), cytokines and adhesion molecules, are induced by OxS. Moreover, chronic low-grade inflammation has been recognized as another common event in the unifying pathogenic view for MetS [4].

Given the dramatic increase in the prevalence of MetS worldwide, the evaluation of oxidant-mediated biomolecule modifications which can also predict clinical outcomes is beneficial. However, the classical definition of OxS as a loss of balance between ROS formation and antioxidant defense [9], does not emphasize on the pivotal role of nitric oxide (•NO) and reactive nitrogen species (RNS) in the pro-oxidative alterations. A relevant oxidative posttranslational protein modification, initialized by •NO, is the nitration of protein tyrosine (Tyr) residues to 3-nitrotyrosine (NT), performed through peroxynitrite and myeloperoxidase (MPO)-dependent nitration pathways [10]. A new term – "nitroxidative stress" has been introduced to reinforce the concept that nitration is caused by •NO-derived oxidants and will be used herein [11]. The nitroxidative stress may represent another mechanism involved in IR and MetS pathogenesis and may also indirectly link the syndrome to its later complications such as T2DM, atherosclerosis and CVD. All of the above mentioned pathologies as well as IR and hyperglycaemia, are associated with increased yield of ROS and RNS, endothelial dysfunction, pro-inflammatory changes and decreased bioavailability of •NO [11, 12]. Furthermore, elevated plasma NT levels have also been documented in diabetes [13] and in high-fat diet [14]. Moreover, the hypothesis for involvement of nitroxidative stress in CVD, has also been supported by an observed strong correlation between circulating protein NT, atherosclerotic risk and prevalence of coronary artery disease (CAD) [15].

The provided data suggest involvement of nitroxidative stress in the pathogenesis of MetS and also highlight the potential of NT to monitor progression of MetS to MetS-related complications. However, studies on serum NT levels in MetS are limited and discordant. It is also unclear whether the accumulation of factors related to MetS increases the degree of underlying nitroxidative stress. Therefore, the aim of the current study was to determine the serum levels of NT in patients with nascent MetS. We also postulated a correlation between NT, serum fasting glucose and homeostasis model assessment (HOMA-IR)-estimated insulin sensitivity.

EXPERIMENTAL

Subjects: The study involved 63 patients with nascent MetS, uncomplicated with T2DM, admitted to the Department of Endocrinology and Metabolic Disorders, University Hospital "Kaspela", Plovdiv, Bulgaria. Patients were diagnosed as having MetS according to the International Diabetes Federation (IDF) global consensus definition, modified by the joint statement of the National Heart, Lung and Blood Institute; the American Heart Association; the World Heart Federation; the International Atherosclerosis Society and the International Association for the Study of Obesity. The presence of any three or more of the following five parameters were considered as diagnostic of MetS: (1) waist circumference: ≥ 94 cm in men, ≥ 80 cm in women; (2) elevated triglyceride (TG) levels ≥1.7 mmol/L or drug treatment for elevated TG; (3) reduced HDL cholesterol: <1.0 mmol/L in men, <1.3 mmol/L in women or history of specific treatment for this lipid abnormality; (4) elevated blood pressure (BP): systolic BP ≥130 mm Hg or diastolic BP ≥85 mmHg or drug treatment for hypertension; and (5) fasting blood glucose (FG) >5.6 mmol/L or drug treatment for hyperglycaemia [1]. The control group consisted of 34 healthy sex- and age-matched subjects who had no history of heart disease, diabetes, hypertension, obesity and smoking. The control subjects were not taking any medications or antioxidant supplements. All the enrolled in the study participants met the following inclusion criteria: have no acute or chronic infections or inflammatory disease, no active immunological disease, no advanced CVD, no other known chronic illness, pregnancy or alcohol abuse.

The study was approved by the Human Ethics Committee of Medical University – Plovdiv (№4/ 21.09.2017) and was conducted in accordance with the Declaration of Helsinki. All participants signed an informed consent.

Laboratory analysis: Fasting blood samples in anticoagulant-free tubes and clinical data were collected. Thirty minutes after blood collection tubes were centrifuged at 3000 g for 10 minutes and se-

rum was separated in Eppendorf tubes. Serum samples for NT detection were stored at –80 °C until analysis. Serum FG concentrations were measured immediately by the standard hexokinase enzymatic method. Serum FG, TG, total and HDL cholesterol were analyzed using an automatic blood analyzer (Beckman Coulter AU480, Beckman Instruments Inc., USA). Serum insulin levels were determined by chemiluminescent immunoassay (Beckman Coulter Access, Beckman Instruments Inc., USA). The homeostasis model assessment (HOMA-IR) was used to detect the degree of IR by measuring the levels of FG and insulin. HOMA-IR was calculated using the following formula: HOMA-IR= (fasting glucose [mmol/L]×fasting insulin [μU/mL]) / 22.5 [16].

The concentrations of serum protein-bound NT (nmol/L) were measured by ELISA method using commercially available kit (Hycult Biotech, Uden, the Netherlands), according to the manufacturer's instructions. The absorbance was red at 450 nm on ELISA reader (HumaReader HS, HUMAN, Wiesbaden, Germany). Concentrations of unknown samples were determined using a standard curve, constructed by plotting absorbance values versus concentrations of standards.

Statistics: Statistical analysis was performed using SPSS software, version 17.0 (SPSS Inc., Chicago, IL, USA). The Kolmogorov-Smirnov test was used to evaluate whether the distribution of continuous variables was normal. Student's *t*-test and the Mann-Whitney *U* test were used for the analysis of parametric and non-parametric data, respectively. Continuous variables were expressed as mean ± SD or as median and interquartile range. Spearman's rank correlation coefficients were used to examine the correlation between NT levels, glycaemia and HOMA-IR. The level of significance was set at $p < 0.05$.

RESULTS AND DISCUSSION

The baseline clinical and metabolic characteristics of the study participants are presented in Table 1.

The MetS patients had significantly higher levels of waist circumference, FG, total cholesterol, TG, systolic BP, diastolic BP and significantly lower HDL cholesterol. Serum NT levels tended to be higher in patients with MetS, although they did not differ significantly from the healthy subjects. So far, the data published about levels of circulating NT in MetS, IGT and T2DM are rather controversial. Some authors have concluded that detection of elevated plasma NT concentrations in patients with MetS [17] and T2DM [13] is sure evidence of OxS, while according to others hyperglycaemia and IGT do not affect systemic NT concentrations [18, 19]. This discrepancy could be partially explained with the age difference between the subjects in the cited investigations as well as with the age difference between patients and controls, since NT accumulates during the aging process [10, 20]. Variety of MetS comorbidities or complications could enhance protein Tyr nitration [20]. However, our age- and sex-matched study conducted newly diagnosed patients with nascent MetS, uncomplicated with T2DM or CVD, and has sufficient power to detect even small differences of NT levels.

Majority of the studies [13, 14, 17–19] have examined NT levels in blood plasma, but the difference in fibrinogen levels have not been taken into account. This acute phase protein is one of the principal targets for Tyr nitration, so a myriad of pro-thrombotic and inflammation-related conditions can augment fibrinogen levels, thus increasing the total concentration of protein-bound NT [21, 22]. Therefore, we detected NT in serum samples.

Table 1. Biochemical and anthropometric characteristics of the study groups

Characteristics	Patients with MetS (n=63)	Control subjects (n=34)	*p*-value
Sex, Male/Female (no.)	28/35	17/17	
Age (years)	43.5 ± 11.6	41.2 ± 10.8	
Waist circumference (cm)	97 ± 14	83 ± 10	<0.001
Serum glucose (mmol/L)	5.25 ± 0.98	4.7 ± 0.41	<0.0001
Total cholesterol (mmol/L)	5.39 ± 1.67	3.68 ± 0.9	<0.0001
HDL cholesterol (mmol/L)	1.18 (1.1–1.26)	1.35 (1.28–1.41)	<0.001
TG (mmol/L)	1.63 ± 0.71	1.24 ± 0.31	<0.0001
Systolic blood pressure (mmHg)	120 ± 11	118 ± 6	0.012
Diastolic blood pressure (mmHg)	86 ± 4	79 ± 5	<0.01
HOMA-IR	2.34 (1.51–3.59)	Not assessed	
NT (nmol/L)	12.59 (3.79–22.68)	4.23 (1.73–18.32)	0.08

Data are presented as mean ± SD or median (25th-75th percentile).

Since OxS and nitroxidave stress are caused by imbalance between ROS/RNS and antioxidants, ameliorated antioxidant defense could counterbalance increased nitroxidave stress in MetS, accounting for the non-significant increase of NT levels. Bo *et al.* reported elevated plasma NT levels only in diabetic patients with lower than recommended daily intake of antioxidant vitamins C and A [19]. Recent studies on MetS have confirmed the hypothesis that in response to aggravated OxS, cells upregulate the primary antioxidant enzymes superoxide dismutase (SOD), glutathione peroxidase and catalase, thus attempting to prevent oxidative injury [23, 24]. On the other hand inactivated through Tyr nitration manganese SOD has been detected in acute and chronic inflammatory processes both in animal models and in humans [25]. Nevertheless, antioxidant status of the research subjects have not been assessed in some of the above-mentioned investigations [14, 17, 18], demonstrating increased NT levels in MetS and T2DM. This was also a limitation of our research.

Although we did not find a significant difference in serum NT levels between the patient and the control groups, NT concentrations significantly and progressively increased with the increase of MetS components. Subjects who fulfilled all the five diagnostic criteria for MetS [1] had significantly higher NT levels, compared both to controls and patients with only three MetS components (Table 2).

These results are in accordance with the study, conducted by Yubero-Serrano *et al*. Yet, this research group did not include healthy controls, but compared only MetS patients with varying from two to five number of MetS components [24]. Any of the MetS components by itself can cause over-activation of NADPH oxidase, increased production of ROS and superoxide radicals ($O_2^{\cdot-}$), in particular [3]. Under conditions of ROS surplus, •NO can be oxidatively inactivated though a diffusion-controlled reaction with $O_2^{\cdot-}$, generating the powerful oxidizing and nitrating agent peroxynitrite (ONOO−) [10, 26]. The production of the short-lived ONOO− (half-life ca. 10 ms) [26] can be indirectly inferred by the presence of the stable NT. Our results of a significant increase of NT levels only

in the cohort with 5 MetS components confirmed that MetS is not merely a cluster of risk factors, but its components can interact and amplify the effect of each other. In addition, the formation of peroxynitrite and NT also leads to a loss of the beneficial anti-inflammatory, anti-proliferative and anti-aggregant actions of •NO, well-known as the major determinant of the normal homeostasis of cardiovascular (CV) system [11]. Thus the progressive increase of NT concentrations in parallel with the number of MetS components suggests a strict association between nitroxidative stress and common CV and metabolic burden.

Furthermore, a positive correlation between serum NT and fasting glucose was established only in the presence of all five MetS components (Fig. 1) which also favored the hypothesis for the profound complexity of MetS. Despite the fact that acute hyperglycaemia has been shown to induce NT overproduction, even in the plasma of healthy subjects [27], we observed that the harmful effect of chronic
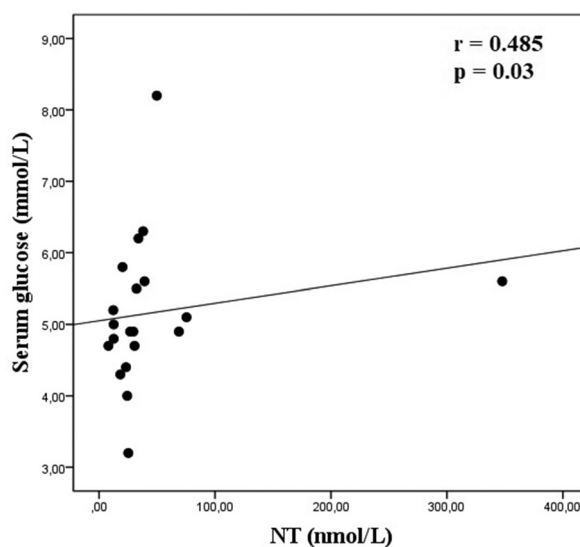
Fig. 1. Correlation between serum nitrotyrosine (NT) and fasting glucose concentrations in patients with five components of metabolic syndrome (n = 20).

Table 2. Serum nitrotyrosine (NT) levels according to the number of MetS components

Measured serum biomarker	Control subjects (n = 34)	Patients with MetS (n=63)		
		Subjects with 3 MetS components (n = 17)	Subjects with 4 MetS components (n = 26)	Subjects with 5 MetS components (n = 20)
NT (nmol/L)	4.23 (1.73–18.32)	6.24 (1.8-9.8)	9.25 (2.99–16.94)	28.13 (19.27–38.58)[a, b]

Data are presented as median (25th–75th percentile). [a] Compared to the control subjects, *p*<0.0001; [b] Compared to the subjects with 3 components of MetS, *p*<0.0001.

hyperglycaemia could only be displayed on the background of the other four MetS features.

Accumulation of MetS components is associated with nitroxidative stress, which may impair the insulin-stimulated glucose uptake in insulin-sensing tissues like liver, muscles and adipose tissue. *In vitro* investigations have shown that ONOO− increases nitration of insulin receptor – beta (IR-β), insulin receptor substrate (IRS)-1, IRS-2 and Akt in muscles [28]. Moreover, Tyr nitration has been associated with hepatic IR and disturbed glucose metabolism regulation in a lipid infused mice model [29]. Recent research has also demonstrated glucose-mediated elevation of Tyr nitration in adipocytes [30]. Furthermore, production of NT reduces •NO bioavailability. At physiological levels •NO acts as a signaling molecule regulating energy homeostasis in adipose tissue by stimulating glucose uptake and insulin-responsive glucose transporter protein-4 (GLUT4) translocation along with increasing glucose and fatty acid metabolism [31]. Thus Tyr nitration has been associated with the onset of IR and subsequent development of compensatory hyperinsulinemia. The full transition to overt T2DM is triggered by β-cell failure. Interestingly, elevated NT-staining in islets from diabetic mice has been related to protein oxidation damage and death of pancreatic β-cells [32].

Considering these data as well as the central role of visceral obesity in the development both of MetS and IR, we hypothesized that nitroxidative stress may be a key link between metabolic abnormalities in MetS and underlying IR. To investigate this suggestion we also evaluated the association between NT levels and insulin sensitivity. Nitrotyrosine concentrations positively correlated with fasting insulin levels and hence with HOMA-IR within the general MetS population (Fig. 2). There was not a significant difference in the magnitude of this correlation between MetS subgroups according to the number of MetS components (data not shown).

The observed weak, but significant positive correlation might indicate that nitroxidative stress alters the intracellular signaling pathways by inducing hyperinsulinemia and IR. This may also be associated with the second, MPO-dependent pathway for Tyr nitration [10, 26] and the increased activity of MPO in obesity-related conditions [33]. MPO is an enzyme expressed abundantly in granules of neutrophils and to a lesser extent in monocytes, the first cells responding to an inflammatory challenge [34]. Therefore, MPO is usually associated with OxS, chronic and acute inflammation. In MetS patients, neutrophils have been correlated with HOMA-IR and the prototypic biomarker of inflammation, high sensitivity C-reactive protein (hsCRP) [35]. Furthermore, serum MPO has also been asso-
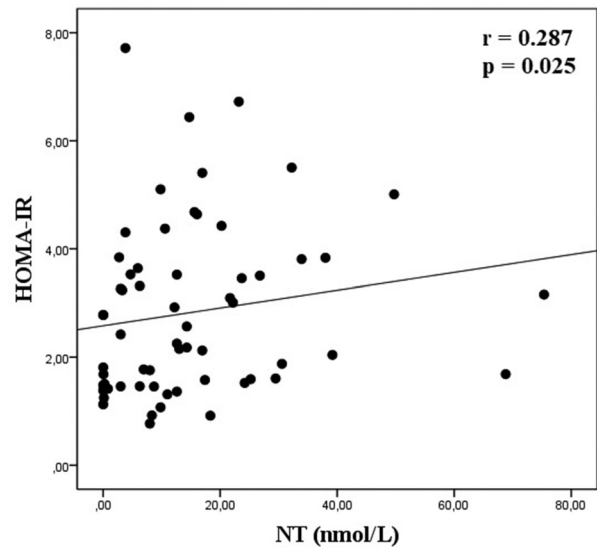
Fig. 2. Correlation between serum nitrotyrosine (NT) concentrations and homeostasis model assessment index (HOMA-IR) in patients with metabolic syndrome (n = 63).

ciated with IL-6 in impaired fasting glucose [36]. Consequently, Heinecke *et al.* proposed MPO as a mediator of IR [37]. This delineates the possible role of MPO-nitration as another mechanism that links increased protein Tyr nitration, chronic subclinical inflammation and IR in MetS.

In addition, peroxinitrite can be directly cytotoxic for endothelial cells and NT has been proposed as a biomarker of diabetic macro-and microvascular complications [38]. MPO has also emerged as a widely used marker for CV risk [11, 33, 39], especially on the background of existing IR and T2DM [40]. Furthermore, a strong correlation between circulating protein NT and the severity of CAD has been recently documented. In the same study, treatment with statins, well known indirect antioxidants, has diminished NT levels [15]. Although larger clinical trials are needed to confirm this finding, it has also suggested the promising role of NT in monitoring vasculoprotective and antioxidant therapies.

CONCLUSIONS

The current study demonstrates a positive correlation between nitroxidative stress, manifested by serum NT concentrations, and insulin resistance, measured by HOMA-IR, in subjects with nascent MetS. This finding suggests possible involvement of nitroxidative stress in MetS pathogenesis, since insulin resistance has been previously recognized as the major underlying mechanism in the develop-

ment of the syndrome. Furthermore, subjects who fulfill all the five diagnostic criteria for MetS may be exposed to a higher level of nitroxidative stress and its detrimental effects. This statement is also supported by the positive correlation between NT and fasting glucose only in the cohort with five MetS components. Therefore, the measurement of serum nitrotyrosine in subjects with metabolic syndrome might contribute to the identification of a subset of patients at increased risk of metabolic and cardiovascular complications.

REFERENCES

1. K. G. Alberti, R. H. Eckel, S. M. Grundy, P. Z. Zimmet, J. I. Cleeman, K. A. Donato, *Circulation*, **120**, 1640 (2009).
2. D. Lann, D. LeRoith, *Med Clin North Am.*, **91** (6), 1063 (2007).
3. S. Tangvarasittichai, *World J Diabetes.*, **6**, 456 (2015).
4. S. J. Chen, C. H. Yen, Y. C. Huang, B. J. Lee, S. Hsia, P. Lin, *PLoS One*, **7**, e45693 (2012).
5. T. Ogihara, T. Asano, H. Katagiri, H. Sakoda, M. Anai, N. Shojima, H. Ono, M. Fujishiro, A. Kushiyama, Y. Fukushima, M. Kikuchi, N. Noguchi, H. Aburatani, Y. Gotoh, I. Komuro, T. Fujita, *Diabetologia*, **47** (5), 794 (2004).
6. K. Vichaiwong, E. J. Henriksen, C. Toskulkao, M. Prasannarong, T. Bupha-Intr, V. Saengsirisuwan, *Free Radic. Biol. Med.*, **47**, 593 (2009).
7. J. S. Kim, V. Saengsirisuwan, J. A. Sloniger, M. K. Teachey, E. J. Henriksen, *Free Radic. Biol. Med.*, **41**, 818 (2006).
8. J. Hirosumi, G. Tuncman, L. Chang, C. Z. Gorgun, K. T. Uysal, K. Maeda, M. Karin, G. S. Hotamisligil, *Nature*, **420**, 333 (2002).
9. H. Sies, *Am. J. Med.*, **91**, 31 (1991).
10. R. Radi, *Proc. Natl. Acad. Sci. USA.*, **101**, 4003 (2004).
11. G. Peluffo, R. Radi, *Cardiovasc Res.*, **75**, 291 (2007).
12. G. Kojda, D. G. Harrison, *Cardiovasc Res.*, **43**, 562 (1999).
13. A. Ceriello, F. Mercuri, L. Quagliaro, R. Assaloni, E. Motz, L. Tonutti, C. Taboga, *Diabetologia*, **44**, 834 (2001).
14. A. Ceriello, L. Quagliaro, L. Piconi, R. Assaloni, R. Da Ros, A. Maier, K. Esposito, D. Giugliano, *Diabetes*, **53**, 701 (2004).
15. M. H. Shishehbor, R. J. Aviles, M. Brennan, X. Fu, M. Goormastic, G. L. Pearce, N. Gokce, J. F. Keaney, Jr, M. S. Penn, D. L. Sprecher, J. A. Vita, S. L. Hazen, *JAMA*, **289**, 1675 (2003).
16. D. R. Matthews, J. P. Hosker, A. S. Rudenski, B. A. Naylor, D. F. Treacher, R. C. Turner, *Diabetologia*, **28**, 412 (1985).
17. K. Esposito, M. Ciotola, B. Schisano, L. Misso, G. Giannetti, A. Ceriello, D. Giugliano, *J. Endocrinol. Invest.*, **29**, 791 (2006).
18. X. L. Wang, D. L. Rainwater, A. Leone, M. C. Mahaney, *Diabet Med.*, **21**, 577 (2004).
19. S. Bo, R. Gambino, S. Guidi, B. Silli, L. Gentile, M. Cassader, G. F. Pagano, *Diabetic Medicine*, **22**, 1185 (2005).
20. H. Ischiropoulos, *Biochem. Biophys. Res. Commun.*, **305**, 776 (2003).
21. C. Vadseth, J. M. Souza, L. Thomson, A. Seagraves, C. Nagaswami, T. Scheiner, *J. Biol. Chem.*, **279**, 8820 (2004).
22. J. Kotur-Stevuljevic, L. Memon, A. Stefanovic, S. Spasic, V. Spasojevic-Kalimanovska, N. Bogavac-Stanojevic, *Clin Biochem.*, **40**, 181 (2007).
23. J. M. Mates, C. Perez-Gomez, I. Nunez de Castro, *Clin. Biochem.*, **32**, 595 (1999).
24. E. M. Yubero-Serrano, J. Delgado-Lista, P. Peña-Orihuela, P. Perez-Martinez, F. Fuentes, C. Marin, I. Tunez, F. Tinahones, F. Perez-Jimenez, *Exp. Mol. Med.*, **21**, 45 (2013).
25. L. A. MacMillan-Crow, J. P. Crow, J. D. Kerby, J. S. Beckman. J. A. Thompson, *Proc. Natl. Acad. Sci. USA*, **93**, 11853 (1996).
26. R. Radi, *J. Biol. Chem.*, **288** (37), 26464 (2013).
27. R. Marfella, L. Quagliaro, F. Nappo, A. Ceriello, D. Giugliano, *J. Clin. Invest.*, **108**, 635 (2001).
28. J. Zhou, K. Huang, *Toxicol. Appl. Pharmacol.*, **241**, 101 (2009).
29. A. Charbonneau, A. Marette, *Diabetes*, **59**, 861 (2010).
30. T. Koecka, B. Willardb, J. W. Crabbc, M. Kinter, D. J. Stuehra, K. S. Aulaka, *Free Radic. Biol. Med.*, **46** (7), 884 (2009).
31. T. Tanaka, K. Nakatani, K. Morioka, H. Urakawa, N. Maruyama, N. Kitagawa, A. Katsuki, R. Araki-Sasaki, Y. Hori, E. C. Gabazza, Y. Yano, H. Wada, T. Nobori, Y. Sumida, Y. Adachi, *Eur. J. Endocrinol.*, **149**, 61 (2003).
32. W. L. Suarez-Pinzon, C. Szabo, A. Rabinovitch, *Diabetes*, **46**, 907 (1997).
33. J. Olza, C. M. Aguilera, M. Gil-Campos, R. Leis, G. Bueno, M. D. Martínez-Jiménez, M. Valle, R. Cañete, R. Tojo, L. A. Moreno, A. Gil, *Diabetes Care*, **35**, 2373 (2012).
34. B. S. van der Veen, M. P. de Winther, P. Heeringa, *Antioxid. Redox Signal.*, **11**, 2899 (2009).
35. H. Kaur, B. Adams-Huet, G. Smith, I. Jialal, *Metab. Syndr. Relat. Disord.*, **11**, 128 (2013).
36. A. Agarwal, A. Hegde, C. Yadav, A. Ahmad, P. A. Manjrekar, R. M. Srikantiah, *Ind. J. Clin. Biochem.*, **32**, 33 (2017).
37. J. W. Heinecke, I. J. Goldberg, *Diabetes*, **63**, 4001 (2014).
38. K. Stadler, *Curr. Med. Chem.*, **18**, 280 (2011).
39. K. Roger, L. P. Schindhelm, T. T. van der Zwan, P. G. Scheffer, *Clin. Chem.*, **55** (8), 1462 (2009).
40. P. Song, J. Xu, Y. Song, S. Jiang, H. Yuan, X. Zhang, *Dis. Markers*, **2015**, 761939 (2015).

3-НИТРОТИРОЗИН КАТО СЕРУМЕН БИОМАРКЕР ЗА „НИТРООКИСЛИТЕЛЕН СТРЕС" И ИНСУЛИНОВА РЕЗИСТЕНТНОСТ ПРИ НЕУСЛОЖНЕН МЕТАБОЛИТЕН СИНДРОМ

Т. Р. Станкова[1]*, Г. Т. Делчева[1], К. И. Стефанова[1], А. И. Манева[1],
С. В. Владева[2, 3], Г. А. Цветкова[4]

[1] *Катедра „Химия и биохимия", Фармацевтичен факултет, Медицински университет – Пловдив, Пловдив, България*
[2] *Клиника „Ендокринология и болести на обмяната", УМБАЛ „Каспела", Пловдив, България*
[3] *Медицински колеж, Медицински университет – Пловдив, Пловдив, България*
[4] *„Клинична лаборатория", УМБАЛ „Каспела", Пловдив, България*

(Резюме)

Метаболитният синдром (МС) представлява комплекс от метаболитни нарушения, включващи централно затлъстяване, хипертензия, хипертриглицеридемия, намалени нива на липопротеиновите комплекси с висока плътност (HDL холестерол) и хипергликемия. Натрупват се все повече доказателства за тясната връзка между „нитроокислителния" стрес с МС и неговите метаболитни и сърдечносъдови усложнения. „Нитроокислителният" стрес може да се оцени чрез нивото на 3-нитротирозин (НТ), който е стабилен продукт на постранслационна модификация на белтъци. Ограничени и доста противоречиви са изследванията върху серумните концентрации на НТ при МС. Затова целта на настоящото проучване е да определи серумните нива на НТ при пациенти с неусложнен МС, както и да изясни връзката между НТ концентрации с нивото на глюкоза на гладно и с инсулиновата чувствителност, оценена чрез хомеостазния модел на инсулинова резистентност (HOMA-IR).

Изследвани са 63 пациенти с МС и 34 здрави контроли. Серумните концентрации на НТ са определени чрез ELISA метод. Не се установява статистически значима разлика в концентрациите на НТ между пациентите с МС [12.59 (3.79–22.68) nmol/L] и здравите контроли [4.23 (1.73–18.32) nmol/L; $p = 0.08$]. Въпреки това пациентите, при които са изпълнени и петте диагностични критерии за МТ, показват значително по-високи НТ нива [28.13 (19.27–38.58) nmol/L; n = 20], спрямо пациентите само с 3 МС конпонента [6.24 (1.8–9.8) nmol/L; n = 17, $p<0.0001$] и здравите контроли [$p<0.0001$]. Положителна корелация между серумните нива на НТ и глюкоза се доказа само при наличие и на петте компонента на МС (n = 20, r = 0.485, $p = 0.03$), докато корелацията с HOMA-IR индекса е валидна за цялата пациентска група (r = 0.287, $p = 0.025$).

„Нитроокислителният стрес" може би е свързан с патогенезата на инсулиновата резистентност при МС и се увеличава пропорционално с нарастването на броя на компонентите на МС.

Aerogels – new materials with promising applications

N. Danchova, D. Paskalev, S. Gutzov*

*Sofia University "St. Kliment Ohridski", Faculty of Chemistry and Pharmacy,
Department of Physical Chemistry, J. Bourchier Blvd. 1, 1164 Sofia, Bulgaria*

This work focuses on the dependence preparation conditions – structure – physical properties of hydrophobic silica aerogel granules and micro powders, all of them prepared under subcritical drying conditions with potential application as insulation materials. The so prepared nanoporous hydrophobic silica aerogel granules and powders are analyzed with scanning electron microscope, infrared spectroscopy, differential scanning calorimetry and thermal conductivity measurements. The physico-chemical properties of the aerogels are compared with that of commercial aerogel granules. It has been proved that a long solvent exchange times and surface hydrophobization lead to aerogel micro powders with a specific surface of about 850 m^2/g and a bulk density of about 0.1 g/cm^3.

Keywords: aerogels, silica, sol-gel, thermal insulation.

INTRODUCTION

Sol-gel technology is a powerful method for the preparation of oxide matrixes at low temperatures. Most important advantages of sol-gel technology are the use of liquid chemicals, the possibility for preparation of complicated chemical compositions and the low temperature preparation. Sol-gel chemistry offers a possibility for the ambient preparation of optical materials like xerogels or layers doped with rare earth ions. In the same way a wide range of useful ceramic materials based on Al_2O_3, ZrO_2, SnO_2, SiO_2 can be easily prepared. Gels are solids confining a solvent in a three-dimensional network. The solvent may be enclosed as quasi-liquid in a pore system. At this state, the gels are called hydrogels (water as solvent) or alcogels (alcohol as solvent), etc. If the network has nano-dimensions or is index-matched, the gel looks transparent. Sol gel-chemistry is based on three basic chemical reactions: water hydrolysis of liquid alkoxides (the most important reagents in sol-gel chemistry) followed by condensation. Condensation (better known as gelation), could be performed as a water condensation or alcohol condensation [1]. The results of sol-gel process strongly depend on the reaction conditions: it is possible to obtain micro or nanopowders,

transparent xerogels, transparent thin films or even aerogels – porous solids with extremely low thermal conductivity and density.

One of the most important advantages of sol-gel chemistry is the preparation of aerogels. Aerogels are a class of porous, solid materials with extreme and valuable materials properties. Most notable aerogels are known for their extreme low densities (which range from 0.001 to 0.5 g/cm^3). In fact, the lowest density solid materials that have ever been produced are all aerogels, including silica aerogels. The advantages of silica aerogels are: low density, theoretically down to (0.001 g/cm^3), optical refraction index (1.002), thermal conductivity (0.02 W/m·K), speed of sound through a material (70 m/s) and a relative dielectric constant 1.008 at 3–40 GHz [2].

There are two main technological strategies for preparation of aerogels: supercritical drying and subcritical drying techniques, leading to bulk aerogels, aerogel powders or granules depending on preparation conditions. The supercritical preparation is combined with liquid carbon dioxide drying of gels at supercritical conditions, following the pioneer investigations of Kistler, 1931[3]. The expensive supercritical drying can be replaced by subcritical drying at low temperature and pressure. This method include several basic steps: preparation of wet gel, solvent exchange of the solvent in the pores of the wet gel, surface hydrophobization and vacuum drying of the materials. In this way powders or bulk materials with the same physical

---

* To whom all correspondence should be sent:
E-mail: sgutzov@chem.uni-sofia.bg

properties as in the case of supercritical drying can be obtained [4, 5].

Despite of the large number of investigations of hydrophobic silica granules and micro powders, there are open questions concerning the physico – chemical nature of solvent exchange taking place in the pore system of aerogels, variation of subcritical drying conditions and microstructure of the aerogel micro powders and granules. Recently we demonstrated for the first time that silica aerogels are suitable matrixes in the production of light emitting composites containing hybrid molecules, $Eu(phen)_2(NO_3)_3$ [6].

The aim of the present contributions is to compare the physico-chemical properties of subcritical produced amorphous silica aerogels in order to achieve a better understanding of preparation – structure – properties relationship of aerogel powders and granules.

EXPERIMENTAL

Millimeter scaled aerogel granules (sample notation SAA). Millimeter scaled aerogel granules were prepared using standard tetraethylortosilicate (TEOS), 99% ethanol (EtOH), 0.23 M hydrochloric acid, 0.14 M ammonia solution, trimethylchlorosilane (TMCS), n-hexane, acetone and distilled water. First, a mixture of TEOS and EtOH was prepared. After 5 minutes stirring distilled water was added followed by the hydrolyzing agent, the 0.23 M HCl. The hydrolysis reaction took about one hour, after that a 0.14 M ammonium solution was used to catalyze the condensation reaction. The gelation time, t_{gel}, was 10–15 minutes, after that EtOH was added to start the solvent exchange reaction at room temperature. The solvent exchange continued for 48 hours followed by hydrophobization in a mixture of TMCS and n-hexane. The hydrophobization continued for 24 hours at room temperature. Drying of the aerogel SAA was performed for 24 hours in a vacuum dryer at 0.5 atm and 70 °C. The bulk density of aerogel granules SAA was 0.1 g/cm³, combined with a very low thermal conductivity, $\lambda = 0.033$ W/m·K and a specific heat $C_p = 1440$ J/kg·K at 30 °C. Details about the thermal insulation properties of aerogel granules depending on preparation conditions are discussed in [4].

During the preparation we used a vacuum drying camera NÜVE EV 018 with a volume V = 1240 cm³ equipped with a LABOR port diaphragm pump (delivery 30 l/min and power 300 W) working at 0.15–0.2 atm.

Subcritical drying at room temperature and 0.150 atm, sample notation S1. Samples obtained at room temperature drying, using the above given

sol-gel preparation conditions (S1) were prepared. The scheme led to granules with bulk density of 0.12 g/cm³. The physical properties expected are close to that of the samples described above because of the dependence between density and thermal properties of aerogels [2, 4]. This confirms that the drying temperature is not a determining factor for the physical properties of aerogel granules.

Aerogel micro powders (sample notations D1 and D2). We developed a new preparation scheme for the preparation of micro powders based on long solvent exchange at room temperature or 40 °C at stirring, followed by drying of the aerogel at subcritical conditions. The preparation of aerogel micro powders was accomplished through four steps, given in Figure 1. The gel preparation and hydrophobi-
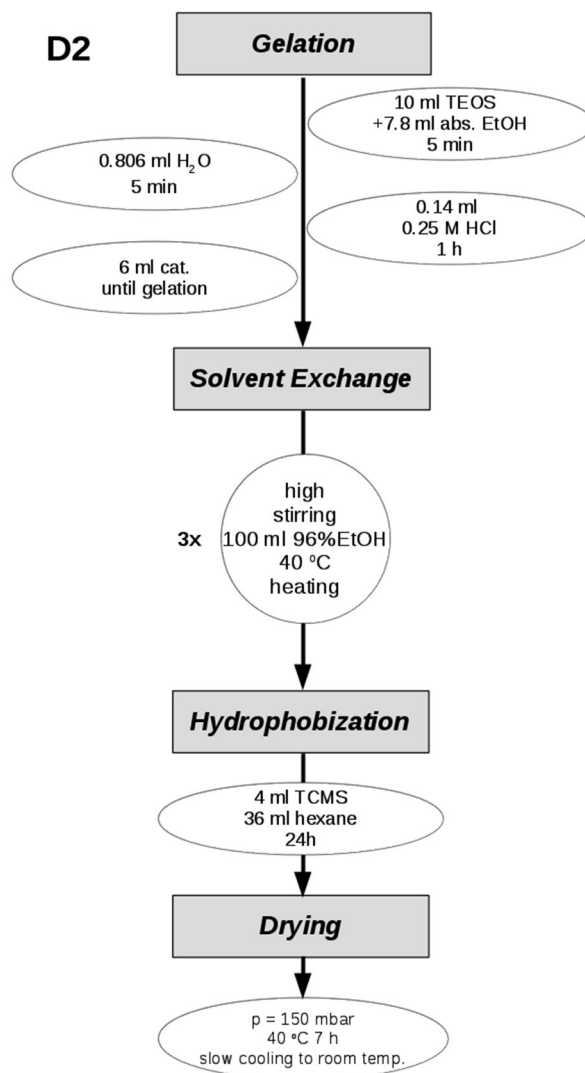
Fig. 1. Sol-gel scheme for preparation of aerogel micro powders at long solvent exchange and 40 °C (sample D2).

zation conditions were close to that of samples SAA and S1, discussed above.

The solvent exchange conditions, however, were changed significantly in order to obtain powders. The solution used here was 100 ml 96% ethanol, the solvent exchange was conducted at stirring. The solvent exchange conditions used were: room temperature and total time of exchange 21 days (*sample D1*) and 40 °C and total time of exchange 11 days (*sample notation D2*). For both samples the solvent was changed two more times.

The last preparation step was the drying of the aerogel micro powders. It was conducted at subcritical conditions – pressure of 0.150 atm and 70 °C temperature for 7 h. The bulk density of these micro powders was about 0.08 g/cm^3 [4].

The amorphous silica micro powders D1 and D2 prepared in this paper possess a typical aerogel morphology, visualized in Figure 2, where a representative SEM picture of aerogel micro powders is given. Here, a wide network of closed and open micrpores and mesopores leads to the low density of the pow-
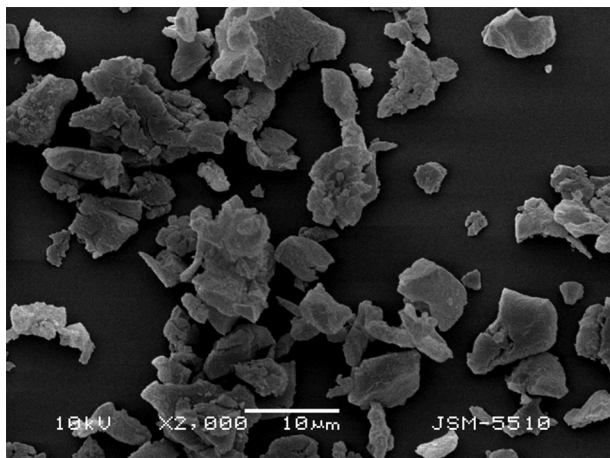
Fig. 2. SEM investigations of aerogel micro powders, sample D2. A typical "cloud – like" morphology of the particles is visible at higher magnifications. The mean particle diameter of powder is in the range of about 5–10 μm.

ders. It is well known, that thermal insulation properties of aerogels depend significantly on the occurrence of nanopores in the range of 10–30 nm [7, 8].

The so prepared, millimeter scaled nanoporous hydrophobic silica aerogel granules and micro powders were analyzed with thermal conductivity measurements and chemical analysis. The thermal conductivity of aerogel granules was measured using a C-THERM TCI–thermal conductivity analyzer using a powder/liquid cell. Scanning electron

microscopic (SEM) investigations were performed using a standard electron microscope JEOL 5510 working on SE regime. Particles were Au – covered. The texture characteristics of the so prepared micro powders and granules were determined by low-temperature (77 K) nitrogen adsorption in a Quantachrome Instrument NOVA 1200e instrument. The nitrogen adsorption-desorption isotherms were analyzed to evaluate the following parameters: specific surface area (S_{BET}), total pore volume (V_t) and associated average pore diameter (D_{av}) [9]. All samples were outgased for 16 h in vacuum at 150 °C before the texture measurements.

Measurements of pH combined with a temperature control were performed using a computer driven pH-meter Hach H270. Infrared (IR) spectra were measured on a standard Thermoscientific 6700 IR spectrophotometer using the KBr preparation technique. Absorption peaks were mathematically treated as overlapping Gaussian curves, peak maxima were determined from second derivative spectra.

RESULTS AND DISCUSSION

The pH dependence vs. time of the solvent exchange process is investigated in order to describe the physico-chemical nature of solvent exchange. Figure 3 displays the experimental data obtained together with temperature measurements; here pH of the solvent exchange solution is measured for a long time continuously together with temperature measurements. The curve obtained can be distinguished into two parts, a fast decrease of pH and an increase of pH. From general chemical point of view the decrease of pH seems to be related to the deprotonation of R-Si-OH groups of the prepared gel. Increasing of pH is due to leaving ammonium cations from the inner pores of the aerogel granules toward the solvent exchange solution of ethanol because ammonium hydroxide is used as a gelation catalyst. The second step is limited by diffusion of the ammonium ions from the pores of the aerogel granules trough the ethanol solution.

Using the pH dependence a rate of the solvent exchange (from point 2 to 3) of 2.5·10^{-4} mol/l·s can be extracted. The deprotonation step (from point 1 to 2) is faster. Further investigation are necessary to develop a kinetic model of solvent exchange describing quantitatively the deprotonation and diffusion limited steps. It is visible that pH measurements could be successfully used to describe microscopically the complicated processes of solvent exchange accompanying the subcritical production of aerogels.

The physicochemical properties of aerogel granules and micro powders discussed here are summa-
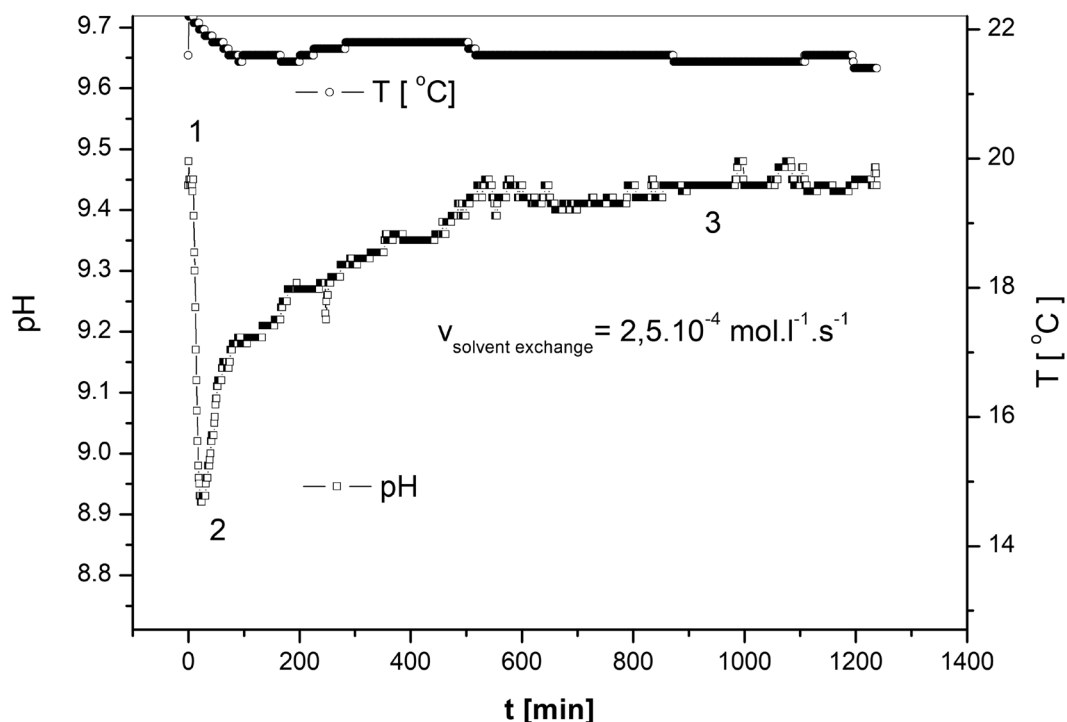
Fig. 3. Representative pH and temperature *vs.* time investigations during solvent exchange.

rized in Table 1, where results from nitrogen adsorption–desorption isotherms are summarized. It is visible that the developed sol-gel scheme leads to the production of high-class aerogel materials, possessing a very high specific surface area. Insulation properties of the produced gels depend strongly on the nanopores, formed in the gels. It is visible, that temperature of drying do not play an important role in aerogel granules production, drying pressure, hydrophobization and solvent-exchange are crucial for the texture properties of aerogel granules and micropowders. The process of powderization of aerogel granules depends strongly on the solvent exchange conditions. The physico-chemical properties of commercial millimeter scaled Cabot Lumira aerogel granules with bulk density of 0.08 g/cm^3 (sample Cabot) are given for comparison.

In Figure 4 IR spectra of Cabot Lumira aerogel granules (sample Cabot) and aerogel granules produced in this contribution are compared.

Figure 4 shows that IR spectra of the investigated samples are identical and demonstrate the reproducibility of the sol-gel technology approach discussed here. Based on [10–12] the intensive peak at wavenumbers near 1090 cm^{-1} or 1220 cm^{-1} correspond to the stretching vibration of Si–O–Si bonds and the peaks at about 840 cm^{-1} and 460 cm^{-1} are assigned to the antisymmetric and symmetric stretching vibration of Si–O–Si, respectively. The bands at

Table 1. Physico-chemical properties of aerogel granules and micropowders. Specific surface area (S_{BET}), the total pore volume (Vt) and associated average pore diameter Dav are given. Samples Cabot, SAA and S1 are millimeter scaled granules, while D1 and D2 are micro powders

Sample	S_{BET}, m^2/g	V_t, cm^3/g	D_{av}, nm
S1	796	3.40	17
D1	840	2.25	11
D2	950	2.67	11
SAA	785	3.12	16
Cabot	699	3.8	21

3440 cm^{-1} and 1632 cm^{-1} represent the stretching and bending vibrations of Si-OH bond and the vibrations of physically adsorbed water. In the spectra a sharp peak coming from Si-CH$_3$ vibrations at about 1260 cm^{-1} is visible, confirming the successful performed hydrophobization.

Using the discussed preparation conditions we produced about 1500 ml hydrophobic granules (sample SAA) and incorporated it as fillers in a glass textulite case-insulation of a Stirling engine cylinder operating at low temperatures. More about the Stirling engine and it components can be found in [13].
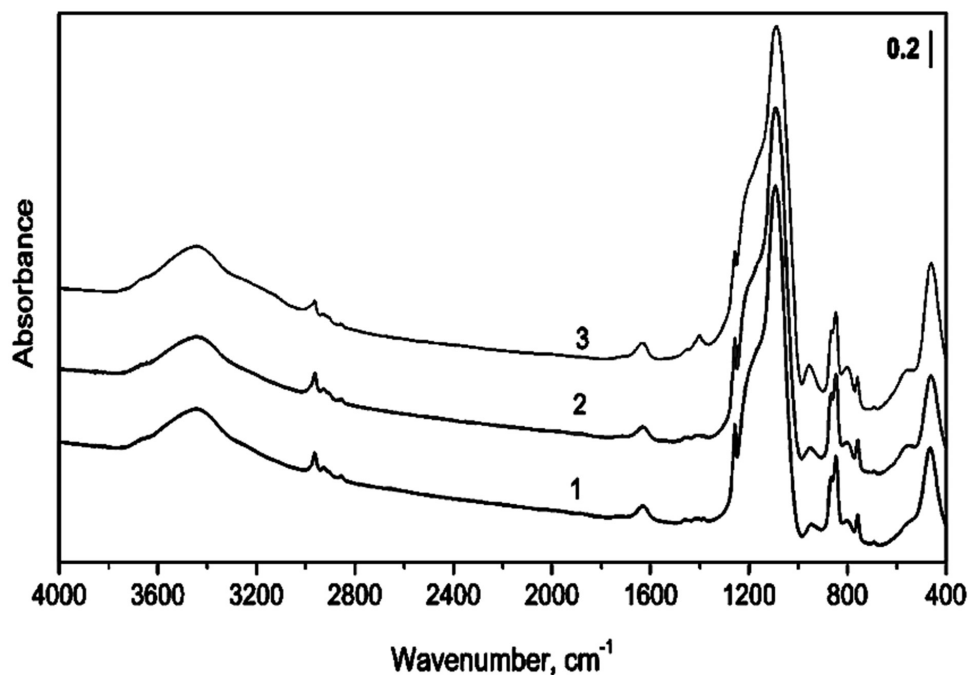
Fig. 4. IR spectra of aerogel millimeter scaled granules: Cabot (1), SAA (2) and (3). Curve 2 and 3 represents spectra of aerogel granule fractions with a density of 0.1 g/cm^3 and 0.2 g/cm^3, respectively.

CONCLUSIONS

A reproducible sol-gel preparation scheme for the production of hydrophobic aerogel granules and micro powders with a specific surface area S_{BET} of about 800 m^2/g and total pore volume of about 3.2 cm^3/g is demonstrated. The insulation properties of aerogel granule and powders in this contribution depend strongly on the nanopores (10–20 nm) formed in the material. The process of powderization of aerogel granules depends on the solvent exchange conditions and drying pressure. The solvent exchange process of aerogels can be separated in two steps, a fast deprotonation reaction and a diffusion limited step. IR spectra are an important tool for controlling the efficiency of aerogel powder production.

REFERENCES

1. C. J. Brinker, G. W. Scherrer, The Physics and chemistry of sol-gel processing, Academic Press INC, New York, 1990.
2. M. A. Aegerter, N. Leventis, M. M. Koebel, Aerogel Handbook, Springer, 2011.
3. S. S. Kistler, *Nature*, **127**, 741 (1931).
4. R. Despande, D. M. Smith, J. Brinker, *US Patent* 5 565 145 (1996).
5. S. Gutzov, N. Danchova, S. I. Karakashev, M. Khristov, J. Ivanova, J. Ulbikas, *J. Sol-Gel Sci. Technol.*, **70**, 511 (2014).
6. S. Gutzov, N. Danchova, R. Kirilova, V. Petrov, S. Yordanova, *Journal of Luminescence*, **183**, 108 (2017).
7. S. S. Kistler, *J. Phys. Chemistry*, **39**, 79, (1935).
8. S. S. Kistler, *J. Phys. Chemistry*, **46**, 19, (1942).
9. N. Stoeva, G. Atanasova, I. Spassova, R. Nikolov, M. Khristova, *Reaction Kinetics, Mechanism and Catalysis*, **118** (1), 199 (2016).
10. T. Kolev, N. Danchova, D. Shandurkov, S. Gutzov, *Spectrochimica Acta Part A: Molecular and Biomolecular Spectroscopy*, **194**, 189 (2018).
11. D. R. Anderson, in: Analysis of Silicones, Wiley-Interscience, New York, Capter 10, 1974.
12. L. J. Bellamy, The infra-red spactra of Complex Molecules, Chapmen and Hall, London, Chapter 20, 1975.
13. S. Gutzov, N. Danchova, J. Ulbikas, J. Bozenko, Report on materials used for increment of Stirling engine efficiency. Development of high efficiency Stirling heat pump. Deliverables: D4.1; D4.2.; D4.2.1., 2013.

АЕРОГЕЛОВЕ – НОВИ МАТЕРИАЛИ С ПЕРСПЕКТИВНИ ПРИЛОЖЕНИЯ

Н. Данчова, Д. Паскалев, С. Гуцов

Софийски Университет „Св. Климент Охридски", Факултет по химия и фармация, катедра Физикохимия

(Резюме)

Настоящото изследване е насочено към изследване на зависимостта препаративни условия – структура – физикохимични свойства на хидрофобни аерогелни гранули и микропрахове от силициев диоксид, получени при субкритични условия. Продуктите са с потенциално приложение като изолационни материали. Получените нанопорьозни гранули и микропрахове са анализирани със сканираща електронна микроскопия, диференциална сканираща калориметрия и термични изследвания. Физикохимичните свойства на получените материали са сравнени с тези на комерсиални аерогелни гранули. Показано е, че продължителният процес на обмен на разтворител води до получаването на аерогелни микропрахове със специфична повърхност около 800 m^2/g и плътност около 0.1 g/cm^3.

A novel monomeric asymmetric tricationic monomethine cyanine dye – Thiazole Orange (TO) analog: synthesis, photophysical and dsDNA binding properties

M. I. Kandinska[1]*, A. A. Vasilev[1], V. S. Videva[1], S. E. Angelova[2]

[1] Faculty of Chemistry and Pharmacy, Sofia University "St. Kliment Ohridski", 1164 Sofia, Bulgaria
[2] Institute of Organic Chemistry with Centre of Phytochemistry, Bulgarian Academy of Sciences, 1113 Sofia, Bulgaria

A new monomeric tricationic cyanine dye **TO-3c-7Cl** – analog of Thiazole Orange (**TO**), has been synthesized using an environmentally benign and simple method and its photophysical properties have been investigated and compared to those of the well-known nucleic acid stain **TO**. Dye **TO-3c-7Cl** has negligible intrinsic fluorescence in Tris-EDTA (TE) buffer, but in the presence of dsDNA its fluorescence intensity increases significantly. DFT and TDDFT calculations are used to compare and contrast the theoretically predicted structure and properties of the new tricationic cyanine dye and **TO**.

Keywords: Thiazole Orange, cyanine dyes, dsDNA, fluorescence.

INTRODUCTION

Cyanine dyes are object of unceasing attention because of their effective and fruitful applications in different scientific areas – laser optics, molecular biology, medicine [1–4].

In recent years, the use of asymmetric cyanine dyes as fluorescent labels or sensors for bioimaging and detection has been of utmost importance. These applications are related to the spectral properties of the dyes and their ability to form fluorescent complexes with variety of biological macromolecules. Such dyes have no or have very weak intrinsic fluorescence, but upon binding to a bio-object the fluorescence intensity can increase dramatically [5]. A wide range of novel molecules with similar characteristics based mainly on **TO** and Oxazole Yellow (**YO**) have been designed, synthesized and commercialized [6, 7].

Continuing our research [8–10] into development of new fluorescent probes for nucleic acids detection, here we report the synthesis of a novel asymmetric monomeric monomethyne cyanine dye **TO-3c-7Cl** – analog of the commercial dsDNA fluorescence binder Thiazole Orange. The preparation of **TO-3c-7Cl** was achieved by using an easy handling, efficient and environmentally benign synthetic procedure. The interactions of the new **TO** derivative with dsDNA have been investigated by absorption and fluorescence spectroscopy. The newly synthesized dye shows quite low fluorescence in TE buffer in the absence of dsDNA, but it becomes strongly fluorescent after binding to the biomolecule. The influence of the substituents attached to the chromophore was investigated by UV-VIS, fluorescence spectroscopy, DFT and TDDFT calculations.

EXPERIMENTAL

All solvents used in the present work were HPLC grade and commercially available. The starting materials **1** and **4** are commercially available and they were used as supplied. Melting point of **TO-3c-7Cl** was determined on a Büchi MP B-545 apparatus and is uncorrected. NMR spectra (^{1}H-, ^{13}C-NMR) were obtained on a Bruker Avance II+ NMR spectrometer operating at 600 MHz for ^{1}H- and 125 MHz for ^{13}C-NMR in DMSO-d$_6$ as solvent. The chemical shifts are given in ppm (δ) using tetramethylsilane (TMS) as an internal standard. UV-VIS spectra were measured on a Unicam 530 UV-VIS spectro-

---

photometer and the fluorescence spectra were obtained on a Varian Cary Eclipse fluorescence spectrophotometer. The intermediate **2** was synthesized by method described in the literature [11].

Synthesis of 3-(4-(4-(dimethylamino)pyridin-1-ium-1-yl)butyl)-2-methylbenzo[d]thiazol-3-ium dibromide (3)

A mixture of 2-methylbenzo[d]thiazole (**1**) 0.76 g (5.1 mmol) and 1-(4-bromobutyl)-4-(dimethylamino)pyridin-1-ium bromide (**2**) 1.71 g (5.1 mmol) was heated at 145 °C for 1.5 h in the absence of a solvent. Then methanol (10 ml) was added and after cooling down of the reaction mixture to room temperature, the product was precipitated with the addition of diethyl ether (25 ml). The precipitate was filtered off and dried at a desiccator. The product **3** was used in the next synthetic route without any additional purification, because of its high hygroscopicity. Yield: 2.79 g (94%).

Synthesis of 4,7-dichloro-1-(4-(4-(dimethylamino) pyridin-1-ium-1-yl)butyl)quinolin-1-ium dibromide (5)

A mixture of 4,7-dichloroquinoline (**4**) 2.00 g (10 mmol) and 1-(4-bromobutyl)-4-(dimethylamino) pyridin-1-ium bromide (**2**) 3.41 g (10 mmol) was heated under argon in 50 ml round bottom flask equipped with a condenser at 145 °C for 10 min in the absence of a solvent. After cooling down of the reaction mixture to room temperature, the product was precipitated with the consecutively addition of methanol (10 ml), acetone (10 ml) and diethyl ether (15 ml). The precipitate was filtered off and dried at a desiccator. The product was used in the next stage of the reaction scheme without any additional purification, because of its high hygroscopicity and low stability. Yield 5.20 g (97%).

Synthesis of (E)-7-chloro-1-(4-(4-(dimethylamino) pyridin-1-ium-1-yl)butyl)-4-((3-(4-(4-(dimethylamino)pyridin-1-ium-1-yl)butyl)benzo[d] thiazol-2(3H)-ylidene)methyl)quinolin-1-ium triiodide (TO-3c-7Cl)

3-(4-(4-(Dimethylamino)pyridin-1-ium-1-yl) butyl)-2-methylbenzo[d]thiazol-3-ium bromide (**3**) (1 mmol) and 4,7-dichloro-1-(4-(4-(dimethylamino) pyridin-1-ium-1-yl)butyl)quinolin-1-ium bromide (**5**) (1 mmol) were mixed and finely ground in a mortar. The mixture was transferred to a 50 ml flask equipped with an electromagnetic stirrer and a reflux condenser and then methanol (10 ml) was added. The mixture was heated at 50 °C for 10 min and

N-ethyldiisopropylamine (DIPEA) (2.2 mmol) was added dropwise. The reaction mixture was stirred vigorously for 2 h without heating and diethyl ether (25 ml) was added. The resulting precipitate was filtered off and the residue was dissolved in methanol (20 ml). Saturated aqueous KI (10 ml) was added to the methanol solution and the resulting precipitate was filtered off and air-dried. The yield of the crude product was over 80%. **TO-3c-7Cl** was purified by multiple recrystallizations from methanol. **TO-3c-7Cl:** Yield 25%, Mp: 260–263°C. Mw = 1047.05. ^{1}H-NMR, δ: 1.75–1.78 (m, CH_2, 4H), 1.80–1.87 (m, CH_2, 4H), 3.17 (s, NCH_3, 12H), 4.02–4.04 (m, N^+CH_2, 4H), 4.22 (t, ^3J = 6. 9 Hz, N^+CH_2, 2H), 4.59 (t, ^3J = 6.8 Hz, N^+CH_2, 2H), 6.89 (s, CH, 1H), 7.02 (d, ^3J = 7.5 Hz, 2H), 7.28 (d, ^3J = 7.2 Hz, 2H), 7.44 (dd, ^3J = 7.6 Hz, 2H), 7.62 (dd, ^3J = 8.0 Hz, 2H), 7.74 (d, ^3J = 7.6 Hz, 2H), 7.82 (d, ^3J = 8.4 Hz, 1H), 8.07 (d, ^3J = 7.8 Hz, 1H), 8.17 (s, 1H), 8.27–8.29 (m, 2H), 8.55 (d, ^3J = 7.4 Hz, 1H), 8.82 (d, ^3J = 9.3 Hz, 1H).

^{13}C, DEPT-135 NMR, δ: 25.66 (CH_2), 27.76 (CH_2), 34.70 (CH_3), 40.24 (CH_3), 53.76 (CH_2), 56.48 (CH_2), 89.22 (CH), 108.14 (CH), 108.18 (CH), 108.25 (CH), 113. 77 (CH), 113.84 (CH), 114.28 (CH), 117.72 (CH), 123.47 (CH), 125.31 (CH), 127.31 (CH), 128.58 (CH), 128.79 (CH), 142.32 (CH), 145.07 (CH). Elemental analysis for N (%): Calculated 8.03, Found 8.31.

COMPUTATIONAL

The B3LYP functional [12, 13] was used in the geometry optimization of the cationic fragments of **TO** and **TO-3c-7Cl** with/without I⁻ counterions. The calculations were performed with the diffuse function-augmented 6-31G(d,p) [14–16] basis set (6-31+G(d,p)) for systems without counterions and with mixed basis set for those with counterions (6-31+G(d,p) basis set for the lighter atoms (C, N, S, Cl and H) and with SDD [17] pseudopotential for the I). The selected combination method/basis set has been proven [9] to reproduce reliably the geometry of 3-(4-((3-methyl-1,3-benzothiazol-2(3H)-ylidene)methyl)-quinolinium-1-yl) propanoate tetrahydrate (CSD ENTRY OVUJUL/ CCDC number 739300) [18]. C_1 symmetry was assumed for all systems and default convergence criteria were used; local minima were verified by establishing that the Hessians had zero negative eigenvalues. The structures with counterions were optimized in methanol by the method developed for implicit treatment of solute-solvent interactions of electronic properties in solution – integral equation formalism polarizable continuum model (IEFPCM) [19]. TDPBE0/6–311+G(2d,p) calculations were

performed to compute the 20 lowest excited states of each structure. Solvent effects were included in TDDFT calculations, also by the IEFPCM. All calculations were performed using Gaussian 09 [20]. The PyMOL molecular graphics system was used to generate the molecular graphics images [21].

RESULTS AND DISCUSSION

In general, monomethine cyanine dyes such as **TO** and its derivatives can be synthesized under condensation of 2-methylthio salt of alkylated benzothizole with another alkylated heterocycle with an activated methyl group (Brooker's method) [1, 22–25], but this method suffers from some disadvantages [26]. In order to avoid the problems concomitant the synthetic strategy usually applied, dye **TO-3c-7Cl** (Scheme 1) was synthesized by simple, efficient and environmentally benign procedure that has been previously used by our group [9, 10, 27, 28]. This approach involves condensation of 2-methylbenzothiazolium salt **3** and 4,7-dichloroquinolinium salt **5** in the presence of the sterically hindered *Hünig's* base (*N*-ethyldiisopropylamine, DIPEA) (Scheme 1). The reactions of quaternization of the starting 2-methylbenzo[d]thiazole (**1**) and 4,7-dichloroquinoline (**4**) with 1-(4-bromobutyl)-4-

(dimethylamino)pyridin-1-ium bromide (**2**) were carried out in the absence of a solvent for a short reaction time[11]. The quaternary salts **3** and **5** were isolated in high yields and in a purity enough for the next synthetic transformation.

The newly synthesized cyanine dye **TO-3c-7Cl** was characterized by NMR-, UV-VIS-spectroscopy and by elemental analysis.

The photophysical properties of the new tricationic dye **TO-3c-7Cl** were evaluated and the data were compared to those of its analog **TO**. The absorption maxima of the studied dyes are at 502 and 513 nm for **TO** and **TO-3c-7Cl**, respectively. The higher value of the molar absorptivity corresponds to **TO-3c-7Cl** – 97000 L·mol^{-1}·cm^{-1}, while **TO** in our conditions is characterized by a molar absorptivity of 86100 L·mol^{-1}·cm^{-1} (Table 1).

The newly synthesized dye **TO-3c-7Cl** in TE buffer in the absence of dsDNA absorbs at 513 nm and this peak is bathochromically shifted to 521 nm in the same buffer in the presence of dsDNA (Table 1). As we mentioned in our previous work [10], this effect could be attributed to an intercalation of the dye into dsDNA, as assumed in other investigations into cyanine dyes [9, 29].

In TE buffer at 538 nm **TO-3c-7Cl** shows fluorescence with low intensity (4.3 au at 1.10^{-7} M and almost zero (below 0.4) at 1.10^{-8} M, Table 1, Fig. 1),
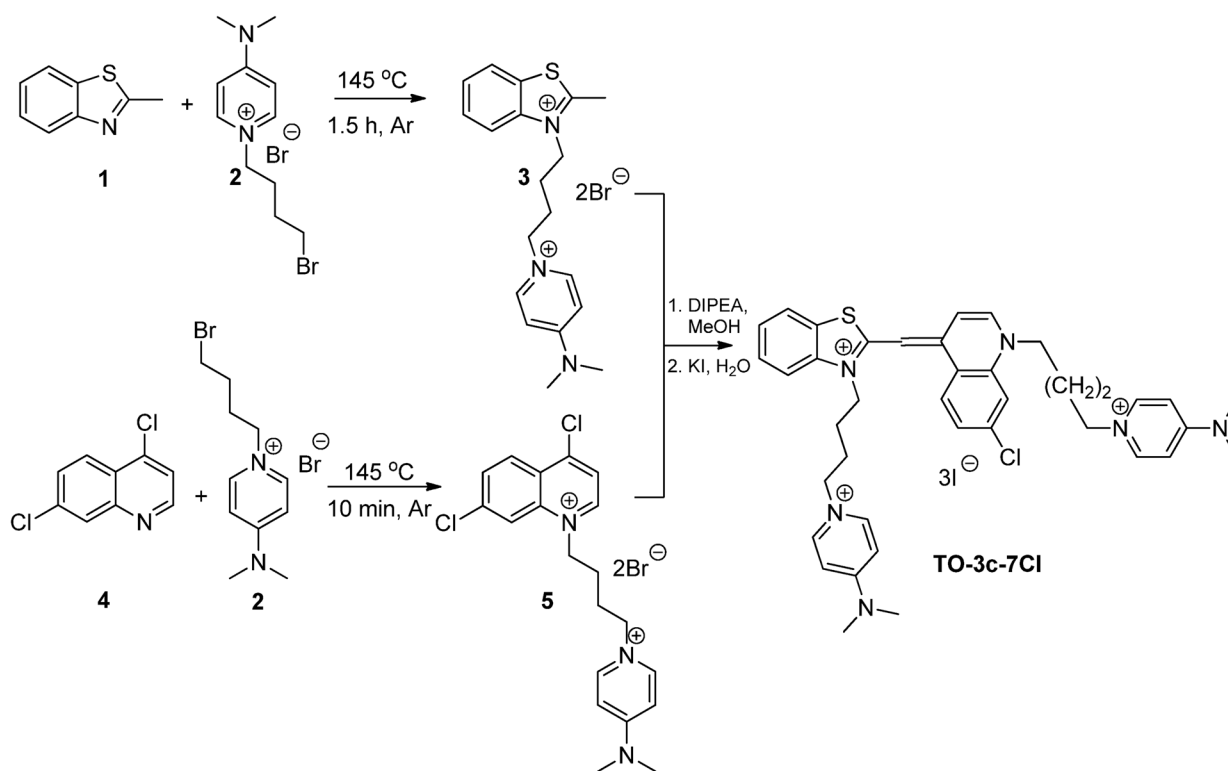
Scheme 1. Synthesis of tricationic monomeric monomethyne cyanine dye **TO-3c-7Cl**.

Table 1. Comparison of the photophysical properties of **TO-3c-7Cl** and TO in the absence and in the presence of dsDNA

Dye	Absorption			Fluorescence				
	Abs[a]	Abs[b]	Abs[c]	λ_{max}^d	I_{fl0}^d	λ_{max}^e	I_{fl}^e	Ratio I_{fl}/I_{fl0}
TO-3c-7Cl	513 (97 000)	513	521	538	0.43*	538	875	>2030
TO	502 (86 100)	502	510	549	0.55	529	252	458

[a] λ_{max} (nm) and molar absorptivity ε (L.mol^{-1}.cm^{-1}) of free dyes in methanol;
[b] λ_{max} (nm) of free dye in TE buffer;
[c] λ_{max} (nm) of dye-dsDNA complex in TE buffer;
[d] λ_{max} (nm) and I_{fl0} of free dye in TE buffer;
[e] λ_{max} (nm) and I_{fl} of complex dye-dsDNA in TE buffer.
*Due to the extremely high fluorescence intensity at 1.10^{-7} M the spectra of the complex dye **TO-3c-7Cl**/dsDNA the spectra was measured at 1.10^{-8} M concentration. The intrinsic fluorescence of the free dye at this concentration is near zero and hardly distinguishable from the instrumental noise.

but excitation at 538 nm in the presence of dsDNA led to a dramatic increase in the fluorescence intensity over 2030-fold (Table 1, Fig. 1). The significant increase of the fluorescence can be attributed to the presence of three positive charges in the dye molecule increasing the binding affinity to dsDNA.

B3LYP/6-31+G(d,p) optimized structures of the cationic fragments of **TO** and **TO-3c-7Cl** are presented in Figure 2 with the respective atom color scheme. A simple structural superimposition of the dyes reveals structural similarity between them with almost identical "TO core" fragment.

TDPBE0 (time-dependent density functional theory calculations using Perdew–Burke–Ernzerhof exchange-correlation functional) calculations with the 6–311+G(2d,p) basis set for all atoms except I and with the Stuttgart-Dresden SDD effective core
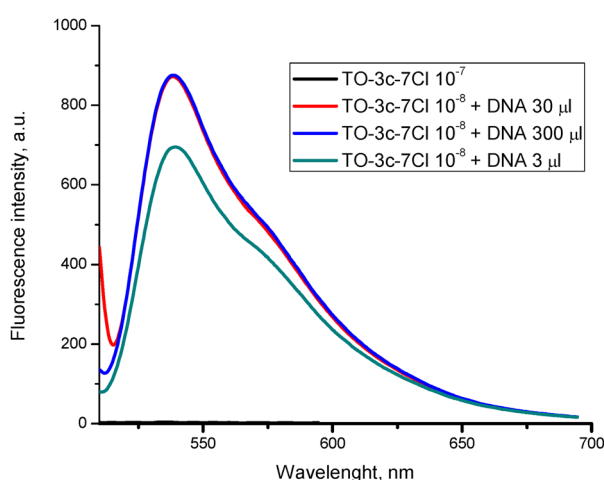
Fig. 1. Fluorescence spectra of free dye **TO-3c-7Cl** in TE buffer and in the presence of dsDNA.
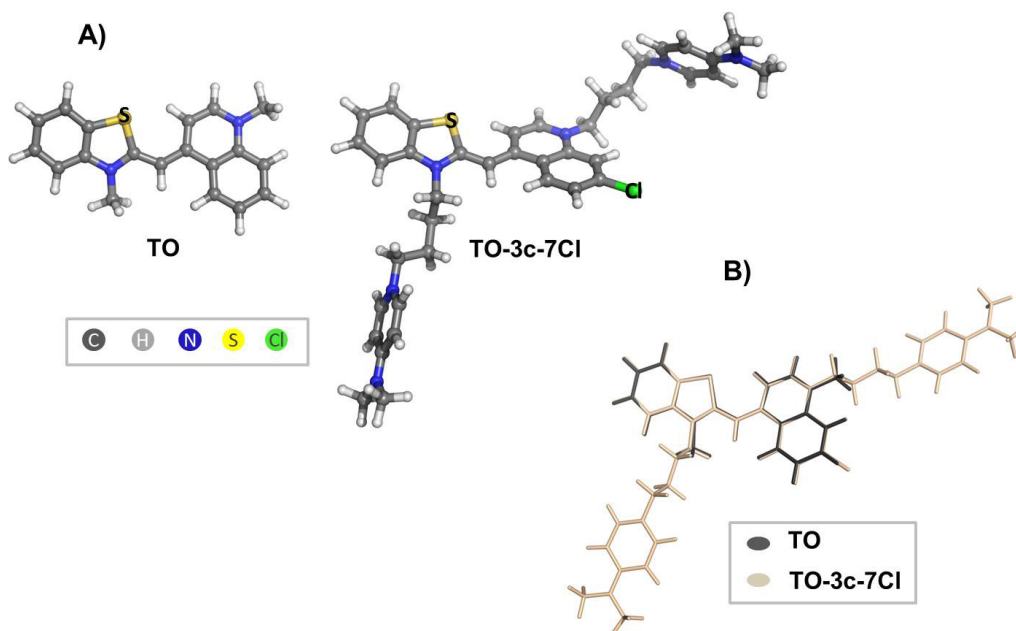
Fig. 2. A) B3LYP optimized structures of the cations of **TO** and **TO-3c-7Cl**; B) superimposed structures of **TO** and **TO-3c-7Cl** cations.

potential (ECP) basis set for I in the range 400–500 nm predict an intensive band for **TO** (at 452 nm) and an intensive band for its tricationic analogue (at 456 nm). The calculated optical parameters such as the absorption maximum (λ_{max}), oscillator strength (f) and frontier orbital energy levels are provided in Table 2.

The $S_0 \rightarrow S_1$ excitation process in the studied dyes can be assigned mainly to HOMO (highest occupied molecular orbital) → LUMO (lowest unoccupied molecular orbital) transition. An examination of the frontier molecular orbitals of the compounds

under investigation can be useful. The qualitative frontier molecular orbital representations for **TO** and **TO-3c-7Cl** are shown in Figure 3.

The oscillator strengths calculated for HOMO → LUMO transition are 0.777 and 1.035 for **TO** and **TO-3c-7Cl**, respectively. The HOMO–LUMO gaps are similar: 3.27 eV and 3.25 eV for the compounds (**TO** and **TO-3c-7Cl**, respectively) in methanol. In **TO-3c-7Cl** the HOMO was found to be populated over the "TO core" fragment. There is no difference between the delocalization of the LUMO in both compounds (Figure 3).

Table 2. TDDFT/PBE0 excitation energies (eV), wavelengths (nm) (in parentheses), oscillator strength *f*, HOMO and LUMO energies and energy differences (HOMO-LUMO gap) (eV) in methanol for **TO** and **TO-3c-7Cl**

	TO	TO-3c-7Cl
HOMO→LUMO		
Excitation energy (wavelength)	2.74 (452)	2.72 (456)
Oscillator strength, *f*	0.777	1.035
HOMO	−5.99	−6.08
LUMO	−2.72	−2.83
HLG	3.27	3.25
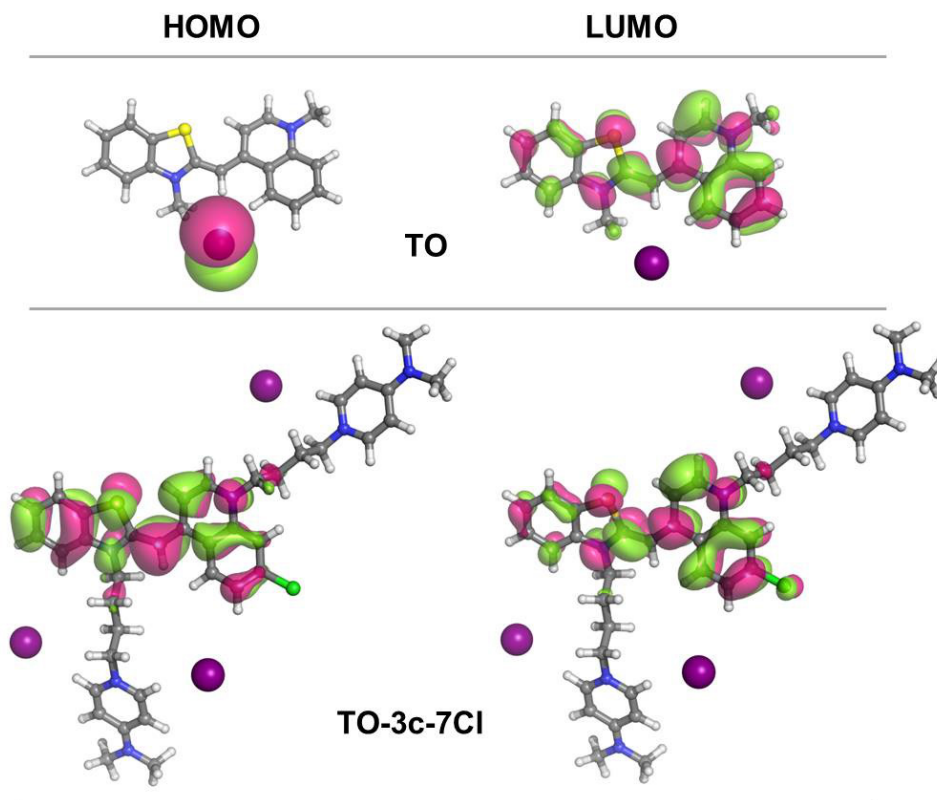
Fig. 3. Graphical representation of the frontier orbitals (isodensity plot, isovalue = 0.02 a.u.).

CONCLUSION

A novel tricationic analog of the commercial nucleic acids binder **TO** was synthesized and its photophysical properties were investigated. **TO-3c-7Cl** possesses typical features of fluorescent DNA label. In the absence of DNA, the dye has negligible fluorescence, but after binding to DNA a significant increase in the fluorescence intensity (2030-fold) was observed. Theoretically predicted (DFT and TDDFT calculated) structure and properties of the new tricationic cyanine dye and **TO** are compared and contrasted. The promising results stimulate us for further investigations in the design, synthesis and application of new polycationic halogen containing analogs of TO as nucleic acid binders.

REFERENCES

1. L. G. Lee, C. H. Chen, L. A. Chiu, *Cytometry*, **7**, 508 (1986).
2. S. Berndl, S. D. Dimitrov, F. Menacher, T. Fiebig, H. A. Wagenknecht, *Chem. Eur. J.*, **22**, 2386 (2016).
3. P. R. Bohländer, M. L. Abba, F. Bestvater, H. Allgayer, H. A.Wagenknecht, *Org. Biomol. Chem.*, **14**, 4961 (2016).
4. H. A. Shindy, *Dyes and Pigments*, **145**, 505 (2017).
5. H. S. Rye, S. Yue, D. E. Wemmer, M. A. Quesada, R. P. Haugland, R. A. Mathies, A. N. Glazer, *Nucleic Acids Res.*, **20**, 2803 (1992).
6. T. Deligeorgiev, A. Vasilev, in: Functional Dyes, Kim S-H (ed.), Elsevier, Amsterdam, New York, Tokyo, (137) 2006.
7. R. P. Haugland, Molecular Probes: Handbook of fluorescent probes and research chemicals, Molecular Probes Inc., 9th ed., 2014.
8. T. G. Deligeorgiev, N. I. Gadjev, A. A. Vasilev, V. A. Maximova, I. I. Timcheva, H. E. Katerinopoulos, G. K. Tsikalas, *Dyes and Pigments*, **75**, 466 (2007).
9. A. A. Vasilev, M. I. Kandinska, S. S. Stoyanov, S. B. Yordanova, D. Sucunza, J. J. Vaquero, O. D. Castaño, S. Baluschev, S. E. Angelova, *Beilstein J. Org. Chem.*, **13**, 2902 (2017).
10. A. A. Vasilev, M. I. Kandinska, Y. Zagranyarski, D. Sucunza, J. J. Vaquero, O. D. Castaño, S. E. Angelova, *Bulg. Chem. Commun.*, in press.
11. T. Deligeorgiev, A. Vasilev, T. Tsvetkova, K-H. Drexhage, *Dyes and Pigments*, **75**, 658 (2007).
12. A. D. Becke, *J. Chem. Phys.*, **98**, 5648 (1993).
13. C. Lee, W. Yang, R. G. Parr, *Phys. Rev. B*, **37**, 785 (1988).
14. W. J. Hehre, R. Ditchfield, J. A. Pople, *J. Chem. Phys.*, **56**, 2257 (1972).
15. T. Clark, J. Chandrasekhar, G. W. Spitznagel, P. v R.Schleyer, *J. Comp. Chem.*, **4**, 294 (1983).
16. M. J. Frisch, J. A. Pople, J. S. Binkley, *J. Chem. Phys.*, **80**, 3265 (1984).
17. G. Igel-Mann, H. Stoll, H. Preuss, *Mol. Phys.*, **65**, 1321 (1988).
18. X. Fei, Y. Gu, Y. Lan et al., *J. Chem. Crystallogr.*, 41, 1232 (2011).
19. J. Tomasi, B. Mennucci, R. Cammi, *Chem. Rev.*, **105**, 2999 (2005).
20. Gaussian 09, Revision D.01, Frisch M J et al., Gaussian, Inc., Wallingford CT, 2013.
21. The PyMOL Molecular Graphics System, Version 1.7.6.6, Schrödinger, LLC.
22. I. Crnolatac, L. Tumir, N. Lesev, A. Vasilev, T. Deligeorgiev, K. Miskovic, L. Glavas-Obrovac, O. Vugrek, I. Piantanida, *Chem. Med. Chem.*, **8**, 1093 (2013).
23. T. Deligeorgiev, N. Gadjev, A. Vasilev, K-H. Drexhage, S. M. Yarmoluk, *Dyes and Pigments*, 70, 185 (2006).
24. L. G. Brooker, G. Keyes, W. Williams, *J. Am. Chem. Soc.*, **64**, 199(1942).
25. B. Beilenson, F. M. Hamer, *J. Chem. Soc.*, **13**, 143 (1939).
26. W. A. Sexton, *J. Chem. Soc.*, **13**, 470 (1939).
27. T. Deligeorgiev, A. Vasilev, T. Tsvetkova, K-H. Drexhage, *Dyes and Pigments*, **75**, 658 (2007).
28. T. Deligeorgiev, A. Vasilev, K-H. Drexhage, *Dyes and Pigments*, **74**, 320 (2007).
29. R. S. Kumar, E. H. Turner, *J. Photochem. Photobiol. A*: *Chemistry*, **74**, 231 (1993).

НОВ МОНОМЕРЕН ТРИКАТИОНЕН МОНОМЕТИНЦИАНИНОВ АНАЛОГ НА ТИАЗОЛ ОРАНЖ (ТО): СИНТЕЗ, ФОТОФИЗИЧНИ И двДНК-СВЪРЗВАЩИ СВОЙСТВА

М. И. Къндинска[1]*, А. А. Василев[1], В. С. Видева[1],
С. Е. Ангелова[2]

[1] *Факултет по химия и фармация, Софийски университет "Св. Климент Охридски",*
1164 София, България
[2] *Институт по органична химия с център по фитохимия, Българска академия на науките,*
1113 София, България

(Резюме)

Синтезирано е ново мономерно трикатионно цианиново багрило **ТО-3с-7Cl** – аналог на Тиазол оранж (**ТО**) посредством лесно приложим и щадящ околната среда метод. Изследвани са фотофизичните свойства на съединението и са сравнени с тези на известния търговски продукт **ТО**. Багрилото **ТО-3с-7Cl** се характеризира с много ниска собствена флуоресценция в Tris-EDTA (TE) буфер, но в присъствието на двДНК, интензитетът му на флуоресценция се увеличава значително. DFT и TDDFT-изчисления са използвани за сравнение и разграничаване на теоретично предсказаните структури и свойства на новополученото трикатионно цианиново багрило и **ТО**.

Amino acids substituted phthalocyanine complexes: an overview on the synthetic approaches and UV-vis properties related to photodynamic applications

V. Mantareva[1]*, M. Aliosman[1, 3], M. Durmuş[2], I. Angelov[1]

*[1] Institute of Organic Chemistry with Centre of Phytochemistry, Bulgarian Academy of Sciences,
1113 Sofia, Bulgaria*
[2] Gebze Technical University Department of Chemistry, P.O. Box 141, Gebze 41400, Kocaeli, Turkey
[3] Institute of Physical Chemistry, Bulgarian Academy of Sciences, 1113 Sofia, Bulgaria

The photosensitizers with biologically active substituents such as amino acids feature one modern strategy to achieve the target- specific photodynamic therapy (PDT). The conjugations of metal phthalocyanines (MPcs) with amino acids or the related short peptides have been studied intensively with respect to PDT applications. The known MPcs with amino acids are recognized with membrane specificity in view of cell receptors or/and with electrostatic interactions based on the charge potential of membranes. This work aims to summarize at presently existing knowledge and our expertise in respect to synthesis and photophysicochemical properties of phthalocyanine complexes conjugated with amino acids for PDT applications.

Keywords: phthalocyanine complexes, amino acids, Click reaction, Sonogashira reaction, photodynamic therapy.

INTRODUCTION

The accelerating problem with drug-resistance towards the conventional therapies reinforces the research and development of new non-traditional curative strategies for combating different pathologic conditions [1–3]. The development of resistance is a consequence of overusing of chemotherapeutics and antibiotics which are leading to adaptation and finally to lowering the effectiveness of these drugs. Photodynamic inactivation (PDI) has been featured as an approach for urgent situation in fighting the life-threatening infections [1, 2]. The procedure includes the harmless drug (photosensitizer, PS) and irradiation with soft dose light of visible or infrared spectra (630–850 nm) for drug excitation [4]. The energy of absorbed light of a PS follows Jablonski diagram. In summary, the radiation transition of a PS goes from its lowest energy singlet excited state (S_1) to the ground state (S_o) by fluorescence. Two possible non-radiative transitions can happen, one of inner conversion between the singlet states and another conversion is the intersystem crossing to the triplet excited state PS. The long-lived triplet state PS can participate in photochemical reactions including the electron or proton transfer (type I mechanism). Most probable is an energy transfer from the triplet state PS to molecular oxygen with generation of reactive singlet oxygen (type II mechanism).

Phthalocyanine complexes (MPcs) conjugated with biologically active moieties have been featured as promising photosensitizers for PDT [5–7]. Nowadays, the complexes of Zn(II)-, Al(III)- and Si(IV)-phthalocyanines are well-known as promising second generation PDT drugs. One critical limitation of these compounds is their low selectivity, followed by undesirable photocytotoxicity. MPcs are related to the natural porphyrin but with the expanded structure of addition four benzene rings. This shifts the absorption in the phototherapeutic window (670–740 nm). The planarity and symmetry in the structure of MPcs allow easy functionalization in peripheral or non-peripheral positions, or at the coordinated ions [8]. Phthalocyanine molecule as a ligand can coordinate most of the metals and semimetals from the periodic table. Moreover MPcs are more studied than their metal free counterparts because of the superior photophysicochemical properties owning to the coordinated ions [9, 10]. The Pc-molecules characterize with very low solubility and high tendency to form photo non-activable spe-

---
* To whom all correspondence should be sent:
E-mail: mantareva@yahoo.com

cies which is not in practical usage for biology and medicine. The proper functionalization of MPcs appears useful tool for improving their photophysico-chemical properties [10]. The conjugation strategy with biomolecules such as amino acids (or short peptides) has been shown to have a great potential for enhancement of PDT properties [7]. The further improvement of MPcs includes the enhancement of their target specificity, localization ability and selectivity. Many efforts are made on the basis of Pc skeleton for structural modifications which include substitutions by different biologically-active and cell-specific molecules such as steroids [5], amino acids and short peptides [7], carbohydrates [11], and others [12].

SYNTHETIC APPROACHES FOR CONJUGATION OF PHTHALOCYANINES WITH AMINO ACIDS

There are two commonly used synthetic pathways which are applicable for preparation of functional phthalocyanine derivatives [13–15]. The so called "phthalonitrile pathway" is based on functionalization of phthalonitriles (Scheme 1a). The synthesis of starting phthalonitriles with substituents A (or AA) includes one or several steps staring from different phthalonitrile with substitution

B and the followed up reactions lead to the desired substituted dinitrile. The second pathway known as "phthalocyanine way" includes the synthesis of Pc with reactive group C which further can be functionalized in a way to obtain the desired Pc with functional group A (Scheme 1b). The structural modifications on the phthalocyanine cycle can generally be performed by the insertion of hydrophilic groups or other functional substituents to the peripheral or non-peripheral position to the ring, or by changing the coordinating ion which can allow addition of bulky groups on axial position [16]. The mixtures of regioisomers which are not easy to separate are obtained in case of tetra- MPcs with peripheral substitutions [17]. Both approaches allow the synthesis of a variety of functionalized phthalocyanines conjugates with properties suitable for biomedical applications [18].

The phthalonitriles (1,2-dicyanobenzenes) are typical precursors for phthalocyanine synthesis. 1,2- Dicyanobenzene was firstly recognized as by-product of the synthesis of o-dicyanodiazoamido-benzene. In the early XX century the phthalonitrile was synthesized by refluxing acetic anhydride and phthalimide [19]. Since then several starting compounds are recognized as suitable precursors but differently substituted phthalonitriles are the most common in usage as precursors in synthetic phthalocyanine chemistry. The synthesis of precursors
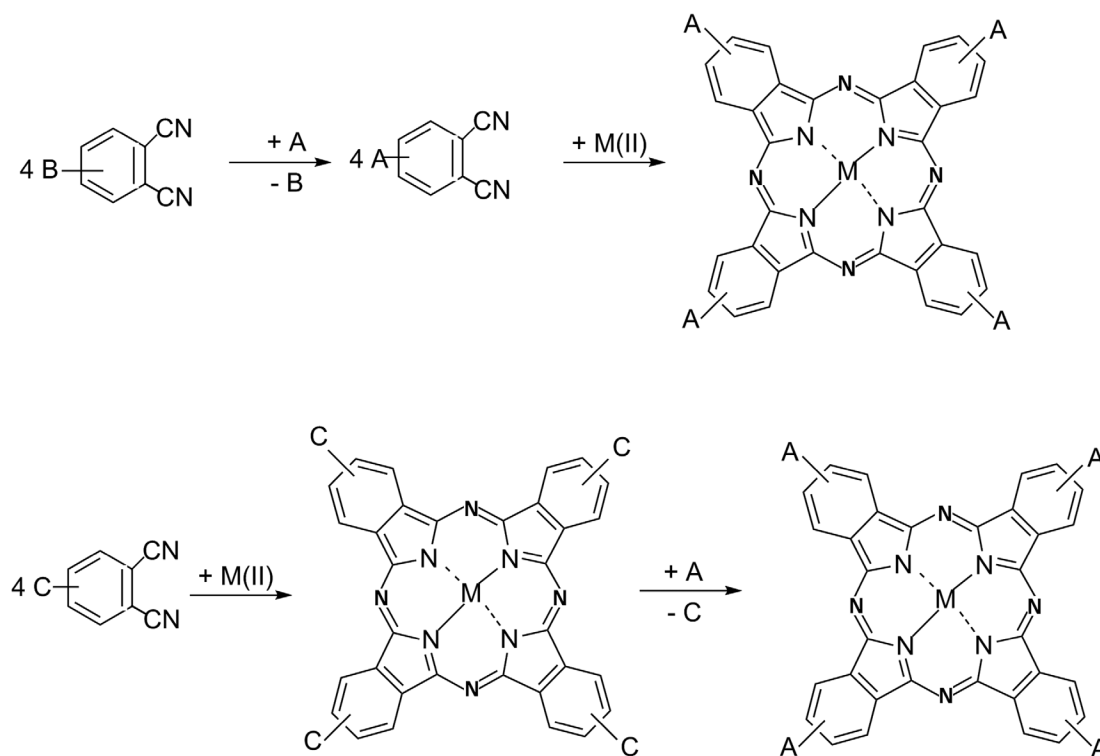
Scheme 1. Synthetic pathways for preparation of metallophthalocyanine conjugates in summarized version.

aims to obtain the starting compounds which are functional for amphiphilic, sterically hindered and soluble phthalocyanines [20, 21]. The synthetical approaches are quite common including the alcohol, base and metal salts [22]. The routine phthalocyanine synthesis starts by cyclotetramerization in a medium of alcohol and the related nucleophilic alkoxides being generated by the addition of non-nucleophilic bases such as quinoline, catalyst 1,8-diazabicyclo [5.4.0] undec-7-ene and the metal salt to serve as a template for the formation of Pc macrocycle. The expected substituted derivatives may be obtained by nucleophilic addition to the nitrile carbon atom; subsequently, the nitrogen atom will add to the other nitrile carbon atom. The second way includes the phthalonitrile molecule forming a *bis*-1,3-diiminoisoindoline which is instable compound and only a few derivatives are isolated for further studies. As mentioned above the metal ions are supposed to assist the cyclotetramerization of intermediates. The coordination, the reaction of nucleophilic additions, the elimination steps and further rearrangements resulted in formation of phthalocyanine core. Phthalocyanines without substituents are almost insoluble due to intermolecular interactions between the planar macrocyclic molecule which limits the investigation in solutions and the application in biomedicine.

A straightforward pathway for synthesis of phthalonitriles suitable for conjugation *via* amide bond was recently proposed [23, 24]. The benefits are due to two unique molecules both with cell specific properties to facilitate the photodynamic process. The structure of amino acids includes carboxyl and amino groups which are thought to facilitate the solubility of conjugated MPcs in biological environment. The reduction of hydrophobic nature was suggested recently for ZnPcs conjugated with short peptides [25]. The biologically active peptides are well documented as suitable for functionalization with MPcs so that the final molecules are compatible in physiological conditions [26, 27]. The synthetical procedures for conjugation of phthalocyanines with biomolecules can include numerous synthetical mechanisms [28, 29]. The amide bond pathway is based on direct covalent binding (Scheme 2).

The "mirror" pathway for amide bounding includes carboxyl groups of MPcs and amino-groups from amino acids. This approach was used for conjugation between the phthalocyanine and other bioactive molecules. The addition of linker group between both molecules aims to improve the rigidity of the linker and facilitate the next reaction step. Moreover the usage of the linker assures the lack of steric hindrance which can obstruct the reaction of conjugation. The symmetrical tetra-substituted MPcs are more soluble than their octa-substituted analogues as a result of the formation of four regioisomers. However the regioisomers of tetra-substituted MPc are not easy to be separated.

The synthesis of octa-substituted phthalocyanine for conjugation with amino acids or short peptides can start from di-nitro or amino- substituted phthalonitriles in pentanol used as solvent/nucleophile (Scheme 3). However the low solubility issue leads to ineffective reaction way of direct cyclometization by using 1,2-amino-phthalonitrile as precursor [22]. The obtained product resulted in a single structure
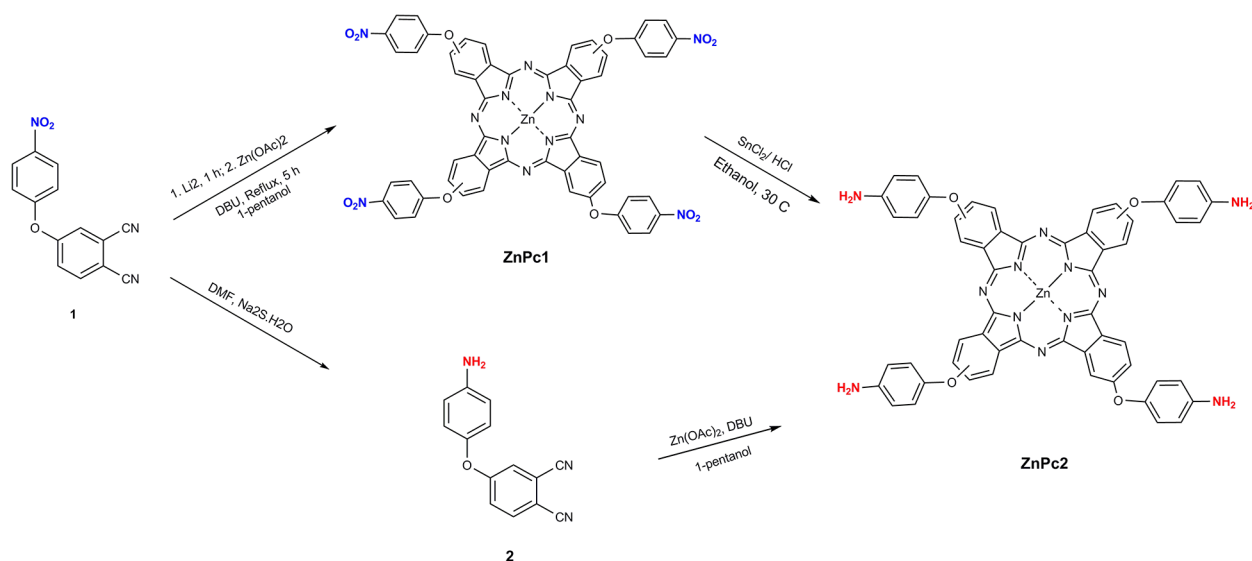
Scheme 2. Synthetic pathways for preparation of *tetra*-aminophenoxy-substituted Zn(II)-phthalocyanine.
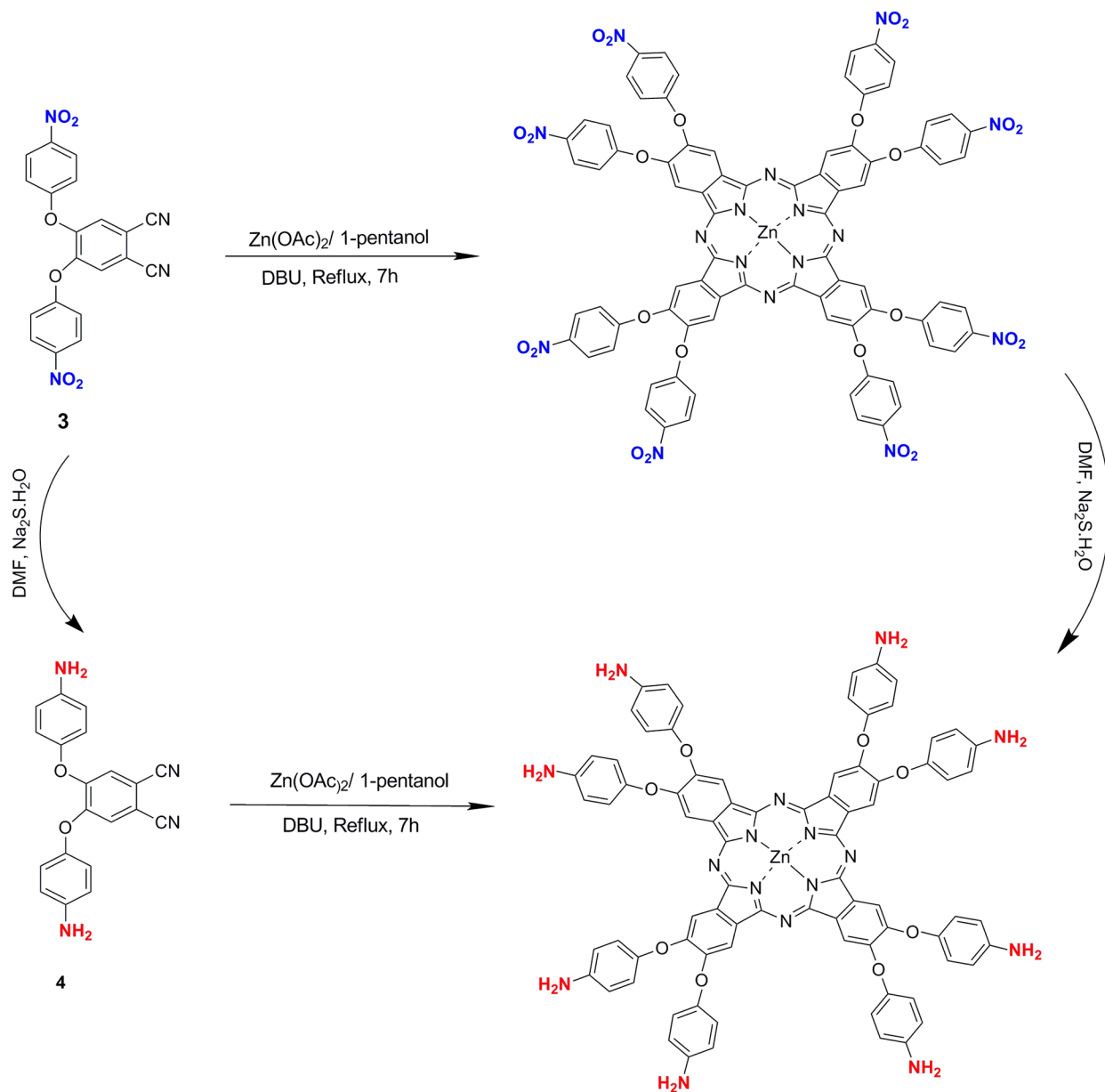
Scheme 3. Synthetic pathways for synthesis of *octa*aminophenoxy-substituted Zn(II)-phthalocyanine.

of the respected octa-substituted MPcs, which have better solubility and the bathochromic shifting of the absorbance in the Q bands to the near infrared region.

Most of the literatures about the conjugation of MPc with selected peptide units referred to the N-terminal position of the peptide forming a sulfonamide or amide bond [30]. However these approaches present some disadvantages if the conjugation of Pc at this position results in loss of peptide activity. The study of Ali et al. [27] reported the use of different Pd-catalyzed cross-coupling reactions (Sonogashira, Buchwald-Hartwig, and Suzuki-Miyaura) for preparation of the new MPc conjugates with selected peptides. The other possible reaction pathway involves the nucleophilic substitution reaction of s-triazine chloride with propargyl alcohol in the presence of NaH/ THF to obtain propargyl alkoxides substituted triazine [31]. This approach was often described for dual molecules with different functionality [32]. The Pc conjugation with amino acids (or short peptides) involves iodine substituted phthalonitrile to obtain the same substituted Pc and the next step is the reaction with triazine in the media of sodium ascorbate and copper sulphate at room temperature. The Cu^{I}-catalysed

azide–alkyne cycloaddition known as the "click" reaction has been developed for routine bioorthogonal ligation reactions with applications to biomaterial conjugation [33]. However, the cytotoxicity of the catalysts has hindered the common usage of this reaction especially in living systems. The "copper-free" click reaction has advantage of prevention the usage of the toxic Cu(I) ion which is not applicable for reactions with biological molecules especially within cells [34]. The solvent-free synthesis and the low-temperature synthesis as methods for synthesis of bioconjugates of phthalocyanines are well described for biologically active molecules [35–37]. Both can be featured as the future in the conjugation strategy for bioactive compounds with application as drugs. Moreover the harsh reactions condition such as toxic catalyst and high temperatures are not useful for substitution with amino functionalized MPcs including amino acids because of racemisation or hydrolysis that begin at high temperature and in the presence of the catalyst.

PHOTOPHYSICOCHEMICAL PROPERTIES OF AMINO ACIDS MPC-CONJUGATES

Properties of the singlet excited state

Phthalocyanines characterize with absorbance within the visible red and infra-red spectral region [38]. Typically the UV-vis spectrum has one sharp intensive Q-band (> 670 nm, $\varepsilon > 10^5$ mol^{-1}.cm^{-1}) and twice less intensive B-band (320–380 nm). The fluorescence spectra of MPcs are red shifted with small shift (8–20 nm) to the near infrared region (> 680 nm). The Q band is a result of the $\pi \rightarrow \pi^*$ transitions from the highest occupied molecular orbital (HOMO) to the lowest unoccupied molecular orbital (LUMO). The B band is starting from the deeper π levels to LUMO transition with spectral region between 320–360 nm for known MPcs. The monomeric molecules of MPcs in solutions can be evidenced by a single (narrow) Q band in the electronic absorption spectra.

Our study with different newly synthesized ZnPcs bearing four amino acids at peripheral positions showed similarity in the absorption spectra (Fig. 1). For example conjugated ZnPcs with amino acids such as tyrosine and lysine showed maximum at ~682 nm which is red shifted by approx. 11–13 nm in respect to unsubstituted ZnPc (671 nm) for recorded UV-vis spectra in different solvents (Fig. 1a).

The similar studies of ZnPcs and SiPcs – peptide conjugates investigated in different solvents also showed the similar position of the absorption bands [39]. The spectra of the conjugates of MPcs with AA (or SPs) possess a single sharp Q band for monomeric molecules with bathochromic shift to the far red spectra. This is explained with the strong conjugation of the structure of molecule containing four, eight or one substitution to the Pc-ring. The known Zn (II)- and Si (IV)- Pcs conjugates in polar media such as buffer, showed a broad low intensity band at around 650 nm which suggested aggregation in water [40].

Recently synthesized by our group different ZnPcs with tyrosine and lysine moieties were studied to have fluorescence maxima bathochromicaly shifted (5–8 nm) in dependence on the solvents. The fluorescence emission spectra of these ZnPcs are presented in Figure 1b. As can be seen the excitation spectra were similar to absorption spectra and both of them represent the mirror images of
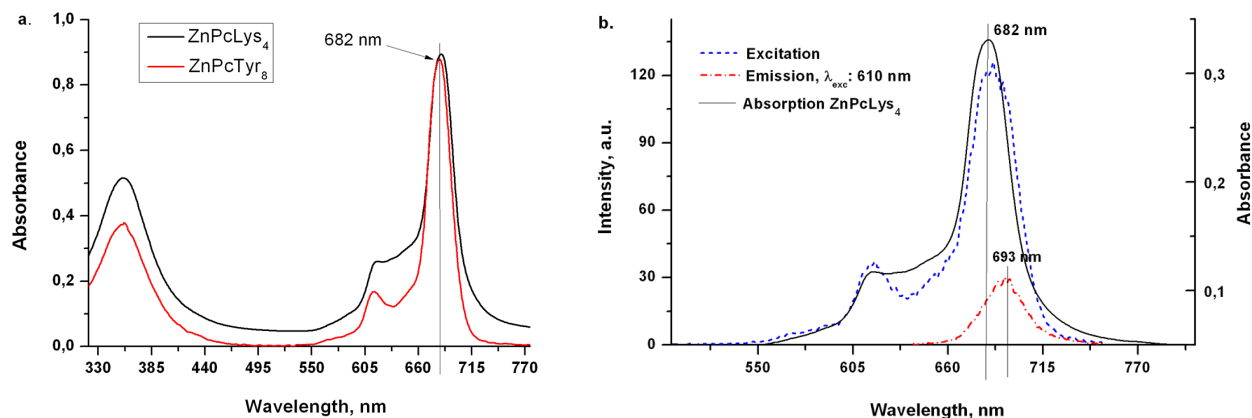
Fig. 1. UV-vis spectra of Zn(II)-phthalocyanine conjugated with amino acids: (**a**) Absorption spectra in DMSO and (**b**) fluorescence and excitation spectra of ZnPcLys$_4$ at exc: 610 nm.

the emission spectra with proves the purity of the studied ZnPcs conjugates. The studied compounds did not undergo the photodegradation during visible light excitation.
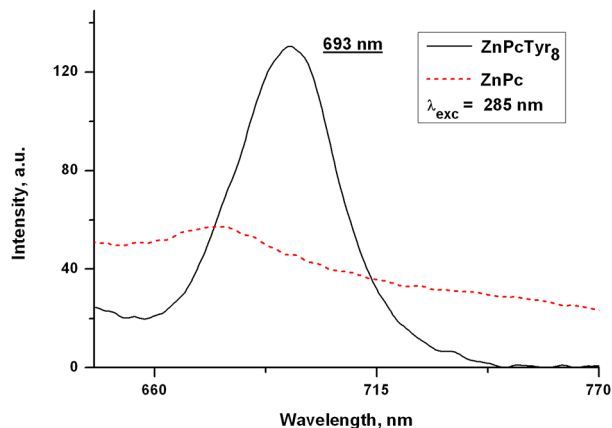
Fig. 2. Fluorescence spectra of a conjugate ZnPcTyr$_8$ (acceptor) and non-conjugate ZnPc, both recorded at exc: 285 nm as absorption maximum of Tyr (donor).

The theory considers that the non-radiative-energy-transfer (quenching) between a quencher and an energy donor proceeds in case of some extent overlap between the absorption spectrum of the quencher and the emission spectrum of the donor [38]. UV-vis study with our newly prepared ZnPc conjugates with tyrosine (ZnPcTyr) and lysine (ZnPcLys) showed the absorption spectra of ZnPc (acceptor) as a quencher and the energy of fluorescence emission of tyrosine molecules (donor) as can be seen in Figure 2. The observed spectral overlapping in the UV region (300–340 nm) suggests the possible energy transfer *via* mechanism Föster (FRET). The phenomenon of energy transfer may occur *via* the aminophenoxy linker between Pc-ring and amino acids. According to theory the distance up to 10 Å allows the energy transfer between two molecules [38]. The overlaps between absorption and fluorescence spectra are observed between spectra of both molecules of conjugate containing ZnPc and selected amino acids (Tyr or Lys). It can be concluded that for effective quenching, the energy levels of a phthalocyanine as quencher should be in a similar energy as the quenching biomolecules.

Singlet oxygen generation and photostability

The photocatalytic process of specific light applied to photosensitizer molecules in case of phthalocyanine is a generation of molecular singlet oxygen [10]. Type II pathway includes energy transfer between the triplet excited state of Pc molecule and the lowest energy state of molecular oxygen which is ground triplet state molecule. The produced other reactive oxygen species (ROS) are also in favour to the efficiency of PDT [12]. Among all possible ROS, it is only the singlet oxygen which is featured with the highest reactivity and harmful capacity towards biomolecules. Phthalocyanine macrocycle facilitates coordination with almost all of the metal and semimetal ions in the Periodic table [22]. The coordinated ion determines the properties of the triplet excited state molecules which are generated by irradiation with a proper light spectrum. The *d*-shell atoms with diamagnetic properties are achieving the optimal parameters of the triplet excited state MPcs. In addition the substitution of MPc with functional groups leads to physical quenching of the generated singlet oxygen. This phenomenon was also observed for our recently synthesized ZnPcs with amino acids tyrosine and lysine which aim to reduce the produced singlet oxygen (Fig. 3).

The photosensitizers for PDT should retain in the target tissue for proper time interval so that after receiving the suitable irradiation dose to initiate the photocatalytic reactions and the effect of photocytotoxicity. The procedure requires that the molecules to be stable without photobleaching activity for the duration of light exposure in order to be part of several cycles of photocatalytic reactions [41]. The high photostability is typical for most of the known MPcs. The presence of amide bond in the conjugated MPc complexes can lead to a limited thermal stability as well as chemical stability due to physiologically existing enzymes.
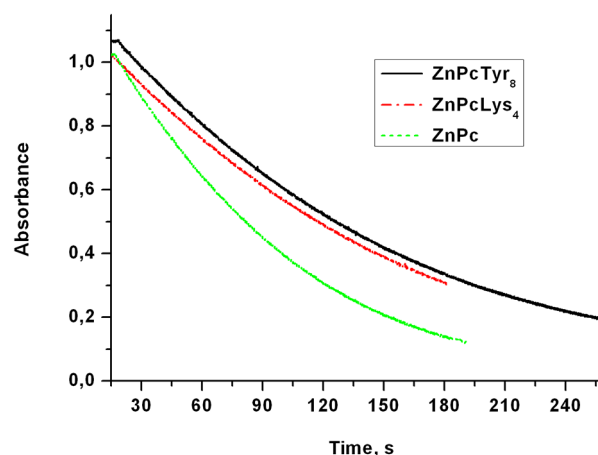
Fig. 3. Absorbance of DPBF at 417 nm as a result of singlet oxygen generation in the presence of ZnPc- amino acids conjugates and unsubstituted ZnPc for comparison.

190

CONCLUSIONS

A number of newly synthesized phthalocyanines conjugated with amino acids have been developed during the last decade, as well as in our research group. The newly developed ZnPc-amino acids conjugates have been synthesized by modification of different well-known synthetic pathways for chemistry of porphyrins and phthalocyanines. The ZnPc-amino acids conjugates are characterized with amphiphilic nature, with advanced photophysicochemical properties as well as an improved cellular uptake and membrane specific localization in tumor cells and pathogenic microbials. The studied optical properties are preconditions for the superior photodynamic action and finally highlight a higher PDT efficiency.

REFERENCES

1. M. Wainwrigh, T. Maisch, S. Nonell, K. Plaetzer, A. Almeida, G. P. Tegos, M. R. Hamblin, *The Lancet Infect Dis.*, **17**(2), 49 (2017).
2. K. S. Sharma, P. Mroz, T. Dai, Y. Huang, T. G. Denis, M. R. Hamblin, *Isr. J. Chem.*, **52**, 1 (2012).
3. D. A. Tekdaş, U. Kumru, A. G. Gürek, M. Durmuş, V. Ahsen, F. Dumoulin, *Tetrahedron Lett.*, **53**, 5227 (2012).
4. F. Moret and E. Reddi, *J. Porphyr. Phthalocyan.*, **21**, 1 (2017).
5. S. Osati, H. Ali, B. Guerin, B., J. E. van Lier, *J. Porphyr. Phthalocyan.*, **21**, 701 (2017).
6. M. Sibrian-Vazquez, J. Ortiz, I. V. Nesterova, F. Fernandez-Lazaro, A. Sastre-Santos, S. A. Soper, G. H. Vicente, *Bioconjugate Chem.* **18**, 410 (2007).
7. F. Li, Q. Liu, Z. Liang, J. Wang, M. Pang, W. Huang, W. Wu, Z. Hong, *Org. Biomol. Chem.*, **14**, 3409 (2016).
8. J. P. Darwent, P. Douglas, A. Harriman, G. Porter, M.-C. Richoux, *Coord. Chem. Rev.*, **44**, 83 (1982).
9. E. A. Luk'yanets, in: *Handbook of Porphyrin Science – The Key Role of Peripheral Substituents in Chemistry of Phthalocyanines,* K. Kadish, K. M. Smith, R. Guilard, R. (eds.), Word Scientific Publishing Co. Pte. Ltd., vol. 3, pp. 2 (2010).
10. M. Durmuş, in: *Photosensitizers in Medicine, Environment, and Security*, T. Nyokong, V. Ahsen (eds.), Springer Dordrecht Heidelberg London New York, (2012).
11. M. Garcia-Iglesias and E. Huerta, *J. Porphyrins Phthalocyanines*, **21**, 1 (2017).
12. V. Mantareva, V. Kussovski, I. Angelov, in: *Photosensitizers: Types, Uses and selected Research*, C. Whitmire (ed.), Nova Science Publ. Inc., NY, pp. 115 (2016).
13. W. Liu, T. J. Jensen, F. R. Fronczek, R. P. Hammer, K. M. Smith, M. G. Vicente, *J. Med. Chem.,* **48**, 1033 (2005).
14. J. Chen, N. Chen, J. Huang, J. Wang, M. Huang, *Inorg. Chem. Commun.*, **9**, 313 (2006).
15. J. Liu, H. X. Zheng, C. Z. Yao, B. F. Sun, Y. Kang, *J. Am. Chem. Soc.* **138**, 3294 (2016).
16. F. Baumann, B. Bienert, G. Rosch, H. Vollman, W. Wolf, *Angew. Chem.* **68**, 133 (1956).
17. B. Barut, Ü. Demirbaş, A. Özel, H. Kantekin, *Int. J. Biol. Macromol.*, **105** (1), 499 (2017).
18. F. Dumoulin, H. Ali, V. Ahsen, J. E. van Lier, *Tetrahedron Lett.,* **52** (34), 4395 (2011).
19. D. Wöhrle, M. Eskes, K. Shigehara, A. Yamada, *Synthesis*, **2**, 194 (1993).
20. M. Göksel, M. Durmuş, D. Atilla, *Photochem. & Photobiol. Sci.*, **15**, 1318 (2016).
21. C. Dubuc, R. Langlois, F. Benard, N. Cauchon K. Klarskov, P. Tonec, J. E. van Lier, *Bioorg. Med. Chem. Lett.*, **18**, 2424 (2008).
22. F. Dumoulin, M. Durmuş, V. Ahsen, T. Nyokong, *Coord. Chem. Rev.*, **254**, 2792 (2010).
23. M. B. Aliosman, I. Z. Eneva, I. B. Stoineva, M. Durmus, V. N. Mantareva, *Bulg. Chem. Comm.*, Special Issue **E**, 79 (2017).
24. M. Aliosman, M. Goksel, V. Mantareva, I. Stoineva, M. Durmus, *J. Photochem. Photobiol. A: Chem.*, **133**, 101 (2017).
25. M. Göksel, M. Durmuş, D. Atilla, *J. Photoch. Photobiol. A: Chem.,* **266**, 37 (2013).
26. E. Ranyuk, N. Cauchon, K. Klarskov, B. Guérin, J. van Lier, *J. Med. Chem.*, **56**, 1520 (2013).
27. H. Ali, S. Mohand, S. Gosselin, J. van Lier, B. Guérin, J. Org. Chem., **76**, 1887 (2011).
28. H. He, P.-C.Lo, S.-L. Yeung, W.P. Fong, D K. P. Ng, *J. Med. Chem.*, **54** (8), 3097 (2011).
29. S. A. Mikhalenko, L. Soloveva, E. A. Lukyanets, *Russ. J. Gen. Chem.*, **74** (3), 451 (2004).
30. C. Dubuc, R. Langlois, F. Benard, N. Cauchon, K. Klarskov, P. Tone, J. E. van Lier, *Bioorg. Med. Chem. Lett.*, **18**, 2424 (2008).
31. H. Yanık, S.Y. Al-Raqa, A. Aljuhanib, M. Durmuş, *Dyes and Pigments*, **134**, 531 (2016).
32. H. Yanık, S. Yesilot, M. Durmus, *Dyes and Pigments*, **40**, 157 (2017).
33. V. Aranyos, A. M. Castaño, H. Greenberg, *Acta Chem. Scand.*, **33**, 714 (1999).
34. C. C. Leznoff, M. Hu, K. J. M. Nolan, *Chem. Commun.*, **1**, 1245 (1996).
35. B. I. Kharisov, U. O. Mendez, J. R. de la Rosa, *Russ. J. Coord. Chem.* **32,** 617 (2006).
36. M. M. Necedova, A. Martinicka, P. Magdolen, V. Novakova, P. Zahradnik, *Dyes and Pigments*, **141**, 448 (2017).
37. A. Nas, S. Fandaklı, H. Kantekin, A. Demirbaş, M. Durmuş, *Dyes and Pigments*, **95**, 8 (2012).
38. M. Durmuş, J.Y. Chen, Z. H. Zhao, T. Nyokong, *Spectrochim. Acta Part A*, **70**, 42 (2008).
39. M. Göksel, M. Durmus, D. Atilla, *Inorg. Chim. Acta*, **456**, 95 (2017).
40. D. Çakır, M. Göksel, V. Çakır, M. Durmuş, Z. Bıyıklıoğlu, H. Kantekin, *Dalton Transactions,* **44**, 9646 (2015).
41. B. G. Fanchiotti, M. P. Z. Machado, L. C. de Paula, M. Durmuş, T. Nyokong, A. S Gonçalves, A. R. da Silva, *J. Photochem. Photobiol. B: Biol.*, **165**, 10 (2016).

АМИНОКИСЕЛИННИ ЗАМЕСТИТЕЛИ НА ФТАЛОЦИАНИНОВИ КОМПЛЕКСИ: ОБЗОР НА СИНТЕТИЧНИТЕ СХЕМИ И СПЕКТРАЛНИТЕ СВОЙСТВА С ПРИНОС КЪМ ФОТОДИНАМИЧНИТЕ ПРИЛОЖЕНИЯ

В. Мантарева[1]*, М. Алиосман[1, 3], М. Дурмуш[2], И. Ангелов[1]

[1] Институт по органична химия с Център по фитохимия, Българска академия на науките, 1113 София, България
[2] Технически университет в Гебзе, 41400 Кошаели, Гебзе, Турция
[3] Институт по физикохимия, Българска Академия на науките, 1113 София, България

(Резюме)

Фотосенсибилизатори с биологично-активни заместители като аминокиселините се очертават като модерна стратегия за постигане на целева фотодинамична терапия (ФДТ). Конюгати на метални фталоцианинови комплекси (МФц) с аминокиселини или къси пептиди се отличават със свойства с принос към ФДТ. Известни МФцс с аминокиселини като заместители показват мембранна специфичност по отношение на рецептори и/или електростатични взаимодействия, основаващи се на заряда на мембраните. Настоящата работа има за цел да обобщи съществуващото научно познание както и нашия принос с нови фталоцианинови комплекси конюгати с тирозин и лизин както по отношение на синтеза, така и при изучаването на фотофизикохимичните им свойства за ФДТ приложения.

In silico ADME and drug-likeness evaluation of a series of cytotoxic polyprenylated acylphloroglucinols, isolated from *Hypericum annulatum* Morris subsp. *annulatum*

Y. Ilieva[1, 2], Z. Kokanova-Nedialkova[1], P. Nedialkov[1], G. Momekov[2]

[1] *Department of Pharmacognosy, Faculty of Pharmacy, Medical University of Sofia, Bulgaria*
[2] *Department of Pharmacology, Pharmacotherapy and Toxicology, Faculty of Pharmacy, Medical University of Sofia, Bulgaria*

Eight polyprenylated acylphloroglucinols, isolated from *Hypericum annulatum* Moris subsp. *annulatum,* and characterized as cytotoxic agents against human cancer cells, were subjected to computational ADME, pharmacokinetic and drug-likeness evaluation, using the web tool SwissADME. The physicochemical parameters assessment shows significant lipophilicity, and low water solubility. The compounds are expected to have good oral bioavailability, and with the only exception of hyperatomarin are not considered to be P-glycoprotein substrates. The evaluation of their inhibitory effects profile in several cytochrome P450 isoforms indicate that all of them as CYP3A4 inhibitors, whereas the expected modulatory effects on other CYPs varied among the series. The drug-likeness evaluation employed five alternative rule-based filters and noteworthy all compounds complied with the Lipinski "rule of five". Taken together, the calculated ADME and pharmacokinetic parameters, give us reason to consider the polyprenylated acylphloroglucinols from *Hypericum annulatum* Moris subsp. *annulatum* as a perspective set of cytotoxic lead compounds for further more detailed oncopharmacological and toxicological evaluation.

Keywords: Polyprenylated acyl phloroglucinols, Anticancer agents, ADME, Drug-likeness.

INTRODUCTION

The exploration of the plant kingdom as a source of novel anticancer drugs comprises a research area of significant interest, driven by the clinical and commercial success of a variety of plant-derived drugs or their semisynthetic analogues, such as Vinca alkaloids, taxanes, epipodophyllotoxins, camptothecins, combretastatins, maytansionoids *etc*. [1, 2]. Moreover, the chemical diversity of the Plant Kingdom is an immense and generally unexplored source of structurally complex molecules, which virtually could not be generated in a chemical lab [1–3].

Among the numerous plant secondary metabolites the polyprenylated acyl phloroglucinols (PAP) comprise an important class of biologically active compounds, peculiar for the plants from the related families Hypericaceae and Clusiaceae (Guttiferae) [4, 5]. The complex substitution patterns involv-

ing different acyl and isoprenoid functionalizations, glycosylation, oxidation, or cyclization of the highly oxygenated phloroglucinol core structure affords the tremendous structural diversity of these fascinating compounds [4–7]. Not surprisingly, this chemical diversity is translated into pleiotropic pharmacological activities, incl. antibacterial, antiprotozoal, antifungal, psychotropic, anti-inflammatory, antiangiogenic, and noteworthy potent cytotoxicity against human cancer cell lines [8, 9].

Our natural phloroglucinol-based drug discovery program has been focused for years on Hypericum species characteristic for the Bulgarian flora [10, 11], and noteworthy on *Hypericum annulatum* Moris subsp. *annulatum* [12–15], an endemic species inhabiting Sardinia, the Balkan Peninsula, East Africa and Saudi Arabia [6, 16]. Phytochemical and bioactivity-guided fractionation has resulted in the identification and oncopharmacological evaluation of several potent cytotoxic agents from this plant [13–15]. Hyperatomarin (**1**), a bicyclic prenylated acylphloroglucinol is a very effective compound, capable of inhibiting the growth of cultured cancer cells and inducing apoptosis at very low micromo-

---

lar concentrations [14, 15]. More recently, a series of acylphloroglucinols (**2–8**) (Fig. 1) were isolated from the same plant and shown to exert cytotoxicity against human tumor cell lines [13].

The promising pharmacological activity however is not a solitary prerequisite for a successful pharmaceutical commercialization of a chemical entity, because it should be accompanied by suitable physicochemical and biopharmaceutical properties, translating in turn into the desired pharmacokinetic parameters [17]. As a high-throughput pre-screen aid in drug discovery a number of *in silico* approaches have been developed for prognosis and estimation of absorption, distribution, metabolism and elimination (ADME) profiles, and for assessment of the so-called drug-likeness, defined as a qualitative prediction of the feasibility for acceptable bioavailability and pharmacokinetics after oral intake [17–21]. The forerunner work of Lipinski *et al.* analysed a comprehensive number of orally active compounds and coined the notorious *Rule-of-five* as a merit of optimal range of the drug's physicochemical ranges to afford optimal pharmacokinetic behaviour after oral intake [22–24].

In order to elucidate the potential of the aforementioned series of prenylated acyl phloroglucinols for further development as antineoplastic agents we herein describe the computational analysis of their pharmacokinetic profile and drug-likeness, using a panel of filters, routinely utilized in the prescreen stage of drug development in the pharmaceutical companies.

EXPERIMENTAL

Target compounds and computational tools

The analysed compounds were isolated from the aerial parts of *Hypericum annulatum* Moris subsp. *annulatum*, collected during the flowering period. The detailed description of the extraction, isolation and identification of the tested compounds has been previously reported [13, 14]. Their structure was confirmed by means of spectral methods (UV, IR, ^{1}H- and ^{13}C-NMR, EI-MS) (Fig. 1, Table 1). The in silico ADMET screening and drug-likeness evaluation was performed using the free webtooll SwissADME, developed by the Swiss Institute of Bioinformatics, and freely available at http://www.swissadme.ch [20].

Hyperatomarin (**1**) is a bicyclic PAP, whereas the other compounds are monocyclic, aromatic PAPs. Compounds **4–7** contain a chroman ring system, which in case of **4** is fused with a cyclohexane
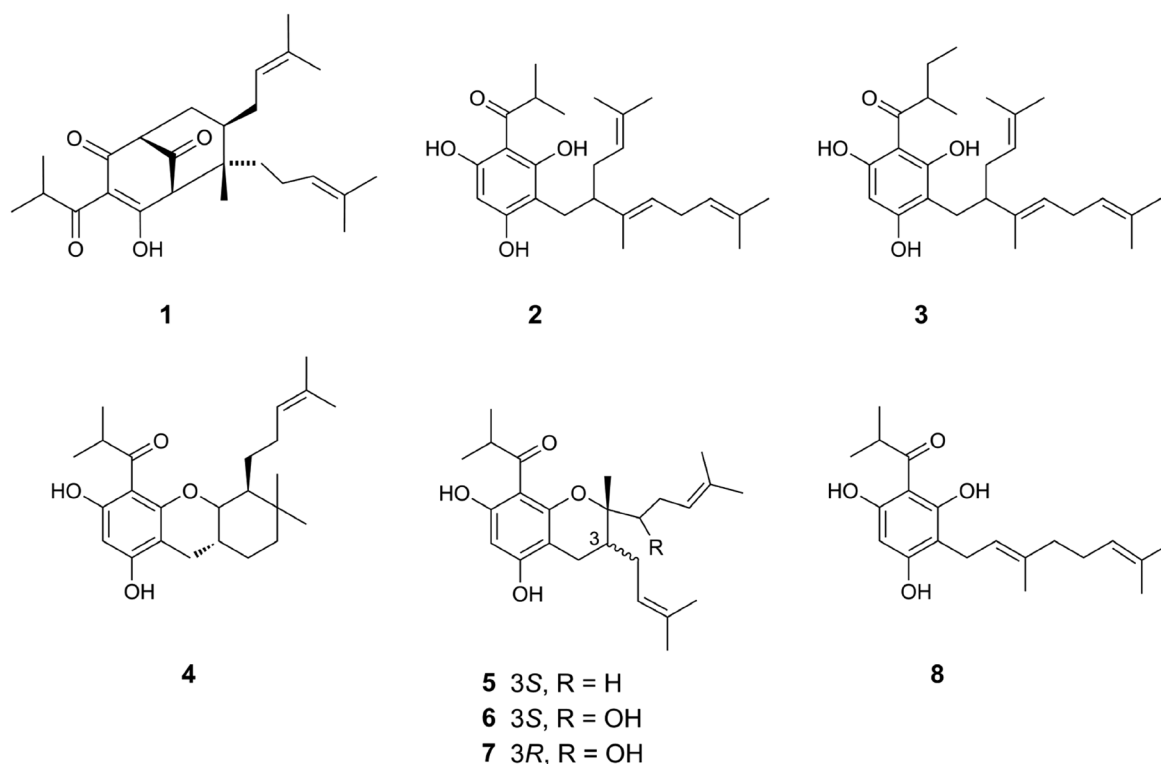
Fig. 1. Chemical structures of the target polyprenylated acylphloroglucinols from *Hypericum annulatum* Moris subsp. a*nnulatum.*

Table 1. Designation of the target compounds

Compound designation	Structure/nomenclature
1	(1R,5R,7R,8S)-4-Hydroxy-3-isobutyryl-8-methyl-7-(3-methyl-2-buten-1-yl)-8-(4-methyl-3-penten-1-yl) bicyclo[3.3.1]non-3-ene-2,9-dione
2	(*E*)-1-(3-(3,7-dimethyl-2-(3-methylbut-2-enyl) octa-3,6-dienyl)-2,4,6-trihydroxyphenyl)-2-methylpropan-1-one
3	(*E*)-1-(3-(3,7-dimethyl-2-(3-methylbut-2-enyl)octa-3,6-dienyl)-2,4,6-trihydroxyphenyl)-2-methylbutan-1-one
4	1-((4aR,9aR)-6,8-dihydroxy-3,3-dimethyl-4a-(4-methylpent-3-enyl)-2,3,4,4a,9,9a-hexahydro-1H-xanthen-5-yl)-2-methylpropan-1-one
5	1-[5,7-dihydroxy-2-methyl-3-(3-methyl-but-2-enyl)-2-(4-methyl-pent-3-enyl)-chroman-8-yl]-2-methyl-propan-1-one; hypercalyxone A
6*	1-((2S,3S)-5,7-dihydroxy-2-(1- hydroxy-4-methylpent-3-enyl)-2-methyl-3-(3-methylbut-2-enyl) chroman-8-yl)-2-methylpropan-1-one
7*	1-((2S,3R)-5,7-dihydroxy-2-(1-hydroxy-4-methylpent-3-enyl)-2-methyl-3-(3-methylbut-2- enyl) chroman-8-yl)-2-methylpropan-1-one
8	3-geranyl-1-(2′-methylpropanoyl)phloroglucinol

* Compounds 6 and 7 are OH-derivatives of **5** and are epimers.

ring. The agents **6** and **7** are hydroxylated derivatives of **5** and are epimers (Fig. 1).

Physiochemical properties and general computational methodology

The SMILES for each structure were generated by the structure file generator, available at the free online tool SwissADME web page. Using the web tool we calculated a number of simple molecular and physicochemical descriptors, such as the molecular weight (MW), molecular refractivity (MR), count of specific atom types and the topological polar surface area (TPSA), the latter proven as a useful descriptor in many models for estimation of membrane diffusion, ADME and pharmacokinetic behaviour. The lipophilicity was assessed by means of five alternative predictive models; i.e. XLOGP; WLOGP; MLOGP; SILICOS-IT, iLOGP, together with a consensus logP estimation, based on the average value of the different computational parameters [20, 25]. Conversely, the aqueous solubility was established, as well, using three alternative models [20].

ADME

The ADME/pharmacokinetics analysis aimed at estimation of core parameters such as gastro intestinal absorption, P-glycoprotein-mediated efflux, ability to penetrate the blood-brain barrier (BBB). Moreover, we analysed whether the target com-

pounds are substrates of a battery of essential isoforms of the cytochrome P450 (CYP) family, namely CYP1A2, CYP2D6, CYP2C9, CYP2C19, and CYP3A4. To meet this objective the SwissADME tool is relying on a robust vector machine algorithm (SVM) with precisely cleaned comprehensive datasets of established inhibitors/non-inhibitors and substrates/non-substrates. The theoretic background, development and validation of these computational approaches have been described in detail elsewhere [20, 26].

Drug likeness estimation

The drug likeness analysis was carried out using the validated rules used as high-throughput screens filters in some of the leading pharmaceutical companies, as follows: Lipinski (*Pfizer*), Ghose (*Amgen*), Veber (*GSK*), Egan (*Pharmacia*) and Muegge (*Bayer*). The Abbott bioavailability score was calculated to predict the probability for a 10% oral bioavailability or Caco-2 diffusion. These filters have been developed to assess drug-likeness, i.e. to predict whether a chemical entity is likely to have useful pharmacokinetic properties, using calculations, based on parameters such as molecular weight, LogP, number of HPA and HBD [17–21]. Moreover the feasibility to explore the presented structures as starting scaffolds or lead compounds in a future synthetic drug discovery program was analysed using specific medicinal chemistry and lead-likeness filters [20].

RESULTS AND DISCUSSION

The basic physicochemical parameters are described in Table 2, whereas the lipophilicity and water solubility estimations are presented in Tables 3 and 4 respectively. Based on the calculated logP values all tested compounds proved to be lipophilic with consensus values ranging 4.25–5.98 (Table 3). These are considered as boundary values for most of the drug-likeness filters employed by the pharmaceutical industry. Conversely these findings were mirrored by the estimation of the water solubility showed that the target compounds are moderately to poorly soluble, depending both on the LogS estimation model and the tested compound (Table 4).

The main ADME parameters of the pharmacokinetic behaviour of the tested phloroglucinols are described in Table 5. With the only exception of compound **3** all agents are estimated to have high absorption in the gastrointestinal tract which is a highly favourable feature of a drug candidate, considering the undisputable advantages of the oral route of administration. With very few exceptions the phloroglucinols are not expected to act as inhibitors of CYP1A2, CYP2C19, CYP2D6, which mediate the biotransformation of a number of important classes of drugs [27]. All of the compounds from the tested series are expected to inhibit CYP3A4, which is a potentially disadvantageous feature, as this CYP isoform is implicated in the metabolism and elimination of the majority of clinically used drugs, such as calcium channel blockers, some statins, immunosuppressors, macrolides, atypical antipsychotics, among others [27, 31]. With the only exception of 6 and 7 the phloroglucinols are expected to act as CYP2C9 inhibitors, as well.

The computational data do not indicate the target compounds as capable of crossing the BBB. The latter feature is disadvantage if considering the possible CNS localization of malignant tumours or metastases thereof, but on the other hand it indicates low risk of CNS side effects, which are at least not impossible having into account the ability of PAP (including hyperatomarin, **1**) to modulate monoam-

Table 2. Basic physicochemical properties and computational descriptors of the tested compounds

Properties	1	2	3	4	5	6, 7	8
Formula	$C_{25}H_{36}O_4$	$C_{25}H_{36}O_4$	$C_{26}H_{38}O_4$	$C_{25}H_{36}O_4$	$C_{25}H_{36}O_4$	$C_{25}H_{36}O_5$	$C_{20}H_{28}O_4$
Molecular weight	400.55 g/mol	400.55 g/mol	414.58 g/mol	400.55 g/mol	400.55 g/mol	416.55 g/mol	332.43 g/mol
Num. heavy atoms	29	29	30	29	29	30	24
Num. arom. heavy atoms	0	6	6	6	6	6	6
Fraction Csp3	0.64	0.48	0.50	0.64	0.56	0.56	0.45
Num. rotatable bonds	7	9	10	5	7	7	7
Num. H-bond acceptors	4	4	4	4	4	5	4
Num. H-bond donors	1	3	3	2	2	3	3
Molar Refractivity	118.55	123.16	127.97	119.28	121.22	122.38	99.60

Table 3. Lipophilicity of the tested compounds

Properties	1	2	3	4	5	6, 7	8
Log $P_{o/w}$ (iLOGP)	4.01	4.17	4.09	3.36	3.88	3.71	2.80
Log $P_{o/w}$ (XLOGP3)	6.61	7.67	8.03	7.25	7.28	6.31	5.92
Log $P_{o/w}$ (WLOGP)	5.54	6.46	6.85	6.04	6.35	5.32	4.88
Log $P_{o/w}$ (MLOGP)	2.81	3.93	4.13	3.70	3.62	2.79	2.93
Log $P_{o/w}$ (SILICOS-IT)	5.80	6.35	6.78	5.60	6.30	5.54	4.73
Consensus Log $P_{o/w}$	4.95	5.72	5.98	5.19	5.49	4.73	4.25

Table 4. Water solubility prediction values, based on three alternative models [20, 25]

Properties	1	2	3	4	5	6, 7	8
Log S (ESOL)	−6.03	−6.71	−6.96	−6.71	−6.60	−6.08	−5.35
Solubility	$3.78.10^{-4}$ mg/ml; $9.43.10^{-7}$ mol/l	$7.73.10^{-5}$ mg/ml; $1.93.10^{-7}$ mol/l	$4.57.10^{-5}$ mg/ml; $1.10.10^{-7}$ mol/l	$7.74.10^{-5}$ mg/ml; $1.93.10^{-7}$ mol/l	$1.00.10^{-4}$ mg/ml; $2.51.10^{-7}$ mol/l	$3.43.10^{-4}$ mg/ml; $8.24.10^{-7}$ mol/l	$1.47.10^{-3}$ mg/ml; $4.43.10^{-6}$ mol/l
Class	Poorly soluble	Poorly soluble	Poorly soluble	Poorly soluble	Poorly soluble	Poorly soluble	Moderately soluble
Log S (Ali)	−7.91	−9.14	−9.52	−8.48	−8.51	−7.93	−7.33
Solubility	$4.92.10^{-6}$ mg/ml; $1.23.10^{-8}$ mol/l	$2.88.10^{-7}$ mg/ml; $7.19.10^{-10}$ mol/l	$1.26.10^{-7}$ mg/ml; $3.04.10^{-10}$ mol/l	$1.34.10^{-6}$ mg/ml; $3.34.10^{-9}$ mol/l	$1.24.10^{-6}$ mg/ml; $3.11.10^{-9}$ mol/l	$4.94.10^{-6}$ mg/ml; $1.19.10^{-8}$ mol/l	$1.56.10^{-5}$ mg/ml; $4.71.10^{-8}$ mol/l
Class	Poorly soluble	Poorly soluble	Poorly soluble	Poorly soluble	Poorly soluble	Poorly soluble	Poorly soluble
Log S (SILICOS-IT)	−4.87	−4.83	−5.23	−5.37	−5.60	−4.65	−3.97
Solubility	$5.39.10^{-3}$ mg/ml; $1.35.10^{-5}$ mol/l	$5.86.10^{-3}$ mg/ml; $1.46.10^{-5}$ mol/l	$2.46.10^{-3}$ mg/ml; $5.93.10^{-6}$ mol/l	$1.72.10^{-3}$ mg/ml; $4.31.10^{-6}$ mol/l	$1.01.10^{-3}$ mg/ml; $2.51.10^{-6}$ mol/l	$9.24.10^{-3}$ mg/ml; $2.22.10^{-5}$ mol/l	$3.55.10^{-2}$ mg/ml; $1.07.10^{-4}$ mol/l
Class	Moderately soluble	Moderately soluble	Moderately soluble	Moderately soluble	Moderately soluble	Moderately soluble	Soluble

Table 5. Calculated ADME and pharmacokinetic parameters

Properties	1	2	3	4	5	6, 7	8
GI absorption	High	High	Low	High	High	High	High
BBB permeant	No	No	No	No	No	No	No
P-gp substrate	Yes	No	No	No	No	No	No
CYP1A2 inhibitor	No	Yes	No	No	No	No	Yes
CYP2C19 inhibitor	Yes	No	No	No	No	No	No
CYP2C9 inhibitor	Yes	Yes	Yes	Yes	Yes	No	Yes
CYP2D6 inhibitor	Yes	No	No	No	No	No	No
CYP3A4 inhibitor	Yes	Yes	Yes	Yes	Yes	Yes	Yes
Log K_p (skin permeation)	−4.05 cm/s	−3.30 cm/s	−3.13 cm/s	−3.60 cm/s	−3.57 cm/s	−4.36 cm/s	−4.12 cm/s

ine neurotransmission [8, 9, 28]. Another beneficial issue for all monocyclic PAPs is that the computational screening indicates them as non-P-gp substrates. This xenobiotic pump mediates the unilateral efflux of anticancer drugs out of cancer cells and hence its overexpression confers multi-drug resistance to a number of chemically and pharmacologically distinct antineoplastic agents [29, 30]. Thus, the findings indicating the target monocyclic PAPs as non-P-gp substrates is a prerequisite for activity against multidrug resistant cancer cells, overexpressing this drug transporter. On the contrary, the computational data for the bicyclic prenylated acyl

phloroglucinol hyperatomarin indicate it as a P-gp substrate. Nevertheless, our pharmacological data from preceding studies shows that this compound is capable of eradicating multidrug resistant leukemic cells, which indirectly indicates that it is actually an inhibitor of the ATP-binding cassette transporters, such as P-gp.

The skin permeation ability of the tested compounds is expected to be very low, based on the calculated LogKp values.

The drug likeness evaluation is summarized in Table 6. All compounds proved to comply with the Lipinski rules, which comprise the pioneering drug

Table 6. Drug likeness, medicinal chemistry and lead-likeness parameters for the tested compounds

Properties	1	2	3	4	5	6, 7	8
Lipinski	Yes; 0 violations	Yes; 0 violations	Yes; 0 violations	Yes; 0 violations	Yes; 0 violations	Yes; 0 violations	Yes; 0 violations
Ghose	Yes	No; 1 violation: WLOGP>5.6	No; 1 violation: WLOGP>5.6	No; 1 violation: WLOGP>5.6	No; 1 violation: WLOGP>5.6	Yes	Yes
Veber	Yes	Yes	Yes	Yes	Yes	Yes	Yes
Egan	Yes	No; 1 violation: WLOGP>5.88	No; 1 violation: WLOGP>5.88	No; 1 violation: WLOGP>5.88	No; 1 violation: WLOGP>5.88	Yes	Yes
Muegge	No; 1 violation: XLOGP3>5	No; 1 violation: XLOGP3>5	No; 1 violation: XLOGP3>5	No; 1 violation: XLOGP3>5	No; 1 violation: XLOGP3>5	No; 1 violation: XLOGP3>5	No; 1 violation: XLOGP3>5
Bioavailability Score	0.56	0.55	0.55	0.55	0.55	0.55	0.55
Brenk	3 alerts: beta/keto/anhydride, isolated alkene, Michael acceptor_4	1 alert: isolated alkene	1 alert: isolated alkene	1 alert: isolated alkene	1 alert: isolated alkene	1 alert: isolated alkene	1 alert: isolated alkene

candidate filter, implemented in the drug discovery screens of Pfizer and are considered the ultimate archetype of all drug-likeness tools. Conversely the tested phloroglucinols had no violations of the rules, implemented in the Veber filter, but had variable success rates in Ghose and Egan filters.

We also calculated the Abbot Bioavailability Score, which measures the probability of a compound to have at least 10% oral bioavailability in rat or measurable Caco-2 permeability [20]. Based on this semi-quantitative score, calculated on the basis of total charge, TPSA, and violation to the Lipinski filter the tested compounds are classified to four classes of compounds with probabilities of 11%, 17%, 56% or 85%. In line with the gastrointestinal absorption data from table 3 all tested compounds were classified as having 56% probability of attaining the aforementioned bioavailability end-points.

Due to their chemical complexity high molecular mass and lipophilicity the tested series generally failed to comply to the Muegge and Brent lead-likeness filters [20], which indicates that if they are to employed as starting scaffolds for a drug discovery programs the synthetic strategies should be focused on structure simplification, elimination of troublesome functionalities and decreased lipophilicity.

CONCLUSION

The global ADME and PK features of the target PAPs generally indicate that the main issue of concern is their significant lipophilicity and low water solubility, otherwise the analysed series of phloroglucinols have a suitable amalgam of physicochemical and biopharmaceutical properties, to afford plausible pharmacokinetic properties. This together with the promising antineoplastic effects give us reason to consider the PAP from *Hypericum annulatum* Moris subsp. *annulatum* as a perspective set of lead compounds for further more detailed pharmacological and toxicological evaluation.

REFERENCES

1. D. J. Newman, G. M. Cragg, *J. Nat. Prod.*, **79**, 629 (2016).
2. C. Basmadjian, Q. Zhao, E. Bentouhami, A. Djehal, C. G. Nebigil, R. A. Johnson, M. Serova, A. de Gramont, S. Faivre, E. Raymond, L. G. Desaubry, *Front. Chem.*, **2**, 1 (2014).
3. D. J. Newman, G. M. Cragg, *J. Nat. Prod.*, **75**, 311 (2012).
4. I. P. Singh, J. Sidana, P. Bansal, W. J. Foley, *Exp. Opin. Ther. Patents*, **19**, 847 (2009).
5. I. P. Singh, J. Sidana, S.B. Bharate, W. J. Foley, *Nat. Prod. Rep.*, **27**, 393 (2010).
6. S. L. Crockett, N. K. Robson, *Med. Arom. Plant Sci. Biotechnol.*, **5**, 1 (2011).
7. S. L. Crockett, B. Schaneberg, I. A. Khan, *Phytochem Anal*, **16**, 479 (2005).
8. X. W. Yang, R. B. Grossman, G. Xu, *Chem. Rev.*, **118**, (2018) (in press).
9. R. Ciochina, R. B. Grossman, *Chem. Rev.*, **106**, 3963 (2006).

10. S. Nikolov, G. Momekov, G. Kitanov, I. Ionkova, I. Krasteva, R. Toshkova, S. Konstantinov, P. Nedialkov, M. Karaivanova, *Biotechnol. Biotechnol. Eq.*, **21**, 471 (2007).

11. P. T. Nedialkov, D. Zheleva-Dimitrova, G. Momekov, K. Karlov, U. Girreser, G. M. Kitanov, *Nat. Prod. Res.*, **25**, 1743 (2011).

12. K. Savikin-Fodulovic, I. Aljancic, V. Vajs, N. Menkovic, S. Macura, G. Gojgic, S. Milosavljevic, *J. Nat. Prod.*, **66**, 1236 (2003).

13. P. Nedialkov, Y. Ilieva, G. Momekov, *Planta Med.*, **81**, 1437 (2015).

14. G. Momekov, D. Ferdinandov, D. Zheleva-Dimitrova, P. Nedialkov, U. Girreser, G. Kitanov, *Phytomedicine*, **15**, 1010 (2008).

15. S. Biljali, G. Momekov, P. Nedialkov, D. Zheleva-Dimitrova, G. Kitanov, D. Momekova, N. Stoyanov, M. Guenova, A. Michova, M. Karaivanova, *J. Pharm. Technol. Drug Res.*, **1**, (2012).

16. N. M. Nürk, S. L. Crockett, *Med. Arom. Plant Sci. Biotechnol.*, **5**, 14 (2011).

17. W. P. Walters, M. A. Murcko, *Adv. Drug Deliv. Rev.*, **54**, 255 (2002).

18. G. Vistoli, A. Pedretti, B. Testa, *Drug Discov. Today*, **13**, 285 (2008).

19. J. R. Proudfoot, *Bioorg. Med. Chem. Lett*, **12**, 1647 (2002).

20. A. Daina, O. Michielin, V. Zoete, *Sci Rep*, **7**, 42717 (2017).

21. M. Brustle, B. Beck, T. Schindler, W. King, T. Mitchell, T. Clark, *J. Med. Chem.*, **45**, 3345 (2002).

22. C. A. Lipinski, F. Lombardo, B. W. Dominy, P. J. Feeney, *Adv. Drug. Deliv. Rev.*, **46**, 3 (2001).

23. C. A. Lipinski, *Adv. Drug. Deliv. Rev.*, **101**, 34 (2016).

24. C. A. Lipinski, *Drug Discov. Today Technol.*, **1**, 337 (2004).

25. A. Daina, O. Michielin, V. Zoete, *J. Chem. Inf. Model.*, **54**, 3284 (2014).

26. A. Daina, V. Zoete, *Chem Med. Chem.*, **11**, 1117 (2016).

27. N. Bozina, V. Bradamante, M. Lovric, *Arh. Hig. Rada Toksikol.*, **60**, 217 (2009).

28. V. Tzankova, P. Nedialkov, G. Kitanov, N. Danchev, *Pharmacologyonline*, **2**, 142 (2010).

29. C. H. Choi, *Cancer Cell Int.*, **5**, 30 (2005).

30. L. Silverton, M. Dean, K. Moitra, *Drug Metabol. Drug Interact.*, **26**, 169 (2010).

31. B. C. Jones, H. Rollison, S. Johansson, K. P. Kanebratt, C. Lambert, K. Vishwanathan, T. B. Andersson, *Drug Metab. Dispos.*, **45**, 35 (2017).

IN SILICO ОЦЕНКА НА ADME ПРОФИЛИТЕ И НА ЛЕКАРСТВЕНОТО ПОДОБИЕ НА СЕРИЯ ОТ ЦИТОТОКСИЧНИ ПОЛИПРЕНИЛИРАНИ АЦИЛФЛОРОГЛУЦИНОЛИ, ИЗОЛИРАНИ ОТ *HYPERICUM ANNULATUS* MORRIS SUBSP. *ANNULATUM*

Я. Илиева[1,2], З. Коканова-Недялкова[1], П. Недялков[1], Г. Момеков[2]

[1] Катедра по фармакогнозия, Фармацевтичен факултет, Медицински университет, София

[2] Катедра по фармакология, фармакотерапия и токсикология, Фармацевтичен факултет, Медицински университет, София

(Резюме)

Осем цитотоксични полипренилирани ацилфлорфлуциноли, изолирани от *Hypericum annulatum* Moris subsp. *annulatum*, бяха подложени на виртуална оценка на ADME, фармакокинетиката и лекарственото подобие, с помощта на уеб платформата SwissADME. Оценката на физикохимичните параметри показва значителна липофилност и ниска водоразтворимост. Въз основа на получените данни се очаква съединенията да имат добра орална бионаличност и с изключение на хиператомарин да не са субстрат на Р-гликопротеина. Оценката на техния профил на модулиращи ефекти спрямо някои изоформи на цитохром Р450 показва, че всички те са инхибитори на CYP3A4, докато очакваните ефекти върху други CYP изоформи варират при отделните съединения. При оценката на лекарствено подобие бяха използвани пет алтернативни филтъра, при което всички съединения са в съответствие с правилото на Липински. В заключение, изчислените ADME и фармакокинетичните параметри ни дават основание да разглеждаме полипренилираните ацилфлорфлуциноли от *Hypericum annulatum* Moris subsp. *annulatum* като перспективна серия от цитотоксични лекарствени кандидати, заслужаващи по-задълбочена онкофармакологична и токсикологична оценка.

Performance of metathesis reactions using different nano-sized ferrite-type catalysts

S. S. Dimova[1]*, K. L. Zaharieva[2], F. S. Ublekov[1], H. P. Penchev[1]

[1] *Institute of Polymers, Bulgarian Academy of Sciences, "Acad. G. Bonchev" St., Bl.103A, 1113 Sofia, Bulgaria*
[2] *Institute of Catalysis, Bulgarian Academy of Sciences, "Acad. G. Bonchev" St., Bl. 11, 1113 Sofia, Bulgaria*

This paper represents a comparative study of our research on metathesis reaction, performed in the presence of different nano-sized ferrite-type catalysts. The obtained products – substituted polyphenylacetylenes, have been characterized by FTIR and ^{1}H-NMR spectroscopy, Size exclusion chromatography (SEC) and Scanning electron microscopy. The monomers used were – 1-phenylacetylene or 1-phenyl-1-propyne, co-monomer – isobutyraldehyde and various nanostructured ferrite-type catalysts – $Ni_xFe_{3-x}O_4$, $Mg_xFe_{3-x}O_4$, $Co_xFe_{3-x}O_4$ (x=0.25, 0.5, 1). The results obtained show that varying of alkyne – carbonyl metathesis reaction conditions – starting monomers, reaction time, temperature and ferrite-type catalysts used, lead to the formation of polyphenylacetylenes with a carbonyl- or olefin end groups. The alkyne – carbonyl metathesis is promising method for preparation of organic compounds and polymers with specific properties.

Keywords: alkyne - carbonyl metathesis, polyphenylacetylenes, ferrite catalysts.

INTRODUCTION

The metathesis carbon-carbon bond forming reactions mediated by transition metal catalysts (all variants of olefin metathesis, metathesis polymerization of alkynes, σ-bond metathesis, etc.) are powerful tools in organic synthesis. Over the last decade, it became an efficient tool to accomplish the synthesis of many complex molecules [1, 2].

The spinel ferrites are interesting materials as they can be used in various fields - catalysts, gas sensors, biomedical applications, targeted drug delivery, hyperthermia treatment. Spinel ferrites exhibit many advantages as catalyst - they are cheap, efficient, reusable and recyclable [3]. In their review I. Bauer et al. [4] report the application of various ferrites as catalysts in different reactions. The metathesis reactions have been studied also in [5–7].

The aim of this present paper is a comparative study of our research concerning the synthesis of polyphenylacetylenes with a carbonyl- or olefin end groups, using metathesis reactions and their physicochemical characterization. A new synthetic route for synthesis of substituted polyphenylacetylenes using different ferrite-type catalysts was developed.

The influence of different synthesis conditions - varying the monomer, co-monomer and the nano-sized ferrite-type catalyst on the products obtained in the alkyne-carbonyl metathesis reactions is discussed.

EXPERIMENTAL

Synthetic procedure

The polymerization was performed under nitrogen in a Schlenk flask, equipped with a three way stopcock placed in an oil bath. Starting materials for each synthesis: isobutyraldehyde (C_4H_8O) (Alfa Aesar), 1-phenyl-1-propyne (C_9H_8) (Alfa Aesar) or 1-phenylacetylene (C_8H_6) (Fluka AG), 4 ml solvent 1,2-dichloroethane ($C_2H_4Cl_2$) and nano-sized ferrite-type catalysts with average crystallite size in 6.5–10 nm. The following co-precipitated ferrite-type materials – $Ni_xFe_{3-x}O_4$, $Mg_xFe_{3-x}O_4$ and $Co_xFe_{3-x}O_4$ (x=0.25, 0.5, 1) – were tested as catalysts. The presence of ferrite and additional iron oxyhydroxide phase has been determined for nickel ferrite-type samples. In the $Mg_xFe_{3-x}O_4$ (x=0.25) sample non-stoichiometric ferrite phase and additional iron oxyhydroxide were registered. For the materials $Mg_xFe_{3-x}O_4$ (x=0.5; 1) the ferrite and additional phases iron oxyhydroxides, as well as

_____
* To whom all correspondence should be sent:
E-mail: dimova@polymer.bas.bg

double layered hydroxides have been established. The single non-stoichiometric ferrite $Co_xFe_{3-x}O_4$ (x=0.25) and cobalt ferrite-type materials $Co_xFe_{3-x}O_4$ (x=0.5;1) containing additional phases – iron oxyhydroxide and double layered hydroxide were also used as catalysts. The synthesis conditions used, according to the end groups of the product, are summarized in Table1 and Table 2.

1,2-Dichloroethane was dried over CaH_2 then distilled and stored under nitrogen. All starting organic materials were characterized by TLC analysis. The reaction mixture was heated at 80–120 °C and stirred at 400–600 rpm for 4 or 24 hours. After cooling the crude mixture was purified using column chromatography with a mixture hexane:ethyl acetate = 1:10. After evaporating the solvent viscous liquids (yellow to brown) were obtained [5–7].

Characterization

The FTIR spectra were recorded from thin films on KBr plates, using Fourier infrared spectrometer Bruker-Vector 22 in the region 400–4000 cm^{-1}.

^{1}H-NMR analysis was performed on Bruker Avance DRX 250 spectrometer, 250 MHz. The peak of the solvent $CDCl_3$ (δ = 7.25 ppm) was used as internal standard.

Size exclusion chromatography was used for the determination of the average molecular weight (M_w), number average molecular weight (M_n) and

Table 1. Synthesis conditions of polyphenylacetylene with a carbonyl end group

Name	Monomer	Co-monomer	Catalyst	Yield,%
P1-CO	1-phenylacetylene 0.007 mmol	isobutyraldehyde 0.005 mmol	$CoFe_2O_4$ 0.0001mmol	70
P2-CO	1-phenylacetylene 0.007 mmol	isobutyraldehyde 0.005 mmol	$Co_{0.5}Fe_{2.5}O_4$ 0.0001mmol	80
P3-CO	1-phenylacetylene 0.007 mmol	isobutyraldehyde 0.005 mmol	$Co_{0.5}Fe_{2.5}O_4$ 0.0001mmol	65
P4-CO	1-phenylacetylene 0.007 mmol	isobutyraldehyde 0.005 mmol	$Co_{0.25}Fe_{2.75}O_4$ 0.0001mmol	60
P5-CO	1-phenylacetylene 0.1 mmol	isobutyraldehyde 1 mmol	$NiFe_2O_4$ 0.000011mmol	65
P6-CO	1-phenylacetylene 7 mmol	isobutyraldehyde 5 mmol	$Ni_{0.5}Fe_{2.5}O_4$ 0.000011mmol	76
P7-CO	1-phenylacetylene 7 mmol	isobutyraldehyde 1 mmol	$Ni_{0.5}Fe_{2.5}O_4$ 0,000011 mmol	80
P8-CO	1-phenylacetylene 7 mmol	isobutyraldehyde 5 mmol	$Ni_{0.25}Fe_{2.75}O_4$ 0.000011mmol	Only for analyses
P9-CO	1-phenylacetylene 0.07 mmol	isobutyraldehyde 0.011 mmol	$Mg_{0.5}Fe_{2.5}O_4$ 0.00001mmol	75

Table 2. Synthesis conditions of polyphenylacetylene with an olefin end group

Product	Monomer	Comonomer	Catalyst	Yield, %
P10-OL	1-phenyl-1-propyne 0.007 mmol	isobutyraldehyde 0.005 mmol	$Co_{0.5}Fe_{2.5}O_4$ 0.0001mmol	75
P11-OL	1-phenyl-1-propyne 7 mmol	isobutyraldehyde 1 mmol	$Ni_{0.5}Fe_{2.5}O_4$ 0.000011 mmol	72
P12-OL	1-phenyl-1-propyne 7 mmol	isobutyraldehyde 1 mmol	$Ni_{0.25}Fe_{2.75}O_4$ 0.000011 mmol	Only for analyses
P13-OL	1-phenyl-1-propyne 0.07 mmol	isobutyraldehyde 0.011 mmol	$Mg_{0.5}Fe_{2.5}O_4$ 0.00001mmol	56
P14-OL	1-phenylacetylene 0.07 mmol	isobutyraldehyde 0.011 mmol	$MgFe_2O_4$ 0.00001mmol	65
P15-OL	1-phenylacetylene 0.07 mmol	–	$Mg_{0.5}Fe_{2.5}O_4$ 0.00001mmol	80
P16-OL	1-phenylacetylene 0.07 mmol	isobutyraldehyde 0.011 mmol	$Mg_{0.25}Fe_{2.75}O_4$ 0.00001mmol	72

R = H, R₁ = Ph, R₂ = (CH₃)₂CH
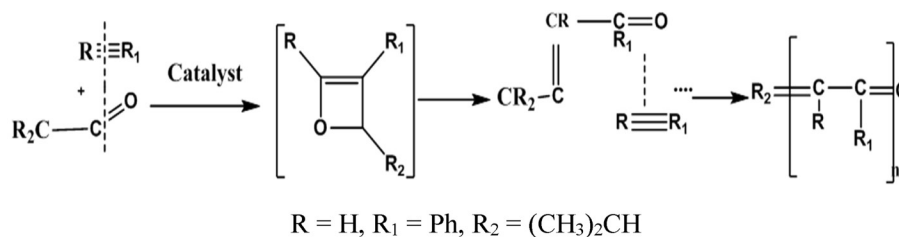
Scheme 1. Alkyne – carbonyl metathesis polyaddition reaction between phenylacetylene and isobutyraldehyde.

molar mass dispersity of products. The SEC system used (Waters, Millipore Corp., USA), was equipped with a double detection – differential refractometer RI M410 and a UV M490 detector. Three different columns were used – Phenogel 50 A; + Phenogel 100 A; + Phenogel 10000 A) calibrated with PS standards, mobile phase – THF, flow rate – 1 ml/min, pressure – 500 psi and temperature – 40 °C [5–7].

The SEM images were recorded on scanning electron microscope JEOL JSM-T200.

RESULTS AND DISCUSSION

The newly developed one-step route for the preparation of substituted polyphenylacetylene

with a carbonyl or olefin end group is presented in Scheme 1. The products obtained are stable in air, well soluble in common volatile solvents like chlorinated hydrocarbons and exhibit the physical properties of conjugated polymers. The yield of polyphenylacetylenes with a carbonyl or olefin end groups is 60–80% (Table 1 and Table 2).

Another advantage of the reaction is that cheap catalysts are used instead of the well-known ones (Ru, W, Mo).

The FTIR spectra of the products are presented in Fig. 1 and Fig. 2. The FTIR spectra of polyphenylacetylenes with a carbonyl end group, prepared using 1-phenylacetylene as monomer and co-monomer – isobutyraldehyde and nano-sized ferrite-type catalysts – samples $M_xFe_{3-x}O_4$ (M – nickel, cobalt
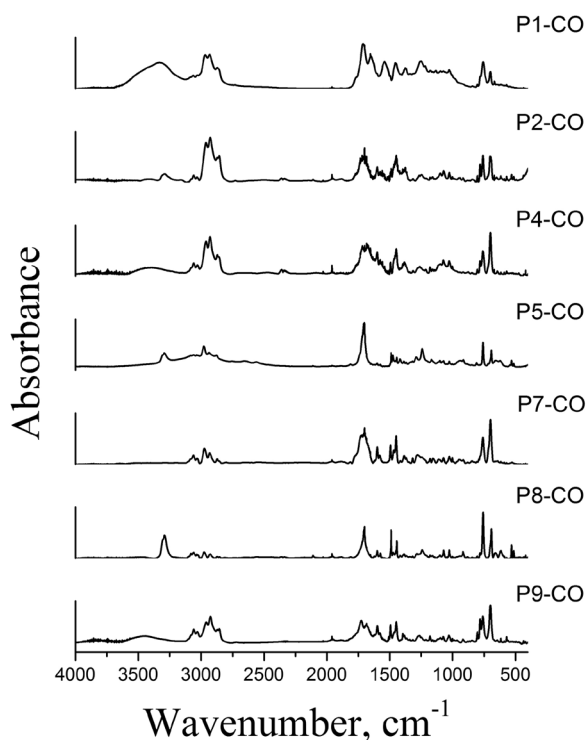
Fig. 1. FTIR spectra of polyphenylacetylene with a carbonyl end group.
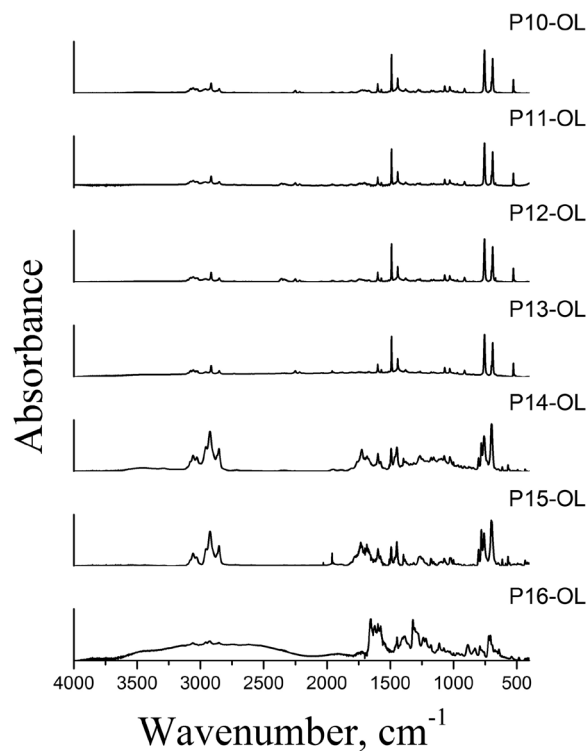
Fig. 2. FTIR spectra of polyphenylacetylene with an olefin end group.

202

and magnesium; x=0.25, 0.5, 1) at different reaction time – 4 or 24 hours are shown in Figure 1. All oligomers showed a band at 1656 cm^{-1} assigned to C=O bond (conjugated ketone end group). Characteristic peaks observed: about 3058 cm^{-1} (=C-H), 2925 cm^{-1}, 2860 cm^{-1} (CH$_2$ and CH$_3$). The double bond -C=C- from the phenylene ring appears around 1597 cm^{-1}, the =C-H aromatic vibrations are in the range of 1180–1029 cm^{-1}, while the =CH- vi-

bration from the polymer backbone is at 1448 cm^{-1}. Figure 2 shows the FTIR spectra of polyphenylacetylenes with an olefin end group. The presence of conjugated –C=C– bonds corresponding to the bands at around 1600 cm^{-1} is observed [5–7, 8].

The ^{1}H-NMR spectra of the synthesized polyphenylacetylenes are shown in Figures 3 and 4. The ^{1}H-NMR (in CDCl$_3$) of P2-CO and P9-CO showed characteristic chemical shift for double bonds
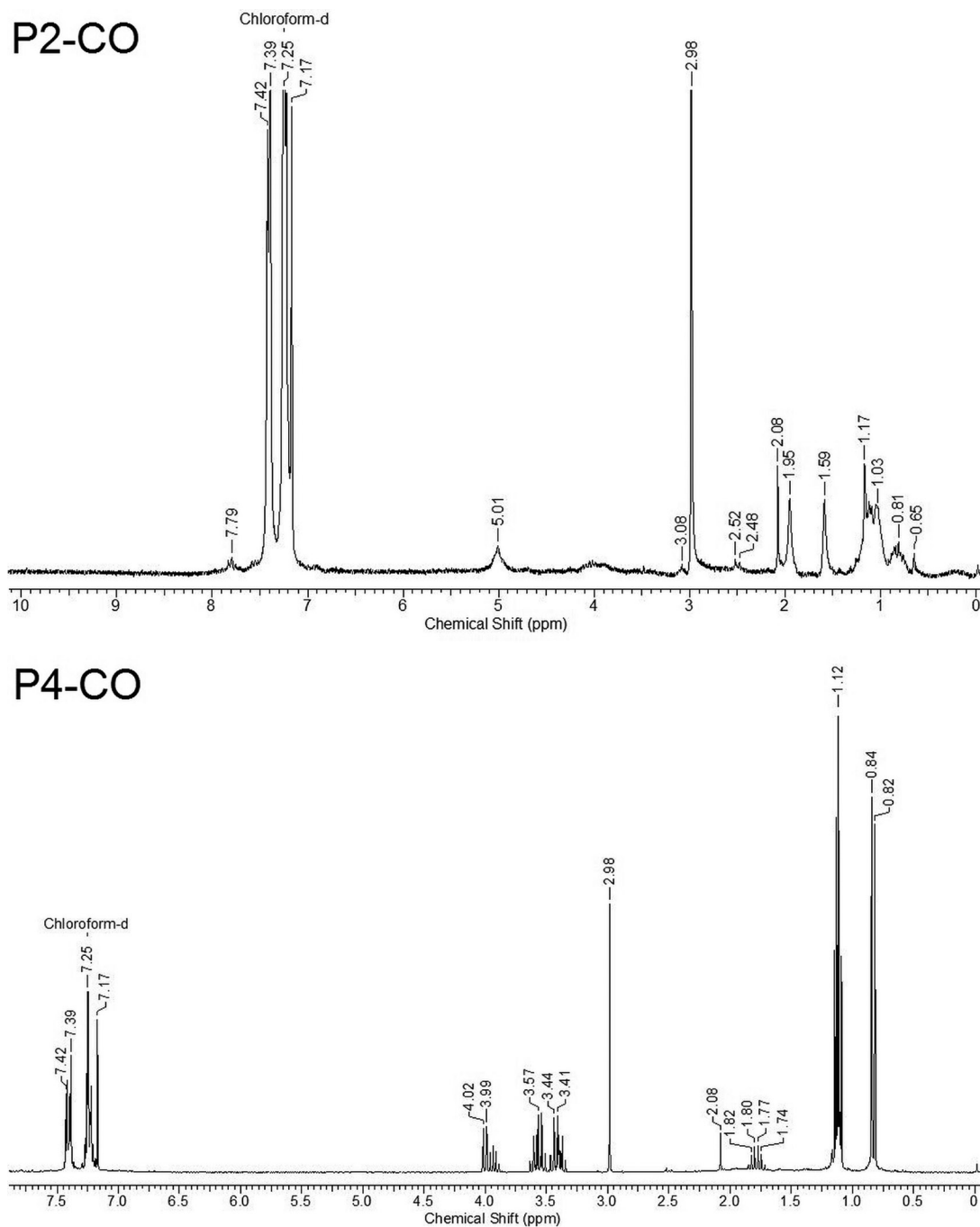
Fig. 3a. ^{1}H-NMR spectra of polyphenylacetylenes with a carbonyl end group (P2-CO, P4-CO).
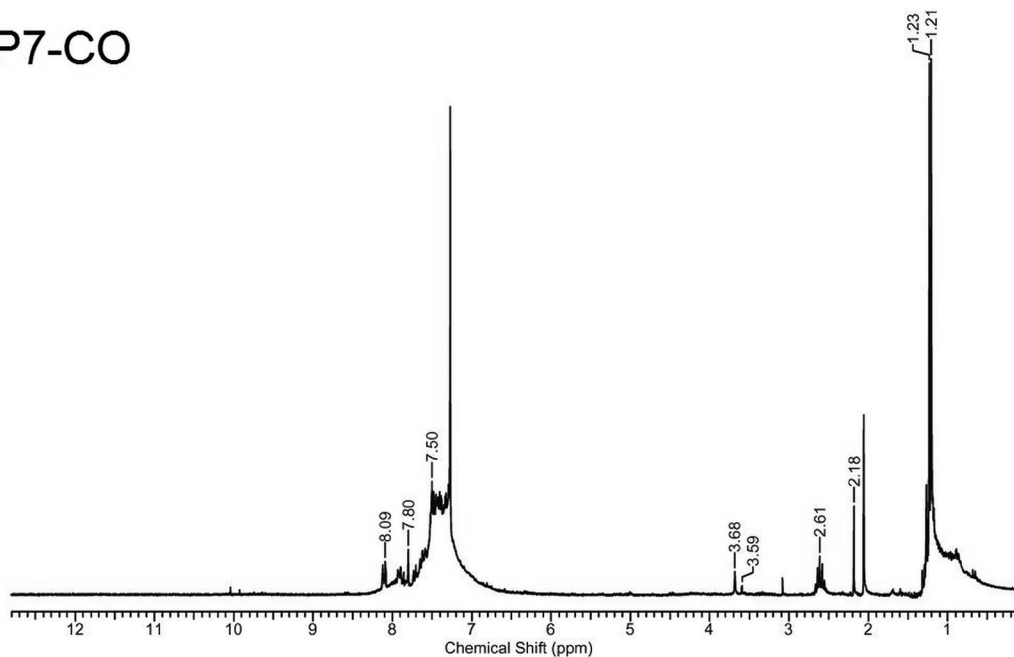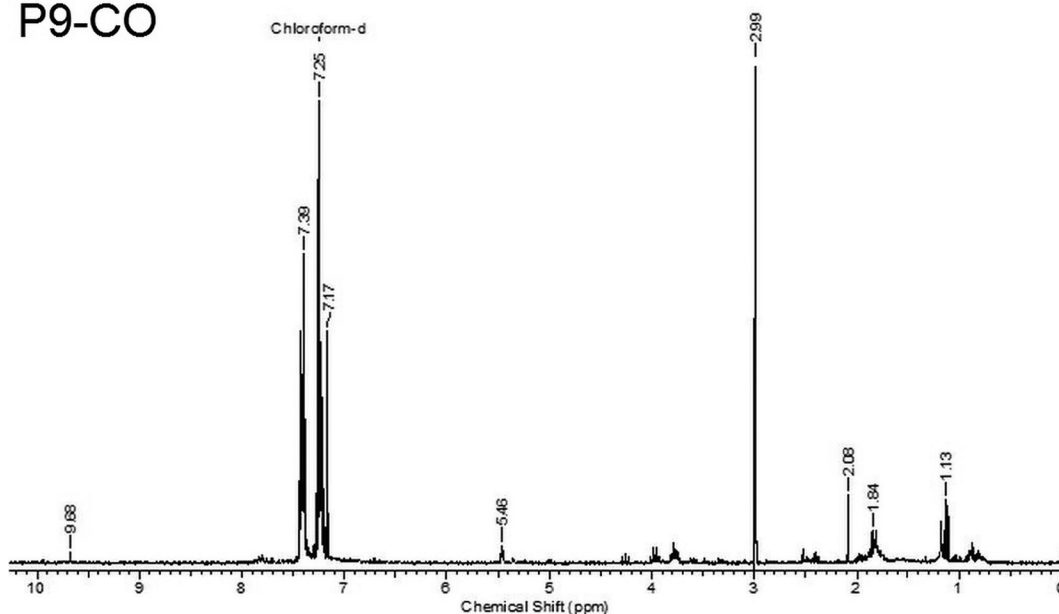
Fig. 3b. ^{1}H-NMR spectra of polyphenylacetylenes with a carbonyl end group (P7-CO, P9-CO).

around 5.07 and 5.4 ppm. The observed signals in the region 7.3–8 ppm are assigned to the protons characteristic for aromatic rings. The chemical shifts between 1.8–2.5 ppm are attributed to the =CH- protons from the backbone. In the ^{1}H-NMR spectrum of the predominantly cis-polyphenylacetylene P9-CO, the peak, characteristic for the proton, attached to the cis-conformation of the double bond, is observed at 5.4 ppm [5–7]. From the literature it is

known that if the polymerization of arylacetylenes is catalyzed by W, Mo, Rh, mainly cis-transoidal structure is obtained [9].

Polyphenylacetylene with a carbonyl end group can be prepared using monomer-1-phenylacetylene, co-monomer – isobutyraldehyde and ferrite-type catalysts – $Mg_{0.5}Fe_{2.5}O_4$, $Ni_xFe_{3-x}O_4$ and $Co_xFe_{3-x}O_4$ (x=0.25, 0.5, 1). The use of 1-phenylacetylene, isobutyraldehyde or only 1-phenylacetylene and

P10-OL

Chloroform-d

P14-OL

Chloroform-d
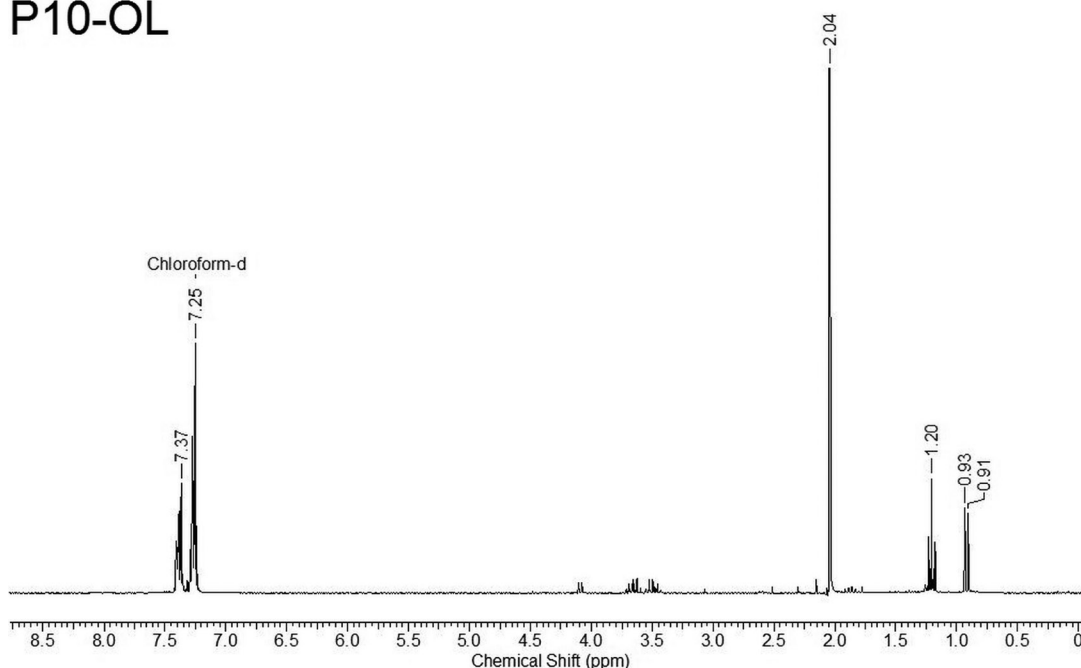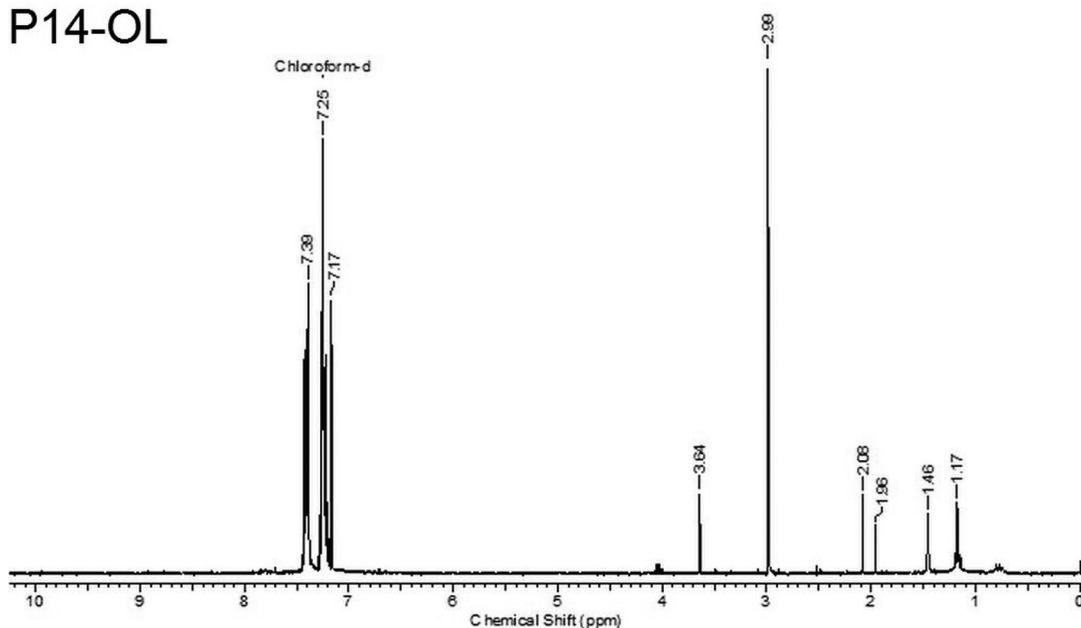
Fig. 4. ^{1}H-NMR spectra of polyphenylacetylenes with an olefin end group.

$Mg_xFe_{3-x}O_4$ (x=0.25, 1) or $Mg_{0.5}Fe_{2.5}O_4$ as catalysts leads to the formation of polyphenylacetylene with an olefin end group. Polyphenylacetylene with an olefin end group can be obtained also in the presence of monomer-1-phenyl-1-propyne, co-monomer – isobutyraldehyde and ferrite-type catalysts – $Mg_{0.5}Fe_{2.5}O_4$, $Ni_xFe_{3-x}O_4$ (x=0.25, 0.5) and $Co_{0.5}Fe_{2.5}O_4$.

The SEC analysis of P16-OL and P14-OL showed various fractions with different molecular masses – 10^2–10^4 g/mol and multimodal molar mass distribution with dispersity index of 2.5.

The highest molecular masses of P16-OL and P14-OL are 548 and about 17000 g/mol [5–7]. The polymerization carried out in 1,2-dichloroethane results in formation of predominantly oligomer prod-
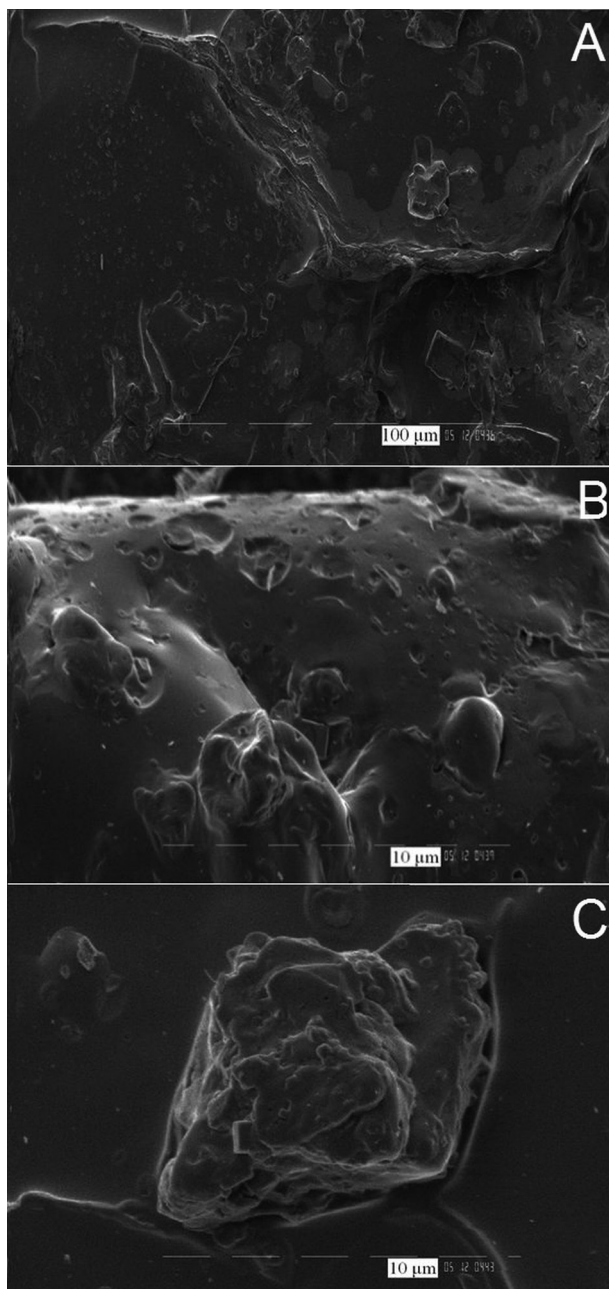
Fig. 5. SEM images of P1-CO at magnifications: 200x (A); 1000x (B); 1000x (C).
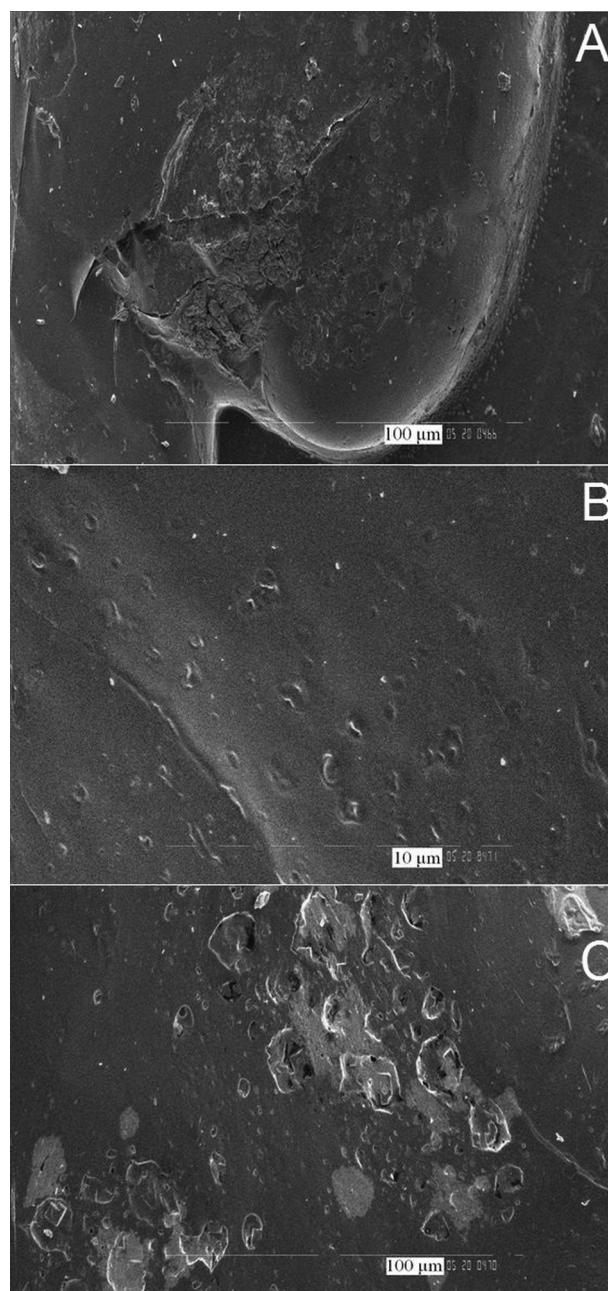
Fig. 6. SEM images of P2-CO at magnifications: 200x (A); 1000x (B); 5000x (C).

uct, irrespectively of the amount of catalyst and the polymerization time.

The SEM images of P1-CO and P2-CO are displayed on Figures 5 and 6 showing different morphological structures of obtained products at different magnifications.

The SEM analysis of the films, prepared from the polymerized samples, show essentially a glass-like matrix structure and enamel-like structure [10].

CONCLUSIONS

The present comparative study shows that by varying the metathesis reaction conditions – starting monomers, reaction time, temperature and ferrite-type catalysts – a series of substituted polyphenylacetylenes with a carbonyl or olefin end groups have been obtained. The structure and chemical composition of these products were investigated in detail

by FTIR, ^{1}H-NMR spectroscopy and Scanning electron microscopy. The results obtained confirm that the materials prepared are oligomers with an alternating C=C double bond system which limits the conjugation in the backbone, having mainly trans-configuration.

REFERENCES

1. A. Szadkowska, C. Samojłowicz, K. Grela, *Pure Appl. Chem.*, **83**, No. 3, 553 (2011).
2. A. Fürstner, *Angew. Chem. Int. Ed.*, **39**, 3012 (2000).
3. S. D. Tapsale, K. M. Jadhav, D. V. Mane, S. G. Patil, *The Pharma Innovation Journal*, **7**(1), 215 (2018).
4. I. Bauer, Hans-Joachim Knölker, *Chem. Rev.*, **115**, 3170 (2015).
5. S. Dimova, K. Zaharieva, Ch. Jossifov, Z. Cherkezova-Zheleva, I. Mitov, *Journal of Chemical Technology and Metallurgy*, **48** (1), 28 (2013).
6. S. Dimova, K. Zaharieva, V. Sinigersky, Z. Cherkezova-Zheleva, Ivan Mitov, *Journal of International Scientific Publications: Materials, Methods & Technologies*, **8**, 233 (2014).
7. S. Dimova, K. Zaharieva, Ch. Jossifov, Z. Cherkezova-Zheleva, I. Mitov, *European Polymer Congress – EPF 2013*, June 16-21, 2013 Pisa, Italy, Book of Abstracts, P1-25.
8. J. M. Sibanyoni, G. B. Bagihalli, S. F. Mapolie, *J. Organometallic Chem.*, **700**, 93 (2012).
9. G. C. Vougioukalakis, R. H. Grubbs, *Chem. Rev.*, **110**, 1746 (2010).
10. M. V. Russo, G. Iucci, D. Ferro, *Polymer*, **34** (2), 257 (1993).

ПРЕДСТАВЯНЕ НА МЕТАТЕЗНИ РЕАКЦИИ, ИЗПОЛЗВАЙКИ РАЗЛИЧНИ НАНОРАЗМЕРНИ ФЕРИТЕН ТИП КАТАЛИЗАТОРИ

С. С. Димова[1]*, К. Л. Захариева[2], Ф. С. Ублеков[1], Хр. П. Пенчев[1]

[1] Институт по полимери, Българска академия на науките, „Акад. Г. Бончев", бл.103А, 1113 София, България
[2] Институт по катализ, Българска академия на науките, „Акад. Г. Бончев", бл. 11, 1113 София, България

(Резюме)

Тази статия представя сравнително изследване върху метатезна реакция в присъствието на различни наноразмерни феритен тип катализатори. Получените продукти – заместени полифенилацетилени, са охарактеризирани чрез FTIR спектроскопия, [1]Н-ЯМР спектроскопия, хроматография с изключване по размера и сканираща електронна микроскопия. Като мономери са използвани – 1-фенилацетилен или 1-фенил-1-пропин, съмономер – изобутиралдехид и различни наноструктурирани феритен тип катализатори – $Ni_xFe_{3-x}O_4$, $Mg_xFe_{3-x}O_4$, $Co_xFe_{3-x}O_4$ (x=0.25, 0.5, 1). Получените резултати показват, че промяната на реакционните условия на алкин-карбониловата метатеза – начални мономери, реакционно време, температура и феритен тип катализатори, води до образуване на полифенилацетилени с крайни карбонилни или олефинови групи. Алкин-карбонилната метатезна реакция е обещаващ метод за получаване на органични съединения и полимери със специфични свойства.

Fluorwavellite from Petroshnitsa river valley, Republic of Macedonia

R. Nikolova[1]*, Sl. Mankov[2], N. Petrova[1], R. Titorenkova[1]

[1] Institute of Mineralogy and Crystallography "Acad. Ivan Kostov", Bulgarian Academy of Sciences, Acad. G. Bonchev Str. Bl. 107, 1113 Sofia, Bulgaria
[2] University of Mining and Geology "St. Ivan Rilski", Prof. Boyan Kamenov Str., 1700 Sofia, Bulgaria

The first finding of fluorwavellite $Al_{2.90}(PO_4)_2(OH)_2 \cdot [F_{0.88}(OH)_{0.12}]5H_2O$ (+0.10H$^+$) from the Balkan Peninsula was studied by XRD, FTIR, Raman spectroscopy and thermal analysis. The unit cell volume of the sample is comparably smaller than that of the wavellite and fluorwavellite studied so far. The vibrational modes of water molecules and hydroxyl groups are detected in their Raman and IR spectra. The results on the thermal decomposition of the fluorine analogue with wavellite structural topology are reported for the first time and different types of water were defined.

Keywords: fluorwavellite, crystal structure, Raman spectroscopy, FTIR spectroscopy, thermal behavior.

INTRODUCTION

New data on lithostratigraphy, petrology and ore mineralogy of the volcanic rocks, exposed along the Petroshnitsa river valley, Republic of Macedonia have been recently reported [1]. In the same study, the complex sulfide mineralization was described as generated during a two-stage mineralization process. Quartz-wavellite and wavellite veins that fill cracks in the intensively quartzified latite – trachytes are referred to the first hydrothermal stage. The preliminary chemical analyzes of the wavellite crystals show a significant amount of fluorine, suggesting the presence of the newly described fluorine analogue of wavellite $Al_3(PO_4)_2(OH)_2(OH_{0.5-x}F_{0.5+x}) \cdot 5H_2O$ [2]. This mineral is identical to the wavellite in terms of structural topology and morphology. The crystal structure is composed of two different chains of corner sharing Al octahedra, additionally connected by PO_4 tetrahedra [3]. The F atoms replace part of the OH groups, linking the Al octahedra.

The aim of the study is to determine the structural and physicochemical characteristics of the first fluorwavellite finding in the Balkan area.

METHODS

Single crystal (colorless prismatic crystals with dimensions $0.6 \times 0.3 \times 0.25$ mm^3) of the studied sample was carefully selected and mounted on a glass capillary. Diffraction data were collected at room temperature by xscan technique, on an Agilent Diffraction SuperNova Dual four-circle diffractometer equipped with Atlas CCD detector using mirror-monochromatized MoKα radiation from a micro-focus source ($\lambda = 0.7107$ Å). The determination of cell parameters, data integration, scaling and absorption correction was carried out using the CrysAlis Pro program package [4]. The structures were solved by direct methods (SHELXS-2014) [5] and refined by full-matrix least-square procedures on F2 (SHELXL-2014). The heavy atoms (P, Al, O) and part of the hydrogen atoms were positioned from difference Fourier maps. It was not possible to obtain the positions of the hydrogen atoms for hydroxyl groups with oxygen atoms, numbered as O5 O9 and O10. The non-hydrogen atoms were refined anisotropically while the hydrogen atoms were constrained to ride on their parent atom with Uiso(H) values of 1.2Ueq (H$_2$O) and 1.5Ueq (OH). A summary of the fundamental crystal and refinement data is provided in Table 1.

Differential thermal analysis and Thermogravimetry (DTA-TG) were carried out on the DTA-TG analyzer SETSYS2400, SETARAM at the following conditions: temperature range from 20 to

* To whom all correspondence should be sent:
E-mail: rosica.pn@clmc.bas.bg

Table 1. Data collection and structure refinement parameters

Diffractometer	Agilent Diffraction SuperNova
X-ray radiation	Mo$K\alpha$ ($\lambda = 0.71075$ Å)
Temperature (K)	290
Chemical Formula	$Al_{2.90}(PO_4)_2(OH)_2[F_{0.88}(OH)_{0.12}] \cdot 5H_2O$ (+0.10H$^+$)
Formula Mass	408.85
Crystal system	Orthorhombic
Space Group	$P\,c\,m\,n$
Unit cell parameters (Å)	$a = 9.6111(4)$
	$b = 17.3422(7)$
	$c = 6.9804(3)$
Unit cell volume (Å^3)	1163.48(8)
No. of formula units per unit cell, Z	4
Density	2.334
F(000)	826
Crystal size (μm)	$60 \times 30 \times 25$
Θ range	3.794–29.334
Index ranges	$-8 \leq h \leq 12; -23 \leq k \leq 22; -7 \leq l \leq 9$
Reflections collected/unique	3144 / 1412
Reflection with I > 2\s(I)	1186
Completnes to Θ (%)	0.99
Min. and max transmission	0.94958 , 1
Refinement method	Full-matrix least squares on F^2
Parameters refined	112
GoF	1.094
R indices [F$_o$ > 4σF]	$R = 0.0341$, $wR = 0.0867$
R indices (all data)	$R = 0.0436$, $wR = 0.0945$
Largest diff. peak / hole (e / Å^3)	+0.567 / –0.457

1000 °C, in a static air atmosphere, with a heating rate of 10 C min^{-1} and 10–15 mg samples mass.

Raman spectrum was collected in backscattering geometry using HORIBA JobinYvon Labram HR spectrometer, Olympus BH2 microscope, 633-nm line of He-Ne laser, CCD detector, and x50 objective.

FTIR spectrum of the powder KBr pallet was collected using Tensor 37 Bruker spectrometer, averaging over 64 scans in the 400–4000 cm^{-1} spectral range.

RESULTS AND DISCUSSION

Spherulitic wavellite aggregates with radial structure (Fig. 1) with a maximum diameter of about 15 mm are formed in the cracks and veins of the hosted volcanic rocks. A colorless needle shaped prismatic crystal was selected for the single crystal analyses. The obtained structural parameters are comparable with that of the previously reported data for wavellite and fluorwavellite (Table 2).

The studied sample exhibit similar structural topology to that of fluorwavellite, where one of the

Fig. 1. Hemispherical fluorwavellite aggregates up to 15 mm in diameter.

OH groups is partially replaced by fluorine atoms. Atomic coordinates and selected bond distances are presented in Tables 3 and 4. The structural packing of the studied compound is shown in Fig. 2.

Table 2. Unit cell parameters for wavellite and fluorwavellite, available in the structural databases

	Wavellite single crystal data	Wavellite – F rich single crystal data	Fluorwavellite single crystal	Fluorwavellite powder data	Fluorwavellite single crystal data
Ref.	[3]	[6]	[2]		**this study**
Formula	$Al_3(PO_4)_2(OH)_3$ $5H_2O$	$Al_3(PO_4)_2(OH)_2$ $[F_{0.53}OH)_{0.47}]$ $5H_2O$	$Al_3(PO_4)_2(OH)_2[F_{0.90}(OH)_{0.10}]$ $5H_2O$		$Al_{2.90}(PO_4)_2(OH)_2[F_{0.88}$ $(OH)_{0.12}]5H_2O$ $(+0.10H^+)$
Unit cell parameters					
SGc	*Pcmn*	*Pcmn*	*Pcmn*	*Pcmn*	*Pcmn*
a (Å)	9.621(2)	9.6422(7)	9.6311(4)	9.6482(4)	9.6111(4)
b (Å)	17.3630(40)	17.4146(15)	17.3731(12)	17.362(12)	17.3422(7)
c (Å)	6.994(3)	7.0094(2)	6.9946(3)	6.9848(3)	6.9804(3)
V (Å³)	1168.34	1176.98	1170.35	1170.04	1163.48(8)

Table 3. Fractional atomic coordinates and displacement parameters

	x	y	z	U_{eq}	Occupancy
Al1	0.22334(12)	0.25	0.37577(15)	0.0064(4)	0.927(6)
Al2	0.24385(8)	0.51608(4)	0.64131(10)	0.0061(3)	0.977(4)
P	0.06048(6)	0.40754(3)	0.39593(8)	0.00697(19)	1
O1	0.14113(18)	0.42751(9)	0.5790(2)	0.0096(4)	1
O2	0.08827(19)	0.32319(10)	0.3445(3)	0.0147(4)	1
O3	−0.09569(17)	0.41666(9)	0.4354(2)	0.0096(4)	1
O4	0.10083(17)	0.45839(10)	0.2256(2)	0.0116(4)	1
O5	0.195(9)	0.25	0.634(13)	0.0167(15)	0.11(6)
F	0.2237(11)	0.25	0.6299(12)	0.0167(15)	0.89(6)
O6	0.32037(18)	0.51776(10)	0.3952(2)	0.0098(4)	1
H6	0.415066	0.52118	0.391898	0.015	1
O7	0.3689(2)	0.32919(11)	0.4017(3)	0.0214(5)	1
H71	0.390826	0.356574	0.495244	0.026	1
H72	0.373627	0.365274	0.299845	0.026	1
O8	0.34954(19)	0.61041(10)	0.6972(3)	0.0137(4)	1
H81	0.365236	0.606614	0.826778	0.016	1
H82	0.294536	0.645815	0.696278	0.016	1
O9	0.1920(13)	0.75	0.720(6)	0.060(8)	0.53(5)
O10	0.220(2)	0.75	0.603(5)	0.052(5)	0.47(5)

Table 4. Comparing Selected bond distances

Distance	Wavellite [3]	Fluorwavellite [2]	This study
Al1 – F		1.7817(17)	1.7770(30)
Al1 – F		1.7982(16)	1.7940(30)
Al1 – OH_2 (x2)	1.8336(42)	1.8346(13)	1.8290(20)
Al1 – OH_2 (x2)	1.9835(46)	1.9715(15)	1.9690(20)
Al1 – OH	1.8031(45)		1.8300(90)
Al1 – OH	1.7758(44)		1.8600(90)
Al2 –OH	1.8795(32)	1.8747(12)	1.8703(18)
Al2 –OH	1.8826(32)	1.8793(12)	1.8754(18)
Al2 –O	1.8947(41)	1.8807(13)	1.8763(19)
Al2 –O	1.8969(41)	1.8973(12)	1.8906(19)
Al2 –O	1.9268(39)	1.9210(13)	1.9164(19)
Al2 –OH_2	1.9799(43)	1.9686(14)	1.9660(20)
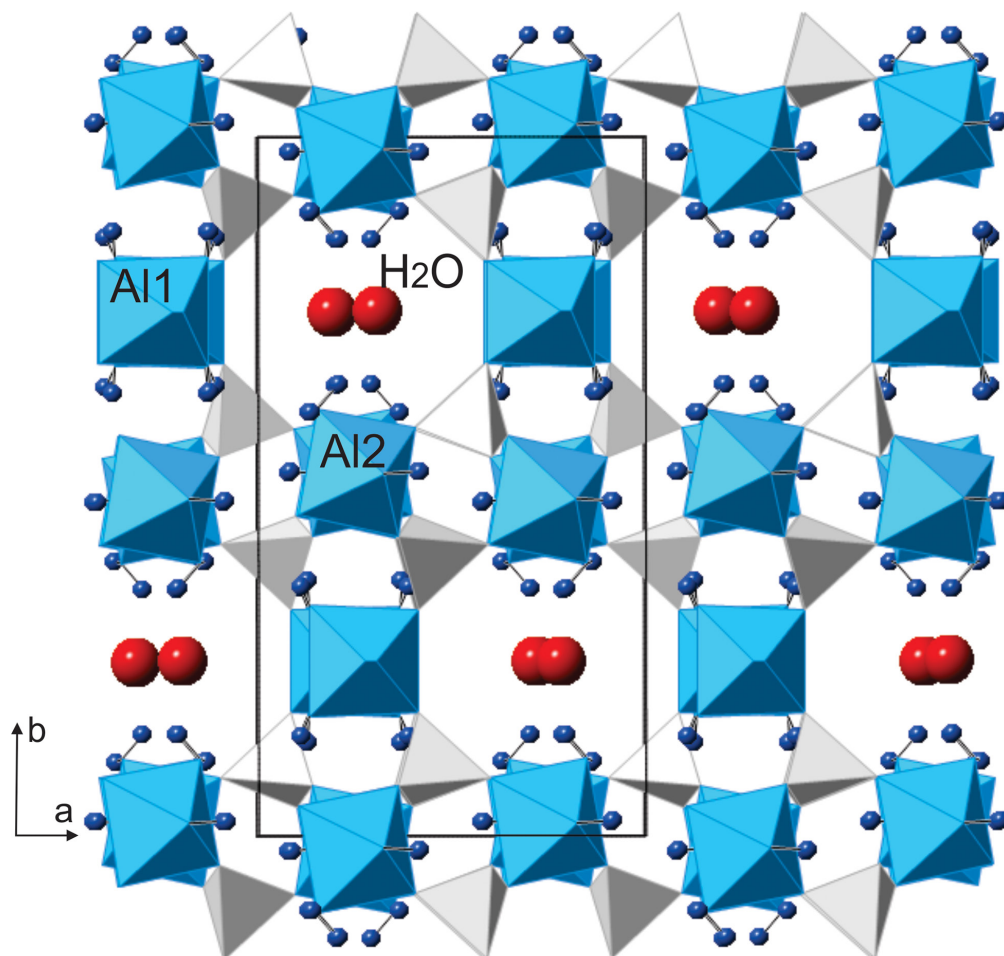
Fig. 2. Structural packing of the fluorwavellite under study.

Our structural refinement confirms splitting of the common (OH, F) position as it is shown on Fig. 3. Considering the difference in the size of the hydroxyl group ion and the fluorine atom, it could be expected that the replacement of the OH groups by F will reduce the unit cell volume. However, this is not unambiguously visible from the data known so far. Most probably the structure density is also affected by the conditions of formation, as fluorwavellite is formed in a variety of environments.

The Raman spectra of fluorwavellite crystals (Fig. 4) reveal intensive peak at 1022 cm^{-1}, assigned to the symmetrical stretching vibration of the phosphate group and other peaks at 410, 543 and 636 cm^{-1} due to bending modes of phosphate group. Peaks at lower frequencies are assigned to Al-O lattice vibrations. In the range of O-H stretching vibrations several peaks can be distinguished. The most intensive and sharp peak at 3508 cm^{-1} is assigned to stretching vibrations of hydroxyl group, while
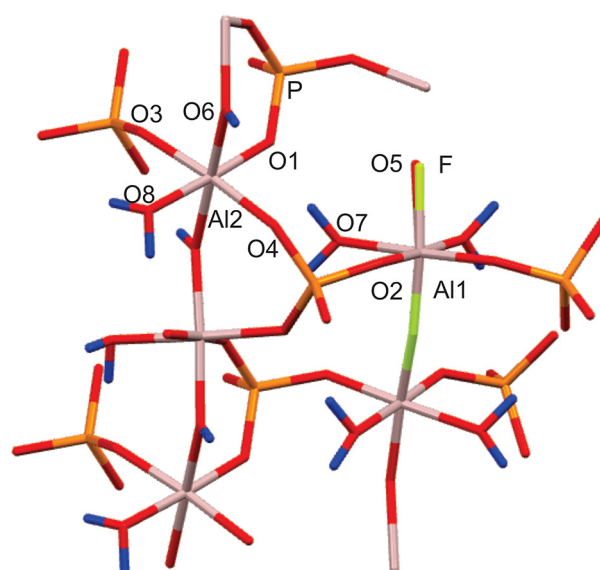
Fig. 3. Structural motive showing the common (OH, F) position splitting.

211
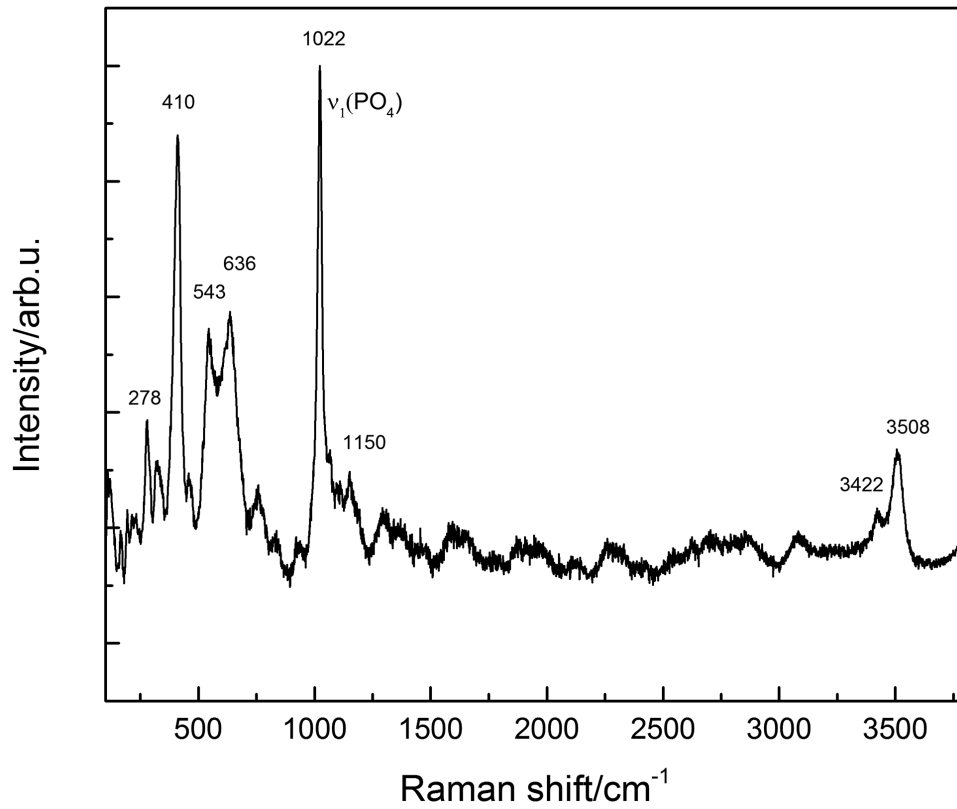
Fig. 4. Raman spectra of fluorwavellite crystals.
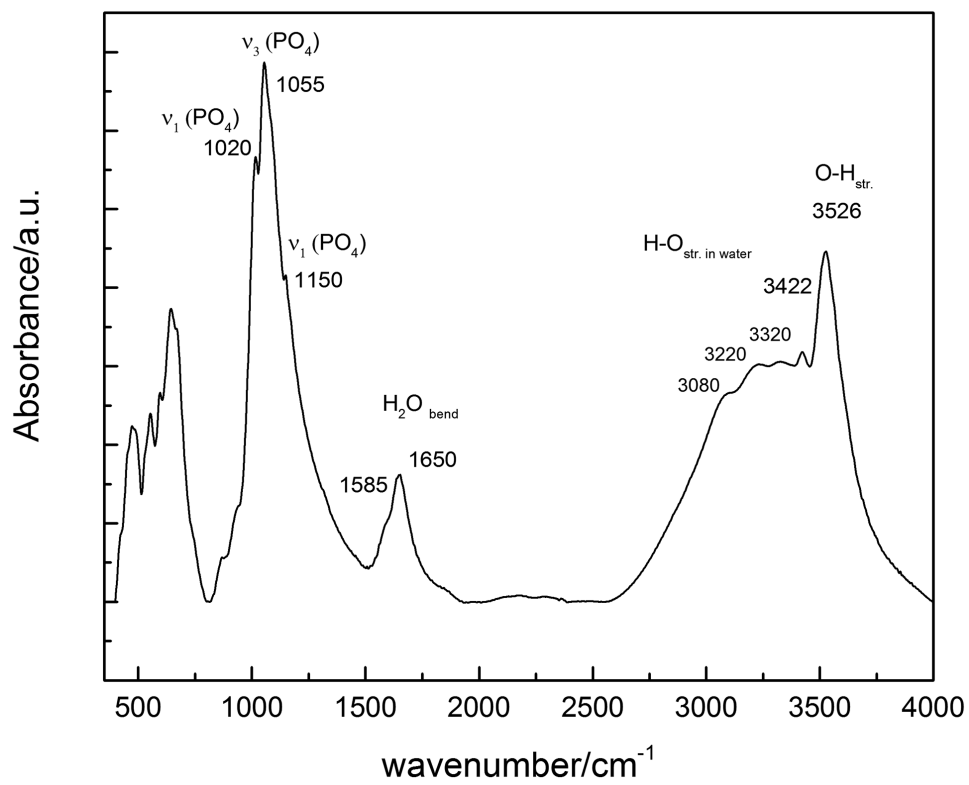
Fig. 5. IR spectra of fluorwavellite crystals.

broader overlapping bands at 3422 and around 3100 cm^{-1} can be related to different water molecules. A strong and sharp peak at 3526 cm^{-1} due to stretching vibrations of OH groups occurs in the same spectral range of IR spectra (Fig. 5). This peak is slightly shifted to higher wavenumbers as compared to previously reported spectral data for wavellite [6]. Several broader absorption bands could be resolved at around 3422, 3320, 3220 and 3080 cm^{-1} due to OH stretching in water molecules, while bending modes are detected at 1650 and 1585 cm^{-1}. This indicates the presence of different water molecules with varying degrees of hydrogen bonding.

Thermal decomposition data of both wavellite and fluorwavellite have not been found so far in the literature. DTA and TG curves, as well as DTG (first derivative of TG) and DDTG (second derivative of TG) curves are presented on Fig. 6. Three endothermal and two exothermal effects can be separated on the DTA curve. First endothermal one is around 97°C and related to the release of physisorption water. The second effect maximizes at 215 °C and corresponds to 21.6 wt% mass loss from the TG curve. This event involves the dehydration of the structure expressed by evolving of 5 molecules of water. Theoretically, this loss is 21.85 wt%, which is in a good agreement with our data. The first water
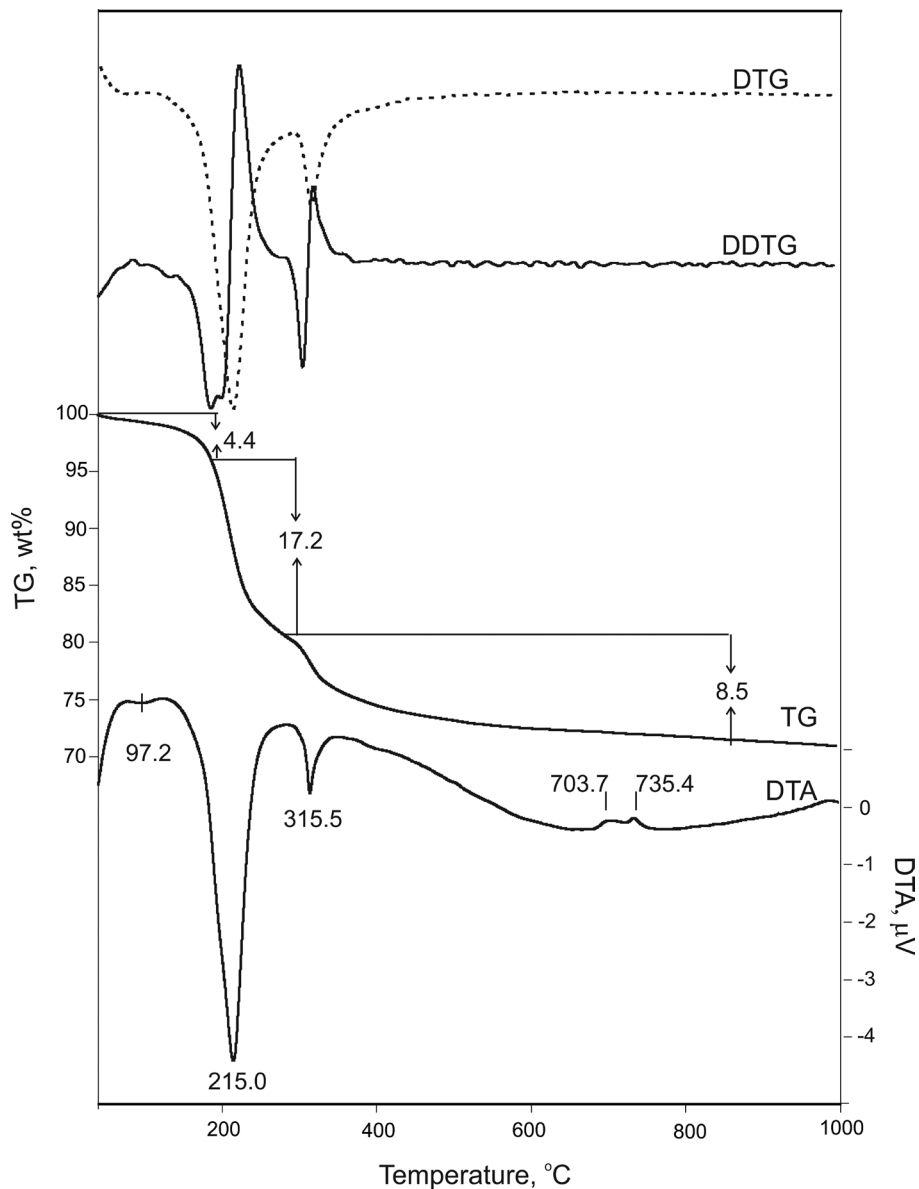
Fig. 6. DTA-TG(DTG and DDTG) curves of the fluorwavellite under study.

213

molecule (4.4 wt% mass loss) could be separated only when the DDTG curve was applied. This water is situated by hydrogen bonds in the structure cavities. The remaining four water molecules are released (17.2 wt%) at a later stage as they are more strongly linked through coordination bonds to the aluminum atoms of the structural octahedrons. The third endothermal effect (maximum of 315.5 °C) is mainly due to the process of dehydroxylation. Probably the defluoridation process starts simultaneously with dehydroxylation. Both exothermal effects at 704 and 735 °C represent the heat released at the formation of new phases, most probably aluminum phosphate and oxides.

CONCLUSIONS

Fluorwavellite from hydrothermal veins crossing early Oligocene volcanic rocks, part of the Kratovo-Zletovo volcanic area, Republic of Macedonia was studied. This is the first described finding of the mineral for the Balkan region.

Structural and spectroscopic data reveal similarity to fluorwavellite, already described by other localities.

Thermal decomposition data of flourwavellite were reported for the first time and respectively different types of water were defined.

REFERENCES

1. Sl. Mankov, M. Antonov, D. Siroshtan, V. Grozdev, Tret Kongres na geolozite na Republika Macedonia, Sbornik trudove, 589 (2016).
2. A .R. Kampf, P. M. Adams, H. Barwood, B. P. Nash, *Amer. Mineral*., **102**, 909 (2017).
3. A. Takaharu, T. Zoltai, *Zeitschrift für Kristallographie*, **127**, 21 (1968).
4. Agilent Technologies, UK Ltd: Yarnton, England, 2011
5. G. M. Sheldrick, *Acta Crystallogr., Sect. A*, **64**, 112 (2008).
6. F. Capitelli, G. Della Ventura, F. Bellatreccia, A. Sodo, M. Saviano, M. R. Ghiara, M. Rossi, *Mineralogical Magazine*, **78**(4), 1057 (2014).

ФЛУОРВАВЕЛИТ ОТ ДОЛИНАТА НА РЕКА ПЕТРОШНИЦА – РЕПУБЛИКА МАКЕДОНИЯ

Р. Николова[1], Сл. Мънков[2], Н. Петрова[1], Р. Титоренкова[1]

[1] *Институт по минералогия и кристалография „Акад. Иван Костов“, Българска академия на науките, ул. „Акад. Г. Бончев“, Бл. 107, София 1113, България*
[2] *Минно-геоложки университет „Св. Иван Рилски“, ул. „Проф. Боян Каменов“, София 1700, България*

(Резюме)

Първата находка на флуорвавелит $Al_{2.90}(PO_4)_2(OH)_2 \cdot [F_{0.88}(OH)_{0.12}]5H_2O$ (+0.10H$^+$) от Балканския полуостров беше изследвана чрез XRD, FTIR, Raman спектроскопия и термичен анализ. Обемът на елементарната клетка на пробата е сравнително по-малък от този на образци на вавелит и флуоравелит, изследвани досега. В рамановите и инфра-червени спектри се констатират вибрационни характеристични линии на водни молекули и хидроксилни групи. За първи път се съобщават резултати от термичното разлагане на флуорния вавелитов аналог, като се диференцират различните типове вода в структурата.

Proton conductive PBI membranes, containing cross-linked polyvinylsulfonic acid, for PEM fuel cells

M. Staneva[1], I. Radev[2], F. Ublekov[1], D. Budurova[1], V. Sinigersky[1], H. Penchev[1]*

[1] Institute of Polymers, Bulgarian Academy of Sciences, 1113 Sofia, Bulgaria
[2] Zentrum für Brennstoffzellen Technik, ZBT GmbH, Duisburg, Germany

Here we present an easy and efficient procedure for the immobilization of proton-donating sulfo-groups in a polymer matrix. Sodium vinyl sulfonate was polymerized/cross-linked in a para-polybenzimidazole (p-PBI) matrix. After acidification semi-interpenetrating networks, comprising p-PBI, containing cross-linked polyvinylsulfonic acid (cr-PVSA), have been obtained. Polymerization/crosslinking has been initiated either thermally or by UV irradiation. Two series of membranes, containing high concentrations of water insoluble acid groups, have been prepared. Proton conductivity was measured at 60, 80 and 95 °C and 100% relative humidity. The highest proton conductivity achieved was 63.2 mS.cm^{-1}.

Keywords: p-Polybenzimidazole-membranes, polyvinylsulfonic acid, cross-linking, semi-interprenetrating network, fuel cells, proton conductivity.

INTRODUCTION

The polymer electrolyte membrane fuel cell (PEM FC) generates electricity from an electrochemical reaction in which oxygen (air) and a fuel (e.g. hydrogen) combine to form water and heat. The polymer electrolyte membrane (PEM) is the heart of the fuel cell. PEM FC with membrane, containing sulfonic groups ($-SO_3H$) are usually operated at temperatures up to 80 °C and high RH (up to 100%).

At present the most widely used proton conductive membranes are based on perfluorinated polyelectrolytes with attached super-acidic sulfo groups (Nafion®, Flemion®, HyflonIon®, Dow membrane). These materials have high proton conductivity, excellent chemical stability, mechanical strength and potentially long term durability. The main drawbacks of these commercial membranes are their high cost and strong dependence of the proton conductivity on water contents in the membrane (difficulties with the so called water-management, due to increased hydrophobicity of the polymer backbone). Such membranes can function properly only in the highly hydrated state. In order to maintain high water content, complex water management is needed and the operation temperature is usually limited to the boiling point of water. Various polymers, containing sulfonic acid groups have been developed during the last years – sulfonated polyetheretherketones and polyether-sulfones, polyimides, sulfonated polybenzimidazoles etc. Despite of being relatively cheaper than the perfluorinated Nafion®-types, these membranes suffer the same restrictions – low operating temperatures and complex water management as well as lower proton-conductivity, inferior to the Nafion membrane.

Different types of PBI membranes with immobilized acidic groups have been described –PBIs with $–SO_3H$ groups in the main chain, PBI, containing cross-linked/grafted polyvinylphosphonic acid (PVPA) [1] and PBI with grafted PVPA chains [2].

The three most widely studied PBIs are meta-, para- and AB-PBI. Ion conductive membranes, based on these materials exhibit excellent phisico-mechanical properties and chemical stability.

The efforts, involved in the preparation of membranes, containing high concentrations of immobilized vinyl phosphonic or vinylsulfonic acid groups, show that the higher contents of such groups results in higher proton conductivity both in the anhydrous and at fully hydrated state of the membrane [2, 3]. Several years ago we have reported membranes, comprising m-PBI, containing cross-linked

_____

* To whom all correspondence should be sent:
E-mail: hpen4ev@gmail.com

polyvinylphoshpnic acid. We also showed that this method can be applied for the preparation of semi-interpenetrating networks PBI/cross-linked polyvinylsulfonic acid.

Here we report a further development of this cheap, extremely easy and efficient method for preparation of p-PBI membranes, containing cross-linked PVSA as well as characterization of the membranes prepared.

EXPERIMENTAL

Materials

2.0 wt.% solution of p-PBI in polyphosphoric acid (PPA) was kindly supplied by BASF Fuel Cell GmbH. Vinylsulfonic acid sodium salt solution 25 wt.% in H_2O (technical grade), EtOH (96%), initiator V50: 2, 2′-Azobis(2-methylpropionamidine) dihydrochloride and crosslinker: triallyl-s-triazine-2, 4, 6 (1H, 3H, 5H)-trion (98%, stabilized) were purchased from Merck and used as received.

Methods

The ^{1}H NMR spectra were recorded in H_2SO_4-d_2 on a Bruker Advance DRX 250 spectrometer using the solvent protons as internal standard. TGA was performed on Perkin Elmer 4000 apparatus – heating rate of 10 °C / min in nitrogen, temperature range 30–300 °C. FT-IR spectra were recorded on FT-IR Bruker-Vector 22 spectrometer (KBr pellets), UV irradiation was performed with Hoenle UV technology 400 W lamp, 20 cm from the filter.

All proton conductivity measurements were performed at Zentrum für Brennstoffzellen Technik ZBT GmbH, Duisburg, Germany. The EasyCell Test method [4], developed at Institute of Electrochemistry and Electrical Sources, Bulgarian Academy of Sciences, has been used.

Proton conductivity measurements were performed at 60, 80 and 95 °C and relative humidity (RH) 100% (Tabl. 1). The proton conductivity measurements were carried out on Solartron Analytical 1287 Electrochemical Interface and 1255 Impedance Phase Analyzer (Farnborough, UK), connected to a computer equipped with CoreWareTM, CoreViewTM, ZPlotTM, and ZViewTM (Scribner Associates, Inc.). The membranes studied were adjusted in four electrode cell placed in the conditioning chamber of the EasyTest Cell [4–6].

Membrane preparation

In order to incorporate high concentrations of immobilized sulfonic acid groups (–SO_3H) in the p-PBI matrix, a method involving simultaneous polymerization/cross-linking of sodium vinyl sulfonate (VSA-Na) in the p-PBI matrix was applied. After acidification, semi-interpenetrating networks p-PBI, containing cross-linked polyvinyl sulfonic acid (further denoted as **PBI-sipn-PVSA**) are obtained as shown in Figure 1.

The procedure for preparation of p-PBI membranes, containing cross-linked PVSA includes the following simple steps (Fig. 2):

Step 1. *Preparation of "starting membrane":*
2.0 wt.% solution of p-PBI in polyphosphoric acid (PPA) was used for casting of the starting membranes. The inherent viscosity of p-PBI used is 3.6 dL/g. It was determined at polymer concentration of 0.2 g/dL in concentrated sulfuric acid (96%) at 30 °C, using an Ubbelohde viscometer.

Using a casting knife (gap 0.6 mm) a membrane was cast on a glass substrate and kept in air for several hours (start of the sol-gel process - hydrolysis of PPA to H_3PO_4).

Step 2. *Preparation of porous p-PBI films, filled with water.*
The membrane was then immersed in a water bath – further hydrolysis of PPA to H_3PO_4 and removal of the acid from the membrane takes place. After abundant washing with water, rests of H_3PO_4
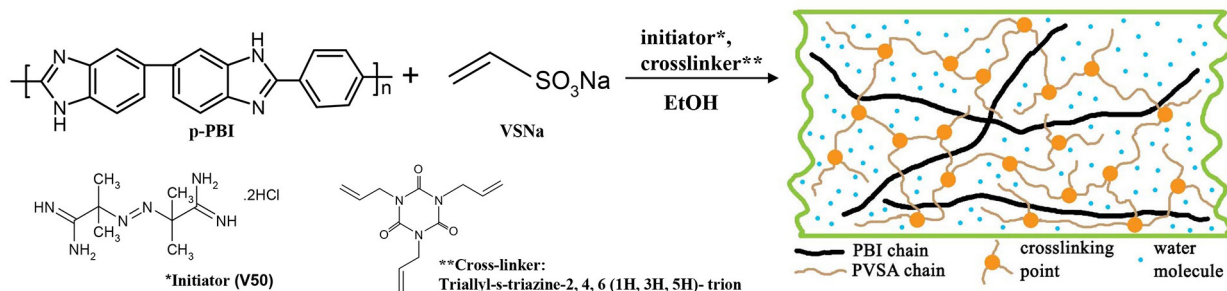
Fig. 1. Preparation of semi-interpenetrating network p-PBI-sipn-PVSA.

```
┌──────────────┐   Washing       ┌──────────────┐   Exchange
│  p-PBI/PA    │  with water     │ Porous p-PBI │
│  membrane    │ ──────────────▶ │ filled with  │   VSNa, Initiator,
└──────────────┘                 │    water     │   Cross-linker
                                 └──────────────┘
                                                   ┌──────────────────┐
                                                   │ p-PBI containing │
                                                   │  VSNa, initiator │
                                                   │ and cross-linker │
                                                   └──────────────────┘
┌──────────────┐                 ┌──────────────┐
│ p-PBI membrane,│  5% HCl       │ p-PBI membrane,│  UV irradiation, Δ
│  containing  │ ◀────────────── │  containing  │
│ cross-linked PVSA│  Water      │ cross-linked PVSNa│ Polymerization/
└──────────────┘                 └──────────────┘   Cross-linking
```
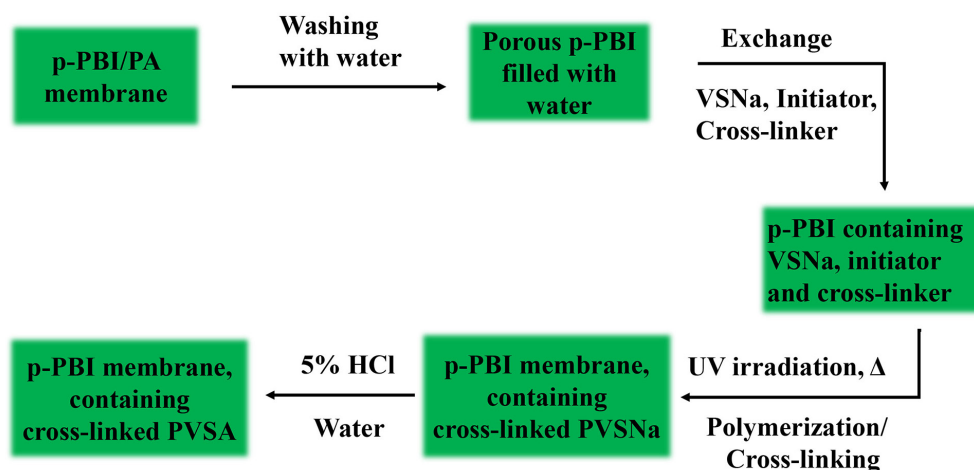
Fig. 2. Procedure for preparation of p-PBI-sipn-PVSA membranes.

were removed with 5 wt.% aqueous NH_3, followed by washing in deionized water. In this way porous p-PBI film, filled with water, is obtained. It contains only 14 wt. % PBI, the rest is water.

Step 3. *Exchanging water with VSA-sodium salt (VSA-Na).*

The membrane obtained in step 2 was transferred into a bath, containing EtOH, 25% aqueous solution of VSA-Na, cross-linker (triallyl-s-triazine-2,4,6 (1H, 3H, 5H)-trion, 2-5 wt.%) and initiator (V 50 – 2, 2′-azobis(2-methylpropionamidine) dihydrochloride, 1–2 wt.%). Exchange of water was completed in about 3 hours at room temperature (RT) in the dark.

Step 4. *Polymerization/ cross-linking of VSA-Na in the PBI matrix, induced thermally or by UV irradiation.*

Simultaneous polymerization/cross-linking of VSA-Na in the p-PBI matrix: The film prepared in Step 3 was irradiated with UV light (up to 4 h) or heated in a furnace (80 °C) for up to 96 h.

Step 5. *Acidification – transformation of PVSA-Na to PVSA.*

The film from step 4 was washed with water (removal of non-crosslinked PVSA), then in with 5% HCl and deionized water. The result is transformation of the $-SO_3Na$ group to $-SO_3H$. Using this procedure membranes of very good quality (smooth, flexible, no defects) were obtained.

For the determination of the amount cross-linked PVSA in the membrane (sulfonic acid groups per PBI repeat unit), two methods have been used:

Method 1: Gravimetrical method: a piece of the porous membrane filled with water was weighted

and dried to constant weight. The difference gives the weight of PBI in the wet membrane (14 wt.%). The same procedure is performed with the final membrane, containing water insoluble $-SO_3H$ groups. From the difference of the weights (dry PBI containing cross linked PVSA and dry PBI in the wet membrane) the amount of $-SO_3H$ groups in the membrane can be calculated.

Method 2: From ^1H NMR: the amount of $-SO_3H$ groups in the membrane can be calculated from the ratio $-CH_2-CH$ protons/aromatic PBI protons.

The values, obtained by both methods are very close. For the membrane M_{UV4} the ratio VSA groups per PBI repeating unit, determined gravimetrically is 4.6, while the value obtained from ^1H NMR analysis was 4.4.

The method used offers vast opportunities for varying different parameters during membrane preparation – in the third step: composition of bath (concentration of VSA-Na, initiator, cross-linker and co-solvent in the bath), temperature and duration of treatment; in the fourth step: intensity and duration of the UV irradiation, temperature and duration of the thermal treatment.

RESULTS AND DISCUSSION

Using the procedure, schematically shown in Figure 2, two series of p-PBI-sipn-PVSA membranes were we prepared:

Series 1: 4 samples (M_{T1}, M_{T2}, M_{T3}, M_{T4}) p-PBI-sipn-PVSA membranes, obtained after thermal treatment – duration 24, 48, 72 and 96 h.

Series 2: 4 samples (M_{UV1}, M_{UV2}, M_{UV3}, M_{UV4}) p-PB-sipn-PVSA membranes, obtained after UV irradiation – duration 1, 2, 3 and 4 h.

The best results (highest proton conductivity) were obtained for the last two samples of each series (i.e. M_{T3}, M_{T4}, M_{UV3}, M_{UV4}), presented in Table l. The other four samples showed much lower proton conductivity, obviously due to lower contents of immobilized $-SO_3H$ groups.

The ^1H NMR spectrum of M_{uv4} (the membrane with highest proton conductivity) is presented in Fig. 3. The peaks for the aromatic protons from the benzimidazole rings (10 protons) appear in the region 7.00–8.00 ppm. The peaks of the aliphatic protons (-CH$_2$-CH-) from VSA (13.2 protons) are observed between 1ppm and 3.5 ppm. As one VSA group has 3 protons, 13.2 protons correspond to 4.4 VSA groups. In this way the membrane contains to 4.4 VSA groups per PBI unit (10 H). This result is very close to the gravimetrically determined value (4.6 VSA groups per PBI unit, Table 1).

The FT-IR spectrum (Fig. 4) of pristine p-PBI showed sharp band around 3435 cm^{-1}, which is

Table 1. Proton conductivity measurements of the best PBI-sipn-PVSA membranes

Membrane p-PBI/cr-PVSA	Method of polymerization/ cross-linking	VSA units per PBI unit	Proton conductivity σ, mS.cm^{-1}		
			60 °C	80 °C	95 °C
M_{T3}	Thermal treatment, 80 °C, 72 h	3.0	25.0	29.2	31.5
M_{T4}	Thermal treatment, 80 °C, 96 h	3.6	28.0	38.2	45.2
M_{UV3}	UV irradiation, 3 h	3.7	29.1	37.3	42.2
M_{UV4}	UV irradiation, 4 h	4.6	51.3	55.3	63.2
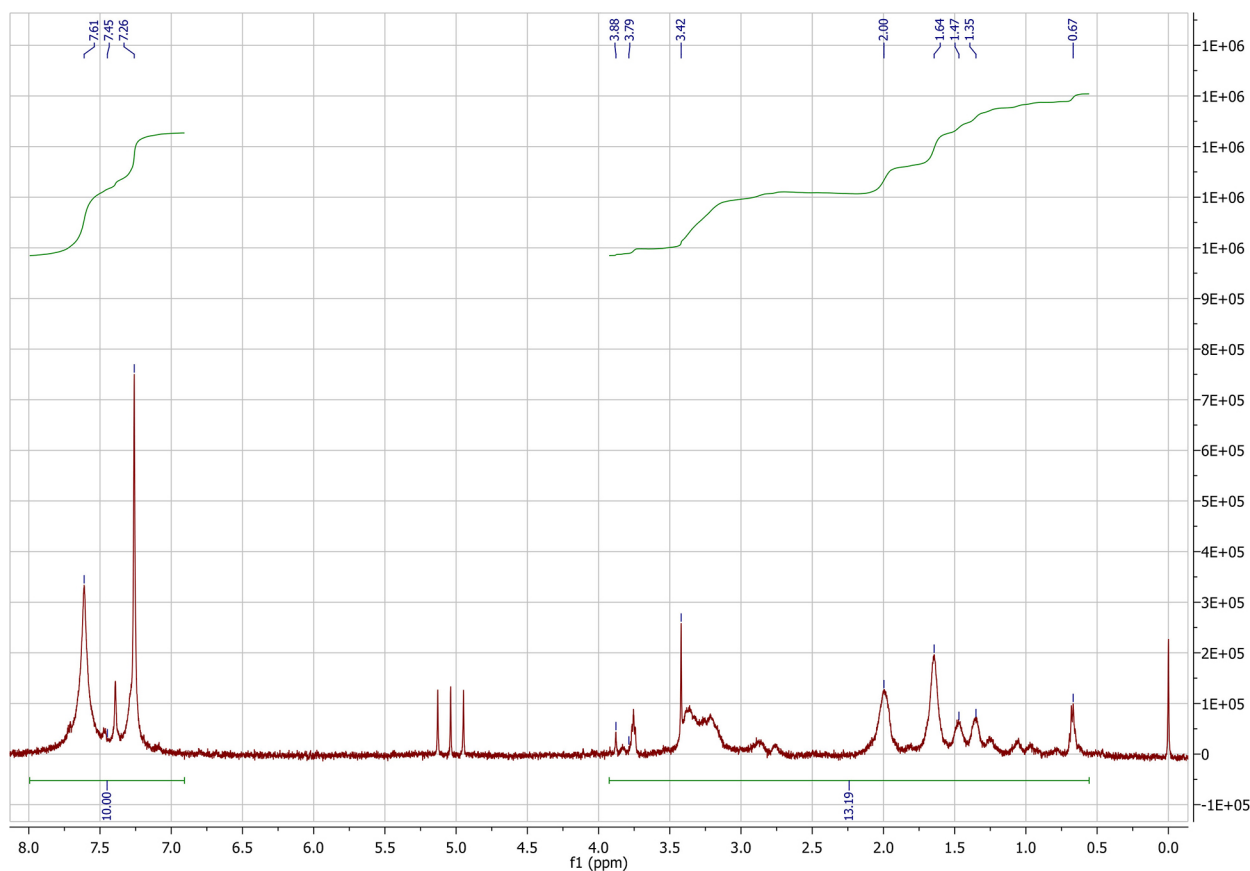
Fig. 3. ^1H NMR spectrum of p-PBI-sipn-PVSA membrane (M_{uv4}).
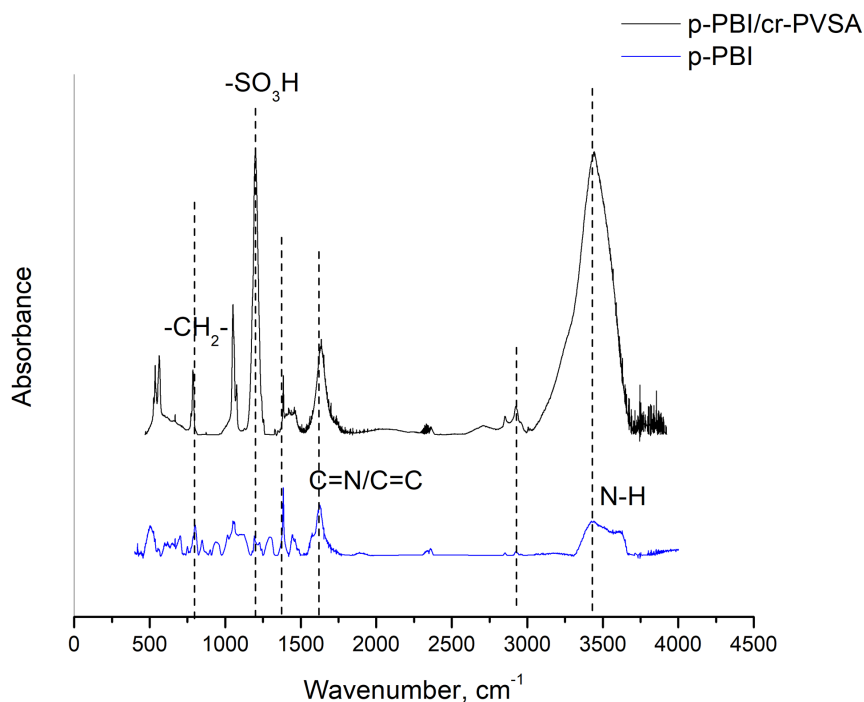
Fig. 4. FT-IR spectra of pristine p-PBI and p-PBI containing PVSA.

attributed to the stretching vibrations of isolated N—H bonds in the imidazole ring. The absorptions in a region of 1630–1500 cm^{-1} are attributed to the vibration of C=C and C=N. The strong band at 1388 cm^{-1} has to be attributed to the in plane deformation of the benzimidazole rings [7–10].

In the FT-IR spectrum of p-PBI-sipn-PVSA (Fig. 4), despite of the bands, characteristic for the p-PBI rings, a medium band at 796 cm^{-1} due to the polymeric methylene group (-CH$_2$-) is clearly visible. The intense peak at 1200 cm^{-1} originates from the sulfonic acid group. The band at 1373 cm^{-1} is assigned to CH$_2$ bond deformation. The band at 2926 cm^{-1} is due to CH$_2$ stretching vibration. Stretching vibration of -OH group of water molecule is a broad band and observed at about 3442 cm^{-1} [10].

As already mentioned, two types of p-PBI-sipn-PVSA membranes were prepared: thermally treated and UV-irradiated. In the PEM FC sulfonated membranes are usually operated at temperatures up to 80 °C and high relative humidity (up to 100%). The thermal stability of the membranes was studied by TGA in the range 30–300 °C (Fig. 5). It can be seen that up to 100 °C the weight loss is only 1–2.5% (Fig. 5). Further loss of water is observed up to 150 °C. Up to 300 °C the weight loss could be attributed to anhydride formation from the sulfonic acid groups. The curves for both materials are almost identical, the difference being only 1–2% in the whole range.

In our opinion for polymerization/cross-linking of VPA-Na in the p-PBI matrix better results were achieve by UV irradiation. Depending on irradiation time up to 75% of the VSA-Na in the film can be cross-liked for 4h. Similar result could be obtained heating at 80 °C for 3–4 days. In both cases films of very good quality (smooth, flexible, no defects) were prepared.

For the best samples very good proton conductivity was obtained. The contents of VSA groups is in the range 3 to 4.6 –SO$_3$H groups per PBI unit. The membrane with highest –SO$_3$H contents showed the best conductivity – 63.2 mS.cm^{-1} at 95 °C and 100% RH (Table 1). Sulfonated Nafion®-type membranes exhibit proton conductivity in the range 85–100 mS.cm^{-1} [11]. The conductivity of phosphoric acid acid-doped sulfonated polysulfones and their blends with polybenzimidazole is 10 mS.cm^{-1} at a very low acid-doping level [12].

CONCLUSION

Using an original method for polymerization/crosslinking of VSA in a p-PBI matrix two series of membranes with high contents of immobilized sulfonic acid groups have been prepared by thermal treatment and UV-irradiation of a p-PBI film, containing VSA-Na salt, cross-linker and initiator. For the best samples the concentration of –SO$_3$H groups

TGA	M$_{UV}$	M$_T$
Weight loss at 100 °C, %	1	2.5
Weight loss at 200 °C, %	4	6
Weight loss at 300 °C, %	10	11
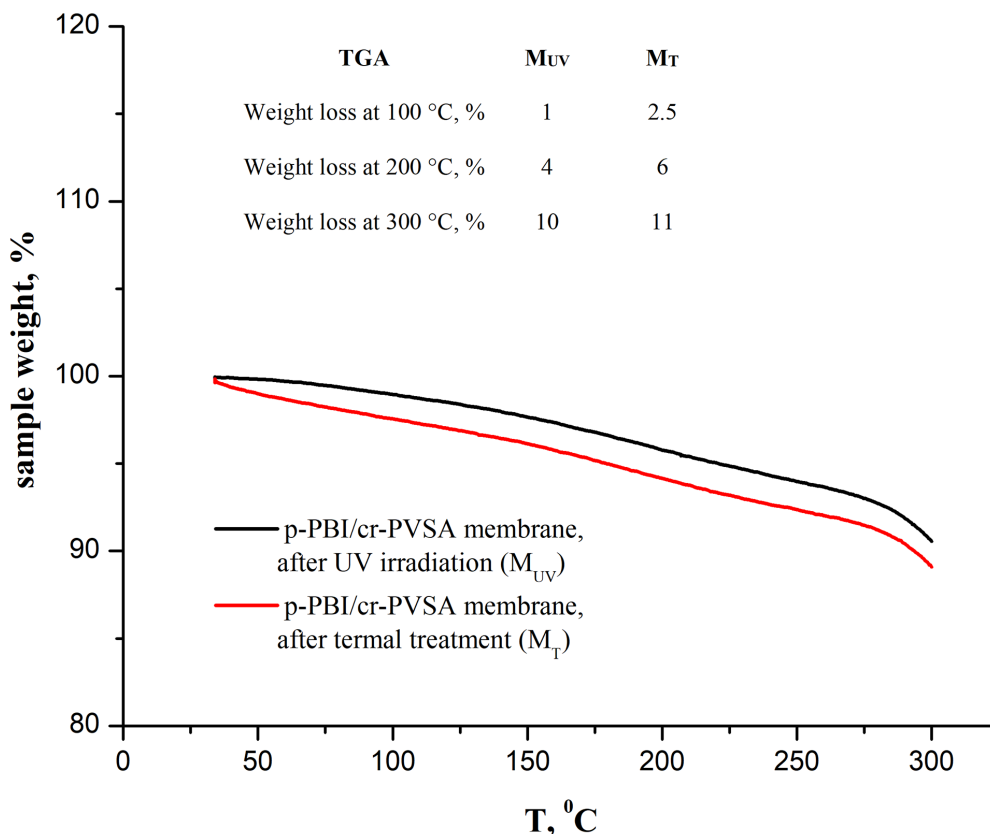
Fig. 5. TGA of PBI-sipn-PVSA membranes, obtained by UV irradiation and thermal treatment.

is 3–4.6 per PBI unit. At 60–95 °C and 100% RH the PBI-sipn-PVSA membranes show proton conductivity close to that of Nafion®-type membranes. Sulfonated Nafion®-type membranes usually exhibit σ = 85–100 mS.cm^{-1}, while our best membrane showed proton conductivity 63.2 mS.cm^{-1}. The results showed that UV irradiation is superior to the thermal treatment as a method for obtaining semi-interpenetrating networks p-PBI-sipn-PVSA. These membranes can be regarded as cheap alternative to the very expensive Nafion type membranes.

REFERENCES

1. L. Gubler, D. Kramer, J. Belack, Ö. Ünsal, T. Schmidt, G. Scherera, *J. Electrochem. Soc.*, **154**, 981 (2007).
2. V. Sinigersky, D. Budurova, H. Penchev, I. Radev, F. Ublekov, *J. Appl. Polymer Science*, **129** (3), 1223 (2013).
3. V. Sinigersky, H. Penchev, F. Ublekov, M. Staneva, D. Budurova, I. Radev, V. Peinecke, in: Proceedings of EFC2013, Fifth European Fuel Cell Technology & Applications Conference – Piero Lunghi Conference, December 11–13, Rome, Italy, 2013, p. 61
4. I. Radev, E. Slavcheva, E. Budevski, U. Schnakenberg, *Electrochim. Acta*, **54**, 1269 (2009).
5. I. Radev, G. Topalov, E. Slavcheva, E. Lefterova, G. Tsotridis, U. Schnakenberg, *Int. J. Hydrogen Energy*, **35**, 2428 (2010).
6. I. Radev, G. Georgiev, V. Sinigersky, E. Slavcheva, *Int. J. Hydrogen Energy*, **33**, 4849 (2008).
7. H. Rong-huan, S. Bao-ying, Y. Jing-shuai, C. Quantong, *Chem. Res. Chinese Universities*, **25** (4), 585 (2009).
8. C. Tosun, H. Gercel, *Int. J. of Adv. in Sci., Eng. and Tech.*, **4** (1), 150 (2016).
9. K. Hwang, J-H. Kim, S.-Y. Kim, H. Byun, *Energies*, **7**, 1721 (2014).
10. S. Ekbote, K. Deshmukh, Z. Qureshi and B. Bhanage, *Green Chemistry Letters and Reviews*, **4** (2), 177 (2011).
11. M. Hickner, H. Ghassemi, Y. Kim, B. Einsla, J. McGrath, *Chem. Rev.*, **104**, 4587 (2004).
12. C. Hasiotis, L. Qingfeng, V. Deimede, J. Kallitsis, C. Kontoyannis, N. Bjerrum, *J. Electrochem. Soc.*, **148** (5), A513 (2001).

ПРОТОН-ПРОВОДЯЩИ МЕМБРАНИ, СЪДЪРЖАЩИ ОМРЕЖЕНА ПОЛИВИНИЛСУЛФОНОВА КИСЕЛИНА, ИЗПОЛЗВАНИ КАТО ПОЛИМЕРЕЛЕКТРОЛИТНИ МЕМБРАНИ ЗА ГОРИВНИ КЛЕТКИ

М. Станева[1], И. Радев[2], Ф. Ублеков[1], Д. Будурова[1],
В. Синигерски[1], Х. Пенчев[1]

[1] *Институт по полимери – БАН, 1113 София*
[2] *Zentrum für Brennstoffzellen Technik, ZBT GmbH, Duisburg, Germany*

(Резюме)

Тук представяме нов подход за имобилизиране на протондонорни сулфо-групи в полимерната матрица. Разработена е лесна и ефикасна процедура за изготвяне на полу-проникващи мрежи от пара-полибензими-дазол (п-ПБИ), съдържащ омрежена поливинилсулфонова киселина (омр-ПВСК). Тя е описана в 5 лесни стъпки. Прилагайки описаната по-горе процедура, изготвихме две серии мембрани, съдържащи водоне-разтворими групи на винилсулфоновата киселина във вискоки концентрации. Най-високата стойност на протонната проводимост, измерена за така получените мембрани е 63.2 mS.cm^{-1} (T = 95 °C, относителна влажност 100%).

Effect of synthesis conditions on the photocatalytic efficiency of NiMnO₃/Mn₂O₃, NiMn₂O₄/NiMnO₃/Mn₂O₃ and Ni₆MnO₈/NiMnO₃/Mn₂O₃ for the degradation of Malachite Green dye under UV-light

K. L. Zaharieva[1]*, K. I. Milenova[1], S. S. Dimova[2], S. V. Vassilev[3], I. D. Stambolova[4], V. N. Blaskov[4]

[1] *Institute of Catalysis, Bulgarian Academy of Sciences, "Acad. G. Bonchev" St., Bl. 11, 1113 Sofia, Bulgaria*
[2] *Institute of Polymers, Bulgarian Academy of Sciences, "Acad. G. Bonchev" St., Bl.103A, 1113 Sofia, Bulgaria*
[3] *Institute of Electrochemistry and Energy Systems, Bulgarian Academy of Sciences, "Acad. G. Bonchev" St., Bl. 10, 1113, Sofia, Bulgaria*
[4] *Institute of General and Inorganic Chemistry, Bulgarian Academy of Sciences, "Acad. G. Bonchev" St., Bl. 11, 1113 Sofia, Bulgaria*

The influence of the type of precursors salts (nitrates or chlorides) and calcination temperatures (450 °C and 650 °C) on the photocatalytic activity of $NiMnO_3/Mn_2O_3$, $NiMn_2O_4/NiMnO_3/Mn_2O_3$ and $Ni_6MnO_8/NiMnO_3/Mn_2O_3$ prepared by precipitation was investigated in this study. The synthesized samples were characterized using the Powder X-ray diffraction analysis and Fourier-transform infrared spectroscopy. The photocatalytic efficiency of obtained materials was tested in the reaction of oxidative degradation of Malachite Green dye as model contaminant from aqueous solution under UV illumination. The results established that the degree of degradation of Malachite Green dye after 120 minutes increases in the following order: $NiMnO_3/Mn_2O_3$, 450°C, chlorides (83%) < $NiMn_2O_4/NiMnO_3/Mn_2O_3$, 650 °C, chlorides (86%) < $NiMnO_3/Mn_2O_3$, 450 °C, nitrates (91%) < $Ni_6MnO_8/NiMnO_3/Mn_2O_3$, 650 °C, nitrates (97%). The photocatalyst prepared at the higher calcination temperature (650 °C) using nitrate precursors demonstrates the highest photocatalytic efficiency.

Keywords: photocatalyst, photocatalytic efficiency, Malachite Green.

INTRODUCTION

The cotton, paper, pulp, leather, wool industries uses many toxic dyes for coloring their final products. The water discharged effluents of these manufactures containing large amount of organic contaminants, leads to pollution of environment. Malachite green dye is cationic dye, which is widely used all over the world in the textile industry as well as in the fish farming industry as fungicide, ectoparasiticide and disinfectant [1–4]. The existence of pigments and dyes in water causes serious damage to the aquatic environment. The color blocks the sunlight access to aquatic flora and fauna, and it decreases the photosynthetic action within the ecosystem [5]. Heterogeneous photocatalysis is a discipline, which includes a large diversity of reactions:

water detoxification, dehydrogenation, mild or total oxidations, hydrogen transfer, O_2^{18}–O_2^{16} and deuterium-alkane isotopic exchange, metal deposition, gaseous pollutant removal, etc. [6, 7]. Photocatalytic degradation of organic contaminants in water by single metal oxides and oxide compounds has attracted the attention of researchers [8]. T. Larbi et al. have investigated photocatalytic degradation of Methylene blue dye by Mn_3O_4, $NiMn_2O_4$ and alloys of Ni-Manganates thin films [9]. $NiO_{0.8}ZnO_{0.2}/ZnO$ and $NiMnO_3/Mn_2O_3$ materials were tested as photocatalysts for degradation of Malachite Green dye under UV-light [10]. Xiaobo He et al. have been synthesized $NiMnO_3/NiMn_2O_4$ oxides with the aid of pollen using a two-step annealing method [11]. Spinel nickel manganese oxide with large specific surface area and suitable pore size has been synthesized from an epoxide-driven sol–gel process and followed by thermal treatment [12]. K. Vijaya Sankar et al. have been obtained sub-micron sized polyhedral shaped $NiMn_2O_4$ particles by a gly-

cine assisted solution combustion method [13]. Murdochite-type Ni_6MnO_8 with variable specific surface areas has been synthesized by H. Taguchi et al. [14].

The goal of the current work is to study the influence of different precursors (nitrates and chlorides) and calcination temperatures (450 °C and 650 °C) on the photocatalytic properties of $NiMnO_3/Mn_2O_3$, $NiMn_2O_4/NiMnO_3/Mn_2O_3$ and $Ni_6MnO_8/NiMnO_3/Mn_2O_3$ materials about degradation of aqueous solution of Malachite Green dye as a model contaminant under UV-light. The tested samples prepared by precipitation and thermally treatment were investigated by Powder X-ray diffraction analysis and Fourier-transform infrared spectroscopy.

EXPERIMENTAL

Preparation and investigation

The tested photocatalysts $NiMnO_3/Mn_2O_3$, $Ni_6MnO_8/NiMnO_3/Mn_2O_3$ and $NiMn_2O_4/NiMnO_3/Mn_2O_3$ were synthesized by precipitation using 0.25M $Ni(NO_3)_2.6H_2O$ (VWR Prolabo BDH chemicals); 0.25M $Mn(NO_3)_2.4H_2O$ (Alfa Aesar); 0.75M $NaHCO_3$ (Valerus Co.) or 0.25M $NiCl_2.6H_2O$ (Valerus Co.); 0.25M $MnCl_2.4H_2O$ (Valerus Co.); 0.75M NaOH (Valerus Co.) aqueous solutions. The precipitant $NaHCO_3$ and NaOH were added dropwise to the mixtures of nitrates or chlorides and at continuous stirring until reaching pH 7 and 12, respectively. The suspension was stirred for one hour after precipitation. The precipitates were filtered and washed with distilled water several times. The obtained precipitates were dried at 35 °C and thermally treated at 450 °C or 650 °C for 3 hours and 30 minutes in air media. The samples obtained by nitrates and calcined at 450 °C and 650 °C were assigned as **MN1** and **MN2** and materials prepared using chlorides and thermally treated at 450 °C and 650 °C – **MC3** and **MC4**.

The Powder X-ray diffraction patterns of the obtained materials were carried out on Philips PW 1050 with Cu K_α-radiation. The presence of the phases in the prepared materials was determined by the ICDD database. The FT-IR investigations were performed on a Fourier infrared spectrometer Bruker-Vector 22 in the region 400–4000 cm⁻¹ and using KBr tablets.

Photocatalytic tests

The photocatalytic activity of $NiMnO_3/Mn_2O_3$, $NiMn_2O_4/NiMnO_3/Mn_2O_3$ and $Ni_6MnO_8/NiMnO_3/Mn_2O_3$ for the oxidative degradation of 5 ppm aqueous solution of Malachite Green dye was investigat-

ed. The photocatalytic test was performed as 0.15 g catalyst sample and 150 ml of dye solution were put in a semi-batch reactor under constant stirring, air flowing at room temperature. The first experiment was performed in the dark in a period of 30 minutes to achieve adsorption-desorption equilibrium. Second UV lamp with power 18 W and λ_{max} 365 nm was turned on and irradiation was carried out for 120 min. To separate the powder from the liquid phase, centrifugation of the samples was performed for a period of 10 minutes. Spectrophotometrically were measured absorption peaks of MG dye – with maximum wavelength at 615 nm using UV-1600PC Spectrophotometer. The degree of degradation of Malachite Green dye was established using dependence:

$$Degradation = \frac{(C_0 - C)}{C_0} 100\%$$

where C_0 and C were initial concentration before turning on the illumination and residual concentration of the dye solution after illumination for selected time interval.

RESULTS AND DISCUSSION

The Powder X-ray diffraction results (see Figures 1 and 2) show that material prepared using nitrate precursors and thermally treatment at 450 °C contains $NiMnO_3$ (PDF-653695); Mn_2O_3 (PDF-721427) and three phases – $NiMnO_3$ (PDF-895878); Mn_2O_3 (PDF-651798); Ni_6MnO_8 (PDF-894619) are established in the sample calcined at 650 °C. The existence of $NiMnO_3$ (PDF-653695) and Mn_2O_3 (PDF-721427) are registered in the PXRD pattern of material synthesized using chlorides as starting materials after thermally treatment at 450 °C. The $NiMnO_3$ (PDF-895878); Mn_2O_3 (PDF-651798) and $NiMn_2O_4$ (PDF-894619) phases are determined in the Powder X-ray diffractogram of sample thermally treated at 650 °C.

FT-IR spectra of prepared materials are shown in the Figure 3. The absorption peaks at around 3440–3442 cm⁻¹ and 1631–1636 cm⁻¹ are attributed to the stretching and bending mode of the OH group of absorbed water molecules [15, 16]. It is known that in the region of 400–1000 cm⁻¹, the characteristic bands of inorganic solids are usually assigned to the vibration of metallic ions in the crystal lattice [17]. The peaks at about 1195–1198 cm⁻¹ and 1051–1058 cm⁻¹ could be assigned of some impurities in the investigated materials.

Photocatalytic degradation of Malachite Green (MG) dye on $NiMnO_3/Mn_2O_3$, $NiMn_2O_4/NiMnO_3/Mn_2O_3$ and $Ni_6MnO_8/NiMnO_3/Mn_2O_3$ samples was
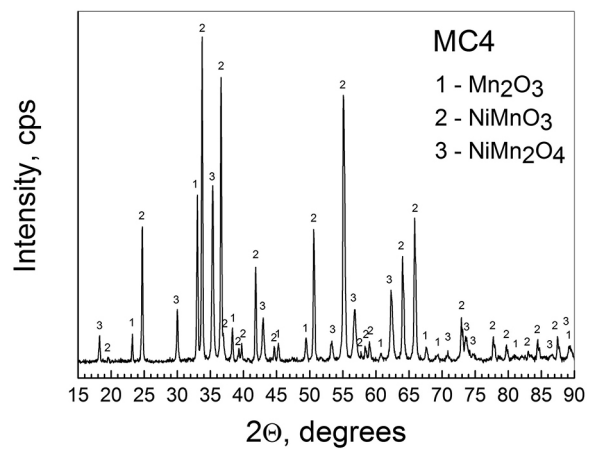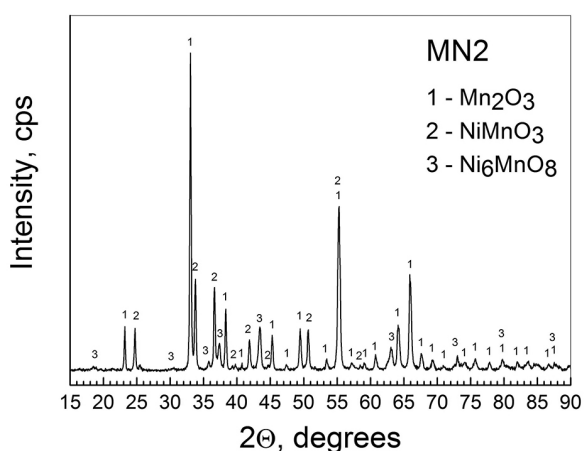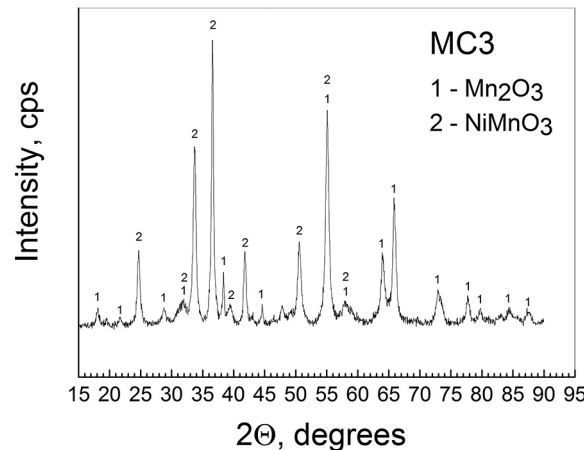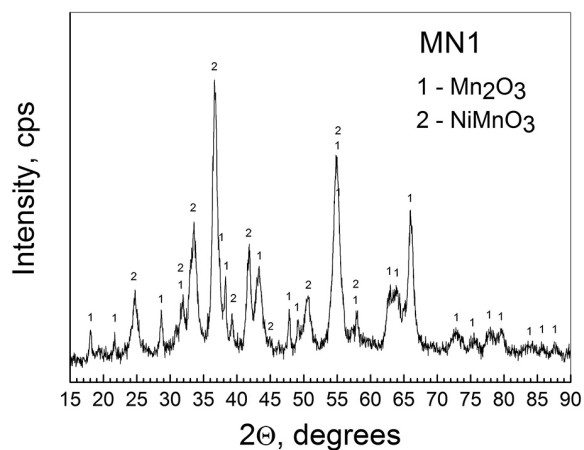
Fig. 1. PXRD patterns of NiMnO$_3$/Mn$_2$O$_3$ and Ni$_6$MnO$_8$/NiMnO$_3$/Mn$_2$O$_3$ materials prepared using nitrate precursors.

Fig. 2. PXRD patterns of NiMnO$_3$/Mn$_2$O$_3$ and NiMn$_2$O$_4$/NiMnO$_3$/Mn$_2$O$_3$ samples prepared using chloride precursors.

investigated under UV-light irradiation. Attention is paid to the influence of different calcination temperatures (450 °C and 650 °C) and precursors (chlorides and nitrates) on the photocatalytic properties of **MN1**, **MN2**, **MC3** and **MC4**. Table 1 shows the data for adsorption capacities and apparent rate constants of the studied materials.

The following formula is used for calculation of the adsorption capacities:

$$Q = \frac{(C_0 - C).V}{m}$$

where C$_0$ and C are the initial and after 30 minutes in the dark concentrations of the dye, V is the volume of the solution and m is the weight of the samples.

The adsorption capacities in ascending order were: **MC3** (0.004 mg/g) < **MN1** (0.041 mg/g) < **MC4** (0.051 mg/g) < **MN2** (0.060 mg/g).

Table 1. Calculated adsorption capacities and apparent rate constants (k) of tested photocatalysts

Sample	Adsorption capacity, mg/g	k (x10^{-3} min^{-1})
MC3	0.004	14.0
MC4	0.051	5.5
MN1	0.041	14.9
MN2	0.060	12.9

In Table 1 the apparent rate constants of investigated materials were defined as pseudo first-order kinetics by logarithmic linear dependence:

$$-\ln\left(\frac{C}{C_0}\right) = k.t \; .$$
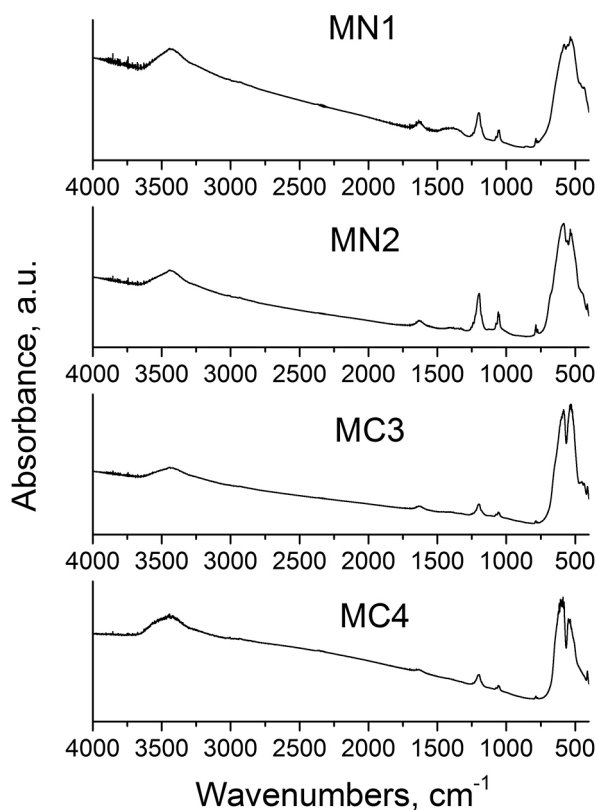
Fig. 3. FT-IR spectra of synthesized materials – **MN1**; **MN2**; **MC3** and **MC4**.
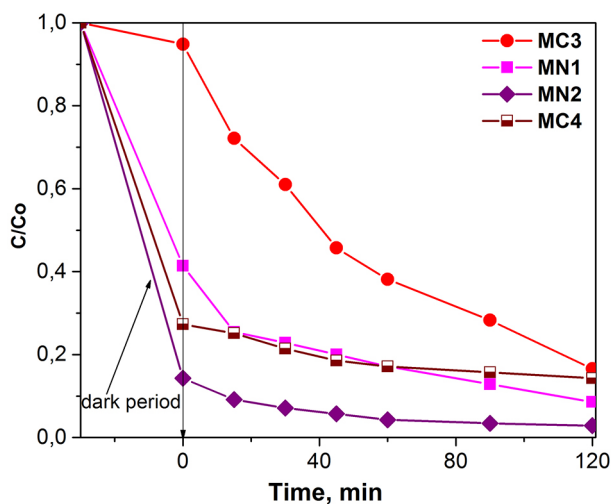
Fig. 4. The concentration ratio C/C$_0$ of Malachite Green dye as a function of the time of UV illumination.

The lowest value of apparent rate constants was for sample **MC4** (5.5 ×10^{-3} min^{-1}) until the highest one was **MN1**, which reached 14.9 ×10^{-3} min^{-1}.

On the Figure 4 are presented the concentration changes C/C$_0$ of degradation of Malachite Green dye as a function of the time of UV irradiation. The
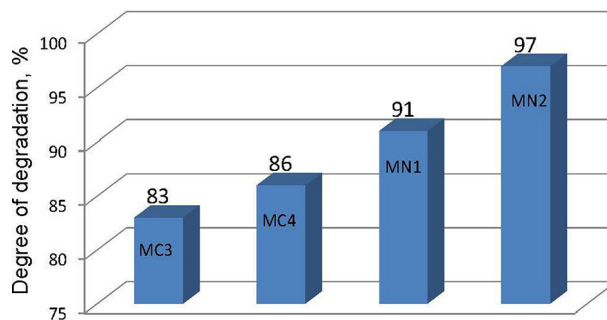
Fig. 5. Degree of degradation of Malachite Green dye after 120 minutes under UV irradiation using prepared photocatalysts – **MN1**; **MN2**; **MC3** and **MC4**.

degree of degradation of Malachite Green dye after 120 minutes UV illumination was showed on Figure 5. Samples **MN1** (91%) and **MN2** (97%) have the best catalytic performance, whereas the degradation degree of **MC3** (83%) and **MC4** (86%) were lower. The obtained data showed that the used precursor affects the catalytic activity, like the samples from nitrate precursors gave maximum results. The different calcination temperatures have influence on the photocatalytic behavior of the systems under investigation. With increasing of the temperature to 650 °C, the degree of degradation of the dye increases for the samples obtained by both types of precursors.

The authors in [18] reported that the excellent catalytic activity of NiMnO$_3$ can be attributed to the composite effect of nickel and manganese oxides for the process of visible light-driven water oxidation. NiMn$_2$O$_4$ nanoparticles demonstrated high photocatalytic activity for degradation of Methyl Orange under UV light, due to the proper size distribution of the pores, high hydroxyl amount and high separation rate of charge carriers [19]. The enhancement of oxygen adsorption leading to more available sites for photocatalytic reaction is the reason for the high photocatalytic reactivity of NiMn$_2$O$_4$ films [9]. Other research groups have explained the photocatalytic activity of Mn$_2$O$_3$ towards degradation of Methylene Blue with the d-d transitions involving Mn$^{2+/4+}$ ions on the photocatalyst surface [20, 21]. It could be supposed that all these factors play role in the enhanced photocatalytic acitivity of investigated nickelum-manganite composite powders in the present study.

CONCLUSIONS

Effect of synthesis conditions on the photocatalytic ability of NiMnO$_3$/Mn$_2$O$_3$, NiMn$_2$O$_4$/NiMnO$_3$/

Mn$_2$O$_3$ and Ni$_6$MnO$_8$/NiMnO$_3$/Mn$_2$O$_3$ about degradation of aqueous solution of Malachite Green dye under UV-light was established in the present study. The photocatalysts prepared using nitrate precursors demonstrate a higher photocatalytic efficiency in comparison with that of the samples synthesized using chlorides. The Ni$_6$MnO$_8$/NiMnO$_3$/Mn$_2$O$_3$ material obtained from nitrate precursors at higher temperature of thermal treatment (650 °C) exhibits the highest degree of degradation of Malachite Green dye (97%).

REFERENCES

1. N. Gupta, A. K. Kushwaha, M. C. Chattopadhyaya, *Arabian Journal of Chemistry*, **9**, S707 (2016).
2. A. Mittal, *Journal of Hazardous Materials B*, **133**, 196 (2006).
3. S. Chowdhury, R. Mishra, P. Saha, P. Kushwaha, *Desalination*, **265**, 159 (2011).
4. S. Sarmah, A. Kumar, *Indian J. Phys.* **85**, 713 (2011).
5. A. G. S. Prado, L. L. Costa, *Journal of Hazardous Materials*, **169**, 297 (2009).
6. Jean-Marie Herrmann, *Catalysis Today*, **53**, 115 (1999).
7. M. I. Litter, *Applied Catalysis B: Environmental*, **23** 89 (1999).
8. M. K. Seery, R. George, P. Floris, S. C. Pillai, *Journal of Photochemistry and Photobiology A: Chemistry*, **189**, 258 (2007).
9. T. Larbi, L. Ben Said, A. Ben Daly, B. Ouni, A. Labidi, M. Amlouk, *Journal of Alloys and Compounds,* **686**, 168 (2016).
10. K. Zaharieva, K. Milenova, S. Vassilev, S. Dimova, I. Stambolova, V. Blaskov, *Bulgarian Chemical Communications*, **49**, Special Issue D, 30 (2017).
11. Xiaobo He, Fengxiang Yin, Yanhui Li, Hao Wang, Jinnan Chen, Yanhong Wang, Biaohua Chen, ACS Appl. Mater. Interfaces, **8** (40), 26740 (2016).
12. Miao Zhang, Shaohua Guo, Lu Zheng, Gaini Zhang, Zhenping Hao, Liping Kang, Zong-Huai Liu, *Electrochimica Acta*, **87**, 546 (2013).
13. K. Vijaya Sankar, S. Surendran, K. Pandi, A. M. Allin, V. D. Nithya, Y. S. Lee, R. Kalai Selvan, *RSC Adv.*, **5**, 27649 (2015).
14. H. Taguchi, S. Tahara, M. Okumura, K. Hirota, *Journal of Solid State Chemistry*, **215**, 300 (2014).
15. V. Jokanović, D. Izvonar, M. D. Dramićanin, B. Jokanović, V. Živojinović, D. Marković, B. Dačić, *J Mater Sci: Mater Med*, **17**, 539 (2006).
16. A. Kaniyoor, T. T. Baby, S. Ramaprabhu, *J. Mater. Chem.*, **20**, 8467 (2010).
17. Maha Hadj-Sadok Ouaguenouni, A. Benadda, A. Kiennemann, A. Barama, *C. R. Chimie*, **12**, 740 (2009).
18. D. Hong, Y. Yamada, A. Nomura, S. Fukuzumi, *Phys. Chem. Chem. Phys.*, **15**, 19125, (2013).
19. S. Khademolhoseini, *J Mater Sci: Mater Electron*, **28**, 7899 (2017).
20. M. Pudukudy, Z. Yaakob, *Journal of Nanoparticles*, ID 8037013 (2016).
21. P. Kar, S. Sardar, S. Ghosh, M. R. Parida, B. Liu, O. F. Mohammed, P. Lemmens, S. K. Pal, *J. Mater. Chem. C*, **3**, 8200 (2015).

ВЛИЯНИЕ НА УСЛОВИЯТА ЗА СИНТЕЗ ВЪРХУ ФОТОКАТАЛИТИЧНАТА СПОСОБНОСТ НА $NiMnO_3/Mn_2O_3$, $NiMn_2O_4/NiMnO_3/Mn_2O_3$ И $Ni_6MnO_8/NiMnO_3/Mn_2O_3$ ЗА РАЗГРАЖДАНЕТО НА МАЛАХИТОВО ЗЕЛЕНО БАГРИЛО ПОД УВ-СВЕТЛИНА

К. Л. Захариева[1]*, К. И. Миленова[1], С. С. Димова[2], С. В. Василев[3], И. Д. Стамболова[4], В. Н. Блъсков[4]

[1] *Институт по катализ, Българска академия на науките, ул. „Акад. Г. Бончев“, бл. 11, 1113 София, България*

[2] *Институт по полимери, Българска академия на науките, ул. „Акад. Г. Бончев“, бл. 103А, 1113 София, България*

[3] *Институт по електрохимия и енергийни системи, Българска академия на науките, ул. „Акад. Г. Бончев“, бл. 10, 1113 София, България*

[4] *Институт по обща и неорганична химия, Българска академия на науките, ул. „Акад. Г. Бончев“, бл. 11, 1113 София, България*

(Резюме)

Изследвано е влиянието на типа прекурсори (нитрати или хлориди) и температури на накаляване (450 °С и 650 °С) върху фотокаталитичната активност на $NiMnO_3/Mn_2O_3$, $NiMn_2O_4/NiMnO_3/Mn_2O_3$ и $Ni_6MnO_8/NiMnO_3/Mn_2O_3$, получени чрез утаяване. Синтезираните проби бяха охарактеризирани чрез рентгенодифракционен анализ и инфрачервена спектроскопия с Фурие трансформация. Фотокаталитичната способност на получените материали беше тествана в реакцията на окислително разграждане на Малахитово Зелено багрило като моделен замърсител от воден разтвор под УВ облъчване. Резултатите установиха, че степента на разграждане на Малахитово Зелено багрило след 120 минути нараства в следния ред: $NiMnO_3/Mn_2O_3$, 450 °С, хлориди (83%) < $NiMn_2O_4/NiMnO_3/Mn_2O_3$, 650 °С, хлориди (86%) < $NiMnO_3/Mn_2O_3$, 450 °С, нитрати (91%) < $Ni_6MnO_8/NiMnO_3/Mn_2O_3$, 650 °С, нитрати (97%). Фотокатализаторът, получен при по-висока температура на накаляване (650 °С), използвайки прекурсори нитрати, демонстрира най-висока фотокаталитична способност.

Sulfur and selenium derivatives of suberoyl anilide hydroxamic acid (SAHA) as a plausible HDAC inhibitors: a DFT study of their tautomerism and metal affinity/selectivity

D. Cheshmedzhieva*, N. Toshev, M. Gerova, O. Petrov, T. Dudev*

Faculty of Chemistry and Pharmacy, Sofia University "St. Kliment Ohridski", 1164 Sofia, Bulgaria

Aberrations in histone deacetilase (HDAC) enzymes are associated with wide range of ailments including some types of cancer, inflammation, metabolic and neurological disorders. In a search for new efficient and body-tolerable HDAC inhibitors two analogs of hydroxamic acid drug (SAHA), containing sulfur- and selenium atoms in the carbonyl group of hydroxamic moiety have been investigated. Questions regarding their physico-chemical properties and metal affinity/selectivity have been addressed by employing density functional calculations combined with polarizable continuum model computations. More specifically, the paper answers the following questions: (1) How does the substitution in the hydroxamic group affect its conformational stability and ionization pattern? (2) What are the preferred deprotonation sites of the hydroxamic moiety and its mode of binding to the metal cation? (3) How does the O→S and O→Se exchange in hydroxamic moiety modulate its affinity and selectivity toward essential biogenic metal cations such as Mg^{2+}, Fe^{2+} and Zn^{2+}? The calculations reveal the key factors governing the ligation properties of the hydroxamic moiety and its sulfur and selenium analogs.

Keywords: Histone deacetylase inhibitors, SAHA, Sulphur derivatives, Selenium derivatives, DFT.

INTRODUCTION

There is an increasing evidence that epigenetic changes in gene expression play important role in progression of cancer. One of the important mechanisms of epigenetic regulation of gene expression is the acetylation and deacetilation of histones. This chromatin modification is controlled by two enzymes with opposing functions: histone acetyl transferases (HAT) and histone acetyl deacetylases (HDAC). The aberration in the action of these enzymes can alter the structure and function of chromatin and is associated with a wide range of ailments including some types of cancer [1, 2], inflammation [3], metabolic and neurological disorders [4, 5]. There are 18 HDACs grouped in four classes: Classes I, II and IV are metal (Zn^{2+} or Fe^{2+}) dependent hydrolases [6, 7]. Class III are NAD^+ dependent sirtuins and do not contain metal cation in the active site. Up to now several classes of small-molecule HDAC inhibitors (HDACi) have been recognized [8–11]. They reduce malignancies by blocking the cell cycle and inducing apoptosis [11] Most of these are hydroxamic acid derivatives, represented by suberoylanilide hydroxamic acid (SAHA) and trichostatin A (TSA) (Fig. 1). Their inhibitory effect stems from chelating the metal ion (Zn^{2+} or Fe^{2+}) in the active site of the enzyme and subsequent disruption of the host enzyme activity [8, 12]. Although hydroxamic acids are regarded as potent inhibitors, they generally have some issues associated with their use such as low oral availability, poor in vivo stability, and undesirable side effects [13, 14]. Therefore, the quest for more efficient and body-tolerable HDAC inhibitors is ongoing.

A series of sulfur and selenium-substituted derivatives of some HDAC inhibitors have been synthesized (Fig. 2) and probed for biological activity [15–17]. Thus, SAHA analogs containing α-mercaptoketone and α-thioacetoxyketone have been found to exhibit higher activity toward isolated histone deacetylases [15]. Derivatives of SAHA, containing one or two selenium atoms in different parts of the molecule (Fig. 2) were found to be 2 to 4-fold more selective against melanoma cells than the unmodified SAHA, and able to decrease melanoma tumor development by up to 87% with negligible toxicity [17, 18].

---

* To whom all correspondence should be sent:
E-mail: dvalentinova@gmail.com
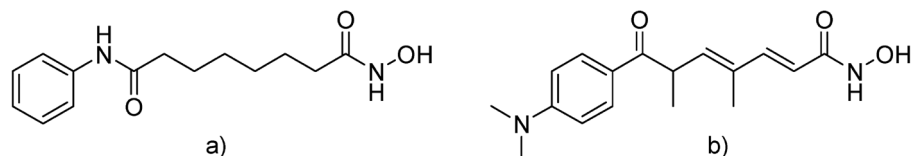
Fig. 1. Structure of a) suberoyl anilide hydroxamic acid (SAHA) and b) trichostatin A (TSA).
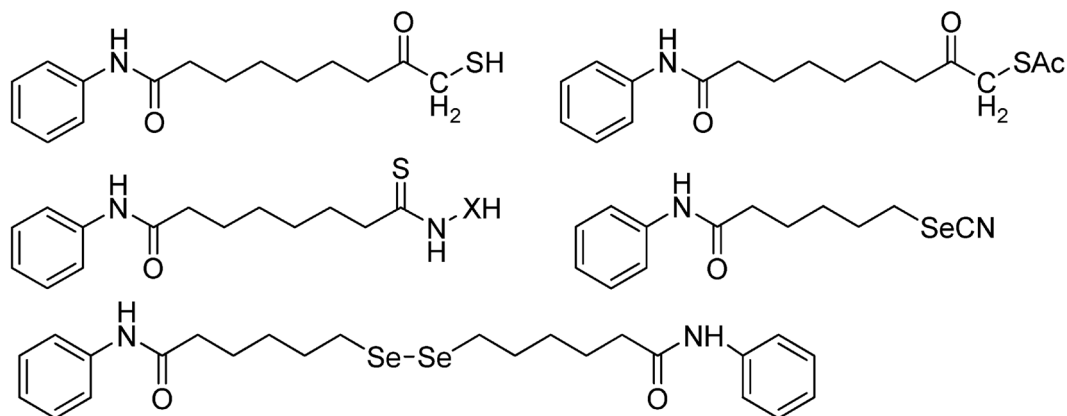
Fig. 2. Structure of sulfur and selenium analogs of SAHA.

Note that derivatives of SAHA where the hydroxamic ligating group –(C=O)−NHOH is modified to –(C=S)−NHOH and –(C=Se)−NHOH, have not been studied (to the best of our knowledge). To determine how incorporation of sulfur and selenium into the metal-binding part of SAHA changes its affinity/selectivity toward biogenic metal cations we modeled and examined the S- and Se-derivatives of the drug by combining density functional theory (DFT) calculations with polarizable continuum model (PCM) computations. In search for novel HDAC inhibitors we studied in detail the geometry and protonation pattern of sulfur- and selenium-containing analogs of SAHA. We investigated how the substitution of carbonyl oxygen in the hydroxamic group with sulfur (carb-S SAHA) and selenium (carb-Se SAHA) would affect its physicochemical and ligating properties as compared to the original unmodified molecule (carb-O SAHA). Several questions were addressed: (1) How does the substitution in the hydroxamic group affect its conformational stability and ionization pattern? (2) What are the preferred deprotonation sites of the hydroxamic moiety and its mode of binding to the metal cation? (3) How does the O→S and O→Se exchange in hydroxamic group modulate its affinity and selectivity toward essential biogenic metal cations such as Mg^{2+}, Fe^{2+} and Zn^{2+}? The calculations reveal the key factors governing the ligation properties of the hydroxamic moiety and its sulfur and selenium analogs.

COMPUTATIONAL METHODOLOGY

Sulfur and selenium carbonyl analogs of SAHA, called for convenience carb-S and carb-Se, were explicitly modeled. All the metal cations under study (Fe^{2+}, Mg^{2+} and Zn^{2+}) are usually hexahydrated in aqueous solution [19, 20]. Hence, their aqua complexes were modeled as $[M(H_2O)_6]^{2+}$ (M = Fe, Mg, Zn). In complexes with organic or protein ligands Mg^{2+} and Fe^{2+} usually retain the six-fold symmetry, whereas Zn^{2+} tend to reduce its coordination number to 4 and form complexes with tetrahedral symmetry [21–24]. Thus, complexes with octahedral symmetry between carb-X (X = O, S or Se) SAHA and Mg^{2+} and Fe^{2+} (high spin; quintuplet) were modeled, while for the complexes with Zn^{2+} tetrahedral symmetry was considered.

All calculations were performed with the Gaussian 09 suite of programs [25]. The B3LYP functional [26–28] in combination with 6-311++G(d,p) [29] basis set was employed in optimizing the structures of the molecules under study and evaluating the respective electronic energies, E_{el}^{ε}, in both the gas

phase ($\varepsilon = 1$) and solution. In the latter case polarizable continuum model (PCM) calculations in water ($\varepsilon = 78$) were performed. The combination between method and basis set was chosen based on: (i) previous theoretical studies on hydroxamic acids [30] and (ii) our own validation with respect to available experimental data [31].

Frequency calculations for each optimized structure were performed at the same level of theory. No imaginary frequency was found for the lowest energy configurations of any of the optimized structures. The vibrational frequencies were used to compute the thermal energies, E_{th}^{ε}, including zero-point energy, and entropies, S^{ε}.

The differences $\Delta E_{el}^{\varepsilon}$, $\Delta E_{th}^{\varepsilon}$, ΔPV (work term) and ΔS^{ε} between the products and reactants were used to evaluate the free energy of the product formation, ΔG^{ε}, in the gas phase and condensed media at T = 298.15 K according to:

$$\Delta G^{\varepsilon} = \Delta E_{el}^{\varepsilon} + \Delta E_{th}^{\varepsilon} + \Delta PV - T\Delta S^{\varepsilon} \qquad (1)$$

A positive ΔG^{ε} implies a thermodynamically unfavorable product formation, whereas negative value implies a favorable one. The free energy of deprotonation reaction in water solution (e = 78) were evaluated by employing the thermodynamic cycle shown in Scheme 1 where the experimental free energy of proton hydration (–264.0 kcal/mol [32]) was used.

$$\Delta G^{\varepsilon} = \Delta G^{1} + \Delta G_{solv}^{\varepsilon} \, (Products) -$$
$$- \Delta G_{solv}^{\varepsilon} \, (Reagents) \qquad (2)$$

RESULTS AND DISCUSSION

Tautomers of carb-S and carb-Se SAHA analogs. The main objective of this study is to assess how the substitution of oxygen atom from the hydroxamic carbonyl moiety by its analogs from the same group of the Periodic table, sulfur and selenium, could alter the tautomeric equilibria in carb-X SAHA. In answering this question, we modeled and thermodynamically characterized the respective S and Se derivatives of this molecule. Two possible tautomeric forms of hydroxamic acids could exist: keto and enol tautomers (Fig. 3). Furthermore, each tautomer can adopt *E*- or *Z*-conformation [33]. Four possible conformers for both S- and Se-derivatives have been modeled. The most stable form in the gas phase and in water solution is the 1Z-keto form (Table 1 and Fig. 3). The stabilization of 1Z tautomer is due to formation of intramolecular hydrogen bond between the -OH group and neighboring substituted carbonyl group (C=S, C=Se) as seen in

Scheme 1. Thermodynamic cycle employed for calculation of the free energy of deprotonation in solution.
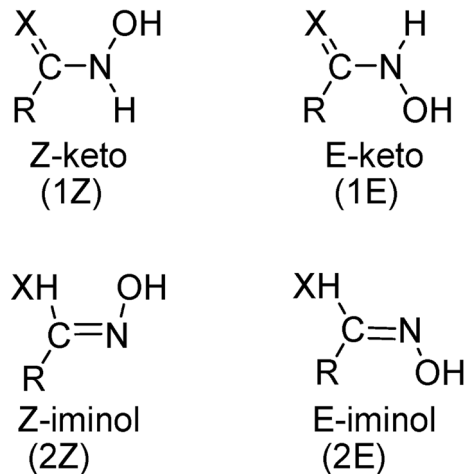
Fig. 3. Keto- and enol forms of hydroxamic acid derivatives; *E* and *Z* isomers.

Table 1. Relative Gibbs free energies (in kcal/mol) of the stable 1Z-keto and 1E-keto iminol tautomers of SAHA in the gas phase, ΔG_{SAHA}^{1}, and water, ΔG_{SAHA}^{78}

	$\Delta G_{\text{carb-O-SAHA}}^{1}$	$\Delta G_{\text{carb-S-SAHA}}^{1}$	$\Delta G_{\text{carb-Se-SAHA}}^{1}$	$\Delta G_{\text{carb-O-SAHA}}^{78}$	$\Delta G_{\text{carb-S-SAHA}}^{78}$	$\Delta G_{\text{carb-Se-SAHA}}^{78}$
1Z	0.0	0.0	0.0	0.0	0.0	0.0
1E	2.1	5.0	5.4	1.9	5.0	4.2
2Z	2.7	0.6	1.1	5.4	3.2	3.8

Fig. 4. The calculations reveal that in all the analogs of SAHA the most stable conformer is the 1Z-keto form (Table 2), as in the unmodified molecule (Table 2). As compared to the unmodified carb-O SAHA molecule, the free energy difference between the 1Z-keto and 1E-keto forms in the heavier-element derivatives are more pronounced (Table 1). Interestingly, the 2Z iminol form in carb-S SAHA (Fig. 4C) carb-Se SAHA appear quite close in energy (just 0.6 kcal/mol and 1.1 kcal/mol free energy

difference respectively) to the 1Z conformer due to the stabilization effect of the intramolecular hydrogen bond. The two most stable conformers for the substituted SAHA analogs are 1Z and 2Z and here is the big difference in comparison to the parent compound carb-O SAHA, where the two most stable conformers are 1Z and 1E (both keto forms).

Hydroxamic acids are weak acids with two labile acidic protons in the hydroxamic moiety (–OH and –NH (Fig. 1)) which could be detached in the
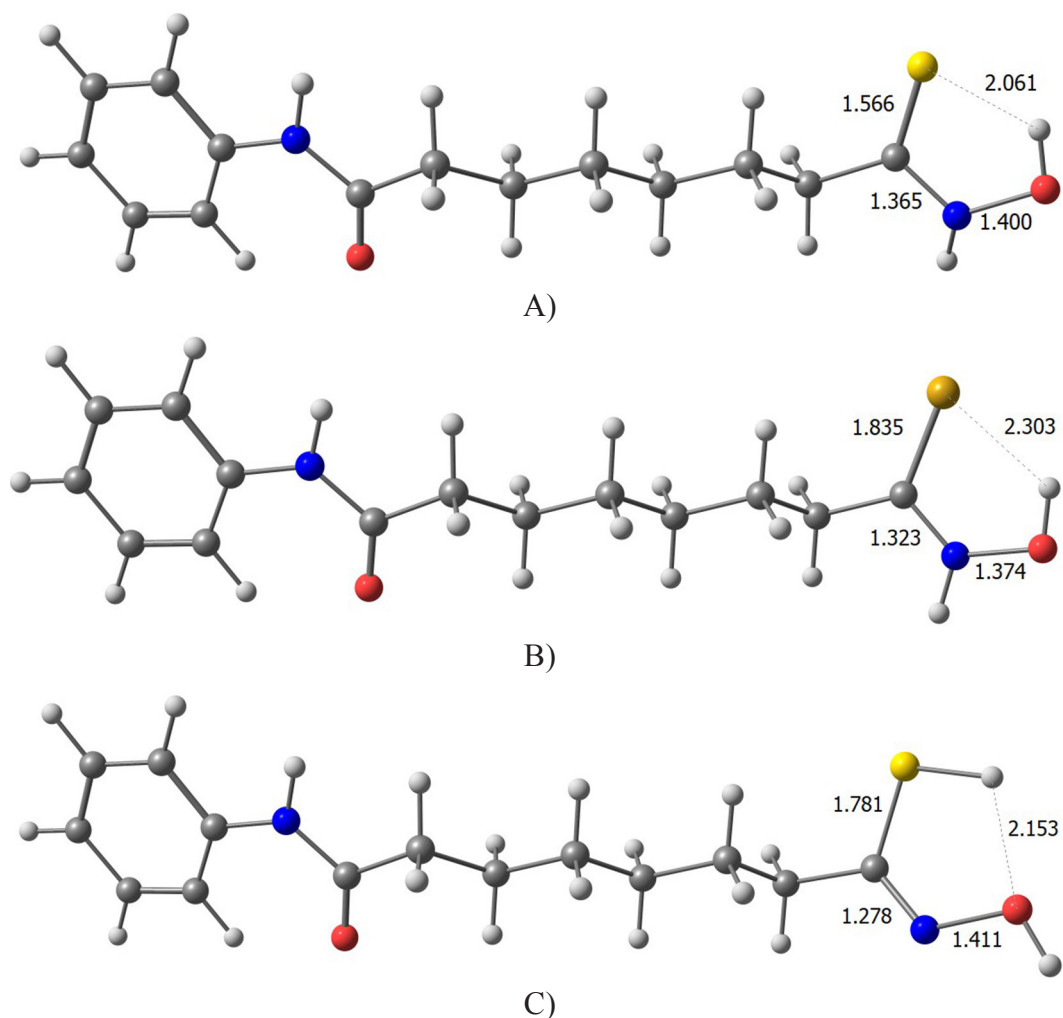
Fig. 4. The optimized geometries of A) 1Z-keto form of carb-S SAHA, B) 1Z-keto form of carb-Se SAHA C) carb-S SAHA 2Z conformer at B3LYP/6-311++G(d,p) level of theory.

Table 2. Change in the Gibbs free energies (in kcal/mol) in the gas phase and water for the reaction of deprotonation of SAHA (AH→A⁻+H⁺). $\Delta G_{solv}^{78}(H^+)$ of −264.0 kcal/mol is taken from the experiment [32]

	$\Delta G_{carb\text{-}O\text{-}SAHA}^{1}$	$\Delta G_{carb\text{-}S\text{-}SAHA}^{1}$	$\Delta G_{carb\text{-}Se\text{-}SAHA}^{1}$	$\Delta G_{carb\text{-}O\text{-}SAHA}^{1}$	$\Delta G_{carb\text{-}S\text{-}SAHA}^{78}$	$\Delta G_{carb\text{-}Se\text{-}SAHA}^{78}$
1Z deprotonated O	347.9	336.7	333.4	24.6	17.5	15.8
1Z deprotonated N	334.2	319.6	316.3	19.9	9.6	7.9

course of chemical/biochemical reaction thus bestowing an OH- or NH-acid properties, respectively, on the parent molecules. [39] What is the deprotonation pattern of the S- and Se-analogs of SAHA? In order to shed light on this question, we modeled the two deprotonation pathways in carb –S/Se SAHA analogs (through OH or NH deprotonation) and evaluated their thermodynamic efficiency (Table 2). The calculations demonstrate that the most stable deprotonated form in the carb –S SAHA derivative in the gas phase is the N-deprotonated 1Z form (Fig. 5b), which is 17.1 kcal/mol more stable in the gas-phase and 7.9 kcal/mol in water medium than the O-deprotonated 1Z form (Table 2). For the Se derivative, these numbers are exactly the same. The stabilization of the N-deprotonated 1Z form is mainly due to the intramolecular hydrogen bond, which is preserved from the original parent structure (structure not shown). The calculations (Table 2) show that carbonyl S- and Se- analogs of SAHA, like the parent unmodified carbonyl O-construct [34] behave essentially as NH acids in both the gas phase and water solution. Data collected in Table 2 reveal that the heavier the heteroatom in the C=O/C=S/C=Se group, the more favorable the proton dissociation at NH location is (decreased free energies of deprotonation in the sequence C=O > C=S > C=Se).

Metal selectivity of SAHA. The nature of the metal cofactor at the enzyme active center greatly affects the thermodynamics and kinetics of the interactions with the respective substrates and enzyme inhibitors. In proteins very often metal cations such as Mg^{2+}, Zn^{2+} and Fe^{2+} compete for the same binding site [20, 35–38] and the proper metal cofactor is selected either by the protein itself or by the cell machinery which strictly regulates the free metal concentration in the intracellular compartments [439]. Note that the identity of the native metal cofactor at the active site of HDACs is still not resolved. Transition metal dications, such as Zn^{2+}, Co^{2+} and Fe^{2+} have been implicated in the enzyme activation. Note, that examples exist of metal-dependent enzymes (including HDAC) that have been reclassified from Zn^{2+}-dependent to Fe^{2+}-dependent enzymes [40–43]. Thus, it is of particular interest to study the metal binding properties of the carb-X (X = O, S, Se) SAHA analogs as possible HDAC inhibitors towards different biogenic metal cations and elucidate the major factors controlling their metal affinity and selectivity.
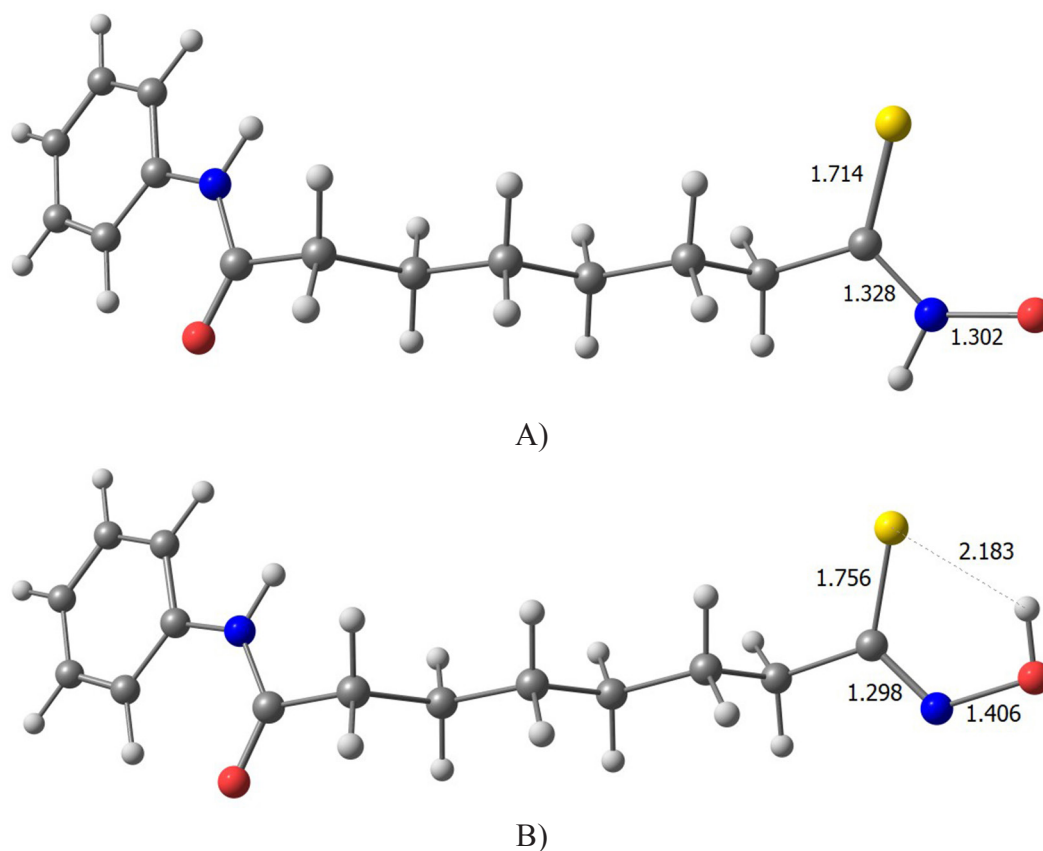
Fig. 5. B3LYP/6-311++G(d,p) optimized structures of carb-S SAHA deprotonated at (A) OH and (B) NH site of the hydroxamic moiety. Bond lengths are given in Å.

Table 3. Change in the Gibbs free energy (in kcal/mol, ΔG^1 gas phase, ΔG^{78} in water) for the $Mg^{2+} \rightarrow Zn^{2+}$ exchange reactions in SAHA, carb-S SAHA, carb-Se SAHA complexes

	ΔG^1	ΔG^{78}
$[Mg(H_2O)_6]^{2+} + [SAHA-Zn(H_2O)_2]^+ + 2H_2O \rightarrow [Zn(H_2O)_6]^{2+} + [SAHA-Mg(H_2O)_4]^+$	−1.7	20.7
$[Mg(H_2O)_6]^{2+} + [carb-S\ SAHA-Zn(H_2O)_2]^+ + 2H_2O \rightarrow [Zn(H_2O)_6]^{2+} + [carb-S\ SAHA-Mg(H_2O)_4]^+$	9.4	31.5
$[Mg(H_2O)_6]^{2+} + [carb-Se\ SAHA-Zn(H_2O)_2]^+ + 2H_2O \rightarrow [Zn(H_2O)_6]^{2+} + [carb-Se\ SAHA-Mg(H_2O)_4]^+$	2.9	30.9

ΔG^1 the free energy change for the reaction in gas phase, ΔG^{78} – in water.

Table 4. Change in the Gibbs free energy (in kcal/mol) for the $Fe^{2+} \rightarrow Zn^{2+}$ exchange reactions in SAHA, SAHA-S, SAHA-Se complexes

	ΔG^1	ΔG^{78}
$[Fe(H_2O)_6]^{2+} + [SAHA-Zn(H_2O)_2]^+ + 2H_2O \rightarrow [Zn(H_2O)_6]^{2+} + [SAHA-Fe(H_2O)_4]^+$	−6.4	16.4
$[Fe(H_2O)_6]^{2+} + [carb-S\ SAHA-Zn(H_2O)_2]^+ + 2H_2O \rightarrow [Zn(H_2O)_6]^{2+} + [carb-S\ SAHA-Fe(H_2O)_4]^+$	0.1	19.2
$[Fe(H_2O)_6]^{2+} + [carb-Se\ SAHA-Zn(H_2O)_2]^+ + 2H_2O \rightarrow [Zn(H_2O)_6]^{2+} + [carb-Se\ SAHA-Fe(H_2O)_4]^+$	2.9	19.3

ΔG^1 the free energy change for the reaction in gas phase, ΔG^{78} – in water.

The SAHA metal ion selectivity can be expressed in terms of the free energy, ΔG^{ε}, for replacing Zn^{2+} bound to the inhibitor by its rival cation, M^{2+} (M = Mg, Fe):

$$[Mg(H_2O)_6]^{2+} + [carb-X\ SAHA-Zn(H_2O)_2]^+ + 2H_2O \rightarrow [Zn(H_2O)_6]^{2+} + [carb-X\ SAHA-Mg(H_2O)_4]^+ \qquad (4)$$

$$[Fe(H_2O)_6]^{2+} + [carb-X\ SAHA-Zn(H_2O)_2]^+ + 2H_2O \rightarrow [Zn(H_2O)_6]^{2+} + [carb-X\ SAHA-Fe(H_2O)_4]^+ \qquad (5)$$
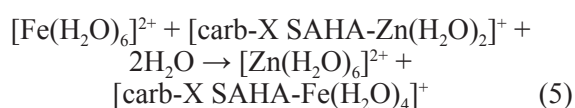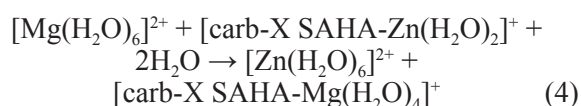
In this model the carb-S and carb-Se derivatives are in their O-deprotonated form and the total charge of the metal complexes is +1. In a previous study [31] it was shown that even SAHA shows NH acidity in gas phase and solution the preferred form of complexation is with O-deprotonated form. In eqs. 4 and 5 a positive ΔG^{ε} implies a Zn^{2+}-selective ligand whereas a negative value implies a Mg^{2+}/Fe^{2+} selective one. The thermodynamic parameters evaluated for carb-X SAHA in the gas phase and condensed media are summarized in Tables 3 and 4. Optimized structures of the metal complexes are shown in Fig. 6. Calculations imply that in the gas phase the substitution reactions for the unmodified SAHA are favorable (negative ΔG^1) but become unfavorable for the S- and Se-substituted analogs evidenced by positive free energies of $Zn^{2+} \rightarrow Mg^{2+}$ and $Zn^{2+} \rightarrow Fe^{2+}$ exchange. This implies that it will be difficult for both metal cations to replace Zn^{2+} in these complexes. The S- and Se-containing SAHA derivatives exhibit higher Zn^{2+} selectivity in condensed media relative to SAHA as well (higher free energies of metal exchange in Tables 3 and 4). The "softer" character of the Zn^{2+} cation relative to that of the Fe^{2+} and Mg^{2+} cations favors the interactions between Zn^{2+} and the "soft" S- and Se-containing ligands in greater extent than those between Fe^{2+} and Mg^{2+} and carb-S SAHA/carb-Se SAHA.

CONCLUSIONS

A systematic theoretical study on sulfur and selenium derivatives of a representative of the family of the HDAC inhibitors – SAHA, has been performed using density functional theory combined with polarizable continuum model calculations. The relative stability of different conformers of the studied molecules was determined. In all cases the most stable is 1Z keto form. The energies of depro-
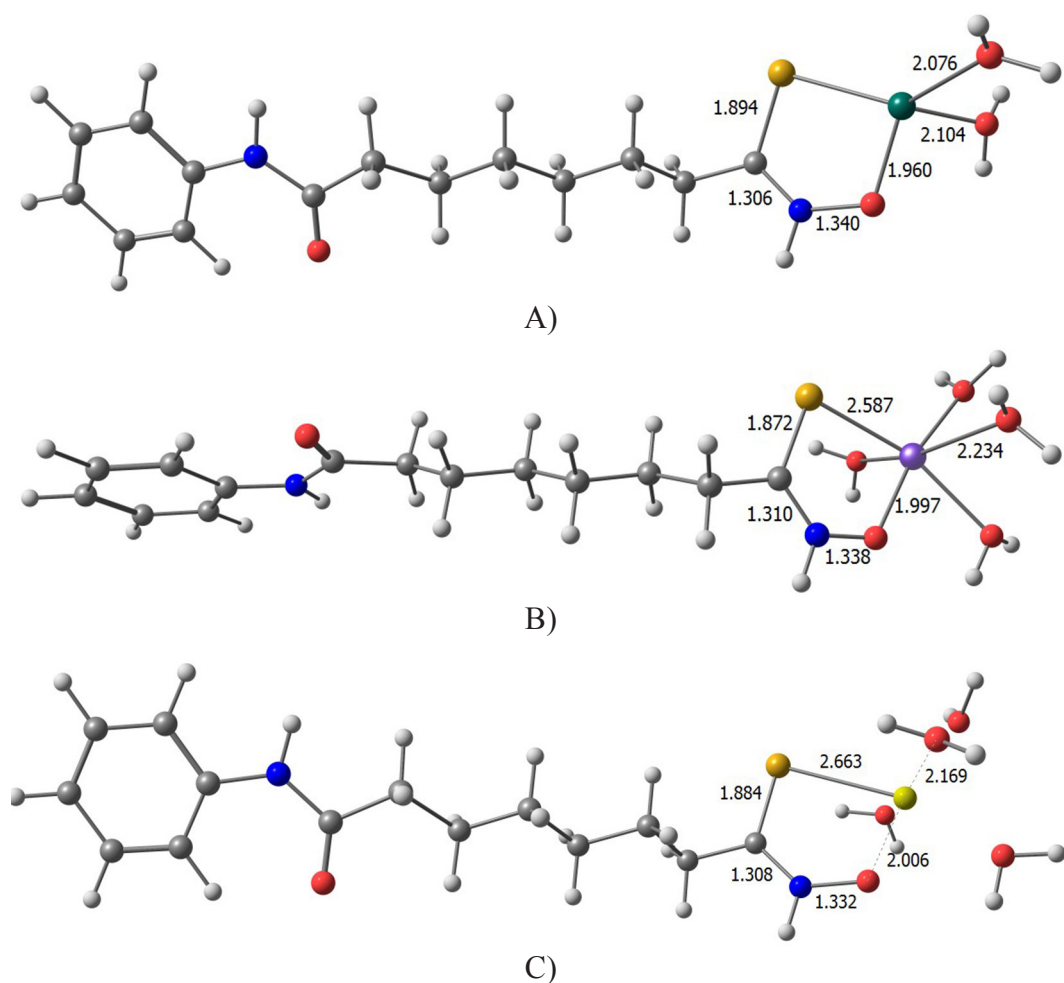
Fig. 6. Optimized structures at B3LYP/6-311++G(d,p) level of theory for the complexes of carb-Se SAHA with A) Zn^{2+}, B) Fe^{2+} and C) Mg^{2+} (Zn^{2+} – green color, Fe^{2+} – purple and Mg^{2+} yellow color).

tonation for the two possible ionizable groups, O-H and N-H, are also determined. It has been found that for the metal-free molecule thermodynamically more favorable is the deprotonation of the N-H group. Sulfur and selenium-containing analogs are deprotonated more easily than the parent SAHA molecule. Deprotonation at the N-H site is more favorable for both compounds. In condensed media SAHA and its sulfur and selenium analogs exhibit greater affinity/selectivity toward Zn^{2+} cations with a noticeable increase in the order O < S ~ Se.

REFERENCES

1. (a) T. Kouzarides, *Curr. Opin. Genet. Dev.*, **9**, 40 (1999). (b) A. H. Lund., M. von Lohuizen, *Genes Dev.*, **18** (19), 2315 (2004). (c) S. B. Baylin, J. E. Ohm, *Nature Rev. Cancer*, **6**, 107 (2006).
2. R. Fendrick, S. W. Hiebert, *J. Cell. Biochem. (Suppl.)*, **30–31**, 194 (1998).
3. M. R. Shakespear, M. A. Halili, K. M. Irvine, D. P. Fairlie, M. J. Sweet, *Trends Immunol.*, **323**, 35 (2011).
4. J. Gräff, D. Kim, M. M. Dobbin, L. H. Tsai, *Physiol. Rev.*, **91**, 603 (2011).
5. N. L. Wiech, J. F. Fisher, P. Helquist, O. Wiest, *Curr. Top Med. Chem.*, **9**, 257 (2009).
6. D. P. Dowling, S. L. Gantt, S. G. Gattis, C. A. Fierke, D. W. Christianson, *Biochemistry*, **47**, 13554 (2008).
7. (a) S. L. Gantt, S. G. Gattis, C. A. Fierke, *Biochemistry*, **45**, 6170 (2006). (b) S. L. Gantt, C. G. Joseph, C. A. Fierke, *J. Biol. Chem.*, **285**, 6036 (2010).
8. J. R. Somoza, R. J. Skene, B. A. Katz, C. Mol, J. D. Ho, A. J. Jennings, C. Luong, A. Arvai, J. J. Buggy, E. Chi, J. Tang, B. C. Sang, E. Verner, R. Wynands, E. M. Leahy, D. R. Dougan, G Snell, M. Navre, M. W. Knuth, R. V. Swanson, D. E. McRee, L. W. Tari, *Structure*, **12**, 1325 (2004).
9. M. Mottamal, S. Zheng, T. L. Huang, G. Wang, *Molecules*, **20**, 3898 (2015).
10. T. A. Miller, D. J. Witter, S. J. Belvedere, *Med. Chem.*, **46**, 5097 (2003).

11. O. Khan, N. B. La Thangue. *Immunol Cell. Biol.*, **90**, 85 (2012).
12. M. S. Finnin, J. R. Donigian, A. Cohen, V. M. Richon, R. A. Rifkind, P. A. Marks, R. Breslow, N. P. Pavletich, *Nature*, **401**, 188 (1999).
13. S. Vassiliou, A. Mucha, P. Cuniasse, D. Georgiadis, K. Lucet-Levannier, F. Beau, R. Kannan, G. Murphy, V. Knaeuper, C. M. Rio, P. Basset, A. Yiotakis, V. Dive. *J. Med Chem.*, **42**, 2610 (1999).
14. G. J. Mulder, J. H. Meerman, *Environ. Health Perspect.*, **49**, 27 (1983).
15. T. Suzuki, A. Kouketsu, A. Matsuura, A. Kohara, S. Ninomiya, K. Kohda, N. Miyata, *Bioorg Med Chem Lett.*, **14**, 3313 (2004).
16. W. Gu, I. Nusinzon, R. D. Smith Jr, C. M. Horvath, R. B. Silverman, *Bioorg. Med. Chem.*, **14**, 3320 (2006).
17. D. Desai, U. Salli, K. E. Vrana, S. Amin, *Bioorg. Med. Chem. Lett.*, **20**, 2044 (2010).
18. R. Gowda, S. V. Madhunapantula, D. Desai, S. Amin, G. P. Robertson, *Cancer Biol. Ther.*, **13**, 756 (2012).
19. Y. Marcus, *Chem. Rev.*, **88**, 1475 (1988).
20. M. Dudev, J. Wang, T. Dudev, C. Lim, *J. Phys. Chem. B*, **110**, 1889 (2006).
21. T. Dudev, C. Lim, *J. Am. Chem. Soc.*, **122**, 11146 (2000).
22. T. Dudev, C. Lim, *J. Phys. Chem. B*, **105**, 4446 (2001).
23. J. M. Berg, H. A. Godwin, *Annu. Rev. Biophys. Biomol. Struct.*, **26**, 357 (1997).
24. W. Gong, X. Zhu, S. Liu, M. Teng, L. Niu, *J. Mol. Biol.*, **283**, 657 (1998).
25. M. J. Frisch, G. W. Trucks, H. B. Schlegel, G. E. Scuseria, M. A. Robb, J. R. Cheeseman, G. Scalmani, V. Barone, G. A. Petersson, H. Nakatsuji, X. Li, M. Caricato, A. Marenich, J. Bloino, B. G. Janesko, R. Gomperts, B. Mennucci, H. P. Hratchian, J. V. Ortiz, A. F. Izmaylov, J. L. Sonnenberg, D. Williams-Young, F. Ding, F. Lipparini, F. Egidi, J. Goings, B. Peng, A. Petrone, T. Henderson, D. Ranasinghe, V. G. Zakrzewski, J. Gao, N. Rega, G. Zheng, W. Liang, M. Hada, M. Ehara, K. Toyota, R. Fukuda, J. Hasegawa, M. Ishida, T. Nakajima, Y. Honda, O. Kitao, H. Nakai, T. Vreven, K. Throssell, J. A. Montgomery, Jr., J. E. Peralta, F. Ogliaro, M. Bearpark, J. J. Heyd, E. Brothers, K. N. Kudin, V. N. Staroverov, T. Keith, R. Kobayashi, J. Normand, K. Raghavachari, A. Rendell, J. C. Burant, S. S. Iyengar, J. Tomasi, M. Cossi, J. M. Millam, M. Klene, C. Adamo, R. Cammi, J. W. Ochterski, R. L. Martin, K. Morokuma, O. Farkas, J. B. Foresman, D. J. Fox, Gaussian09, Revision A.02, Gaussian, Inc., Wallingford CT, 2009.
26. A. D. Becke, *J. Chem. Phys.*, **98**, 5648 (1993).
27. A. D. Becke, *J. Chem. Phys.*, **104**, 1040 (1996).
28. C. T. Lee, W. T. Yang, R. G. Parr, *Phys. Rev. B*, **37**, 785(1988).
29. K. Raghavachari, J. S. Binkley, R. Seeger, J. A. Pople, *J. Chem. Phys.*, **72**, 650 (1980).
30. R. Kakkar, R. Grover, P. Chadha, *Org. Biomol. Chem.*, **1**, 2200 (2003).
31. D. Cheshmedzhieva, N. Toshev, M. Gerova, O. Petrov, T. Dudev, *J. Mol. Model.*, **24**, 114 (2018).
32. M. D. Tissandier, K. A. Cowen, W. Y. Feng, E. Gundlach, M. H. Cohen, A. D. Earhart, J. V. Coe, T. R. Tuttle Jr., *J. Phys. Chem. A*, **102**, 7787 (1998).
33. D. Brown, W. Glass, B. G. R. Mageswaren, *Mag. Res. Chem.*, **26**, 1705 (1988).
34. M. Decouzon, O. Exner, J. F. Gal, P. C. Maria, *J. Org. Chem.*, **55**, 3980 (1990).
35. P. Ciancaglini, J. M. Pizauro, C. Curti, A. C. Tedesco, F. A. Leone, *Int. J. Biochem.*, **22**, 747 (1990).
36. G. S. Lukat, A. M. Stock, J. B. Stock, *Biochemistry*, **29**, 5436 (1990).
37. G. Sun, R. J. A. Budde, *Biochemistry*, **38**, 5659 (1999).
38. L. V. Lee, R. R. Poyner, M. V. Vu, W. W. Cleland, *Biochemistry*, **39**, 4821 (2000).
39. T. Dudev, C. Lim, *Chem. Rev.*, **114**, 538 (2014).
40. B. C. Tripp, C. B. Bell III, F. Cruz, C. Krebs, J. G. Ferry, *J. Biol. Chem.*, **279**, 6683 (2004).
41. J. Zhu, E. Dizin, X. Hu, A. S. Wavreille, J. Park, D. Pei. *Biochemistry*, **42**, 4717 (2003).
42. D. P. Dowling, S. G. Gattis, C. A. Fierke, D. W. Christianson, *Biochemistry*, **49**, 5048 (2010).
43. B. Kim, A. S. Pithadia, C. A. Fierke, *Protein Sci.*, **24**, 354 (2015).

СЯРА И СЕЛЕН СЪДЪРЖАЩИ ПРОИЗВОДНИ НА СУБЕРОИЛ АНИЛИД ХИДРОКСАМОВА КИСЕЛИНА (SAHA) КАТО ПОТЕНЦИАЛНИ HDAC ИНХИБИТОРИ: DFT ИЗСЛЕДВАНЕ НА ТАВТОМЕРИЯТА И МЕТАЛНИЯ ИМ АФИНИТЕТ/СЕЛЕКТИВНОСТ

Д. Чешмеджиева*, Н. Тошев, М. Герова, О. Петров, Т. Дудев*

*Факултет по химия и фармация, Софийски университет „Св. Климент Охридски",
бул. Дж. Баучер 1, 1164 София, България*

(Резюме)

Нарушаването на действието на ензимите от групата на хистон деацетилазите (HDAC) се свързва с широк спектър от заболявания, включително някои видове рак, възпаления, метаболитни и неврологични заболявания. В търсене на нови ефикасни и по-толерантни HDAC инхибитори, са изследвани два аналога на утвърденото лекарство субероил анилид хидроксамова киселина (SAHA), съдържащи серни и селенови атоми в карбонилната група на хидроксамовия остатък. С помощта на теорията на плътностния функционал (density functional theory – DFT) са изследвани техните физикохимични свойства както и афинитета/селективността им към метали в газова фаза и разтворител. По-конкретно, статията отговаря на следните въпроси: (1) Как заместването в хидроксамовата група влияе върху нейната конформационна стабилност? (2) Какви са предпочитаните места за депротониране на хидроксамовата част и начина на свързване към металния катион? (3) Как обменът на O → S и O → Se в хидроксамовата част модулира афинитета и селективността към основни биогенни метални катиони като Mg^{2+}, Fe^{2+} и Zn^{2+}? Изчисленията разкриват ключовите фактори, определящи лигиращите свойства на хидроксамовата част на инхибитора и нейните серни и селенови аналози.

Pd(II) and Pd(IV) complexes with new hydantoin based ligand. Synthesis, characterization, computational and pharmacological studies

E. Cherneva[1]*, R. Buyukliev[1], N. Burdjiev[2], R. Michailova[3], A. Bakalova[1]

*[1] Department of Chemistry, Faculty of Pharmacy, Medical University – Sofia,
2 Dunav Str., 1000 Sofia, Bulgaria*
*[2] Department of Organic Chemistry and Pharmacognosy, Faculty of Chemistry and Pharmacy,
Sofia University, 1 James Bourchier Blvd., 1164 Sofia, Bulgaria*
*[3] Department of Pharmacology, Pharmacotherapy and Toxicology, Faculty of Pharmacy,
Medical University – Sofia, 2 Dunav Str., 1000 Sofia, Bulgaria*

New Pd(II) and Pd(IV) complexes with 3-amino-5-methyl-5-benzylhydantoin have been synthesized and characterized using different spectroscopic techniques, such as FTIR, NMR and elemental analysis. DFT calculations have been employed to investigate the structure of the ligand and its complexes. The free ligand and the metal complexes have been tested *in vitro* for their cytotoxic activity against HL-60, REH and HT-29 human tumor cell lines.

Keywords: Pd complexes;hydantoins; IR spectra; DFT calculations; cytotoxicity.

INTRODUCTION

Transition metal complexes play a crucial role in medical and pharmaceutical chemistry due to their pharmacological effects based on the antitumor activity [1–3]. Given the similar structure, chemical properties and coordination modes between platinum and palladium, palladium complexes [4–8] are of great interest. It is supposed that they will have the same cytotoxic activity like platinum complexes. The similarity and side effects of the platinum complexes lead to the study of Pd complexes as antitumor drugs [3, 9, 10]. In several cases the palladium complexes show significant cytotoxic activity in normal tumor cells and lower resistance of tumor cells to clinical treatments as well as lower side effects than their platinum counterparts [4]. From a thermodynamic and kinetic point of view, the palladium compounds are more labile than the corresponding platinum compounds [11].

Herein is presented the synthesis, spectral investigation and cytotoxic activity of Pd(II) and Pd(IV) complexes with 3-amino-5-methyl-5-benzylhydantoin. In order to get more information about their molecular structure, the new synthezed compounds were studied by computational methods.

EXPERIMENTAL

General: All chemicals were purchased from Fluka (UK) and Sigma-Aldrich. The new Pd(II) and Pd(IV) complexes were characterized by elemental analyses, melting points, IR and NMR spectra. The elemental analyses were carried out on a "EuroEA 3000 – Single", EuroVectorSpA apparatus (Milan, Italy). Corrected melting points were determined, using a Bushi 535 apparatus (Bushi Labortechnik AG, Flawil, Switzerland). The IR spectra were recorded on Thermo Scientific Nicolet iS10 spectrophotometer (Thermo Scientific, USA) in the range of 4000-400 cm^{-1} as Attenuated Total Reflection Fourier Transform Infrared Spectroscopy (ATR-FTIR). The ^{1}H and ^{13}C NMR spectra were registered on Bruker WM 500 (500 MHz) spectrometers in DMSO-d$_6$. The mass spectrum of the ligand was recorded on LC-MS (Thermo Scientific q Exactive Plus – Dionex 3000RSLC).

Synthesis

Preparation of the 5-benzyl-5-methyl hydantoin (2)
The organic compound 5-benzyl-5-methyl hydantoin was obtained by different synthetic pathway from this described by Herbst et al. [12]. Phenylacetone (**1**) (4.02 g, 30 mmol) was dissolved in an aqueous ethanol. 2.45 g (50 mmol) NaCN and 5.3 g (60 mmol) (NH$_4$)$_2$CO$_3$ were added. The

* To whom all correspondence should be sent:
E-mail: e.d.cherneva@gmail.com

resulting mixture was stirred, heated at 65 °C for 24 hours and acidified with conc. HCl to pH = 5. The precipitate was filtered off, recrystallized from aqueous ethanol and dried. Yield: 4.05 g (66%), m.p. 227–228 °C (lit. m.p. 228–229 °C). ^{1}H NMR (500 MHz, DMSO-d$_6$): 10.45 (s, 1H, NH-3); 8.58(s, 1H, NH-1); 7.21–7.18 (m, 5H, C$_6$H$_5$); 2.94; 2.74(dd, AB quartet, 2H, CH$_2$); 1.33 (s, 3H, CH$_3$). ^{13}C NMR (125 MHz, DMSO-d$_6$): 174.7 (C-4); 155.7 (C-2); 135.6; 130.4; 128.4; 127.3(C$_6$H$_5$); 60.8 (C-5); 43.3 (CH$_2$); 24.5 (CH$_3$). Mass-spectrum – M+ = 204.

Preparation of 3-amino-5-benzyl-5-methyl hydantoin (3)

5-benzyl-5-methyl hydantoin (2.043 g, 10 mmol) and 20 ml hydrazine hydrate were heated with reflux condenser for 3 hours. The solution was diluted with 50 ml water and placed in refrigerator for 12 hours. The forming precipitate was filtered off and recrystallized from aqueous ethanol. Yield: 1.05 g (43%), m.p. 232–233°C. IR (ATR, cm^{-1}): 3323, 3284, 3202, 1763, 1722, 1626. ^{1}H NMR (500 MHz, DMSO-d$_6$): 8.58(s, 1H, NH-1); 7.21–7.18 (m, 5H, C$_6$H$_5$); 4.51 (s, 2H, NH$_2$); 2.95; 2.75(dd, AB quartet, 2H, CH$_2$); 1.34 (s, 3H, CH$_3$). ^{13}C NMR (125 MHz, DMSO-d$_6$): 174.9 (C-4); 155.6 (C-2); 135.7; 130.4; 128.4; 127.3(C$_6$H$_5$); 60.9 (C-5); 43.3 (CH$_2$); 24.5 (CH$_3$). Mass-spectrum – M+ = 219.

Preparation of 3-amino-5-benzyl-5-methyl hydantoin dichlorido palladium(II) – [PdLCl$_2$] (complex 4)

An aqueous ethanol solution of (3) (0.0996 g, 0.45 mmol) was added dropwise to an aqueous solution of K$_2$[PdCl$_4$] (0.0903 g, 0.22 mmol) with constant stirring. The homogenous solution obtained was stirred for 9–10 h at ambient temperature. Subsequently, the reaction mixture was concentrated and cooled to 4 °C. The light yellow precipitate obtained was filtered off, washed several times with Et$_2$O and dried in a vacuum desiccator. The product was recrystallized from EtOH. The substance is soluble in DMSO and slightly soluble in water. Yield: 73%, m.p. 213 °C (dec.). IR (ATR, cm^{-1}): 3191, 1772, 1712, 1607. ^{1}H NMR (500 MHz, DMSO-d$_6$): 8.20(s, 1H, NH-1); 7.35–7.27 (m, 5H, C$_6$H$_5$); 7.15 (s, 2H, NH$_2$); 2.99; 2.81(dd, AB quartet, 2H, CH$_2$); 1.35(s, 3H, CH$_3$). ^{13}C NMR (125 MHz, DMSO-d$_6$): 177.7(C-4); 158.8 (C-2); 138.7; 133.5; 131.5; 130.3(C$_6$H$_5$); 63.9 (C-5); 46.4 (CH$_2$); 27.5 (CH$_3$).

Preparation of 3-amino-5-benzyl-5-methyl hydantoin dichlorido palladium(IV) – [PdLCl$_4$] (complex 5)

An aqueous solution of K$_2$[PdCl$_6$] (0.0990 g, 0.3033 mmol) was added dropwise to an aqueous

ethanol solution of (3) (0.1305 g, 0.4826 mmol) at constant stirring. The homogenous solution obtained was stirred for 8–9 h at ambient temperature. Then, the reaction mixture was concentrated and cooled to 4 °C. The yellow precipitate obtained was filtered off, washed several times with Et$_2$O and dried in a vacuum desiccator. The product was recrystallized from EtOH. The substance is soluble in DMSO and slightly soluble in water. Yield: 82%, m.p. 227 °C (dec.). IR (ATR, cm^{-1}):3199, 1771, 1708, 1608. ^{1}H NMR (500 MHz, DMSO-d$_6$): 8.20(s, 1H, NH-1); 7.35–7.27(m, 5H, C$_6$H$_5$); 7.14 (s, 2H, NH$_2$); 2.99; 2.81(dd, AB quartet, 2H, CH$_2$); 1.34(s, 3H, CH$_3$). ^{13}C NMR (125 MHz, DMSO-d$_6$): 177.6(C-4); 158.9 (C-2); 138.7; 133.5; 131.3; 130.4(C$_6$H$_5$); 63.9 (C-5); 46.4 (CH$_2$); 27.4 (CH$_3$).

Computational details

The molecular structures and vibrational spectra of the ligand (3) and its complexes (4, 5) were studied by computational methods. All theoretical calculations were performed using the Gaussian 03 package of programs [13]. Optimization of the structures of the ligand and its complexes was carried out by hybrid DFT calculations, employing the B3LYP (Becke's three-parameter non-local exchange) [14, 15] correlation functional and 6-311++G** basis set for all non-metal atoms and LANL2DZ basis set for metal center.

Cytotoxic activity

Cytotoxicity of the ligand (3) and complexes (4, 5) was evaluated *in vitro* against three human tumor cell lines (Table 1). The cell lines used for the experiments were: (i) HL-60 (acute myeloid leukemia, established from the peripheral blood of a patient with acute promyelocyte leukemia), (ii) REH (acute lymphoblastic leukemia, established from the peripheral blood of a 15-year-old North African girl with acute lymphoblastic leukemia in 1973), (iii) HT-29 (colon adenocarcinoma, established from the primary tumor of a 44-year-old Caucasian woman with colon adenocarcinoma in 1964). The cell lines were obtained from DSMZ German Collection of Microorganisms and Cell Cultures and were well validated in our laboratory as a proper test system for metal complexes. Their DSMZ catalogue numbers are as follows: HL-60 (ACC 3), REH (ACC 22) and HT-29 (ACC 299). Cytotoxicity of the compounds was assessed using the MTT [3-(4,5-dimethylthiazol-2-yl)-2,5-diphenyltetrazolium bromide] dye reduction assay as described by Mossman [16] with some modifications [17]. Exponentially growing cells were seeded in 96-well microplates (100 μL/well at a density of 3.5 × 10^5 cells/mL for the ad-

herent and 1×10^5 cells/mL for the suspension cell lines) and allowed to grow for 24 h prior the exposure to the studied compounds. Stock solutions of the investigated Pd(II) and Pd(IV) complexes were freshly dissolved in DMSO and then promptly diluted in RMPI-1640 growth medium, immediately before treatment of cells. At the final dilutions the solvent concentration never exceeded 0.5%. Cells were exposed to the tested compounds for 72 h, whereby for each concentration a set of 8 separate wells was used. Every test was run in triplicate, *i.e.* in three separate microplates. After incubation with the tested compounds MTT solution (10 mg/mL in PBS) aliquots were added to each well. The plates were further incubated for 4 h at 37 °C and the formazan crystals formed were dissolved by adding 110 μL of 5% HCOOH in 2-propanol. Absorption of the samples was measured by an ELISA reader (UniscanTitertec) at 580 nm. Survival fraction was calculated as percentage of the untreated control. In addition IC_{50} values were calculated from the concentration-response curves. The experimental

data was processed using GraphPadPrizm software and was fitted to sigmoidal concentration/response curves *via* non-linear regression.

RESULTS AND DISCUSSION

The method of obtaining of the organic compound 5-benzyl-5-methyl hydantoin (**2**) described by Herbst et al [12] was improved and shortened. Synthetic pathway to obtain the new ligand and its complexes is illustrated on the Scheme 1. The structure of the ligand (**3**) and its metal complexes (**4**, **5**) were confirmed by various spectroscopic techniques such as IR, ^{1}H NMR, ^{13}C NMR spectra and elemental analyses. The results were consistent with the assigned structures.

The complexes (**4**, **5**) were stable in solid state at room temperature and their melting points were over 200 °C. As a result of elemental analyses, metal complexes were supposed to have the following general formulas $[PdLCl_2]$ and $[PdLCl_4]$.
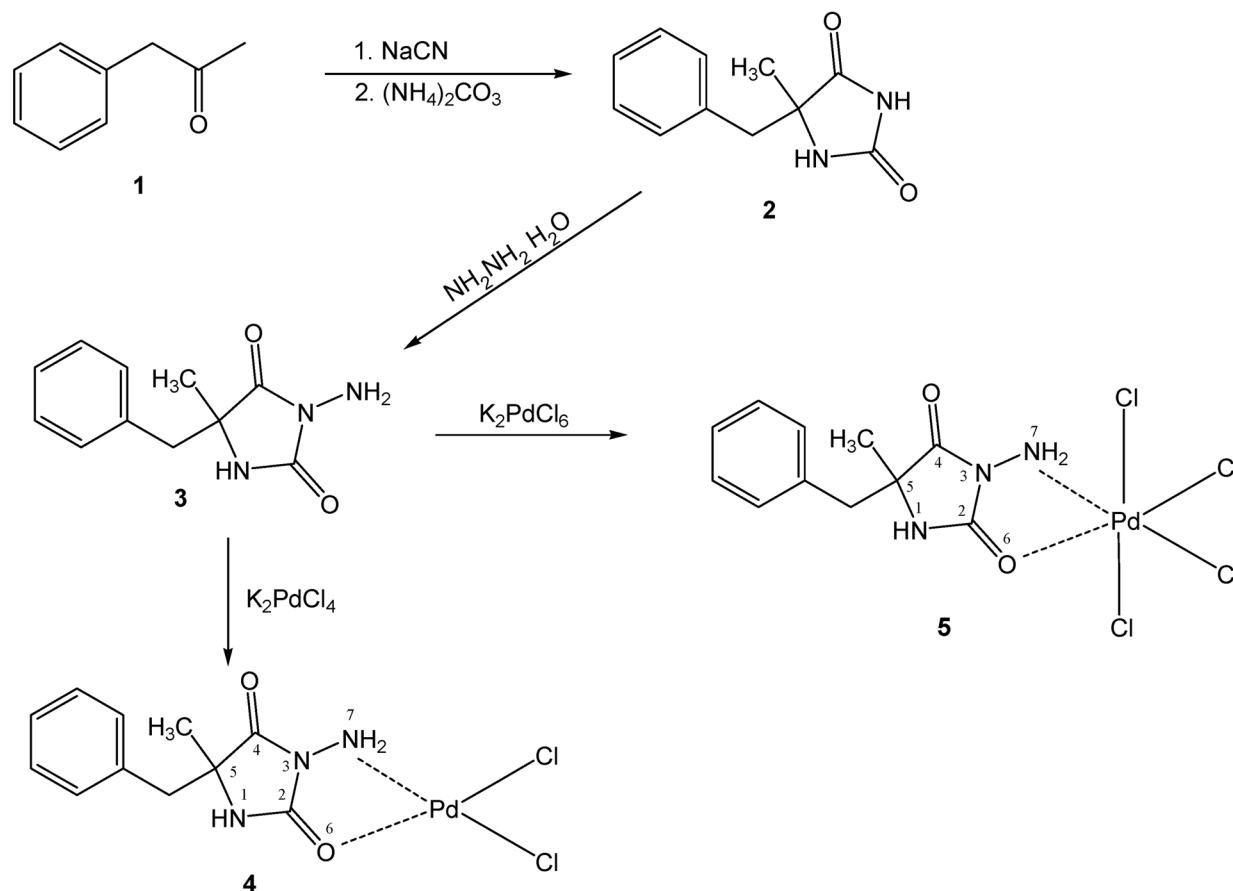
Scheme 1. Synthesis of 5-benzyl-5-methyl hydantoin (**2**), ligand (**3**), Pd(II) and Pd(IV) complexes (**4**, **5**).

The structural characterization

Infrared spectra

The accurate assignment of the main experimental frequencies of ligand and complexes (**4**, **5**) to the corresponding normal modes was supported by DFT method employing B3LYP functional, 6-311++G** basis set was selected for C, N, H and O atoms and LANL2DZ was applied for the Pd atom. All calculated frequencies are positive. This is confirmed that the structures are correctly optimized.

The IR spectrum of the free ligand shows three characteristic bands in the region 3323–3202 cm^{-1} (theor. 3520–3372 cm^{-1}) associated with the stretching modes of the NH and NH$_2$ groups, which is typical for hydrogen bonded systems. While in the spectra of the complexes (**4**, **5**), they are shifted to lower frequencies (exp. 3205–3110 cm^{-1}/theor. 3554–3344 cm^{-1}).

The bands observed at 1764 and 1723 cm^{-1} corresponding to υ(C=O) vibrations in the ligand are slightly shifted to higher frequencies in the complexes: 1772, 1712 cm^{-1} in Pd(II) and 1772, 1708 cm^{-1} in Pd(IV) complex. The band at 1626 cm^{-1} attributed to the δ(NH$_2$) vibration in the spectrum of the ligand is slightly shifted to lower wavenumbers by 18 cm^{-1} in the complexes.

NMR spectra

In the ^{1}H NMR spectra of the ligand the signal of NH(1) is at 8.59 ppm, the signals of two diastereotopic CH$_2$ protons are in the 2.75–2.95 ppm. N-NH$_2$ protons are singlet at 4.51 ppm. The comparative analysis of the ^{1}H NMR spectra of the complexes (**4**, **5**) and the ligand (**3**) showed that there was a significant shifting of the signal of N-NH$_2$ group (from 4.51 in the ligand to 7.15–7.20 ppm in the complexes). The signals of the other protons were not shifted extraordinary. This shows that the coordination of the ligand with metal ions was realized by nitrogen atom of the amino group.

In the ^{13}C NMR spectra, as well as in the ^{1}H spectra of the complexes, the signals of two carbonyl groups are slightly influenced. But the shifting of the C-2 carbonyl carbon (C=O-2) is relatively great (from 155.6 to 158.9). It revealed that ligand coordinates with palladium cation bidentate, through C-2 carbonyl oxygen and the amine group. All other carbon atoms do not shift significantly after coordination.

Theoretical analysis

The theoretical calculations were used to obtain the important information about structural characteristics due to the difficulties to obtain crystals suitable for X-ray analysis. The geometries of the ligand and complexes were optimized at the B3LYP level, 6-311++G ** and LANL2DZ basis sets (Fig. 1).

The palladium(II) ion has square planar environments with the ligand, bonded through the nitrogen atom from amine group and carbonyl oxygen atom

3

4   **5**
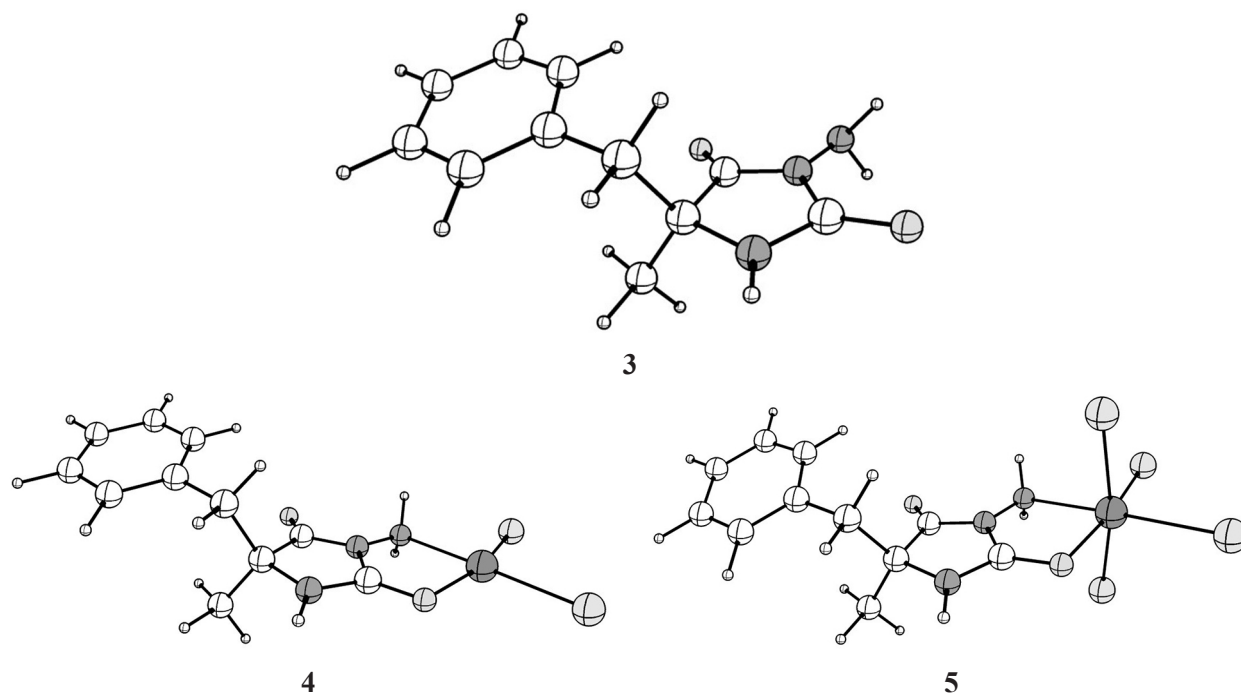
Fig. 1. Optimized structures of the ligand (**3**) and its complexes (**4**, **5**).

Table 1. *In vitro* evaluation of cytotoxicity of the ligand (**3**) and complexes (**4**, **5**) in comparison with referent drug cisplatin in three human tumour cell lines

Compounds	$IC_{50}(\mu M)$		
	HL-60	REH	HT-29
Ligand	167 ± 10	> 200	> 200
Complex Pd(II)	127 ± 5	> 200	> 200
Complex Pd(IV)	133 ± 5	> 200	> 200
Cisplatin	8.7	1.07	170

(C=O-2). The last one is more stable by 0.33 kJ/mol compared to coordination of metal ion with C=O group on fourth position. In case of complex (**5**) the metal adopts a distorted octahedral coordination.

Theoretical analysis showed that the bond lengths in the complexes are slightly longer than the ligand by 0.03–0.05 Å. The Pd–N and Pd–O bond lengths are 2.16 Å and 2.21 Å, respectively, consistent with those found in other palladium compounds [18, 19]. The angle, $N_5N_3C_2$ is slightly affected upon complexation by 2.9–3.9°. The computed values of angles N_5PdO_6 in complexes are 79.84° and 80.81° respectively.

In vitro cytotoxicity

Cytotoxicity of the ligand (**3**) and complexes (**4**, **5**) was evaluated *in vitro* against three human tumor cell lines (Table 1). Pd(II) and Pd(IV) complexes showed higher cytotoxic activity than the ligand on HL-60 cell line. This cell line maybe is more sensitive to palladium complexes than the other two lines. The new complexes are less active than the referent cisplatin.

CONCLUSIONS

The paper describes synthesis, characterization and theoretical analysis of 3-amino-5-methyl-5-benzyl hydantoin as a ligand and its palladium complexes. Their structures were determined by several spectroscopic methods. The DFT calculations show that palladium ion exhibit a square planar geometrical arrangement in Pd(II) complex and distorted octahedral coordination in Pd(IV) complex. Theoretical analysis confirmed the experimental data for bidentate coordination of the ligand with metal ions. Pd(II) and Pd(IV) complexes showed higher cytotoxic activity than the ligand on HL-60 cell line.

REFERENCES

1. K. M. Deo, B. J. Pages, D. L. Ang, C. P. Gordon, J. R. Aldrich-Wright, *Int. J. Mol. Sci.*, **17**, 1818 (2016).
2. K. Karami, Z. Mehri Lighvan, H. Farrokhpour, M. Dehdashti Jahromi, A. A. Momtazi-Borojeni, *J. Biomol. Struct. Dyn.*, 1 (2017).
3. Taotao Zou, Chun-Nam Lok, Pui-Ki Wan, Zhi-Feng Zhang, Sin-Ki Fung, Chi-Ming Che, *Current Opinion in Chemical Biology*, **43**, 30 (2018).
4. A. R. Kapdi, I. J. S. Fairlamb, *Chem. Soc. Rev.*, **43**, 4751 (2014).
5. H. Mansouri-Torshizi, M. Saeidifar, F. Khosravi, A. Divsalar, A. A. Saboury, F. Hassani, *Bioinorganic Chemistry and Applications*, **2011**, 1, (2011).
6. H. Mansouri-Torshizi, M. Saeidifar, A. Divsalar, and A. A. Saboury, *Journal of Biomolecular Structure and Dynamics*, **28**, 805 (2011).
7. N. T. Abdel Ghani, A. M. Mansour, *J. Mol. Struct.*, **991**, 108 (2011).
8. S. Rubino, R. Busà, A. Attanzio, R. Alduina, Vita Di Stefano, M. A. Girasolo, S. Orecchio, L. Tesoriere, *Bioorg. Med. Chem.*, **25**, 2378 (2017).
9. M. D. Coskun, F. Ari, A. Y. Oral, M. Sarimahmut, H. M. Kutlu, V. T. Yilmaz, E. Ulukaya, *Bioorg. Med. Chem.*, **21**, 4698 (2013).
10. T. Lazarević, A. Rilak, Ž. D. Bugarčić, *Eur. J. Med. Chem.*, **142**, 8 (2017).
11. E. J. Gao, K. H. Wang, X. F. Gu, Y. Yu, Y. G. Sun, W. Z. Zhang, H. X. Yin, Q. Wu, M. C. Zhu, X. M. Yan, *J. Inorg. Biochem.*, **101**, 1404 (2007).
12. R. Herbst, T. Johnson, *J. Am. Chem. Soc.*, **54**, 2463 (1932).
13. M. J. Frisch, G. W. Trucks, H. B. Schlegel, G. E. Scuseria, M. A. Robb, J. R. Cheeseman, Jr., J. A. Montgomery, T. Vreven, K. N. Kudin, J. C. Burant, J. M. Millam, S. S. Iyengar, J. Tomasi, V. Barone, B. Mennucci, M. Cossi, G. Scalmani, N. Rega, G. A. Petersson, H. Nakatsuji, M. Hada, M. Ehara, K. Toyota, R. Fukuda, J. Hasegawa, M. Ishida, T. Nakajima, Y. Honda, O. Kitao, H. Nakai, M. Klene, X. Li, J. E. Knox, H. P. Hratchian, J. B. Cross, V. Bakken, C. Adamo, J. Jaramillo, R. Gomperts, R. E. Stratmann, O. Yazyev, A. J. Austin, R. Cammi, C. Pomelli, J. W. Ochterski, P. Y. Ayala, K. Morokuma,

G. A. Voth, P. Salvador, J. J. Dannenberg, V. G. Zakrzewski, S. Dapprich, A. D. Daniels, M. C. Strain, O. Farkas, D. K. Malick, A. D. Rabuck, K. Raghavachari, J. B. Foresman, J. V. Ortiz, Q. Cui, A. G. Baboul, S. Clifford, J. Cioslowski, B. B. Stefanov, G. Liu, A. Liashenko, P. Piskorz, I. Komaromi, R. L. Martin, D. J. Fox, T. Keith, M. A. Al-Laham, C. Y. Peng, A. Nanayakkara, M. Challacombe, P. M. W. Gill, B. Johnson, W. Chen, M. W. Wong, C. Gonzalez, J. A. Pople, Gaussian 03, Revision C.02, Gaussian, Inc., Wallingford CT, 2004.

14. P. J. Stephens, F. J. Devlin, C. F. Chabalowski, M. J. Frisch, *J. Phys. Chem.*, **98**, 11623 (1994).
15. C. T. Lee, W. T. Yang, R. G. Parr, *Phys. Rev.*, B, **37**, 785 (1988).
16. T. Mosmann, *J. Immunol. Methods*, **65**, 55 (1983).
17. S. Konstantinov, H. Eibl, M. Berger, *Br. J. Haemat.*, **107**, 365 (1999).
18. A. M. Mansour, N. T. Abdel-Ghani, *Inorg. Chim. Acta*, **438**, 76 (2015).
19. M. R. Shehata, M. M.Shoukry, M. S. Ragab, *J. Mol. Struc.*, **1159**, 216 (2018).

КОМПЛЕКСИ НА Pd (II) И Pd (IV) С НОВ ХИДАНТОИНОВ ЛИГАНД: СИНТЕЗ, ОХАРАКТЕРИЗИРАНЕ, ТЕОРЕТИЧНИ И ФАРМАКОЛОГИЧНИ ИЗСЛЕДВАНИЯ

Е. Чернева[1], Р. Буюклиев[1], Н. Бурджиев[2], Р. Михайлова[3], А. Бакалова[1]

[1] Катедра „Химия", Фармацевтичен факултет, Медицински университет – София, ул. „Дунав" 2, 1000 София, България
[2] Катедра „Химия и фармакогнозия", Факултет по химия и фармация, Софийски Университет, бул. „Джеймс Баучер" 1, 1164 София, България
[3] Катедра по фармакология, фармакотерапия и токсикология, Фармацевтичен факултет, Медицински университет – София, ул. „Дунав" 2, 1000 София, България

(Резюме)

Нови комплекси на Pd(II) и Pd(IV) с 3-амино-5-метил-5-бензилхидантоин бяха синтезирани и охарактеризирани, използвайки различни спектроскопски методи като ИЧ, ЯМР и елементен анализ. Квантово-химични изчисления бяха приложени за изследване на структурата на лиганда и неговите комплекси. Свободният лиганд и комплексите бяха тествани *in vitro* за цитотоксична активност върху три човешки туморни клетъчни линии: HL-60, REH и HT-29.

Insights in the photophysics of 2-[2'-hydroxyphenyl]-quinazolin-4-one isomers by DFT modeling in the ground S_0 and excited S_1 states

J. Kaneti, S. M. Bakalova*, I. P. Angelov

Institute of Organic chemistry with Centre of Phytochemistry Bulgarian Academy of Sciences, Acad. G. Bonchev str., Block 9, 1113 Sofia, Bulgaria

2-[2'-hydroxyphenyl]-quinazolin-4-one, HPQ, is believed for a long time to be a typical compound capable of keto-enol tautomerism. As such it would normally be expected to exhibit a characteristic absorption spectrum for the tautomers potentially present in solution. Moreover, fluorescence should also exhibit features of possible excited state proton transfer, ESIPT. Contrary to expectations, the absorption spectra of HPQ do not directly indicate tautomerism, whereas the observed fluorescence is relatively weak. For these reasons in this paper we look for additional DFT and TD-DFT computational, as well as experimental, insight into the spectroscopic properties of the title compound. The results indicate the simultaneous presence of enol and keto forms both in the ground and first excited singlet state, as well as multiple overlapping emissions.

Keywords: tautomerism, photophysics, DFT and TD-DFT calculations, solvent effect.

INTRODUCTION

The visible absorption spectrum of 2-[2'-hydroxyphenyl]-quinazolin-4-one (HPQ) has been recorded routinely by a number of groups [1, 2, 3] and shown to possess an intense peak at *ca.* 30.10^3 cm^{-1}, accompanied by a longer wavelength absorption (shoulder) at *ca.* 25.10^3 cm^{-1} in proton acceptor solvents as N,N-dimethyl formamide, DMF, and dimethylsulfoxide, DMSO [2]. Solutions of HPQ fluoresce at concentrations *ca.* 10 μM at ca. 21.10^3 cm^{-1}, while its crystals show either blue or green fluorescence [2]. The offered common interpretation of the observed fluorescence emission involves dimer aggregates as the emitting species [2]. Traditionally fluorescence of compounds with similar structural fragments is referred to their expected capability to undergo ESIPT, which is usually associated with anomalously large Stokes' shift of the order of 10^4 cm^{-1} [4]. Reported absorption and steady state fluorescence spectra of HPQ, with a Stokes shift of ca. 9.10^3 cm^{-1} [1–3] indeed conform to the mentioned requirements. The reason for the present report is that the dynamics of tautomerization and

internal rotations of HPQ, as well as its observed electronic absorption and emission features in solution are apparently still incompletely understood.

EXPERIMENTAL

Computational DFT and TD-DFT modeling has been carried out using the Gaussian 09 program system, rev. D01 [5], DFT and TD DFT (TD=nstates=6) theory. B3LYP and CAM-B3LYP functionals have been employed. Solvent interactions are calculated within the PCM formalism [6, 7]. UV-visible spectra are recorded on a Perkin Elmer Lambda 25 UV/Vis Spectrometer and fluorescence spectra are recorded on a Perkin Elmer LS-55 Luminescence Spectrometer. Time resolved photophysical studies have been performed using a 1 cm path length quartz cuvette at room temperature. Fluorescence lifetimes with a time resolution less than 100 ps have been obtained by Time Correlated Single-Photon Counting (TCSPC) using a Fluorolog®-3 (HORIBA Jobin Yvon S.A.S., Longjumeau, France) spectrofluorimeter and picosecond light pulses generated from a pico-LED source at 365 nm. The decay curves have been deconvoluted using DAS-6 decay analysis software and the acceptability of the fits was assessed by χ^2 criteria and visual inspection

---

* To whom all correspondence should be sent:
E-mail: bakalova@orgchm.bas.bg

of the residuals of the fitted functions to the data. Time-resolved fluorescence decay *I(t)* is described by the following expression:

$$I(t) = \sum_i \alpha_i \tau_i \qquad (1).$$

The average fluorescence lifetimes are calculated using the following equation [8]:

$$\tau_{i0} = \frac{\sum_i \alpha_i \tau_i^2}{\sum_i \alpha_i \tau_i} \qquad (2)$$

in which α_i is the pre-exponential factor corresponding to the *i-th* decay time constant, τ_i.

RESULTS AND DISCUSSION

Several possible tautomeric forms of HPQ are shown on Scheme 1. Evidently HPQ isomers shown in Scheme 1 may arise from one another either via proton transfer processes, or partially hindered internal rotation around the formal single C – C bond connecting the two aromatic fragments, or both.

We start computational modeling of isomers **1–4** in the ground (S$_0$) and the first excited singlet (S$_1$) states at CAM-B3LYP/6-31G(d,p) in five solvents of very different polarity and hydrogen bonding ability – tetrahydrofuran (THF), dichloromethane (DCM), N,N-dimethylformamide (DMF), dimethylsulfoxide (DMSO) and water (H$_2$O). We have been unable to locate the keto isomer **3** at this level of theory in any of the solvents considered; any attempt led to the more stable isomer **1** instead. Results for isomers **1, 2** and **4** indicate insignificant solvent dependence of their electronic spectra on solvent polarity. This computational result is in agreement with the published fluorescence spectra in THF and THF/water mixtures up to 99% of water [1].

We further explore the influence of the basis set on the energies and predicted electronic spectra in a
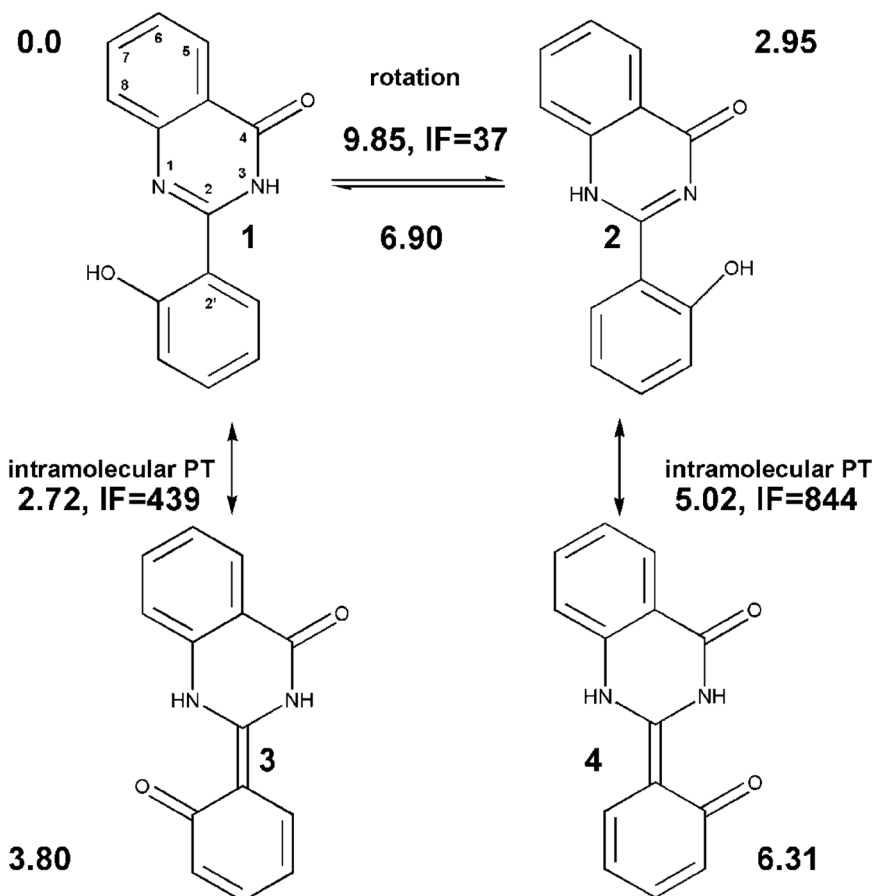
Scheme 1. Some of the possible prototropic and rotational isomers of HPQ, with computed CAM-B3LYP/6-31+G(d,p) relative Gibbs free energies $E + \Delta G_0$ (kcal.mol^{-1}) in the S$_0$ electronic state in solvent DMF, PCM. Activation free energies of interconnecting transition structures (TSs) are given in kcal.mol^{-1} together with the computed imaginary frequencies, IFs, in cm^{-1}. Note the conversion of **1** to **2** requires rotation and proton transfer, N$_3$H to N$_1$.

solvent of medium polarity, DMF (Table 1) and the following discussion is based on the results in DMF. The results show that CAM-B3LYP/6-31G+(d,p) performs best as a compromise between accuracy and computational cost. Moreover, all four considered isomers (Scheme 1) have been located in the ground (S_0) state at this level of theory. The addition of a second diffuse function does not make difference, presumably because the hydrogen bonds are very strong. We estimate this by comparing the energies of enols **1** and **2** (which have hydrogen bonds with distances 1.64 Å and 1.62 Å, resp.) with their respective isomers **anti-1** and **anti-2** (Table 2 and Fig. 1) in which no H bond is possible. Results show that the H-bond stabilization is 7.6 kcal.mol^{-1} in the case of **1** and 8.7 kcal.mol^{-1} for **2**, consistent with the notion of strong, low barrier, hydrogen bonding, Fig. 1 [9].

Table 2 shows the values of the rotational barrier between **1** and **2**, as well as the barriers for proton transfer interconnecting **1** and **3** and **2** and **4**, respectively.

Computational results (Table 1) show that the enol form **1** is the prevailing species in the ground state. Computed energy of the $S_0 - S_1$ absorption electronic transition is 306.9 nm (32580 cm^{-1}), while the experimentally reported longest-wavelength absorption maximum [2] is at 335 nm (29850 cm^{-1}). The overestimation of absorption transition energy by 2730 cm^{-1} may be considered acceptable. This vertical absorption transition is an almost pure HOMO $\rightarrow$ LUMO π-excitation. The complex form of the longest-wavelength absorption maximum, together with the observed shoulder at ca. 390–400 nm in DMF and DMSO [2] is an indication of the presence of quinoid keto-forms, **3** and/or **4** in solution as well.

Table 1. Electronic (E) and Gibbs free (E+ΔG) energies and electronic spectra in DMF, predicted by (TD) CAM-B3LYP calculations with various basis sets. Energies are given in hartrees, relative free energies ΔΔG in kcal.mol^{-1}. Transition wavelengths are in nm, and oscillator strengths in absolute units. λ_{abs} correspond to vertical excitations and λ_{Fl} – to relaxed TD emission energies from the S_1 excited state

Str	S_0			S_0–S_1		S_0–S_2		S_1	
	E	E+ΔG	ΔΔG	λ_{abs}	f_{osc}	λ_{abs}	f_{osc}	λ_{Fl}	f_{osc}
				6-31+G(d)					
1	−799.15279	−798.97554	0.00	305.8	0.75	273.6	0.07	363.1	0.90
2	−799.14705	−798.97056	3.17	304.8	0.58	273.7	0.18	441.1	0.52
3	−799.14526	−798.96956	3.81	373.8	0.56	286.8	0.06	436.3	0.48
4	−799.14296	−798.96655	5.73	380.2	0.60	290.5	0.00	433.8	0.55
				6-31G(d,p)					
1	−799.14107	−798.96371	0.00	304.1	0.68	267.2	0.10	357.6	0.78
2	−799.13464	−798.95808	3.59	302.8	0.53	270.9	0.03	434.1	0.49
3	−								
4	−799.12842	−798.95238	7.22	367.9	0.56	289.4	0.00	425.1	0.52
				6-31+G(d,p)					
1	−799.17417	−798.99734	0.00	306.9	0.74	273.9	0.07	363.6	0.87
2	−799.16864	−798.99263	2.95	306.7	0.58	273.6	0.18	438.7	0.52
3	−799.16539	−798.99128	3.80	364.6	0.55	283.5	0.07	425.0	0.52
4	−799.16281	−798.98729	6.31	374.8	0.59	285.4	0.01	432.6	0.55
				6-31++G(d,p)					
1	−799.17430	−798.99753	0.00	306.9	0.74	273.9	0.07	363.5	0.87
2	−799.16873	−798.99273	3.01	306.7	0.58	273.6	0.18	433.0	0.55
3	−799.16550	−798.99153	3.76	364.6	0.55	283.5	0.07	425.0	0.52
4	−799.16289	−798.98744	6.33	374.8	0.59	285.5	0.01	432.6	0.55
				6-311G(d,p)					
1	−799.32703	−799.15055	0.00	304.8	0.70	268.9	0.09	360.7	0.84
2	−799.32067	−799.14468	3.74	303.2	0.55	268.0	0.17	437.0	0.51
3	−799.31711	−799.14263	5.05	366.5	0.55	281.6	0.01	423.9	0.50
4	−799.31459	−799.13928	7.18	373.1	0.60	290.1	0.00	429.9	0.53

*We could not locate isomer **3** using the 6-31G(d,p) basis set.

Table 2. CAM-B3LYP/6-31+G(d,p) ground state electronic and Gibbs free energies of HPQ tautomeric species shown on Scheme 1 and Figure 1 with connecting transition structures rts for internal rotation and hts for intramolecular hydrogen (proton) transfer. Solvent DMF. Energies in hartrees, $\Delta\Delta G$ in kcal.mol^{-1} and imaginary frequencies in cm^{-1}

Str.	E	E+ΔG	$\Delta\Delta G$	IF
1	−799.17417	−798.99734	0.00	
Anti-1	−799.16073	−798.98527	7.57	
1-2 rts	−799.15845	−798.98164	9.85	37
1-3 hts	−799.16533	−798.99301	2.72	439
2	−799.16864	−798.99263	2.95	
Anti-2	−799.15447	−798.97870	11.70	
3	−799.16539	−798.99128	3.80	
4	−799.16281	−798.98729	6.31	
2-1 rts	−799.15845	−798.98164	6.90	37
2-4 hts	−799.16212	−798.98934	5.02	844

0.0   7.6   11.7   3.0
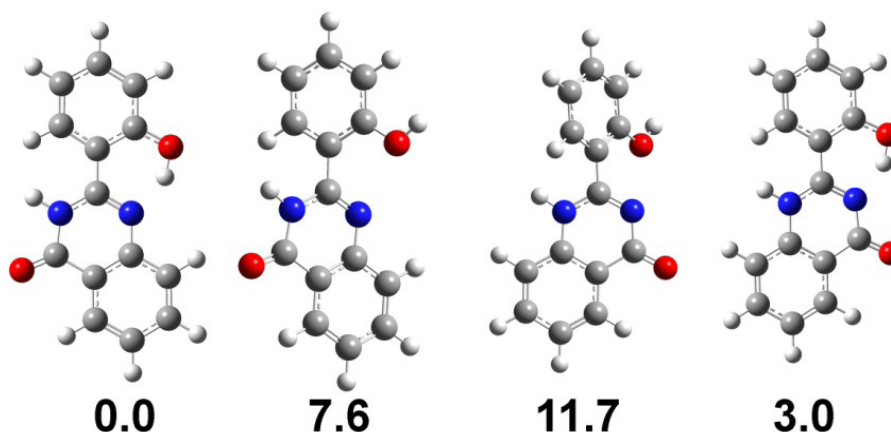
Fig. 1. Tautomers **1, anti-1** and **anti-2, 2** with or without H-bond, resp. Relative free energies $\Delta\Delta G_0$ in kcal.mol^{-1}.

Computational results for the relaxed excited S_1 state show, that three isomers may be present – **1***, **3*** and **4*** (Fig. 2). Any attempt to locate the enol form **2*** leads to its simultaneous conversion to the corresponding keto form **4***. The keto forms **3*** and **4*** are predicted to fluoresce at much longer wavelengths (Table 1) than the enol form **1**, thus accounting for the large Stokes' shift found by experiment. Although, similar to the case of absorption, computationally predicted values of emission energies are higher than experimentally found ones, the computed Stokes' shift of ca. 9000 cm^{-1}, indicative of ESIPT, is gratifying.

Table 3 shows the relaxed computational results obtained at B3LYP/6-31+G(d,p). It can be seen that in this case predicted absorption spectra are shifted bathochromically relative to experimental values, the energy differences with the experimentally observed spectra being much smaller than at

CAM-B3LYP/6-31+G(d,p). The energy differences with fluorescence experiment at TD B3LYP/6-31+G(d,p) are also much smaller than at TD CAM-B3LYP/6-31+G(d,p). The conclusions however are the same with the two DFT functionals.

Reported absorption and emission spectra of HPQ in the literature are little [1, 2], if at all, influenced by solvent polarity, which does not completely conform to our own experimental spectra, see Figure 3. The absorption spectrum in DMF and DMSO has a fine structured band at $30–33.10^3$ cm^{-1}, with a secondary bathochromically shifted absorption at 26.10^3 cm^{-1} in DMF, which we attribute to the keto-tautomer **3**. Our absorption spectra correspond roughly to the data reported earlier [1, 2]. Present emission spectra in the same solvents show some more detail and indicate the presence of at least two fluorescence bands in DMF and DMSO, which on the basis of the computational results may
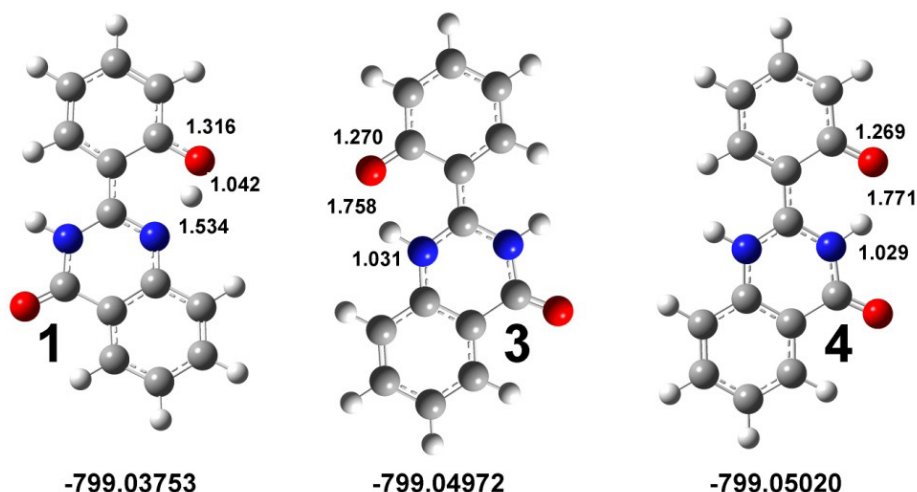
Fig. 2. Equilibrium geometries of **1***, **3*** and **4*** in the S_1 excited state, solvent DMF, CAM-B3LYP/6-31+G(d,p). C=O, O--H and N--H distances are shown in Å; total electron energies are in hartrees (au).

Table 3. Electronic (E) and Gibbs free (E+ΔG) energies and electronic spectra, predicted by TD B3LYP/6-31+G(d,p) calculations. Energies are given in hartrees, relative free energies ΔΔG in kcal.mol^{-1}. Transition wavelengths are in nm, and oscillator strengths in absolute units. λ_{abs} correspond to vertical excitations, and λ_{Fl} – to relaxed TD emission energies from the S_1 excited state. No relaxed S_1 structure **3** could be found by these calculations

Str	S_0			S_0–S_1		S_0–S_2		S_1	
	E	E+ΔG	ΔΔG	λ_{abs}	f_{osc}	λ_{abs}	f_{osc}	λ_{Fl}	f_{osc}
1	−799.57580	−799.40215	0.00	342.7	0.66	309.4	0.04	393.0	0.77
2	−799.57016	−799.39762	2.88	346.7	0.47	308.9	0.17	513.6	0.33
3	−799.56824	−799.39814	2.56	408.0	0.46	369.1	0.02		
4	−799.56571	−799.39297	5.85	422.5	0.45	358.2	0.08	488.0	0.37
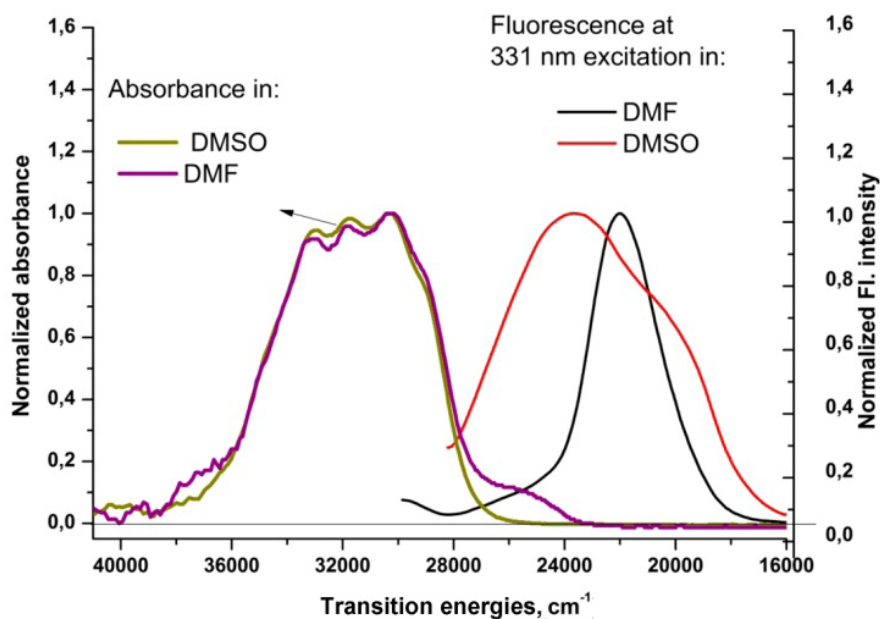
Fig. 3. Normalized absorption and emission spectra of HPQ.
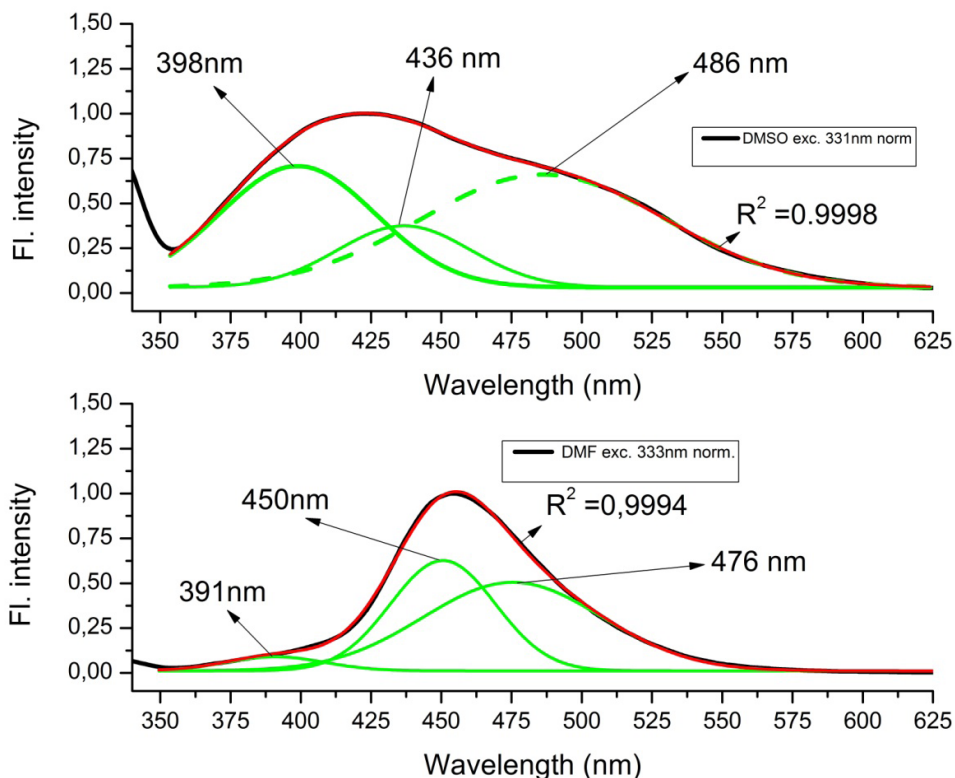
Fig. 4. Overlapping fluorescence spectral bands obtained by curve fitting of the observed fluorescence spectra of HPQ in DMSO and DMF.
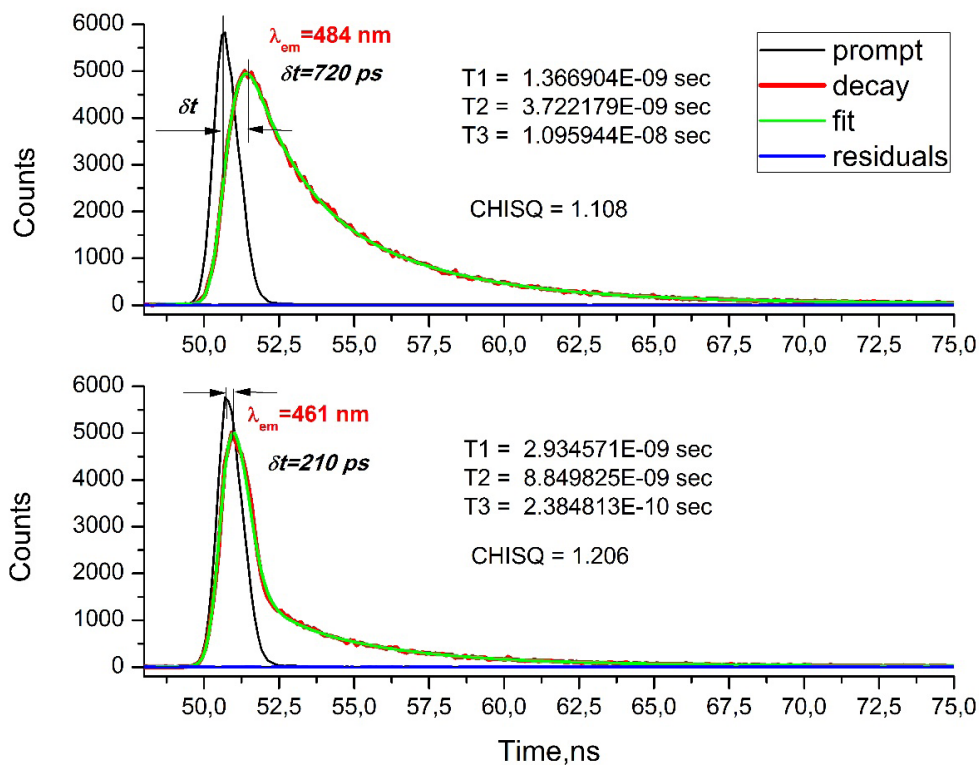
Fig. 5. Fluorescence emission decay curves and lifetimes for HPQ in DMF. Excitation at 365 nm.

be attributed to the excited tautomers **1*** and **3*** or/and **4*** resp. (see Tables 1 and 3).

Present fluorescence spectra seem to corroborate, in agreement with computational predictions, the presence of at least two different species in the first excited singlet state S_1. The difference in the bandshapes of the fluorescence spectra can well be attributed to different percentage distribution of the species in the two solvents, which are of different polarity and basicity. Decomposition of the fluorescence spectral curves of HPQ in DMSO and DMF (Fig. 4) suggests with high probability, that the emitting species are actually three. This is also clearly demonstrated by measurement of fluorescence lifetimes. The obtained results, observed as different behavior of decay curves from two levels of energy (Fig. 5) are indicative of at least two species, emitting from the S_1 level.

As the enol tautomer **1*** is computed as a shorter wavelength emitter than the respective keto-isomers **3*** and **4***, we may attribute the longer wavelength emissions, Fig. 4, to the keto-isomers. At longer emission wavelength, 484 nm, the decay curve is the result only from emission by keto-isomers and with high accuracy can be interpreted as nearly monoexponential with a lifetime of about 4 ns. At shorter emission wavelength (460 nm), the decay curve is the result of emissions from all 3 forms showing significant difference from monoexponential decay.

CONCLUSION

Joint computational and photophysical studies of HPQ provide a detailed picture of its internal molecular dynamics and provide a tool to assign the origin of observed light absorption and emission phenomena to specific isomeric species of the molecule.

REFERENCES

1. M. Gao, S. Li, Y. Lin, Y. Geng, X. Ling, L. Wang, A. Qin, B. Z. Tang, *ACS Sens. 1*, 179 (2016).
2. S. P. Anthony, *Chem. Asian J.*, **7**, 374 (2012).
3. X. B. Zhang, G. Cheng, W. J. Zhang, G. L. Shen, R. Q. Yu, *Talanta*, **71**, 171 (2007).
4. D. L. Williams, A. Heller, *J. Phys. Chem.*, **74**, 4473 (1970).
5. M. J. Frisch, G. W. Trucks, H. B. Schlegel, G. E. Scuseria, M. A. Robb, J. R. Cheeseman, G. Scalmani, V. Barone, B. Mennucci, G. A. Petersson, H. Nakatsuji, M. Caricato, X. Li, H. P. Hratchian, A. F. Izmaylov, J. Bloino, G. Zheng, J. L. Sonnenberg, M. Hada, M. Ehara, K. Toyota, R. Fukuda, J. Hasegawa, M. Ishida, T. Nakajima, Y. Honda, O. Kitao, H. Nakai, T. Vreven, J. A. Montgomery, Jr., J. E. Peralta, F. Ogliaro, M. Bearpark, J. J. Heyd, E. Brothers, K. N. Kudin, V. N. Staroverov, T. Keith, R. Kobayashi, J. Normand, K. Raghavachari, A. Rendell, J. C. Burant, S. S. Iyengar, J. Tomasi, M. Cossi, N. Rega, J. M. Millam, M. Klene, J. E. Knox, J. B. Cross, V. Bakken, C. Adamo, J. Jaramillo, R. Gomperts, R. E. Stratmann, O. Yazyev, A. J. Austin, R. Cammi, C. Pomelli, J. W. Ochterski, R. L. Martin, K. Morokuma, V. G. Zakrzewski, G. A. Voth, P. Salvador, J. J. Dannenberg, S. Dapprich, A. D. Daniels, O. Farkas, J. B. Foresman, J. V. Ortiz, J. Cioslowski, D. J. Fox, Gaussian, Inc., Wallingford CT, 2013.
6. J. Tomasi, B. Menucci, R. Cammi, *Chem. Rev.*, **105**, 2999 (2005).
7. C. R. Guido, D. Jaquemin, C. Adamo, B. Mennucci, *J. Chem. Theory Comput.*, **11**, 5782 (2015).
8. J. R. Lakowicz, Principles of Fluorescence Spectroscopy, 3rd ed., Springer, 2006.
9. C. L. Perrin, J. B. Nelson, *Annual Rev. Phys. Chem.*, **48**, 511 (1997).

ВИЖДАНИЯ ЗА ФОТОФИЗИКАТА НА ИЗОМЕРИ НА 2-(2'-ХИДРОКСИФЕНИЛ)-ХИНАЗОЛИН-4-ОН ВЪЗ ОСНОВА НА МОДЕЛИРАНЕ С ТФП (DFT) В ОСНОВНО S₀ И ВЪЗБУДЕНО S₁ СЪСТОЯНИЕ

Х. Канети, С. М. Бакалова*, И. П. Ангелов

Институт по органична химия с Център по фитохимия, Българска академия на науките,
1113 София, България

(Резюме)

2-(2'-хидроксифенил)-хиназолин-4-он (HPQ) е съединение, за което от дълго време се смята, че има възможност да проявява кето-енолна тавтомерия. Би трябвало да се очаква, че то притежава абсорбционен спектър характерен за тавтомерите, потенциално съществуващи в разтвор. Флуоресценцията също трябва да показва възможността за пренос на протон във възбудено електронно състояние, ESIPT. Противно на очакванията абсорбционните спектри на HPQ не показват тавтомерия директно, а наблюдаваната флуоресценция е относително слаба. По тези причини ние предприемаме допълнителни изследвания с помощта на теорията на функционала на плътността ТФП и зависимата от времето ТФП, както и експериментални изследвания, върху спектроскопските свойства на HPQ. Резултатите показват едновременното наличие на енолни и кето форми в разтвор както в основно, така и в първо възбудено синглетно състояние, както и наличието на суперпозиция от припокриващи се емисии.

Coordination of bis((dimethylphosphinyl)methyl)amine to copper(II). Synthesis and single-crystal structure of its mononuclear octahedral copper(II) complex

Zh. V. Georgieva[1], A. G. Ugrinov[2], R. P. Nikolova[3], B. L. Shivachev[3], S. Y. Zareva[1], S. G. Varbanov[4], T. D. Tosheva[4], G. G. Gencheva[1]*

[1] *Faculty of Chemistry and Pharmacy, Sofia University "St. Kliment Ohridski", 1164 Sofia, 1 J. Bourchier Blvd., Bulgaria*

[2] *Department of Chemistry and Biochemistry, North Dakota State University, Fargo, ND 58102, United States*

[3] *Institute of Mineralogy and Crystallography "Acad. Ivan Kostov", Bulgarian Academy of Sciences, Acad. G. Bonchev str., bl. 107, 1113 Sofia, Bulgaria*

[4] *Institute of Organic Chemistry with Center of Phytochemistry, Bulgarian Academy of Sciences, 1113 Sofia*

The synthesis and structural characterization of a mononuclear complex of bis((dimethylphosphinyl)methyl)amine, L with a composition $[CuL_2]Cl_2.3H_2O$ has been discussed in a comparison with series of copper(II) complexes in order to study the mode of the ligand coordination as a function of the electronic properties of the metal ion and the particular reaction conditions. All copper(II) coordination compounds of the titled ligand have been obtained as a result of its interaction with $CuCl_2.2H_2O$ at different M:L molar ratios in ethanol and were isolated as neutrals compounds containing different counter ions (Cl^-, AsF_6^-). The compound $[CuL_2]Cl_2.3H_2O$ crystallizes in orthorhombic *Fdd*2 space group with unit cell parameters a = 19.123(16), b = 21.657(16), c = 13.107(11) Å and Z = 8. Its crystal structure consists of complex $[Cu^{2+}L_2]^{2+}$ cations, chloride anions and water molecules. The L ligands are coordinated in a tridentate mode each of them forming two five-membered Cu-O-P-C-N rings. The Cu^{2+} in the CuO_4N_2-chromophores exhibits tetragonally compressed octahedral coordination.

Keywords: Cu^{2+} complex, tetragonally compressed octahedral coordination, bis((dimethylphosphinyl)methyl)amine.

INTRODUCTION

Among the essential elements, copper has an important role for the biological systems [1]. Many enzymes and proteins have coordinated copper ions and thus their active sites are formed [2]. The biological functions of copper containing proteins and enzymes involve electron transfer, dioxygen transport and control on processes of oxidation, reduction and disproportionation. The importance of copper transporters for the selective cellular uptake of the platinum based antitumor drugs was established [3, 4]. Drug transport, intracellular shuffling and export, carried out by the high-affinity copper transporters contribute cumulatively to the chemo-sensitivity of platinum drugs and thus for improvement of their mode of action.

Metallobiomolecules and in particular, copper biomolecules [5] can be considered as complicated coordination complexes whose active sites are constructed from one or more metal ions together with the donor atoms in their inner co-ordination sphere originating from the proteins and enzymes. The complexity of the biological systems makes the detailed study on their mechanism of action very difficult. An approach to circumvent the problem is to elucidate the structures and model mechanisms on simpler coordination compounds. Thus, in order to mimic the physicochemical properties of the metalloproteins numerous new simple coordination compounds have been synthesized.

The investigations on the coordination chemistry of copper(II) is stimulated by the construction of models for copper proteins [6]. An additional

_____

* To whom all correspondence should be sent:
E-mail: ggencheva@chem.uni-sofia.bg

challenge for the intensive studies in this field is to understand the factors which give rise to the seemingly infinite variety of distortions from regular stereochemistry observed for Cu(II) complexes [7–9]. The cooper compounds containing Cu^{2+} with its d^9 electron configuration are strongly affected by the Jahn–Teller effect [10–12]. The metal atom in the cooper(II) compounds display square-planar, square pyramidal, trigonal bipyramidal or octahedral coordination which due to the Jahn–Teller effect could be tetragonally compressed or elongated [13–16]. Very few of the Cu^{2+} complexes with regular square pyramidal and trigonal bipyramidal geometry are known as most of the complexes adopt geometries that are intermediate between these extremes [17].

Here we report the synthesis and the single crystal structure of a mononuclear Cu^{2+} complex of bis((dimethylphosphinyl)methyl)amine [18],
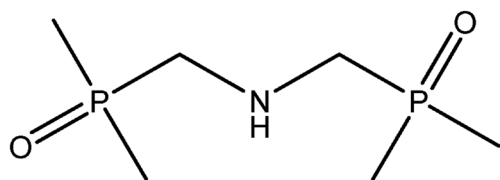
Scheme 1. Molecular structure of bis((dimethylphosphinyl) methyl)amine.

Scheme 1, with tetragonally compressed octahedral geometry and composition $[CuL_2]Cl_2.3H_2O$ (Fig. 1).

The ligand belongs to the group of aminophosphine oxides [19] and especially to functionalized nitrogen-containing tertiary phosphine oxides (AmPOs). The organophosphorus compounds, including AmPOs are extensively studied in the past years because of their various industrial applications and ability of the phosphorus substituents to regulate important cellular processes. It is proved already that the introduction of organophosphorus functionalities in simple synthons may afford useful substrates for the preparation of biologically active compounds [20]. AmPOs have additional N-containing functional groups that together with highly basic P=O groups and the substituents at the pentavalent phosphorus atom determine their special behavior in regard to coordination ability, flexibility, lipophilicity, etc. The diverse properties of the AmPOs are the basis for their application as molecular precursors to produce new polymeric materials, in catalytic organic reactions, in selective separation mostly for lanthanides and actinides, etc.. Due to their biological importance there has been growing interest in coordination chemistry [21, 22] of this class of ligands. Here, we discuss the mode of coordination of bis((dimethylphosphinyl) methyl)amine as a function of the copper(II) nature and the reaction conditions on the basis of a series complexes (Scheme 2).
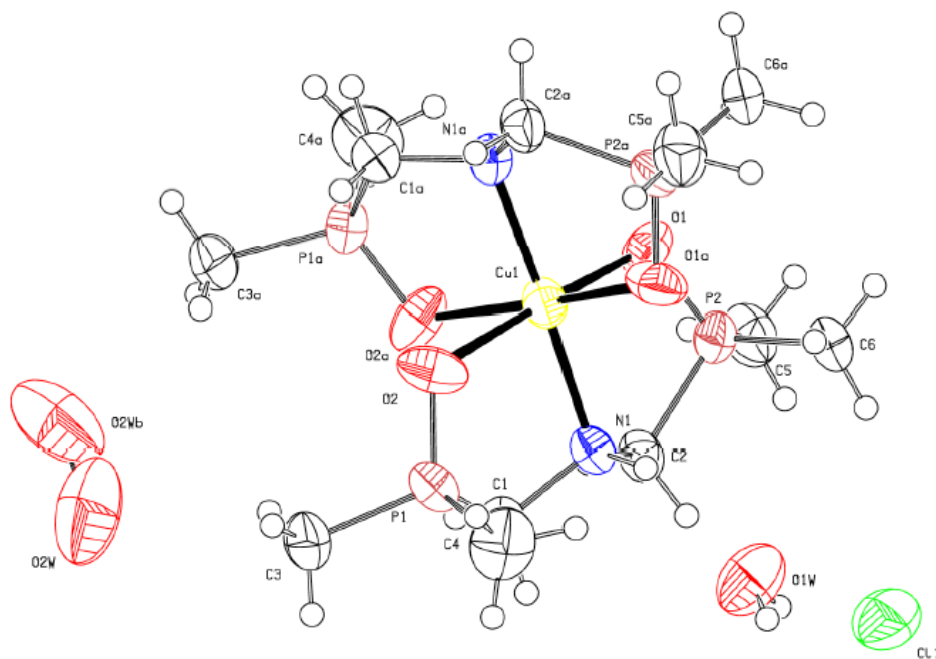
Fig. 1. ORTEP drawing of the molecular structure of the compound **2**. The thermal displacement ellipsoids are drawn at the 50% probability.
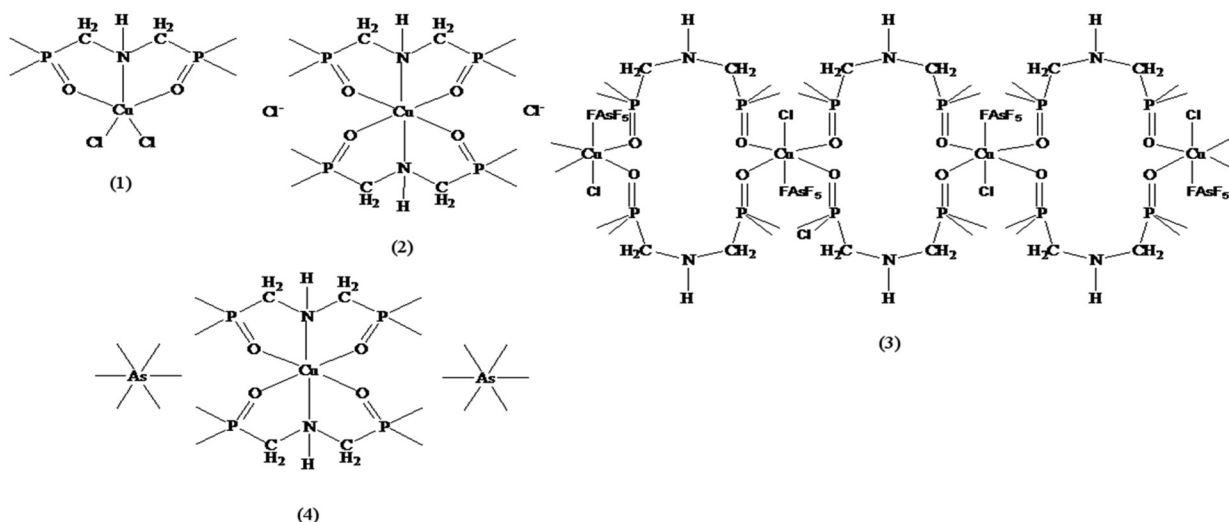
Scheme 2. A series of copper(II) complexes of bis((dimethylphosphinyl)-methyl)amine.

EXPERIMENTAL

Synthesis

The ligand bis((dimethylphosphinyl)methyl) amine was synthesized as described in the literature [18]. All other reagents were of analytical grade and were used without further purification and drying; $CuCl_2.2H_2O$ and $LiAsF_6$ (Fluka) and C_2H_5OH (Merck).

Synthesis of *[CuLCl_2]*, **1**: 0.0170 g (0.10 mmol) of $CuCl_2.2H_2O$ and 0.0381 g (0.19 mmol) L (L:Cu^{2+}=2) were dissolved each in 5 mL C_2H_5OH. Then the two solutions were mixed, stirred magnetically and heated (40 °C) for 3 hours. The complex was obtained as blue crystals by slow evaporation at room temperature for a week. *Anal. Calc. for* **1**, $C_6H_{17}NP_2O_2Cl_2Cu$ (MM = 331.60 g/mol); C%=21.73, H%=5.17, N%=4.22; *Found:* C%=21.74, H%=5.13, N%=4.23).

Synthesis of *[CuL_2]Cl_2.3H_2O*, **2**: 0.0085 g (0.05 mmol) of $CuCl_2.2H_2O$ was dissolved in 2 mL C_2H_5OH and 0.0394 g (0.2 mmol) of the ligand was dissolved in 5 mL C_2H_5OH (L:Cu^{2+}=4). Then, both solutions were mixed, stirred and heated at 60 °C for 4 hours. The complex was obtained as light blue crystals suitable for X-ray analysis after repeated re-crystallization in ethanol. Compound **2** crystallizes in orthorhombic *Fdd*2 space group with cell parameters a =19.123(16), b = 21.657(16), c =13.107(11) Å and Z = 8.

Synthesis of *{[Cu(L)ClAsF_6].H_2O}n*, **3**: An ethanol solution (3 mL) of $CuCl_2.2H_2O$ (0.0171 g, 0.1 mmol) was mixed with an ethanol solution (3 mL) of the ligand (0.0395 g, 0.2 mmol) (L:Cu^{2+}=2). Then the reaction mixture was stirred and heated at 50 °C for 1 hour. $LiAsF_6$ (0.0782 g, 0.4 mmol) was dissolved in 4 mL C_2H_5OH and then the solution was added to the initial mixture. A light blue powder was precipitated for a few minutes. The interaction was continued with stirring and heating (50 °C) for 2 more hours. The obtained precipitate was filtered while the solution was left for evaporation on air at room temperature. Dark blue crystals of a polymeric compound were obtained after repeated evaporation of the solvent. *Anal. Calc. for* **3**,$\{C_6H_{19}NP_2O_3ClF_6AsCu\}_n$ (MM(monomer) = 502.08 g/mol); C%=14,32, H%=3.81, N%=2.78; *Found:* C%=14.07; H%=3.73, N%=2.79.

Synthesis of *[CuL_2](AsF_6)_2.2H_2O*, **4**: $CuCl_2.2H_2O$ (0.0171 g, 0.1 mmol) was dissolved in 3 mL C_2H_5OH and 0.0395 g (0.2 mmol) of the ligand was dissolved in 5 mL C_2H_5OH. Then, both solutions were mixed (L:Cu^{2+}=2), stirred and heated at 50 °C for 1 hour. An amount of 0.0782 g (0.4 mmol) of LiAsF6 was dissolved in 4 mL C_2H_5OH and was added to the reaction mixture. A light blue powder precipitated after a few minutes (~4–5 min). The interaction was continued with stirring and heating (50 °C) for 2 more hours. The obtained complex was filtrated and recrystallized repeatedly from ethanol solution. *Anal. Calc. for* **4**, $C_{12}H_{38}N_2O_6P_4F_{12}As_2Cu$ (M=871.70 g/mol); C%=16.53 H%=4.39, N%=3.21; Found: C%=16.36; H%=4.15, N%=3.18.

Single-crystal XRD structural analysis

A light blue crystal of complex **2** suitable for X-ray analysis with size 0.50×0.48×0.20 mm^3 was selected for data collection at room temperature. The crystal was mounted on a Bruker SMART

X2S diffractometer using a monochromatic Mo-Kα ($\lambda = 0.71073$ Å) radiation from a micro-focus source and APEX-II CCD detector. Data collection, cell refinement and data reduction were performed using APEXII software [23]. SADABS-2014/5 (Bruker, 2014/5) was used for absorption correction [23]. The ratio of minimum to maximum transmission is 0.6538. The structure was solved by *ab-initio* methods using ShelXD and refined with the ShelXL [24]. All hydrogen atoms were placed on calculated positions. To refine the structure, the program SHELXL97 [24], version 2014/7 implemented in program OLEX2 [25] was used. Full-matrix least-squares refinement was carried out till the final refinement cycles converged to an $R = 0.0650$ and $wR(F^2) = 0.1457$ for all observed data. The OLEX software was applied to prepare the materials for publication. The crystallographic, X-ray data collection and refinement statistics for the compound are given in Table 1. Selected bond lengths and bond angles are summarized in Table 2 and hydrogen bonding interactions are given in Table 3. ORTEP diagram for the studied compound is shown on Fig. 1. The crystallographic data for **2** were deposited at the Cambridge Crystallographic Data Centre and allocated the deposition number CCDC 1831416. Copies of the data can be obtained, free of charge, on application to CCDC, 12 Union Road, Cambridge CB2 1EZ, UK; tel: +441223762910; fax: +441223336033; e-mail: deposit@ccdc.cam.ac.uk; http://www.ccdc.cam.ac.uk/deposit. The drawings were prepared using Mercury version 3.3 [26].

RESULTS AND DISCUSSION

Syntheses and crystallography

The ligand bis((dimethylphosphinyl)methyl) amine is well soluble in ethanol. All copper coordination compounds the synthesis we report here were obtained as a result of the interaction ligand (L) with $CuCl_2.2H_2O$ (M) at a different molar L:M ratio in ethanol (with traces of water). The complexes were isolated as neutral compounds with the counter ions (Cl^- or AsF_6^-). Complexes **1** and **2** were obtained solely from the interaction of the starting copper salt and ligand L with successively substitution of solvate (complex **1**) and Cl^- (complex **2**) ligands from Cu^{2+}-inner coordination sphere with one and

Table 1. Crystal data and structure refinement for **2**

Empirical formula	$C_{12}H_{38}Cl_2CuN_2O_7P_4$
Formula weight	580.10
Temperature/K	300.15
Crystal system	*orthorhombic*
Space group	*Fdd*2
a/Å	19.123(16)
b/Å	21.657(16)
c/Å	13.107(11)
α/° ≡ β/° ≡ γ/°	90
Volume/Å³	5428(8)
Z	8
ρ_{calc} g/cm³	1.420
μ/mm⁻¹	1.268
F(000)	2421.0
Crystal size/mm³	0.5 × 0.48 × 0.2
Radiation	MoKα ($\lambda = 0.71073$)
2θ range for data collection/°	5.684 to 50.048
Index ranges	$-22 \leq h \leq 22, -24 \leq k \leq 25, -15 \leq l \leq 15$
Reflections collected	12187
Independent reflections	2369 [$R_{int} = 0.1762$, $R_{sigma} = 0.1572$]
Data/restraints/parameters	2369/1/141
Goodness-of-fit on F²	0.953
Final R indexes [I>=2σ (I)]	$R_1 = 0.0650$, $wR_2 = 0.1278$
Final R indexes [all data]	$R_1 = 0.1092$, $wR_2 = 0.1457$
Largest diff. peak/hole / e Å⁻³	0.42/–0.56
Flack parameter	0.00(4)
CCDC number	1845615

Table 2. Geometrical parameters for the complex cation of the compound **2** (Å, °)

Bond Lengths			
Cu(1)–O(1)[1]	2.159(9)	P(1)–C(3)	1.786(12)
Cu(1)–O(1)	2.159(9)	P(1)–C(4)	1.781(12)
Cu(1)–O(2)	2.211(9)	P(2)–O(1)	1.505(7)
Cu(1)–O(2)[1]	2.211(9)	P(2)–C(5)	1.789(11)
Cu(1)–N(1)	2.026(8)	P(2)–C(6)	1.776(11)
Cu(1)–N(1)[1]	2.026(8)	P(2)–C(2)	1.829(11)
P(1)–O(2)	1.517(8)	N(1)–C(1)	1.502(14)
P(1)–C(1)	1.830(10)	N(1)–C(2)	1.481(12)
Bond Angles			
O(1)[1]–Cu(1)–O(1)	95.1(4)	O(2)–P(1)–C(4)	111.7(6)
O(1)[1]–Cu(1)–O(2)[1]	174.1(3)	C(3)–P(1)–C(1)	109.1(6)
O(1)[1]–Cu(1)–O(2)	174.1(3)	C(4)–P(1)–C(1)	107.3(6)
O(1)–Cu(1)–O(2)	90.0(3)	C(4)–P(1)–C(3)	108.0(7)
O(1)–Cu(1)–O(2)[1]	90.0(3)	O(1)–P(2)–C(5)	114.8(6)
O(2)[1]–Cu(1)–O(2)	85.1(4)	O(1)–P(2)–C(6)	111.9(5)
N(1)[1]–Cu(1)–O(1)[1]	89.1(3)	O(1)–P(2)–C(2)	106.6(5)
N(1)–Cu(1)–O(1)[1]	92.4(3)	C(5)–P(2)–C(2)	106.9(5)
N(1)[1]–Cu(1)–O(1)	92.4(3)	C(6)–(2)–C(5)	107.8(6)
N(1)–Cu(1)–O(1)	89.1(3)	C(6)–P(2)–C(2)	108.6(5)
N(1)[1]–Cu(1)–O(2)	90.7(3)	P(2)–O(1)–Cu(1)	108.7(5)
N(1)–Cu(1)–O(2)[1]	90.7(3)	P(1)–O(2)–Cu(1)	109.7(5)
N(1)[1]–Cu(1)–O(2)[1]	87.6(3)	C(1)–N(1)–Cu(1)	109.0(7)
N(1)–Cu(1)–O(2)	87.6(3)	C(2)–N(1)–Cu(1)	110.2(6)
N(1)[1]–Cu(1)–N(1)	177.7(5)	C(2)–N(1)–C(1)	113.7(8)
O(2)–P(1)–C(1)	108.1(5)	N(1)–C(1)–P(1)	108.5(7)
O(2)–P(1)–C(3)	112.5(6)	N(1)–C(2)–P(2)	108.4(7)

[1] 1-X, 1-Y,+Z

Table 3. Hydrogen bonds and weak C–H…O interactions (Å, °) in the crystal structure of **2**

D—H⋯A	d(D-H)	d(H-A)	d(D-A)	D-H-A
O(1W)—H(1WA)⋯O(2)[1]	0.85	1.97	2.807(12)	170.2
O(1W)—H(1WB) Cl(1)	0.85	2.33	3.135(11)	157.9
C(2)—H(2A) O(1W)[2]	0.97	2.54	3.477(16)	162.2

[1] 5/4-X,-1/4+Y,-1/4+Z; [2] -1/4+X, 3/4-Y,1/4+Z

two bis((dimethylphosphinyl)methyl)amine molecules (Scheme 2) for **1** and **2** respectively. Complex **1** was obtained from a comparatively concentrated reaction mixture (2×10^{-2} mol/L in respect of Cu^{2+}) at molar ratio M:L=1:1.9 (some insufficiency of L in respect to L:M = 2) for approximately 3 hours. Whereas complex **2** was prepared from a more diluted system ($5x10^{-3}$ mol/L in respect of Cu^{2+}) at molar ratio M:L=1:4 for a slightly longer period (~4 hours). The complexes **3** and **4** were obtain from the M:L=1:2 reaction system (concentration of $Cu^{2+} \sim 1\times10^{-2}$ mol/L) with a four-fold excess of AsF_6^-. Although AsF_6^- counter-anions exhibit very

weak coordinating tendencies towards transition metals, it was found that the competition between $[F-AsF_5]^-$ and Cl^- for the inner coordination sphere of copper(II) in the reaction system directs the mode of coordination of bis((dimethylphosphinyl)methyl) amine. Thus, the complexes **3** and **4** were isolated from the filtrate and from the powder of one and the same reaction system (Scheme 2).

Light blue crystals of *[CuL$_2$]Cl$_2$.3H$_2$O*, **2** suitable for X-ray analysis were obtained after repeated recrystallization from ethanol. Crystallographic data of complex **2** are summarized in Table 1. The data for the bond lengths and angels are listed in

Table 2. Molecular structure and hydrogen bonds together with weak C–H…O interactions (Table 3) are shown in Figs. 1 and 2. The Cu^{2+} ion is situated in a special crystallographic position and is surrounded by two symmetrically equivalent bis((dimethylphosphinyl)methyl)amine molecules (L) to form complex $[CuL_2]^{2+}$ cation. The organic molecules are bonded as a tridentate ligands through secondary amino group and two tertiary phosphine oxide donors thus forming two five-membered rings. The Cu–O bond lengths are not equal and differ with 0.051(1) Å (Cu-O1 = 2.159 (9) and Cu-O2 = 2.211(9) Å. As it is expected the Cu–N bonds are shorter than the Cu–O ones being 2.026 (8) Å. The O–Cu–O angles vary between 85.1(4)° to 95.1(4)° and only O(1)–Cu–O(2) in the coordination plane is 90.0(3)°. The N-Cu-O angles differ in the range 87.6(3)° to 92.(4)° while N-Cu-N is 177.7(5)°. Thus the octahedral coordination geometry of the complex cation can be described as axially compressed octahedra. The distance Cu-Cl (Cl⁻) of 6.270 Å shows that the chloride ions are in the outer coordination sphere of the complex **2**. The Cl⁻ ions together with the water molecules and O(2) from the coordinated P=O group build up the hydrogen-bonding network (Table 3).

Mode of coordination of bis((dimethylphosphinyl) methyl)amine

The ligand bis((dimethylphosphinyl) methyl)amine has polydentate nature due to its three func-tional donor groups, namely a secondary amino group and two tertiary phosphine oxide groups. The mode of coordination has been studied by IR spectra analysis. The solid state IR spectral data about the ligand and its copper(II) complexes are represented in Table 4. The assignments of the bands are made in accordance with IR data and NCA published [27, 28] for transition metal complexes of aminomethyl-phosphine oxides.

In order to assess the mode of coordination the analysis of the IR data has been done on the basis of the IR spectrum of compound **2** since X-ray single-crystal structure data for **2** is available. In this spectrum as well as in the spectra of the compounds **1** and **4** (Table 4) all bands concerning the second-ary amino group and phosphoryl groups are affected from the coordination. The bands for NH-stretching and CNH deformation together with P=O stretch-ing vibrations are shifted to lower frequencies. Only in the spectrum of compound **3**, the bands for NH-stretching and CNH deformation are poorly affected and this indicates only for participation of the amino group in hydrogen bonding formation. In addition, the new bands assigned to Cu-O, Cu-N as well Cu-Cl vibration modes prove the composition of in-ner coordination sphere of the complexes. These results together with the elemental analysis data show that the interaction between the $CuCl_2.2H_2O$ and L in ethanol solution proceeds with consist-ent coordination of two bis((dimethylphosphinyl) methyl)amine molecules. In the complex **1**, the li-gand is coordinated as a tridentate O,N,O ligand
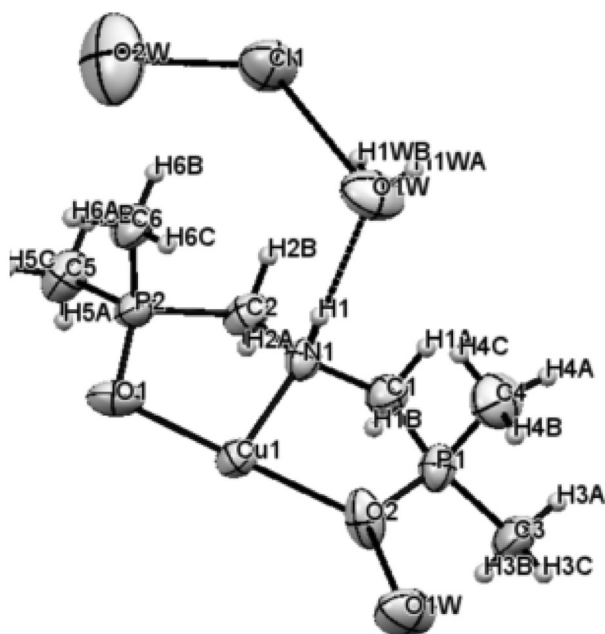
Fig. 2. An asymmetric unit with hydrogen-bonding in the crystal structure of **2**.

Table 4. Selected frequencies from the infrared spectra of the free ligand and its Cu^{2+} complexes

Bands, cm^{-1}	Compounds				Assignment
	[CuLCl$_2$]	[CuL$_2$]Cl$_2$.3H$_2$O	{[Cu(L)ClAsF$_6$].H$_2$O}n	[CuL$_2$](AsF$_6$)$_2$.2H$_2$O	
L	1	2	3	4	
		3405br	3423br	3430br	$\nu^{as,a}$ (H$_2$O)
3317s	3139s	~3227w Overlapped from $\nu^{as,a}$ (H$_2$O)	3265	3113s	ν(NH)
2956 2925 2870 2850 2811 2791	3002 2979 2967 2931 2911 2898	2987 2916	2989 2919	3016 2979 2926 2902	$\nu^{as,a}$ (CH$_3$, CH$_2$)
		1662	1655 1638	1630	δ(H$_2$O)
1560vw 1545vw	1460s	1543w 1489w	1560w 1548w	1487w 1458w	δ(CNH)
1458 1446 1436 1428 1405 1378 1364	1419 1411 1402 1392	1422 1392	1430 1420	1425 1422 1403	δ(CH$_3$,CH$_2$)
1332 1317 1303 1294 1286 1258 1236	1321 1314 1304 1291 1261	1301 1272	1326 1311 1304	1238 1216	δ(P-CH$_3$)
1161s 1119m 1077 1042	1104 1090 1067	1138 1100 1039	1105 1089 1040	1143 1097 1087	ν(P=O)
954 924 906 892	974 953 915 905	947 905 866	955 924 905 865	957 939 902 862	ρ(P-CH$_3$)
755 750 734 724	762 743	758 745 733	764 747 699	697 681	δ(P-CH$_2$)
	509	484	520 498	518	ν(Cu-O)
	473	457 447		465	ν(Cu-N)
	410		447		ν(Cu-Cl)
			697	699	ν_3(AsF$_6$)
			574		ν(Cu-F-AsF$_5$)

257

without displacement of the two Cl^- ions. In the complex **2**, the second L molecule is coordinated by displacing of the Cl^- and as a result the formation of a CuO_4N_2-chromophore with compressed octahedral coordination is observed. In the presence of AsF_6^-, the complicated equilibrium is directed toward a substitution of Cl^- with AsF_6^-. As a result, the displacement of Cl^- with AsF_6^- produces two different complexes in which the ligand in addition of the tridentate coordination is also coordinated with two the phosphoryl O-donors. Despite the preferred N-containing donor functional groups from Cu^{2+}, in all complexes presented here, the ligand is bonded only through (compound **3**) or with the participation of phosphoryl O-donor atoms (compounds **1**, **2**, **4**). The determined protolytic constant (pK_a) of 2.54 for the ligand [18] proves the low basicity of the nitrogen donor. The decreased electron density around the nitrogen atom in the molecular structure of the ligand is a consequence of the electronegative effects of the phosphoryl groups. This results in a comparatively equal affinity of these two donor functional groups to copper(II). The structure of the complexes is additionally stabilized from the formation of chelate rings.

CONCLUSION

A series of copper(II) coordination compounds has been synthesized with a ligand belonging to the family of tertiary phosphine oxides functionalized with secondary amino groups. The complexes were obtained from the interaction of the ligand with copper(II) in ethanol solution in the presence of Cl^- and AsF_6^- as counterion. The investigation on the structures of the complexes was done on the basis of X-ray data for the complex with composition $[CuL_2]Cl_2.3H_2O$, IR spectra and elemental analysis. The studied ligand as a chelating ligand, coordinates by formation of two five-membered N,O-chelate rings in mononuclear complexes or as a bridging O,O-linker between metal ions in polynuclear structures.

REFERENCES

1. R. N. Mukherjee, *Indian J. Chem.*, **47A**, 2175 (2003).
2. E. Bouwman, W.L. Driesse, J. Reedijk, *Coord. Chem. Rev.*, **104**, 143 (1990).
3. S. B. Howell, R. Safaei, C. A. Larson, M. J. Sailor, *Mol. Pharmacol.*, **77**, 887 (2010).
4. T. C. Johnstone, K. Suntharalingam, S. J. Lippard, *Chem Rev.*, **116**, 3436 (2016).
5. U. Ryde, M. H. M. Olsson, K. Pierloot, in: Theoretical Biochemistry – Processes and Properties of Biological Systems, Leif A. Eriksson (ed.), vol. 9, 1, Elsevier, Amsterdam, 2001.
6. A. J. Alabdali, F. M. Ibrahim, *Journal of Applied Chemistry*, **6**, 60 (2014).
7. M. Melník, M. Kabešová, L. Macášková, C. E. Holloway, *J. Coord. Chem.*, **45**, 31 (1998).
8. M. Melník, M. Kabešová, L. Macášková, C. E. Holloway, *J. Coord. Chem.*, **50**, 117 (2000).
9. M. Melnik, M. KabeSova, M. Dunaj-JurEo and C.E. Holloway, *J. Coord. Chem.*, **41**, 35 (1997).
10. T. Chaudhary, J. Khamar, P. Chaudhary, V. Chaudhary, M. Barot, Dh. J. Sen, *Journal of Drug Discovery and Therapeutics*, **3**, 9 (2015).
11. J. Echever, E Cremades, A. J. Amorosob, S. Alvarez, *Chem. Commun.*, 4242 (2009).
12. P. K. Olshin, O. S. Myasnikova, M. V. Kashina, A. O. Gorbunov, N. A. Bogachev, V. O. Kompanets, S. V. Chekalin, S. A. Pulkin, V. A. Kochemirovsky, M. Yu. Skripkin, A. S. Mereshchenko, *Chemical Physics*, **503**, 14 (2018).
13. K. Hegetschweiler,V. Gramlich, M. Ghisletta, H. Samaras, *Inorg. Chem.*, **31**, 2341 (1992).
14. Z. D. Matovic, B. Ristic, M. Joksovic, S. R. Trifunovic, *Trans. Met. Chemistry*, **25**, 720 (2000).
15. Z. Mazej, I. Arcon, P. Benkic, A. Kodre, A. Tressaud, *Chem. Eur. J.*, **10**, 5052 (2004).
16. G. A. McLachlan, G. D. Fallon, R. L. Martin, L. Spiccia, *Inorg. Chem.*, **34**, 254 (1995).
17. M. A. Halcrow, *Dalton Trans.*, 4375 (2003).
18. S. V. Arbanov, T. Tosheva, E. Russeva, Phosphorus, Sulfur, and Silicon and the Related Elements, **127**, 27 (1997).
19. E. V. Goud, A. Sivaramakrishna, K. Vijayakrishna, *Top Curr. Chem. (Z)*, **375**, 10 (2017).
20. S. E. Denmark, J. Fu, D. M. Coe, Xiping Su, Norman E. Pratt, B. D. Griedel, *J. Org. Chem.*, **71**, 1513 (2006).
21. V. Vassileva, G. Gencheva, E. Russeva, S. Varbanov, R. Scopelliti, E. Tashev, *Inorg. Chim Acta*, **358**, 3671 (2005).
22. A. Bogomilova, M. Günther, Ernst Wagner, G. Hägele, K. Troev, *J. Coord. Chem.*, **65**, 1093 (2012).
23. Bruker (2014/5). SADABS-2014/5 Madison, Wisconsin, USA; Bruker (2013). APEX2 and SAINT. Bruker AXS Inc., Madison, Wisconsin, USA.
24. G. M. Sheldrick, *Acta Cryst.*, **C71**, 3 (2015).
25. O. V. Dolomanov, L. J. Bourhis, R. J. Gildea, J. A. Howard, H. Puschmann, *J. Appl. Cryst.,* 42, 339 (2009).
26. C. F. Macrae, I. J. Bruno, J. A. Chisholm, P. R. Edgington, P. McCabe, E. Pidock, L. Rodriguez-Monge, R. Taylor, J. Van de Streek, P. A. Wood, *J. Appl. Crystallogr.*, **41**, 466 (2008).
27. N. Trendafilova, I. Georgieva, G. Bauer, S. Varbanov, N. Dodoff, *Spectrochimica Acta Part*, **A** **53**, 819 (1997).
28. K. Nakamoto, Infrared and Raman Spectra of Inorganic and Coordination Compounds, Part B, 5th ed., Wiley, New York, 1997.

КООРДИНАЦИЯ НА БИС((ДИМЕТИЛФОСФИНИЛ)МЕТИЛ)АМИН КЪМ МЕД(II). ПОЛУЧАВАНЕ И КРИСТАЛНА СТРУКТУРА НА МОНОЯДРЕН ОКТАЕДРИЧЕН КОМПЛЕКС НА МЕД(II)

Ж. В. Георгиева[1], А. Г. Угринов[2], Р. П. Николова[3], Б. Л. Шивачев[3], С. Й. Зарева[1], С. Г. Върбанов[4], Т. Д. Тошева[4], Г. Г. Генчева[1]*

[1] *Факултет по химия и фармация, СУ „Св. Кл. Охридски", 1164 София, Дж. Баучер 1, България*

[2] *Факултет по химия и биохимия, Държавен университет на Северна Дакота, 58102 Фарго, САЩ*

[3] *Институт по минералогия и кристалография „Акад. Иван Костов", Българска академия на науките, ул. „Акад. Г. Бончев", бл. 107, 1113 София, България*

[4] *Институт по органична химия с Център по фитохимия, Българска академия на науките, 1113 Sofia*

(Резюме)

Получаването и структурата на моноядрен комплекс на бис((диметилфосфи-нил)метил)амин, L, със състав $[CuL_2]Cl_2.3H_2O$, са обсъдени в сравнение със серия мед(II) комплекси на този лиганд, с цел да бъде изучен начина на координация на лиганда в зависимост от природата на металния йон и конкретните реакционни условия. Всички комплекси са получени от взаимодействието на лиганда с $CuCl_2.2H_2O$ в етанол при различни M:L молни съотношения и са изолирани като неутрални съединения с противойоните Cl^-, AsF_6^-. Комплексът $[CuL_2]Cl_2.3H_2O$ кристализира в орторомбична *Fdd*2 пространствена група с параметри на елементарната клет-ка $a = 19.123(16)$, $b = 21.657(16)$, $c = 13.107(11)$ Å и $Z = 8$. Кристалната структура се състои от комплексни катиони със състав $[Cu^{2+}L_2]^{2+}$, два хлоридни аниона и три водни молекули. Лигандите L се координират като тридентатни, като всеки от тях образува по два петчленни Cu-O-P-C-N хелатни пръстена. Cu^{2+} в комплекса е с тетрагонално деформирана октаедрична координация.

4-Methylquinolinium hydrogensquarate – crystal structure and spectroscopic elucidation

S. Kotov[1]*, H. Mayer-Figge[2], S. Zareva[3]

[1] University "Prof. Dr. As. Zlatarov", Bourgas, Bulgaria
[2] Lehrstuhl für Analytische Chemie, Ruhr-Universität Bochum, Universitätsstraße 150, 44780 Bochum, Germany
[3] University of Sofia, Faculty of Chemistry, Department of Analytical Chemistry, Sofia 1164, Bulgaria

4-Methylquinolinium hydrogensquarate (**1**) has been synthesized, and its structure and spectroscopic properties have been elucidated by means of single crystal X-ray diffraction, linear-polarized solid state IR-spectroscopy, UV-spectroscopy, ^{1}H-NMR, TGA, DSC, DTA and positive and negative ESI-MS. Quantum-chemical calculations were used to obtain the electronic structure, vibrational data and electronic spectrum of the target compound. The effects of N-protonation on the optical and magnetic properties were estimated by comparing the data of the protonated and neutral compound.

Keywords: 4-methylquinolinium hydrogensquarate, crystal structure, solid-state linear polarized IR-spectroscopy, UV-spectroscopy, quantum chemical calculations, ^{1}H-NMR.

INTRODUCTION

Quinolinium salts are a class of very important synthetic compounds. Similarly to other heteroarenium salts, they contain cyclic nitrogen atom with formal positive charge and lone electron pair bound to proton, alkyl, aryl or other organic fragments. Some representatives of this class are known to possess valuable physiological properties [1] such as anti-microbial, anti-tumor, hypotensive, ganglion-blocking ones, *etc*. Moreover, quinolinium salt fragments are included in the molecular structures of a number of polymethine dyes [2]. Certain quinolinium derivatives were found to act as plant growth regulators [3]. Recently, N-butyl-6-methylquinolinium salt was reported to be successfully applied as ionic liquid in dye-sensitized solar cells [4]. In another study, Engel *et al.* [5] have demonstrated generation of intramolecular photo-induced electron transfer in zwitterionic quinolinium salts, depending on the type of substituents, attached to the quinoline moiety. These interesting properties of the quinolinium salts, and previous publications in this field [6, 7] prompted us to synthesize and explore the properties of 4-methylquinolinium hydrogensquarate as a potential material for the synthesis of new stilbazolium-type salts. The latter possess extended π-conjugated system with very large second-order nonlinear optical (NLO) susceptibilities. This has attracted a lot of scientific attention, due to the potential of the salts for use in electro-optic modulation [8], frequency conversion [9] and THz-wave generation and detection [10]. Todorova *et al.* have published structural and spectroscopic elucidation of a new stilbazolium dye with enlarged or conjugated system, which was synthesized by *Knoevenagel*-type condensation between 4-mehtylquinolinium iodide and the 4-dimethylaminonaphthaldehyde [11].

Squaric acid (H_2Sq) represents an attractive template for generating tightly hydrogen-bonded self-assemblies from polarizable cations in general, and basic amino acids in particular. During the last 15 years, series of non-centrosymmetric crystals were synthesized, isolated, and spectroscopically and structurally elucidated by means of single crystal X-ray diffraction studies. Squaric acid as a strong organic acid gives rise to stabilized hydrogensquarate (HSq^-) anion and squarate dianion (Sq^{2-}), which allows for the control of their self-assembly in crystals and for tuning their spectroscopic, optical and nonlinear-optical properties. New structural motifs of squaric acid derivatives of amino acids,

---

amino acid amides and diamides were previously described by Kolev and co-workers [12–21] and other authors [22–30].

Therefore it seems important to expand the scope of these studies by elucidating the structural and spectroscopic properties of quinolinium salts of squaric acid. To this purpose, the target compound, 4-methylquinolinium hydrogensquatate was synthesized, according to Scheme 1, purified and further characterized. The present investigation is a continuation of systematic studies on the protonation and coordination capabilities of various substituted heterocycles [31–37]. Now we report the synthesis as well as the spectroscopic and structural elucidation of novel 4-methylquinolinium hydrogensquarate (**1**), both in solution and in solid-state by using single crystal X-ray diffraction, ^{1}H-NMR, positive and negative ESI mass spectrometry, UV-spectroscopy, conventional and linear polarized IR-spectroscopy, and the TGA and DSC. Quantum-chemical calculations at the DFT and MP2 levels of theory with the 6-31++G** basis set were employed for predicting and supporting the experimentally observed optical properties of the compounds studied. Regardless of the number of published studies on different substituted quinoline derivatives, crystallographic data, concerning 4-methylquinolinium salts are rare. Ten structures of cobalt, copper, ruthenium and osmium complexes [38–46] and only one structure of the salt have been reported so far such as 4-methylquinolinium chloro-trioxo-chromium(vi) complex [47].

The structure of 4-methylquinolinium hydrogensquarate is outlined below (Scheme 1):
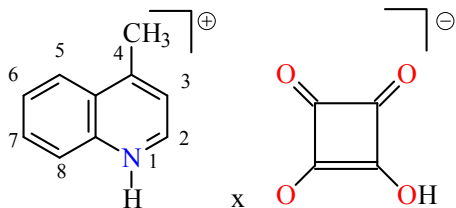
Scheme 1. Chemical diagram of the 4-methylquinolinium hydrogensquarate (**1**).

EXPERIMENTAL

Methods

The *X-ray diffraction* intensities were measured in the w scan mode on a Siemens P4 diffractometer equipped with Mo *Kα* radiation (λ = 0.71073 Å θ_{max} = 25°). The structure was resolved by direct methods and refined against F^2 [48, 49]. *An ORTEP plot* illustrates the anion and cation moieties, *ADP* are at the 50% probability level. Relevant crystallographic data and refinement details are presented in Table 1. Both the conventional and polarized IR-spectra were measured on a Thermo Nicolet 6700 FTIR-spectrometer (4000–400 cm^{-1}, 2 cm^{-1} resolution, 200 scans). *Non-polarized solid-state IR spectra* were recorded using the KBr pellet technique. The oriented samples were obtained as a colloid suspension in a nematic liquid crystal ZLI 1695 (Merck, Germany). The theoretical approach, the experimental technique for preparing the samples, the procedures for polarized IR-spectra interpretation, and the validation of this new linear-dichroic infrared (IR-LD) orientation solid-state method for accuracy and precision have previously been published by Ivanova *et al*. [50]. The influence of the liquid crystal medium on the peak positions and integral absorbance of the guest molecule bands, the rheological model, the nature and balance of the forces in the nematic liquid crystal suspension system, and the morphology of the suspended particles were also discussed by Ivanova, *et al*. [50–53].

The positive and negative ESI mass spectra were recorded on a Fisons VG Autospec instrument. *Ultraviolet (UV-) spectra* were recorded on Tecan Safire Absorbance/Fluorescence XFluor 4 V 4.40 spectrophotometer operating between 190 and 900 nm, using acetonitrile as solvent (Uvasol, Merck) at a concentration of $2.5.10^{-5}$ M, and 0.0921 cm quartz cells.

Quantum chemical calculations were performed with GAUSSIAN 98 program packages [54]. The output files were visualized by means of the ChemCraft program [55]. The geometry of protonated form of the compound was optimized at two levels of theory: second-order Moller-Pleset perturbation theory (MP2) and density functional theory (DFT) using the 6-31++G** basis set. The DFT method employed is B3LYP, which combines Becke's three-parameter non-local exchange function with the correlation function of Lee, Yang and Parr. The absence of the imaginary frequencies as well as of negative eigenvalues of the second-derivative matrix confirmed that the stationary points correspond to minima of the potential energy hypersurfaces. The calculations of vibrational frequencies and infrared intensities were checked to establish which level of performed calculations are in good agreement with the obtained experimental data. The B3LYP/6-31++G** data were presented for above-discussed modes, where a modification of the results using the empirical scaling factors 0.9614 was made to achieve better correspondence between the experimental and theoretical values.

The *thermal analyses* were performed in the 300–500 K range on a Differential Scanning Calorimeter

Table 1. Crystal and refinement data for (**1**)

Empirical formula	$C_{14}H_{11}NO_4$
Formula weight	257.24
Temperature (K)	293(2)
Wavelength (Å)	0.71073
Crystal system, space group	Triclinic, $P\bar{1}$
Unit cell dimensions	$a = 8.0666(16)$Å $\alpha = 87.97(3)°$
	$b = 8.5919(17)$ Å $\beta = 77.46(3)°$
	$c = 9.7079(19)$Å $\gamma = 66.34(3)°$
Volume (Å^3)	600.6(2)
Z	2
Calculated density (Mg·m^{-3})	1.423
Absorption coefficient (mm^{-1})	0.106
F(000)	268
Crystal size (mm)	$0.45 \times 0.43 \times 0.38$
θ range for data collection	$2.15 \leq \theta \leq 25.27$
hkl indices	$0 \leq h \leq 6, -8 \leq k \leq 10, -11 \leq l \leq 11$
Reflections collected / unique	1875/1716, R(int) = 0.0468
Absorption correction	multi-scan
Goodness-of-fit on F^2	1.022
Final R indices [I>2σ (I)]	R1 = 0.0696, wR2 = 0.1525
R indices (all data)	R1 = 0.1618, wR2 = 0.1977
max./min. res. (e·A^{-3})	0.221/ –0.280

Perkin-Elmer DSC-7, and a Differential Thermal Analyzer DTA/TG (Seiko Instrument, model TG/DTA 300). The *elemental analysis* was carried, out according to the standard procedures for C and H (as CO_2, and H_2O) and N (by the Dumas method).

Synthesis

4-Methylquinolinium hydrogensquarate (**1**) was synthesized by the following procedure: Squaric acid 342 mg (3 mmol) was dissolved in 50 ml distilled water. 435 mg of 4-methylquinoline (3 mmol) dissolved in 10 ml methanol were added dropwise to the aqueous solution by continuous stirring at room temperature for 6 h. After complete dissolution, the reaction mixture was set aside to crystallize for two weeks. The product was then purified by multiple recrystallizations from distilled water, and was finally obtained in 85% yield. Crystals suitable for X-ray diffraction studies were grown by slow evaporation from a mixture of water- methanol (1:1 *v/v*). After several weeks, colorless crystals were isolated, filtered and dried at room temperature. (Found: C, 65.4; H, 4.3; N, 5.4; [$C_{14}H_{11}NO_4$] calcd.: C, 65.4; H, 4.3; N, 5.40%). The strongest signal in the positive ESI mass spectrum corresponded to the peak at *m/z* 144.62 which represents singly-charged cation [$C_{10}H_{10}N$]$^+$ with a molecular weight of 144.20. The

TGA and DSC data recorded within the temperature range of 300–500 K showed that solvent molecules were not incorporated in the crystal structure of the target compound.

RESULTS AND DISCUSSION

Crystal structure of (1) and molecular geometry of the 4-methylquinolinium cation

Compound (**1**) crystallizes in the centrosymmetric space group $P\bar{1}$. The ORTEP diagram of the asymmetric unit is given in Fig. 1. The structure consists of infinite layers (Fig. 2), formed by means of intermolecular $N^+H…O=C_{(Sq)}$ hydrogen bonds of length 2.752 Å between the cations and anions. The hydrogensquarate moieties form stable dimers, which is a typical structural motif in the crystals with differently substituted pyridinium counter ions [34–36] *via* strong hydrogen $_{(Sq)}OH…O=C_{(Sq)}$ bonds (2.595 Å) (Fig. 2). In the unit cell, the two cations are disposed in a co-planar manner (Fig. 2), thus leading to a co-linear orientation of the out-of-plane (*o.p.*) normal modes of the quinoline-fragment (see below). The cation is effectively flat with a dihedral angle between the planes of the fused aromatic rings of only 0.8(2)°. The geometrical parameters of
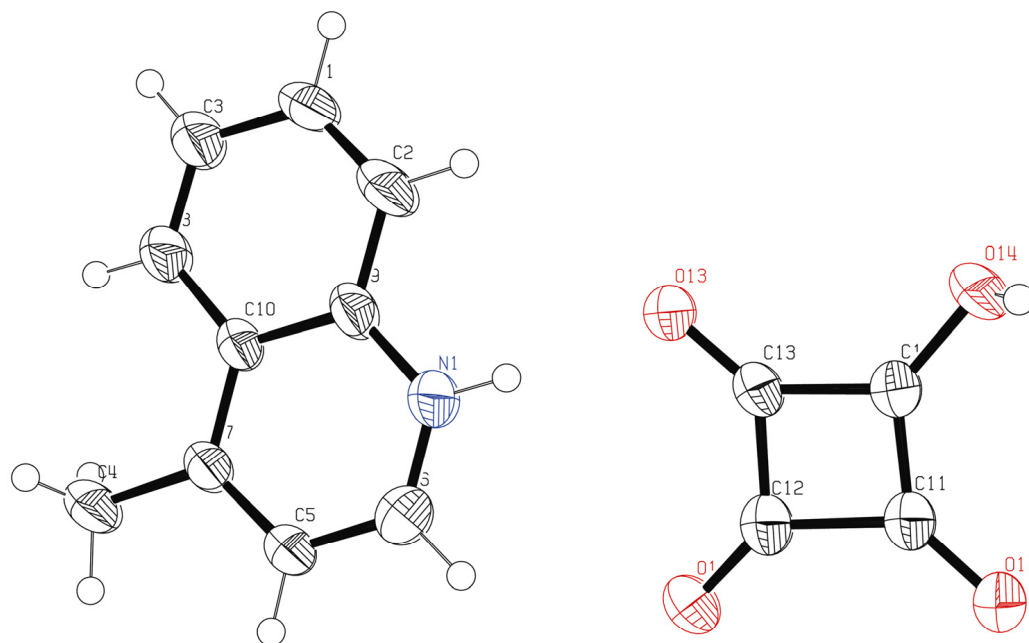
Fig. 1. The molecular structure of (**1**). Displacement ellipsoids are drawn at the 50% probability level.

(a)   (b)   (c)
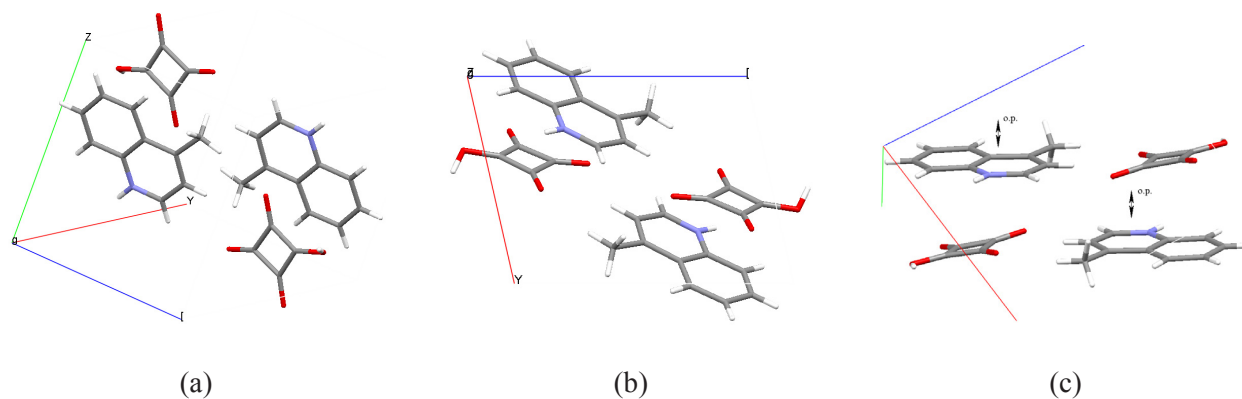
Fig. 2. Unit cell (a), view along *b*-axis (b) and visualization of the direction of the out-of-plane normal modes (c) of the 4-methylquinoline fragment obtained by group analysis.

the cationic moiety lie within the range of the previously reported salt [47].

The calculated electronic structure of the protonated 4-methylquinoline correlated well with the experimentally obtained structure. The calculations at the approximation used generated a structure (Fig. 3), with geometry parameters differing from the experimental values by maximum values of 0.021 Å and 1.6(3)°. Therefore, a very good coincidence between the experimental and calculated values exists.

Electronic spectra

The UV-vis spectrum of (**1**) in acetonitrile is depicted in Fig. 4. According to literature data, the electronic spectrum of the neutral form is characterized by three bands within the 265–275 nm, 300–305 nm and 310–315 nm ranges, depending on the solvent type. The corresponding ε-values were, approximately, 4000, 2300 and 2100 l.mol^{-1}.cm^{-1}, respectively [57]. The effect of protonation led to a hypsochromic shift of the discussed maxima.
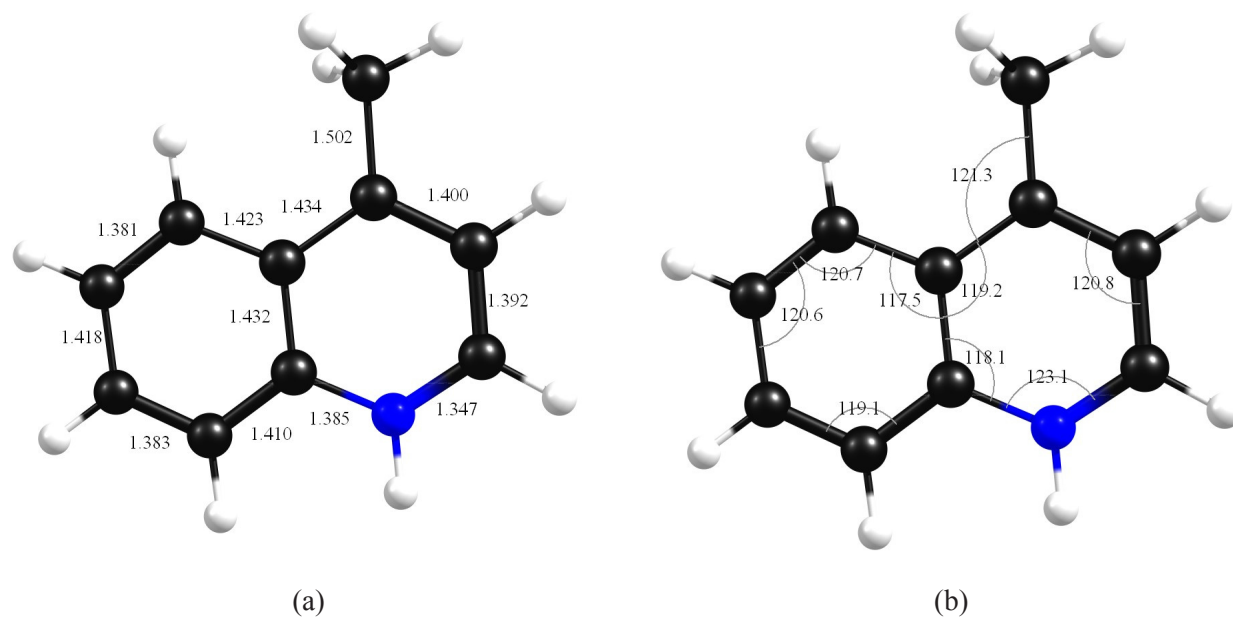
Fig. 3. Predicted geometry parameters of protonated 4-methylquinoline, the bond lengths are given in [Å] (a), bond angles in [°] (b), respectively.

The corresponding values amounted to 238 nm (ε = 4467 l.mol^{-1}.cm^{-1}), 254 nm (ε = 2231 l.mol^{-1}.cm^{-1}) and 277 nm (ε = 2000 l.mol^{-1}.cm^{-1}). The low intensity bands at about 310 nm with ε value of 1000 l.mol^{-1}.cm^{-1} corresponds to hydrogensquarate species.

The experimentally observed data correlate well with the theoretically predicted electronic spectra of protonated 4-methylquinoline. The observed absorption bands were 235 nm (coefficient of the probability of the transition, f = 0.0330), 260 nm (f = 0.0610) and 280 nm (f = 0.0098), respectively. The differences between the theoretically predicted and experimentally observed data obtained were less than 5 nm. These results suggest that the N-protonation leads to a partial charge re-distribution within the 4-methylquinoline molecule (Fig. 4).
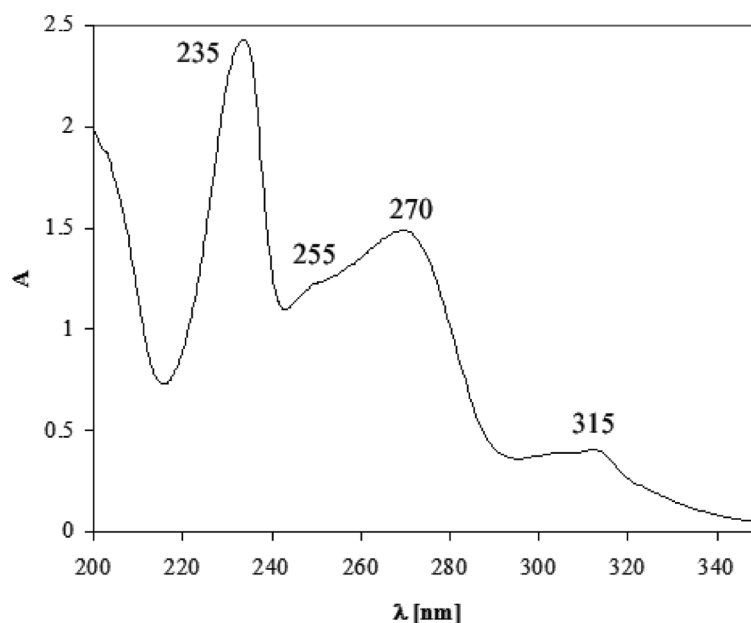
Fig. 4. UV-Vis spectrum of (**1**) in acetonitrile at concentration 2.5.10^{-4} mol/l.

The theoretical data indicate that the structural shift is predominantly localized in the conjugated plane and that the groups, not belonging to the conjugated plane do not change significantly (Fig. 5).

IR-spectroscopic data

The IR-spectroscopic elucidation of (**1**) was performed by comparing the experimental IR-char-acteristics (Fig. 6) with the corresponding theoretical vibrations of protonated 4-methylquinoline (Fig. 7).

The experimental IR-spectrum of (**1**) was characterized by a broad absorption band within the 3000–1900 cm^{-1} region, corresponding to overlapped $\nu_{OH(Sq)}$ and ν_{N^+H} stretching vibrations (Fig. 6). The last vibration was theoretically predicted at 3576 cm^{-1} (Fig. 7), but the participation of the N$^+$H group in intermolecular hydrogen bonding leads

(a)   (b)
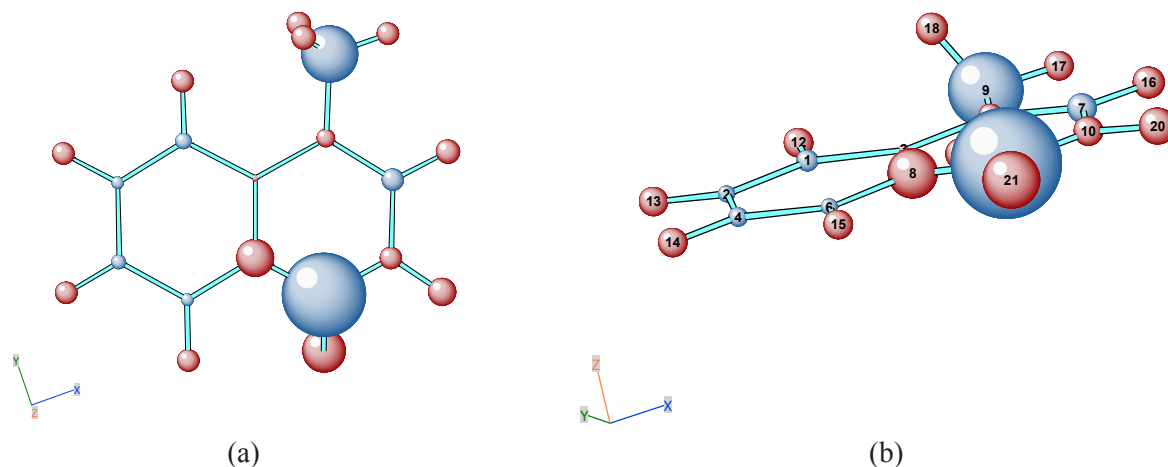
Fig. 5. Theoretical predicted single atomic charges of protonated 4-methylquinoline (a) and another view (b). The sizes of the spheres are proportional to charges on atoms.
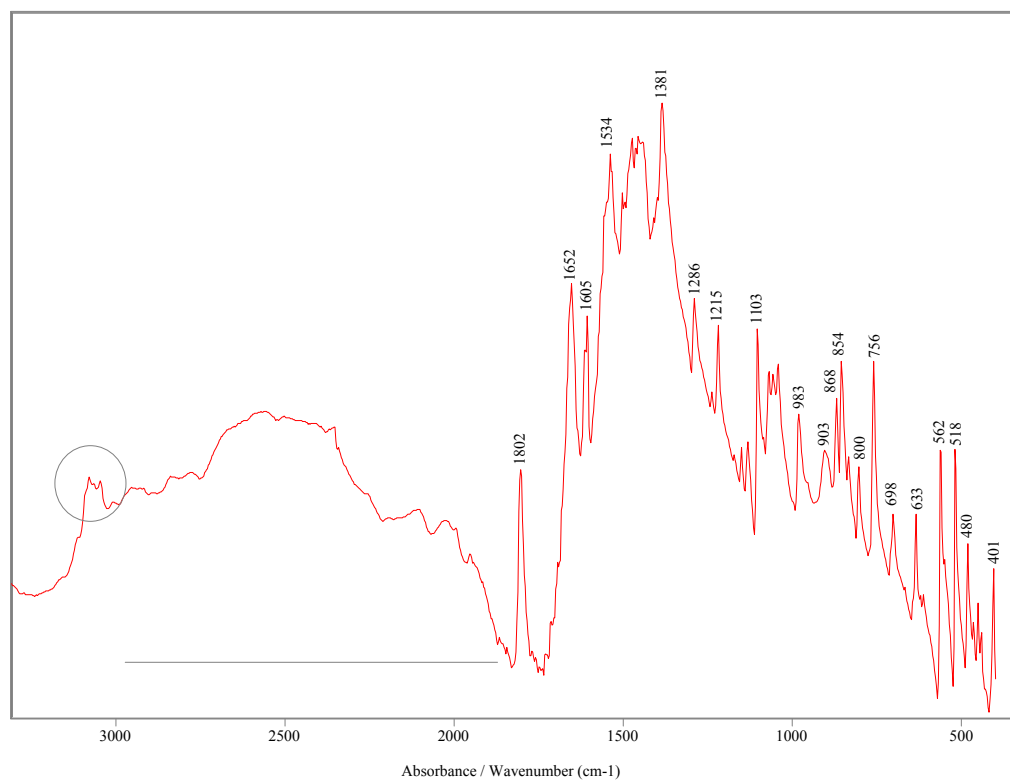
Fig. 6. IR-spectrum of (**1**) in KBr pellet.
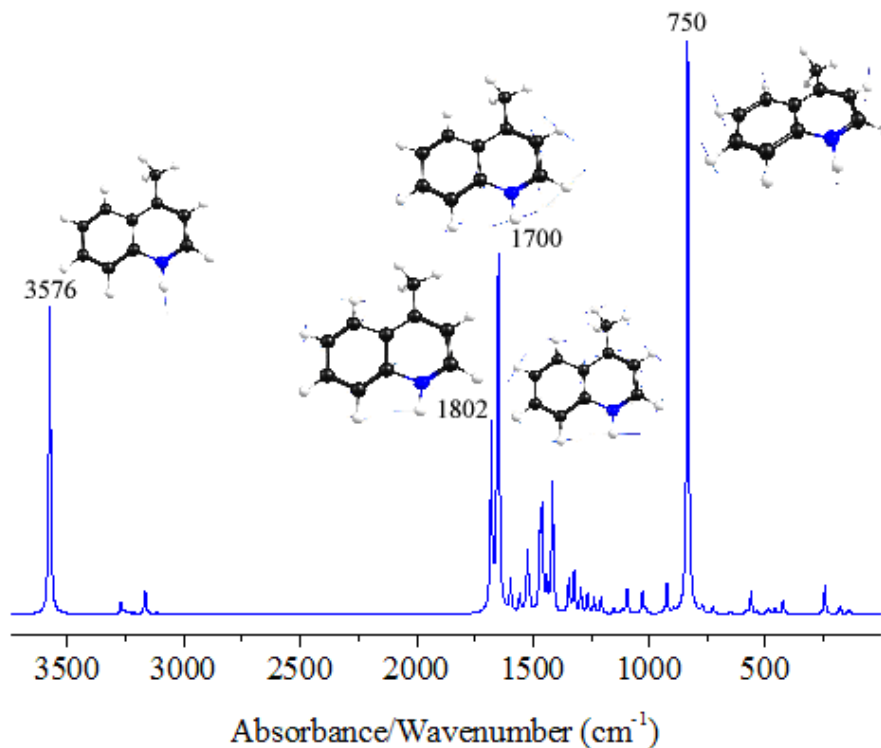
Fig. 7. Theoretical IR-spectrum of protonated 4-methylquinoline and visualization of selected directions of the molecular motion.

to a significant low-frequency shifting. The series of bands within the 3100–3000 cm^{-1} region corresponds to in-plane (*i.p.*) stretching vibrations ν_{ArH} in both the theoretical and experimental IR-spectra. The bands at 1802, 1700 and 1534 cm^{-1} belong to $\nu^s_{C=O(Sq)}$, $\nu^{as}_{C=O(Sq)}$ and $\nu_{C=C(Sq)}$ stretching vibrations of the hydrogensquarate anion, respectively (Fig. 6). The bands at 1652 cm^{-1} and 1605 cm^{-1} could be attributed to δ_{N+H} bending vibrations and *i.p.* vibrations of the quinoline fragment (Fig. 7). The corresponding theoretical values are 1633 cm^{-1} and 1604 cm^{-1}, respectively. The high-frequency shift of δ_{N+H} results from intermolecular interactions in the solid-state, and the obtained difference of 19 cm^{-1} for the first IR-band is therefore expected. The IR-spectrum of (**1**) is characterized by strong band at 1381 cm^{-1}, belonging to *i.p.* vibrations of quinoline fragment (theoretical value of 1380 cm^{-1}). The other IR-bands observed within the 1300–950 cm^{-1} range also belonged to the *i.p.* vibrations of the latter fragment. The broad band at 903 cm^{-1} (Fig. 6) could be assigned to the γ_{N+H} mode (theoretical value of 750 cm^{-1}). Similarly to δ_{N+H}, the participation of the N$^+$H group in the intermolecular interactions leads to a high-frequency shift of the γ_{N+H} IR-band as well.

The bands at 869, 854 and 833 cm^{-1} (theoretical values of 870, 855 and 833 cm^{-1}, respectively) belong to the out of-plane (*o.p.*) bending vibrations

of the 4-lepidine fragment. A direct experimental confirmation of their assignment follows from the obtained elimination of these maxima at an equal dichroic ratio (Fig. 8). Regardless of this observation, the discussed IR-bands are split into pairs as a result of the crystal field splitting in the case of Z = 2. Total disappearance of the maxima during the elimination procedure was observed. At the same time, disappearance of the band at 903 cm^{-1} was also found (Fig. 8), which was in accordance with the geometry obtained, since the normal modes of the *o.p.* and γ_{N+H} modes are oriented in a mutually co-linear manner.

Hence the vibrational assignment of the bands belonging to structure (**1**) was made on the basis of calculated IR frequencies, and their intensities were supported by the polarization IR spectral data. The coincidence between calculated and measured frequencies was found to be satisfactory.

^{1}H- and ^{13}C-NMR data

According to literature data, the chemical shift signals of the C2H, C3H, C5H-C7H (Scheme 1) in the ^{1}H NMR spectrum of the neutral molecule 4-methylquinoline are observed at about 8.77, 7.21. 7.98, 7.55, 7.70 and 8.10 ppm, while the signal of -CH$_3$ is at 2.79 ppm [57, 58]. The effect of
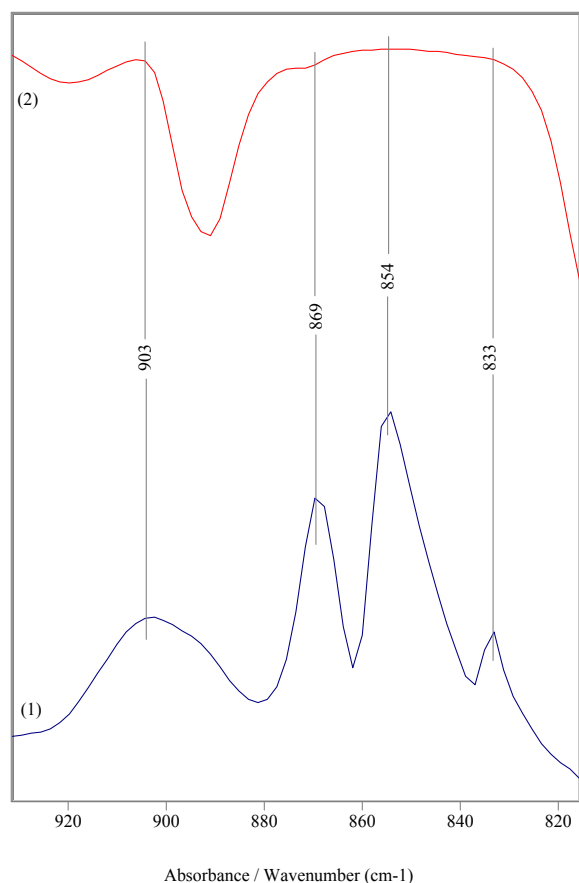
Fig. 8. Non-polarized IR-(**1**) and reduced IR-LD (**2**) spectra of (**1**) after elimination of the band at 854 cm^{-1}.

N-protonation leads to a downfield shifting of the signals of C2H and C3H by about 0.5–0.7 *ppm*.

CONCLUSIONS

The new compound, 4-methylquinolinium hydrogensquarate has been synthesized, isolated, and spectroscopically and structurally elucidated by using single crystal X-ray diffraction, IR-LD spectroscopy, UV-spectroscopy, ^{1}H-NMR, thermal methods and mass spectrometry. Quantum chemical calculations are used to obtain the electronic structure, vibrational data and electronic spectra. The effects of N-protonation on the optical and magnetic properties are elucidated by comparing the data of the protonated and neutral compound. Compound crystallizes in the centrosymmetric space group P$\bar{1}$, and the structure consists of infinite layers, formed by intermolecular N$^+$H…O=C$_{(Sq)}$ hydrogen bonds (2.752 Å) between the cations and anions. The hydrogensquarate moieties form stable dimers by

means of strong hydrogen $_{(Sq)}$OH…O=C$_{(Sq)}$ bond (2.595 Å). The two cations are found to be in coplanar arrangement within the unit cell, thus indicating a successful application of the reducing-difference-procedure for polarized IR-LD spectra interpretation. Moreover, the N-protonation leads to a partial charge redistribution of the protonated 4-lepidine.

SUPPORTING INFORMATION

Crystallographic data for the structural analysis have been deposited with the Cambridge Crystallographic Data Centre; CCDC 705630 Copies of this information can be obtained from the Director, CCDC, 12 Union Road, Cambridge, CB2 1EZ, UK (Fax: +44 1223 336 033; e-mail: deposit@ccdc.cam.ac.uk or http://www.ccdc.cam.ac.uk).

REFERENCES

1. B. Gutsulyak, *Russ. Chem. Rev.*, **41**, 187 (1972).
2. J. Bricks, Y. Slominskii, I. Panas, A. Demchenko, *Methods Appl. Fluoresc.*, **6**, 1 (2018).
3. Varbanova, *Nauch. Trud. Vissh. Veterinarnomed. Institut*, **23**, 211 (1973) (*in Bulgarian*).
4. V. Sundararajan, G. Selvaraj, H. M. Ng, S. Ramesh, K. Ramesh, C. D. Wilfred, S. Bashir, *Electrochim. Acta*, **240**, 361 (2017).
5. Th. Engel, G. Käb, H. Lanig, *Z. Phys. Chem.*, **216**, 305 (2002).
6. A. Popova, M. Christov, A. Vasilev, *Corrosion Science*, **49**, 3276 (2007).
7. A. Vasilev, M. Kandinska, S. Stoyanov, S. Yordanova, D. Sucunza, J. J. Vaquero, O. D. Castaño, S. Baluschev, S. E. Angelova, *Beilstein J. Org. Chem.*, **13**, 2902 (2017).
8. A. Zarkov, A. Vasilev, T. Deligeorgiev, S. Stoynov, M. Nedelcheva-Veleva, *Molecular Imaging*, **12** (2), 90 (2013).
9. Ch. Bosshard, M. Bösch, I. Liakatas, M. Jäger, P. Günter, in: Nonlinear Optical Effects and Materials, Springer Series in Optical Sciences, P. Günter (ed.), vol. 72, Chapter 3, Springer-Verlag, Berlin, 2000, p. 163.
10. S. Marder, J. Perry, W. Schaefer, *Science*, **245**, 626 (1989).
11. M. Todorova, R. Bakalska, Ts. Kolev, *Spectrochim. Acta – Part A*, **108**, 211 (2013).
12. O. Angelova, R. Petrova, V Radomirska, T. Kolev, *Acta Crystallographica*, *C***52**, 2218, (1996).
13. O. Angelova, V. Velikova, T. Kolev, V. Radomirska, *Acta Crystallographica*, *C***52**, 3252 (1996).
14. T. Kolev, Z. Glavcheva, R. Stahl, H. Preut, P. Bleckmann, V. Radomirska, *Acta Crystallographica*, *C* **53**, IUC9700010 – CIF access (1997).
15. T. Kolev, H Preut, P. Bleckmann, H. Preut, V. Radomirska, *Acta Crystallographica*, **C53**, 805 (1997).

16. T. Kolev, H. Preut, P. Bleckmann,V. Radomirska, *Zeitschrift für Kristallographie – New Crystal Structures*, **212**, 414 (1997).

17. T. Kolev, R. Stahl, H. Preut, P. Bleckmann, V. Radomirska, *Zeitschrift für Kristallographie – New Crystal Structures*, **212**, 415 (1997).

18. T. Kolev, R. Stahl, H. Preut, L. Koniczek, P. Bleckmann, V. Radomirska, *Zeitschrift für Kristallographie – New Crystal Structures*, **212**, 417 (1997).

19. T. Kolev, R. Stahl, H. Preut, L. Koniczek, P. Bleckmann, V. Radomirska, *Zeitschrift für Kristallographie – New Crystal Structures*, **213** (1), 167 (1998).

20. T. Kolev, Z. Glavcheva, R.Stahl, H. Preut, P. Bleckmann, V. Radomirska, *Zeitschrift für Kristallographie – New Crystal Structures*, **214**, 193 (1999).

21. T. Kolev, M. Spiteller, B. Koleva, *Amino Acids*, **38**, 45 (2010).

22. G. Gilli, V. Bertolasi, P. Gilli, V. Ferretti, *Acta Crystallogr.*, **B57**, 859 (2001).

23. I. Karle, D. Ranganathan, V. Haridas, *J. Am. Chem. Soc.*, **118**, 7128 (1996).

24. O. Yesilel, *J. Mol. Struct.*, **874**, 151 (2008).

25. O. Yesilel, Z. Pasaoglu, H. Yilanve, O. Buyukgungor, *Z. Naturforsch.* **62b**, 823 (2007).

26. O. Yesilel, M. Odabasoglu, H. Olmez, O. Buyukgungor, *Z.Naturforsch.,* **61b***,* 1243 (2006).

27. I. Ucar, A. Bulut, O. Yesilel, O. Buyukgungor, *Acta Crystallogr.*, **C60**, 585 (2004).

28. A. Bulut, O. Yesilel, N. Dege, H. Icbudak, H. Olmez, O. Buyukgungor *Acta Crystallogr.*, **C59**, 727 (2003).

29. Z. Dega-Szafran, A. Kania, B. Nowak-Wydra, M. Szafran, *J. Mol. Struct.*, **322**, 223 (1994).

30. M. Aniola, S. Dega-Szafran, A. Katrusiak, *New J. Chem.*, 38, 3556 (2014).

31. B. Ivanova, H. Mayer-Figge, *J. Coord. Chem.*, **58**, 653 (2005).

32. B. Ivanova, M. G. Arnaudov, H. Mayer-Figge, *Polyhedron*, **24**(13), 1624 (2005).

33. B. Koleva, E. Trendafilova, M. Arnaudov, W.S. Sheldrick, H. Mayer-Figge, *Trans. Met. Chem.*, **31**(7), 866 (2006).

34. B. Koleva, T. Kolev, T. Tsanev, St. Kotov, H. Mayer-Figge, R. W. Seidel, W. S. Sheldrick, *J. Mol. Struct.*, **881**, 146 (2008).

35. B. Koleva, T. Kolev, T. Tsanev, St. Kotov, H. Mayer-Figge, R. Seidel, W.S. Sheldrick, *Struct. Chem.*, **19**, 13 (2008).

36. B. Koleva, T. Tsanev, T. Kolev, H. Mayer-Figge, W.S. Sheldrick, *Acta Cryst.*, **E63**, 3356 (2007).

37. B. Koleva, Ts. Kolev, R. Seidel, H.Mayer-Figge, M. Spiteller, W.S. Sheldrick,*J. Phys. Chem. Part A*, **112**(13), 2899 (2008).

38. J. Davies, A. Rivera, G. M. Sheldrick, *Acta Crystallogr.*, **33B**, 156 (1977).

39. N. Begum, D. Bennett, G. Hossain, S. Kabir, A. Sharmin, D. Haworth, T. Siddiquee, E. Rosenberg, *J. Cluster Sci.*, **16**, 413 (2005).

40. S. E. Kabir, T. A. Siddiquee, E. Rosenberg, R. Smith, M. B. Hursthouse, K. M. A. Malik, K. I. Hardcastle, M. Visi, *J. Cluster Sci.*, **9**, 185 (1998).

41. P. Siega, L. Randaccio, P.A. Marzilli, L.G. Marzilli, *Inorg. Chem.*, **45**, 3359 (2006).

42. M. B. Hursthouse, S. E. Kabir, K. M. A. Malik, M. Tesmer, H. Vahrenkamp, *J. Organomet. Chem.*, **568**, 133 (1998).

43. S. E. Kabir, H. Vahrenkamp, M. B. Hursthouse, K. M. A. Malik, *J. Organomet.Chem.*, **536**, 509 (1997).

44. E. Arcia, D.S. Kolwaite, E. Rosenberg, K. Hardcastle, J. Ciurash, R. Duque, R. Gobetto, L. Milone, D. Osella, M. Botta, W. Dastru, A. Viale, I. Fiedler, *Organometallics*, **17**, 415 (1998).

45. M. A. S. Goher, F. A. Mautner, *Z. Naturforsch.*, **B 46**, 687 (1991).

46. M. A. Mottalib, N. Begum, S. M. T. Abedin, T. Akter, S. E. Kabir, M. A. Miah, D. Rokhsana, E. Rosenberg, G. M. G. Hossain, K. I. Hardcastle, *Organometallics*, **24**, 4747 (2005).

47. P.A. Lorenzo Luis, P. Martin-Zarza, P. Gili, C. Ruiz-Perez, M. Hernandez-Molina, X. Solans *Acta Crystallogr.*, **52C**, 1441 (1996).

48. G. M. Sheldrick, 1995, SHELXTL, Release 5.03 for Siemens R3 crystallographic research system. Siemens Analytical X-Ray Instruments, Inc., Madison, USA.

49. G. M. Sheldrick, 1997, SHELXS97 and SHELXL97. University of Goettingen, Germany.

50. B. Ivanova, M. Arnaudov, P. Bontchev, *Spectrochim. Acta*, **60A**, 855 (2004).

51. B. Ivanova, D. Tsalev, M. Arnaudov, *Talanta*, **69**, 822 (2006).

52. B. Ivanova, V. Simeonov, M. Arnaudov, D. Tsalev, *Spectrochim. Acta*, **67**, 66 (2007).

53. B. B. Koleva, T. M. Kolev, V. Simeonov, T. Spassov, K. Dimitrov, M. Spiteller, *J. Inclus. Prenomen.*, **61**, 319 (2008).

54. M. J. Frisch, G. W. Trucks, H. B. Schlegel, G. E. Scuseria, M. A. Robb, J. R. Cheeseman, G. Scalmani, V. Barone, B. Mennucci, G.A. Petersson, H. Nakatsuji, M. Caricato, X. Li, H.P. Hratchian, A. F. Izmaylov, J. Bloino, G. Zheng, J. L. Sonnenberg, M. Hada, M. Ehara, K. Toyota, R. Fukuda, J. Hasegawa, M. Ishida, T. Nakajima, Y. Honda, O. Kitao, H. Nakai, T. Vreven, J.A. Montgomery, J. E. Peralta, F. Ogliaro, M. Bearpark, J. J. Heyd, E. Brothers, K.N. Kudin, V.N. Staroverov, R. Kobayashi, J. Normand, K. Raghavachari, A. Rendell, J. C. Burant, S.S. Iyengar, J. Tomasi, M. Cossi, N. Rega, J. M. Millam, M. Klene, J. E. Knox, J. B. Cross, V. Bakken, C. Adamo, J. Jaramillo, R. Gomperts, R. E. Stratmann, O. Yazyev, A. J. Austin, R. Cammi, C. Pomelli, J. W. Ochterski, R. L. Martin, K. Morokuma, V. G. Zakrzewski, G. A. Voth, P. Salvador, J. J. Dannenberg, S. Dapprich, A. D. Daniels, O. Farkas, J. B. Foresman, J. V. Ortiz, J. Cioslowski, D. J. Fox, Gaussian 09, Revision A1, Gaussian Inc., Wallingford, CT, 200?.

55. G. A. Zhurko, D. A. Zhurko, *ChemCraft: Tool for treatment of chemical data*, 2005.

56. R. Mondelli, L. Merrlini, *Tetrahedron*, **22**, 3253 (1966).

57. R. J. Abraham, M. Reid, *J. Chem. Soc., Perkin Trans.*, **2**, 1081 (2002).

4-МЕТИЛХИНОЛИНИЕВ ХИДРОГЕНСКВАРАТ: КРИСТАЛНА СТРУКТУРА И СПЕКТРАЛНА ОЦЕНКА

Ст. Котов[1], Х. Майер-Фиге[2], С. Зарева[3]

[1] *Университет „Проф. Д-р Ас. Златаров“, Бургас, България*
[2] *Катедра „Аналитична химия“, Рурски университет Бохум, ул. „ Университетска“ 150, 44780 Бохум, Германия*
[3] *Софийски университет, Химически факултет, катедра „Аналитична химия“, 1164 София, България*

(Резюме)

Синтезирано е съединението 4-метилхинолиниев хидрогенскварат и са определени неговата структура и спектрални характеристики чрез инструментални методи, като монокристален рентгеноструктурен анализ, линейно поляризирана инфрачервена спектроскопия в твърдо състояние, UV-спектроскопия, ^{1}H-NMR, TGA, DSC, DTA и ESI-MS. Използвани са квантово-химични изчислителни процедури, за да се генерират електронната структура, както и теоретични спектрални данни за изследваното съединение. Влиянието на протонирането при азотния атом върху оптичните и магнитни свойства е оценено чрез сравняване на съответните данни за протонираната и непротонирана форма на 4-метилхинолиниев хидрогенскварат.

Structural and chemical evolution of mineral forms of tungsten in the oxidation zone of the Grantcharitza deposit (Western Rhodopes, Bulgaria)

M. P. Tarassov*, E. D. Tarassova

Institute of Mineralogy and Crystallography "Acad. Ivan Kostov", Bulgarian Academy of Sciences, Acad. Georgy Bonchev Str., bl. 107, 1113 Sofia, Bulgaria

Two principal trends of structural and chemical evolution of mineral forms of W are distinguished in the oxidation zone of the Grantcharitza tungsten deposit. The first trend concerns the processes that occur when the overall pH of supergene solutions decreases. The first group of processes include: (1) dissolution of scheelite, $CaWO_4$, accompanied by the formation of polytungstate ions in the solution at pH ~6–4; (2) pseudomorphic replacement of scheelite by poorly crystalline $WO_3.xFe_2O_3.nH_2O$ (iron-containing meymacite) at pH ~4–1; (3) crystallization of tungstite, $WO_3.H_2O$, and hydrotungstite, $WO_3.2H_2O$, at the expense of meymacite at pH <1. The second group of processes proceeds in the overall trend of increasing pH of supergene solutions and includes: (1) partial dissolution of meymacite upon increasing the pH and the K, Na and W content in the solution (pH ~1–3); (2) occasionally, precipitation of amorphous gels $WO_3.xFe_2O_3.nH_2O$ – chemical counterparts of meymacite (pH ~1–3); (3) crystallization of hydrokenoelsmoreite, $(W,Fe)_2(O,OH)_6.H_2O$ – the second chemical counterpart of meymacite with the pyrochlore structure type, as result of the interaction of meymacite and solution enriched with K, Na, Ca and, most probably W, at pH ~3–4; (4) formation of mineral bearers of W: goethite, α-FeOOH, hematite, α-Fe_2O_3, undefined amorphous $SiO_2.xAl_2O_3.yFe_2O_3.nH_2O$ gels, and, rarely, of $CaWO_4$, and stolzite, $PbWO_4$, at pH>4. It is shown that the increase of pH from <1 to 4 causes the successive change of the structure types: ReO_3 (ReO_3-type layers in the structures of tungstite and hydrotungstite), hexagonal tungsten bronze (HTB) (HTB-type layers in the structure of $WO_3.1/3H_2O$, meymacite), and pyrochlore (structure of hydrokenoelsmoreite).

Keywords: scheelite alteration, oxidation zone, secondary tungsten minerals, structure types.

INTRODUCTION

In 1981, Th. G. Sahama in his review [1] devoted to the secondary W minerals wrote that "The secondary tungsten minerals form a group of species with no crystallographic interrelationship". For the decades since then, new data on the secondary W minerals were collected and a number of new secondary W minerals with simplified formula $(W,Fe)(O,OH)_3.nH_2O$ (hydrokenoelsmoreite, pittongite) were discovered [2–4]. Several new phases of $WO_3.nH_2O$ (1/3, 1/2) with structures of hexagonal tungsten bronze and pyrochlore were synthesized using the soft chemistry (chemie douce) approach [5]. These new phases have their natural analogues as hydrokenoelsmoreite with a pyrochlore type of

structure [2] and poorly crystalline $WO_3.1/3H_2O$ [6]. The obtained so far data show that the structures of the secondary W minerals of the type $(W,Fe)(O,OH)_3.nH_2O$ and their artificial counterparts have similar structure elements such as layers of hexagonal tungsten bronze or/and ReO_3 perovskite [5]. Such minerals as pittongite and phyllotungstite [3, 4] are characterized with combined pyrochlore and tungsten bronze types of structure.

Thus, the crystallographic interrelationships between the secondary W minerals do exist. However, it is difficult to relate these minerals and their structure to certain physicochemical conditions. The synthesis conditions can hardly be used directly to interpret the natural conditions as they depend on numerous geological factors.

The processes of weathering occurring in W deposits cause a significant change in the mineral composition and properties of W ores, which makes them unsuitable for flotation and gravity beneficia-

---

* To whom all correspondence should be sent:
E-mail: mptarassov@gmail.com

tion. The behavior of W in the oxidation zone is very complicated due to complex aquatic chemistry of the element and its ability to polymerize. Recently, W has become the subject of scientific focus due to the possible toxicity of W in drinking water [7]. Weathering of W deposits is considered as one of the possible sources of W in ground waters [8].

The processes of weathering affect significant part of the Grantcharitza deposit (Western Rhodopes), the largest tungsten deposit in Bulgaria. In the present paper, the authors discuss the principal features of the development of the oxidation zone in the Grantcharitza tungsten deposit and the structural and chemical evolution of different secondary mineral forms of W by connecting them with certain physicochemical conditions.

BREAF INFORMATION ABOUT THE GRANCHARITSA DEPOSIT

The Grantcharitza tungsten deposit is situated in the Western Rhodopes Mountains, 18 km southwest of the town of Velingrad (Plovdiv region, Bulgaria). The deposit is localized in porphyritic biotite granites and amphibole-biotite granodiorites of the so-called "unit 1" of the composite Rila-Western Rhodopes Batholith [9]. The ore mineralizations occur in pegmatoid quartz-feldspar veins characterized by almost sub latitudinal strike – dipping to NW ~350° with slope of ~30° and in the wall-rock as vein-disseminated ores ("mineralized granitoids"). The mineral composition of the vein ores is characterized by strong domination of quartz, SiO_2, and potassium feldspar, $KAlSi_3O_8$ (microcline) among the gangue minerals and of pyrite, FeS_2, and scheelite, $CaWO_4$, among the ore minerals. The region of the deposit is characterized by broken terrain which causes fragmentariness of the weathering crust. The oxidation zone of the deposit is developed unevenly. Most intensive supergene processes are observed in the southern upper area of the most economically important Grantcharitza-Center section of the deposit. There, a significant part of the relief is presented by a gentle slope (~30°) of the Grantcharitza River valley. This slope is subparallel to the ore zone and thus ensures nearly even access to the ore zone of the weathering agents – water, atmospheric oxygen, microorganisms, etc. The textural and structural features of the primary ores and their mineral composition (presence of quartz and potassium feldspar which screen the ore minerals from the weathering agents) contribute to the inhomogeneous development of the supergene processes which are controlled by the fracture zones in the ores.

The most important supergene process that ultimately modifies the primary ores is the oxidation of pyrite and the generation of natural sulfuric acid. Goethite, α-FeOOH, and jarosite, $KFe_3(SO_4)_2(OH)_6$, are two most dominated minerals in the oxidation zone of the deposit indicating very high variation of pH of the supergene solution – from neutral to strongly acid, and Eh being very close to the values typical for waters being in direct contact with atmospheric oxygen [10]. All altered ores in the oxidation zone are clearly divided into two groups: limonitized ones with dominated ferric iron oxides/oxyhydroxides and non-limonitized ones, containing jarosite and a variety of secondary tungsten minerals.

MATERIAL AND METHODS

Representative samples from a personal collection of the authors taken from the oxidation zone of the Grantcharitza deposit (Center section) are used for the present study. Scanning electron microscopy and electron probe microanalysis (Philips SEM515 – WEDAX3A and ZEISS EVO LS25 – EDAX Trident) at 15–20 kV acceleration voltage, and micro-Raman spectroscopy (MicroDil 28 (Dilor Co.) with an Olympus 100x microscope objective, 488-nm line of an Ar^+ laser, laser power below 2 mW at the sample surface) were the main methods for the sample characterization. For a part of the samples, transmission electron microscopy (Philips TEM420) at 120 kV and Powder X-Ray diffraction analysis (DRON-UM1, CoKα and CuKα radiations) were also applied. For better understanding the supergene processes in the oxidation zone of the deposit, the authors have constructed series of Eh–pH diagrams for the systems W–Ca–Fe–S–K–O–H and W–Fe–O–H at 298 K and 1 atm. using the thermodynamic data from [11–13] and the activities of chemical components ($\Sigma Fe – 10^{-4}$, $Ca^{2+} – 10^{-4}$, $\Sigma S – 10^{-2}$, $K^+ – 10^{-3}$) in aqueous solutions typical for the oxidation zones of ore deposits [10, 14]. The thermodynamic activity of W for the system W–Fe–O–H was chosen equal to 10^{-5} – the value corresponding well to the $CaWO_4$ solubility in water according to [15]. For simplification, only the monomeric tungstate ion $[WO_4^{2-}]$ was taken into account.

RESULTS AND DISCUSSIONS

The following W minerals and W-bearing minerals are established in the oxidized ores: (i) hypogene minerals – scheelite $CaWO_4$ (intact and relic – most common); (ii) supergene minerals: iron-containing meymacite $WO_3.xFe_2O_3.nH_2O$ (important), tungstate $WO_3.H_2O$, hydrotungstite $WO_3.2H_2O$,

iron-containing hydrokenoelsmoreite (ferritungstite) $(W,Fe)_2(O,OH)_6.H_2O$, stolzite $PbWO_4$ (rare), colloform supergene scheelite $CaWO_4$ (rare), amorphous $WO_3.xFe_2O_3.nH_2O$ gels; (iii) mineral bearers of tungsten: goethite α-FeOOH (most widespread), hematite α-Fe_2O_3, amorphous $SiO_2.xAl_2O_3.yFe_2O_3.nH_2O$ gels.

Scheelite, CaWO₄, (endogenic) is the most important mineral form of W in the oxidized ores. The mineral is represented by: (1) intact crystals (most spread from), (2) crystals with pronounced signs of dissolution without formation of secondary minerals (wide spread form), and (3) relic forms replaced by secondary W mineral, $WO_3.xFe_2O_3.nH_2O$. The case (2) is shown in Fig. 1: the most intensive dissolution of the scheelite crystals takes place along the {101} crystallographic planes corresponding to the cleavage planes. The development of the dissolution process along {101} causes the formation of etch hillocks and pits with {101} faces and large empty channels along [001].

The calculated concentration of W in aqueous solution as a result of equilibrium dissolution of $CaWO_4$ ($CaWO_4 = Ca^{2+} + WO_4^{2-}$, ΔGr (298) = +50.16 kJ; thermodynamic data are from [11]) is equal to $4 \cdot 10^{-5}$ m ($\sim 4 \cdot 10^{-5}$ M or 7.4 mg/L) and well corresponds to the experimental data of [15]. This value exceeds the highest concentration of W (10^{-5} M) in an aqueous solution that contains only monomeric ion and molecular W forms [16] thus indicating that the polymeric forms of W should play a significant role in the interaction scheelite – supergene solution. According to [15] at pH < 6 the concentration of W in the aqueous solution in contact with scheelite becomes notably higher than that in the neutral solutions as a sequence of the increased role of polymeric forms of W as paratungtstate-B

$[H_2W_{12}O_{42}]^{10-}$, α-metatungstate $[H_2W_{12}O_{40}]^{6-}$ and other isopolytungstate ions. The role of monomeric forms of tungsten WO_4^{2-} is significant at pH>6. These data show that, at least at the beginning stages of scheelite alteration, at pH<6 to about 4 the only process of changing the mineral is its dissolution which proceeds with the formation of polytungstate ions. These ion forms of W are able to be transported over long distances in a supergene solution. The speciation of tungsten in aqueous solutions is expected to be more complex in the presence of Fe, Al, Si and P (typical for supergene solutions) due to the formation of tungsten heteropolyanions [17].

The second type of scheelite alteration in the Grantcharitza deposit is illustrated in Fig. 2: the mineral is pseudomorphically replaced by the secondary $WO_3.xFe_2O_3.nH_2O$ product (iron-containing meymacite or iron-containing ochre) in the acid medium of the oxidation zone enriched with Fe ions. The replacement is crystallographically controlled by the {101} cleavage planes of scheelite (Fig. 2b). The two fields ($WO_3.H_2O$ + α-FeOOH) and ($WO_3.H_2O$ + $KFe_3(SO_4)_2(OH)_6$) in the Eh-pH diagram (Fig. 2c) appear to reflect realistically the conditions of the alteration of scheelite and the formation of $WO_3.xFe_2O_3.nH_2O$, since the boundaries in the diagram between the W phases are independent of the type and concentration of the dissolved W species.

Iron-containing meymacite (ochre), $WO_3.xFe_2O_3.nH_2O$, is the most widespread supergene mineral of W in the deposit and the earliest product of scheelite alteration, and occurs as full or partial pseudomorphs after scheelite (Figs. 2a, b; 3a). The material has a glassy appearance and color in different nuances of yellow and brown – from light-yellow to dark- and black-brown. In the formula $WO_3.xFe_2O_3.nH_2O$ of the iron-containing meymacite, the coefficient x varies in the range 0.12–0.25 (~0.15 is the most common) and positively correlates with the coefficient n for water molecules varying in the range 1.8–3.9. The content of iron correlates with the color of the material: a higher content of iron corresponds to a darker color. All varieties of meymacite are poorly crystalline: their XRD patterns consist of two distinct peaks at 3.85 and 1.925 Å and asymmetric amorphous halos.

The performed observations reveal that all varieties of iron-containing meymacite are derivatives/ modifications of the earliest variety of meymacite with Fe/W atomic ratio equal to ~0.2. The modification of the earliest meymacite includes also the textural changes of the material as a result of the aging processes (aging of gels) [18]. The results of the aging process are shown in Fig. 3a and b: the material consists of two parts – glassy massive one (a) and spongy aggregates (b) in the cavities of the
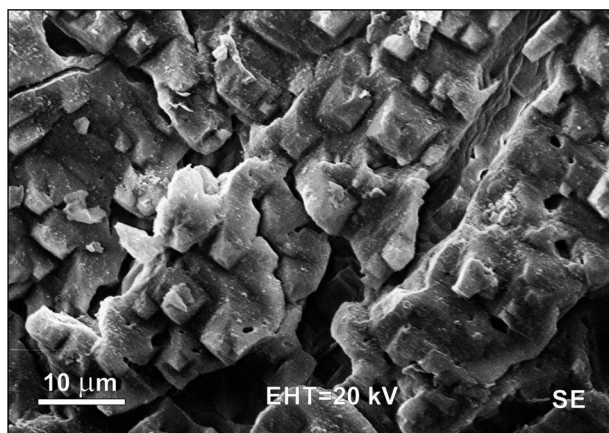
Fig. 1. Natural dissolution of scheelite, $CaWO_4$, in the oxidation zone of the Grantcharitza deposit. {101} faced hillocks and pits and channels along [001] are formed.
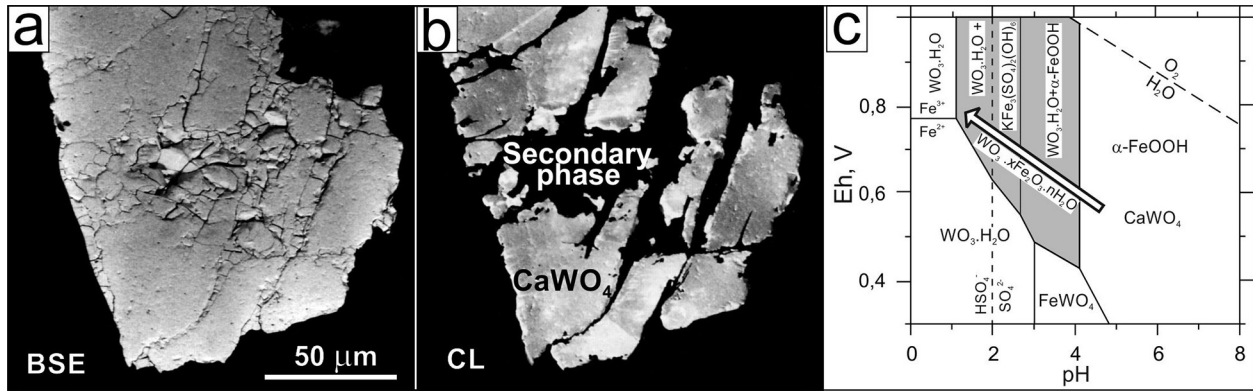
Fig. 2. (a) and (b) pseudomorphic replacement of scheelite by secondary $WO_3.xFe_2O_3.nH_2O$ material (iron-containing meymacite) in an acid medium enriched with Fe ions (images in backscattered electrons (a) and cathode luminescence (b)); (c) Eh–pH diagram with outlined (shaded) areas corresponding to the conditions of alteration scheelite via a pseudomorphic replacement by $WO_3.xFe_2O_3.nH_2O$.

first part. The spongy aggregates are macroscopically white or light-yellow. The Raman spectra of all meymacite varieties including the spongy aggregates are very similar – they are composed of broadened peaks in the whole studied spectral range 100–1050 cm^{-1} (Fig. 3c), and correspond well to the Raman spectra of crystalline $WO_3.1/3H_2O$ (S.G. Fmm2, a=7.359 Å, b=12.513, c=7.704) [19, 20].

The TEM investigation reveals that that the spongy aggregates are the most structurally ordered part of the meymacite. It is found that every single spongy particle represents a thin quasi-crystal consisting of coalesced elongated nanocrystals with length of 20–25 nm and width of 2–3 nm (Fig. 4). The single crystal type of electron diffraction patterns from a spongy particle was obtained only using the convergent beam electron diffraction (CBED)

method (Fig. 4a see the insert). The corresponding high resolution (HR) image with two-dimensional lattice fringes is shown in Fig. 4b. The recorded CBED pattern is actually a superposition of several patterns slightly rotated relative to each other, which hinders accurate measurement of d-spacing and reliable zone and phase identification. The HR image shows that the nanocrystals constituting the spongy particle are not ideally stacked – there are some angle discordances and displacements between the atomic planes of neighbor nanocrystals (Fig. 4b). For a more precise determination of the d-spacings, a Fast Fourier Transform (FFT) of the HR image was performed (Fig. 4b). The final measured d-spacings are: 3.85 Å (perpendicularly to the elongation of the particle) and 3.68 Å (in parallel to the elongation of the particle). These d-spacings
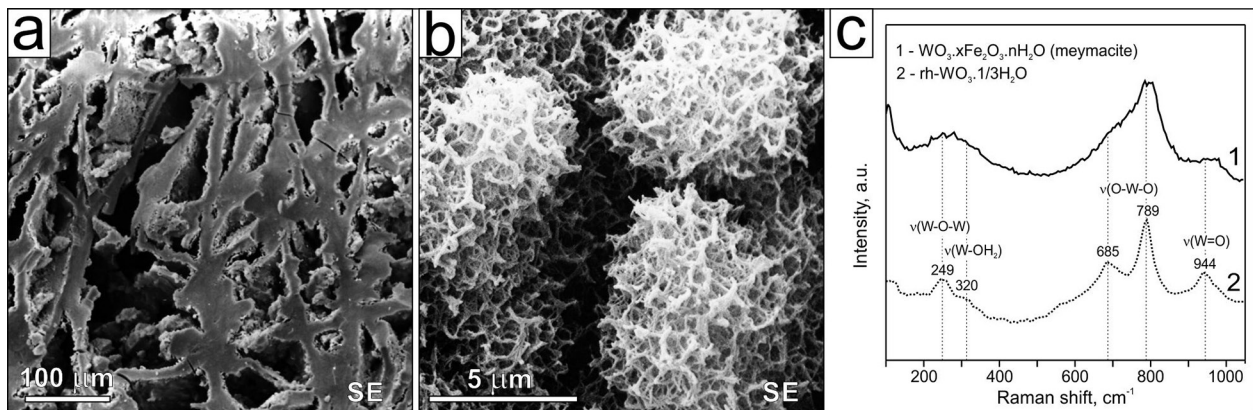
Fig. (3). (a and b) two parts of the iron-containing meymacite with atomic ratio Fe/W ~0.3: massive glassy one (a) and spongy aggregates in cavities of the first part (b); (c) unpolarized Raman spectra of the studied meymacite (1) and crystalline rh-$WO_3.1/3H_2O$ (2).

273
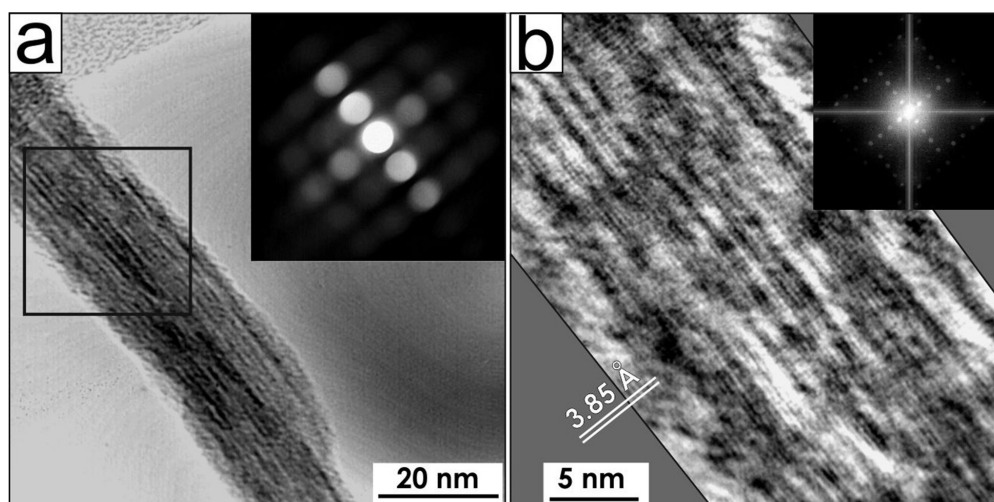
Fig. 4. (a) TEM bright-field image of a single spongy particle of iron-containing meymacite and corresponding convergent beam electron diffraction (CBED) pattern in the insert; (b) high-resolution (HR) image of the area outlined in (a) visualizing fragmented two-dimensional lattice fringes with d-spacings 3.85 and 3.68 Å and corresponding FFT image in the insert.

correspond to [010] zone of $WO_3.1/3H_2O$ (Fmm2): $d_{002} = 3.852$ Å and $d_{200} = 3.680$ Å. No other larger d-spacings typical for $WO_3.1/3H_2O$ (Fmm2) as d_{111} = 4.897 Å and $d_{020} = 6.257$ Å were found in the material under study. The reason for this is in the specific morphology of the studied nanocrystals and the manner of their stacking in the spongy particles. The nanocrystals are very narrow (~2 nm) and elongated (~20 nm) in the [001] direction and across to the elongation may accommodate to 2 unit cells only, as the b parameter of $WO_3.1/3H_2O$ is equal to 1.25 nm. The structure of $WO_3.1/3H_2O$ [20] consists of layers of WO_6 octahedra sharing their corners and forming six-membered rings typical for hexagonal WO_3 and hexagonal tungsten bronzes (HTB). The stacking of the layers is along the [001] direction, every layer being shifted by a/2 relative to the adjacent layer. In the [010] direction there is an alternation of more dense layers of WO_6 shared their corner according to the ReO_3 structure type and layers with two times fewer WO_6 octahedra [20]. Our experimental data (Fig. 4b) provide evidence that the $WO_3.1/3H_2O$ nanocrystals are stacked to each other by connecting their most dense (010) atomic planes. This stacking well explains the observed morphology of the spongy quasi-crystals (Fig. 4a) – they are very thin in the [010] direction and very long in the [001] direction of $WO_3.1/3H_2O$. Because the nanocrystals contain Fe^{3+}, their formula, in analogy with hydrokenoelsmoreite, can be presented as $(W, Fe^{3+}) (O,OH)_3.1/3H_2O$.

The obtained results well corresponds to our earlier TEM studies of the structural and orientation relationships between $CaWO_4$ and $WO_3.1/3H_2O$ during the decomposition of $CaWO_4$ in dilute solutions of sulfuric acid at 120°C [21]. It was shown in [22] that the transformation of $CaWO_4$ into $WO_3.1/3H_2O$ is topotactic one. The transformation is most intensively carried out along the {101} planes of $CaWO_4$, which to a greater extent predetermines the formation of $WO_3.1/3H_2O$ nanocrystals elongated in [001] direction.

Tungstite, $WO_3.H_2O$, and hydrotungstite, $WO_3.2H_2O$, are rare secondary tungsten minerals in the oxidation zone of the Grantcharitza deposit (Fig. 5a, b). The field ($WO_3.H_2O$ + Fe^{3+}) in the Eh-pH diagram (Fig. 2c) seems to realistically represent the strongly acid (pH≤1) conditions of crystallization of two tungsten trioxide hydrate minerals in the supergene media enriched with iron ions. We have nowhere observed that the two minerals directly replace the primary scheelite – in all examined samples, these minerals occur with iron-containing meymacite and are formed at the expense of meymacite. The hydrotungstite occurs as bright-yellow aggregates in cavities of meymacite. The individual crystals are with size to 50–60 μm. Twins and intergrowths are very common (Fig. 5a). In SEM, the mineral is easily distinguished by desiccation fissures in the crystals due to evaporation of a part of the structural water. The tungstite is fine-crystalline (<10 μm) (Fig. 5b). The mineral is represented by bright-yellow platy crystals and without complex twining. The presence of tungstite and hydrotungstite in the oxidation zone of the deposit indicates that the supergene processes occur in a relatively wide temperature range, because tungstite crystallizes at ≥50°C and hydrotungstite – at ≤50°C.
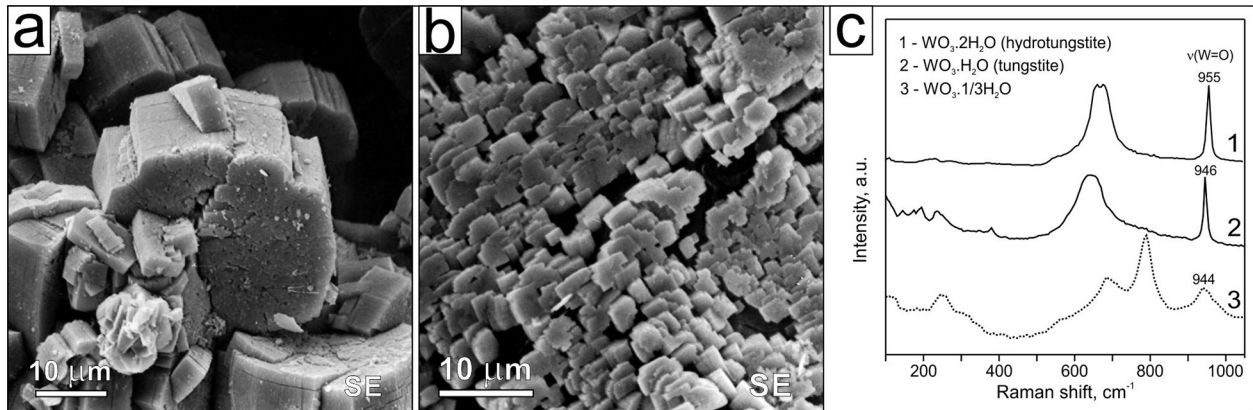
Fig. 5. (a) twinned crystals of hydrotungstite, $WO_3.2H_2O$, in cavity of meymacite; (b) platy crystals of tungstite covering quartz in close proximity to meymacite; (c) unpolarized Raman spectra of $WO_3.nH_2O$ phases (n=2, 1, 1/3)

The structures of the two minerals [23, 24] consist of layers of WO_5OH_2 octahedra sharing their 4 corners in a manner typical of the ReO_3 structure. The two other corners of the octahedra are occupied by non-shared oxygen (terminal W=O bond) and water molecule (W-OH_2 bond). In tungstite, the layers are connected by hydrogen bonds. In the structure of hydrotungstite, additional water molecules are intercalated between adjacent layers. The Raman spectra of hydrotungstite and tungstite (Fig. 5c) well correspond to the literature data [19].

The considered above consecutive processes, namely, (1) scheelite dissolution, (2) replacement of scheelite by iron-containing meymacite, and (3) crystallization of tungstite and hydrotungstite at the expense of meymacite, proceed in the overall trend of decreasing pH (increasing concentration of H_2SO_4).

In the interaction of natural sulfuric acid with scheelite and other minerals (quartz and microcline), the acidity of the supergene solutions are gradually neutralized with a simultaneous increase in the concentration of potassium and sodium. This is a reason that the further structural and chemical evolution of tungsten mineral forms is realized in the general trend of increasing pH.

Amorphous $WO_3.xFe_2O_3.nH_2O$ gels. This natural amorphous material is described here for the first time. The material is macroscopically light-yellow and can be mistaken for fine-crystalline tungstite and hydrotungstite. It is chemical counterpart of iron-containing meymacite. The material is found in quartz fractures (Fig. 6a) without clear positional connections with scheelite and other secondary tungsten minerals indicating that W and Fe were introduced here by supergene solutions.
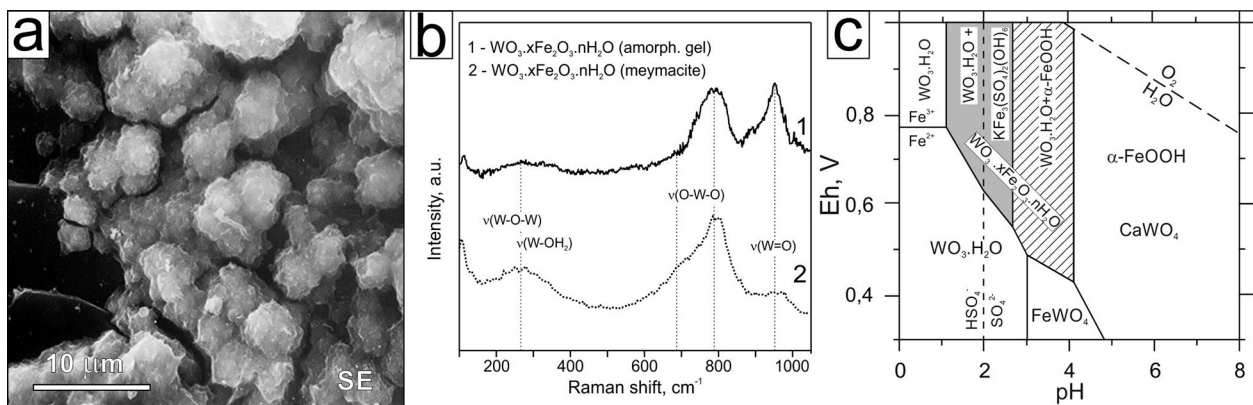
Fig. 6. (a) crust of amorphous $WO_3.xFe_2O_3.nH_2O$ gels on the surface of quartz; (b) Raman spectra of $WO_3.xFe_2O_3.nH_2O$ gel and meymacite; (c) Eh-pH diagram with shaded area corresponding to the most probable gel formation conditions (the hatched area represents less probable conditions).

Dissolution of either tungstite and hydrotungstite or iron-containing meymacite by a supergene solution, followed by transport and a sol-gel process could produce such a type of natural amorphous gels. Dissolution of scheelite can also be a possible source of tungsten in the solution. Normally the gel is accompanied by jarosite, $KFe_3(SO_4)_2(OH)_6$, therefore the field ($WO_3.H_2O + KFe_3(SO_4)_2(OH)_6$) in the Eh–pH diagram (Fig. 6c) can be considered as an approximation to the material formation conditions but keeping in mind that the gel is amorphous.

The Raman spectrum of the studied gel differs significantly from that of the iron-containing meymacite (Fig. 6b). The peak at 950 cm^{-1} corresponding to W=O terminal bond in the gel spectrum has a much higher intensity as is typical for amorphous WO_3 materials/films obtained in various ways including sol-gel process [25, 26] and reflects a significant role of the surface W=O bonds in the tungsten-oxygen clusters composing the materials. In the spectral range 650–850 cm^{-1} corresponding to the stretching vibration of W-O bonds in WO_3 compounds [19], the spectrum of the gel demonstrates a relatively narrow intense peak at 780 cm^{-1} (Fig. 6b). This peak may indicate that the gel clusters are compact and consist of WO_6 octahedra sharing not only their apexes but also edges. This suggestion to a greater extent is confirmed in [27] where radial distribution function (RDF) analysis made for amorphous $WO_3.xFe_2O_3.nH_2O$ gels reveals the presence of a weak peak at 3.2 Å corresponding to W-W nearest-neighbor distance in WO_6 octahedra sharing edges [28] which is typical for polytungstate acid.

Iron-containing hydrokenoelsmoreite (W,Fe)$_2$ (O,OH)$_6$.H$_2$O (ferritugstite) is the third chemical counterpart of the iron-containing meymacite with the pyrochlore-type structure. The mineral is rare.

It sporadically crystalizes in situ in the cavities of meymacite. Macroscopically, it is bright-yellow. The mineral is encountered as well faced octahedral crystals with size 10–20 μm, their twins and intergrowths (Fig. 7a). Besides WO_3, Fe_2O_3 and H_2O, the following chemical components Na_2O, K_2O, CaO and PbO are established in the chemical composition of the mineral. The detailed observation shows that hydrokenoelsmoreite is the result of the interaction of meymacite and supergene solution. This is evidenced by the fact that hydrokenoelsmoreite is formed only there, where there is a meymacite, and the crystallization of hydrokenoelsmoreite is accompanied by the destruction of meymacite – the latter becomes very fragile and friable. The composition of hydrokenoelsmoreite indicates the presence of K, Na, Ca and Pb in the supergene solution. Most likely, this solution contained also W and Fe ions. The ($WO_3.H_2O + \alpha$-FeOOH) field in Fig. 7c tentatively corresponds to the conditions of crystallization of hydrokenoelsmoreite (pH ~3–4). The proposed pH range is very close to pH of ~3 of the precursor tungsten solutions used for synthesis of the pyrochlore type tungsten trioxide hydrates [29, 30].

The Raman spectrum of hydrokenoelsmoreite (Fig. 7b) is characterized by two broad bands in the spectral ranges 600–750 and 850–1000 cm^{-1} corresponding to symmetric and asymmetric stretching of W-O bonds, respectively [31]. It is notable, that although the mineral is well crystalline, its Raman peaks in the range 600–1000 cm^{-1} are essentially broader than the Raman peaks of the chemical counterparts of the mineral – cryptocrystalline meymacite and amorphous gels. According to [31] broadening of the Raman lines results from structural disorder caused by the presence of iron atoms.
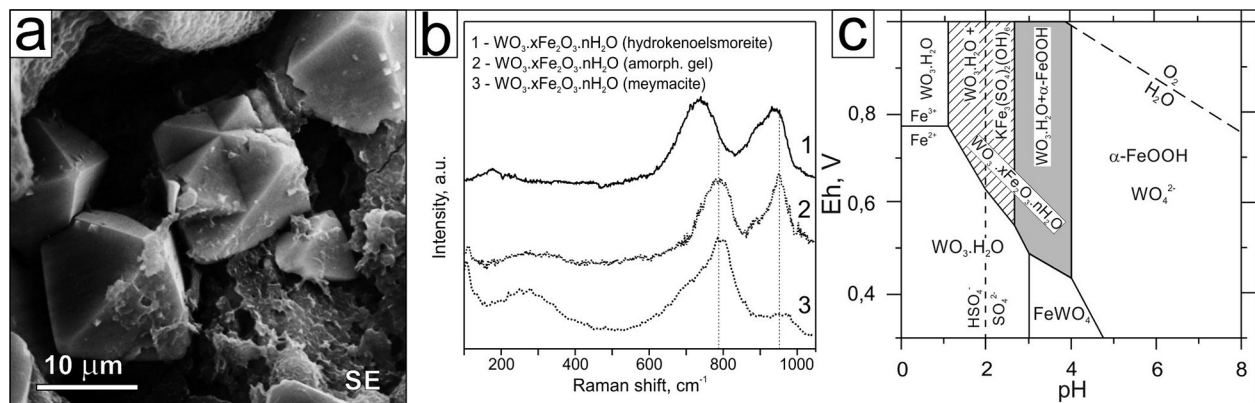
Fig. 7. (a) octahedral crystals and crystal intergrowths of iron-containing hydrokenoelsmoreite in the cavity of iron-containing meymacite; (b) Raman spectra of three $WO_3.xFe_2O_3.nH_2O$ supergene forms of W: hydrokenoelsmoreite, amorphous gel and meymacite; (c) Eh-pH diagram with outlined (shaded) area tentatively corresponding to the hydrokenoelsmoreite formation conditions.
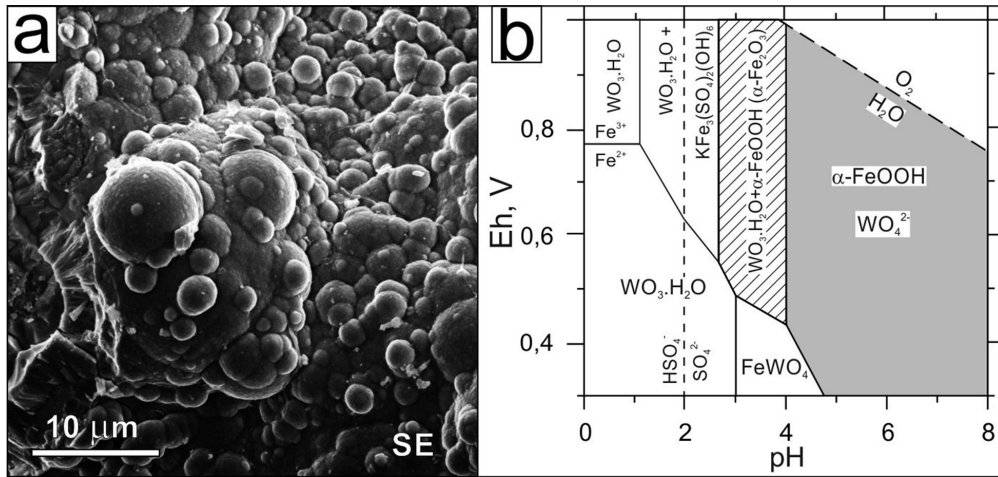
Fig. 8. (a) colloform W-bearing goethite, α-FeOOH, (b) Eh-pH diagram with outlined (shaded) area corresponding to the formation of W-bearing goethite.

Tungsten-bearing goethite, α-FeOOH, is widespread supergene mineral in the oxidation zone of the deposit and most important secondary bearer of tungsten. The mineral is presented by colloform compact mass (Fig. 8a), macroscopically black-colored, filling the fissures and cavities remained after dissolution of scheelite and pyrite, and powder ochreous mass colored in brown to yellow. The established concentration of WO_3 in the goethite aggregates varies in the range 1–10 wt.% [32]. It is shown that to ~2 wt.% of W are structurally incorporated in goethite. The other most enriched in W part of the goethite aggregates is related to a strongly disordered ferrihydrite-like phase (phase Fw) with WO_3 content to 25 wt.%. The presence of tungsten in goethite can be related to two different processes: (1) co-precipitation of Fe and W from colloidal solution causing the formation of colloform goethites, and (2) adsorption of tungsten species by goethite and ferrihydrite. Tungsten adsorption is more extensive at circumneutral pHs of solutions containing monomeric tungstate forms [33]. Tungstate polymerization significantly decreases W adsorption. The $(\alpha\text{-FeOOH}+WO_4^{2-})$ field in Fig. 8b seems to be a reasonable approximation to the conditions of formation W-bearing goethite (pH>4).

Tungsten-bearing hematite α-Fe₂O₃ occurs rarely in local places of compact tungsten-bearing goethite and is characterized by a content of WO_3 of 0.5–2.0 wt.% corresponding to the structural incorporation of W in hematite [32]. The hematite crystallizes via a multistage process including dissolution of goethite, reprecipitation of the material in the form of tungsten-bearing ferrihydrite and subsequent solid-state conversion of ferrihydrite into hematite. According to [34] in both hematite and goethite the

structural incorporation of W is realized via protonation scheme: $3Fe^{3+} = W^{6+}+3H^++2\square^0$. Similarly to the goethite, the $(\alpha\text{-FeOOH}+WO_4^{2-})$ field in Fig. 8b is an approximation to the conditions of formation W-bearing hematite (pH>4).

Amorphous tungsten-containing $SiO_2.xAl_2O_3.$ $yFe_2O_3.nH_2O$ gel is widespread undefined product of sol-gel processes taken place in the oxidation zone. It is commonly presented by surface yellow-brawn powdery materials with variable content of Fe_2O_3 and WO_3 (to 2 wt.%). The field $(\alpha\text{-FeOOH} + WO_4^{2-})$ outlined in the pH-Eh diagram in Fig. 8c corresponds to the possible conditions for the gels formation. The presence of W in the gel most probably is due to adsorption of monotungstate WO_4^{2-} ions.

Stolzite, $PbWO_4$, and colloform scheelite, $CaWO_4$, are rarely occurred supergene forms of W in the deposit. The field $(CaWO_4 + \alpha\text{-FeOOH})$ in the pH-Eh diagrams (Figs. 2c, 6c) well defines conditions of crystallization of these minerals.

CONCLUSIONS

A relatively simple mineral composition of primary ores in the Grantcharitza deposit, strongly dominated by pyrite and scheelite, creates a very wide diversity of secondary W minerals and secondary mineral bearers of W in the oxidations zone in the southern part of the Grantcharitza-Center section. The processes are carried out over a wide range of pH, high oxidation potential Eh corresponding to that characteristic of the waters which are in direct contact with atmospheric oxygen, and with a very important role of Fe^{3+}. In fact, the most important
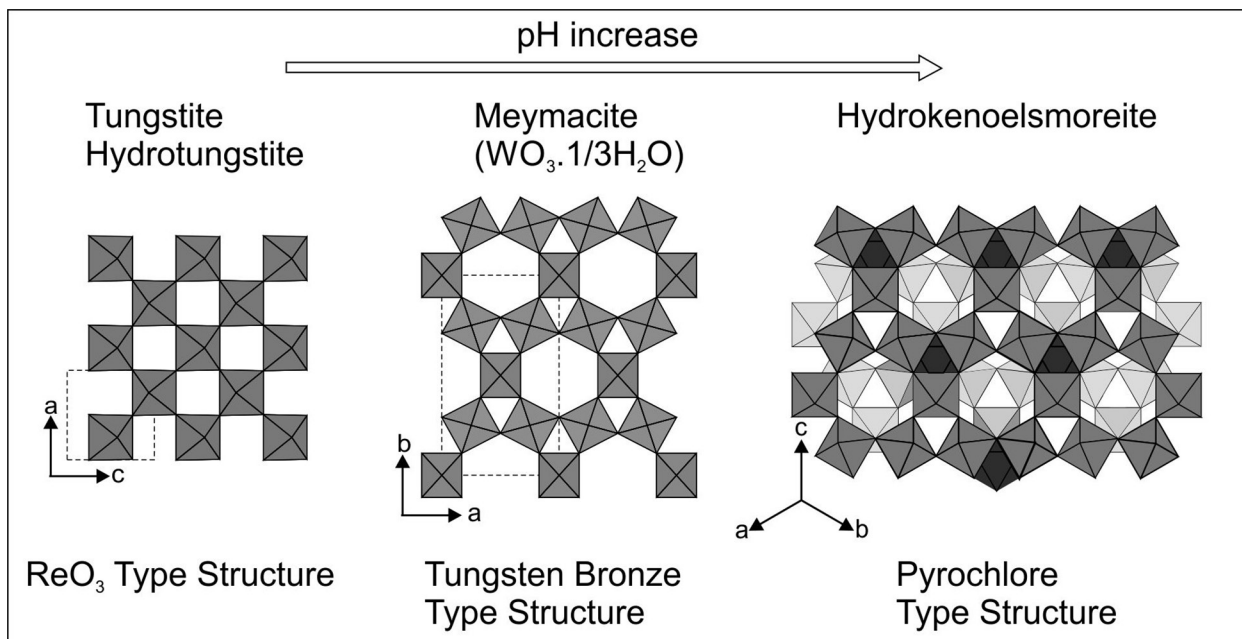
Fig. 9. Summary scheme: dependence of the structure type of secondary tungsten mineral on the pH of solution in the presence of iron ions.

secondary W mineral forming processes in the deposit are realized within the WO_3–Fe_2O_3–H_2O system. These processes are carried out *in situ* and *ex situ* with involving the ground waters and essential transport of dissolved W including its polytungstate ion forms.

Two principal trends of structural and chemical evolution of mineral forms of W are distinguished in the oxidation zone of the deposit. The first trend concerns the processes that occur when the overall pH of supergene solutions decrease. The first group of processes include: (1) dissolution of scheelite accompanied by the formation of polytungstate ions in the solution at pH ~6–4; (2) pseudomorphic replacement of scheelite by poorly crystalline $WO_3.xFe_2O_3.nH_2O$ (iron-containing meymacite) at pH ~4–1; (3) crystallization of tungstite, $WO_3.H_2O$, and hydrotungstite, $WO_3.2H_2O$, at the expense of meymacite at pH <1. It is shown that the most ordered part of the meymacite is represented by nanocrystals with a structure of $WO_3.1/3H_2O$ (Fmm2).

The second group of processes proceeds in the overall trend of increasing pH of supergene solutions and includes: (1) partial dissolution of meymacite upon increasing the pH and the K, Na and W content in the supergene solution (pH ~1–3); (2) occasionally, precipitation of amorphous gels $WO_3.xFe_2O_3.nH_2O$ – chemical counterparts of meymacite, commonly accompanied by jarosite, $KFe_3(SO_4)_2(OH)_6$ (pH ~1–3); (3) crystallization of iron-containing hydrokenoelsmoreite, $(W,Fe)_2(O,OH)_6.H_2O$ – the second chemical counterpart of meymacite with the

pyrochlore structure type, as result of the interaction of meymacite and supergene solution enriched with K, Na and Ca and most likely containing W and Fe ions at pH ~3–4; (4) formation of mineral bearers of tungsten: goethite, α-FeOOH, hematite, α-Fe_2O_3, undefined amorphous $SiO_2.xAl_2O_3.yFe_2O_3.nH_2O$ gels, and very rarely of tungstate minerals – supergene scheelite, $CaWO_4$, and stolzite, $PbWO_4$, at pH>4.

Based on the data obtained for the oxidation zone of the Grantcharitza deposit, the authors propose the following summary scheme describing the dependence of the structure type of the secondary tungsten mineral on the pH of the solution in the presence of iron ions (Fig. 9). The increase of pH of the solution is accompanied by the consecutive change of the structure types: ReO_3 type (ReO_3-type layers in the structures of tungstite and hydrotungstite), hexagonal tungsten bronze type (HTB) (HTB-type layers in the structure of $WO_3.1/3H_2O$, meymacite), and pyrochlore type (structure of hydrokenoelsmoreite). According to this scheme, it becomes more apparent the conditions of formation of such tungsten minerals as pittongite and phyllotungstite [3, 4] with combined pyrochlore and tungsten bronze types of structure.

REFERENCES

1. Th. G. Sahama, *Mineral. Rec*, **12**, 81 (1981).
2. P. A. Williams, P. Leverett, J. L. Sharpe, D. M. Colchester, J. Rankin, *Can. Mineral.*, 43, 1061 (2005).

3. I. E. Grey, W. D. Birch, C. Bougerol, S. J. Mills, *J. Solid State Chem.*, **179**, 3860 (2006).
4. W. D. Birch, I. E. Grey, S. J. Mills, C. Bougerol, A. Pring, S. Ansermet, *Can. Mineral.*, **45**, 857 (2007).
5. M. Figlarz, *Prog. Solid State Chem.*, **19**, 1 (1989).
6. M. P. Tarassov, *Geochem. Mineral. Petrol., Sofia*, **30**, 19(1995).
7. A. Koutsospyros, W. Braida, C. Christodoulatos, D. Dermatas, N. Strigul, *J. Hazard Mater.*, **136**, 1 (2006).
8. R. L. Seiler, K. G. Stollenwerk, J. R. Garbarino, *Appl. Geochem.*, **20**, 423 (2005).
9. B. Kamenov, I. Peytcheva, L. Klain, K. Arsova, Y. Kostitsin, E. Salnikova, *Geochem. Miner. Petrol., Sofia*, **36**, 3 (1999).
10. R. M. Garrels, Ch. L. Christ, Solutions, Minerals and Equilibria, Harper & Row Publishers, New York, 1965.
11. A. G. Bulah, K. G. Bulah, Physicochemical properties of minerals and components of hydrothermal solutions. Nedra, Leningrad, 1978.
12. S. Crouch-Baker, P. G. Dickens, S.A. Kay, *J. Chem. Thermodyn.*, **17**, 797 (1985).
13. J. B. Brown, *Miner. Depos.*, **6**, 245 (1971).
14. L. K. Yahontova, A. P. Grudev, Supegene zone of ore deposits, Publishing House of the Moscow University, Moscow, 1978.
15. K. I. Marinakis, G. H. Kelsall, *Colloids Surf.*, **25**, 369 (1987).
16. M. V. Mohosoev, N. A. Shevtsova, Molybdenum and tungsten speciation in aqueous solutions, Buryat Publishing House, Ulan-Ude, 1977.
17. M. T. Pope, Heteropoly and Isopoly oxometalates (Inorganic Chemistry Concepts, vol. 8), Springer Verlag, Berlin, 1983.
18. G. W. Scherer, *J. Non-Cryst. Solids*, **100**, 1–3, 77 (1988).
19. M. F. Daniel, B. Desbat, J. C. Lassegues, *J. Solid State Chem.*, **67**, 235 (1987).
20. B. Gerand, G. Nowogrocki, M. Figlarz, *J. Solid State Chem.*, **38**, 312 (1981).
21. M. P. Tarassov, V. Dimov, N. Khaltakova, *Comp. rend. Acad. bulg. Sci.*, **51**, 11–12, 65 (1998).
22. M. P. Tarassov, N. Khaltakova, *Comp. rend. Acad. bulg. Sci.*, **52**, 1–2, 61 (1999).
23. J. T. Szimanski, A. C. Roberts, *Can. Mineral.*, **22**, 681 (1984).
24. B. Von Krebs, *Acta Cryst.*, **B28**, 2222 (1972).
25. A. Chemseddine, M. Henry, J. Livage, *Rev. Chim. miner.*, **21**, 487 (1984).
26. Y. A. Yang, J. N. Yao, *J. Phys. Chem. Solids*, **61**, 647 (2000).
27. N. S. Zotov, M. P. Tarassov, *Mater. Sci. Forum*, **133–136**, 945 (1993).
28. T. Nanba, S. Takano, I. Yasui, T. Kudo, *J. Solid State Chem.*, **90**, 47 (1991).
29. J. R. Günter, M. Amberg, H. Schmalle, *Mat. Res. Bull.*, **24**, 289 (1989).
30. A. Coucou, M. Figlarz, *Solid State Ionics*, **28–30**, 1762 (1988)
31. M. P. Tarassov, M. S. Marinov, L. L. Konstantinov, N. S. Zotov, *Phys. Chem. Miner.*, **21**, 1/2, 63 (1994).
32. M. Tarassov, B. Mihailova, E. Tarassova, L. Konstantinov, *Eur. J. Mineral.*, **14**, 977 (2002).
33. J. Sun, B. C. Bostick, *Chem. Geol.*, **417**, 21 (2015).
34. S. Kreissl, R. Bolanz, J. Göttlicher, R. Steininger, M. Tarassov, G. Markl, *Am. Mineral.*, **101**, 2701 (2016).

СТРУКТУРНА И ХИМИЧНА ЕВОЛЮЦИЯ НА МИНЕРАЛНИ ФОРМИ НА ВОЛФРАМА В ОКИСЛИТЕЛНАТА ЗОНА НА НАХОДИЩЕ ГРЪНЧАРИЦА (ЗАПАДНИ РОДОПИ, БЪЛГАРИЯ)

М. П. Тарасов*, Е. Д. Тарасова

Институт по минералогия и кристалография „Академик Иван Костов", Българска Академия на науките, ул. Акад. Георги Бончев, бл. 107, 1113 София, България

(Резюме)

Две основни тенденции на структурната и химична еволюция на минералните форми на W са проявени в зоната на окисление на шеелит-пиритовото ($CaWO_4$–FeS_2) находище Грънчарица. Първата тенденция е свързана с процесите, които протичат при общо намаляване на pH на супергенните разтвори. Най-ранният процес включва взаимодействие на първичния шеелит със супергенния разтвор, което води до: (а) разтваряне на минерала, придружено от образуване на поливолфраматни йони в разтвора при pH ~6–4, и (б) псевдоморфно заместване на минерала от криптокристален $WO_3.xFe_2O_3.nH_2O$ (желязо-съдържащ меймацит) при pH ~4–1. Показано е, че най-подредената част на меймацита е представена от удължени нанокристали със структура на $WO_3.1/3H_2O$ (Fmm2). При pH<1 за сметка на меймацита се формират тунгстит, $WO_3.H_2O$, и хидротунгстит, $WO_3.2H_2O$. Втората група процеси протича при обща тенденция на повишаване на pH на супергенните разтвори. При повишаване на pH и съдържанието на K и Na в супергенния разтвор меймацитът частично се разтваря и волфрамът преминава в разтвор и в други вторични фази. В някои случаи разтворените волфрам и желязо се утаяват, образувайки аморфни гели $WO_3.xFe_2O_3.nH_2O$ – химични аналози на меймацит, обикновено придружени от ярозит, $KFe_3(SO_4)_2(OH)_6$ (pH ~1–3). Взаимодействието на такъв разтвор с меймацит при pH ~3–4 води до частичното или почти пълното разтваряне на меймацита и кристализация на втория химичен аналог на меймацит – желязо-съдържащ хидрокеноелсмореит, $(W,Fe)_2(O,OH)_6.H_2O$, с пирохлоров тип структура. При pH> 4 основните носители на волфрама стават гьотитът α-$FeOOH$ (най-широко разпространен минерал), хематитът α-Fe_2O_3 и аморфните $SiO_2.xAl_2O_3.yFe_2O_3.nH_2O$ гелове. В редки случаи в тези условия се формират супергенен шеелит, $CaWO_4$, и щолцит, $PbWO_4$. На базата на получените данни е предложена обобщена схема за зависимостта на структурния тип на вторичния волфрамов минерал от pH на разтвора в присъствието на железни йони. При нарастване на pH от <1 до 4 настъпва последователна смяна на следните структурни типове: тип ReO_3 (слоеве от ReO_3-тип в структурите на тунгстит и хидротунгстит), тип хексагонален волфрамов бронз (HTB) (HTB-тип слоеве в структурата на $WO_3.1/3H_2O$, меймацит) и тип пирохлор (структура на хидрокеноелсмореит).

Instructions about Preparation of Manuscripts

General remarks: Manuscripts are submitted in English by e-mail. The text must be typed on A4 format paper using Times New Roman font size 11, normal character spacing. The manuscript should not exceed 15 pages (about 3500 words), including photographs, tables, drawings, formulae, *etc*. Authors are requested to use margins of 2 cm on all sides.

Manuscripts should be subdivided into labelled sections, e.g. **Introduction**, **Experimental**, **Results** and **Discussion**, *etc*. **The title page** comprises headline, author's names and affiliations, abstract and key words. Attention is drawn to the following:

a) **The title** of the manuscript should reflect concisely the purpose and findings of the work. Abbreviations, symbols, chemical formulas, references and footnotes should be avoided. If indispensable, abbreviations and formulas should be given in parentheses immediately after the respective full form.

b) **The author**'s first and middle name initials and family name in full should be given, followed by the address (or addresses) of the contributing laboratory (laboratories). **The affiliation** of the author(s) should be listed in detail by numbers (no abbreviations!). The author to whom correspondence and/or inquiries should be sent should be indicated by asterisk (*) with e-mail address.

The abstract should be self-explanatory and intelligible without any references to the text and containing not more than 250 words. It should be followed by key words (not more than six).

References should be numbered sequentially in the order, in which they are cited in the text. The numbers in the text should be enclosed in brackets [2], [5, 6], [9–12], *etc*., set on the text line. References are to be listed in numerical order on a separate sheet. All references are to be given in Latin letters. The names of the authors are given without inversion. Titles of journals must be abbreviated according to Chemical Abstracts and given in italics, the volume is typed in bold, the initial page is given and the year in parentheses. Attention is drawn to the following conventions: a) The names of all authors of a certain publications should be given. The use of "*et al*." in the list of references is not acceptable. b) Only the initials of the first and middle names should be given. In the manuscripts, the reference to author(s) of cited works should be made without giving initials, e.g. "Bush and Smith [7] pioneered...". If the reference carries the names of three or more authors it should be quoted as "Bush *et al*. [7]", if Bush is the first author, or as "Bush and co-workers [7]", if Bush is the senior author.

Footnotes should be reduced to a minimum. Each footnote should be typed double-spaced at the bottom of the page, on which its subject is first mentioned. **Tables** are numbered with Arabic numerals on the left-hand top. Each table should be referred to in the text. Column headings should be as short as possible but they must define units unambiguously. The units are to be separated from the preceding symbols by a comma or brackets. Note: The following format should be used when figures, equations, *etc*. are referred to the text (followed by the respective numbers): Fig., Eqns., Table, Scheme.

Schemes and figures. Each manuscript should contain or be accompanied by the respective illustrative material as well as by the respective figure captions in a separate file (sheet).As far as presentation of units is concerned, SI units are to be used. However, some non-SI units are also acceptable, such as °C, ml, l, *etc*. The author(s) name(s), the title of the manuscript, the number of drawings, photographs, diagrams, *etc*., should be written in black pencil on the back of the illustrative material (hard copies) in accordance with the list enclosed. Avoid using more than 6 (12 for reviews, respectively) figures in the manuscript. Since most of the illustrative materials are to be presented as 8-cm wide pictures, attention should be paid that all axis titles, numerals, legend(s) and texts are legible.

The authors are required to submit the text with a list of three individuals and their e-mail addresses that can be considered by the Editors as potential reviewers. Please, note that the reviewers should be outside the authors' own institution or organization. The Editorial Board of the journal is not obliged to accept these proposals.

The authors are asked to submit **the final text** (after the manuscript has been accepted for publication) in electronic form by e-mail. The main text, list of references, tables and figure captions should be saved in separate files (as *.rtf or *.doc) with clearly identifiable file names. It is essential that the name and version of the word-processing program and the format of the text files is clearly indicated. It is recommended that the pictures are presented in *.tif, *.jpg, *.cdr or *.bmp format.

The equations are written using "Equation Editor" and chemical reaction schemes are written using ISIS Draw or ChemDraw programme.

EXAMPLES FOR PRESENTATION OF REFERENCES

REFERENCES

1. D. S. Newsome, *Catal. Rev.–Sci. Eng.*, **21**, 275 (1980).
2. C.-H. Lin, C.-Y. Hsu, *J. Chem. Soc. Chem. Commun.*, 1479 (1992).
3. R. G. Parr, W. Yang, Density Functional Theory of Atoms and Molecules, Oxford Univ. Press, New York, 1989.
4. V. Ponec, G. C. Bond, Catalysis by Metals and Alloys (Stud. Surf. Sci. Catal., vol. 95), Elsevier, Amsterdam, 1995.
5. G. Kadinov, S. Todorova, A. Palazov, in: New Frontiers in Catalysis (Proc. 10th Int. Congr. Catal., Budapest, (1992), L. Guczi, F. Solymosi, P. Tetenyi (eds.), Akademiai Kiado, Budapest, 1993, Part C, p. 2817.
6. G. L. C. Maire, F. Garin, in: Catalysis. Science and Technology, J. R. Anderson, M. Boudart (eds.), vol. 6, SpringerVerlag, Berlin, 1984, p. 161.
7. D. Pocknell, *GB Patent* 2 207 355 (1949).
8. G. Angelov, PhD Thesis, UCTM, Sofia, 2001, pp. 121–126.
9. JCPDS International Center for Diffraction Data, Power Diffraction File, Swarthmore, PA, 1991.
10. CA 127, 184 762q (1998).
11. P. Hou, H. Wise, *J. Catal.*, in press.
12. M. Sinev, private communication.
13. http://www.chemweb.com/alchem/articles/1051611477211.html.

Texts with references which do not match these requirements will not be considered for publication!!!

CONTENTS

СЪДЪРЖАНИЕ